THE OXIDATION OF LIQUID ALUMINIUM

BY

R. DHOLIWAR

Submitted for the degree of

Doctor of Philosophy

1985

Brunel University,
Department of Metallurgy,
Uxbridge, Middlesex, UB8 3PH.

Ramesh Dholiwar

The Oxidation of Liquid Aluminium

Ph.D. Degree

1983

ABSTRACT

Structures and growth kinetics of oxide films formed on molten aluminium have been studied to provide information in the context of melt losses and melt quality.

Consideration of water vapour potentials at the boundaries of oxide films predicts that in air of normal humidity, a slightly hydrated transitional alumina (η - Al_2O_3) is stable at the oxide/atmosphere interface, and the dehydrated α- Al_2O_3 is stable at the metal/oxide interface. Structures observed in oxide films lifted from the liquid metal are consistent with this concept.

The morphology of α- Al_2O_3 growing at the metal/oxide interface depends on the impurities incorporated within the oxide, and according to circumstances it can appear as degenerate dendritic shapes or plate like structures.

The oxidation kinetics in moist oxygen are characterised by a rapid initial rate during which η - Al_2O_3 plays a dominant but diminishing role, followed by much slower kinetics after the α- Al_2O_3 subfilm is fully established and exercises rate control.

Oxidation kinetics in dry oxygen of samples obtained from high purity aluminium conform to the parabolic growth law after an initial period during which linear kinetics are observed. The kinetics of samples obtained from commercial purity aluminium are much simpler and conform to the parabolic growth law.

CONTENTS

1. INTRODUCTION

Aluminium is available from the electrolytic reduction cells as a liquid at 1173 K (900°C), and as much as possible is cast into ingots. For complex alloying and recovery of secondary metal the economics depend on the melting capacity.

During the melting and holding of aluminium a surface oxide is formed, which must be removed periodically. The 'skim' which is removed from the surface of the metal contains not only the oxide but also adherent metal. A major problem confronting the aluminium industry is the loss of metal incurred by skimming[1].

The problem is not new, (its been recognised for over sixty years) but it has gained added significance due to the escalation in energy costs over the last decade, as shown in Table 1.

Melt losses can be severe, and may even influence the choice of future melting systems as suggested by the results of a cost comparison analysis by Mittmann[2]. The total cost of melting aluminium in an induction furnace is slightly less than melting in a rotary or hearth furnace (Table 2), despite the relatively high cost of electricity, due mainly to the very low melting losses incurred during melting in induction furnaces.

Although the quantity of skim generated is usually taken as a measure of the melt loss, it is common practice to extract the entrapped metal before discarding the residue.

1.1 'Skim' Reclamation Techniques

The composition of the 'skim' tends to vary considerably, Table 3 gives typical values. The quantity of skim generated depends primarily on the nature of the metal being melted as shown in Table 4. It has been estimated[3] that some 200,000 tons of skim are generated annually and its most valuable consistuent is the entrapped metal.

Several techniques[3-7] to recover this metal have been developed. Some 25 years ago rather crude processes were used, in which the skim was ball milled and screened. The coarse material was remelted in a rotary furnace or in a side well furnace with some salt flux. The fines and the salt flux were dumped. Some of these techniques are still used and the plants are noisy, hot and extremely dusty.

Development over the years has in certain cases improved these methods greatly. For example the introduction of low frequency coreless induction furnace for recovery of metal from skim has simplified the process considerably. The skim and a suitable quantity of flux are charged into the induction furnace in which a molten heel of metal is already present. The metal in the skim melts and agglomerates in the heel while the alumina and other non metallic materials float on top of the molten metal. In routine operations it is possible to recover well over 90% of the entrapped metal.

Attempts have also been made to return the skim to the reduction cells in primary smelters. In this way it was hoped to recover, in one step, the metallic content, the oxides and fluorine compounds, Unfortunately, it was found that these additions seriously upset operation of the reduction cells.

1.2 Scope of Present Work

Future strategy to control the melt losses must take into account

a) Consistent use of better skim reclamation techniques

b) Control of surface oxidation during melting and all associated processing

Whereas skim reclamation technology has been developed to a high level of sophistication and efficiency, comparatively little effort has been devoted to minimising the oxidation of the molten metal. The few studies which have been published tend to be rather empirical[8] from which only crude codes of practice can be devised.

Opportunities to reduce oxidation losses can be more clearly perceived if the fundamental processes by which surface oxide films grow on liquid metal in furnace environments are correctly conceived. One of the difficulties of approach is that the problem arises in the melting (foundry) shop, but its resolution lies in the purview of the corrosion scientist.

Although oxidation losses are particularly severe for alloys such as Al/Mg and Al/Li , this study is confined to the oxidation of pure metal, with the aim of laying a foundation for studying the oxidation of more complex alloys.

To understand the oxidation of pure molten aluminium the structure of the oxide films must be related to the kinetics. It is also important to realise that the system is complex which requires consideration of, not only oxygen and aluminium, but also the water vapour in the environments

These matters together with principles of oxidation will be reviewed in the next few sections.

The understanding of the nature of oxide films may also prove useful in alleviating problems due to,

a) Hydrogen absorption[9], since the kinetics of absorption are known to depend on the nature of the oxide film

b) Oxide inclusions which can adversely effect quality of finished products.

The practical effects of these problems have been reviewed by Ferguson[10].

2. PRINCIPLES OF OXIDATION

In this section a number of generalised concepts and theories which may be applied to interpret the phenomena observed in the present work will be considered. Initially the growth mechanisms and theories of compact, continuous oxide films will be described. Such theoretical models are usually developed by making numerous simplifying assumptions for ease of mathematical manipulation so that they are seldom directly applicable to phenomena observed experimentally. Examples of factors which can contribute to deviations from idealised models include impurities in the metal leading to multiphase oxide structures, and cracking or spalling of the film which may result in complex oxidation kinetics.

2.1 Oxygen Adsorption and Oxide Nucleation

When oxygen impinges on a clean metal surface it is adsorbed[11, 12]. The adsorption process is accompanied by the decrease in the entropy of the system[13], due to loss, by the gas molecules, of the translational degrees of freedom. Since the surface free energy is also reduced, adsorption is an exothermic process, by virtue of the definitional relation $G = H - T S$. In considering the adsorption process it is customary to distinguish between physical and chemical adsorption.

In physical adsorption gases are bound to the surface by Van der Waals forces[11], and the process proceeds without significant activation energy so that the rate controlling step is the imping-

ment of the gas molecules on the surface. It is generally accepted that physisorption is restricted to temperatures below the boiling point of the gaseous phase. It is therefore unlikely that physisorption is significant at the temperatures relevant to this study and hence it will not be considered further. However detailed treatments of the subject are available elsewhere[11, 12].

It is most likely that on a clean molten aluminium surface the adsorption is predominantly chemisorption, although it is not always possible to distinguish between the relative proportions of physical and chemisorption. In the chemisorption process the adsorbed species and surface atoms are bonded by electron transfer. Although this is obviously an activated process very rapid chemisorption rates have in fact been demonstrated on clean metal, without a significant activation energy[14, 15].

On an atomistic scale chemisorption is still imperfectly understood, due mainly to the practical difficulties in producing a 'clean' surface. It is considered, however, that initially almost every molecule impinging on the metal adheres to the surface and is adsorbed dissociatively on adjacent metal atoms[16, 17]. Dissociative chemisorption of the oxygen molecules can occur if an oxygen atom adjacent to the adsorbed molecule changes place with the underlying metal atom in a place exchange process as shown in Fig. 1[18]. Reduction of the free energy of the system requires a transition from a chemisorbed layer to a three dimensional oxide and the place exchange marks the beginning of this transition. The

net result of a single exchange of atoms is the formation of an oxide nucleus and multiple nuclei formed in this way coalesce to form one or more oxide layers. The nature of this transition has aroused considerable interest but its progress has hitherto been impeded by experimental problems.

More recently some progress in this field has been stimulated by the development of new techniques such as Low Energy Electron Diffraction[14] (LEED) and Field Ion Microscopy[19]. The usefulness of LEED technique, for example was demonstrated by Jona[20] who detected very thin amorphous layers on aluminium, and May[21] et al who found distinct 'two dimensional' surface crystals on nickel, which by reordering blend gradually into a three dimensional oxide structure Fig. 2[22]. The above discussion gives only a very brief simplistic description of an extremely controversial and complex phenomena. The next stage is to consider the subsequent growth of the established oxide film.

2.2 Defect Structures and Transport Mechanisms in Oxides

The essential feature of all oxide growth theories is that they require the diffusion of reacting species through the oxide film. An analysis of the mechanisms therefore requires some fundamental knowledge or assumptions concerning possible diffusion paths. Transport phenomena can be described in terms of simplified models of the physical character and lattice defect structures of the oxides. In cases where the defects are predominantly of one type the concepts adequately represent observed behaviour. For

oxidation products on aluminium in humid atmospheres the interpretation is much more difficult than for most oxides because of the variety and structural complexities of phases which might be expected, from the phase relationships in the alumina-water system.

2.2.1 Statistical Analysis of Defect Stability

At the absolute zero, atoms or ions occupy all the normal lattice sites, in a crystal, and remain immobile. At higher temperatures, however, atoms in the crystal vibrate around the lattice sites with a mean energy proportional to temperature. Due to random fluctuations in the vibrational energy, single atoms or groups of atoms acquire energy considerably higher than the mean value, the fluctuations of thermal motion leading to the formation of intrinsic atomic point defects e.g. vacancies or interstitial atoms.

Energy expended in the formation of defects at higher temperatures produces an increase in enthalpy. The increase in defect concentration also increases the entropy.

The total entropy is composed of a configuration entropy term S_c and vibration entropy term S_v.

The configurational entropy associated with the possible arrangement of N atoms and n vacancies over a total number of (N + n) lattice sites is

$$S_c = k \log \frac{(N + n)!}{N!\ n!} \qquad (1)$$

where k is the Boltzmann constant.

The Gibbs free energy, induced by the presence of defects is therefore

$$\Delta G = n \times \Delta H_f - n T \Delta S_v - k T \log \frac{(N + n)!}{N!\ n!} \qquad (2)$$

where

ΔH_f is the enthalpy of formation of one defect

ΔS_v is the change in vibrational energy of the crystal due to the presence of one defect.

Fig. 3 shows schematically how each term is dependent on the total number of defects. The equilibrium condition, namely that the free energy of the system is minimum, is satisfied at a definite defect concentration (n_e).

In a solid several types of lattice defects can occur but the pertinent imperfections when considering the transport phenomena through protective oxide films are usually classified as point defects. The system of notation developed by Kroger[23], (given in Appendix I) to describe the point defects will be adopted.

Several excellent texts are available in which various defect structures are described[13, 23, 24]. It is sufficient here to summ-

arise this information as a prelude to a discussion of the more complex defect structure of α - Al_2O_3.

2.2.2 Non-Stoichiometric Oxides

Many oxides exhibit deviation from the stoichiometric compositions, where the electrical neutrality of the crystal is conserved through the formation of complimentary valence or electronic defects, which confer semi-conducting properties. In such oxides the predominant defects are confined either to the oxygen or to the metal lattice. It is usual to categorise oxides further according to whether the conduction takes place by electronic hole migration (p - type) or by the migration of free electrons (n - type).

In n - type oxides the electronic defect is an electron in the conduction band, so that the lattice defects must be species contributing excess positive charge i.e. either an interstitial cation as in ZnO or anion vacancy as in TiO_2 (c.f e.g Shrier[24]).

The electronic defect in a p - type oxide is a "hole" in the conduction band, so that the lattice defect must be contributing excess negative charge to the structure e.g. cation vacancy in NiO.

It is important to remember, as discussed earlier that many types of defects are present in all oxides and the above classification merely refers to the most predominant.

Although, in principle, non-stoichiometry always occurs, deviation from stoichiometry is open to question for a few oxides e.g. α - Al_2O_3.

2.2.3 Stoichiometric Oxides

In an oxide of stoichiometric composition equivalence between metal and oxygen is maintained during the formation of point defects. Although numerous types of atomic defects are possible, in practice the two most common are Schottky and Frenkel disorders, schematically represented in Figs. 4 and 5. Schottky disorder comprises equivalent concentration of anion and cation vacancies whereas Frenkel disorder is limited to either the cation or anion sub lattice.

Frenkel disorder has little application in the present context but a detailed analysis of Schottky disorder is given in Appendix II anticipating its significant contribution to the defect structure of α - Al_2O_3 which emerges from the review given in section 2.2.5.

In the course of this analysis the following results emerge. For low oxygen pressures [e'] and [$V_o^{\bullet}$] decrease whereas [h$^{\bullet}$] and [V'_m] increase with Po_2.

For high oxygen pressure [e'] and [$V^{\bullet}_o$] decrease whereas [h$^{\bullet}$] and [V'_m] increase with Po_2. More significant than these extremes is the intermediate pressure range, in which two alternative limiting

conditions need consideration.

a) If the electronic intrinsic ionization predominates then [e'] and [h°] are independent, whereas [V'_m] increases and [$V^\bullet_o$] de--creases, with oxygen pressure.

b) If however internal disorder (i.e. Schottky) predominates then [V'_m] and [$V^\bullet_o$] are independent, [h°] increases and [e'] decreases with increasing oxygen pressure.

The variations of point and electronic defects as a function of the oxygen pressure, illustrating these two limiting conditions in the intermediate pressure range are given in Fig. 6a and b respectively. Fig. 6a is typical of electronic semi-conductors and Fig. 6b is typical of ionic conductors, although, of course, in principle both types of conduction contribute to the overall conductivity in both cases.

2.2.4 Diffusion

The various defect species introduced in the previous two sections are, of course mobile, and it is their ability to diffuse within the oxide which sustains the growth of a continuous oxide film, and any transformation which occur within it.

This opens up a vast subject which is outside the scope of the present work. Many excellent textbooks are available describing both the mathematics and phenomenology[25-29] of diffusion, but for the present purpose a brief description will suffice.

On a macroscopic scale, provided that a diffusion is singly-activated and comprises non-interacting species of the same kind diffusing in a single phase, its progress is described by Ficks law:

$$\frac{\partial C}{\partial t} = \text{div (D grad C)} \qquad (3)$$

where $\partial C/\partial t$ is rate of concentration change

D is Diffusion coefficient

So that diffusion processes are described by the standard solutions to this equation. Provided that the temperature range is not too wide, diffusion coefficients for a singly-activated process vary with temperature according to an Arrhenius-type relation:

$$D = D_o \exp - \frac{E}{RT} \qquad (4)$$

where E is the activation energy for diffusion and D_o is a constant, normally referred to as the frequency factor. Failure of equations (3) and (4) to represent particular observed behaviour is often evidence that the simplifying assumptions made in their derivation, are not justified and that the process is in fact more complex.

On an atomic scale the diffusion can be analysed statistically as net effect of random atomic motion. In a lattice this atomic motion takes place through the movement of point defects and three simple models are available, reflecting different mechanisms

of diffusion as illustrated schematically in Fig. 7a, b, c and described below.

i) Vacancy mechanism

Diffusion takes place by this mechanism when the atom on a normal site jumps into an adjacent unoccupied site.

ii) Interstitial mechanism

This involves the movement of an atom on an interstitial site to a neighbouring interstitial site. Such a movement may introduce considerable distortion in the lattice, and hence this mechanism is probable only when the interstitial atom is considerably smaller than the atoms on the normal lattice positions. Diffusion of interstitially dissolved atoms (e.g C and H) in metals provide the best known examples of this mechanism.

iii) Interstitialcy mechanism

The interstitial mechanism is improbable, where the distortion cannot be accommodated in the lattice with ease. In such cases the interstitial atom may move by the interstitialcy mechanism in which it displaces its nearest neighbour on a normal lattice site into another interstitial position, itself occupying the original site of the displaced atom.

These mechanisms are based on highly idealised models of solids and for which equations 3 and 4 may be expected to apply since it is usually possible to identify, in principle, a rate controlling step and thereby treat the process as singly-activated to a reasonable approximation. If applied to interpret transport phenomena due to such highly complex defect structure as exists in oxides, these simple theories require considerable modification to take into account the presence of impurities, grain boundaries, dislocations etc. One way in which such complications are manifest is the breakdown of equations 3 and 4. A schematic illustration is given in Fig. 8 where the variation of D with T for an oxide divides into two parts, a high temperature region and a low temperature region, referred to as intrinsic and extrinsic respectively. Different values for E and D_o are required for the two regions reflecting different transport kinetics induced, for example, by the greater influence of foreign species at low temperatures. This effect is of particular importance for α- Al_2O_3 and will be considered in some detail in the following section.

Diffusion through the lattice is supplemented in polycrystalline material by enhanced diffusion along grain boundaries due to the lower activation energy required in the disordered region. Although the contribution to the diffusion path is very small, grain boundary diffusion can predominate when lattice diffusion is slow. Because the activation energy for grain boundary diffusion is lower than for lattice diffusion its contribution to total diffusion increases with decreasing temperature. Grain boundary assisted diffusion is

more characteristic for anion than for the cation, an example is Laurent and Bernard's[30] observations that anion diffusion is greater in polycrystalline sodium and potassium halides than in single crystals, and that it is increased with decreasing grain size in accord with increasing grain boundary area. By contrast, it has been demonstrated on a number of occasions that cation diffusion is independent of grain size for most ionic compounds.

Paladino and Coble[31] have applied the concept of anionic diffusion to polycrystalline α- Al_2O_3 in an attempt to predict diffusion coefficients as a function of grain size from those available for single and some polycrystals. By extrapolation they predicted that the diffusion coefficient for anions should exceed that for cations, (in α- Al_2O_3) for grain size < 20,000 nm.

2.2.5 Defect Structure of α- Al_2O_3

The non-stoichiometry in α- Al_2O_3 is relatively small and has as yet not been measured by analytical techniques presently available. Indeed all work of this kind is hindered by difficulties in producing α - Al_2O_3 single crystal of sufficiently high purity.

It is intructive to review, briefly, some studies which have contributed to the understanding of the transport phenomena in α - Al_2O_3. This will provide a background from which features can be selected to interpret the oxidation phenomena. The experimental

evidence is broadly of two kinds, i.e. of electrical properties and of ionic transport.

a) Electrical Properties

Cohen[32] reviewed the published literature related to the electrical conductivity of $\alpha - Al_2O_3$. Information from several studies was compared and this highlighted the large discrepancies in the results. At lower temperatures the spread in values for the conductivity ranges through six orders of magnitude, and values of the activation energies range from 4×10^{-20} J to 64×10^{-20} J. At high temperatures the divergence is less presumably because the properties are less "structure sensitive" Cohen[32] cites Hartmann's[33] measurements in which he found that the D.C. conductivity of sintered $\alpha - Al_2O_3$ in vacuum increases with time at any prescribed constant temperature. He explained this effect by assuming that $\alpha - Al_2O_3$ dissociated when heated in vacuum losing oxygen and thereby increasing the conductivity by virtue of excess cationic charge. The oxygen is replenished when $\alpha - Al_2O_3$ is reheated in air restoring the original condition. This behaviour is characteristic of a n - type oxide and so Hartmann classified $\alpha - Al_2O_3$ as n - type.

Heldt and Hasse[34] could not accept this interpretation because it was in conflict with their own results. They found in similar

experiments that less pure α - Al_2O_3 exhibited a higher conductivity than pure material, and furthermore the less pure material yielded two different values for the activation energies 38 x 10^{-20} J and 40 x 10^{-20} J according to whether temperature was below or above 1373 K (1100°C). This evidence was taken to imply that there was a transition from extrinsic to intrinsic conductivity at this temperature. In contrast the pure material exhibited only a single activation energy, i.e. 40 x 10^{-20} J implying that conductivity in the pure material was intrinsic throughout the temperature range. For this reason they offered an alternative explanation for Hartmann's results, based on an increase in conductivity due to progressive dissolution of impurities.

Pappis and Kingery's[35] work illustrates the complexity of the defect structure in α - Al_2O_3 and shows that the defect type as well as concentration are sensitive to oxygen pressure. They studied the electrical properties of the material using measurements both of conductivity and of the thermoelectric power in the temperature range 1573 K (1300°C) - 2023 K (1750°C) as functions of oxygen pressure (Po_2). The electrical conductivity results for single crystals exhibit a minimum for $Po_2 \simeq 10^{-5}$ atmospheres as illustrated in Fig. 9 , and can be represented by the relations:

$$\theta = K\, Po_2^{0.20 \pm 0.03} \text{ for } 10^{-3} < {}^{Po_2}/_{1 \text{ atmosphere}} < 1$$

$$\theta = \text{independent of } Po_2 \text{ for } 10^{-7} < {}^{Po_2}/_{1 \text{ atmosphere}} < 10^{-3}$$

$$\theta = K\, Po_2^{-(0.17 \pm 0.03)} \text{ for } 10^{-10} < {}^{po_2}/_{1 \text{ atmosphere}} < 10^{-7}$$

where θ is the conductivity

K is constant

Po_2 is oxygen pressure

The results for polycrystalline material Fig. 10 were similar but the minimum was less marked. From measurements of the thermoelectric power the authors deduce that the oxide is an amphoteric semiconductor, since it behaves as a p - type conductor at Po_2 = 1 atmosphere and as an n - type conductor at Po_2 = 10^{-10} atmospheres.

Harrop and Creamer[36] drew attention to the extrinsic complications especially as introduced by small concentrations of iron ions as impurities. They suggest a similarity between α - Al_2O_3 and MgO which exhibits a similar minimum in the electrical conductivity at $Po_2 = 10^{-5}$ atmospheres and which is profoundly influenced by small concentrations of iron. By analogy they were inclined to interpret Pappis and Kingery's[35] results in the same way i.e that the variation of conductivity with oxygen pressure is controlled by the presence of iron ions. Such a view is not unreasonable because at 1573 K (1300°C) values for conductivities of MgO and α - Al_2O_3 are the same, both for $Po_2 = 10^{-5}$ atms and $Po_2 = 10^{-20}$ atms, which suggests a mechanistic similarity.

Harrop and Creamer's[36] own measurements on high purity single crystal α - Al_2O_3 with less than 2×10^{-5} mol fraction iron produced values for conductivity in the range 1073 K (800°C) - 1773 K (1500°C) sli ghtly less than those given by Pappis and Kingery[35]. They ascribed this difference to impurities possibly present in the material used by Pappis and Kingery.

They also confirmed Pappis and Kingery's findings that the charge carriers are p - type at Po_2 = 1 atmosphere, from their own measurements of thermoelectric power.

Dasgupta and Hart[37] measured the thermoelectric power of α - Al_2O_3 single crystals at various pressures of argon and air in the temperature range 600 K (327°C) - 1100 K (827°C). Their results indicate that the thermoelectric power of α - Al_2O_3 is a function of the air pressure. Peters[38] attempted to determine the electric conductivity and the thermoelectric power of α - Al_2O_3 single crystals as a function of temperature between 673 K (400°C) - 1273 K (1000°C). The variation of thermoelectric power with temperature is shown in Fig. 11, where the positive values for the thermoelectric power indicate that the charge carriers are positive, confirming previous results[37, 39]. The author suggests that the conductivity measurements are typical of an extrinsic-type of conduction process.

b) Ionic Transport

Oishi and Kingery[40] determined the self diffusion of oxy-

gen in single crystal and polycrystalline α- Al_2O_3, as a function of temperature by isotopic exchange between ^{16}O in the sample and ^{18}O in the gas phase at temperatures $\langle$2053 K (1780°C).

Their results for single crystal are given in Fig. 12 which seems to indicate intrinsic and extrinsic modes of oxygen diffusion at high and low temperatures respectively. At high temperatures the intrinsic character reflects either Frenkel or Schottky disorder, but the authors prefer the latter in view of the close packing of α- Al_2O_3 lattice, and the relatively large anionic radius.

For the polycrystalline material the self-diffusion coefficients (Fig. 12) are considerably greater at all temperatures than those observed on single crystal samples, implying that grain boundaries play a significant role in the diffusion process. There is a break in the plot at ~1723 K (1450°C), presumably, due to greater influence of impurities at the lower temperatures. Indeed it was found that prior heat treatment of the samples, which may dissolve impurities, alter grain boundary structure, or cause changes in the stoichiometry, markedly influenced the results.

Paladino and Kingery[41] measured the self-diffusion coefficient of aluminium ions in polycrystalline α - Al_2O_3, in

the temperature range 1943 K (1670°C) - 2178 K (1905°C) using ^{26}Al as a radioactive tracer. The principle of the technique was to allow interdiffusion between a cylindrical disc of α - Al_2O_3 enriched with the active isotope and a similar disc of inactive material placed in intimate contact with it. The active material transferred across the interface was determined by counting. The results given in Fig. 12 show that the aluminium ions are much more mobile than oxygen ions in polycrystalline α - Al_2O_3[40]. The mobility of oxygen ion does, however, approach that of aluminium ion when assisted by grain boundary diffusion as described earlier. The activation energy for aluminium ion diffusion is constant over the whole temperature range from which Paladino and Kingery[41] deduce intrinsic behaviour.

Davies[42] in a critical re-evaluation of available information, based solely on activation energies, considered the possibility that α - Al_2O_3 behaves as a pure ionic conductor, similar in nature to MgO in which the conductivity is controlled by oxygen ion transport. This attempt to assess the nature of conductivity by using observed activation energies as a guide is unreliable because, as Kofstad[43] has remarked, in an oxide with complicated conductivity characteristics the sole use of activation energies is an insufficient basis for evaluating transport mechanisms in detail.

c) Appraisal of Defect Character

The foregoing survey indicates the extremely complex transport phenomena within α - Al_2O_3. Indeed a rather confused picture emerges and as several authors[43] have remarked, it is not possible to form an unequivocal concept of transport through α- Al_2O_3. However, by selecting particular features, the review can be used constructively as a guide to interpret observations made in the present research.

To interpret a diffusion-controlled oxidation process (in cases where the film is compact and adherent) equations must be formulated to describe the formation and mutual interaction of defects. For an oxide in which the deviation from stoichiometry and types of defects which predominate are known, the reaction equations can be formulated with relative ease. For example in copper (I) oxide, which is p - type cation vacant, the excess oxygen is incorporated within the oxide by the formation of vacant cation sites (V'_{cu}) and vacant electron levels ($h^{\cdot}$). The reaction giving non-stoichiometric Cu_2O may then be written as:

$$\tfrac{1}{2}O_2 \rightleftharpoons Cu_2O + 2\,[V'_{cu}] + 2\,[h^{\cdot}] \qquad (5)$$

The equilibrium concentration of defects is given by:

$$K = [V'_{cu}]^2\,[h^{\cdot}]^2\,Po_2^{-\frac{1}{2}} \qquad (6)$$

The defect concentration, therefore, increases with the oxygen pressure. The rules and techniques for formulating such equations are well documented (c.f e.g. Shrier[24]).

For α - Al_2O_3 the formulation of the equations is inevitably speculative because the degree of non-stoichiometry is uncertain, and the predominating defects have not been clearly established. It is clear however, that any non-stoichiometric model is inadequate because of the overwhelming evidence that both anionic and cationic species can migrate. A model based on Schottky disorder, although not established with certainty, overcomes these difficulties and has been proposed by various authors[40-42] in explaining their results and this model will be used. Indeed Davies[42] claims that α - Al_2O_3 is a pure ionic conductor.

On this basis Fig. 6b characterises the defects in pure α - Al_2O_3. The diagram is also in agreement with the experimental observation of Pappis and Kingery[35] i.e. at low Po_2 the oxide is n - type and at high Po_2 it behaves as a p - type conductor.

It is interesting to relate Fig. 6b to the conditions which prevail when α - Al_2O_3 is growing on aluminium. The Po_2 at the metal/oxide interface is exceedingly low, and is equal to the dissociation pressure of α - Al_2O_3, whereas

at the oxide/atmosphere interface the Po_2 is equal to the oxygen pressure in the atmosphere. Fig. 6b then predicts that at the inner interface corresponding to low values of Po_2, anion vacancies predominate, and at the oxide/-atmosphere interface cation vacancies predominate.

From the overwhelming evidence given earlier it is virtually certain that $\alpha - Al_2O_3$ of normal purity behaves wholly extrinsically except at very high temperatures. Values of critical temperatures for the extrinsic/intrinsic transition of $\alpha - Al_2O_3$ of normal or even the highest attainable purity are uncertain, presumably, because small impurity levels that are significant are below the range of available analytical methods. However, the highest value given is 1373 K (1100°C) by Heldt and Hasse[34] based on conductivity measurements. Oishi and Kingery[40] place it as high 1723 K (1450°C) from their measurement of oxygen self diffusion and certainly Peters[38] conductivity measurements imply extrinsic character below 1273 K (1000°C). Hence at temperatures relevant to the present work, < 1023 K, (< 750°C) it is safe to assume that $\alpha - Al_2O_3$ of normal purity behaves extrinsically.

Besides their role in confering extrinsic character, dissolved impurities can have other effects on crystals e.g size difference between impurity and parent atom induces strain, and

there may be differences in the polarization effects between the impurity and native atoms.

2.2.6 Defect Structures in Hydrated Aluminas

It will become apparent that the film formed on molten aluminium exposed to humid atmospheres is duplex consisting of α - Al_2O_3, and a slightly hydrated η - Al_2O_3, of the so-called transitional alumina series.

The defect structure and diffusion through α - Al_2O_3 has been discussed in the foregoing section, but η - Al_2O_3 has not been considered at all, due to the lack of readily available published data. This necessitates speculation and making tentative assumptions based on the results of present work, as will become apparent in the discussion section.

2.3 Coherent Films and Growth Theories

The growth mechanisms of thin (< 10 nm) and thick oxide films will be treated separately for the following discussion, as is customary.

2.3.1 Thin Films and the Cabrera-Mott Theory

It is often found that at low temperatures, where the oxide films on many metals are classified as 'thin', the growth kinetics conform to logarithmic or inverse logarithmic relationship

i.e

$X = K_{log} \log (t + t_o) + A$ Direct logarithmic (7)

$^1/_X = B - K_{II} \log t$ Inverse logarithmic (8)

where X is thickness of the oxide

t is time

A, B and t_o are constants

K_{log} and K_{II} are rate constants.

Logarithmic growth kinetics have been observed for a number of metal/gas systems e.g the oxidation of mild steel in air or oxygen[44, 45] and the reaction of calcium with water vapour[46]. Inverse logarithmic kinetics have been observed during film growth on aluminium[47] in oxygen at 293 K(20°C) and the oxidation of iron[48] in oxygen in the temperature range 273 K (0°C) - 393 K (120°C).

Several models have been proposed to explain the kinetics in the thin film range. However, proof has been extremely difficult to establish by reason of extreme experimental difficulties. The model proposed by Cabrera and Mott[49] and subsequently developed by others[50-55] is perhaps the most fruitful and has gained general acceptance.

Cabrera and Mott[49] introduced the idea that ions and electrons move independently within an existing chemisorbed layer on a metal surface. At low temperatures, the ions cannot diffuse by

thermal activation through the film, so that some alternative activation potential is required. Mott[56] suggested that an electric potential is developed across the film providing the driving force for diffusion of the reacting species. Electrons are assumed to penetrate the thin film by thermionic emission or by the quantum concept of the 'tunnel effect'. Capture of these electrons by adsorbed oxygen atoms would form cations at the metal/oxide interface, and oxygen ions at the oxide/gas interface. The strong electrical field thereby produced across the oxide would provide a potential sufficient to drive ions through the film. It has been estimated that the field strength corresponding to a film thickness of 5 nm is $\simeq 10^9$ Vm^{-1}. An inverse logarithmic relationship can be derived for these conditions.

The model is based on several assumptions e.g. that the defect concentration within the film remains constant, and that the rate is controlled by the transfer of metal ions across the metal/oxide interface. Mott[56] had earlier derived a direct logarithmic rate equation on the assumption that tunnelling of the electrons through the film is rate determining.

Several alternative models have been proposed to explain logarithmic and inverse logarithmic kinetics[54, 57] but they are not relevant to the current discussion.

The Cabrera-Mott theory applies less rigorously as the film thickens because the field strength progessively decreases. As an

example, it is inappropriate for films thicker than $\simeq$ 3nm on aluminium at 300K (27°C). For thicker films, theories of this kind are replaced by those based on diffusion control as described in the following section.

2.3.2 Thick Films and the Parabolic Law

The very early oxidation studies by Tammann[58] and Pilling and Bedworth[59] showed that at high temperatures, providing that the film is continuous and relatively 'thick', oxidation follows a parabolic growth law. The compact scale formed,acts as a barrier to the reacting species, and as it grows the diffusion distance increases so that the overall oxidation rate decreases. Perhaps the most important single contribution to the understanding of high temperature oxidation of metals is Wagner's[60] well known and widely applied theory of high temperature parabolic oxidation.

The theory is based on the concept that the film behaves as an electrolyte, through which electrons and ions migrate independently. The directional diffusion of species through the film requires a concentration gradient across the oxide.

It is assumed that the reactions at the phase boundaries are instantaneous i.e. thermodynamic equilibrium is established between the oxide and gaseous oxygen, and between the metal and oxide at the oxide/atmosphere and metal/oxide interfaces respectively, so

that concentration gradients are established through the oxide. This is illustrated schematically in Figs. 13a and b for scales in which metal and oxygen vacancies predominate respectively. The partial pressure of oxygen at the metal/oxide interface corresponds to the dissociation pressure of the oxide in equilibrium with its metal (Po_2^d) while at the oxide/atmosphere interface it is equal to the oxygen pressure in the gaseous phase (Po_2^g).

Wagner derived an expression for the growth rate in terms of the conductivity of the oxide, transport numbers of the cations, anions and electrons, and the free energy change of the oxidation reaction. Wagner's original derivation is available in several publications[61, 62] but for the present purpose a much simpler approach developed by Jost[61] and Hoar and Price[63] using an electrochemical analogy is given in Appendix III.

The Wagner theory cannot be faulted on its theoretical merit, and providing all of the assumptions are satisfied it must also apply in practice. It is the manner in which the theory is sometimes applied that must be critically considered, since the implicit assumptions are frequently overlooked. It is interesting to consider the limitations imposed by these assumptions.

a) The theory requires not a constant concentration gradient but a constant concentration difference. This implies that a multiphase oxide film may not conform to the Wagner mechanism because the interfacial equilibria are disturbed.

b) Gray[64] in his particularly severe assessment of the practical application discusses the limitations imposed due to the anisotropic nature of an oxide film.

c) It has also been suggested[64] that the mechanism involving ionic mobility, as implied in the Wagner mechanism applies only at temperatures above the oxide Tammann temperature, and therefore the parabolic kinetics observed below this temperature perhaps require some alternative explanation.

d) The principle limitation of the theory is imposed by the assumption that the film is continuous and adherent, and hence the growth characteristics of a discontinuous film must deviate from parabolic kinetics. This aspect is considered in the following Section 2.4.

2.4 Discontinuous Oxide Films

Many oxide/metal systems are characterised by the growth of discontinuous oxide films. Since several unrelated factors collectively contribute in varying degrees to the formation of these films, it is unrealistic to expect that all of the observed phenomena can be interpreted within a single generalised concept. Instead, an alternative strategy is required in which the intervention of the various factors is assessed from empirical oxidation rate laws found for the formation of discontinuous films. Some of the concepts which emerge from this approach have an important bearing on oxide growth theories for molten aluminium developed later in Section 5.

2.4.1 Empirical Growth Laws

a) Oxidation at Linear Rate

When discontinuous or porous oxide films are formed it is often found that the kinetics can be represented by a linear rate law, which may be expressed thus:

$$dx/dt = K_L \qquad (9)$$

where x is thickness

t is time

K_L is rate constant

The phenomena leading to such a law may be interpreted either as periodic failure of the oxide on reaching a critical thickness so that the diffusion path remains effectively constant or as extension of the porosity to the metal/oxide interface so that the rate is controlled by the reactions at this metal/oxide interface.

b) Paralinear Oxidation

In some cases a gradual transition from initial parabolic kinetics to decreased linear kinetics is observed. This is a well recognised phenomenon and is referred to as paralinear rate law [65, 66, 67] which may be observed if the oxide layer consists of a compact inner layer, whose rate is

controlled by diffusion of species through the film and an outer porous layer.

If y and z are thicknesses of inner and outer layers respectively then

$$dy/dt = a/y - b \qquad (10)$$

$$dz/dt = fb \qquad (11)$$

where a and b are constants,

z is mass of oxygen in porous layer

y is mass of oxygen in compact layer

f is ratio of oxygen content per gram atom of metal in outer layer to that in the inner layer.

The overall weight gain is given by summation of (10) and (11) as shown diagrammatically in Fig. 14. The thickness of inner layer tends to a maximum value (y_{max}) so that

$$y_{max} = a/b \qquad (12)$$

and the overall mass gain is then given by

$$dw/dt = fb \qquad (13)$$

c) Breakaway Oxidation Kinetics

In some cases an oxide film growing parabolically may crack and the oxidation rate increases eventually transforming to the linear rate law Fig. 15. It has been suggested[68] that the breakaway kinetics occur if the cracks are more difficult to nucleate than to propagate. This allows the oxide to attain a certain critical thickness, before sufficient stresses are developed to activate crack nucleation.

The oxidation may not exhibit linear kinetics immediately after the breakaway since the whole film does not fail at the same time. In fact several hours can elapse before the linear rate is attained. The oxidation of magnesium[69] at 800 K, (525°C), niobium[70, 71] at 723 K (450°C) and titanium[72], provide examples where breakaway kinetics have been observed.

Caplan and Cohen[73] observed interesting kinetics, during the oxidation of Fe/Cr alloys, which may be considered as a special case of the breakaway phenomena. The oxidation curve, shown in Fig. 16, exhibits a series of parabolas punctuated by breaks which correspond to tne periodic fracturing of the film. Caplan and Cohen[73] proposed the following mechanism to account for their observations. Initially the oxide film grows according to the parabolic law

(branch OA Fig. 16) and consists of a chromium oxide scale with minor amounts of iron oxide. The oxidation rate decreases due to silica accumulating at the metal/oxide interface, forming a barrier to cations diffusing into the scale. The scale isolated from the metal then cracks (region AB Fig. 16) admitting oxygen to the inner interface and the whole cycle is then repeated.

The foregoing description of discontinuous oxides and their kinetics implied that the characteristic feature is the presence of stresses which develop during the film growth. This theme will now be developed by analysing the origins of these stresses and the factors which influence them.

2.4.2 Development of Stress in Oxide Films

It has been recognised for over fifty years that stresses are developed within an oxide growing on a metal surface, which may eventually cause the film to rupture, and thus cease to act as an effective barrier between the reacting species. Stresses within an oxide film often become apparent, when a scale fails in a manner indicative of stress systems acting in the plane of the interfaces. Compressive[74] stresses are often manifest by blistering, and shear cracking, whereas fractures indicate the presence of tensile stresses.

The existence of stresses in a continuous nickel oxide film was demonstrated by Evans[75], in a series of classic experiments. Since then many techniques have been developed, to quantify the stresses, and some of these have been reviewed by Stringer[76].

The origins of stresses within an oxide film have been a subject of some concern and not a little controversy. It is extremely unlikely that one factor can explain all the stresses in every metal/oxide system. Thus the causes of stresses in any oxide are peculiar to that particular system. Perhaps the best approach is to outline the most probable factors, and then to consider their application to stresses in the oxide film formed on molten aluminium.

The earliest theory concerning the origins of growth stresses in oxide films was proposed by Pilling and Bedworth[59] who based their theory on the assumption that oxygen ions are the only species mobile in the scale. They considered the nature of stresses in their classification of various oxide/metal systems according to whether

a) the oxide is physically discontinuous

b) the oxide is physically continuous

This was based on the often quoted Pilling and Bedworth ratio (PBR) which is written

$$PBR = \frac{Wd}{wD} \qquad (14)$$

where

W = molecular weight of oxide

w = formula weight of metal

D = density of oxide

d = density of metal

If this ratio is less than unity, the oxide produced was presumed to be discontinuous, or cellular whereas a compact continuous oxide is produced if the ratio is greater than one. It is, of course, well recognised that Pilling and Bedworth's concept of the oxidation process was inadequate by reason of limitations imposed due to the assumptions. For example, Vermilyea[77] suggests that, an oxide film is expected to be stress-free if the cation is mobile within it, and therefore the Pilling/Bedworth rule is invalid in this case. Even if this were true stresses can still develop in films by alternative mechanisms regardless of cationic conduction. The PBR has also been criticised on the grounds that it fails to predict the magnitude of stresses e.g. quite thick layers of Ta_2O_5 and Nb_2O_5 can grow without fracture, despite the great volume change. This implies much lower stresses than those predicted by the rule, possibly indicating stress relief which is overlooked in the PBR. Stringer[76] has further argued that even if a metal ion is immobile in the oxide lattice it may have sufficient mobility at the interface and so contribute to stress relief.

Several authors[73, 78] have identified changes in composition of either the oxide or the metal as the source of growth stresses. This mechanism obviously applies to the oxidation of alloys. Howes and Richardson[79] for example, consider the gradual development of stresses during the oxidation of Fe/Cr alloys, resulting from compositional changes within the oxide film. The volume changes are developed by the volume change upon the dissolution of one phase as the oxidation progresses.

Changes in composition leading to interfacial stresses must also be considered for pure metals if duplex or multiphase films form.

Another factor worthy of consideration is the contribution to the overall stresses by oxide growth within the oxide layer. Jaenicke[80] suggested that when the stresses exceed a certain value an oxide develops defects, (pores and cracks) which admit oxygen, permitting the formation of oxide within the body of the scale. This theory has been advanced by Rhines and Wolf[81] to explain growth stresses in Ni O (Fig. 17).

Transformations such as recrystallisation within an oxide can also influence the stresses in the film. However the influence of recrystallisation is not clear. On one hand it has been suggested that recrystallisation may promote stresses, but on the other hand Stringer[76] argues that it may relieve stress, particularly if it is induced by growth stresses.

In addition to the factors outlined above stresses in oxide films may also be created by epitaxial constraints. However, these constraints diminish as films thicken. The stresses produced by epitaxial growth are insignificant in the present work, this is due mainly to the nature of the liquid metal surface, where there is only short range order subject to statistical fluctuations owing to the high mobility of atoms in the surface.

In a growing oxide the defect gradient referred to earlier may also contribute to the development of stresses, but it is difficult to assess the magnitude and significance of this effect.

2.5 Oxidation of Pure Aluminium

It is scarcely 50 years since the study of oxidation was placed on any kind of theoretical basis. As with so many other branches of science the initial interpretations were formulated to provide limiting laws with which growth rates can be correlated. For a considerable period the role of structure was not accorded adequate recognition, and in common with other systems, oxidation studies of aluminium have suffered from this oversimplistic approach. Of course in the case of aluminium the situation has been further aggravated due to the required sensitivity of measurements.

It is now recognised that kinetic studies must be linked with structural information. These two aspects will now be considered.

2.5.1 Kinetics of Oxidation

In 1859 Deville[82] first remarked on the apparent slowness of the oxidation reaction, but the first serious quantitative measurements were not made until 1923 when Pilling and Bedworth[59] included aluminium amongst the range of metals in their classic work.

This work was carried out before the development of standard mechanistic theories of oxidation, and using equipment which by todays standards would be considered wholly inadequate, but they were at least able to recognise that over an oxidation period of several hundred hours, at 873 K (600°C) in oxygen (97.4% O_2 and 0.07% H_2O) the oxidation followed a two part growth law, which they referred to as 'quadratic law' and the 'cessation' as illustrated in Fig. 18.

Gulbransen[83] recognised the need for equipment of very high resolution to measure the mass changes expected, in the early stages of oxidation and developed a silica fibre torsion microbalance for the purpose. Gulbransen and Wysong[84] used the microbalance to study oxidation kinetics, principally in the temperature range 673 K (400°C) - 823 K (550°C), for periods of up to 2 hours in oxygen of unspecified dryness and purity. They found that for $T < 748$ K (475°C) the kinetics were parabolic, implying, diffusion control but at higher temperatures the growth approaches linear kinetics following a brief initial parabolic period. Gulbransen[84]

et al could not accept that this deviation from parabolic kinetics was due to any loss of protection afforded by the film on the grounds that the film was too thin to crack, and they were therefore inclined to speculate that the linear kinetics were due to rate control by ion formation rather than diffusion.

Gulbransen and Wysong's[84] work exemplifies the importance of maintaining a constant sample preparation scheme, if work of this nature is to provide reproducible unambiguous results. The marked effect of variation in surface finish and impurity content are well illustrated in Figs. 19 and 20, taken from their results. A further effect of sample condition was manifest in stimulated oxidation, in an isolated experiment at 473 K (200°C), which was attributed to the effect of an unspecified heat treatment referred to as "degassing" at 748 K (475°C) for 20 mins which presumably means heat treatment. This may be a further illustration of the influence of impurities because such a treatment would not only reduce hydrogen content but would also remove volatile impurities from the metal.

Smeltzer[85] extended Gulbransen and Wysong's[84] work to much longer periods of oxidation Fig. 21a i.e. 24 hours and at higher temperatures 873 K (600°C) using a similar technique. He broadly confirmed their general results that the kinetics are parabolic at T < 748 K (475°C) The results of Smeltzer's tests at 823 K (550°C) are interesting. The parabolic plot of these results (Fig. 21b)

consists of a linear section which undergoes a transition to a second linear section of a greater slope and this in turn gives way to a section with a lower slope. Obviously such a treatment yields two values of activation energies for each parabolic component. The values given for thin and thick film regions were 172 KJ/mol and 214 KJ/mol. These values are in the wrong order to comply with Cabrera - Mott equation for thick and thin films and illustrates the limitations of theories based on diffusion control without regard to other factors.

Aylmore[86] et al produced experimental results (Fig 22) which broadly confirm Smeltzer's work i.e. the marked departure from simple parabolic kinetics at high temperatures but they were unable to identify a sequence of parabolas. In their interpretation they recognised the limitations imposed by idealisations implicit in models based exclusively on diffusion control and introduced as an additional factor the influence of structural changes taking place within the film which had been observed by others as discussed in the following section.

The central feature of their interpretation was the rate control exercised by a barrier film produced during a preparatory vacuum anneal. Further oxide produced during the course of oxidation experiment termed "amorphous" oxide was assumed to offer no impediment until it transformed in its turn. In this way Aylmore[86] et al could account for both the linear and subsequent decrease in the rate.

In Dignam's[87] later study direct structural observations were made to interpret features in thermograms which he obtained at temperatures within a range 678 K (405°C) - 873 K (600°C). He first observed crystal nuclei after 10 hours at 727 K (454°C), corresponding with a point of inflection on the thermogram as in Fig. 23. At successively higher temperatures both the detection of crystal nuclei and observations of the inflection were advanced to progressively earlier times. Detailed mathematical analysis of the oxidation kinetics at 727 K (454°C) showed that during the amorphous film growth, the kinetics conformed to the inverse logarithmic law derived by Cabrera - Mott for the growth of thin films. Thus Dignam's[87] contribution was to substantiate Aylmore et al speculation and at the same time to reconcile it with the Cabrera - Mott theories for conditions in which the assumptions are reasonable.

Beck[88] et al also studied the relation between the kinetics and structure of oxide films formed on high purity aluminium, in nominally dry oxygen over a similar temperature range i.e 723 K (450°C) - 848 K (575°C) but for greatly extended periods of time. The overall growth was treated as a summation of two independent and distinct processes, the growth of the overlying "amorphous" film, and the growth of $\gamma - Al_2O_3$ crystals *. The growth

* In the terminology used in the present work this phase will be identified as $\eta - Al_2O_3$. Its detection implies some source of water vapour despite the nominally dry atmosphere.

kinetics of the amorphous films (Fig. 24) complied accurately with the parabolic law in disagreement with Dignam's[87] analysis,

The growth kinetics of γ - Al_2O_3 crystals could accurately be described by applying Evans'[89] equation for expanding circles nucleated instantaneously and distributed randomly. The overall growth was adequately described by summation of the parabolic law and the expanding circle principle.

Cochran and Sleppy[90] took account of the nature of the atmosphere in which oxidation proceeds. They examined the oxidation of high purity aluminium in the temperature range 723 K (450°C) - 913 K (640°C) in oxygen of unspecified dryness, moist air, and water vapour for periods of up to 167 hours.

In all cases the oxidation was initially linear and subsequently decreased to a low rate (e.g. after 66 hrs and 20 mins at 748 K (475°C) and 913 K (640°C) respectively).

The oxidation rate was slightly faster in moist air than in dry oxygen for T > 823 K (550°C) but slightly slower for T < 823 K (550°C). The oxidation kinetics in moist air were identical to that in water vapour implying a passive role, of oxygen and nitrogen if water vapour is present.

2.5.2 Structural Studies of Oxide Films

The principal difficulty in structural studies has been the availability of techniques adequate to provide appropriate information and the problems have been resolved over a long period by a combination of electron optical instrument development and personal ingenuity. Successive advances in structural concepts have followed the introduction of particular techniques, as illustrated in the following review.

a) Early Electron Diffraction Studies

The advent of electron diffraction techniques offered a degree of resolution for use in thin films not accessible to x-ray diffraction, although electron diffraction lacks the accuracy of x-ray diffraction for indexing. The first results were obtained using purpose built electron diffraction equipment not associated with image formation. Although they are quoted frequently, the results obtained with such equipment are ambiguous due partly to the primitive stage of electron diffraction development and partly to inadequate appreciation of all factors which influence oxide structure.

Preston and Bircumshaw[91] and later De Brouckere[92] found by electron diffraction that the films formed on solid and liquid aluminium by heating in air up to 1573 K

(1300°C) were essentially γ - Al_2O_3, but among the diffraction rings observed there were a number which could not be assigned to γ - Al_2O_3. With hindsight, these can be ascribed to the presence of some additional phase e.g. α - Al_2O_3. Certainly more recent studies[93, 94] have confirmed that α - Al_2O_3 is observed on molten aluminium oxidised at high temperatures. De Brouckere's work in particular must be considered with some reservations since it reported the presence of γ - Al_2O_3 on aluminium at 1573 K (1300°C) at which temperature it is unstable with respect to α - Al_2O_3 for all practical water vapour pressures[95].

Harrington and Nelson[96] later examined films formed on aluminium heated up to 160 hours in air at temperatures up to 923 K (650°C). They could not obtain distinct diffraction patterns for films formed at temperatures between 573 K (300°C), and 723 K (450°C), consequently they regarded them as amorphous. The patterns obtained for films formed at temperatures between 573 K (300°C) - 723 K (450°C) were indexed as those for α - Al_2O_3 a result which the authors could not accept because in their view the phase can not be stable at such low temperatures. Such a view implies that temperature is the only variable determining the phase stability, a matter which is taken up later.

The patterns obtained for films formed at temperatures over 823 K (550°C) were so complex that they defied analysis suggesting a multiphase structure. With the advent of modern electron imaging equipment, electron diffraction has acquired a new prominence as an adjunct to the TEM, and in this role the two techniques in concert are very powerful as reviewed in the following section.

b) Correlated Electron Diffraction and TEM Observations Of Detached Oxide Films

The TEM over the past 25 years has proved to be a very effective tool in studying the nature of the thin films formed on aluminium. Its value in this role was demonstrated by Thomas and Roberts[97] who examined the properties of oxide films formed on aluminium foil during heat treatments in various oxidising atmospheres in the temperature range 673 K (400°C) - 873 K (600°C). Atmospheres which are normally regarded as "high vacuum" are in fact oxidising to aluminium at temperatures of normal practical interest. Their basic observations are summarised in Table 5 showing a variation in the oxide morphologies according to the 'quality' of the vacuum in which the prior heat treatments were carried out. It is particularly interesting to note that in very low pressures i.e. 1.3×10^{-8} atmospheres where the partial pressure of oxygen was $\simeq 1.3 \times 10^{-10}$ atmospheres

the film formed contained isolated needles, attributed to growth constraints in the film, whereas at higher pressures contiguous growths were observed. The work does not positively indicate whether these crystals are formed by direct oxidation of the aluminium at its interface with the oxide or, as the authors assume by crystallisation of the 'amorphous' oxide. In fact later work has suggested an alternative view. Both Doherty and Davis[98] and Randall and Bernard[99] conducted experiments on barrier films formed by anodising in non-solvent electrolytes. They used this technique as an expedient to produce thick structureless ('amorphous') films for studying crystallisation induced, subsequently, by thermal oxidation at 873 K (600°C). The number of crystals observed using the TEM were found to be inversely proportional to the initial thickness of the anodic film. Both sets of authors argue that this is evidence for direct formation of crystals by oxygen transport to the metal/oxide interface rather than the 'devitrification' (i.e. crystallisation) of the 'amorphous' film although they differ in their views of the transport mechanism, Doherty and Davis[98] favour diffusion of oxygen from the atmosphere whereas Randall and Bernard[99] prefer to attribute oxygen transport by direct access via cracks formed in the oxide, because there appears to be insufficient driving potential gradient through the film to justify Doherty and Davis's[98] view. In their interpretation, neither of these

authors considered the influence of impurities in imparting conduction to the oxide which is known to be important.

Of course there is the further reservation in their implicit assumption that kinetic information for 'anodic' film is equally applicable to the amorphous film formed thermally at low temperatures.

Doherty and Davis[98] also applied the TEM to observations intended to assess the influence of substrate orientation on the oxide film. Electropolished pure (99.992%) aluminium tricrystals (exhibiting (100), (110), (111) planes) were oxidised for 15 minutes at 773 K (500°C) and 873 K (600°C) in air. Oxide samples were detached for examination by an unusual technique in which excess vacancies quenched into the metal were condensed at the metal/oxide interface to induce decohesion. The films formed at low temperatures were "amorphous" i.e. without resolvable structure but exhibited an apparently orientation-dependent feature. Although the oxide/metal interfaces were all smooth with CLA $< \pm$ 1 nm, the profiles of the oxide/atmosphere interfaces were smooth, grooved and scalloped respectively on the (100), (110) and (111) crystallographic faces of the metal respectively. The authors sought an explanation using Mott's theory[56] of interface rate-control and associated with the orientation-dependence of the activation energy

for transfer of aluminium from the metal to interstitial solution as ions in the oxide. These results have been strongly criticised by Randall and Bernard[99] on the basis of their own experience in applying the same techniques to the study of oxide films formed on polycrystalline 99.98% pure aluminium foil. They found that scalloped faces were produced by electropolishing the metal and moreover that the topographical periodicity of the oxide could be varied by varying the electropolishing technique. For this reason they were inclined to ascribe Doherty and Davis's undulating oxide/atmosphere profiles to electropolishing artefacts introduced during initial sample preparation rather than to a genuine oxidation phenomena. The two opposing interpretations are compared in Fig. 25, and Fig. 26.

With the advent of the high voltage ($\propto 10^6$ V) TEM it has become feasible to observe the oxidation of thin aluminium foil directly "in-situ" in the microscope because the penetrating power of the beam permits observation of the oxide film through the thin substrate and because a gas reaction cell can be accommodated within the larger specimen chamber. Such experiments are possible for aluminium because of the free energy change of the reaction :

$$2\,Al + \tfrac{3}{2}O_2 \rightleftharpoons Al_2O_3 \quad \Delta G^{\ominus} = -1704 - 0.02\,T \log T + 0.36\,T \text{ kJ} \quad \ldots \quad (15)$$

is so high that the oxygen pressure in the microscope may be adjusted to a value for which the instrument will function and yet which is oxidising to the metal.

Scamans and Butler[100] applied the technique to obtain further information on the crystallisation known to occur within the 'amorphous' alumina. At temperatures much below 748 K (475°C) no crystals were observed, but at 748 K (475°C) the growth of $\gamma - Al_2O_3$ crystals could be followed early because nucleation was preceded by an incubation period which the authors ascribed to the time needed for the development of critical oxygen concentration at nucleation sites. At higher temperatures , 793 K (520°C), the incubation period was so short that crystal nucleation was virtually instantaneous. The critical temperature for nucleation, i.e. 748 K (475°C) is in broad agreement with other observations quoted earlier.

Hart and Maurin[101] used direct TEM observations to study the initial stages in the thickening of air formed filmson samples of aluminium foil oxidised in the microscope in temperature and pressure ranges 623 K (350°C) - 813 K (540°C) and 1.3×10^{-7} - 6.5×10^{-10} atmospheres respectively. The oxidation in the microscope occurred by nucleation, growth and coalescence of oxide islands after an incubation period. The distribution of the islands was

temperature and pressure independent and they were formed in one or either of two morphological variations.

a) well defined crystallographic forms

b) dendritic polycrystalline aggregates

The authors offer no comment on the nature of the morphologies observed, but they extracted kinetic information from enlarged electron micrographs marking stages in the growth of island and diminution of the remaining surface. It is questionable whether kinetic information obtained from two-dimensional photomicrographs, can be applied to a three dimensional process such as crystal growth and this perhaps explains why the activation energies obtained are inconsistent with activation energies determined thermogravimetrically.

c) Use of Electrochemical Polarization Techniques

The technique had its origin in work by Hunter and Fowle[102] who developed a simple rapid electrochemical technique for measuring the thickness of anodically formed films on aluminium. It was based on the principle that the electrical potential (EMF) at which a leakage current could be observed, on an anodised sample in a suitable electrolyte, was a measure of the barrier layer thickness, i.e. thickness was 1.4 nm/V. On further reflection Hunter and Fowle[102]

considered that the technique would be equally valid for thermally formed films on the assumption that the structures of the two kinds of films were similar.

Dignam[103] applied this technique to study the nature of the films formed thermally and anodically on normal high purity aluminium, and some of its binary alloys. Leakage current i.e. (polarization curves) were determined for samples previously exposed to dry oxygen (purified by distillation through liquid nitrogen) at 523 K, (250°C), 623 K (350°C), 723 K (450°C).

The polarization curves of normal high purity (99.99%) aluminium oxidised at 723 K (450°C) in dry oxygen are given in Fig. 27. These were interpreted as indicating structural change within the oxide formed after oxidising for 16 hours. No such phenomena was observed for samples oxidised at lower temperatures. In Dignam's[103] view the structural change was related to the nucleation and growth of crystals within the initially formed film. Supporting TEM work confirmed that crystals were indeed present in the sample in which they were suspected. The crystals were orientated with respect to the metal substrate in a manner suggesting epitaxial growth providing further evidence that they nucleated from the 'amorphous' film at the metal/oxide interface.

Dignam's[103] comments on the role of the impurities are of special interest. He was aware that magnesium present as an impurity reduces the temperature at which δ-Al_2O_3 crystals nucleate and grow within the "amorphous" oxide film, and since γ- Al_2O_3 is isomorphous with the spinel $MgAl_2O_4$ he suggested that the role of 0.001% Mg present as an impurity in the metal, could promote nucleation e.g by forming clusters of magnesium atoms in the disorder at the metal/oxide interface, copper and silicon additions had the opposite effect (e.g 0.24% Si added to high purity aluminium suppressed crystallisation as illustrated by the polarization curves given in Fig. 28). Dignam offered an explanation for these effects using an argument based on size factors, relative diffusivities and affinities between solute atoms, asserting that copper and silicon inhibit the nucleation induced by magnesium.

d) Ellipsometry

Badia[104] employed the ellipsometry technique to analyse the amorphous oxide film growth, and crystalline oxide development during thermal oxidation of aluminium.

This technique which is normally used on films which are homogeneous, with smooth interfaces, involves the measurement of phase changes (Δ) between two mutually perpendi-

cular plane polarized light waves and the ratio of their amplitudes (ψ) upon reflection off a surface.

In this study Badia uses the technique to show the changes of an initially smooth interface, due to the formation of crystals beneath the amorphous film.

The method adopted was to calculate the changes in Δ and ψ for the ideal case of smooth interfaces, (the calculations were confirmed experimentally by measurements on an alumina film deposited on polished aluminium) and then to compare these values with the data obtained from aluminium surfaces, oxidised at 793 K (520^{o}C). The two sets of data are shown in Fig. 29.

The deviations, of the measurements on the oxide from the ideal model, were interpreted as the perturbations, of the initially smooth interface, due to the formation of crystals.

During the course of thermal oxidation a 'minimum' occurs in the Δ , ψ plot (marked A, Fig. 29). The experimental points for Δ . ψ obtained after prolonged oxidation lie close to the ideal curve, which suggests that the smooth interface is reproduced presumably due to the coalescence of the crystals.

Although this study demonstrated the applicability of the

technique, clearly the data obtained can only be interpreted with supplementary structural studies. Whether the ellipsometry technique can contribute, in addition to the more commonly used techniques (electron microscopy and thermogravimetry), to understanding of the oxidation process remains doubtful, in its present state of development.

2.6 The Alumina-Water System

From the observations reported in the preceding section it is clear that the structures found in films formed on aluminium in normal atmospheres must be interpreted not within the simple aluminium-oxygen system in which the metal and corundum are the only stable phases, but in a wider context of the ternary aluminium-oxygen-water system. Fortunately the alumina-water system has been very extensively studied because of the technological importance of Bayer process in which aluminium trihydrates are calcined to provide corundum as feedstock for the production of aluminium by electrolytic reduction, and because of commercial applications of alumina products e.g for use as absorbents.

2.6.1 Nomenclature

The first point which requires clarification is the usage of the term "alumina". This term is used rather ambiguously in the literature to denote[105].

i) aluminous material of all types taken collectively

ii) the anhydrous and hydrous aluminium oxides taken indiscriminately

iii) the calcined or substantially water-free aluminium oxides without distinguishing the phases present

iv) corundum or α - Al_2O_3 specifically.

Unfortunately the significance assigned to the term is sometimes hard to determine, from the context in which it is given. More than 25 solid phases of alumina have been described and it is doubtful whether some of these really exist[95, 105]. The phases found in nature and some of the artificially produced types of alumina, have common mineralogical names. Most of these phases are also identified by Greek letters, but due to many systems used by various investigators, there is no general agreement on terminology. The historical development and basis used for various systems of nomenclature have been reviewed by Gitzen[105] and Wefers and Bell[95]. The systems in use are shown in Table 6. The ALCOA system will be used throughout this work; the other systems are given only for comparison.

2.6.2 Classification and Characterisation of Phases

The phases which have been identified in the alumina-water system

can be divided into three main groups:-

i) the hydrous aluminas i.e. the trihydrates, gibbsite, bayerite and norstrandite and the monohydrates boehmite and diaspore

ii) the transition aluminas

iii) the anhydrous high temperature phase corundum (α - Al_2O_3)

This classification has evolved traditionally from the dehydration sequence followed in the calcination of the trihydrates during the preparation of α- Al_2O_3 by the Bayer process. Within this broad classification the particular variants of the general forms have also been characterised according to the methods by which they can be prepared or obtained.

i) The Hydrous Aluminas

The trihydrates gibbsite and bayerite and the monohydrates boehmite and diaspore are all naturally occurring constituents of mineral deposits. Together with the other two members of the group they can also be prepared artificially as described elsewhere[95, 105]. These phases are of interest in the present work only in so far as they can yield information as precursors of the transitional aluminas and of corundum. No further elaboration of their particular nature is necessary.

ii) The Transitional Aluminas

The transitional aluminas comprise a group of phases which fall between the monohydrates and corundum (α - Al_2O_3). They had originally been grouped together and referred to as "gamma" alumina. All of these phases may be produced by thermal transformations and in some cases by hydrothermal transformations, of the aluminium hydroxides and by the oxidation of aluminium. All of these forms are hydrous to some extent and have various uses, particularly as absorbents, catalysts, coatings and soft abrasives.

Stumpf et al[106] have described the x-ray patterns, transition sequences, and temperature ranges of seven transitional aluminas. They found that the sequence of phases is influenced by the water vapour in the atmosphere and by the impurities. Complete surveys on transitional phases have sincebeen made by many investigators[95, 107-109]. Lippens[110] classified the transitional aluminas into two groups; low temperature forms, dehydrated below 873 K (600°C) and containing up to 2% H_2O which includes ρ, χ, η, γ and high temperature forms obtained at 1073-1273K (800 - 1000°C) which are nearly anhydrous and include the phases κ, θ, δ. Some of the possible transition sequences are shown in Fig. 30, but these are not necessarily hard and fast rules. The sequences are

affected not only by the starting materials but also by their crystal size, heating rates and impurities.

η - Al_2O_3 is of particular significance in the present work as will become apparent later but because of the confusion occasioned by its structural similarities to γ - Al_2O_3 and use of different systems of nomenclature it cannot be discussed in isolation.

γ - Al_2O_3, according to Stumpf[106] et al is the phase with a cubic structure obtained by heating bayerite or boehmite at 773 K (500°C). Rooksby[108] determined that γ - Al_2O_3 is a spinel, which probably coincides with the η - Al_2O_3 described by Stumpf[106] γ - Al_2O_3 is distinguished from η - Al_2O_3 by differences in the relative intensity and sharpness of lines produced by x-ray diffraction i.e the line corresponding to 0.46 nm for η - Al_2O_3 and splitting of the line corresponding to 0.197 nm for γ - Al_2O_3. In other respects the patterns are very closely related so that it is difficult to distinguish between them.

Houben and De Boer[111] suggest that the crystal structure of γ - Al_2O_3 is probably due to the presence of about 3.4% water which fills all open spaces in the spinel lattice. Additional water may react with the surface of the oxide until the surface composition can be represented by the

formula Al O OH while the internal structure is the spinel H Al_5O_8.

Maciver, Tobin and Barth[112], differentiated δ - Al_2O_3 from γ - Al_2O_3 by its higher water content. This was thought to be due to molecular water strongly adsorbed on the surface of the δ - Al_2O_3. Yanagida, Yamaguchi and Kubota[113] distinguished between two types of water associated with the transitional aluminas, "non-lattice water" which does not substantially change the d-spacings as determined by heating curves, and "lattice water", which produces changes in lattice dimensions.

iii) Corundum (α - Al_2O_3)

The principle sources of α - Al_2O_3 are native corundum and the manufactured product derived from boehmite. The most common methods for preparing α - Al_2O_3, are calcination of aluminium hydroxides, transitional aluminas and aluminium salts and by solidification from melts[105]. α - Al_2O_3 can be produced with a wide range of properties. Purity, crystal size and orientation depend very much upon the conditions under which the oxide is produced.

According to Stumpf[106] et al, Rooksby[108] and Tertian and Pappee[107], the temperature of formation of α -

Al_2O_3 from the transitional aluminas varies between 1373 K (1100°C) and 1423 K (1150°C). There are however many factors that influence this temperature. These include the starting material, particle size, nature of gases in the calcining atmosphere impurities, and additions that either promote or suppress crystal growth, or affect other properties.

Steinheil[114] prepared a phase he termed "episilon alumina" by oxidising aluminium. Upon heating to melt off the metal, he observed that " γ - Al_2O_3" was obtained. In contact with aluminium the transition to α - Al_2O_3 appears to be lowered to 933 K (660°C). Beghi[115] et al noted that if the metal is dissolved away from the oxide the transition to α - Al_2O_3 occurs at much higher temperatures (> 1173 K (900°C).

In 1887, Le Chatelier[116] made the unexpected observation that there is a sudden heat release at about 1123 K (850°C) during calcination of "alumina" prepared from nitrates and chlorides but not when prepared from sodium aluminate. Heat evolution in the latter case can in fact be induced by small amounts of added fluorides indicating some kind of catalytic activity in nucleating the new phase. This effect has a practical application in the Pechiney process[117] to increase the mineralisation of the alumina and to conserve

fuel by reducing the calcination temperature required to produce non-hygroscopic alumina. Furthermore according to Lindsay[118] there is also an influence on the growth kinetics, increasing the crystal size until a maximum is attained for an aluminium fluoride concentration of 1.4%. Roberts and Jukkola[119] used the Pechiney method of adding volatile fluoride to reduce the conversion temperature to α- Al_2O_3 during fluid calcination of finely divided alumina.

The transitional aluminas can serve as excellent absorbents because of the ease with which they can be rehydrated and subsequently reactivated. However, if the reactivation is taken too far so that the alumina is totally dehydrated, it transforms to α- Al_2O_3 and subsequent rehydration is no longer possible[120].

2.6.3 The Structures of Aluminas

The structures of the aluminas have been reviewed by several authors[95, 105] but for the present purpose it is sufficient to consider only η , δ and α- Al_2O_3.

Many oxides exhibit a mixed type of ionic and covalent bonding in the solid state[121]. Generally the amount of ionic bonding is lowered as the cation size and its co-ordination number, in the

oxide, is decreased. This is illustrated by the estimations of ionic bonding in several oxides (Table 7).

The large proportions of ionic bonding in alumina implies that the structure is close packed since the bonds are not directed.

It may be shown, by simple geometry, that cation co-ordination number in oxides with close packed structure, is related to the ratio of cation to anion radii. Typical values for basic and acidic oxides are shown in Table 7. If the radius ratio is 0.414 it is not possible to place six oxygen ions in contact with one cation. The tetrahedral co-ordination is usually formed when the radius ratio is in the range 0.255-0.414, whilst an eight-fold co-ordination is found for radius ratios greater than 0.732. The radius ratio for aluminium is close to the critical value, and although the cations are usually in six-fold co-ordination, with oxygen anion or hydroxyl groups, and are located in interstices of octahedral anion groups, there are occasions when the cation may be in fourfold co-ordination, as in glass or mullite. All these factors are characteristic of amphoteric oxides.

Both cubic and hexagonal close-packing have been observed in the aluminas. In cubic close packing, the ions of one plane occupy the hollows formed by three ions of the adjacent plane. Every fourth plane of ions in the crystal lattice is repeated in the sequence ABCABC yielding the face centred cubic cell. In the hexagonal

close packing the close packed anionic planes recur at every third plane in the sequence ABAB. In general the octahedra and tetrahedra are distorted by cations. Empty octahedra are larger than those filled by aluminium ions[105].

γ - Al_2O_3 is described as a spinel, having a similar structure to $MgAl_2O_4$. Taking this view, Verwey[122] describes γ - Al_2O_3 as a spinel with 32 oxygen ions and consequently $21\ ^1/3$ aluminium ions. The formula Verwey suggested is

$$Al_8\ [\ Al\ 40/3\ \square\ \ 8/3\ ]\ O_{32} \qquad (16)$$

Aluminium ions and cation vacancies in the square brackets are distributed at octahedral sites.

Stumpf[106] et al suggested that γ - Al_2O_3 produced from bayerite is cubic, Saalfled[123], showed that γ - Al_2O_3 produced from gibbsite has a tetragonal structure. Tertian and Pappee[107] showed that a slow dehydration rate leads to the formation of the more ordered tetragonal form, whereas a fast dehydration may produce the cubic form. According to Glemser and Reick[124] γ - Al_2O_3 has water strongly bound as hydroxyl ions, a view supported by Maciver[112] et al.

The structures of the transitional aluminas have been considered in terms of two alternative models.

De Boer and Houben[125] proposed a model based on estimated densities of various alumina samples, in which they assigned to η - Al_2O_3* the empirical formula 5 Al_2O_3 n H_2O. Their results given in Fig 31 exhibited a sharp discontinuity for n = 1 a composition representing the limiting composition for a 3 : 1 spinel. Rearranging this limiting formula as H Al_5O_8 demonstrates the analogy of the empirical formula with that for ζ - Al_2O_3 spinel, Li Al_5O_8, where Li^+ ion enters octahedral spaces to redress the charge imbalance. Taking this structure as a guide[125] the framework on which the γ - Al_2O_3 is based on is written as

$$Al_8 [Al_{13} 1/3 \ \square_2 2/3] O_{32} \qquad (17)$$

The eight aluminium ions before the brackets represent those which are bound in tetrahedral interstices, and those within brackets occupy octahedral holes. On average 13 1/3 octahedral interstices are occupied by aluminium ions and 2 2/3 are vacant. The limiting composition 5 Al_2O_3 H_2O is written as

$$Al_8 [Al_{12} H_4] O_{32} \qquad (18)$$

representing substitution of aluminium ions in the octahedral interstices by a number of hydrogen ions bearing an equivalent positive charge. The increase in configurational entropy for (18) as compared with (17) is the basis of the stabilization of the spinel

---

* δ - Al_2O_3 in their terminology

structure by other cation species. When hydrogen is the second species it is often convenient to speak of the effect as stabilization by hydration. Equations (17) and (18) are structurally similar and they are of course schematic representations and account neither of inherent structural instability of (17) nor the geometric problem in assigning a bare proton to interstitial site.

The geometric problem posed by the need to accommodate the proton in the hydrogen substituted spinel is solved in the alternative model proposed by Anderson[126] where the hydrogen is accommodated as protonated anions i.e as hydroxyl groups.

Verwey's[127] discussion on the structure of various spinels gives further insight into Anderson[126] model. The spinel $LiFe_5O_8$ can be considered in terms of the unit cell:

$$Fe_8 [Fe_{12} Li_4] O_{32} \qquad (19)$$

where the ions between the brackets occupy octahedral sites. This spinel shows a reversible order-disorder phenomenon with a transition point in the neighbourhood of 1023 K (750°C). Samples heated above the transition temperature and cooled rapidly show the normal spinel structure as determined by x-ray methods indicating a disordered arrangement with only short range order of 12 Fe and 4 Li cations about each octahedral hole. X-ray diffraction patterns of samples annealed at temperatures < 1023 K (750°C)

exhibit a number of extra lines, which Braun[128] explained in terms of a long range order of Fe and Li cations (in the ratio 3 : 1) in the octahedral sites.

This structure also represents both γ - Fe_2O_3 and η - Al_2O_3. Samples of γ - Fe_2O_3 were prepared by Gorter[129] which produced x-ray diffraction patterns similar to that for ordered $LiFe_5O_8$. These samples contained various amounts of water up to the empirical compositions H Fe_5O_8. The scattering power of Li^+ and H^+ for x-rays is negligible compared with that for other ions and in consequence they do not contribute to the patterns so that the structural arrangment is

$$Fe_8 [Fe_{12} H_4] O_{32} \qquad (20)$$

by the DeBoer and Houben model or

$$Fe_8 [Fe_{12} [ ]_4] O_{28} (OH)_4 \qquad (21)$$

by the Anderson model where the protonated anion is adjacent to a cation vacancy.

Similarly, the structural arrangement for η - Al_2O_3 may be represented by either

$$Al_8 [Al_{12} H_4] O_{32} \qquad (22)$$

(DeBoer and Houben) or more realistically

$$Al_8 [Al_{12} [ ]_4] O_{28} (OH)_4 \quad \text{(Anderson)} \qquad (23)$$

When water is taken up beyond the amount required for the spinel structure it is bound to the outer surface of the oxide. The dotted line in Fig. 31 is calculated suggesting that the density of adsorbed water is equal to liquid water. The first mono-layer of these water molecules must be considered to be bound by chemical forces, forming OH^- groups at the surface. Fig. 32 gives the percentage of water after heating at various temperatures, for eight hours in an atmosphere in which the water vapour pressure is 6×10^{-3} atmospheres. There is a sharp discontinuity in the curve at 4% water which represents a point higher than that corresponding to the formula $H\ Al_5O_8$. From these results De Boer and Houben[125] suggested that up to 4% water is taken up by chemical forces in the lattice and on the surface of $\eta - Al_2O_3$. They further suggested that the water in lattice contributes to the normal constituents of lattice, as described previously. Water chemically bound on the surface was typified as forming OH^- group. When still more water is taken up, it is physically adsorbed, initially as single molecules, then as a continuous mono-molecular layer, followed by multimolecular adsorption.

Maciver[112] et al interpreted their results as showing that the entire water content of $\gamma - Al_2O_3$ could be attributed to surface

hydroxyl groups. This view is quite inconsistent with the concensus of other workers and will be disregarded.

The structure of α - Al_2O_3 (corundum) was determined in 1915 by Bragg and Bragg[130] who found it to be rhombohedral using x-ray techniques. This has since been confirmed by other investigators[131]. According to Newnham and Haan[132] the oxygen anions are hexagonally close packed and the cations occupy two-thirds of the octahedral interstices . α - Al_2O_3 crystals usually appear as thin hexagonal plates and less often as triangular plates. Small differences in the mode of crystal growth are observed, mainly concerning the thickness of the plates, the edge faceting, size, and degree of perfection of the crystal. The mode of growth is affected by several factors which include temperature, and presence of fluorides, borates, phosphates, and other mineralisers. A good example of this, is the effect of fluorides upon the thickness of the crystals. Added cryolite produces thin sharp cornered plates, whereas calcium fluorides produced thick rounded crystals[95, 105].

2.6.4 Films Formed on Pure Aluminium in Water

Although at first sight it appears unrelated to the general theme of high temperature oxidation it is useful to include a brief review of published work concerned with the phases formed on pure aluminium in the presence of water. The literature is extensive, but

since only the principle and the nature of phases are of direct interest in the present context it is inappropriate to present an exhaustive review, which would only serve to detract from the main theme. Therefore details of theoretical mechanistic models and the numerical analysis of kinetic data are largely ignored in this discussion.

The compositions of the films formed in water are primarily temperature-dependent and hence it is convenient to consider the information available within loosely defined temperature ranges.

i) Films formed between 293 K (20°C) 0 353 K (80°C)

The results of several studies on the phases formed on aluminium within this loosely defined temperature range have been published[133-135].

Hart[133] reported weight gain and electron diffraction analysis of samples immersed in pure water at temperatures between 293 K (20°C) - 353 K (80°C) for periods up to 20 days. At temperatures below 333 K (60°C) a duplex layer is formed, consisting of trihydrate crystals, bayerite overlying the monohydrate, boehmite. As the temperature of the water was increased the number of bayerite crystals progressively decreased, until at 353 K (80°C) only boehmite was detected, although small crystals of bayerite formed on some specimens after prolonged exposure.

Alwitt[134] et al also studied the growth of hydrated oxide films and obtained SEM micrographs of the duplex films, clearly confirming the presence of bayerite crystals, but their electron diffraction patterns of the inner layer differed from those obtained by Hart, which corresponded to crystalline boehmite. Instead the diffraction pattern was characteristic of a poorly crystalline form of boehmite, which is often referred to as "pseudo-boehmite".

An interesting feature in both of these studies is the observation that the two layers remain quite separate, and even during their growth there was total absence of mutual penetration.

ii) Films formed between 363 K (90°C) - 373 K (100°C)

The films formed by reaction with boiling water have, perhaps, been the most extensively studied of hydrated oxide films on aluminium[136, 137]. This may be because only one phase is present, the films grow rapidly in easily reproducible conditions, and they are of commercial importance in corrosion protection, sealing of porous anodic oxides, and manufacture of dielectric oxide layers.

The films formed within this temperature at 1 atmosphere pressure consists entirely of fairly well crystallised pseudo

boehmite. Bayerite can also be formed, but only at much higher pressures[137] (700 atmospheres).

iii) Films formed between 373 K (100°C) - 647 K (374°C)

It is generally accepted that at 1 atmosphere pressure the films formed within this temperature range almost invariably consists of boehmite[138-141] although diaspore has been observed after prolonged exposure[138]. It is possible to form bayerite at very high pressures (700-2000 atmospheres) at temperatures between 373 K (100°C) and 423 K (150°C), but above 423 K (150°C) only boehmite is observed.

iv) Films formed above 647 K (374°C)

Reaction above the critical temperature of water, results in the formation of γ - Al_2O_3 and α - Al_2O_3[138].

3. EXPERIMENTAL PROCEDURES

The review of previous work on oxidation of solid aluminium at high temperatures highlighted the requirement to utilise both structural and kinetic information to form an adequate concept of the oxide films.

The experimental approach for the present work was programmed in two parts

a) Structural analysis of oxide films

b) Growth kinetics of oxide films

3.1 Structural Studies

3.1.1 Preparation of Melts

During the initial stages oxide samples were obtained from large melts (α 6 Kg) which were prepared by melting in a gas fired furnace and held at constant temperature in an electric furnace.

This technique was inadequate for several reasons, among them the following.

a) The poor temperature control during melting and holding adversely affected reproducibility of the results (e.g compositional changes arising from inconsistent superheating

during melting are particular undesirable since the oxide structures are sensitive to incorporated impurities.

b) Contamination of the metal from the crucible and furnace atmosphere.

c) The oxidising atmosphere could not be controlled with sufficient accuracy.

A smaller melting and holding furnace Fig. 33 was constructed to overcome these difficulties. The advantages of the system are.

a) The metal can be melted and held in a clean environment, and without superheating.

b) The contamination of the metal from crucible is eliminated by using recrystallised alumina crucibles.

c) The oxidising atmosphere can be controlled with greater precision.

d) The temperature can be maintained at 1003 K (730°C) to within $\pm$ 1°C over long periods of time.

3.1.2 Sampling Procedure

0.05 kgs of metal were melted and held at 1003 K (730°C) $\pm$1°C in the electric furnace. The required oxidising atmosphere over the melt was maintained by means of a lance positioned $\simeq$ 0.015 m from the melt surface. Gas 'trains' for various atmospheres are

shown in Fig. 34. Water vapour pressure in the atmosphere was controlled by passing oxygen through a saturator (A) comprising a series of Dreschal bottles (D) filled with distilled water and immersed in a water bath controlled accurately at the dew point appropriate for the prescribed humidity. Similarly, volatile fluoride was introduced into the atmosphere by passing oxygen through a bottle containing hydrofluoric acid.

Prior to sampling the surface of the melt was skimmed clean, using a scraper constructed of alumina, and allowed to oxidise for the prescribed time period. The oxide formed was lifted by withdrawing a copper wire loop through melt surface, so that the oxide and adherent metal formed a continuous film across the loop.

3.1.3 Examination of Oxide Films

The following techniques were selected to study the structure and constituents of the oxide films.

1) Electron Microscopy
   - a) Transmission Electron Microscopy (TEM)
   - b) Scanning Electron Microscopy (SEM)
2) X-ray Photoelectron Spectroscopy (XPS).

3.1.4 Electron Microscopy

It will become apparent later, that the main features of interest in

the oxide films are small crystallites, typically 125 nm, across, which cannot be resolved using light optical microscopy. Electron microscopes on the other hand, are ideally suited to study the structure of oxide films, not only due to the superior resolution but also due to the several additional features capable of yielding information to fully characterise the films.

3.1.5 Transmission Electron Microscopy

The mechanism of image formation in the normal transmission mode of operation in which the image is formed by a combination of the unscattered beam and the scattered electrons, are well documented in several texts[142-144]. Considerably more information may be gained from specimens if other modes of operation are also employed. Electron diffraction and dark field imaging modes are particularly useful for identifying phases within a structure and merit a brief description.

a) Electron Diffraction

A crystalline specimen will diffract the electron beam strongly through certain angles, θ, dependent on electron wavelength and crystal spacing given by Bragg's law.

$$n\lambda = 2\,d\,\sin\theta \qquad (24)$$

where d is lattice spacing, λ is the electron wavelength and n is an integer.

These diffracted electrons are brought to focus in the back focal plane of the objective lens (Fig. 35). In normal magnification mode of operation, the intermediate image formed by the objective lens is the object plane for the first (intermediate) projector lens. If the strength of this projector lens is so weakened that the object plane of this lens becomes the back focal plane of the objective lens, then the diffraction pattern will be imaged by the first projector and enlarged by further projector lenses. Both the image plane and the diffraction pattern contain information about the specimen, and both are always present to be viewed at will by selection of the strength of the intermediate lens.

An aperture inserted in the objective lens image plane can be used to select areas from which diffraction patterns may be obtained. This technique is known as selected area diffraction and is extremely useful for identifying phases within a structure. It is unfortunate[143] however, that the technique cannot be used to define regions much smaller than $\simeq$ 1000 nm diameter.

b) Dark Field Microscopy

A dark field image is produced when the unscattered elect-

rons are removed, so that the image is formed only from the scattered electrons. This image is of much greater contrast than a bright field image, although, of course, the intensity is very much reduced.

The simplest way in which a dark field image can be formed is by displacement of the objective aperture disc so that the aperture in the disc accepts no part of the central unscattered beam. The image is of poor quality, because the aperture is accepting off-axis electrons subject to larger aberrations than those on the object lens axis.

Dark field images of high quality can be obtained by tilting the electron beam at an angle so that the diffracted beam of interest travels down the objective lens axis. The technique is referred to as High Resolution Dark Field Imaging.

A Jeol 120 CX Temscan operated at 100 KV was used in the present work. Under ideal conditions it's resolution is $\simeq$ 1 nm.

c) Sample Preparation for TEM

Operation of the TEM requires preparation of samples through which an electron beam can be transmitted without too great a loss of intensity. The maximum usable sample

thickness depends on the atomic number of the material, and is typically 500 nm or more for specimens composed of light elements, decreasing to less than half this value for materials of higher atomic number.

Oxide samples cut from the copper wire loops cannot be examined in the TEM without first removing the metal adhering to its underside. The following techniques for isolating the oxide from metal were considered.

a) Removal of metal by passing dry HCl gas over the sample. This technique suffers from a number of drawbacks, for example the sample has to be heated to $\simeq$ 200°C, and the removal can take several hours.

b) Dissolution of metal in $HgCl_2$ solution. This technique is inconvenient because mercury deposits may adhere to the oxide leading to complications during microscopical examination.

c) Dissolution of metal in a dry methanol 3% bromine solution. This technique was selected because it dissolved away the metal without reacting with oxide and the time required for dissolution is relatively short $\simeq$ 20 mins.

3.1.6 Scanning Electron Microscopy

The Scanning Electron Microscope (SEM) is particularly effective

for studying topographical details of oxide/atmosphere and oxide/metal interfaces.

Cambridge S.600, Cambridge S.4 and High Resolution SEM (HRSEM) facility on the Jeol 120 CX Temscan were used in the present work. The Cambridge microscopes were used far more extensively than the Jeol Temscan, due mainly to their ease of operation and greater availability.

Details of their principles of operation can be found in reference (145), and for the present a brief description will suffice.

In a Scanning Electron Microscope a finely focussed beam of electrons is rastered on the specimen surface. The raster is synchronised with a cathode ray tube (CRT). Primary and secondary electrons emitted from the specimen are collected, amplified and used as a signal to modulate the brightness of the CRT.

When the image is formed using mainly the secondary electrons the contrast is due to changes, over the specimen surface, in the angle of tilt to the collector and also to the beam. The contrast can be increased by forming the image using primary electrons, but details inside holes and recessive surfaces may be lost. The proportion of primary and secondary electrons entering the detector is controlled by varying the potential of a Faraday cage positioned in front of the collector. The potential can be varied between +250 V and -50 V. At the first extreme most of the electrons are

collected, and as the potential is varied through zero to negative values the low energy secondary electrons are progressively excluded.

In the HRSEM system on the Jeol Temscan, the image is formed using secondary electrons. The image tends to lack contrast and its depth of focus is not as large as the image formed in a conventional SEM. However, the resolution of the HRSEM can be $\simeq$ 1 nm under ideal conditions. The resolution of a conventional SEM is $\simeq$ 10 nm.

The resolution of Scanning Electron Microscopes is limited by the spot size of the incident beam. The smaller the spot size the greater the resolution. In practice, however, a small spot size may not always be appropriate since the signal/noise ratio can become intolerably low.

Other factors which degrade the resolution include beam penetration, and specimen charging. The latter factor can be minimised by coating the specimen with a conductive layer.

a) Sample Preparation for Scanning Electron Microscopy

The oxide samples were lifted from the melt surface using copper wire loops as described previously. Examination of the oxide/metal interface was only possible after removal of the adherent metal, using dry methanol/3% bromine solution

as described previously. The oxide samples were lifted from the solution using TEM copper sample grids and washed carefully in methanol.

The grids were mounted on an aluminium stub especially designed to fit on the specimen stage in the SEM.

For examination of the oxide/atmosphere interface small segments were cut from the copper wire loop samples and mounted on aluminium stubs.

As mentioned in the preceding section the loss of resolution through specimen charging can be minimised by coating the sample with a conductive layer. In general any such coating should

1) be a good secondary electron emitter

2) be continuous

3) not display any structural features of its own at the resolution of the SEM.

For these reasons Au, Au/Pd or Pt coatings are generally used. In the present study, samples to be examined using the conventional SEM were sputter coated with Pt or Au/Pd.

It was found, however, that metallic coatings were unsuitable for examination using the HRSEM, since these coatings displayed their own features which were resolvable using this technique. Thus for

examination using HRSEM the samples were coated with C. which was deposited on the specimen in an evaporation unit.

The conventional SEM and the HRSEM were operated at 20 kV and 100 kV respectively.

3.2 X-ray Photoelectron Spectroscopy (XPS)

It will become apparent in later discussion that the structure and growth kinetics of oxide films formed on liquid aluminium are profoundly influenced by impurities incorporated within the oxide. Attempts to identify the impurities using Energy Dispersive Analysis of X-rays (EDAX) system fitted on Cambridge S-600 SEM proved unsatisfactory since the depth from which x-rays are obtained (e.g. $\simeq$ 1000 nm at $\simeq$ 30 kV accelerating voltage) is greater than the thickness of oxide films being studied.

Clearly the requirement is for a technique which has a greater surface sensitivity and XPS provides an elegant alternative. Although this technique is documented[146], it is relatively new and some comment on its principle of operation is justified.

3.2.1 Electron Spectroscopy

A complete spectrum of electrons obtained when a sample is irradiated with x-rays (e.g. Al Kα) consists of valence electrons, core electrons and secondary electrons (including Auger electrons) (Fig.

36). The total width of the spectrum is ($\bar{h}w$ - ϕ) where $\bar{h}w$ is the exciting energy and ϕ is the work function of specimen.

Core electrons and valence electrons in the spectrum result from primary excitation process, and XPS is primarily concerned with the determination of binding energies of core electrons.

The binding energy of an emitted electron is given by subtracting ($\bar{h}w - \phi$) from the measured kinetic energy. Small variations in the binding energies of core electrons from a particular atom may be observed depending on the chemical environment. This effect is known as chemical shift.

The 'hole' created in the core shell by excitation and emission of a core electron can be filled either by radiative process, giving rise to a characteristic x-ray spectrum or by an Auger process. Electrons emitted by the Auger process, which is the dominant de-excitation mechanism for elements lighter than $Z = 35$ are observable in the XPS spectrum.

The depth from which information is obtained is limited by electron mean free path to $\simeq$ 5 nm.

A Kratos ES 300 Electron Spectrometer was used in the present study. Al Kα and Mg Kα x-rays were used to irradiate the sample.

a) Sample Preparation for XPS

The films from the copper wire loops were backed with aluminium foil to provide rigidity. These foils were then mounted on a platinum or tin wire which was secured on the sample probe by means of a chuck specially designed for holding thin wires[146].

3.3 Colour Changes in Oxide Films

In the course of the work it became apparent that the colour of oxide changes depending on circumstances. When first noticed this effect, although unrelated, appeared to have no significance but as other work progressed it assumed considerable importance and so some special experiments were designed to examine this more closely.

To examine this effect an experiment was conducted in which a series of oxide samples were obtained at hourly intervals from the normal high purity aluminium held at 1003°C (730 K) for a total period of 8 hours. For every sample the surface was skimmed clean and allowed to oxidise for 10 mins before sampling.

3.4 Oxidation Kinetics

To produce results of adequate accuracy the first task is to select

a suitable thermobalance with certain obvious requirements.

a) From reported oxidation thermograms of aluminium at elevated temperatures, the expected mass increase through oxidation may be approximated as 0.15 mg (assuming the surface area is 4 cm^2). Thermobalances with 0.1 mg sensitivity are unsuitable and the requirement is for a balance with sensitivity in microgram range.

b) The balance must have a loading capacity of at least 10 g, which is the combined mass of sample and crucible.

c) The temperature and the oxidising environment must be closely controllable.

3.4.1 Selection and Description of Microbalance

A Sartorius microbalance (model 4410) was selected since it has a sensitivity of 1 µg, loading capacity of 25 g, and a provision to incorporate ancillary apparatus for controlling the temperature and atmosphere.

One of its special features is that the whole weighing system is in a sealed unit which can be evacuated to high vacuum or filled with any desirable atmosphere.

The complete apparatus (Fig. 37) consists of

a) Balance weighing mechanism

b) Ancillary recording apparatus

c) Vacuum system

d) Specimen chamber

e) Furnace

a) Balance Weighing Mechanism

The weighing system functions on the principle of automatic electromagnetic force compensation. The beam is maintained in equilibrium with only a minimal deflection (max. 0.2 mm at the end of the beam) while the compensation current required for this purpose comes automatically and is the measure of the weight to be determined.

The light weight balance beam Fig. 38 of metallized quartz tube ensures excellent mechanical and thermal stability. The beam is supported on a torsion band; frictional resistance is therefore eliminated.

b) Ancillary Apparatus

The ancillary recording apparatus (Fig. 39) comprises a

Digital Voltmeter (DVM) Digital/Analog (D/A) converter and a chart recorder.

The output from the balance is displayed on the DVM. The D/A converter converts measured values into proportional voltages which are fed into the chart recorder.

c) Vacuum System

The simple vacuum system shown in Fig 40, comprises a

1) Mercury and glass diffusion pump

2) Rotary pump

3) Liquid nitrogen trap

4) Pirani gauge, and a manometer.

The system is capable of lowering pressure in the specimen chamber to $\simeq 10^{-7}$ atmospheres.

d) Specimen Chamber

The specimen chamber is constructed of pyrex and silica glass, and can be secured to the microbalance tube with a spring clamp on an 'O' ring ball joint. This facilitates easy dismantling for sample loading etc.

A thermocouple is inserted into the specimen chamber, ≃ 1.5 mm from the sample, by means of a cone and socket arrangement, which is gas sealed with picien wax (Fig. 41). The temperature in the chamber can be maintained to ± 1°C.

Radiation shields (Fig. 41) are mounted on the tube to protect the balance and 'O' ringed joint from the furnace heat. The balance mechanism is further protected by a series of baffles located in reaction chamber.

e) Furnace Assembly (Fig. 37)

The furnace, mounted on linear bearings, can be raised around the specimen chamber and secured in position. The furnace temperature is controllable to ± 1°C.

3.4.2 Sources of Error and Precautions

To make full use of the potential of the balance a number of precautions were observed.

1) The balance was mounted rigidly in a location where it remains unaffected by vibrations from normal laboratory activities.

2) The balance is located in an environment where ambient temperature fluctuations do not affect its sensitivity.

3) The crucible and suspension wires were constructed of inert materials i.e recrystallised alumina and silica respectively.

4) The sensitivity of the balance is adversely affected by static electricity generated on the specimen chamber. These were eliminated by earthing a Nichrome wire wound around the specimen chamber (Fig. 41).

5) The furnace tube was wound with Nichrome wire. Electromagnetic fields generated within the furnace can have an adverse affect on the sensitivity of the balance. This field was negated by winding the furnace non-inductively.

6) The crucibles must be preconditioned to remove adsorbed volatile substances (e.g water) prior to testing. This was accomplished by holding the crucibles at 800^{o}C in vacuum for 8 hours.

7) Thermal convective noise.

There is a further source of error characteristic of the complete system, namely the instability due to interaction of convective currents with balance suspension and crucible.

Preliminary experiments were undertaken to analyse this problem and establish suitable experimental procedures. The following relationships were assessed.

a) Variation of 'noise' with temperature at constant pressure of 1 atm.

b) Variation of 'noise' with pressure, at constant temperature of 1003 K (730°C).

The result of first study (Fig. 42a) shows that the balance is essentially 'noise' free at atmospheric pressure and room temperature. The noise increases as the temperature increases reaching an unacceptably high level (≃ 0.2 mg) at the operating temperature 1003 K (730°C). Repeating the test without the crucible on the suspension wire reduced the noise to very low levels (0.001 mg) confirming the work of Cox[147] et al.

The result of the second study (Fig. 42b) shows that the balance sensitivity (at 730°C) degrades as the pressure in the system increases.

On the basis of these results all tests were carried out in pure oxygen at 0.2 atms. In effect the dilutant gases in the atmosphere, mainly nitrogen, are removed to facilitate the testing. This necessitates the assumption that nitrogen is unreactive in the oxidation process.

Using these precautions the sensitivity of the balance is better than the inherent scatter expected from variations in sample composition and preparation.

3.4.3 Test Procedure

The microbalance was calibrated using the procedures and standard weights supplied by Sartorius Instruments. The calibration of the balance was checked periodically throughout the test period.

The samples were machined in the form of discs to fit snugly into the crucible. Prior to testing, the discs were prepared, by grinding the oxidising surface to a standard 600 grit finish, washing in 5% NaOH to remove surface contaminants, and cleaning ultrasonically in distilled water and methyl alcohol.

The sample was placed in a preconditioned alumina crucible suspended in the specimen chamber. The entire system was evacuated and the preheated furnace raised and secured in position around the specimen chamber. Temperature in the specimen chamber rose to 1003 K (730^{o}C) within 10 mins. A further 20 min. were allowed for melting the specimen before admitting the oxidising atmosphere into the chamber. The time allowed for the specimen to acquire the test temperature was estimated by a preliminary test in which the furnace was lowered momentarily (after various time periods) for a visual inspection of the sample.

For tests in dry atmosphere, oxygen was passed successively through silica gel, and a liquid nitrogen 'trap' before admitting it, very slowly, into the system, until the pressure increased to 0.2 atms. The balance was tared and, immediately, a record of mass increase through oxidation was initiated on the chart recorder. A vacuum flask containing liquid nitrogen placed around the side tube (Fig. 40) ensured that the low water vapour pressure was maintained in the system during the course of the test.

For tests in wet atmosphere, oxygen was passed successively through a series of Dreschal bottles containing water at a temperature for which the saturated vapour pressure is of a prescribed value. In admitting any required atmosphere it is of course essential that the atmosphere must be of the required composition but in addition it is also essential to maintain it at this value during testing. This was achieved by maintaining a droplet of water, in the side tube, at the corresponding temperature. During the melting period, a flask containing liquid nitrogen was placed around the tube to suppress evaporation. Prior to admission of oxygen, the liquid nitrogen was replaced with water for which the saturated water pressure is of a prescribed value. The water vapour pressure was measured using the manometer.

3.4.4 Two Stage Tests

A number of tests were carried out in which a dry oxidation test

was interrupted after a predetermined time and continued in moist environments.

The procedure for the first stage was similar to the tests in dry atmosphere. During this period a flask containing liquid nitrogen was placed around the side tube containing a droplet of water. After a predetermined time the entire system was evacuated using the rotary pump. The liquid nitrogen around the side tube was replaced with water at the temperature for which the saturated water vapour pressure is of the required value, and the system was refilled with moist oxygen for the second stage.

Using this technique it was found possible to change the atmosphere abruptly and hence observe the influence of the moist atmosphere on a film formed initially under dry conditions.

3.5 Materials

Oxide films formed on the following metals were analysed using the techniques described.

1) Normal high purity aluminium (Billet A)

Chemical Analysis (Billet A)

Element	Cu	Fe	Mg	Mn	Si	Ti	Cr	Na	Zn
%	0.001	0.002	0.001	0.001	0.001	<0.001	0.004	0.0006	0.001

2) The normal high purity metal further purified by selective oxidation of impurities. The normal high purity metal was held at (1073) K, 800°C for periods of up to 8 hours. The surface was skimmed every 20 mins.

Chemical Analysis

Billet	Holding time hrs	Cu	Fe	Mg	Mn	Si	Ti	Zn	Cr	Na
B	1	0.001	0.002	0.001	<0.001	0.001	<0.001	<0.001	0.004	0.0005
C	2	0.004	0.002	0.001	<0.001	0.002	<0.001	0.001	0.005	0.0001
D	4	0.002	0.001	0.001	<0.001	0.003	<0.001	0.001	0.002	0.0002
E	8	0.001	0.002	<0.001	<0.001	0.003	<0.001	0.001	<0.001	<0.0001

3) Normal commercial purity aluminium

Chemical Analysis

Element	Cu	Fe	Mg	Mn	Si	Ti	Zn	Cr	Na
%	0.001	0.16	0.001	0.002	0.040	0.001	0.017	<0.001	0.0009

4. RESULTS

4.1 Electron Microscopy

Fig. 44a shows a transmission electron micrograph of an oxide film formed on high purity aluminium at 1003 K (730°C) after 10 mins. in moist oxygen (P_{H_2O} = 0.03 atms.). The associated diffraction pattern is shown in Fig. 44(b).

All the diffraction patterns observed in this study consisted of concentric rings, characteristic of fine grain size material. The normal technique for indexing such a pattern is to use the identity

$$\lambda l = r d \qquad (25)$$

where λ = wavelength

l = camera length

r = ring radius

d = lattice spacing.

Since the value of the camera length is not known to the required precision the patterns were indexed by comparing ratios of ring radii to the ratios of 'd' spacings (Table 8) thereby eliminating 'λl'

i.e. $$r_1/r_2 = d_2/d_1 \qquad (26)$$

where r_1 and r_2 are radii of rings, and d_1 and d_2 are 'd' spacings

corresponding to the rings. Analysis of diffraction pattern (Fig. 44(b)) is given in Table 9 and it indicates that the oxide film (Fig. 44(a)) is duplex in nature, consisting of a slightly hydrated phase $\eta - Al_2O_3$ and dehydrated phase $\alpha - Al_2O_3$.

Fig. 45 shows a scanning electron micrograph of the oxide/metal interface of an oxide film formed in moist oxygen. It clearly reveals that the $\alpha - Al_2O_3$ crystals are stable at the metal/oxide interface and their penetration into the metal are clearly evident from the strong relief. The corresponding scanning electron micrograph of the oxide/atmosphere interface shows no evidence of the $\alpha - Al_2O_3$ crystals, and establishes that $\eta - Al_2O_3$ is stable at this interface (Fig. 46).

The wrinkles evident in the oxide film, shown in Fig. 46, formed during the solidification of metal adhering to the underside of the film, and bear no structural significance. Removal of adherent metal relieves the oxide film of this constraint as demonstrated in transmission electron micrographs (e.g. Fig. 44a) and the scanning electron micrographs of oxide/metal interface (e.g. Fig. 45).

Figs. 47 and 48 are transmission electron micrographs which show the two forms of $\alpha - Al_2O_3$. The coarse crystals are primary α

- Al_2O_3 and the fine crystallites in the background are the secondary α - Al_2O_3. The fine secondary α - Al_2O_3 crystals can be seen in Fig. 48 with greater clarity.

Figs. 49 (a-n) show the morphological variants of the primary α - Al_2O_3 growths.

Figs. 49 (a-d) are micrographs which show examples of the acicular morphology. This morphology will be referred to as Type a.

Figs. 49 (e-h) are micrographs illustrating the globular dendritic morphology of α - Al_2O_3. This morphology will be referred to as Type b.

Figs. 49 (i-l) illustrate degenerate forms of the globular dendrites. The globular dendrites and the degenerate forms are by no means exclusive. Fig. 49 (j) for example shows areas in which both these forms are present.

Fig. 49 (m) is a scanning electron micrograph of oxide/metal interface, illustrating the unassociated crystals of α - Al_2O_3. This is the simplest form of α - Al_2O_3 and will be referred to as Type d. Further example is shown in the transmission electron micrograph Fig. 49 (n).

Fig. 50 is a transmission electron micrograph which shows that

the spikey dendrites (Fig. 49a) are in fact assemblages of platelets each resembling the unassociated crystals shown in Fig. 47.

Fig 55 shows a series of transmission electron micrographs of oxide films formed on samples obtained from normal high purity metal (Billet A) at 1003 K (730°C) when exposed to moist oxygen (P_{H_2O} = 0.03 atms). The micrographs show a development of acicular (Type a) morphology of α - Al_2O_3 as a function of time. The significant feature in this series is the complete coverage of cross-section by α - Al_2O_3 subfilm after 10 mins. oxidation time.

Figs. 56 are transmission electron micrographs of oxide films formed at 1003 K (730°C) in moist oxygen (P_{H_2O} = 0.03 atms on samples obtained from normal high purity metal purified further by selective oxidation (Billet D). The micrographs show a development of unassociated crystals (Type d) of α - Al_2O_3. The significant feature in this series of micrographs is that the complete coverage of cross-section by the α - Al_2O_3 subfilm takes $\simeq$ 30 mins.

Fig. 60 shows a scanning electron micrograph (HRSEM) of the oxide/atmosphere interface of a sample obtained from normal high purity aluminium (Billet A) which had been exposed at 1003 K (730°C) to dry oxygen ($P_{H_2O} < 10^{-8}$ atms). The micrograph reveals outcrops of α - Al_2O_3 which closely resemble the degenerate α - Al_2O_3 dendrites at the oxide/metal interface of

films formed in moist oxygen (Fig. 49g).

Figs. 61 (a-c) show micrographs which illustrate the effect volatile flourides in the atmospheres, on the morphology of the α - Al_2O_3 crystals. There is a dramatic increase in the growth rates of the crystals when fluorides are present in trace quantities. It is particularly interesting to compare the morphology of α - Al_2O_3 in the oxide films, with the morphology of α - Al_2O_3 which has been obtained by calcining gibbsite in the presence of fluorides. The rectangular and disc-like platelets of α - Al_2O_3 in Fig. 61a and Fig. 61c bear a remarkable resemblance to those in Fig. 62b and Fig. 62c respectively.

Figs. 67(a), (b) and (c) are transmission electron micrographs of oxide films formed, in moist oxygen (P_{H_2O} = 0.03 atms) at 1003 K (730°C), on samples obtained from commercial purity metal. The micrographs show a much slower development of α - Al_2O_3 sub-film as compared with the oxide films shown in Figs. 55(a) (b) and (c) and Figs .56(a) (b) and (c).

Fig. 82 gives a scanning electron micograph of the oxide/atmosphere interface of a sample which had previously been tested according to the two-stage test. A film, presumably γ - Al_2O_3, can be seen overlying α - Al_2O_3 crystals formed during oxidation in dry oxygen during the first stage.

4.2 X-ray Photoelectron Spectroscopy

The results obtained using XPS are shown in Figs. 53(a, b) and Fig. 69, where the kinetic and binding energies of the emitted electrons are plotted on the abscissa scale. All the spectra shown were obtained using Al Kα radiation as the excitation source.

The spectra contain peaks corresponding to both Auger electrons and core electrons. Peaks corresponding to core electrons were interpreted by comparing the binding energies (obtained by substracting the experimentally determined kinetic energies from the energy of Al Kα radiation, 2.4×10^{-16} J (1486 eV) with those given in Table 10. The agreement between calculated and tabulated binding energies are within $\pm$ 6.4×10^{-19} J (4 eV).

The peaks corresponding to Auger electrons were initially indentified by comparing the measured kinetic energies to those given in Table 11 and subsequently confirmed by using MgKα (2.3×10^{-16} J (1446 eV)) radiation as the excitation source. This technique for differentiating between Auger and core electrons is made possible because the kinetic energies of electrons emitted by Auger process are independent of the primary excitation source.

A comparison of Fig. 53a with Fig. 53b shows that the levels of Na and, more importantly, Ca incorporated in the oxide formed on purified metal are lower than those incorporated in the oxide formed on normal high purity metal.

Fig.69 shows that Cu and Fe are the main impurities incorporated in the oxide formed on commercial purity metal.

The Sn_{3p} and Sn_{3d} electrons originate from the Sn wire used to support the sample.

4.3 Colour Changes in Oxide Films

The results of the experimental described in Section 3.3 are shown in Fig.52 and Figs.54 (a), (b), (c) and (d).

The macrograph in Fig. 52, shows that the colour of oxide films formed on aluminium at 1003 K (730°C) after 10 mins in moist oxygen (P_{H_2O} = 0.03 atms), becomes progressively lighter as the metal is purified.

Figs.54 (a), (b), (c) and (d) are transmission electron micrographs which show that the colour of oxide films is related to the morphology of α - Al_2O_3. The micrographs reveal a progressive degeneration of α - Al_2O_3 dendrites as the metal is purified.

4.4 Oxidation Kinetics

Results obtained using the microbalance are described in this section.

Mass gains during oxidation were obtained from continuous chart recorder traces, converted to mass gain/unit area and plotted as a function of time. The oxidising surface area was evaluated a 4 cm^2 taking into account the truncated cone shape assumed by the sample when molten.

Mathematical equations describing the curves are given in Appendix. (IV).

Fig. 63a shows the oxidation kinetics of normal high purity aluminium (Billet A) at 1003 K (730°C) in moist oxygen (P_{H_2O} = 0.03 atms). Results of four individual tests are given, and the important feature is that the curves consist of initial rapid kinetics (Stage I) followed by much slower kinetics (Stage II). Curves Aw_1, Aw_2, Aw_3 exhibit these two regions quite distinctly, but the transition to Stage II is complicated in Aw_4 by the inflection at t≃16 mins, and it was unprofitable to analyse this curve further.

The transition to Stage II in curves Aw_1, Aw_2 takes place after t = 10 - 20 mins, but in Aw_3 the transition is delayed to t ≃ 30 mins.

The kinetics in Stage II conform to the parabolic law as shown in Fig. 63 (b) and Fig. 63 (c), where (mass gain/unit area)^2 is proportional to time. The parabolic rate constants determined from these plots are given in Table 12(a).

Plots of log (Δ m) against log t are useful since they can reveal the existence of power laws by the presence of linear portions. Fig. 63 (d) gives a log/log plot of results in Fig. 63 (a), and it demonstrates that during Stage I the mass gain/unit area is not related to time by a power law.

Fig. 65(a) shows the oxidation kinetics of further purified normal high purity aluminium (Billet D) at 1003 K (730^{o}C) in moist oxygen (P_{H_2O} = 0.03 atms). All the curves exhibit Stages I and II, and the transition between stages takes place within t = 20-30 mins.

Fig. 65(b) and Fig. 65(c) demonstrate that the kinetics during Stage II conform to the parabolic law since (mass gain/cm^2)^2 is proportional to time. The parabolic rate constants (K_p) determined from these plots are given in Table 12(b). The scatter in the curve Dw_3 is $\simeq$ 12% greater than in curves Dw_1 and Dw_2; hence the parabolic rate constant for Dw_3 could not be determined.

The log/log plot of the results in Fig. 65(a), given in Fig. 65(d), again illustrates that the kinetics in Stage I do not conform to a power law.

The oxidation kinetics in moist oxygen (P_{H_2O} = 0.03 atms) at 1003 K (730^{o}C) of samples obtained from commercial purity aluminium are given in Fig. 66(a). Curves CPw_1 and CPw_2 exhibit a smooth transition from Stage 1 to Stage II, but the transition to

Stage II in CPw_3 is complicated by an inflection at t $\simeq$ 25 mins, and it was not analysed further. Fig. 66(a) shows that in curves CPw_1 and CPw_2 Stage II is established after t > 30 mins.

Figs.66(b) and (c) show that once Stage II is established the kinetics conform to the parabolic law, and the rate constants obtained from these plots are given in Table 12(c). The log/log plots (Fig. 66(d)) of the results in Fig.66(a) show that the kinetics in Stage I do not conform to a power law.

The parabolic rate constants for curves Aw_1 and Aw_2 could be determined with greater accuracy than for any of the other curves presented so far. The reason for this is the weighing technique used. During Stage I the oxidation rate is rapid and the balance can only be operated using 0.01 mg sensitivity range. The kinetics during Stage II however are much slower and ideally the balance sensitivity should be increased to 0.001 mg range. This was appreciated late in the test program and was only performed on tests yielding curves Aw_1 and Aw_2.

The oxidation kinetics in moist oxygen (P_{H_2O} = 0.03 atms) at 1003 K (730°C) of samples obtained from normal high purity aluminium (Billet A), further purified high purity aluminium (Billet D) and commercial purity aluminium are compared in Fig. 68. The enclosed areas envelope all results obtained for samples from particular billets.

From Fig 68 the following observations can be made:-

(a) The overall mass gains during the oxidation of samples obtained from commercial purity aluminium are greater than those obtained from normal high purity aluminium (Billet A) and further purified aluminium (Billet D), and furthermore the transition to Stage II is delayed.

(b) The overall mass gains during the oxidation of samples obtained from normal high purity (Billet A) are greater than those obtained from further purified aluminium (Billet D) and Stage II is established more rapidly.

Fig.70 and Fig.71 show the effect of water vapour pressure on the oxidation at 1003 K (730^{o}C) of samples obtained from normal high purity aluminium (Billet A) and commercial purity aluminium respectively.

In both cases the overall oxidation increases as the water vapour pressure in the oxidising atmosphere is increased.

Fig.72(a) shows the oxidation kinetics at 1003 K (730^{o}C) of samples obtained from normal high purity aluminium (Billet A) in dry oxygen (P_{H_2O} < 10^{-8} atms). Results of four individual samples are given.

The general log/log plot of the curves in Fig. 72(a) given in Fig.

72(b), show that the curves Ad_1, Ad_3 and Ad_4 exhibit two portions, which as plotted suggest the indices 'n' in the relationship

$$m^n \propto t \qquad (27)$$

are 1 and 4.3. However, when the (mass gain/cm^2)^2 are plotted as a function of time the index 4.3 is shown to be false and is infact 2 (Fig.72(c)). Thus (with the exception of Ad_2) all the curves are composed of linear kinetics, which can extend to t = 20 mins (Ad_4) followed by parabolic kinetics. In curve Ad_2 the kinetics preceding the parabolic portion do not conform to a linear rate law and since this in an anomaly, further analysis serves no useful purpose.

The rate constants for linear and parabolic regions were determined from Fig.72(a) and Fig.72(c) respectively and are given in Table 13a.

The parabolic plots of curves in Fig.72(a) given in Fig.72(d) show that when the straight lines from parabolic portions are extrapolated they intersect at a common origin i.e. t = - 45 mins.

Fig. 73(a) shows the oxidation kinetics at 1003 K (730°C) in dry oxygen ($P_{H_2O} < 10^{-8}$ atms) of samples obtained from further purified high purity aluminium (Billet B). The log/log plots of curves in Fig.73(a) are given in Fig.73(b) and they show that the curves consist of two portions. From the linearity of the plots in

Fig. 73(a) and the unit slope of plots in Fig .73(b) it is apparent that kinetics in the early stages (t < 10 mins) are linear. Fig. 73(a) yield the rate constants given in Table 13(b).

Fig .73(c) which gives the parabolic plot of curves in Fig. 73(a), suggests that the kinetics in the second portion conform to the parabolic rate law. The rate constants for the parabolic portions were determined from Fig .73(c) and are given in Table 13b.

Fig.74(a) shows the oxidation kinetics at 1003 K (730°C) in dry oxygen ($P_{H_2O} < 10^{-8}$ atms) of samples obtained from further purified high purity aluminium (Billet C).

The log/log plots of curves in Fig.74(a) given in Fig.74(b) consist of two portions of different slopes. From Figs.74(a) and Fig.74(b) it can be seen that kinetics during the early stages (t < 10 mins) conform to the linear rate law, and the linear rate constants determined from Fig.74(a) are given in Table 13(c).

Fig. 74(c) gives the parabolic plots of the results in Fig. 74(a). Although the experimental scatter for such small mass gains preclude accurate analysis of the kinetics, Fig. 74(c) indicates that the linear kinetics during early stages of oxidation are followed by parabolic kinetics. Approximate values for the parabolic rate constants, determined from Fig .74(c) are given in Table 13(c).

Fig.75(a) shows the oxidation kinetics at 1003 K (730°C) in 'dry' oxygen ($P_{H_2O} < 10^{-8}$ atms) of samples obtained from further purified high purity aluminium (Billet D). The overall mass gains of Dd_3 and Dd_4 are greater than Dd_1 and Dd_2, which is due to the faster kinetics during the early stages of oxidation, since, beyond 20 mins. the rates of all samples appear to be similar.

Fig.75(b) gives parabolic plots of curves in Fig.75(a) and it shows that Dd_1 and Dd_2 conform to parabolic kinetics after $t \simeq 20$ mins and $t \simeq 10$ mins respectively. The parabolic rate constants determined from Fig.75(b) are given in Table 13(d). The experimental scatter in Fig.75(b) for curves Dd_3 and Dd_4 is so great that it precludes accurate determination of parabolic rate constants.

The data for the stage preceding the parabolic kinetics are inadequate to define the kinetics. However, in view of the foregoing analysis of oxidation in dry oxygen of samples obtained from Billets A, B and C it seems reasonable to assume that oxidation kinetics during the early stages conform to a linear law.

Fig. 76 compares the oxidation kinetic in dry oxygen at 1003 K (730°C) of samples obtained from normal high purity aluminium (Billet A) and further purified normal high purity aluminium (Billets B, C and D). The comparison shows that the overall final mass gains decrease as the metal is purified.

Fig. 77(a) gives the oxidation kinetics at 1003 K (730°C) in dry oxygen ($P_{H_2O} < 10^{-8}$ atms) of samples obtained from commercial purity aluminium. It shows that although the balance sensitivity was sufficient to follow the early stages of oxidation i.e. for t < 25 mins. further mass gains were so exceedingly small that they were beyond the resolution of the equipment and hence the rate laws governing the latter stages cannot be assessed.

The log/log plots and parabolic plots of curves in Fig. 77(a) are given in Fig. 77(b) and Fig. 77(c) respectively. These plots indicate that during the early stages i.e. t < 15 mins, the kinetics are parabolic, but beyond this the experimental scatter precludes accurate assessment of the data. The parabolic rate constants estimated from Fig. 77(c) are given in Table 13e.

4.5 Two-Stage Tests

The results of the two stage tests are shown in Figs. 79-81.

Fig. 79 and Fig. 80 show the oxidation of samples obtained from normal high purity aluminium and commercial purity aluminium. The water vapour pressure in the environment during the second stage was 0.03 atms.

Fig. 81 shows the oxidation of samples obtained from commercial purity aluminium. The water vapour pressure in the environment

during the second stage was 0.012 atms.

All the tests were carried out at 1003 K (730°C) and the significant features in the results are the abrupt increases in the oxidation rate when the dry oxygen is substituted with moist oxygen.

5. DISCUSSION

The investigation has yielded valuable information on several aspects of the structure, chemical composition and growth kinetics of oxide films formed on liquid aluminium. In evaluating the significance of this information the first requirement is to collate it so that it may be applied to develop a model of the overall oxidation process which explains numerous new observations apparently not reported earlier.

5.1 Thermodynamic Considerations

It is convenient to begin with a thermodynamic treatment of the Al/H_2O system to predict phase relationships as a guide in evaluating the oxide growth kinetics. Of the known oxides and hydrated oxides which exist in the system those which actually form in the film are determined not only by temperature as implied in Fig. 30 but also on the water vapour pressure present in the system. These two factors are taken into account in Fig. 43 where the free energies for the reactions of the type:

$$\text{Less hydrated phase} + H_2O \rightleftharpoons \text{More hydrated phase}$$

are plotted as function of temperature i.e the diagram is plotted on the same principles as those for the familiar oxygen potential diagram devised by Ellingham.

The location of lines at the water vapour pressures approaching atmospheric pressure are known with some certainty because the transition temperatures for the dehydration of hydrates have received special attention in view of their industrial importance in Bayer process [95, 105]. The lines for the various reactions considered are drawn straight and with positive slopes (≃ 190 J/deg mol H_2O) [148] assuming that the contribution of water vapour to overall entropy change is very large in relation to the entropy difference between the condensed phases. The diagram is thus divided into domains of stability for the species considered in terms of temperature and water vapour potentials.

The general form of the diagram can be checked against earlier experimental observations before applying it to present work. For example it shows that the phases expected on aluminium at low temperatures (< 373 K (100°C)) are the monohydrate and trihydrate, in agreement with observations reported elsewhere [133, 135]. At slightly higher temperatures (423°K (150°C)) the monohydrate, boehmite is predicted, as is also observed.

Further lines have been added to indicate water vapour pressures in the oxidising environments used in present work (i.e. 0.03 atms and 0.012 atms) and the water vapour pressure in equilibrium with pure aluminium using values of Gibbs free energy change given by

$$G^{\ominus} = -958650 - 72.2\ T \log T + 415\ T\ J/mol$$

for the reaction

$$2\,Al + 3\,H_2O \rightleftharpoons Al_2O_3 + 3\,H_2 \qquad (28)$$

Consider now an oxide film separating a liquid aluminium surface and an atmosphere containing oxygen and water vapour as reacting species. Provided that the film is sufficiently thick (> 10.0 nm) the Wagner assumption is justified i.e. local equilibrium is maintained at the bounding interfaces. This assumption is particularly appropriate for the present system, because the oxide is suspended between two fluids so that diffusion effects in the bounding phases can be ignored. Application of the water vapour potential diagram to this system at 1003 K (730°C) predicts that $\eta - Al_2O_3$ is stable at the oxide/atmosphere interface, if the water vapour pressure is greater than α 6.5 x 10^{-6} atms and $\alpha - Al_2O_3$ is stable at the oxide/metal interface.

These principles may now be compared with the experimental observations.

Fig. 44a is a transmission electron micrograph of the oxide film formed on molten aluminium after 10 mins in moist environment , which shows that the film is duplex in nature as predicted, the dark crystals appearing superimposed within an apparently structureless matrix. The analysis of the associated electron diffraction pattern Fig.44b, Table 9, shows that the crystals are $\alpha - Al_2O_3$, and the matrix as $\eta - Al_2O_3$. These observations therefore validate the thermodynamic approach.

It is, however, not possible using Fig. 44 to locate the α - Al_2O_3 crystals with respect to the outer and inner interfaces of the oxide film. The Scanning Electron Microscope perhaps provides the most convenient technique for this purpose. This is most effectively illustrated in Figs. 45 and 46 showing the metal/oxide and oxide/atmosphere interfaces respectively. These micrographs conclusively establish that α - Al_2O_3 is stable at the inner interface, and the featureless γ - Al_2O_3 (within the resolution of the technique) is stable at the outer interface, which is consistent with the water vapour potential concept.

Having established the nature of the oxide, and the relative localities of the phases, the next matter concerns the possible growth mechanisms which may be involved. The oxidation process in the very early stages is envisaged as follows. Initially γ - Al_2O_3 is formed, which is followed by nucleation and growth of α - Al_2O_3 at the inner interface.

This approach will be elaborated in developing latter arguments but in its fundamental form it is sufficient to initiate a discussion on the nucleation and growth of α - Al_2O_3, at the metal/oxide interface of a growing oxide film.

5.2 Nucleation and Growth Mechanisms of α - Al_2O_3

The structures observed in films formed on liquid aluminium sugg-

est that at least two independent mechanisms contribute to the formation of α - Al_2O_3 yielding characteristic morphologies which may be distinguished by the terms,

a) Primary α - Al_2O_3

b) Secondary α - Al_2O_3

The use of these terms can be justified subsequently. The two forms can be compared in Fig 47 which illustrates typical coarse agglomerates of primary α - Al_2O_3 together with dispersed fine particles of secondary α - Al_2O_3. The secondary form is revealed with greater clarity in the dark field micrograph Fig.48.

5.2.1 Mechanisms of Primary α - Al_2O_3 Formation

The micrograph of the oxide/metal interface given in Fig.45 show that the primary α - Al_2O_3 crystals protrude into the liquid metal providing evidence that they nucleate and grow at the metal/oxide interface, implying direct reaction between oxygen and aluminium. This process requires transport of oxygen (anions) through the overlying initially formed γ - Al_2O_3 layer. Unfortunately, as intimated in the earlier discussion on oxide defect structures, little information is available for use in assessing the extent of anionic mobility in γ - Al_2O_3. We may be guided to some degree by earlier work on defect structure of thin oxide films on solid aluminium.

In the discussion on the isothermal oxidation of solid aluminium films formed during the very early stages (< 5 nm) were described as a poorly crystalline δ - Al_2O_3. The oxidation product is probably identical with γ - Al_2O_3 now observed on molten aluminium using an alternative system of nomenclature. Several attempts have been made[149-151] to assess the defect structure of these thin films on aluminium. It is in fact commonly accepted that the atomic structure of very thin oxide films (< 5 nm) differs from that of substantially thicker films[149] especially in respect of the metal to oxygen ion ratio, which is abnormally high, and presumably such an effect will apply also to the inner regions of a more substantial oxide film in the vicinity of the metal surface, where it is perturbed by the electric field from the metal.

The nature of the metal excess near the interface in thin aluminium oxide films has never been clarified. For example Gurnberg and Wright[150] suggest that the most probable configuration is an F'-centre structure, where there is a deficiency of oxygen ions with two electrons trapped in the vicinity of each oxygen ion vacancy. They reject the idea that aluminium ions occupy interstitial sites with electrical neutrality preserved by similarly trapped electrons. Another possibility is that the excess aluminium ions occupy otherwise vacant cation sites, electrical neutrality being maintained by the provision of three electrons trapped in the vicinity of each excess aluminium ion. This model is favoured by Pryor[149].

The foregoing discussion suggests that a gradient exists within the γ - Al_2O_3, providing the driving force for the anionic transport. This gradient would probably be small, since the defects are restricted to a region in close proximity to the metal/oxide interface. This implies that the anionic diffusion through pure γ - Al_2O_3 formed on aluminium is relatively slow, thereby exerting a strong influence on the nucleation, growth and physical form of primary α - Al_2O_3.

This line of reasoning can be extended to account for the observed morphological variations of α - Al_2O_3 growths and their dependence on the diffusion rate of anions through the γ - Al_2O_3 as discussed in the following section.

5.2.2 Description of Primary α - Al_2O_3 Morphologies

The morphologies of the primary α - Al_2O_3 vary considerably Fig. 49 (a-n) serve both to illustrate a selection of the variants observed and to define a convenient terminology to classify them as an aid for discussion.

Type (a)	Acicular dendrites	(Fig.49 a-d)
Type (b)	Globular dentrites	(Fig.49 e-h)
Type (c)	Degenerate globular dendrites	(Fig.49 i -l)
Type (d)	Unassociated crystals	(Fig.49 m-n)

The globular dendrites (Type (b)) and the degenerate globular dendrites (Type (c)) are not mutually exclusive. Fig. 49(j) shows a field in which both types occur in the same oxide film. No further detail can be resolved in either of these forms even at magnifications of $\simeq$ 100 KX. In contrast although the acicular dendrites appear at first sight to be simple crystals which radiate from a central spine, it is possible to resolve them at higher magnifications (Fig. 50), into assemblages of platelets orientated in a dendritic morphology. In this respect they resemble similar growths in other systems e.g Cd I[152]. It is interesting to note that the forms of individual platelets are identical to those of unassociated crystals (Type (d)) i.e triangular and rectangular platelets, and rhombohedral forms, Fig. 47, which are all characteristic of the forms observed for α - Al_2O_3 in bulk calcined alumina hydrates[95, 105].

5.2.3 Factors Controlling Morphologies of Primary α - Al_2O_3

Very little of the available information on the oxidation of aluminium is of value in developing this theme. The striking differences in α - Al_2O_3 morphologies which now require explanation have not been reported in earlier studies of oxide films formed on aluminium. There are however other circumstances in which similar morphological differences have in fact been observed. In this respect it is particularly interesting to consider the morphologies of alumina inclusions in steel during deoxidation with

aluminium and theoretical approaches to explain them. In common with the present work, it is found that the morphology of α- Al_2O_3 inclusions can vary considerably as shown in Fig.51.

Several authors[153-157] have considered factors, which influence the morphologies of the α- Al_2O_3 inclusions formed in molten steel. From early observations it was first assumed that alumina inclusions in steel were frequently rounded. To account for this it was suggested[153] that they were formed in an initially fluid or viscous state because the temperature was locally increased due to enthalpy of formation of alumina. The theory was subsequently invalidated by Waudby and Salter's[154] calculation showing that the heat released is insufficient to cause incipient melting. In their own observations Waudby and Salter[154] found that the constitution of alumina-based inclusions in steel depended on the elapsed time following deoxidation and on the quantity of aluminium added. Ooi[155] et al observed that alumina clusters changed their morphology if the melt was stirred; in quiescent melts well defined dendritic inclusions were formed whereas in a stirred bath the inclusions were formed as spherical particles. Work of this kind demonstrates that the rounding of particles requires explanation based on the kinetics of their formation rather than subsequent events. Steinmetz[156] related the morphological variations of the inclusions to the initial oxygen content of the melt. For low values the inclusions formed were globular, for high values dendritic growths were observed, and in

the intermediate range the inclusions developed a coral-like morphology. On the basis of these observations he deduced that the alumina clusters or corals grow independently, and are not formed by the agglomeration and sintering of amputated dendrite arms. The coral like morphology should therefore be considered as special forms of columnar and dendritic growths. Robinson[157] et al also found that for high oxygen and high aluminium contents the inclusions were very branched and dendritic (Fig. 51(a)). For lower oxygen contents the dendritic growth of alumina was more degenerate, the dendritic arms tending to spherodise (Fig. 51(b)). At very low oxygen contents the growth became almost spheroidal (Fig. 51(c)).

From the foregoing brief review it is evident that the mechanisms of inclusion formation in steel during deoxidation have not been fully explored but experimental observations certainly indicate that morphology of inclusions is profoundly influenced by the initial oxygen content of the melt. It is very significant that Robinson[157] et al could vary the inclusion morphology from acicular, dendritic structures to degenerate forms by controlling the oxygen content. Their micrographs (Fig. 51 (a)-(c)) have been arranged as a series to emphasize this progressive controlled structure degeneration.

If the concept developed above for the formation of α- Al_2O_3 in steel is applied to the growth of α- Al_2O_3 underlying the γ -

Al_2O_3 on molten aluminium, the variation in morphology is expected to correlate with the local value of oxygen potential. This potential is controlled by the supply of oxygen through the η - Al_2O_3 layer so that it is logical to seek an explanation for differences in α - Al_2O_3 morphology in terms of differences in oxygen diffusivity in η - Al_2O_3 induced by the operation of some variable extrinsic factor.

In Section 2.2.5, a discussion on the relationship between intrinsic/extrinsic diffusion and temperature led to the conclusion that at temperatures relevant to the present study the diffusion mechanism is likely to be predominantly extrinsic. Let us now examine the possible role of impurities on the oxygen diffusion through η - Al_2O_3 and hence on the morphology of α - Al_2O_3. In accordance with Hauffe's valency rules for the preservation of electroneutrality it is expected that the substitution of aluminium cations within the η - Al_2O_3 lattice by a divalent or monovalent cation leads to an increase in the number of oxygen ion vacancies, thereby increasing the rate of oxygen diffusion. Application of surface analysis techniques described in Section 3.2 provided information on the type of the incorporated impurities. The results of the simple experiment given in Fig. 52, indicate on a qualitative basis a relationship between the impurities and α - Al_2O_3 morphology. The colour of the sample becomes progressively lighter as the holding time increases. This effect is probably due to the scattering of light, which is related to structure of the metal/oxide

interface and also, possibly to total thickness of oxide, since reflection from metal/oxide interface becomes progressively weaker as the oxide thickens, as Evans[158] suggested.

The effect of increased holding time and periodic skimming is to reduce progressively the quantity of impurities entering the oxide. Fig. 53 illustrates XPS studies which verify this point. Comparison of the traces shows that the calcium and sodium level in the initially formed oxide are considerably higher than in the oxide obtained after four hours holding time. It is therefore most probable that the calcium and/or sodium incorporated within $\eta - Al_2O_3$ is responsible for the increased oxygen diffusion. Progressive degeneration of well defined acicular dendrites is evident in the transmission electron micrographs given in Fig. 54. These observations establish a link between the levels of incorporated calcium and/or sodium $\eta - Al_2O_3$ and variations in the morphologies of $\alpha - Al_2O_3$.

The next aspect to consider concerns the kinetics of $\alpha - Al_2O_3$ growths. The series of micrographs Figs. 55 and 56 shows a progressive development of the two extreme morphologies from which it is clear that the acicular well defined dendritic morphology grows far more rapidly than the globular or the unassociated particles.

Although it is difficult to discuss atomistic mechanisms, for the formation of crystallographic and globular α - Al_2O_3 with the available information, a possible mechanism is illustrated in Fig. 57, and Fig. 58. Aluminium cations diffuse more rapidly than oxygen anions through single crystal α - Al_2O_3, implying that the growth of a single α - Al_2O_3 crystal takes place at the oxide/metal interface, (since oxygen cannot diffuse into the metal), and the crystal therefore grows into the liquid metal. This process continues as long as a sufficient concentration of oxygen is maintained at the interface. The crystallographic dendrites observed are infact an assemblage of these single crystal platelets (Fig. 50). If however the oxygen activity is low, the precipitate may only be capable of growing laterally as shown diagramatically in Fig. 58 . The resulting crystal then tends towards a spheroidal shape growing along the interface, because the depleted oxygen supply cannot maintain the crystallographic form.

The foregoing discussion relates to the formation of primary α - Al_2O_3 crystals. There remains the problem of secondary α - Al_2O_3 formation, i.e the very fine α - Al_2O_3 precipitates which will be discussed in the next section.

5.2.4 Mechanism of Secondary α - Al_2O_3 Formation

The arguments advanced in the preceding section for direct formation of primary α - Al_2O_3 by oxygen diffusion through γ - Al_2O_3 depend on the thermodynamic stability of α - Al_2O_3 at the metal/oxide interface. As a corollary, the η - Al_2O_3 initially formed near the metal surface is of course unstable, and may be expected to transform, yielding additional α - Al_2O_3 as the transformation product. By implication this is the origins of the very fine α - Al_2O_3 observed in η - Al_2O_3 matrix, illustrated in Fig. 48 i.e. it is a secondary phase in the accepted sense. Any discussion on the transformation of η - Al_2O_3 centres on factors which influence the structure of the phase and thereby determines its stability.

Recalling the arguments given earlier in Section 2.6.3 on the configuration of the spinel structure it seems appropriate to accept Andersons model of hydroxyl ion replacement of oxygen ion, in preference to De Boer's concepts of hydrogen ion replacement of aluminium ions in octahedral interstices on the grounds that a bare proton will be captured by an adjacent O^{2-} ion to form OH^- ion.

The transformation of η - Al_2O_3 to α - Al_2O_3 at the metal/-oxide interface is difficult to describe on an atomic scale, but it is probably initiated by the destabilisation of the η - Al_2O_3 lattice in contact with metal,[159] through the annihilation of OH^-

ions, liberating hydrogen. The overall reaction may then be written as:-

$$4Al + 3 \quad Al_8 [Al_{12} [\ ]_4] O_{28} (OH)_4 \quad = 32\ \alpha\text{-}Al_2O_3 + 12H \tag{29}$$

The hydrogen is liberated in close proximity to the metal/oxide interface where the $Po_2 \sim 3 \times 10^{-48}$ atmospheres. By virtue of the small diffusion distance most of this enters the liquid metal, but there is of course a simultaneous loss into the atmosphere by diffusion through the oxide film.

During the early stages of oxidation when η - Al_2O_3 near the metal/oxide interface is transforming the gas content of the melt increases. As primary and secondary α - Al_2O_3 develop the source of hydrogen progressively recedes towards the oxide/atmosphere interface so that after complete coverage of the metal surface by α - Al_2O_3 hydrogen loss predominates.

Such an effect was invariably observed by Stevenson[159] in the course of an extensive investigation to establish the kinetics of hydrogen absorption by liquid aluminium exposed to humid atmospheres (Fig. 59).

These considerations establish a link between the structure of the oxide film and hydrogen absorption kinetics.

5.3 Structures of Oxide Films Formed in 'Dry' Environments

The discussion so far, has been confined to the formation and development of oxide films on molten aluminium in moist environments and it has been demonstrated that the water in the atmosphere plays a dominant role, in the oxidation process. This leads on to an intriguing question, concerning the nature of the films formed in the absence of moisture.

From the preceding discussion on γ - Al_2O_3, regarded as a hydrogen aluminium spinel, it is expected that in a perfectly dry atmosphere, the film consists wholly of α - Al_2O_3.

Fig. 60 shows a scanning electron micrograph of a film formed on a sample obtained from normal high purity aluminium (Billet A). The sample was exposed at 1003 K (730°C) to an oxidising environment in which the water vapour pressure was $<10^{-8}$ atms. The water vapour potential diagram predicts that under these conditions the oxide film consists wholly of α - Al_2O_3. This appears to be quite consistent with the experimental observations, as shown in Fig. 60, where the degenerate globular dendrites at the oxide/atmosphere interface resemble the α - Al_2O_3 degenerate dendrites at the oxide/metal interface of the duplex films formed in moist environments (Fig. 49g).

Despite its theoretical importance this concept has no practical

significance since it presupposes a degree of dryness unattainable in industrial processes.

It will become apparent that oxidation rates in moist atmospheres is several orders of magnitude greater than the oxidation rate in dry atmospheres. By implication, additives in the furnace which promote the formation of α - Al_2O_3 are expected to be beneficial in minimising the melt losses.

Traces of volatile fluorides in the atmosphere have a dramatic effect in promoting the formation of α - Al_2O_3 as evident from the micrographs in Figs. 61 (a-c).

This effect can be interpreted readily by an analogy with similar effects that are well known in the dehydration of bulk alumina, produced by Bayer process, in which it is a common practice to add fluorides in the environment to facilitate the process. The effect is illustrated in Figs. 62 (a-c) taken from "An atlas of alumina" (BA Chemicals Ltd)[160] which show the remarkable effect of fluorine on both the rate of formation and morphology of α - Al_2O_3.

There is a clear similarity between these structural effects and those for oxides formed on pure aluminium. No clear explanation has been given but it may be due to the clustering of hydroxyl ions around fluoride ions, which are known to solvate readily, thus

destabilizing $\eta - Al_2O_3$.

5.4 Oxidation Kinetics

In the discussion so far the behaviour of oxide films on liquid metal has been considered only in thermodynamic and structural terms, and although this analysis has been useful in revealing some important aspects of the oxidation process it yields no information on oxidation rates. Acquisition of such important measurements requires direct measurements of the kind made in the present study. Not only do these measurements yield results of immediate practical value but in combination with the structural studies they provide a very powerful approach to characterise completely the oxidation process.

5.4.1 Oxidation Kinetics in Moist Environments

Thermogravimetric results must be considered within the framework of the thermodynamic considerations and structural changes observed on liquid metal exposed to moist environments.

The simple fundamental assumptions from which idealised oxidation rate laws are derived obviously do not apply and as expected the oxidation kinetics change with time. Over the short term exposure relevant to the present work the plots of mass gain against time can be considered in two parts:-

a) An initial stage during which an α - Al_2O_3 sub-film is forming at the metal surface under the overlay of γ - Al_2O_3, in which the γ - Al_2O_3 film plays a dominant but diminishing role in the kinetics.

b) The subsequent stage during which the α - Al_2O_3 sub-film is continuous across the metal surface creating two dissimilar media through which reacting species diffuse.

These two periods are well illustrated in Fig. 63a which shows the oxidation kinetics of normal high purity aluminium (Billet A) at 1003 K (730°C) in moist oxygen (P_{H_2O} = 0.03 atms). The results of four individual tests are given, and the essential feature in plots of this kind is that the oxidation rate is rapid during initial stages (Stage I in Fig. 63a) of oxidation while γ - Al_2O_3 exercises rate control, but once α - Al_2O_3 sub-film is continuous it acts as a barrier to continued oxidation. These concepts are particularly well supported for curves Aw_1 and Aw_2 by the transmission electron micrographs (Fig. 55) showing the progressive development of α - Al_2O_3 barrier layer. The acicular primary α - Al_2O_3 crystals are well developed after only 5 minutes and have grown until they completely cover the cross-section after 10 minutes corresponding with transition in the curves. The transition to Stage II is delayed to $\simeq$ 30 mins. in curve Aw_3 (Fig. 63a); presumably this is due to slower establishment of α - Al_2O_3 sub-film in this particular specimen. The transition to Stage II in curve Aw_4 is discontinuous where the inflection at $\simeq$ 16 mins. is

due to cracking and healing of film.

From the time at which the α - Al_2O_3 sub-film is continuous the oxidation kinetics conform to a parabolic rate law as shown in Fig. 63(b) and 63(c) where the (mass gain/unit area)^2 is proportional to time (t). The parabolic rate constants k_p for Aw_1, Aw_2, and Aw_3 obtained from Fig. 63 b&c are given in Table 12a and the kinetics can be associated with Wagner's theory of diffusion rate control through a single phase i.e. it is diffusion through the α - Al_2O_3 layer which controls the overall rate of oxidation and not diffusion through η - Al_2O_3 layer, nor the rate process at its bounding interfaces. Such a situation is not unusual for other pure metals on which a sequence of different oxides is formed e.g. the overall growth rate of thick oxide scales on iron is controlled by the outer layer of Fe_2O_3 and not by FeO which constitutes the main mass of the scale[161].

The argument becomes clearer on considering the transport mechanism available in the two oxides, η - Al_2O_3 and α- Al_2O_3, for reacting species. As discussed earlier, the η - Al_2O_3 lattice is based on a face centred cubic oxygen lattice in which a significant fraction of the interstitial positions are vacant and thus available for diffusion of Al^{3+} cations. In comparison the anionic (O^{2-}) diffusion must be negligible; accordingly the oxide growth must take place at the η - Al_2O_3/atmosphere interface.

Taking a simple view, the cathodic reaction at the γ - Al_2O_3/ atmosphere interface is

$$^1/2\ O_2 + 2e \longrightarrow O^{2-} \qquad (30)$$

with the simultaneous protonation needed for stability:

$$O^{2-} + H_2O \longrightarrow 2(OH)^- \qquad (31)$$

The neutrality is preserved by the current of electrons and Al^{3+} cations diffusing through vacant interstices, the rate control being exercised by supply of Al^{3+} and electrons available at the γ - Al_2O_3/ α - Al_2O_3 interface from the α - Al_2O_3 (Fig. 64).

The above arguments do not preclude earlier arguments for the direct formation of α - Al_2O_3 at the metal/oxide interface by oxygen diffusion through γ - Al_2O_3, which is conceived as a very much slower process.

This explains the observed kinetics in Stage II of oxidation. During Stage I of course, in which α - Al_2O_3 is growing the rate control is continuously changing and hence the oxidation kinetics are expected to be complex, (Fig. 63d). A rigorous mathematical analysis of kinetics in Stage I requires more precise information than is available.

The arguments outlined above rests on the relationships between structural developments within the oxide film and kinetics of its formation, so that factors which modify the structural developments are also expected to modify the oxidation kinetics. Support for this line of reasoning is found in the results for further purified normal high purity aluminium (Billet D) and commercial purity aluminium.

The micrographs (Fig. 56) of oxide films formed on samples obtained from further purified aluminium (Billet D) at 1003 K (730°C) in moist oxygen (P_{H_2O} = 0.03 atms) show a slower and morphologically different form of α- Al_2O_3 as compared with the oxides formed on samples obtained from normal high purity aluminium (Fig. 55). For the further purified material complete coverage of the cross-section by an α- Al_2O_3 sub-film is delayed to $\simeq$ 30 mins, which is reflected in the delayed transition to Stage II of the kinetics as shown in Fig. 65(a). The oxidation kinetics in Stage II conform to the parabolic laws. The parabolic rate constants obtained from Figs. 65(b) and 65(c) are given in Table 12b. The log/log plots of results given in Figure 65a shown in Fig. 65d indicate that during Stage I mass gain/unit area is not related to time by a power law.

Oxidation kinetics of samples obtained from commercial purity aluminium can be interpreted similarly. Fig. 66a shows oxidation kinetics at 1003 K (730°C) in moist oxygen (P_{H_2O} = 0.03 atms) of three samples obtained from commercial purity aluminium.

The kinetics in Stage II conform to the parabolic rate law as shown in Figs. 66b, and 66(c). The parabolic rate constants given in Table 12c were obtained from Fig. 66(b) and Fig. 66(c).

The log/log plots of the results in Fig. 66(a) given in Fig. 66(d) indicate that the kinetics during Stage I are complex.

The transition to Stage II is discontinuous in CPw_3 where the inflection at $t \simeq 25$ mins. is due to cracking and rehealing of the oxide, and because of this complication obvious in Fig. 66(a) it was unprofitable to analyse this curve further.

Transmission electron micrographs (Fig. 67) of oxide films formed on commercial purity metal when exposed to moist oxygen show a much slower development of $\alpha - Al_2O_3$ sub-film as compared with the micrographs in Fig. 55, and Fig. 56. This is consistent with the prolongation of Stage I and the delayed transition to Stage II, during the oxidation of samples obtained from commercial purity aluminium.

5.4.2 Role of Impurities During Oxidation in Moist Oxygen

Oxidation kinetics, at 1003 K (730°C) in moist oxygen, of samples obtained from Billet A, Billet D and commercial purity aluminium are compared in Fig. 68. These results together with the analysis (Fig. 53), using XPS, yield the following information.

a) Calcium and/or sodium incorporated in oxide films formed on normal high purity aluminium in moist oxygen increases the overall oxidation and reduces the time before Stage II is fully established.

b) The overall mass gains are greater and Stage I is prolonged during the oxidation of samples obtained from commercial purity aluminium. The main impurities incorporated within the oxide are iron and copper (Fig. 69).

Providing that no new phase is introduced an impurity element may exercise its influence on the oxidation kinetics by changing the defect structure of the parent oxide.

In applying the principles developed by Hauffe several factors require consideration, among them the following.

a) The size of the foreign cation in relation to sites available for occupation and the need to maintain co-ordination.

b) The type of electrical charge compensation required to accommodate differences of valency between the parent and foreign cation.

c) The possibility of charge compensation by valency changes of either parent or foreign cation.

d) The possibility of charge compensation by change in the degree of non-stoichiometry.

e) The possibility of charge compensation by protonation of the anions.

Table 14 provides the relevant information for analysing the incorporation of calcium, in η - Al_2O_3 and α - Al_2O_3.

In considering the incorporation of Ca^{2+} into the η - Al_2O_3 it is interesting that calcium promotes the formation of α - Al_2O_3, i.e. it increases anion diffusion.

Table 14 shows that Ca^{2+} cannot be accommodated in either tetrahedral or octahedral sites without considerable lattice distortion. However an interesting discussion can be initiated by making the tentative assumption that Ca^{2+} is incorporated in octahedral sites. Inspection of other spinel lattices indicates that this is not an unreasonable assumption, for example in $Mg\ Al_2O_4$ the Mg^{2+} ions occupy tetrahedral sites even though the radius of Mg^{2+} is 0.065 nm.

Ca^{2+} incorporated in octahedral interstices may be represented by

$$Al_8\ [Al_{12}\ Ca\ [\ ]_3\ ]\ O_{28}\ (OH)_4 \qquad 32$$

In writing formula 32 no account has been taken of charge imbalance, but since Ca^{2+} is a fixed divalent, substitution for a trivalent Al^{3+} ion, the charge compensation is required either by replacing octahedral Al^{3+} cations with a proportionally greater

number of Ca^{2+} ions i.e.

$$Al_8 [Al_{10} Ca_3 [\,]_3\,] O_{28} (OH)_4 \qquad 33$$

or by introducing anion vacancies i.e.

$$Al_8 [Al_{10} Ca_2 [\,]_4\,] O_{27} [\,] (OH)_4 \qquad 34$$

The work needed to create anion vacancies can be compensated by the opportunity for the increase of configuration entropy afforded by the distribution of calcium ions on vacant octahedral sites. It can be assumed therefore, that at least some anion vacancies are introduced. This is consistent with the increased anion diffusion manifest by rapid growth of primary α- Al_2O_3 sub-film.

The activities of Na^+. Cu^{2+} and Fe^{2+} in η - Al_2O_3 are expected to be exceedingly low by virtue of the low oxygen potentials. According to Hauffe's valency rules the lattice defect concentration remains largely unaffected by the incorporation of Na, Cu and Fe, and the only effect that these impurities could have is short range distortion of the lattice.

The reasoning appears to be consistent with the much slower development of α - Al_2O_3 sub-film during the oxidation in moist oxygen (P_{H_2O} = 0.03 atms) at 1003 K (730^{o}C) of samples obtained from commercial purity aluminium, where the main impurities incorporated within the oxide are Fe and Cu.

In the same sense as we have considered calcium to be a foreign cation we may regard protonation as foreign cations i.e O^{2-} is replaced by OH^-. Taking this view the reasoning applied to the influence of calcium should apply also to the introduction of univalent anion OH^-. The population of OH^- ions as anion substituents is controlled by the water vapour pressure in the atmosphere.

In introducing Anderson's model the structure was formally written as

$$Al_8 [Al_{12} [\ ]_4\ ] O_{28} (OH)_4$$

for the sake of establishing certain principles. Since a characteristic of spinels is their stability over ranges of composition the influence of increased protonation of O^{2-} must be considered. For example, as illustrated by

$$Al_8 [Al_{11} [\ ]_5\ ] O_{25} (OH)_7 \qquad 35$$

From this it follows that charge compensation requirements are met by increasing the vacancy population which promotes the diffusion of Al^{3+} cations. This provides an explanation for the influence of water vapour pressure in increasing the rate of formation of $\gamma - Al_2O_3$, before the sub-film of $\alpha - Al_2O_3$ is fully established and exercises rate control (Figs. 70, 71).

5.4.3 Oxidation Kinetics in Dry Environments

Oxidation kinetics at 1003 K (730°C) in dry oxygen ($P_{H_2O} < 10^{-8}$ atm) of four samples obtained from normal high purity aluminium Billet A, are shown in Fig. 72(a). The log/log plots (Fig. 72(b)) and the parabolic plots (Fig. 72(c)) of the results in Fig. 72(a), reveal that the kinetics conform to a parabolic growth law following an initial period in which the growth conforms to a linear rate law.

It is interesting that when the parabolic portions are extrapolated back they correspond to oxidation which started at a time before the true zero. This is demonstrated in Fig. 72(d) where the parabolic portions intersect at -45 min . The implication is that the parabolic oxidation starts with a finite thickness of protective oxide which would occur if an initially formed non-protective oxide were to become protective during the course of oxidation.

A non-protective oxide implies easy access of oxygen to the metal surface, usually provided by cracking, and if such a cracking film were subsequently to heal its growth kinetics would be similar to those observed.

Oxidation kinetics at 1003 K (730°C) in dry oxygen ($P_{H_2O} < 10^{-8}$ atm) of samples obtained from Billets B, C, D are shown in Figs. 73(a), 74(a) and 75(a) respectively. (high purity metal further purified by selective oxidation)

The log/log plots (Fig. 73b, Fig. 74b) and parabolic plots (Fig. 73c, Fig 74c) show that the oxidation kinetics of samples obtained from Billets B and C conform to the parabolic law following an initial period during which linear kinetics are observed. Due to the small mass gains (Fig. 75a) the oxidation kinetics, during early stages, of samples obtained from Billet D cannot be identified positively. However, the parabolic plots (Fig. 75b) of results in Fig. 75a show that curves Dd_1 and Dd_2 conform to a parabolic law after the early stages ($t > 10$ mins, and 20 mins respectively). Curves Dd_3 and Dd_4 could not be further analysed, because of the experimental scatter evident in Fig. 75b.

Linear rate constants obtained from Figs. 72a, 73a and 74a are given in Tables 13a, 13b and 13c. Parabolic rate constants obtained from Fig. 72c, 73c, 74c and 75b are given in Tables 13a, 13b, 13c and 13d.

A comparison of Fig. 72(a), Fig. 73(a), Fig 74(a) and Fig. 75(a), given in Fig. 76, shows that the final overall mass gains are lowered as the metal is purified.

The oxidation kinetics at 1003 K (730°C) in dry oxygen ($P_{H_2O} < 10^{-8}$ atms) of samples obtained from commercial purity aluminium are shown in Fig. 77(a). The log/log plots (Fig. 77(b)) and the parabolic plots (Fig. 77(c)) of the results in Fig. 77(a) indicate that the kinetics conform to the parabolic rate law, at least up to $t \simeq$

15 mins. The mass gains after t = 15 mins are exceedingly small and beyond the resolution of the experimental technique used.

Absence of a linear portion, preceding the parabolic portion suggests that the films formed on commercial purity aluminium are continuous, and their growth is controlled by diffusion of species through the film.

The parabolic rate constants obtained from Fig. 77(c) are given in Table 13(e).

The next important matter concerns the lack of reproduciblity in oxidation kinetics of samples exposed to dry oxygen. It is convenient to explore the reasons for the irreproducibility by considering the results given in Fig. 72(a), which show the oxidation kinetics of samples obtained from normal high purity aluminium.

The irreproducibility in the results shown in Fig. 72(a) could be due to inadequacies in the experimental technique or to minor compositional variations from sample to sample. In this respect it is noteworthy that the parabolic rate constants (k_p) (Table 13a) obtained from Fig. 72(c) range from 6.9×10^{-13} $gm^2/cm^4/sec$ to 5×10^{-13} $gm^2/cm^4/sec$ reflecting changes in either the activation energy, E, or the pre-exponential factor, A, by virtue of the relationship

$$K_p = A \exp - \frac{E}{RT} \qquad 36$$

The activation energy is constant for any particular diffusion mechanism and therefore the irreproducibility is due to variations in the pre-exponential factor which is sensitive to the lattice defect concentration, and therefore to impurities incorporated in the oxide film.

Validity of the foregoing argument is qualitatively supported by the results given in Fig. 78 which show the dramatic variation in oxidation kinetics between samples obtained from different ingots of the same nominal composition.

5.4.4 Role of Impurities During Oxidation in Dry Oxygen

Fig. 76 shows that the overall final mass gains during oxidation of samples obtained from normal high purity aluminium are greater than the overall final mass gains during oxidation of samples obtained from further purified billets.

XPS showed that the main impurities incorporated in oxide films formed in moist oxygen on high purity aluminium are calcium and sodium. The levels of these impurities being higher in oxides formed on samples obtained from Billet A than in oxides formed on samples obtained from Billet D.

Presumably this also applies to the oxide films formed in dry oxygen, and on this basis the differences in oxidation kinetics between samples obtained from Billets A, B, C and D may be explained in terms of variation in diffusion kinetics through α - Al_2O_3 induced by incorporated Ca^{2+} ions. The activity of Na^+ ions in α - Al_2O_3 is expected to be exceedingly low, and according to Hauffe's valency rules, should not profoundly influence the oxidation kinetics.

In describing the transport phenomena through α - Al_2O_3 (Section 2.2.5) some experimental measurements were cited which showed that the diffusion of aluminium is many orders of magnitude greater than the diffusion of oxygen. This however only applies to within the intrinsic region and for single crystals.

In polycrystalline α - Al_2O_3 anionic diffusion becomes significant which progressively increases as the grain size is reduced, so that below $\simeq$ 20,000 nm anionic diffusion predominates over cationic diffusion. Extending these results to the present case it is expected that the significant growth of α - Al_2O_3 film takes place at the metal/oxide interface.

The mechanism by which Ca^{2+} exerts its influence on oxidation kinetics in dry oxygen may be explained by combining Hauffe's valency rules and the generally accepted model of diffusion through polycrystalline α - Al_2O_3 first proposed by Laurent and Bernard[30], in which diffusion takes place not only along grain

boundaries but in a measurable volume adjacent to grain boundaries. The width of this region was estimated as ≃ 20 nm. Given the nature of α- Al_2O_3 as discussed earlier, given the trivalency of the parent cation and divalency of the calcium ion as an impurity cation, Hauffe's valency principle predicts that the anion vacancy population will increase. The oxidation kinetics are thus expected to increase as the level of incorporated calcium increases, which is consistent with experimental measurements given in Fig. 76.

XPS showed that the main impurities incorporated in oxide films formed in moist oxygen on samples obtained from commercial purity aluminium are Fe and Cu. Presumably these impurities would also be present in films formed on commercial purity aluminium in dry oxygen.

The activities of Fe^{2+} and Cu^{2+} ions in α- Al_2O_3 are exceedingly low, by virtue of the low oxygen potentials. Application of Hauffe's valency rules predicts that the incorporation of Fe and Cu should not profoundly influence the defect structure and hence the kinetics, which is consistent with the very small mass gains observed during the oxidation of samples obtained from commercial purity aluminium (Fig. 77(a)).

The only other effect that foreign atoms could have is lattice distortion, which is difficult to quantify using the available data. However, the parabolic kinetics observed suggest that the stresses

resulting from lattice distortion are insufficient to disrupt the continuity of the film.

Linear kinetics observed during the early stages of oxidation in 'dry' oxygen of samples obtained from high purity aluminium suggest that the films contain cracks through which reacting species migrate. This disruption of the film could occur during the rapid ingress of oxygen through regions adjacent to grain boundaries, analogous to the model proposed by Rhines and Wolf[81] for the growth of NiO (Fig. 17).

5.5 Two-Stage Tests

Most of the present arguments have been devoted to the control of oxidation by α - Al_2O_3 both as a single phase film formed in dry atmosphere and in duplex films formed in humid atmospheres where it develops as a sub-film underneath the initially formed layer of η - Al_2O_3.

This is in marked contrast to the disruption of a protective α-Al_2O_3 layer when it is formed first as happens in the two stage tests, where the metal was exposed to dry atmosphere and then to moist atmosphere.

Figs. 79-81 show that the oxidation rate invariably increases immediately in response to substitution of initial dry atmosphere

with humid atmosphere. This effect can be associated with the appearance of an additional phase formed on top of α- Al_2O_3 (Fig. 82) which by implication is a new growth of γ- Al_2O_3.

The results of the present work have shown that the short term oxidation characteristics of pure liquid aluminium can be very complex. The present work has established certain basic principles which apply to short term oxidation of pure liquid aluminium, notably those which concern the role of atmospheric components especially humidity and of impurities which enter the oxide from metal. These have been applied to follow and to explain structural changes which occur in the first hour or two. The marked effects these changes have on the oxidation rate shows the irrelevance of deductions made from results of measurements over very long periods. In this respect some comment is required on results (Fig. 83) published by Thiele[93] some years ago. These results were obtained using thermogravimetric equipment for which the early stages of oxidation were inaccessible because of inadequate sensitivity of equipment and inability to prevent oxidation during melting of sample.

Thiele[93] found that over very long periods of up to $\simeq$ 120 hours during which very thick oxide films are formed the mass of oxide in dry atmosphere is greater than that formed in humid atmospheres. This effect must be attributed to special features which influence the integrity of very thick films of α- Al_2O_3 which has no relevance to the present work. Since these results have

entered the literature a warning must be sounded on the fallacious arguments that can be based on these results if applied to short term oxidation of interest during the time scale for melting and casting.

6 CONCLUSIONS AND FURTHER WORK

6.1 Conclusions

1) The oxide film formed on pure molten aluminium at 1003 K (730 C) in moist oxygen is duplex in nature consisting of a slightly hydrated phase ,η–Al_2O_3 overlying the dehydrated phase ,α–Al_2O_3, which is stable at the oxide/metal interface. This is consistent with predictions based on water vapour potentials at the bounding interfaces of the oxide films.

2) The oxide film formed on pure molten aluminium at 1003 K (730 C) in dry oxygen is single phase, consisting of α–Al_2O_3.

3) The morphology of α–Al_2O_3 formed as a sub-film under the η–Al_2O_3 in moist oxygen can vary from well defined acicular dendrites to degenerate forms and depends on impurities incorporated within η–Al_2O_3.

4) The oxidation kinetics at 1003 K (730 C) of samples obtained from pure and commercial purity aluminium are characterised by a rapid initial kinetics followed by a transition to much slower kinetics which conform to parabolic growth law.

5) The transition to the parabolic growth rate takes place when the α–Al_2O_3 sub-film is fully established at the metal/oxide interface.

6) The oxidation kinetics at 1003 K (730 C) in dry oxygen of samples obtained from pure aluminium conform to linear kinetics followed by parabolic kinetics.

7) The oxidation kinetics at 1003 K (730 C) in dry oxygen of samples obtained from commercial purity aluminium conform to parabolic kinetics, at least up to $t \leqslant 15$ minutes, after which the kinetics cannot be identified since the mass gains are exceedingly small and beyond the resolution of the technique used.

8) The effects of calcium incorporated in the oxide films formed on pure aluminium in moist oxygen are to,

   a) increase overall oxidation

   b) decrease the transition time from the rapid initial kinetics to the slower parabolic kinetics.

9) The effect of incorporated calcium on the oxidation kinetics of pure aluminium in dry oxygen is to increase the overall oxidation.

6.2 Further Work

Since the completion of this work the author has carried out an extensive study of oxidation of molten Al/Mg alloys, in collaboration with Willis[162].

Although attention is now being focused onthe Al/Mg alloys, there are many areas in the oxidation of pure metal which require further investigation. Further work should be aimed to:-

1) Define further the effect of impurities on oxidation, by controlled additions to very pure aluminium produced by zone refining.

2) Develop a microbalance technique to measure oxidation rates of aluminium in environments containing aggresive additives such as fluorides.

3) Evaluate the oxidation kinetics as a function of heating rates, to simulate melting in a real furnace.

4) Compare the nature of oxide films formed in induction furnaces to the oxide films formed in electric or gas fired furnaces.

REFERENCES

1. N Whittner, Foundry Trade Journal 1980 2, 264.

2. E Mittmann, Giesserei 1976, 63 (1), 4 BISI 14265.

3. H Spoel, Light Metals, AIME, 1976, 2, 313.

4. C Moser, Light Metals, 1976, 2, 299.

5. M Dolezil, M Patera, L Ludvikova, 11th International Mineral Processing Congress 1975, Cagliori Paper 53.

6. C Heins, Process for Recovery of Fine Aluminium From Aluminium Dross. US Patent Number 3,155,494 November 3rd, 1964.

7. E Freisz, G Langley, Light Metals, AIME, 1975, 2, 101.

8. N Cochran, D Belitkus, D Kinosz. Metal Transactions, 1977, 8B, 323.

9. D Talbot, International Metals Review, 1975, 20, 166.

10. D Ferguson, Master of Technology Thesis Brunel University (Metallurgy Dept) 1981.

11. D Hayward and B Trapnell, Chemisorption Butterworths, London, 1964.

12. D Young and D Crowell, Physical Adsorption of Gases. Butterworths, London 1962.

13. P Kofstad, High Temperature Oxidation of Metals, Wiley, New York. 1966

14. G Ehrlich, in Metal Surfaces: Structure Energetics and Kinetics. Am. Soc. Metals, P. 221. 1966.

15. W Ruhl, Z Physik, 1963, 409. 176 (quoted in ref. 18).

16. J Tompkins, Chemisorption of Gases on Metals, Academic Press 1978.

17. G Ehrlich, Trans 8th Vacuum Symposium and 2nd International Congress. Pergamon Press, New York 1962, 126.

18. F Felner and N Mott. Oxidation of Metals, 1970, 2, (1), 59.

19. S Brenner, P305, Metal Surfaces: Structure, Energetics and Kinetics. Am. Soc. Mets. 1963.

20. F Jona, J Phys. Chem. Solids. 1967, 28, 2155.

21. J May and L Germer, Surface Sci. 1968 11, 443.

22. W Orr. Oxide Nucleation and Growth, Thesis Cornell University Microfilm Inc. Ann. Arbor Mich. Onr Rept. 5 1962.

23. F Kroger, The Chemistry of Imperfect Crystals, North Holland Publ. Amsterdam, 1964.

24. L Shrier, Corrosion V I Newness Butterworths, London 1976.

25. J Crank, The Mathematics of Diffusion, Oxford Clarendon Press 1956.

26. R Barrer, Diffusion in and Through Solids. Cambridge Univ. Press 1951.

27. H Carslaw and J Jaeger. Conduction of Heat Through Solids, Oxford Univ. Press. 1947.

28. P Shewmon, Diffusion in Solids, McGraw Hill New York 1963.

29. J Stark, Solid State Diffusion, Wiley, London 1976.

30. J Laurent and J Bernard, Compt. Rend. 1955, 241, (18), 1204.

31. A Paladino and R Coble. J. Am. Cer. Soc. 1963, 46, 3, 133.

32. J Cohen, Bull. Am. Cer. Soc. 1959, 38 (9), 441.

33. W Hartmann, Z Physik. 1936, 102, (11/12), 709.

34. K Heldt and G Hasse, Z Angew Phys. 1954, 6 (4), 157 (quoted in reference 32)

35. J Pappis and W Kingery, J. Am. Cer. Soc. 1961, 44, 459

36. P Harrop and R Creamer, Brit. J. App. Phys. 1963, 14, 335.

37. S Dasgupta and J Hart, ibid 1965, 16, 725.

38. D Peters, J. Phys. Chem. Solids. 1966, 27, 1560.

39. V Johnson, K Lark-Horowitz, Phys. Rev. 1953, 92, 226.

40. Y Oishi and W Kingery, J. Chem. Phys. 1960, 33 (2), 480

41. A Paladino and W Kingery, ibid. 1962, 37 (5), 957.

42. M Davies, NASA Tech. Note. NASA TND 2765.

43. P Kofstad, Non-Stoichiometry, Diffusion and Electrical Conductivity in Oxides. Wiley and Sons London.

44. E Gulbransen, Trans. Electrochem. Soc. 1942, 81, 327.

45. E Gulbransen, ibid, 1942, 82, 357.

46. H Svec and J Appel. J Electrochem. Soc. 1957, 104, 346.

47. R Hart. Proc. Roy. Soc. 1956, 68A, 236.

48. M Roberts, Trans. Faraday Soc. 1961, 57, 99.

49. N Cabrera and N Mott. Rept. Progr. Phys. 1948-49, 12, 163.

50. N Cabrera, Phil Mag 1949, 40, 175.

51. A Fromhold and E Cook, J Chem. Phys. 1966, 44, 4564.

52. A Fromhold and E Cook, Phys. Rev. 1967, 158, 600.

53. J Boggio and R Plumb, J Chem. Phys. 1966, 44, 1081.

54. D Eley and P Wilkinson, Proc. Roy. Soc. London Ser. A. 1960, 254, 327.

55. C Kirk and E Huber, Surface Sci 1968, 9, 217.

56. N Mott, Trans Fara. Soc. 1947, 43, 429.

57. M Lanyon and E Trapnell Proc. Roy. Soc. London Ser. A. 1955, 227, 387.

58. G Tammann, Zeitschrift Fur. Anorganisrhe Chemie. 1920, 111, 78.

59. N Pilling and R Bedworth, J Inst. Mets. 1923, 29, 529.

60. C Wagner, Z Phys. Chem. 1933, 21(B), 25.

61. W Jost, Diffusion in Solids, Liquids and Gases. Academic Press, New York. 1952.

62. A Fromhold, Theory of Metal Oxidation. North Halland Co. Amsterdam 1976.

63. T Hoar and L Price, Trans. Fara. Soc. 1938, 34, 867.

64. T Gray, The Defect Solid state. Interscience Publishers Inc. New York 1957.

65. J Loriers, Compt. Rend. 1949, 229, 547, USAEC Translation HW 61492.

66. W Webb, J Norton and C Wagner, J. Electrochem. Soc. 1956, 103, 107.

67. E Haycock, J. Electrochem. Soc. 1959, 106, 771.

68. Wanklyn, Quoted in U R Evans Corrosion and Oxidation or Metals Edward-Arnold 1960, P. (263).

69. S Gregg W Jepson, J Inst. Mets. 1959, 81, 187.

70. D Aylmore, S Gregg and W Jepson, J Electrochem. Soc. 1960, 107, 495.

71. E Gulbransen and K Andrew, J. Electrochem. Soc. 1958, 105, 4.

72. A Jenkins, J. Inst. Mets. 1953, 82, 213.

73. D Caplan and M Cohen, J Met. 1951, 3, 155.

74. U Evans, Trans. Electrochem. Soc. 1947 91, 547.

75. U Evans, Inst. Mets. Symposium on Internal Stress in Metals and Alloys. 1947, 219.

76. J Stringer, Corrosion Sci. 1970, 10, 513.

77. D Vermilyea, Acta. Metall. 1957, 5, 492.

78. J Richmond, I Leslie, P Wriet, Trans. Am. Soc. Mets. 1964, 57, 294.

79. V Howes and R Richardson, Corrosion Sci. 1969, 9, 385.

80. W Jaenicke, S Leistikow and A Sadler, J Electrochem. Soc. 1964, 111, 1031.

81. F Rhines and J Wolf. Personnal Communication to J Stringer, Reference 76.

82. H Deville. "De L' Aluminium", 1859.

83. E Gulbransen, Advance Catalysis, 1953, 5, 119.

84. E Gulbransen and Y Wysong, J Phys. Colloid Chem. 1947, 51, 1087.

85. W Smeltzer, J. Electrochem Soc. 1956, 103, 209.

86. D Aylmore, S Gregg and W Jepson, J. Inst. Mets. 1959, 88, 205.

87. M Dignam, W Fawcett, H Bohni, J. Electrochem. Soc. 1966, 113, 656.

88. A Beck, M Heine, E Caule, and M Pryor, Corrosion Sci. 1967, 7, 1.

89. U Evans, Trans. Fara. Soc. 1945, 41, 365.

90. N Cochran and W Sleppy, J. Electrochem. Soc. 1961, 108, 322.

91. G Preston and L Bircumshaw, Phil. mag. 1936, 22, 654.

92. L De. Brouckere, J. Inst. Met. 1945, 71, 131.

93. W Thiele, Aluminium 1962, 38, 707.

94a. E Strum and H Winterhagen, Aluminium 1978, 58, (6), 380.

94b. Ibid, 1978, 54, (7), 441.

95 K Wefer, Oxides and Hydroxides of Aluminium Alcoa Technical Paper No. 19.

96. R Harrington and H Nelson, Metals Technology, 1940, 7, 1.

97. K Thomas and M Roberts, J. App. Phys. 1961, 32, 70.

98. P Doherty and R Davis, Ibid 1963, 34, 619.

99. J Randall and W Bernard, Ibid, 1964, 35, 1317.

100. G Scamans and P Butler, Met. Trans. 1975, 6A, 2055.

101. R Hart and J Maurin, Surface Sci. 1970, 20, 285.

102. M Hunter and P Fowle, J Electrochem. Soc. 1954, 103. 481.

103. M Dignam, Ibid, 1962, 109, 184.

104. M Badia, Thin Solid Films 1972, 13, 329.

105. W Gitzen, Alumina as a Ceramic Material. Am. Cer. Soc. 1970.

106. H Stumpf, J Newsome, C Tucker, A Russell, Ind. Eng. Chem. 1950, 42, (7), 1398.

107. R Tertian, Pappee, J. Chim, Phys. 1958, 55, 341.

108. H Rooksby, X-Ray Identification and Crystal Structure of Clay Minerals, (Edt Brindley) The Minerlogical Soc. Brit. Museum, London 1951.

109. M Day, V Hill, J. Phys. Chem. 1953, 57, 946.

110. B Lippens, Thesis, Delft (1961). Structure and Textures of Aluminas.

111. G Houben and J De Boer, Trans. Intern, Cer. Congr. 3rd Congr. Paris 1952, p. 77.

112. D Maciver, H Tobin, R Barth. J. Catalysis, 1963, 2, (6), 485.

113. H Yanagida, G Yamaguchi, and J Kubota. Bull. Chem. Soc. Japan 1965, 38, 2194.

114 A Steinheil, Ann. Phyzik 1934, 19, 465.

115. G Beghi, Cazzanda, G Riatti, J. Nucl. Mats. 1966, 18, 237.

116. H Le Chattelier, Bull. Soc. Min. 1887, 10, 204, Compt. Rend. 1887, 104, 1443.

117. A Pechiney, French Patent, No. 394709, (4.5.1904)

118. J Lindsay, Am. Ceram. Soc. meeting Dallas, Texas, 8th May 1957.

119. E Roberts and W Jukkola, US Patent No. 2,833,622, 5.8.1958.

120. G Ervin and E Osborn, J. Geol. 1951, 59, 381.

121. L Pauling, Nature of the Chemical Bond, Cornell Univ. Press 1945.

122. E Verwey, J. Chem. Phys. 1935, 3, 592.

123. H Saalfled, Clay Minerals Bull 1958, 3, 249.

124. O Glemser and G Reick, Z. Angew Chem. 1955, 67, 652.

125. J De Boer and Houben, Proc. Intern. Symp. Reactivity of Solids Gotenburg, 1952, 237.

126. J Anderson, in reference (125).

127. E Verwey, in reference (125).

128. P Braun, in reference (125).

129. Gorter, in reference (125).

130. W Bragg and W Bragg, "X-Rays and Crystal Structure", Bell and Sons, London 1915.

131. H Swanson, M Cook, T Issacs, E Evans, Standard X-Ray Powder Diffraction Patterns, Natl. Bureau Stds. Circ. 1960, 9, 539.

132. R Newnham and Y Haan, Z Krist, 1962, 117 (2-3), 235.

133. R Hart, Trans. Fara. Soc. 1957, 53, 1020.

134. R Alwitt and L Archibald, Corrosion Sci. 1973, 13, 687.

135. W Bernard and J Randall, J Electrochem Soc. 1960, 107, 483.

136. R Hart, Trans. Fara. Soc. 1954, 50, 269.

137. W Vedder and D Vermilyea, Ibid, 1969, 65, 561.

138. P Gigl, Phd. Thesis Pennsylvania State Univ. 1972.

139. R Hart and J Maurin, Corrosion 1965, 21, 222.

140. J Draley and W Ruther, Ibid, 1956, 12, 441 t

141. V Troutner, Ibid, 1959, 15, 9t.

142. D Bowen and C Hall., Microscopy of Materials, MacMillan Press Ltd. 1975, London.

143. A Agar, R Alderson, D Chescoe, Principles, and Practice of Electron Microscope Operation, North Holland Pub. 1974.

144. A Glavert, Practical Methods in Electron Microscopy, North Holland Pub. 1972.

145. J Goldstein and H Yakawitz (ed), Practical Scanning Electron Microscopy, Plenum Press, New York, 1975.

146. D Briggs (Ed) Handbook of X-Ray and Photoelectron Spectroscopy. Heyden and Sons Ltd. 1977.

147. M Cox, B McEnaney and V Scott, Vacuum Microbalance Techniques.

148. O Kubachewski and C Alcock, Metallurgical Thermochemistry, Pergamon 1979.

149. M Pryor, Oxidation of Metals, 1971, 3 (6), 523.

150. I Gurnberg and K Wright, Proc. Roy. Soc., 1955, A232, 403.

151. M Heine and P Sperry, J. Electrochem Soc., 1965, 112 (3), 359.

152. D Saratovkin, Dendritic Crystallization, Consultants Bureau, New York, 1959.

153. A Choudhuary and M Wahlster, Keistahl Tech. 1966, 4, 111. (quoted in reference 154).

154. P Waudby and W Salter, JISI, 1971, 7, 518.

155. H Ooi, J Sekine and J Kasai, Trans. ISIJ, 1975, 15, 371.

156. E Steinmetz and P Hammerschmid, Arch, Eisen, 1977, 48 (11), 569. BISI Translation 16510.

157. S Robinson, I Martin, and F Pickering, Metals Technology, 1979, 5, 157.

158. U Evans, The Corrosion and Oxidation of Metals, London, Edward Arnold Pub. 1971.

159. D Stevenson, Phd. Thesis, Brunel University, 1978.

160. British Aluminium Co. Atlas of Aluminas.

161. O Kubachewski and B Hopkins, Oxidation of Metals and Alloys, Butterworths 2nd Edition 1967, p 111.

162. P Willis, Oxidation of Molten Aluminium/Magnesium Alloys, 4th Year Project Brunel University 1982.

APPENDIX I

Notation for point defects

Symbol	*Defect*	*Effective charge in units q*
e'	Quasi-free electron in the conduction band	−1
$h^{\cdot}$	Quasi-free hole in the valence band	+1
V_A^X	A vacancy	0
V_A'''	A vacancy	−2
V_B^X	B vacancy	0
A_B'	A at a B site	−1
B_A^X	B at an A site	0
$A_i^{\cdot}$	A at an interstitial site	+1
A_A^X	A at an A site	0
B_B^X	B at a B site	0
V_I^X	Unoccupied interstitial site	0
F_A^X	Foreign atom F at A site	0

APPENDIX II

CONCENTRATION OF POINT DEFECTS IN AN OXIDE CONTAINING SCHOTTKY DISORDER

Consider an oxide with sites of two types occupied by M and O atoms respectively. A small fraction of either type of site may be vacated as follows:

$$\text{Zero} = V_m^x + V_o^x \qquad [V_m^x][V_o^x] = K_s \qquad 1a$$

$$V_m^x = V_m^{'} + h^{\cdot} \qquad \frac{[V_m^{'}][h^{\cdot}]}{[V_m^x]} = K_a \qquad 2a$$

$$V_o^x = V_o^{\cdot} + e^{'} \qquad \frac{[V_o^{\cdot}]\ [e^{'}]}{[V_o^x]} = K_b \qquad 3a$$

in addition, further electronic defects are formed by intrinsic ionization, exciting electrons from the valence band leaving electron holes:

$$\text{Zero} = e^{'} + h^{\cdot} \qquad [e^{'}]\ [h^{\cdot}] = K_i \qquad 4a$$

The combination of 1a, 2a, and 3a yields

$$\text{Zero} = V_m^{'} + V_o^{\cdot} \qquad [V_m^{'}][V_o^{\cdot}] = K_s^{'} \qquad 5a$$

and also

$$K_s^{'} = \frac{K_s\ K_a\ K_b}{K_i} \qquad 6a$$

To preserve electrical neutrality

$$[e^{'}] + [V_m^{'}] = [h^{\cdot}] + [V_o^{\cdot}] \qquad 7a$$

Equilibrium with the gaseous phase is maintained by :

$$\tfrac{1}{2}\,O_2(g) = O_o^x + V_m^x \qquad \frac{[O_o^x]\ [V_m^x]}{P_{O_2}^{\frac{1}{2}}} \approx \frac{[V_m^x]}{P_{O_2}^{\frac{1}{2}}} = K_{O_2 v} \qquad 8a$$

$$M\ (g) = M_m^x + V_o^x \qquad \frac{[M_m^x]\ [V_o^x]}{P_m} \approx \frac{[V_o^x]}{P_m} = K_{mv} \qquad 9a$$

using equations (4a-9a) an approximate graphical method can be used, to express the concentration of all defects in terms of P_{O_2} (c.f Kofstad[13])
It is convenient to express defects in terms of the relationship:

$$P_{O_2}^{\frac{1}{2}}\ K_{O_2 v} = R$$

For low values of P_{O_2} oxygen vacancies are the predominating defects, ionising to give $V_o^{\bullet}$ and free electrons in the conduction band. To preserve electrical neutrality,

$$[e'] = [V_o^{\bullet}] \gg [h^{\bullet}] \text{ and } [V_m']$$

and the various concentrations are given by

$$[V_m^x] = R, \qquad [V_o^x] = \frac{K_s}{R} = \frac{K_s'\ K_i}{R\ K_a K_b}$$

$$[e'] = [V_o^{\bullet}] = \left(\frac{K_b\ K_s}{R}\right)^{\frac{1}{2}} = \left(\frac{K_i\ K_s'}{K_a\ R}\right)^{\frac{1}{2}}$$

$$[h^{\bullet}] = \frac{K_i}{[e']} = K_i \left(\frac{K_a\ R}{K_i\ K_s'}\right)^{\frac{1}{2}}$$

$$[V_m'] = \frac{K_s'}{[V_o^{\bullet}]} = K_s' \left(\frac{K_a\ R}{K_i\ K_s'}\right)^{\frac{1}{2}}$$

$[e']$, $[V_o^{\bullet}]$ decrease and $[h^{\bullet}]$ and $[V_m']$ increase with $R^{\frac{1}{2}}$

Similarly for high values of P_{O_2} metal vacancies predominate so that :

$$\left[V_m^{'}\right] = \left[h^{\bullet}\right] \gg \left[e^{'}\right] \text{ and } \left[V_O^{\bullet}\right]$$

The concentration of various defects are :

$$\left[V_m^{'}\right] = \left[h^{\bullet}\right] = \left(K_a R \right)^{\frac{1}{2}}$$

$$\left[e^{'}\right] = \frac{K_i}{(K_a R)^{\frac{1}{2}}}$$

$$\left[V_O^{\bullet}\right] = \frac{K_s^{'}}{(K_a R)^{\frac{1}{2}}}$$

Thus $\left[e^{'}\right]$ and $\left[V_O^{\bullet}\right]$ decrease whereas $\left[h^{\bullet}\right]$ and $\left[V_m^{'}\right]$ increase with $R^{\frac{1}{2}}$. For intermediate values of P_{O_2} the following alternative limiting conditions need consideration.

CASE A

Electronic intrinsic ionization predominates so that $K_i > K_s^{'}$ and electroneutrality condition is represented by

$$\left[e^{'}\right] = \left[h^{\bullet}\right]$$

The defect concentrations are :

$$\left[e^{'}\right] = \left[h^{\bullet}\right] = (K_i)^{\frac{1}{2}}$$

$$\left[V_m^{'}\right] = \frac{K_a R}{(K_i)^{\frac{1}{2}}}$$

$$\left[V_O^{\bullet}\right] = \frac{K_s^{'} (K_i)^{\frac{1}{2}}}{K_a R}$$

$\left[e^{'}\right]$ and $\left[h^{\bullet}\right]$ are therefore independent of P_{O_2}. $\left[V_m^{'}\right]$ increases while $\left[V_O^{\bullet}\right]$ decreases with P_{O_2}

CASE B

Internal disorder predominates (e.g Schottky) i.e $K_s' > K_i$ so that electroneutrality is preserved by

$$[V_m'] = [V_o^\bullet]$$

and the concentrations of various defects are given by

$$[V_m'] = [V_o^\bullet] = (K_s')^{\frac{1}{2}}$$

$$[h^\bullet] = \frac{K_a R}{(K_s')^{\frac{1}{2}}}$$

$$[e'] = \frac{K_i (K_s')^{\frac{1}{2}}}{K_a R}$$

$[V_m']$ and $[V_o^\bullet]$ are independent of P_{O_2}. $[h^\bullet]$ increases while $[e']$ decreases with P_{O_2}

APPENDIX III

DERIVATION OF PARABOLIC GROWTH RATE USING AN ELECTROCHEMICAL MODEL

The reacting system is considered to be an electrochemical cell in which the oxide scale serves as an electrolyte for the ionic transport and as a circuit for transport of electrons.

The cathodic reaction at the oxide/atmosphere interface is represented by:

$$O_2 + 2e^- \longrightarrow O^{2-}$$

and the anodic reaction at the metal/oxide interface is represented by

$$Me \longrightarrow Me^{2+} + 2e$$

The total resistance ,R, (ionic plus electronic) of a film with area A cm^2 and thickness y cm

$$R = R_{ionic} + R_{electronic}$$

If K is specific conductivity, then

$$R = \left[\frac{\tau_a + \tau_c + \tau_e}{(\tau_a + \tau_c) K} + \frac{\tau_a + \tau_c + \tau_e}{\tau_e K} \right] \frac{y}{A}$$

where τ_a , τ_c and τ_e are transport numbers of anions, cations and electrons respectively.
Since $\tau_a + \tau_c + \tau_e = 1$

$$R = \frac{y}{(\tau_a + \tau_c)\ \tau_e\ A K}$$

Providing Ohms law is obeyed then the current , i , flowing through the cell is

$$i = \frac{E\ (\tau_a + \tau_c)\ \tau_e\ K\ A}{y}$$

where E is the EMF of the cell
A current flowing for dt seconds produces i.dt coulombs
These will produce i.dt.J/ F volume of oxide, where J is equivalent weight of oxide, ρ = density of oxide, and F = Faraday constant
In dt seconds the volume of oxide produced = d y . A
hence,

$$dy = \frac{i.dt.J}{\rho\ F\ A}$$

substituting for i

$$\frac{dy}{dt} = \frac{E\ (\tau_a + \tau_c)\ \tau_e K\ J}{\rho\ F\ y}$$

From this

$$\frac{dy}{dt} = \frac{k}{y}$$

where k is a constant

and

$$y^2 = kt$$

APPENDIX IV

The equations describing the oxidation kinetics in moist oxygen (P_{H_2O} = 0.03 atms) and dry oxygen at 1003 K (730C) of samples obtained from

1) normal high purity aluminium (Billet A)
2) further purified high purity aluminium Billet B, Billet C, and Billet D
3) commercial purity aluminium

are given in Table A IV

All equations except for those corresponding to curves CP_{d1}, CP_{d2}, and CP_{d3} were obtained using a computer programme supplied with Hewlett Packard micro-computer, (model HP 9845).

The equations describing curves CP_{d1}, CP_{d2}, and CP_{d3} were derived. These equations describe the kinetics during $t < 15$ mins when the kinetics conform to the parabolic growth law.

TABLE A IV

CURVE		EQUATION
A_{w1}	Fig 63a	$m = 7.237 \times 10^{-6} t^3 - 0.005 t^2 + 0.108 t + 0.056$
A_{w2}	Fig 63a	$m = -2.24 \times 10^{-9} t^6 + 4.291^{-7} \times 10^{-7} t^5 - 3.237 \times 10^{-5} t^4 + 1.224 \times 10 t^3 - 2.431 \times 10^{-2} t^2 + 2.407 \times 10^{-1} t - 1.615 \times 10^{-1}$
A_{w3}	Fig 63a	$m = 1.327 \times 10^{-8} t^5 - 2.372 \times 10^{-6} t^4 + 1.643 \times 10^{-4} t^3 - 5.569 \times 10^{-3} t^2 + 9.453 \times 10^{-2} t + 2.035 \times 10^{-2}$
A_{w4}	Fig 63a	$m = -6.456 \times 10^{-9} t^6 + 9.406 \times 10^{-7} t^5 - 5.383 \times 10^{-5} t^4 + 1.532 \times 10^{-3} t^3 - 2.295 \times 10^{-2} t^2 + 1.873 \times 10^{-1} t - 3.144 \times 10^{-2}$
D_{w1}	Fig 65a	$m = -1.865 \times 10^{-6} t^4 + 1.585 \times 10^{-4} t^3 - 5.452 \times 10^{-3} t^2 - 9.551 \times 10^{-2} t - 5.892 \times 10^{-2}$
D_{w2}	Fig 65a	$m = 1.744 \times 10^{-5} t^3 - 1.725 \times 10^{-3} t^2 + 5.687 \times 10^{-2} t + 3.047 \times 10^{-2}$
D_{w3}	Fig 65a	$m = -7.399 \times 10^{-7} t^4 + 8.916 \times 10^{-5} t^3 - 4.071 \times 10^{-3} t^2 + 8.583 \times 10^{-2} t - 4.227 \times 10^{-2}$
CP_{w1}	Fig 66a	$m = -1.905 \times 10^{-7} t^4 + 3.841 \times 10^{-5} t^3 - 2.822 \times 10^{-3} t^2 + 9.004 \times 10^{-2} t - 5.899 \times 10^{-2}$
CP_{w2}	Fig 66a	$m = -9.903 \times 10^{-8} t^4 + 2.326 \times 10^{-5} t^3 - 1.890 \times 10^{-3} t^2 + 6.444 \times 10^{-2} t + 8.579 \times 10^{-2}$
CP_{w3}	Fig 66a	$m = -1.543 \times 10^{-7} t^4 + 2.431 \times 10^{-5} t^3 - 1.597 \times 10^{-3} t^2 + 5.774 \times 10^{-2} t - 1.426 \times 10^{-2}$

TABLE A IV (contd.)

CURVE		EQUATION
A_{d1}	Fig 72a	$m= 2.767 \times 10^{-13} t^7 - 8.832 \times 10^{-11} t^6 + 1.161 \times 10^{-8} t^5 - 8.126 \times 10^{-7} t^4 + 3.266 \times 10^{-5} t^3 - 7.595 \times 10^{-4} t^2 + 1.005 \times 10^{-2} t + 4.999 \times 10^{-4}$
A_{d2}	Fig 72a	$m= 2.081 \times 10^{-7} t^3 - 4.275 \times 10^{-6} t^2 + 2.963 \times 10^{-3} t + 2.576 \times 10^{-3}$
A_{d3}	Fig 72a	$m= -9.669 \times 10^{-9} t^4 + 1.986 \times 10^{-6} t^3 - 1.478 \times 10^{-4} t^2 + 4.989 \times 10^{-3} t - 6.312 \times 10^{-3}$
A_{d4}	Fig 72a	$m= -3.956 \times 10^{-9} t^4 + 9.650 \times 10^{-7} t^3 - 8.611 \times 10^{-5} t^2 + 3.531 \times 10^{-3} t - 4.109 \times 10^{-3}$
B_{d1}	Fig 73a	$m= -1.193 \times 10^{-8} t^4 + 2.195 \times 10^{-6} t^3 - 1.442 \times 10^{-4} t^2 + 4.101 \times 10^{-3} t + 7.701 \times 10^{-4}$
B_{d2}	Fig 73a	$m= -4.349 \times 10^{-9} t^4 + 9.012 \times 10^{-7} t^3 - 6.774 \times 10^{-5} t^2 + 2.352 \times 10^{-3} t + 8.527 \times 10^{-3}$
C_{d1}	Fig 74a	$m= 5.742 \times 10^{-10} t^5 - 1.218 \times 10^{-7} t^4 + 9.762 \times 10^{-6} t^3 - 3.645 \times 10^{-4} t^2 + 6.344 \times 10^{-3} t - 1.318 \times 10^{-2}$
C_{d2}	Fig 74a	$m= -2.249 \times 10^{-11} t^6 + 5.5 \times 10^{-9} t^5 - 5.302 \times 10^{-7} t^4 + 2.538 \times 10^{-6} t^3 - 6.337 \times 10^{-4} t^2 + 8.017 \times 10^{-3} t - 1.863 \times 10^{-2}$
D_{d1}	Fig 75a	$m= 6.819 \times 10^{-8} t^3 - 1.022 \times 10^{-5} t^2 + 5.773 \times 10^{-3} t + 2.534 \times 10^{-3}$
D_{d2}	Fig 74a	$m= 7.905 \times 10^{-8} t^3 - 1.175 \times 10^{-5} t^2 + 6.765 \times 10^{-4} t + 1.194 \times 10^{-3}$
D_{d3}	Fig 74a	$m= 2.707 \times 10^{-7} t^3 - 2.958 \times 10^{-5} t^2 + 1.076 \times 10^{-3} t + 8.146 \times 10^{-3}$
D_{d4}	Fig 74a	$m= 1.011 \times 10^{-7} t^3 - 1.298 \times 10^{-5} t^2 + 5.881 \times 10^{-4} t + 1.092 \times 10^{-2}$
CP_{d1}	Fig 77a	$m= (1.25 \times 10^{-5} t)^{\frac{1}{2}}$
CP_{d2}	Fig 77a	$m= (4.50 \times 10^{-6} t)^{\frac{1}{2}}$
CP_{d3}	Fig 77a	$m= (3.33 \times 10^{-6} t)^{\frac{1}{2}}$

TABLE 1 - COMPARISON OF ENERGY AND METAL PRICES

YEAR	OIL P/LITRE	ELECTRICITY P/Kwh	METAL £/tonne (LM6)
1970	0.835	0.654	266
1980	10.120	2.8	1000

TABLE 2 - APPROXIMATE COST CALCULATION FOR MELTING 1 TONNE OF ALUMINIUM.
(POSITION AT THE END OF 1974)
MITTMAN[2]

FURNACE		CRUCIBLE		ROTARY		HEARTH		MEDIUM FREQUENCY CURRENT
TYPE OF HEATING		OIL	NATURAL GAS	OIL	NATURAL GAS	OIL	NATURAL GAS	
1	Capital cost (DM)	6.5	6.5	6.0	6.0	6.7	6.7	15
2	Lining cost (DM)	7.6	7.6	2.9	2.9	5.0	5.0	2.50
3	Energy cost (DM)	40.0	47.3	20.0	24.3	25.0	31.0	47.60
4	Additional cost (DM/$_t$)	16.6	16.6	0.5	0.5	0.32	0.32	14
5	Sum of 1 to 4	70.7	78	29.4	33.7	37.02	43.02	79.1
6	Melting losses DM/$_t$	22.0	22.0	88.0	88.0	65.0	65.0	22.0
	Total sum of (5+6) DM/$_t$	92.7	100	117.4	121.7	102.0	108.0	101. 1.

TABLE 3 - COMPOSITION OF SKIM FROM NON-MAGNESIUM CONTAINING MELT

Constituents	Quantity present in skim
Aluminium	20 - 80%
Aluminium Oxides	80 - 20%
Aluminium Carbides	2%
Aluminium Nitrides	2%
Other Metals and Components	2 - 5%

TABLE 4 - Quantity of Skim Generated

Process	Total Skim Generated % of Metal Throughput
Primary Smelter (making range of ingot products)	1%
Secondary Smelter:	
(a) Clean process scrap	2 - 5%
(b) Loss grade scrap (painted, foil etc)	20 - 30%

TABLE 5

Temperature ^{o}C	Oxidising Conditions (Pressure)	Time (Hours)	Morphology
600	10^{-7} atmospheres	6	Acicular crystals
600	1 atmosphere	1	Contiguous crystals
550	10^{-9} atmospheres	20	Unassociated random 'needles'
550	1 atmosphere	1	Contiguous crystals
450	10^{-7} atmospheres	20	'Amorphous') occasional) indication
450	1 atmosphere	1	'Amorphous') of crystalline material

Table 6 NOMENCLATURE OF OXIDES AND HYDROXIDES OF ALUMINIUM

Mineralogical name	USA Alcoa	British	French	Germany
Gibbsite	α-$Al_2O_3\,3H_2O$	γ-$Al_2O_3\,3H_2O$		$Al(OH)_3$
Bayerite	β-$Al_2O_3\,3H_2O$	α-$Al_2O_3\,3H_2O$		$Al(OH)_3$
Nordstrandite				$Al(OH)_3$
Boehmite	α-$Al_2O_3\,H_2O$	γ-$Al_2O_3\,H_2O$		Al OOH
Diaspore	β-$Al_2O_3\,H_2O$			
	Chi	Chi+Gamma	Chi+Gamma	Chi
	Eta	Gamma	Eta	Eta
	Gamma	Delta	Gamma	Gamma
	Delta	Delta + Theta	Delta	Delta
	Kappa	Kappa + Theta	Kappa + Theta	Kappa
Corundum	Alpha	Alpha	Alpha	Alpha

TABLE 7 - RATIO OF ION RADII AND CO-ORDINATION NUMBER FOR SOME PURE OXIDES

Oxide	Cation Radius (nm)	% Ionic Bond	Radius Ratio Cation/Anion	Co-ordination Number
CaO	0.099	80	0.71	6
MnO	0.080		0.57	6
FeO	0.075		0.54	6
MgO	0.065	75	0.46	6
Al_2O_3	0.050	65	0.36	4
SiO_2	0.051	50	0.29	4

TABLE 8 X- RAY DIFFRACTION DATA FOR $\alpha - Al_2O_3$ AND $\gamma - Al_2O_3$ (ASTM diffraction file)

$\alpha - Al_2O_3$		$\gamma - Al_2O_3$	
d spacing nm	Intensity	d spacing nm	Intensity
0.3479	74	0.455	10
0.2552	92	0.2782	15
0.2379	42	0.2387	35
0.2165	1	0.2283	20
0.2085	100	0.1977	100
.1740	43	0.1521	10
0.1601	81	0.1398	90
0.1546	3	0.1142	5
0.1510	7	0.1029	3
0.1404	35	0.0989	5
0.1374	48	0.0884	5
0.1276	2	0.0807	15
0.1289	16		
0.1190	6		

The ASTM diffraction file uses the nomenclature favoured by Rooksby[10] and Day and Hill[11] so that δ-Al_2O_3 in Table 8 is tabulated as γ-Al_2O_3 in Table 9 (ALCOA system)

Table 9 ANALYSIS OF DIFFRACTION PATTERN SHOWN IN FIGURE 44b

Ring number	Experimental values for d spacings		Recommended values for d spacings ASTM x-ray diffraction file	
	Measured ring diameter cms	Calculated d spacings nm	d spacings nm	Phase
1	5.90	0.29	0.2782	η -Al_2O_3
2	6.85	0.25	0.2552	α -Al_2O_3
3	7.15	0.24	{0.2379 0.2387}	α η > Al_2O_3
4	7.80	0.22	0.2282	η -Al_2O_3
5	8.35	0.21	0.2085	α -Al_2O_3
6	8.85	0.19	0.1977	η -Al_2O_3
7	10.15	0.17	0.1740	α -Al_2O_3
8	10.85	0.16	0.1601	α -Al_2O_3
9	12.00	0.14	0.1398	η -Al_2O_3
10	13.90	0.13	0.1289	α -Al_2O_3
11	14.50	0.12	0.1142	η -Al_2O_3

TABLE 10 FREE ATOM SUBSHELL BINDING ENERGIES

Z		1s	2s	2p1/2	2p3/2	3s	3p1/2	3p3/2	3d3/2	3d5/2	4s	4p1/2	4p3/2	4d3/2	4d5/2	4f5/2	4f7/2	5s	5p1/2	5p3/2	5d3/2	5d5/2	5f5/2	5f7/2	6s	6p1/2	6p3/2	6d3/2 5/2	7s
1	H	13.60																										
2	He	24.59																										
3	Li	58	5.392																									
4	Be	115	9.322																									
5	B	192	12.93	8.298																								
6	C	288	16.59	11.26																								
7	N	403	20.33	14.53																								
8	O	538	28.48	13 62																								
9	F	694	37.85	17.42																								
10	Ne	870.1	48.47	21.66	21.56																							
11	Na	1075	66	34	34	5.139																						
12	Mg	1308	92	54	54	7.646																						
13	Al	1564	121	77	77	10.62	5.986																					
14	Si	1844	154	104	104	13.46	8 151																					
15	P	2148	191	135	134	16.15	10 49																					
16	S	2476	232	170	168	20.20	10 36																					
17	Cl	2829	277	208	206	24.54	12.97																					
18	Ar	3206.3	326.5	250 6	248.5	29.24	15.94	15.76																				
19	K	3610	381	299	296	37	19	18.7			4 341																	
20	Ca	4041	441	353	349	46	28	28			6.113																	
21	Sc	4494	503	408	403	55	33	33	8		6.540																	
22	Ti		567	465	459	64	39	38	8		6.820																	
23	V		633	525	518	72	44	43	8		6.740																	
24	Cr		702	589	580	80	49	48	8.25		6.765																	
25	Mn		755	656	645	89	55	53	9		7.434																	
26	Fe		851	726	713	98	61	59	9		7.870																	
27	Co		931	800	785	107	68	66	9		7.864																	
28	Ni		1015	877	860	117	75	73	10	10	7.635																	
29	Cu		1103	958	938	127	82	80	11	10.4	7.726																	
30	Zn		1198	1047	1024	141	94	91	12	11.2	9.394																	
31	Ga		1302	1146	1119	162	111	107	21	20	11	6.00																
32	Ge		1413	1251	1220	184	130	125	33	32	14.3	7.90																
33	As		1531	1362	1327	208	151	145	46	45	17	9.81																
34	Se		1656	1479	1439	234	173	166	61	60	20.15	9.75																
35	Br		1787	1602	1556	262	197	189	77	76	23.80	11.85																
36	Kr		1924.6	1730.9	1678.4	292.8	222.2	214.4	95.0	93.8	27.51	14.65	14															
37	Rb		2068	1867	1807	325	251	242	116	114	32	16	15.3					4.18										
38	Sr		2219	2010	1943	361	283	273	139	137	40	23	22					5.69										
39	Y		2375	2158	2083	397	315	304	163	161	48	30	29	6.38				6.48										
40	Zr		2536	2311	2227	434	348	335	187	185	56	35	33	8.61				6.84										
41	Nb		2702	2469	2375	472	382	367	212	209	62	40	38	7.17				6.88										
42	Mo		2872	2632	2527	511	416	399	237	234	68	45	42	8.56				7.10										
43	Tc		3048	2800	2683	551	451	432	263	259	74	49	45	8.6				7.28										
44	Ru		3230	2973	2844	592	488	466	290	286	81	53	49	8.50				7.37										
45	Rh		3418	3152	3010	634	526	501	318	313	87	58	53	9.56				7.46										
46	Pd		3611	3337	3180	677	565	537	347	342	93	63	57	8 78	8.34													
47	Ag		3812	3530	3357	724	608	577	379	373	101	69	63	11	10			7.58										
48	Cd		4022	3732	3542	775	655	621	415	408	112	78	71	14	13			8.99										
49	In		4242	3943	3735	830	707	669	455	447	126	90	82	21	20			10	5.79									
50	Sn		4469	4160	3933	888	761	719	497	489	141	102	93	29	28			12	7.34									
51	Sb			4385	4137	949	817	771	542	533	157	114	104	38	37			15	8.64									
52	Te				4347	1012	876	825	589	578	174	127	117	48	46			17.84	9.01									
53	I					1078	937	881	638	626	193	141	131	58	56			20.61	10.45									
54	Xe					1148.7	1002.1	940.6	689.0	676.4	213.2	157	145.5	69.5	67.5			23.39	13.43	12.13								
55	Cs					1220	1068	1000	742	728	233	174	164	81	79			25	14	12.3								
56	Ba					1293	1138	1063	797	782	254	193	181	94	92			31	18	16								
57	La					1365	1207	1124	851	834	273	210	196	105	103			36	22	19								
58	Ce					1437	1275	1184	903	885	291	225	209	114	111	6		39	25	22	5.75							
59	Pr					1509	1342	1244	954	934	307	238	220	121	117	6		41	27	24	6							
60	Nd					1580	1408	1303	1005	983	321	250	230	126	122	6		42	28	25								
61	Pm					1653	1476	1362	1057	1032	335	261	240	131	127	6		43	28	25								
62	Sm					1728	1546	1422	1110	1083	349	273	251	137	132	6		44	29	25								
63	Eu					1805	1618	1484	1164	1135	364	286	262	143	137	6		45	30	26								
64	Gd					1884	1692	1547	1220	1189	380	300	273	150	143	6		46	31	27	6							
65	Tb					1965	1768	1612	1277	1243	398	315	285	157	150	6		48	32	28	6							
66	Dy					2048	1846	1678	1335	1298	416	331	297	164	157	6		50	33	28								
67	Ho					2133	1926	1746	1395	1354	434	348	310	172	164	6		52	34	29								
68	Er					2220	2008	1815	1456	1412	452	365	323	181	172	6		54	35	30								
69	Tm					2309	2092	1885	1518	1471	471	382	336	190	181	7		56	36	30								
70	Yb					2401	2174	1950	1580	1531	490	399	349	200	190	8	7	58	37	31								
71	Lu					2499	2270	2032	1640	1596	514	420	366	213	202	13	12	62	39	32	6.6							
72	Hf					2604	2369	2114	1720	1665	542	444	386	229	217	21	20	68	43	35	7.0							
73	Ta					2712	2472	2197	1796	1737	570	469	407	245	232	30	28	74	47	38	8 3							
74	W					2823	2577	2283	1874	1811	599	495	428	261	248	38	36	80	51	41	9.0							
75	Re					2937	2686	2371	1953	1887	629	522	450	278	264	47	45	86	56	45	9.6							
76	Os					3054	2797	2461	2035	1964	660	551	473	295	280	56	54	92	61	49	9.6							
77	Ir					3175	2912	2554	2119	2044	693	581	497	314	298	67	64	99	66	53	9.6							
78	Pt					3300	3030	2649	2206	2126	727	612	522	335	318	78	75	106	71	57	9.6							
79	Au					3430	3153	2748	2295	2210	764	645	548	357	339	91	87	114	76	61	12.5	11.1						
80	Hg					3567	3283	2852	2390	2300	806	683	579	382	363	107	103	125	85	68	14	12						
81	Tl					3710	3420	2961	2490	2394	852	726	615	411	391	127	123	139	98	79	21	19						
82	Pb					3857	3560	3072	2592	2490	899	769	651	441	419	148	144	153	111	90	27	25						
83	Bi					4007	3704	3185	2696	2588	946	813	687	472	448	170	165	167	125	101	34	32						
84	Po					4161	3852	3301	2802	2687	994	858	724	503	478	193	187	181	139	112	41	38						
85	At					4320	4005	3420	2910	2788	1044	904	761	535	508	217	211	196	153	123	48	44						
86	Rn					4483	4162	3452	3109	2890	1096	951	798	567	538	242	235	212	167	134	55	51						
87	Fr						4324	3666	3134	2998	1153	1003	839	603	572	268	260	231	183	147	65	61						
88	Ra						4491	3793	3254	3111	1214	1060	884	642	609	296	287	253	201	161	77	73						
89	Ac							3921	3374	3223	1274	1116	928	680	645	322	313	274	218	174	88	83						
90	Th							4049	3494	3335	1333	1171	970	717	679	347	338	293	233	185	97	91						
91	Pa							4178	3613	3446	1390	1225	1011	752	712	372	362	312	248	195	104	97	6					
92	U							4308	3733	3557	1446	1278	1050	785	743	396	386	329	261	203	110	101	6					
93	Np							4440	3854	3669	1504	1331	1089	819	774	421	410	346	274	211	116	106	6					
94	Pu								3977	3783	1563	1384	1128	853	805	446	434	356	287	219	122	111	6					
95	Am								4102	3898	1623	1439	1167	887	836	467	452	355	301	220	123	112	6					
96	Cm								4236	4014	1664	1493	1194	919	864	494	479	384	314	239	126	119	11					
97	Bk								4366	4133	1729	1554	1236	955	898	520	504	401	329	248	142	124	12					
98	Cf								4492	4247	1789	1610	1273	987	925	546	529	412	338	251	142	129	9					
99	Es									4369	1857	1674	1316	1024	959	573	554	429	353	260	148	135	9					
100	Fm									4498	1933	1746	1366	1068	1000	606	587	453	375	275	160	145	15					
101	Md										1998	1807	1404	1100	1029	627	607	464	384	278	160	144	11					
102	No										2071	1876	1449	1139	1064	654	633	483	400	287	166	149	14	11				
103	Lw										2153	1954	1501	1186	1106	689	666	509	424	303	178	160	20	17				
104											2237	2034	1554	1233	1149	724	700	535	448	318	190	171	26	23				
105											2324	2117	1609	1281	1193	760	735	562	473	335	203	183	32	29				
106											2413	2202	1664	1330	1238	797	770	590	499	350	216	194	39	35				

Z		4p1/2	4p3/2	4d3/2	4d5/2	4f5/2	4f7/2	5s	5p1/2	5p3/2	5d3/2	5d5/2	5f5/2	5f7/2	6s	6p1/2	6p3/2	6d3/2 5/2	7s
37	Rb	4.18													3.89				
38	Sr	5.69													5.21				
39	Y	6.48													5.58				
40	Zr	6.84													5.65				
41	Nb	6.88													5.42				
42	Mo	7.10													5.49				
43	Tc	7.28													5.55				
44	Ru	7.37													5.63				
45	Rh	7.46													5.68				
46	Pd														6.16				
47	Ag	7.58													5.85				
48	Cd	8.99													5.93				
49	In	10	5.79												6.02				
50	Sn	12	7.34												6.10				
51	Sb	15	8.64												6 18				
52	Te	17.84	9.01												6.25				
53	I	20.61	10.45												7.0				
54	Xe	23.39	13.43	12.13											7.3				
55	Cs	25	14	12.3											7.9				
56	Ba	31	18	16											8.0				
57	La	36	22	19											7.9				
58	Ce	39	25	22	5.75										8.5				
59	Pr	41	27	24	6										9.1				
60	Nd	42	28	25											9.0				
61	Pm	43	28	25											9.23				
62	Sm	44	29	25											10.4				
63	Eu	45	30	26											8	6.11			
64	Gd	46	31	27	6										10	7.42			
65	Tb	48	32	28	6										12	7.29			
66	Dy	50	33	28											15	8.43			
67	Ho	52	34	29											19	11	9.3		
68	Er	54	35	30											24	14	10.7		
69	Tm	56	36	30											33	19	14		4.0
70	Yb	58	37	31											40	25	19		5.28
71	Lu	62	39	32	6.6										45	29	22	5.7	6.3
72	Hf	68	43	35	7.0										50	33	25	6	6
73	Ta	74	47	38	8 3										50	32	24	6	6
74	W	80	51	41	9.0										52	34	24	6.1	6
75	Re	86	56	45	9.6										54	35	25	6	6
76	Os	92	61	49	9.6										53	34	23		6
77	Ir	99	66	53	9.6										54	44	36		6.0
78	Pt	106	71	57	9.6										60	39	27	5	6
79	Au	114	76	61	12.5	11.1									63	41	27	4	6
80	Hg	125	85	68	14	12									61	39	25		6
81	Tl	139	98	79	21	19									63	40	25		6
82	Pb	153	111	90	27	25									69	45	29	4	7
83	Bi	167	125	101	34	32									67	43	26		6
84	Po	181	139	112	41	38									69	44	26		6
85	At	196	153	123	48	44									76	49	30	4	7
86	Rn	212	167	134	55	51									82	55	33	5	8
87	Fr	231	183	147	65	61									89	60	36	6	8
88	Ra	253	201	161	77	73									96	65	39	7	9
89	Ac	274	218	174	88	83													
90	Th	293	233	185	97	91													
91	Pa	312	248	195	104	97	6												
92	U	329	261	203	110	101	6												
93	Np	346	274	211	116	106	6												
94	Pu	356	287	219	122	111	6												
95	Am	355	301	220	123	112	6												
96	Cm	384	314	239	126	119	11												
97	Bk	401	329	248	142	124	12												
98	Cf	412	338	251	142	129	9												
99	Es	429	353	260	148	135	9												
100	Fm	453	375	275	160	145	15												
101	Md	464	384	278	160	144	11												
102	No	483	400	287	166	149	14	11											
103	Lw	509	424	303	178	160	20	17											
104		535	448	318	190	171	26	23											
105		562	473	335	203	183	32	29											
106		590	499	350	216	194	39	35											

		Kinetic energy eV
80	MERCURY	76
4	BERYLLIUM	104
38	STRONTIUM	110
15	PHOSPHOROUS	120
39	YTTRIUM	127
65	TERBIUM	146
40	ZIRCONIUM	147
79	GOLD	150
66	DYSPROSIUM	151
16	SULPHUR	152
67	HOLMIUM	157
68	ERBIUM	163
69	THULIUM	166
41	NIOBIUM	167
78	PLATINUM	168
74	TUNGSTEN	169
70	YTTERBIUM	170
77	IRIDIUM	171
75	RHENIUM	176
71	LUTETIUM	177
5	BORON	179
73	TANTALUM	179
17	CHLORINE	181
37	RUBIDIUM	183
72	HAFNIUM	185
41	NIOBIUM	197
18	ARGON	215
75	RHENIUM	218
42	MOLYBDENUM	221
77	IRIDIUM	229
78	PLATINUM	237
64	GADOLINIUM	238
79	GOLD	239
19	POTASSIUM	252
6	CARBON	272
44	RUTHENIUM	273
20	CALCIUM	291
63	EUROPIUM	293
45	RHODIUM	302
70	YTTERBIUM	308
71	LUTETIUM	319
72	HAFNIUM	329
46	PALLADIUM	330
71	LUTETIUM	330
72	HAFNIUM	339
21	SCANDIUM	340
73	TANTALUM	342
74	TUNGSTEN	350
47	SILVER	356
48	CADMIUM	376
7	NITROGEN	381
22	TITANIUM	387
49	INDIUM	404
22	TITANIUM	418
50	TIN	430
23	VANADIUM	437
51	ANTIMONY	454
23	VANADIUM	473
52	TELLURIUM	483
24	CHROMIUM	489
8	OXYGEN	510
53	IODINE	511
24	CHROMIUM	529
55	CESIUM	563
55	CESIUM	575
56	BARIUM	584
25	MANGANESE	589
56	BARIUM	600
57	LANTHANUM	625
9	FLUORINE	650
26	IRON	651
58	CERIUM	681
59	PRASEODYMIUM	699
60	NEODYMIUM	730
27	COBALT	775
62	SAMARIUM	814
28	NICKEL	848
63	EUROPIUM	858
64	GADOLINIUM	895
29	COPPER	920
65	TERBIUM	933
66	DYSPROSIUM	976
11	SODIUM	990
30	ZINC	994
68	ERBIUM	1057
31	GALLIUM	1070
34	SELENIUM	1093
69	THULIUM	1096
33	ARSENIC	1117
66	DYSPROSIUM	1136
70	YTTERBIUM	1141
32	GERMANIUM	1147
35	BROMINE	1172
67	HOLMIUM	1175
12	MAGNESIUM	1186
33	ARSENIC	1226
34	SELENIUM	1315
13	ALUMINIUM	1396
35	BROMINE	1396
69	THULIUM	1449
70	YTTERBIUM	1514
37	RUBIDIUM	1565
71	LUTETIUM	1573
14	SILICON	1619
72	HAFNIUM	1624
38	STRONTIUM	1640
73	TANTALUM	1680
74	TUNGSTEN	1735
39	YTTRIUM	1746
75	RHENIUM	1799
40	ZIRCONIUM	1845
77	IRIDIUM	1908
41	NIOBIUM	1949
78	PLATINUM	1967
79	GOLD	2024
42	MOLYBDENUM	2044

Handbook of Auger electron spectroscopy
Physical electronics industries 1972

Table 12a

Curve	Parabolic rate constants k_p $g^2\ cm^{-4}\ sec^{-1}$	Source
A_{w1}	4.6×10^{-11}	Fig 63b
A_{w2}	5.3×10^{-11}	Fig 63b
A_{w3}	2.5×10^{-12}	Fig 63c

Table 12b

Curve	Parabolic rate constants k_p $g^2\ cm^{-4}\ sec^{-1}$	Source
D_{w1}	1.4×10^{-11}	Fig 65b
D_{w2}	1.5×10^{-11}	Fig 65c

Table 12c

Curve	Parabolic rate constants k_p $g^2\ cm^{-4}\ sec^{-1}$	Source
CP_{w1}	4.5×10^{-11}	Fig 66b
CP_{w2}	8.6×10^{-12}	Fig 66c

Table 13a

Curve	Linear rate constants k_l g cm^{-2} sec^{-1}	Source	Parabolic rate constants k_p g^2 cm^{-4} sec^{-1}	Source
A_{d1}	1.1×10^{-6}	Fig 72a	6.9×10^{-13}	Fig 72c
A_{d2}	5×10^{-7}	Fig 72a	5.3×10^{-13}	Fig 72c
A_{d3}	4.6×10^{-8}	Fig 72a	5.7×10^{-13}	Fig 72c
A_{d4}	3.6×10^{-8}	Fig 72a	5.0×10^{-13}	Fig 72c

Table 13b

Curve	Linear rate constants k_l g cm^{-2} sec^{-1}	Source	Parabolic rate constants k_p g^2 cm^{-4} sec^{-1}	Source
B_{d1}	5.4×10^{-8}	Fig 73a	2.5×10^{-13}	Fig 73c
P_{d2}	5.4×10^{-8}	Fig 73a	2.7×10^{-13}	Fig 73c

Table 13c

Curve	Linear rate constants k_l g cm^{-2} sec^{-1}	Source	Parabolic rate constants k_p g^2 cm^{-4} sec^{-1}	Source
C_{d1}	4.5×10^{-8}	Fig 74a	1.1×10^{-13}	Fig 74c
C_{d2}	3.4×10^{-8}	Fig 74a	1.0×10^{-13}	Fig 74c

Table 13d

Curve	Parabolic rate constants k_p g^2 cm^{-4} sec^{-1}	Source
D_{d1}	6.2×10^{-14}	Fig 75b
D_{d2}	6.2×10^{-14}	Fig 75b

Table 13e

Curve	Parabolic rate constants k_p g^2 cm^{-4} sec^{-1}	Source
CP_{d1}	2.1×10^{-13}	Fig 77c
CP_{d2}	7.5×10^{-14}	Fig 77c
CP_{d3}	5.6×10^{-14}	Fig 77c

TABLE 14 - RADII OF IMPURITY IONS AND INTERSTICES IN

$\eta - Al_2O_3$ and $\alpha - Al_2O_3$

Species	Radius (nm)
Aluminium cation	0.050
Calcium cation	0.099
Iron cation	0.075
Copper cation	0.096
Oxygen anion	0.139
Octahedral interstice in $\eta - Al_2O_3$ and $\alpha - Al_2O_3$	0.058
Tetrahedral interstice in $\eta - Al_2O_3$ and $\alpha - Al_2O_3$	0.031

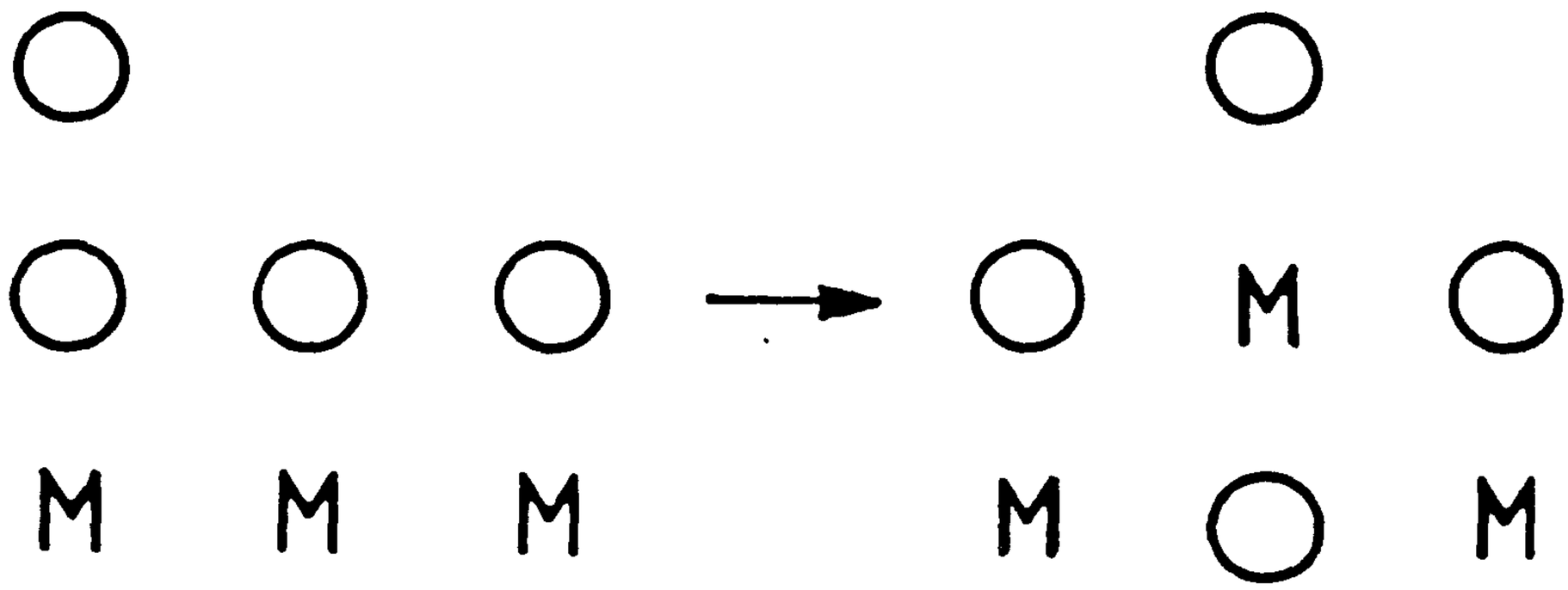

Fig.1 Model of place exchange process(after Felner and Mott)[18]

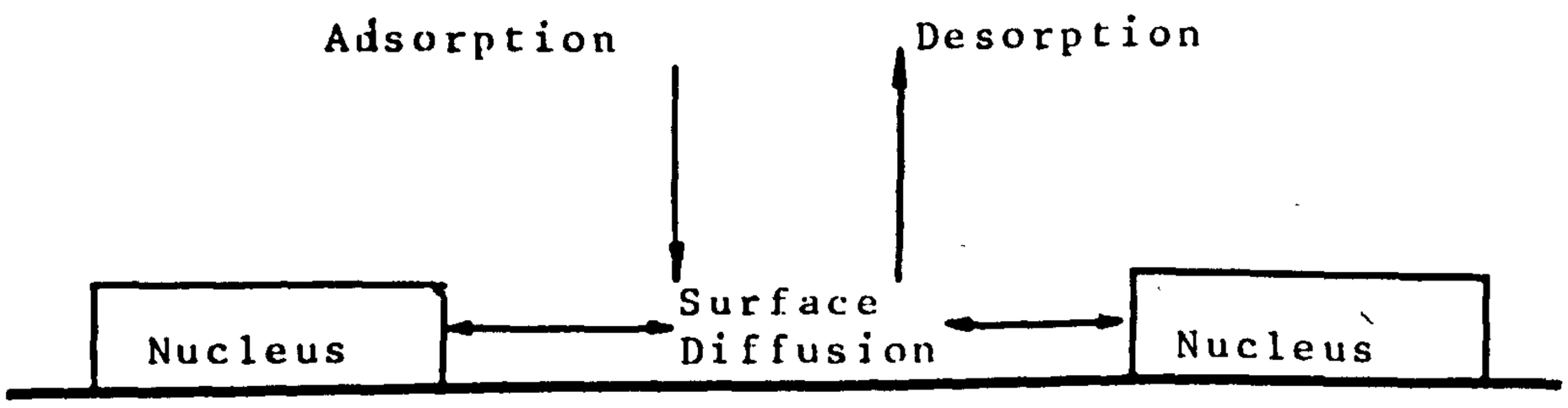

Fig.2. Schematic model of initial oxide formation on magnesium (after Orr)22

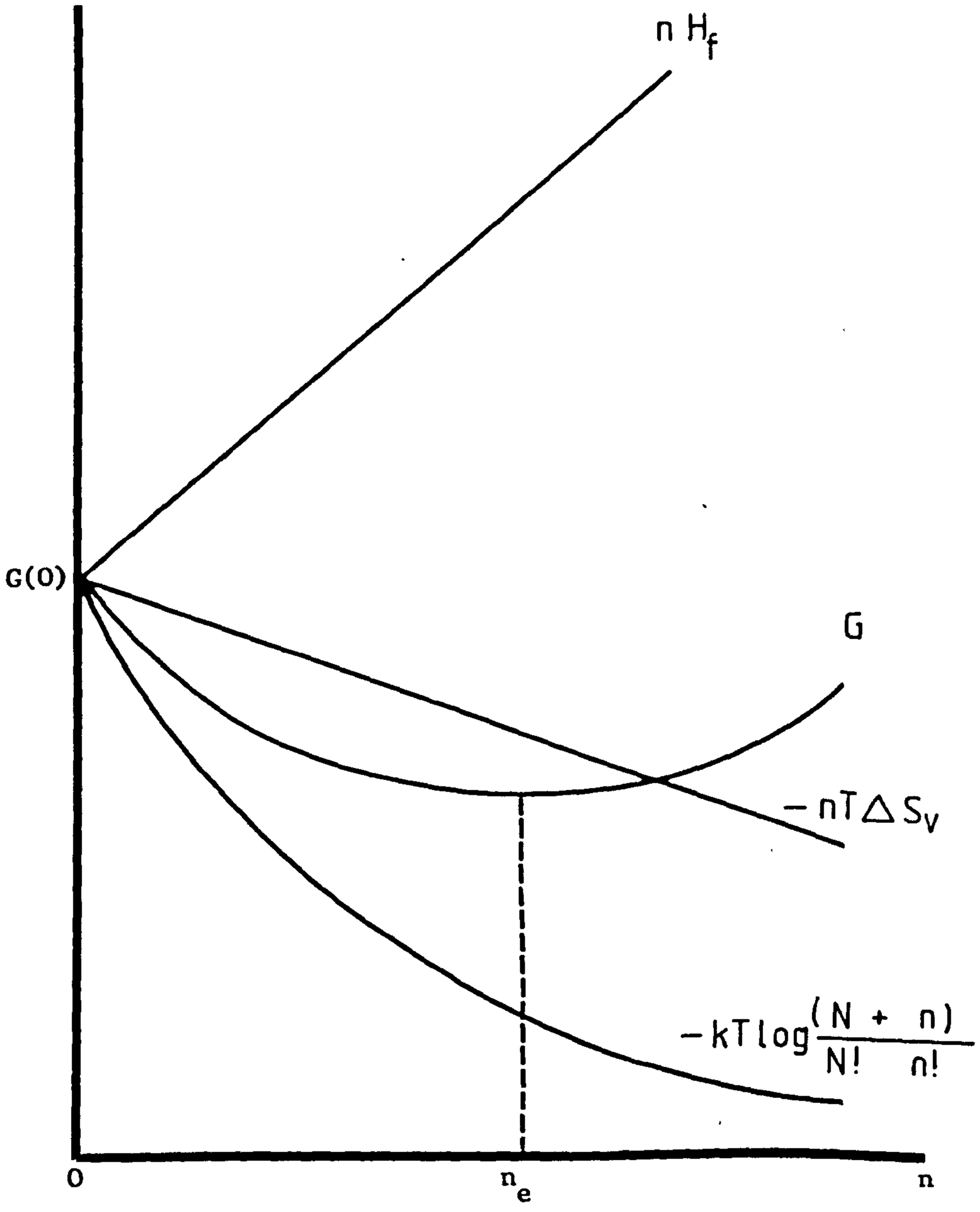

Fig.3. Dependence of Gibbs free energy and its component terms on the concentration of defects.

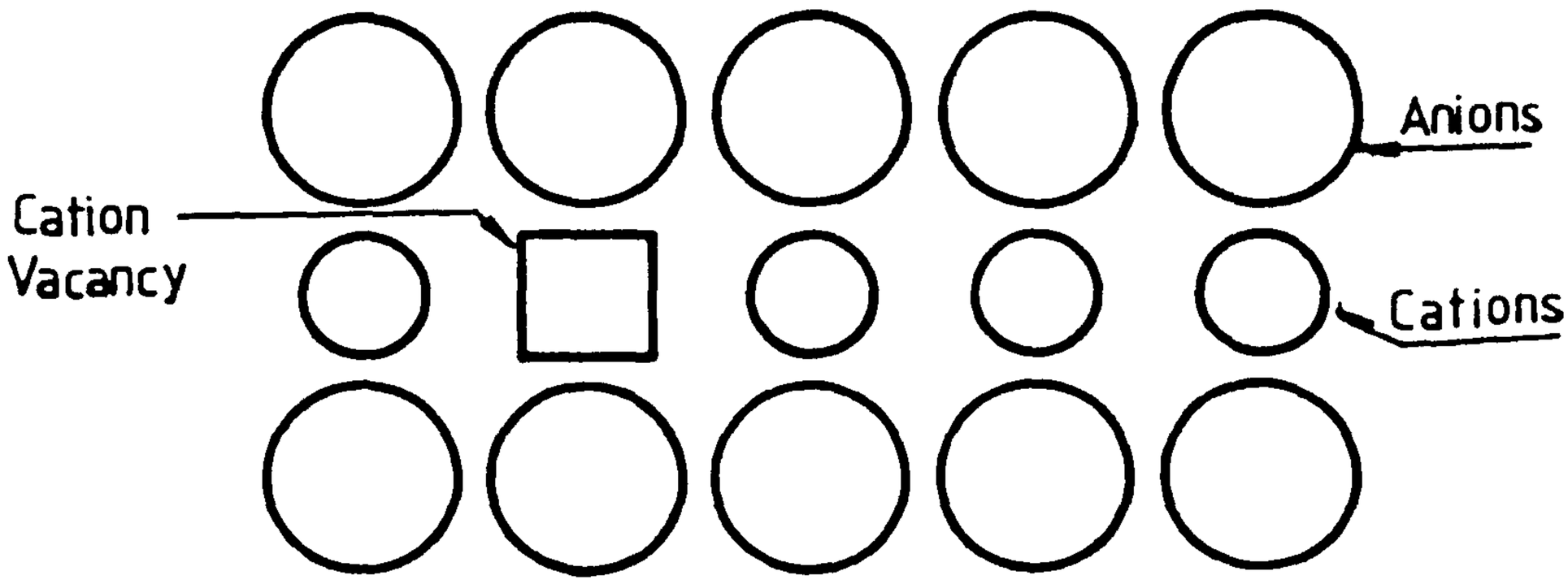

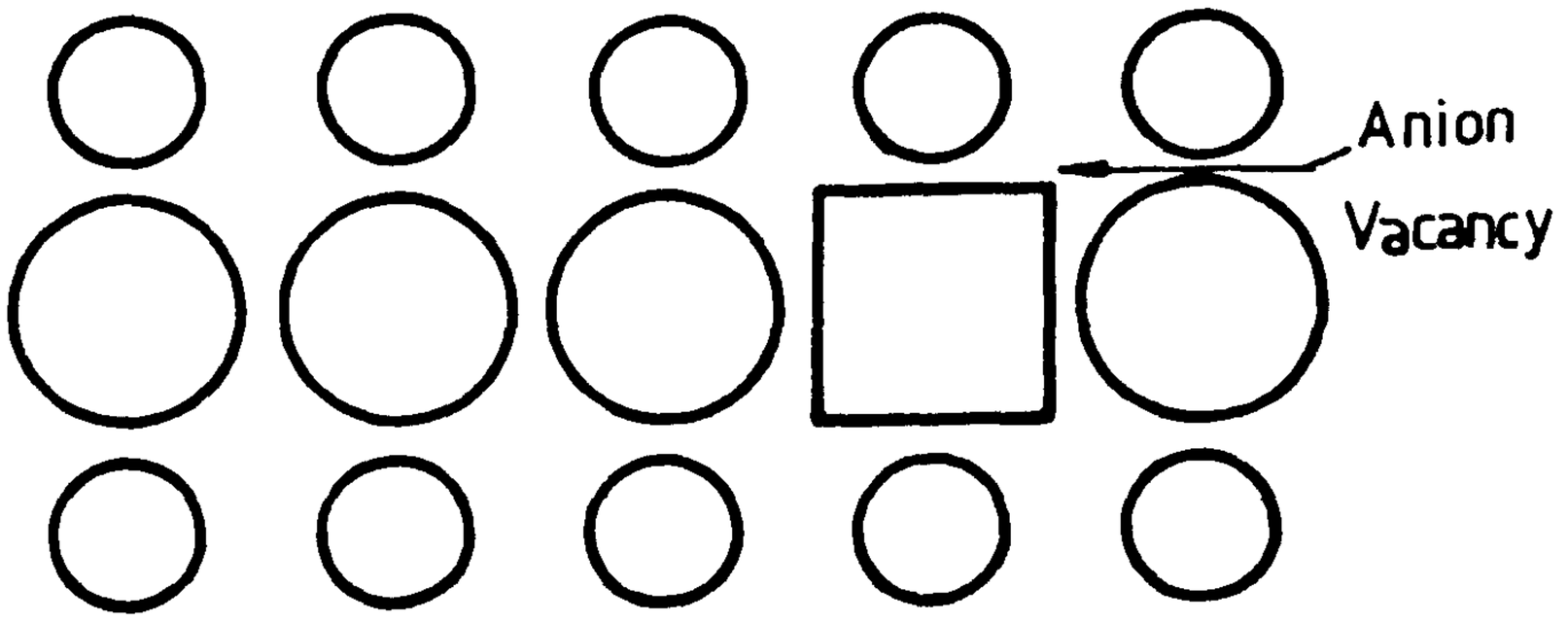

Fig.4. Schematic model of Schottky defect.

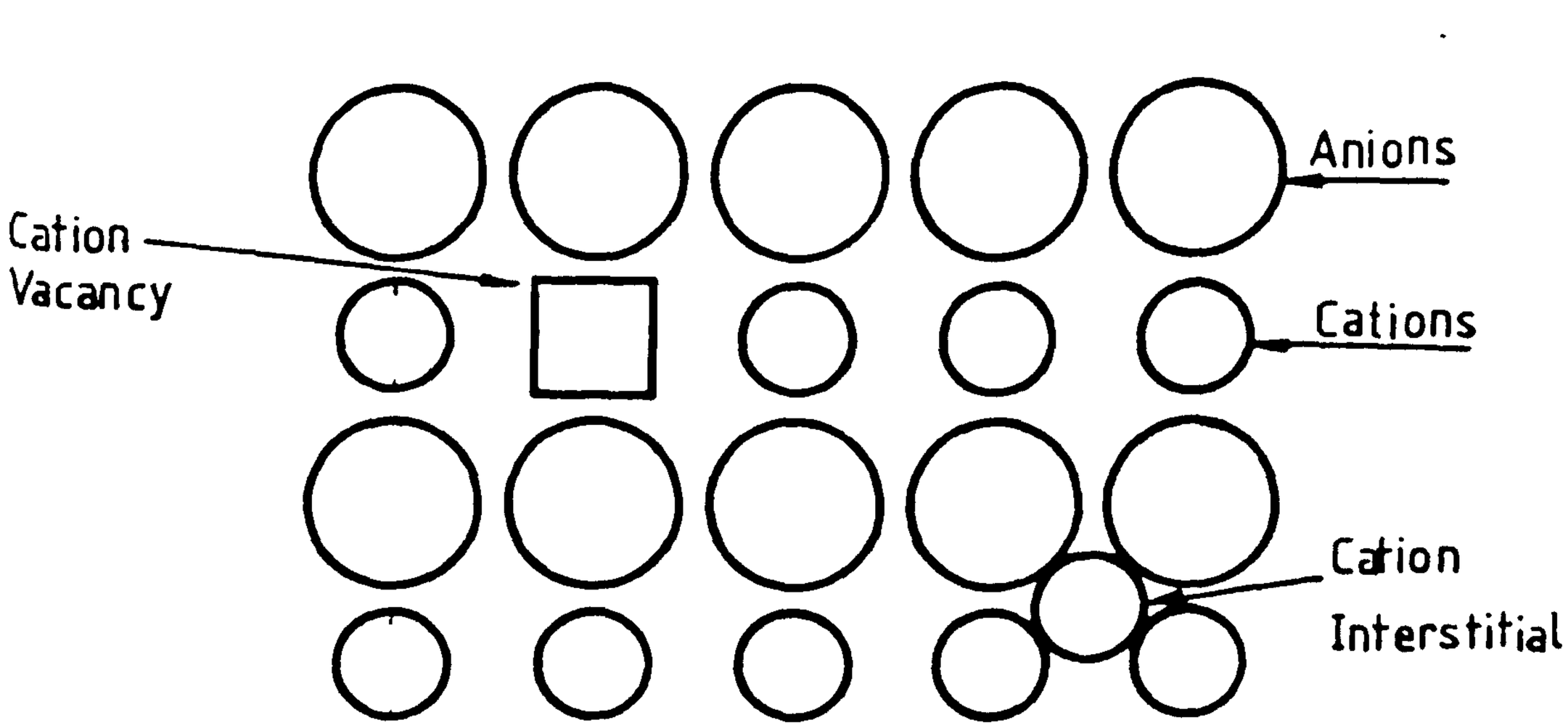

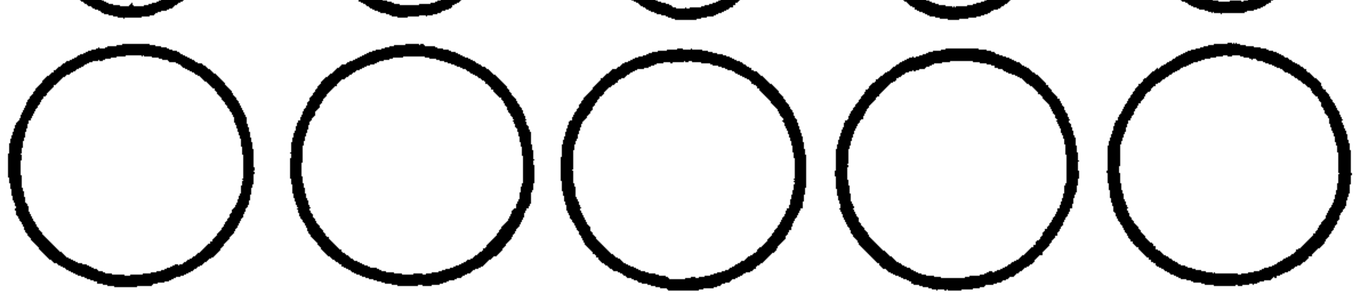

Fig.5. Schematic model of Frenkel defect.

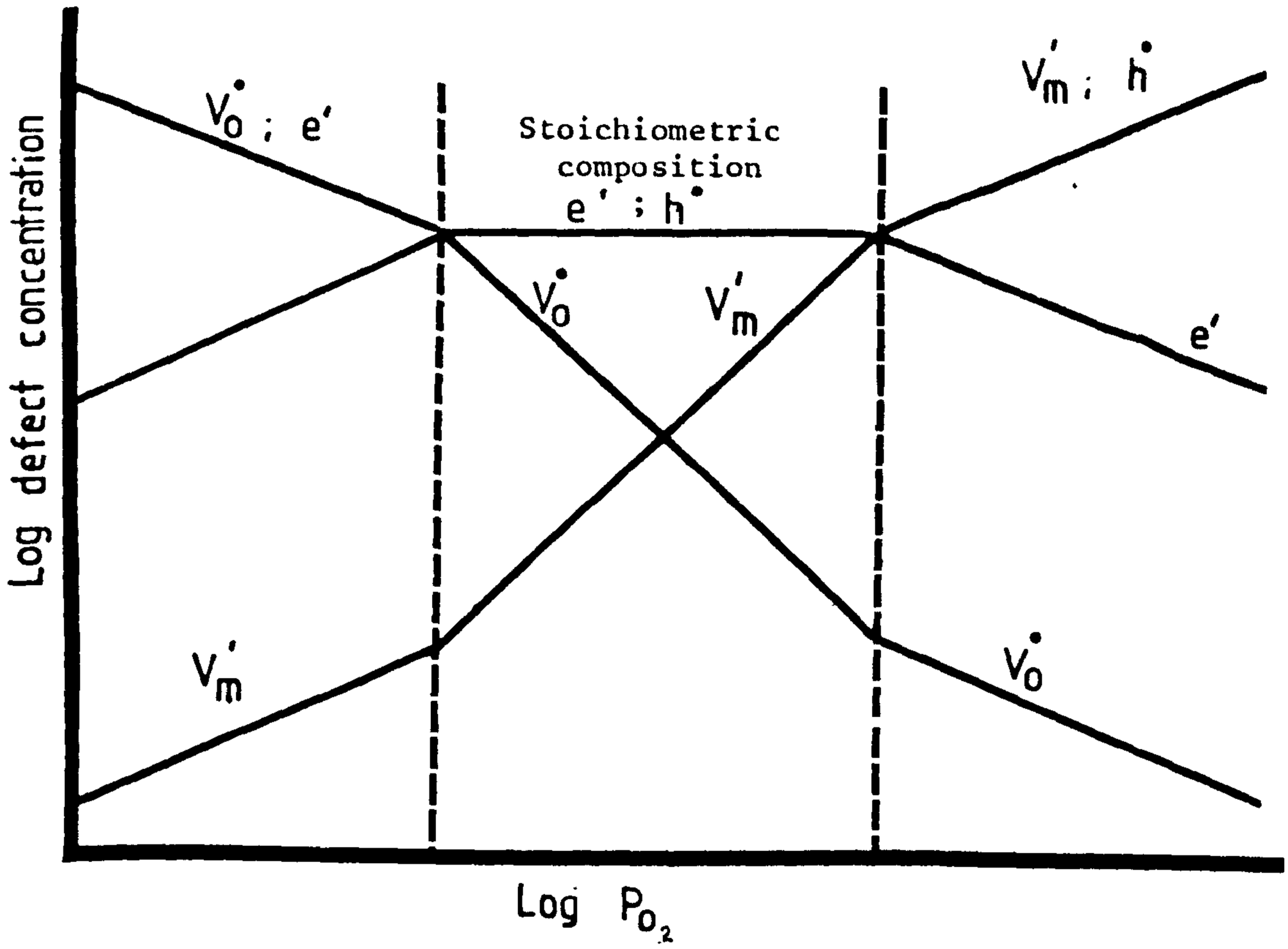

Fig.6a. Schematic illustration of concentration of defects for an electronic conductor (Case A)

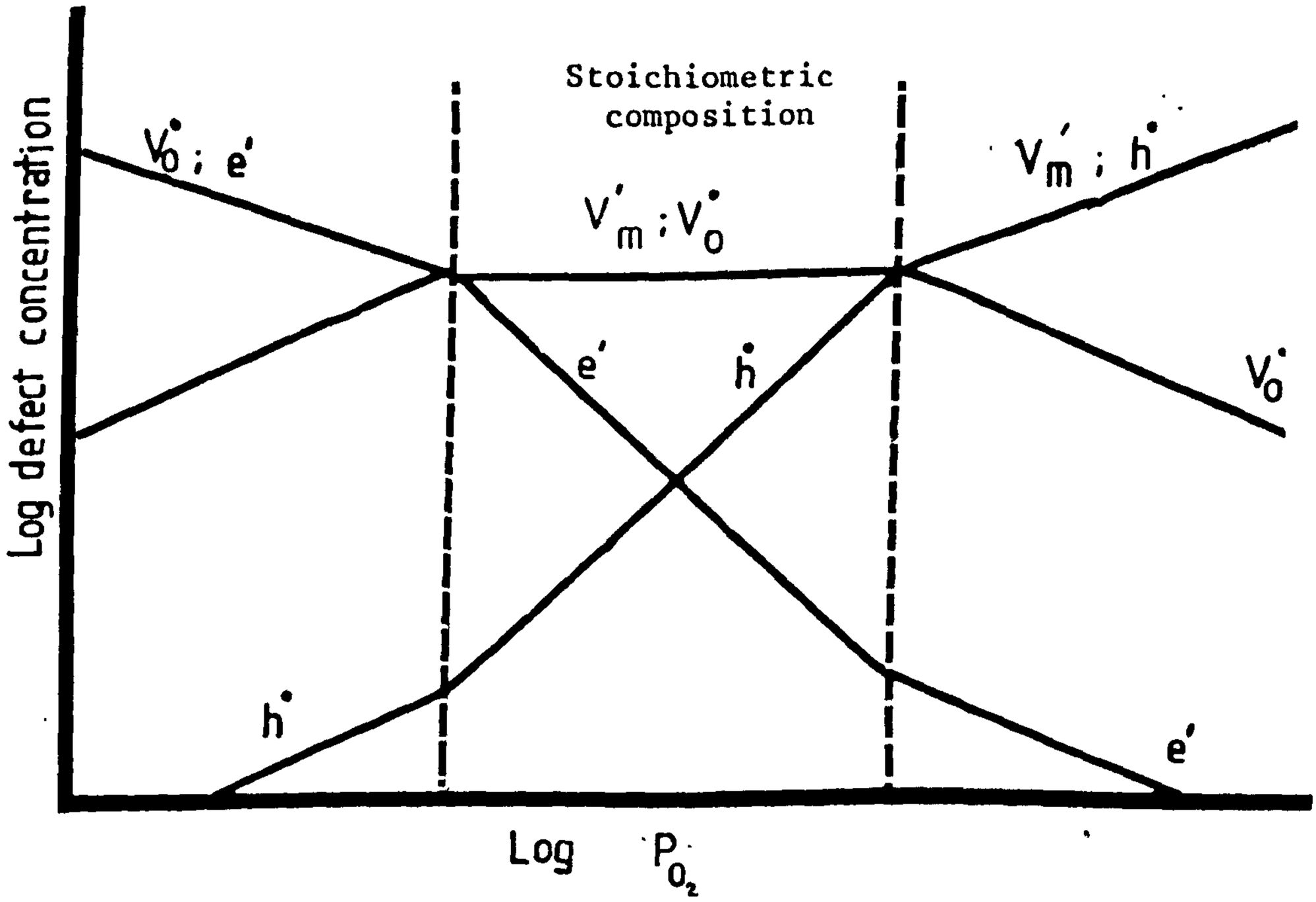

Fig.6b Schematic illustration of concentration of defects for an ionic conductor (Case B)

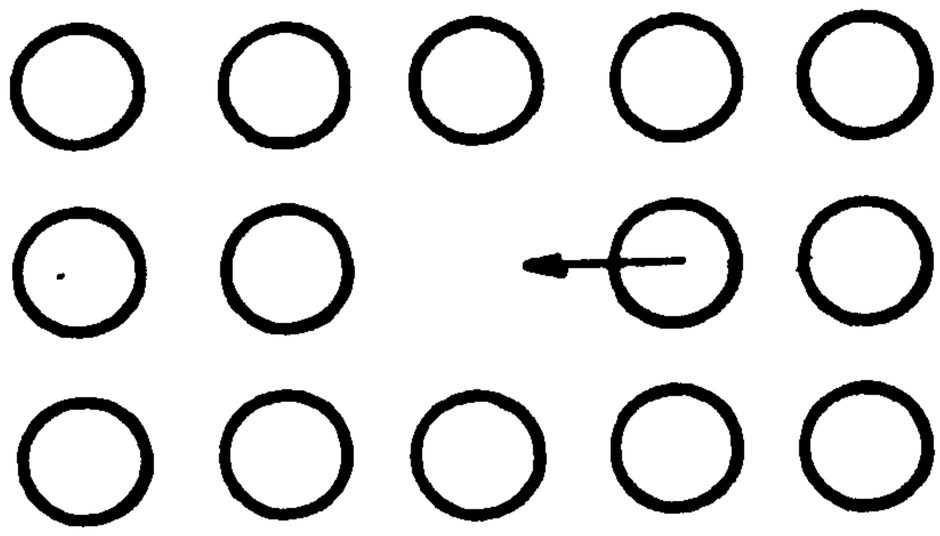

Fig.7a. Schematic illustration of vacancy diffusion in solids.

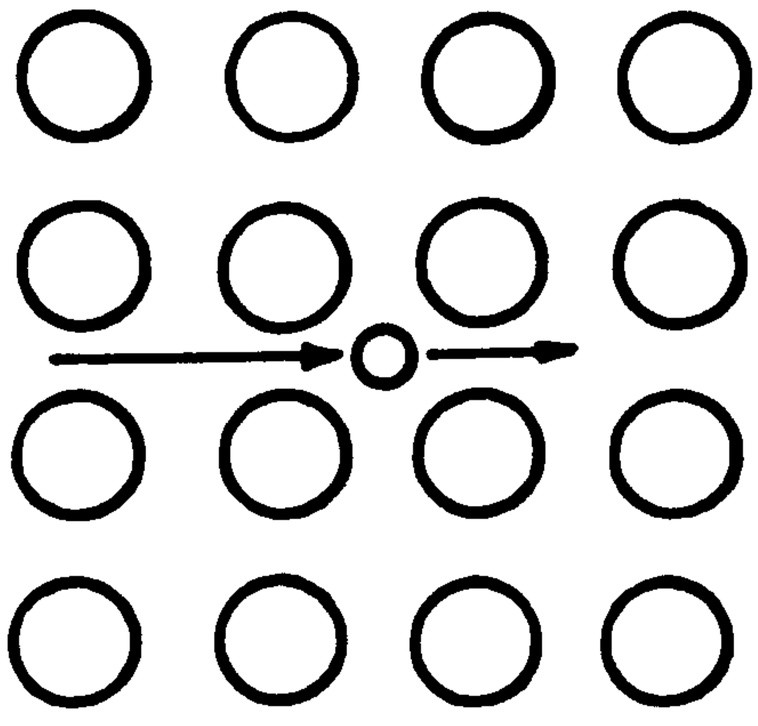

Fig.7b. Schematic illustration of interstitial diffusion in solids.

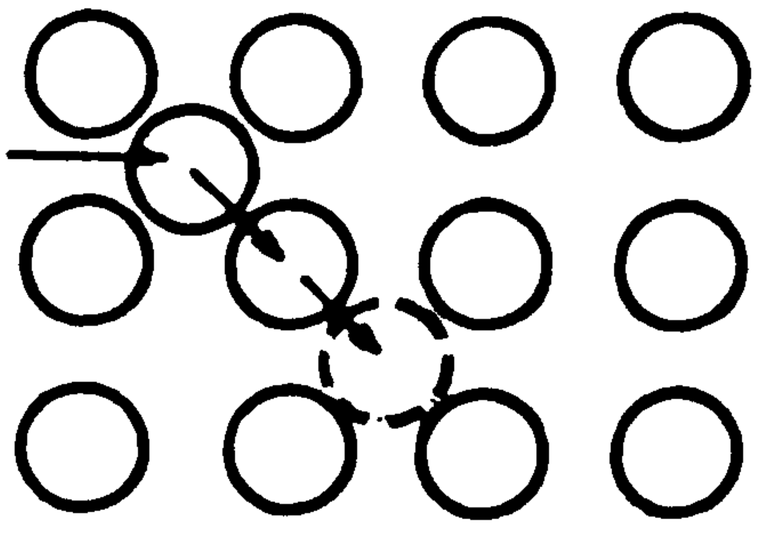

Fig.7c. Schematic illustration of interstitialcy mechanism of diffusion in solids.

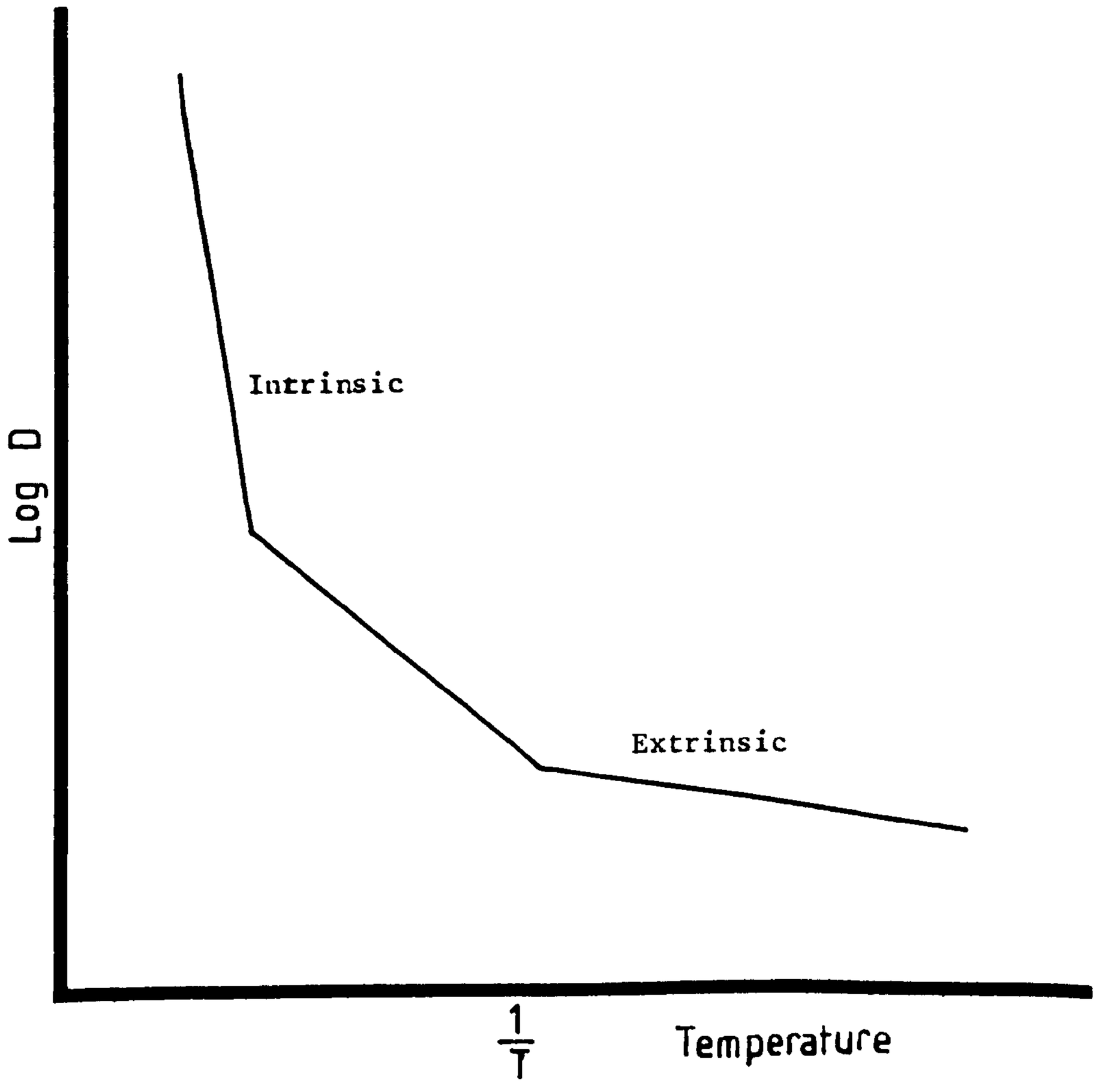

Fig.8. Relationship between diffusion coefficient(D) of an ion in a solid, and temperature (T), showing regions of different activation energies.

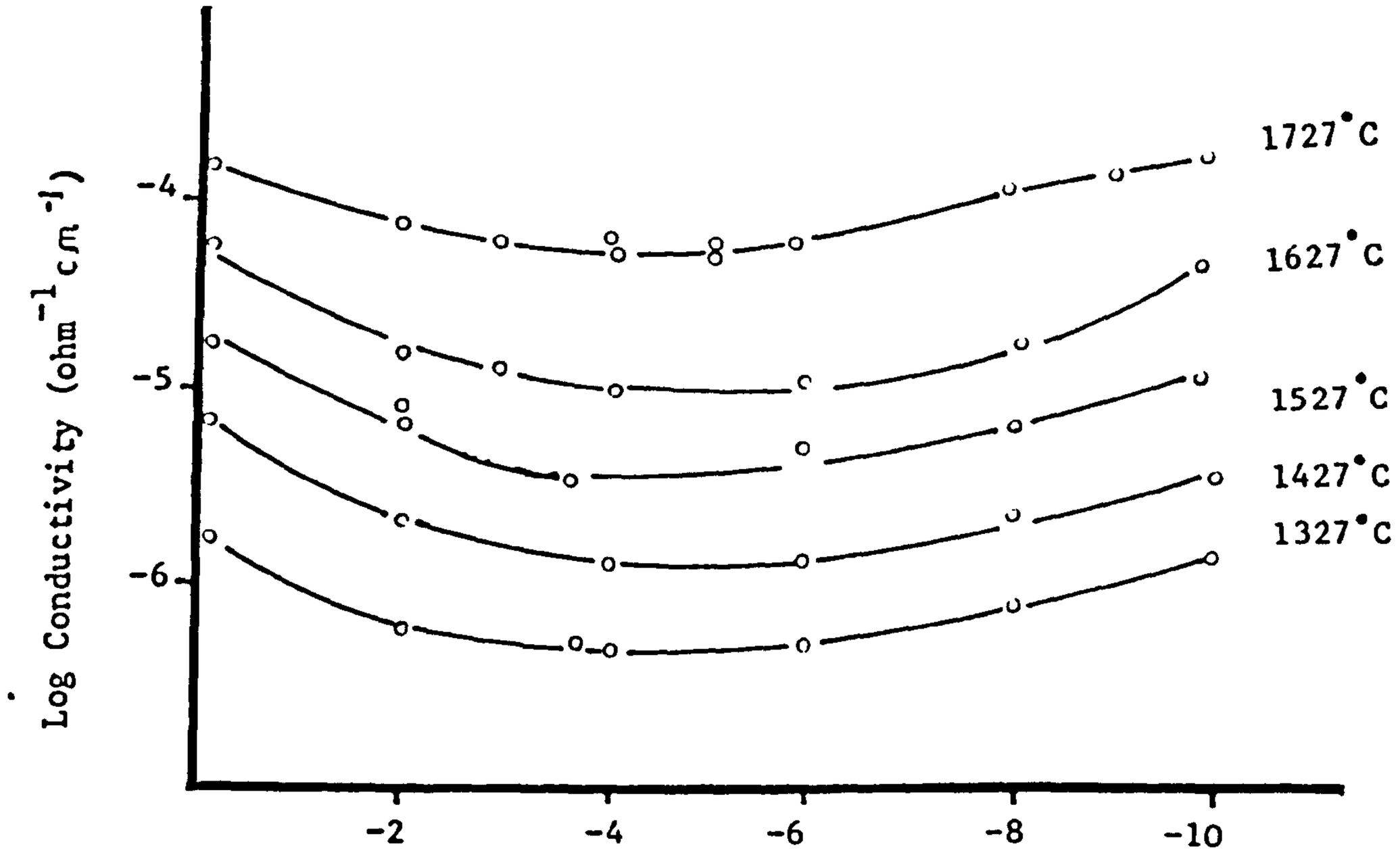

Fig.9 Effect of oxygen partial pressure on electrical conductivity of single-crystal α-Al_2O_3 (Pappis and Kingery)[35]

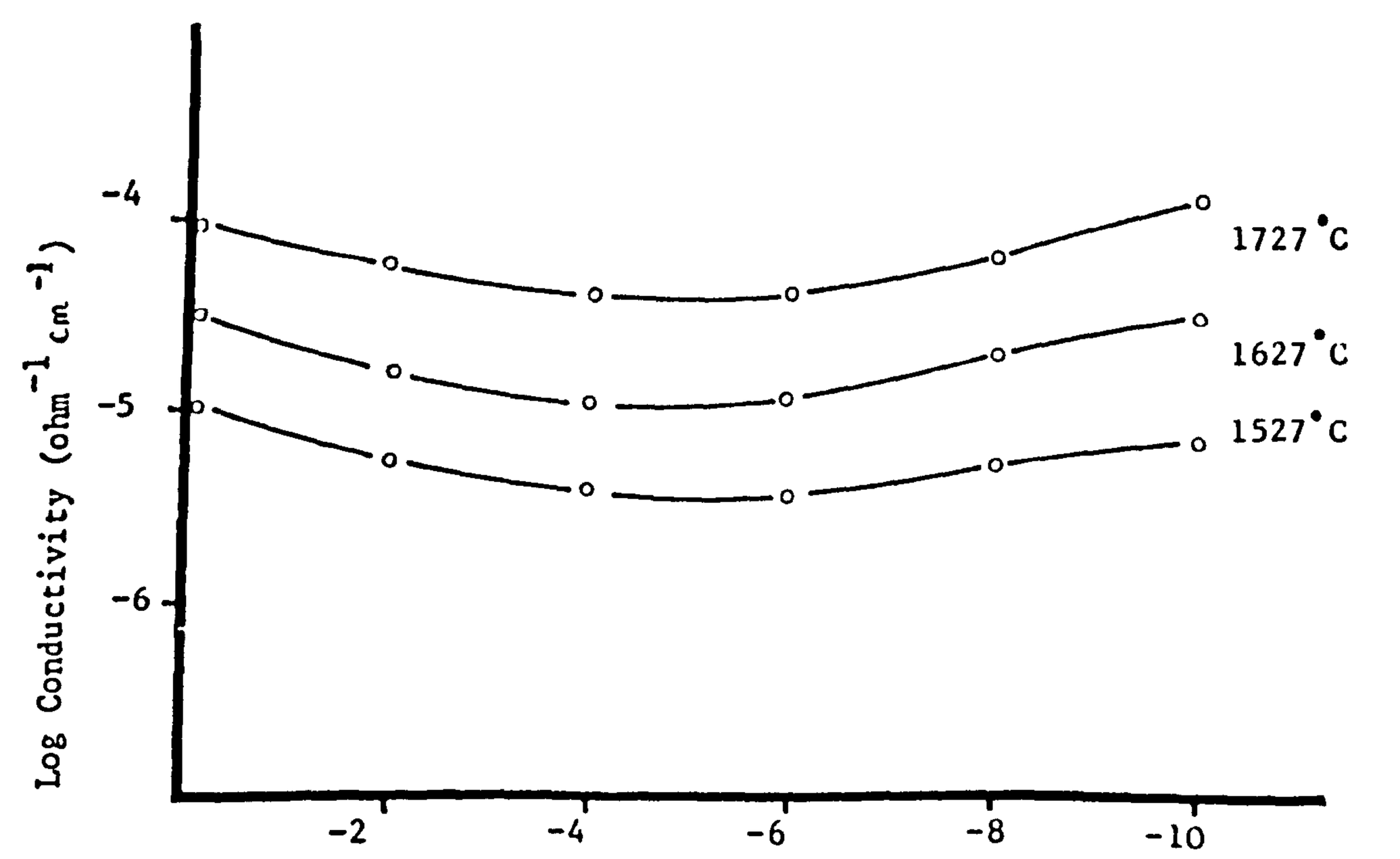

Fig. 10 Effect of oxygen partial pressure on electrical conductivity of polycrystalline α-Al_2O_3 (Pappis and Kingery)[35]

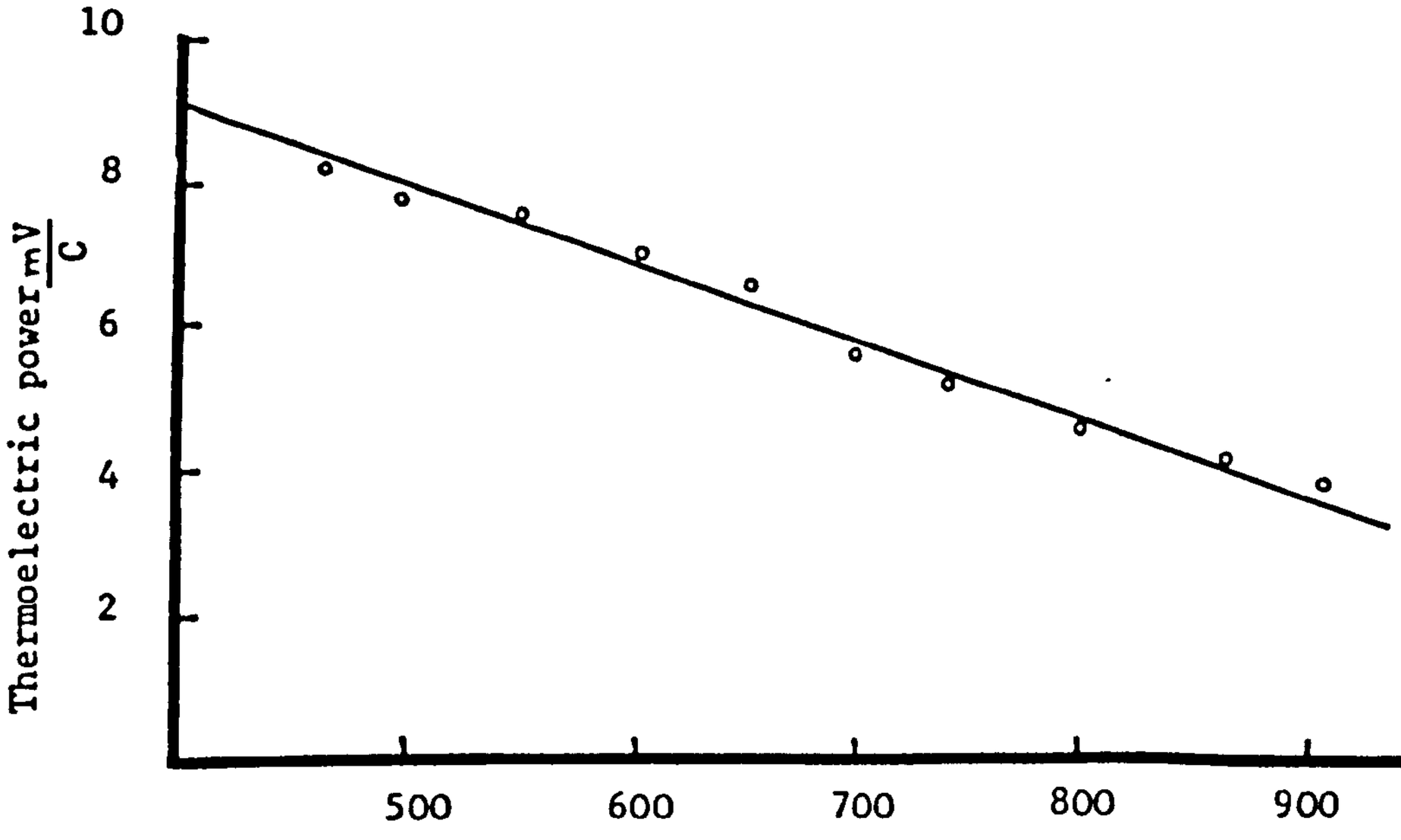

Fig.11 Thermoelectric power of single-crystal α-Al_2O_3 (Peters) [38]

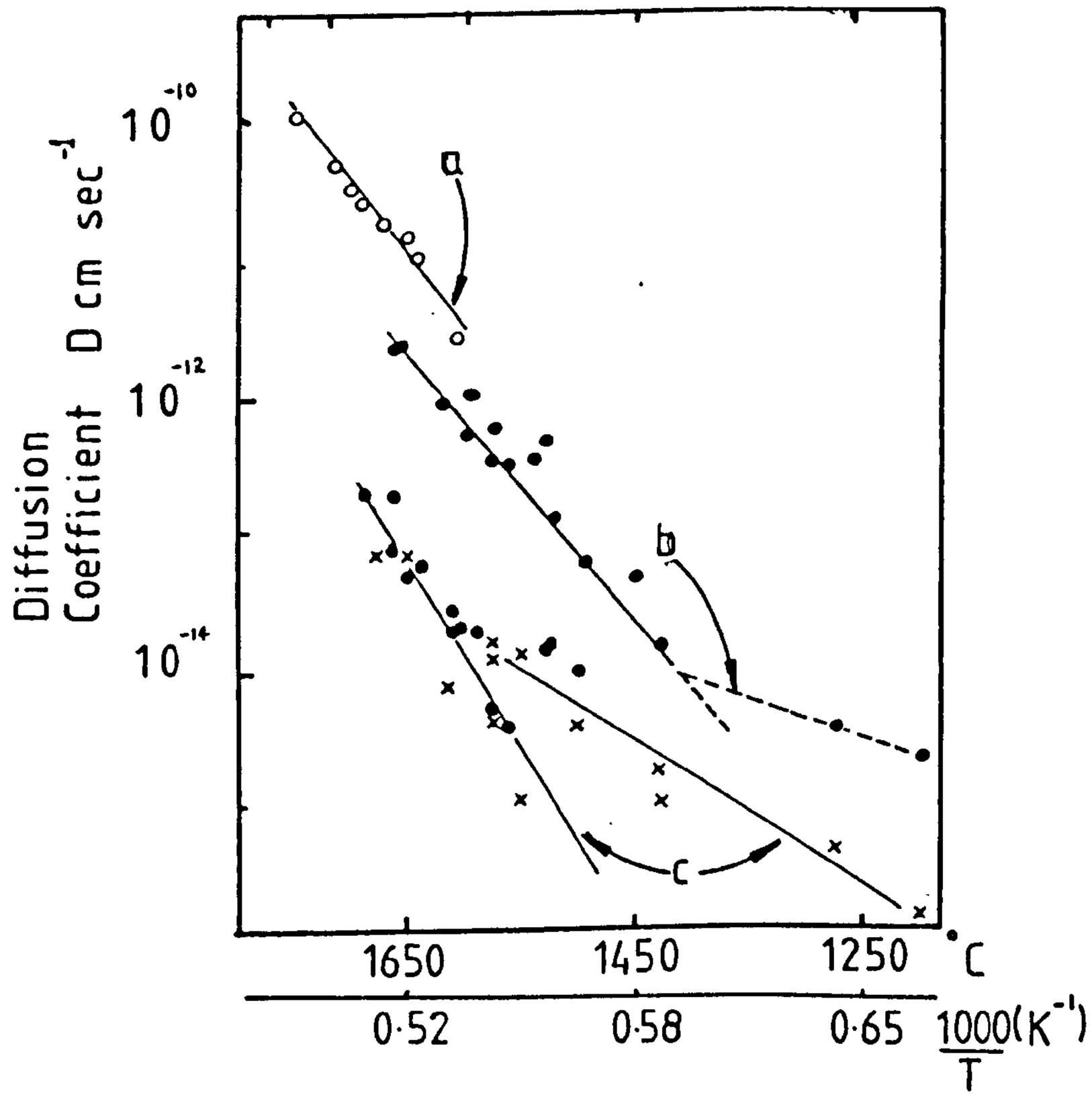

Fig 12 Comparison of aluminium ion self diffusion coefficients with oxygen ion self diffusion coefficients in $\alpha \cdot Al_2O_3$.
a) Aluminium ion diffusion in polycrystalline α-Al_2O_3
b) Oxygen ion diffusion polycrystalline α-Al_2O_3
c) Oxygen ion diffusion in single crystal $\alpha \cdot Al_2O_3$ (Oishi and kingery)[40]

Spheres • °

Grains ×

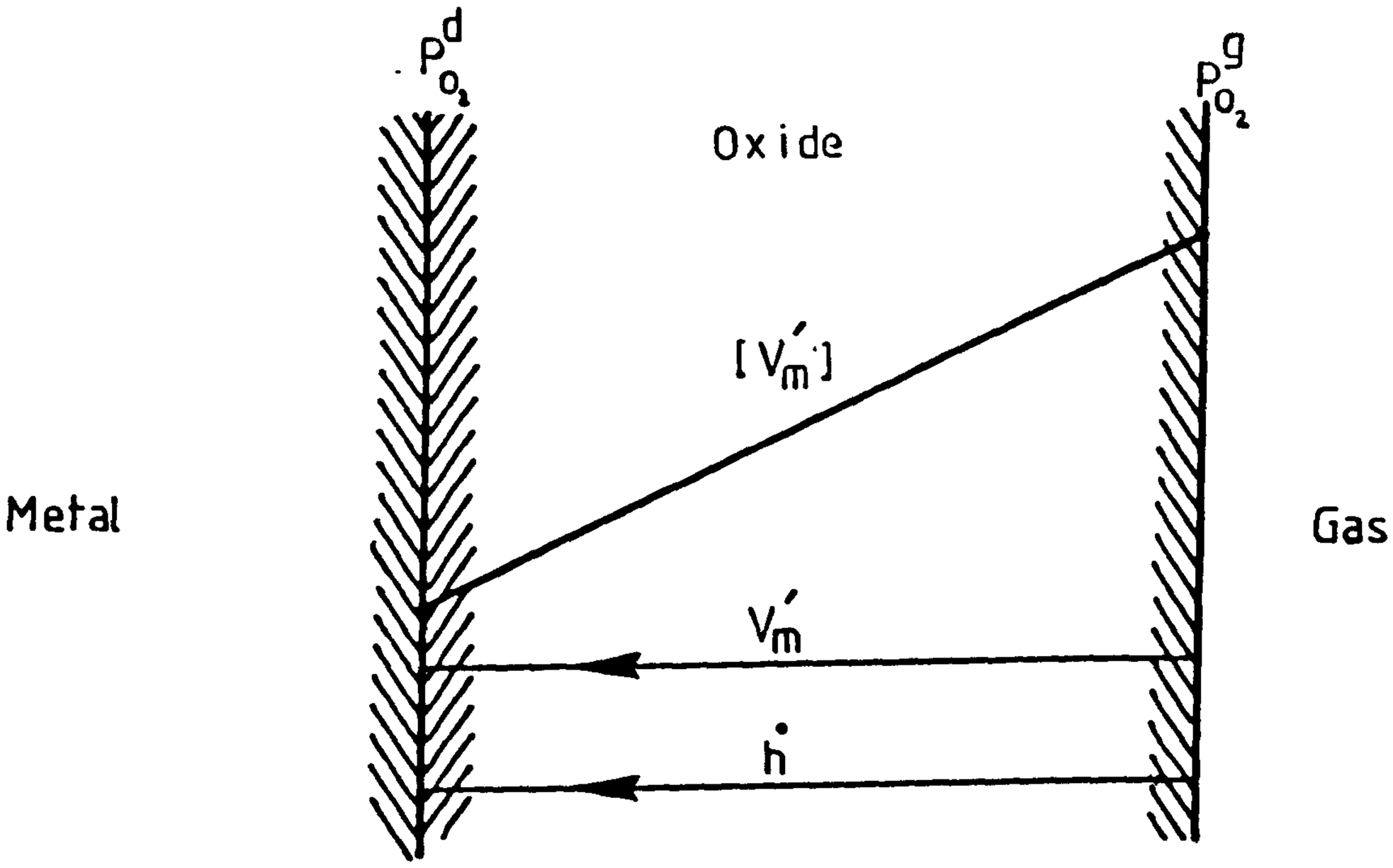

Fig 13a Schematic representation of concentration gradients and transport phenomena in an oxide containing metal ion vacancies

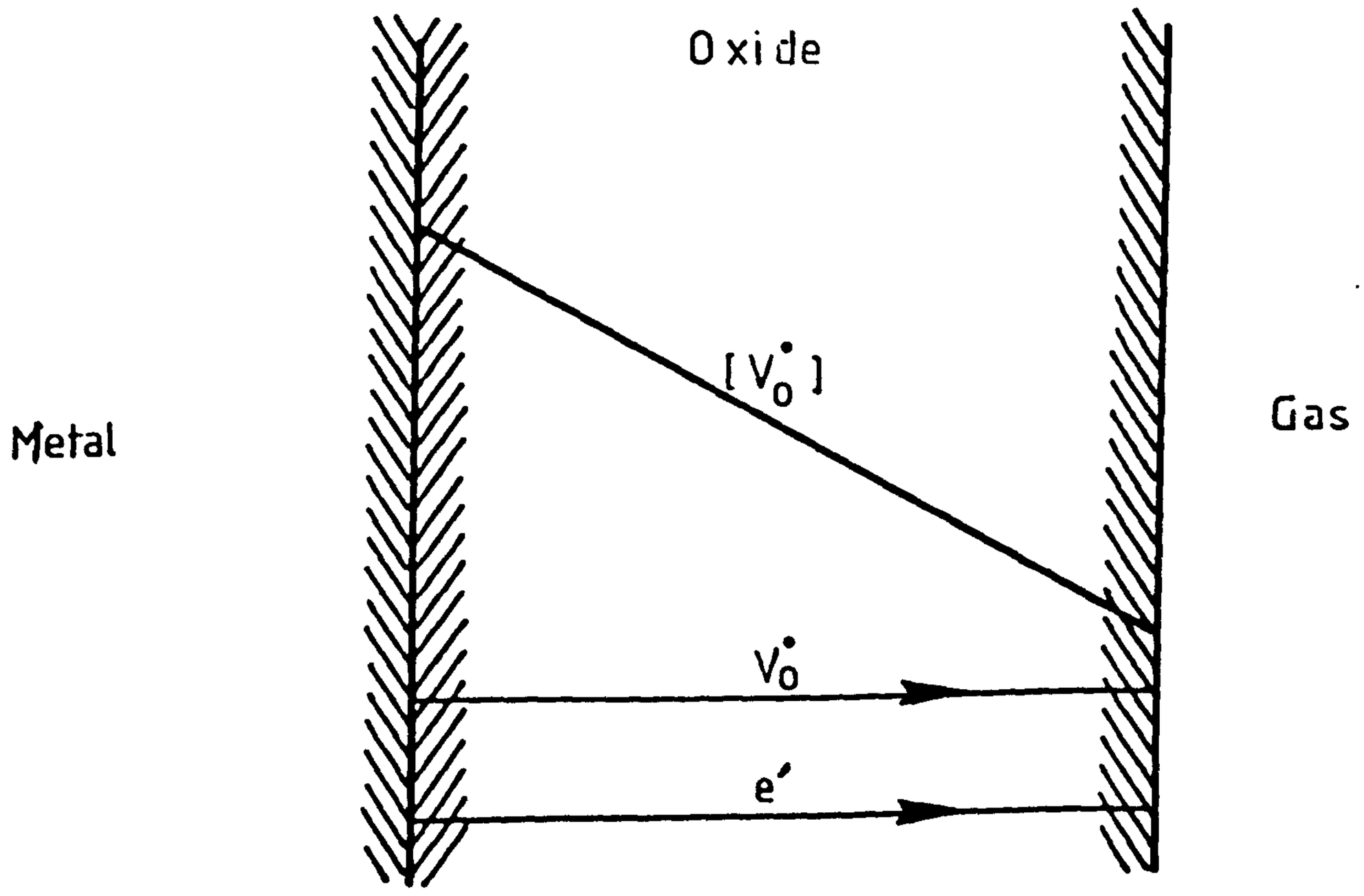

Fig 13b Schematic representation of concentration gradients and transport phenomena in an oxide containing oxygen ion vacancies

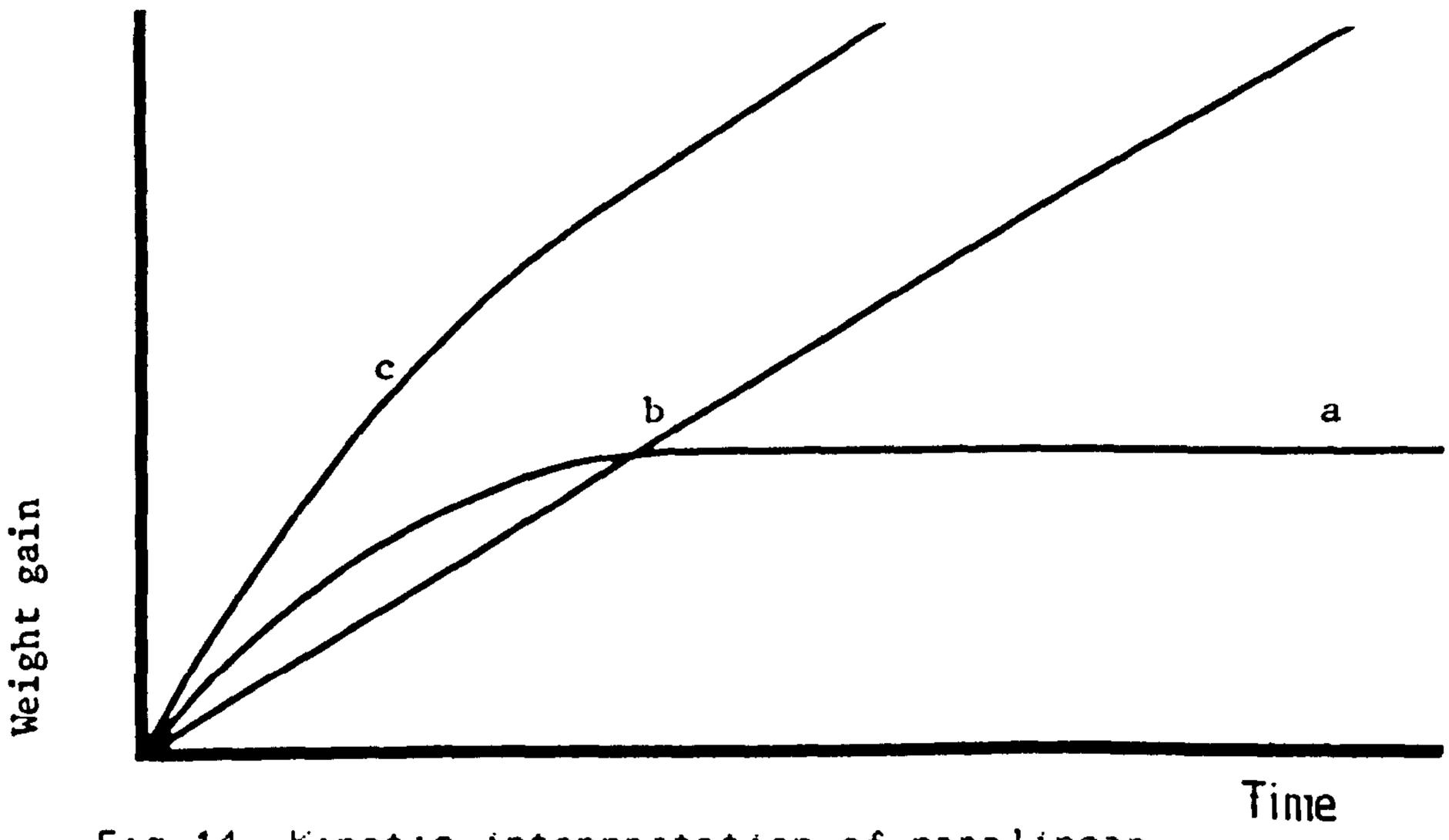

Fig 14 Kinetic interpretation of paralinear oxidation. Curves a and b correspond to the growth of inner and outer porous layer respectively; curve c represents the total weight gain and is the algebraic sum of curves a and b. As oxidation proceeds the growth of inner layer progressively decreases and it's thickness tends to a limiting value.

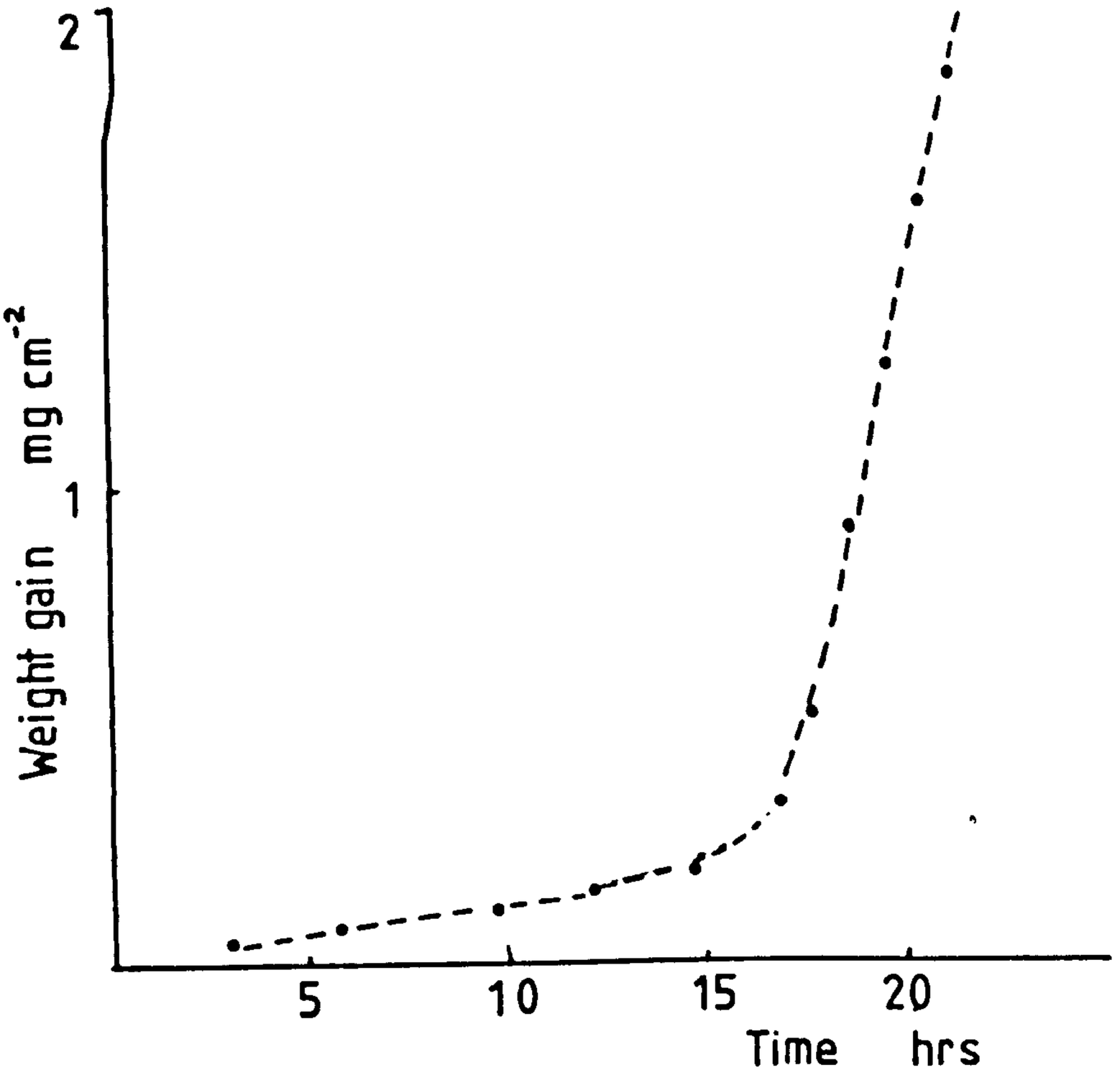

Fig 15 Oxidation of magnesium at 525 C in dry oxygen, illustrating 'breakaway kinetics.
(Gregg and Jepson)[69]

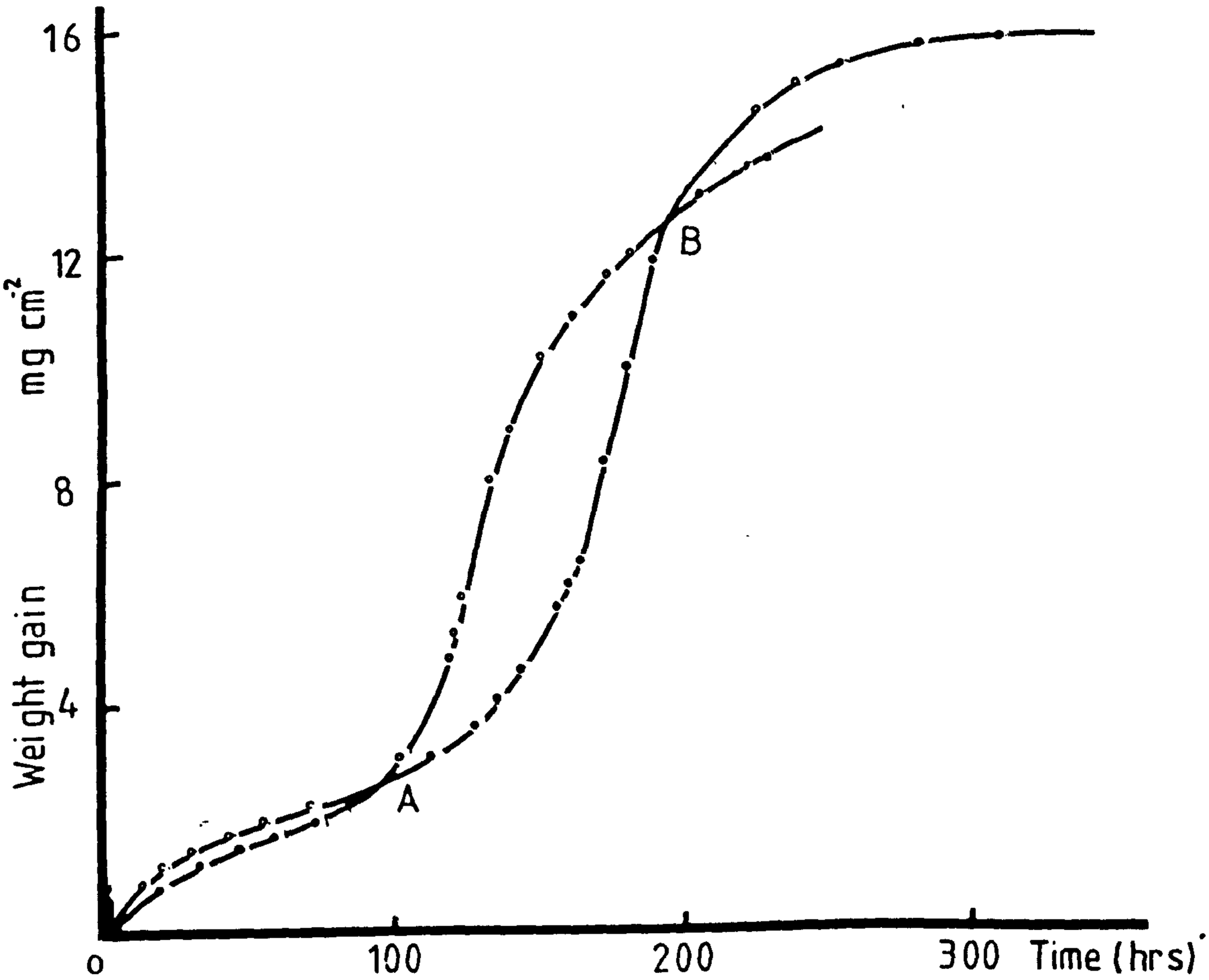

Fig 16 Oxidation of stainless steel (309) in moist air at 1093 °C exemplifing breakaway kinetics.
(Caplan and Cohen)[73]

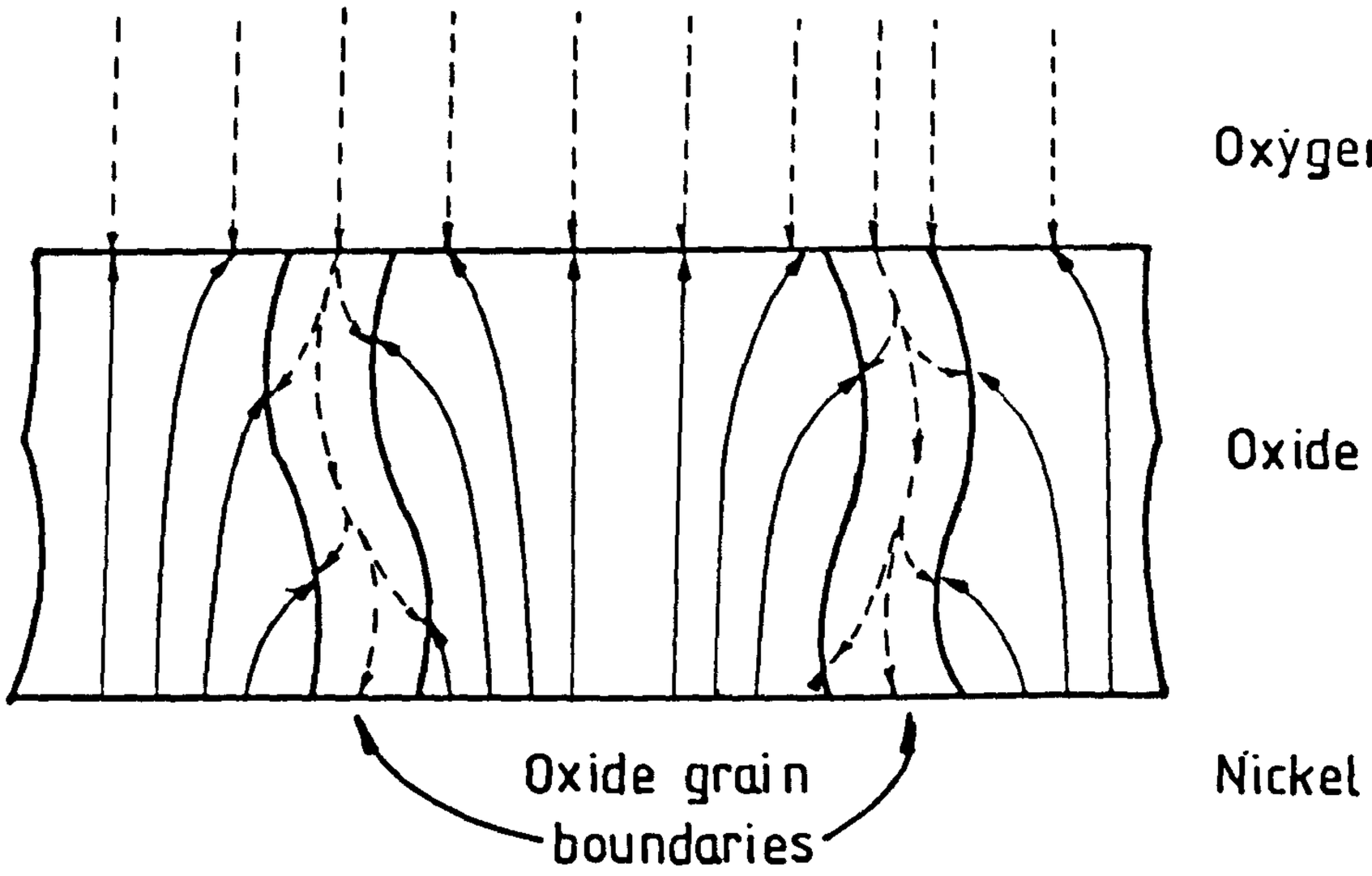

Fig 17 A schematic diagram showing diffusion paths of nickel and oxygen during formation of NiO.
(Rhines and Wolf)[81]
Nickel path ——
Oxygen path ------

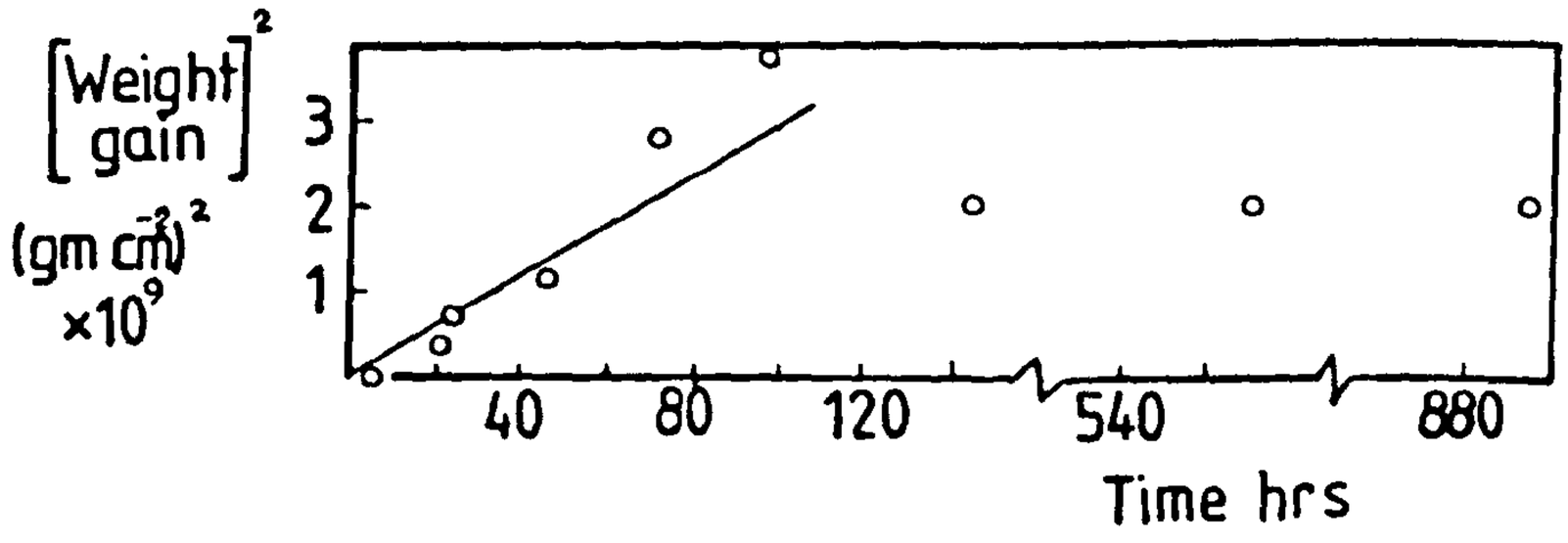

Fig 18 Oxidation of aluminium at 600 °C in moist oxygen (P_{H_2O} = 7×10⁻⁴ atms)
(Pilling and Bedworth)[59]

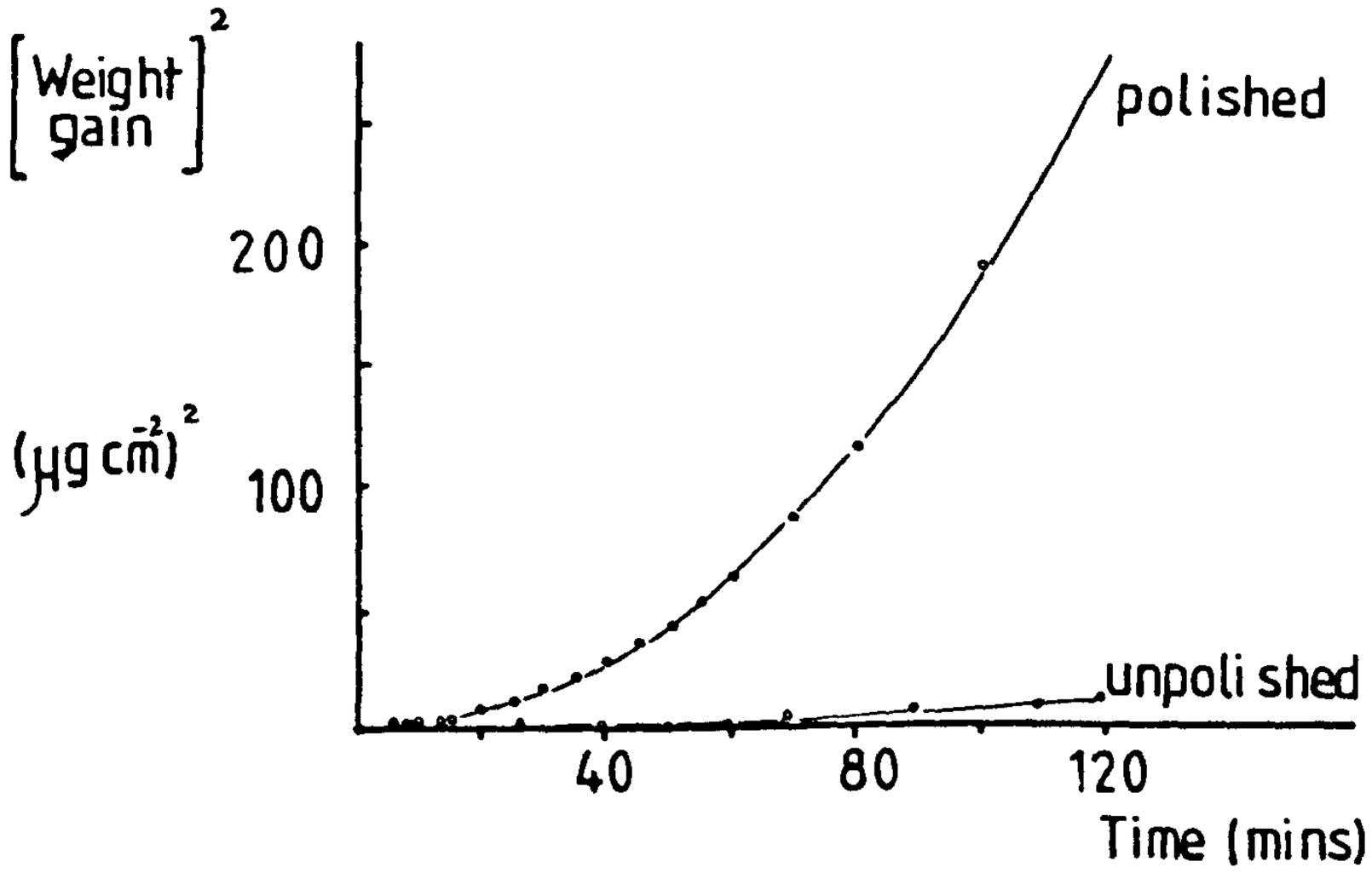

Fig 19 Oxidation kinetics of aluminium at 500 °C showing the influence of surface finish.
(Gulbransen and Wysong)[84]

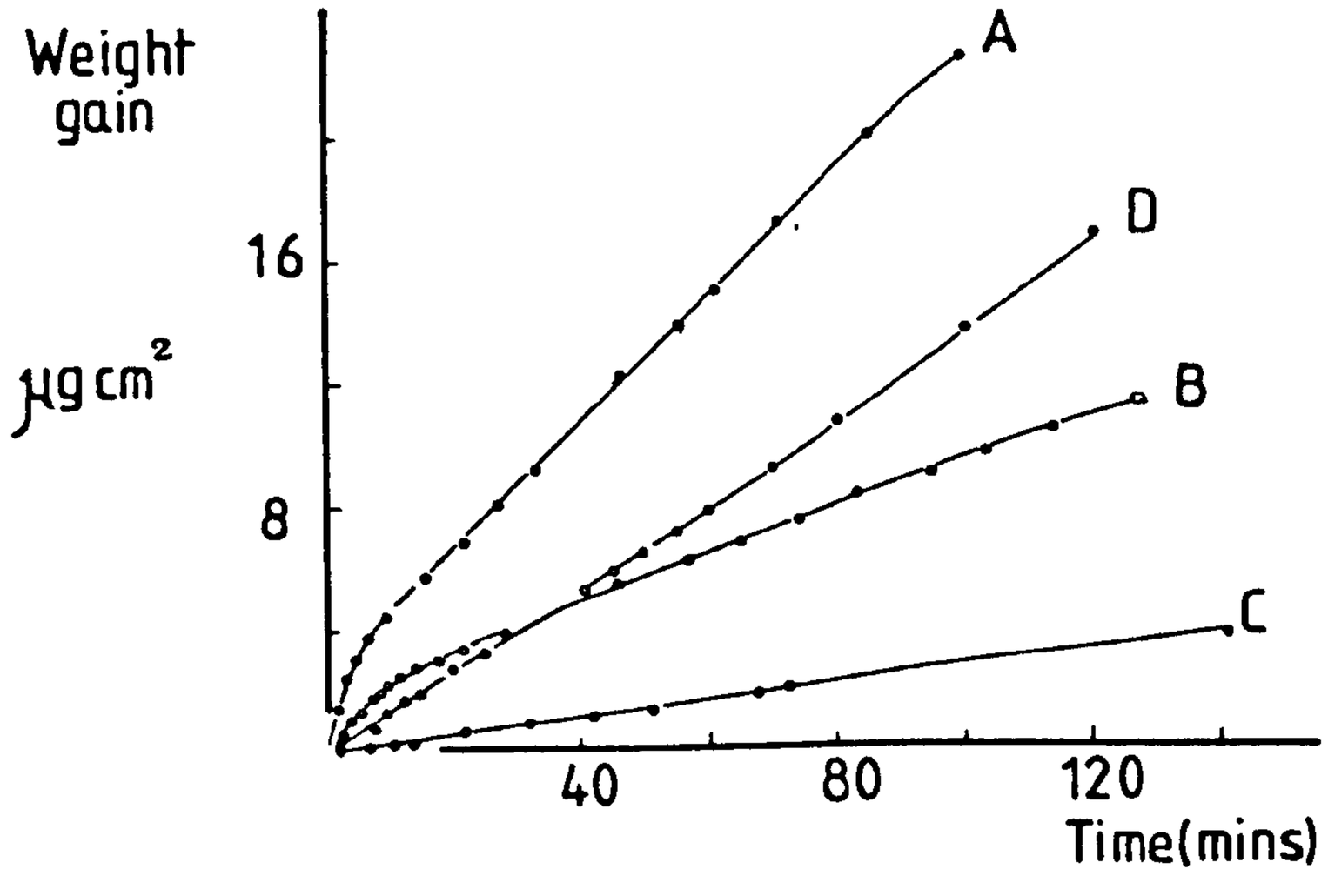

Fig 20 Oxidation kinetics of aluminium at 500 °C
(Gulbransen and Wysong)[84]

A, B: 99.985% Al Samples obtained from sheet roll

C, D: 99.978% Al Samples obtained from ingots and given a pre-treatment of electrolytic brigtening, rolling, annealing and washing in phosphoric/chromic acid solution followed by distilled water.

(All samples polished)

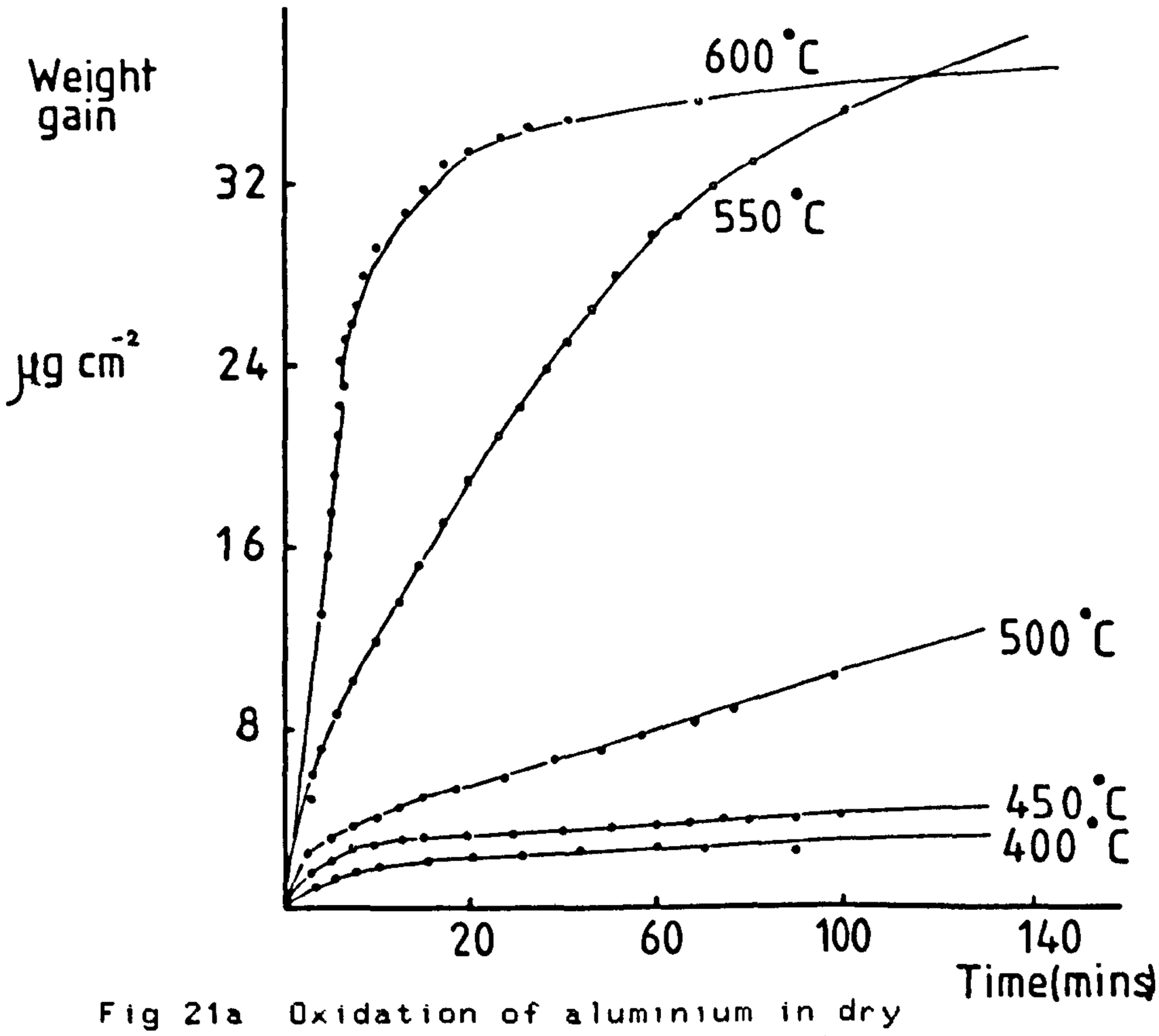

Fig 21a Oxidation of aluminium in dry oxygen within the temperature range 400 °C - 600 °C
(Smeltzer)[85]

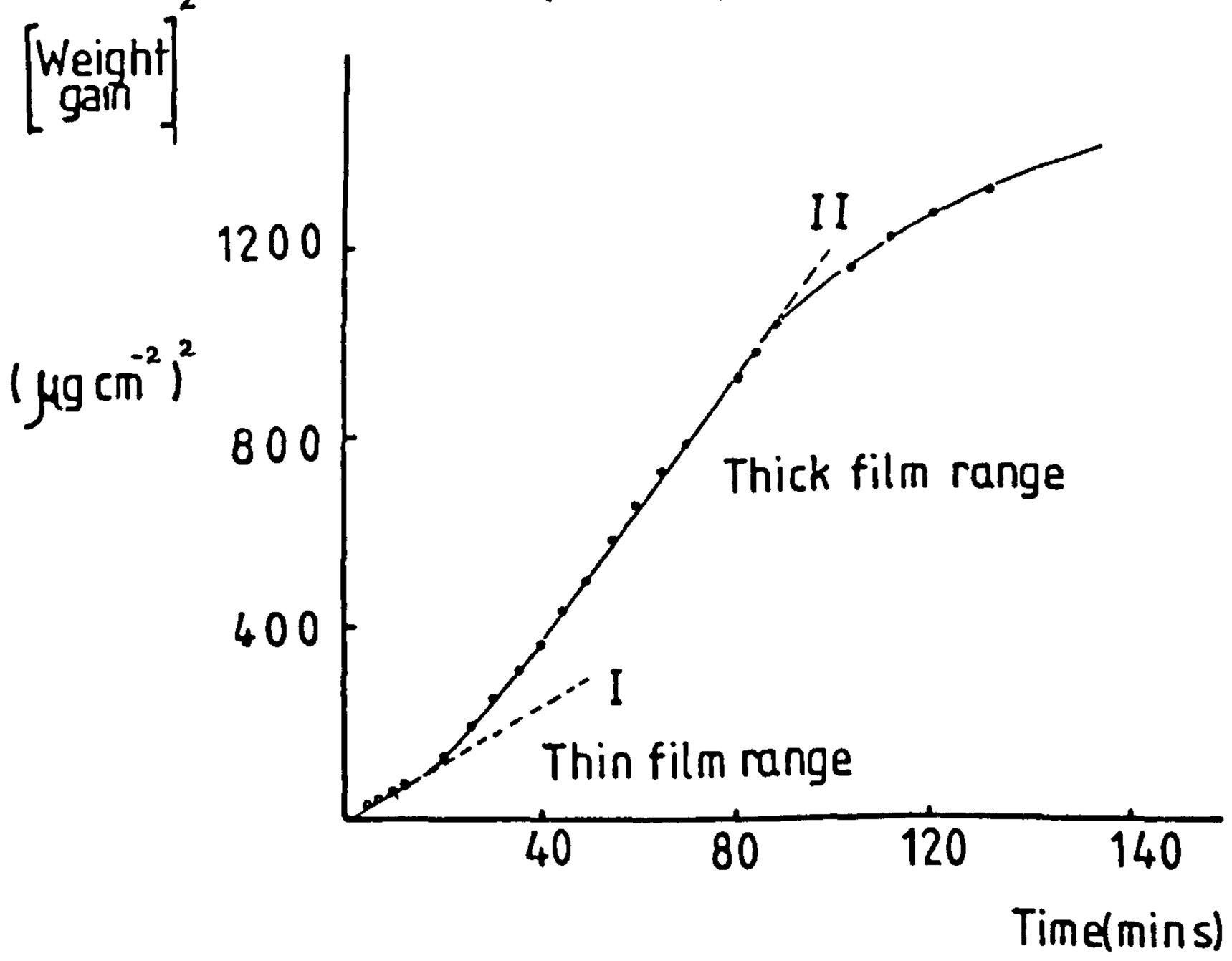

Fig 21b Parabolic plot of oxidation data at 550 °C (Fig 21a) exhibiting two linear sections (I and II)
(Smeltzer)[85]

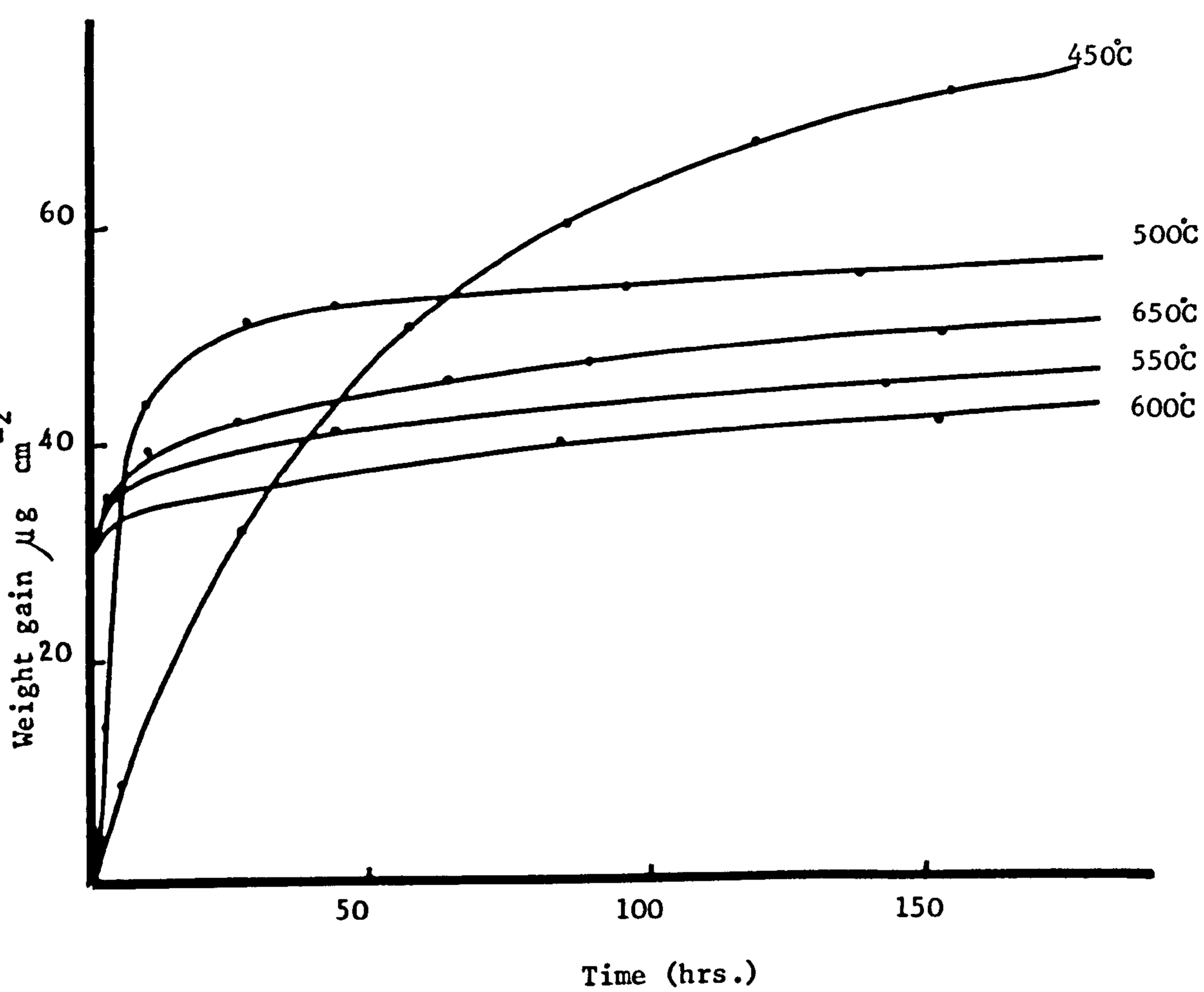

Fig 22 Oxidation kinetics of normal high purity aluminium in dry oxygen (P_{O_2} = 0.1 atmosphere) [86] (Rylmore et al)

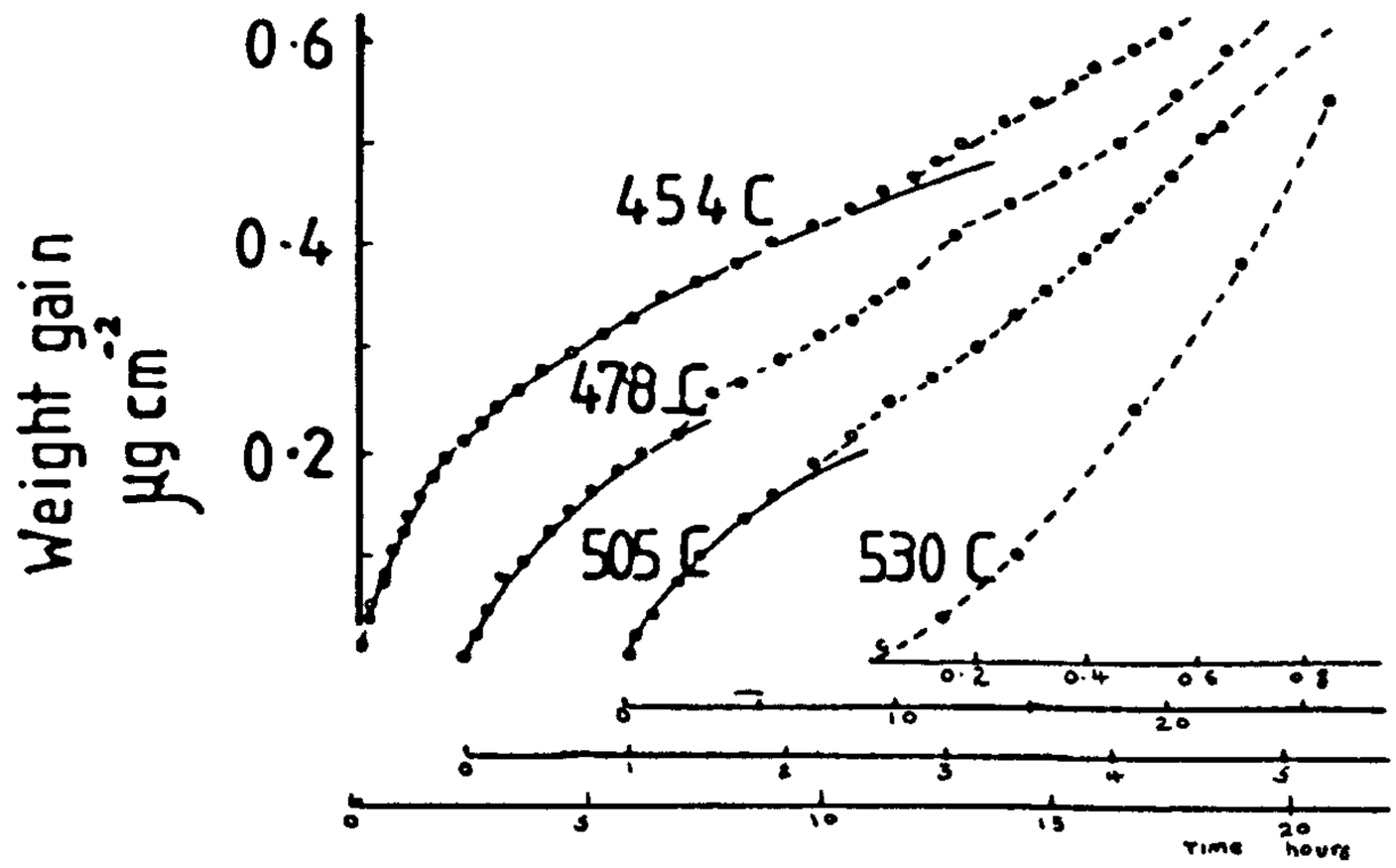

Fig 23 Oxidation kinetics of aluminium in dry oxygen. Full lines indicate the growth of amorphous oxide before nucleation of δ- Al_2O_3 crystals.

(Dignam et al)[87]

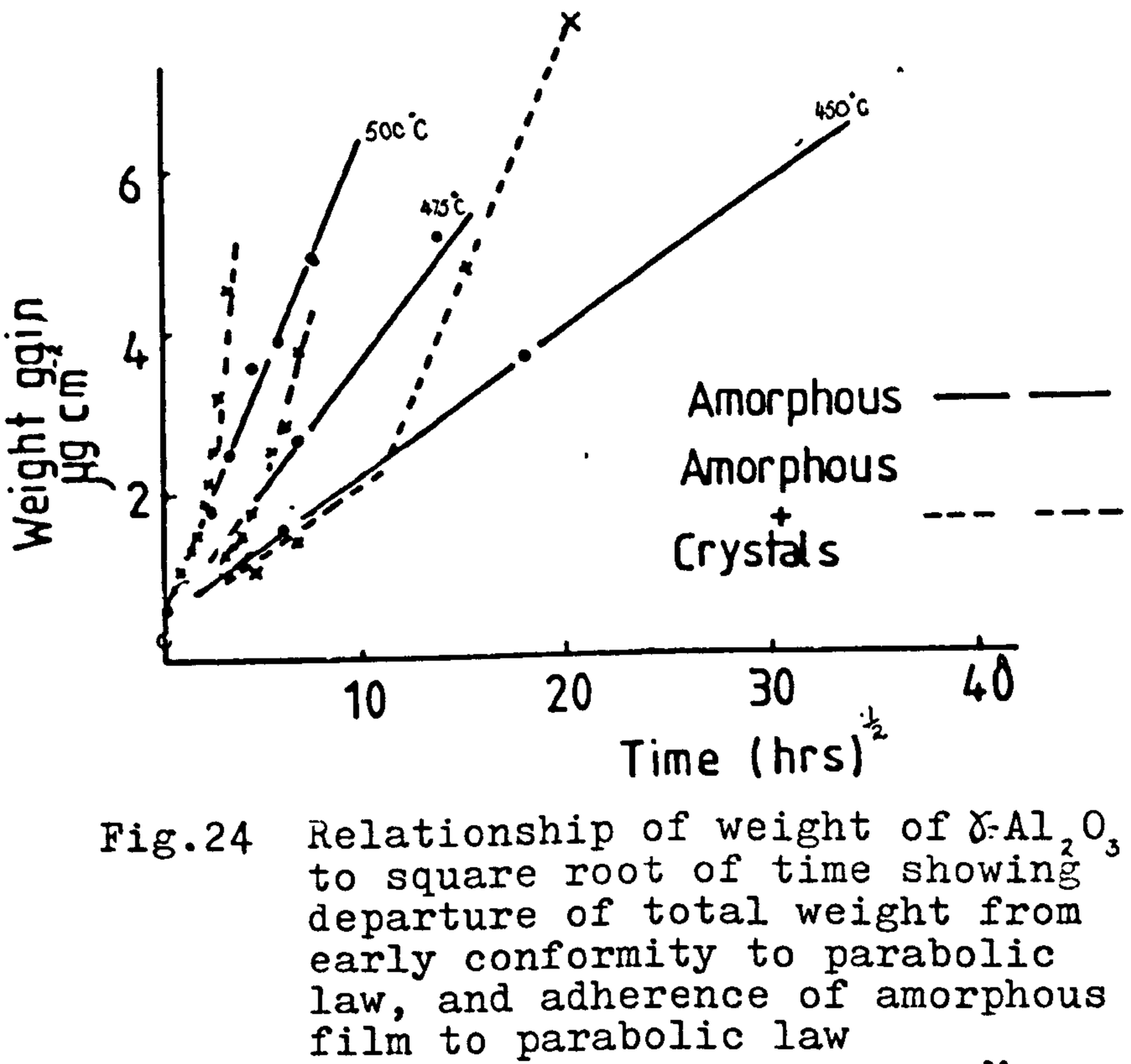

Fig.24 Relationship of weight of δ-Al_2O_3 to square root of time showing departure of total weight from early conformity to parabolic law, and adherence of amorphous film to parabolic law

(Beck et al)[88]

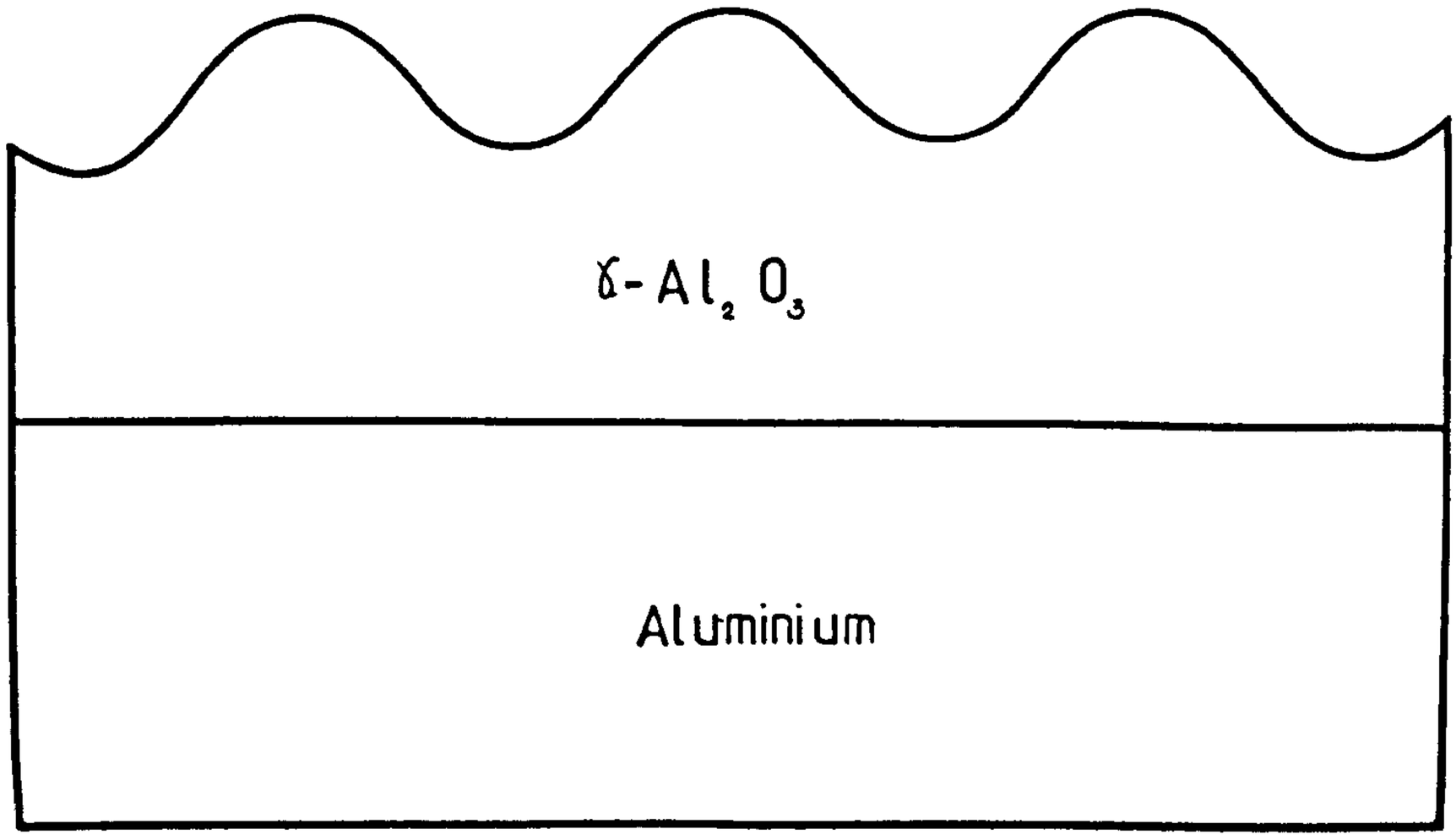

Fig.25. Expected cross section of amorphous γ-Al_2O_3 on (110) aluminium face from observations of Doherty and Davis (98)

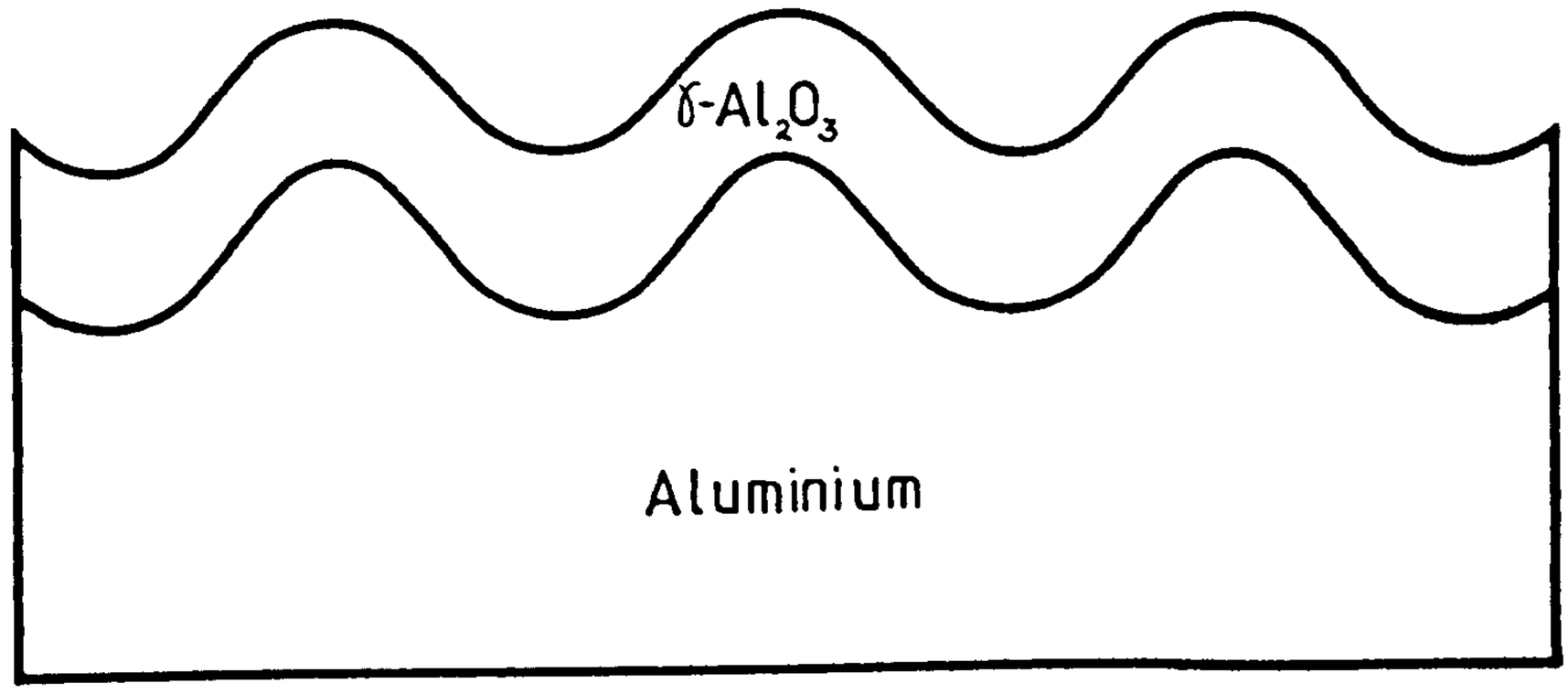

Fig.26. Alternative model of γ-Al_2O_3 film on (110) aluminium face, proposed by Randall and Bernard. (99)

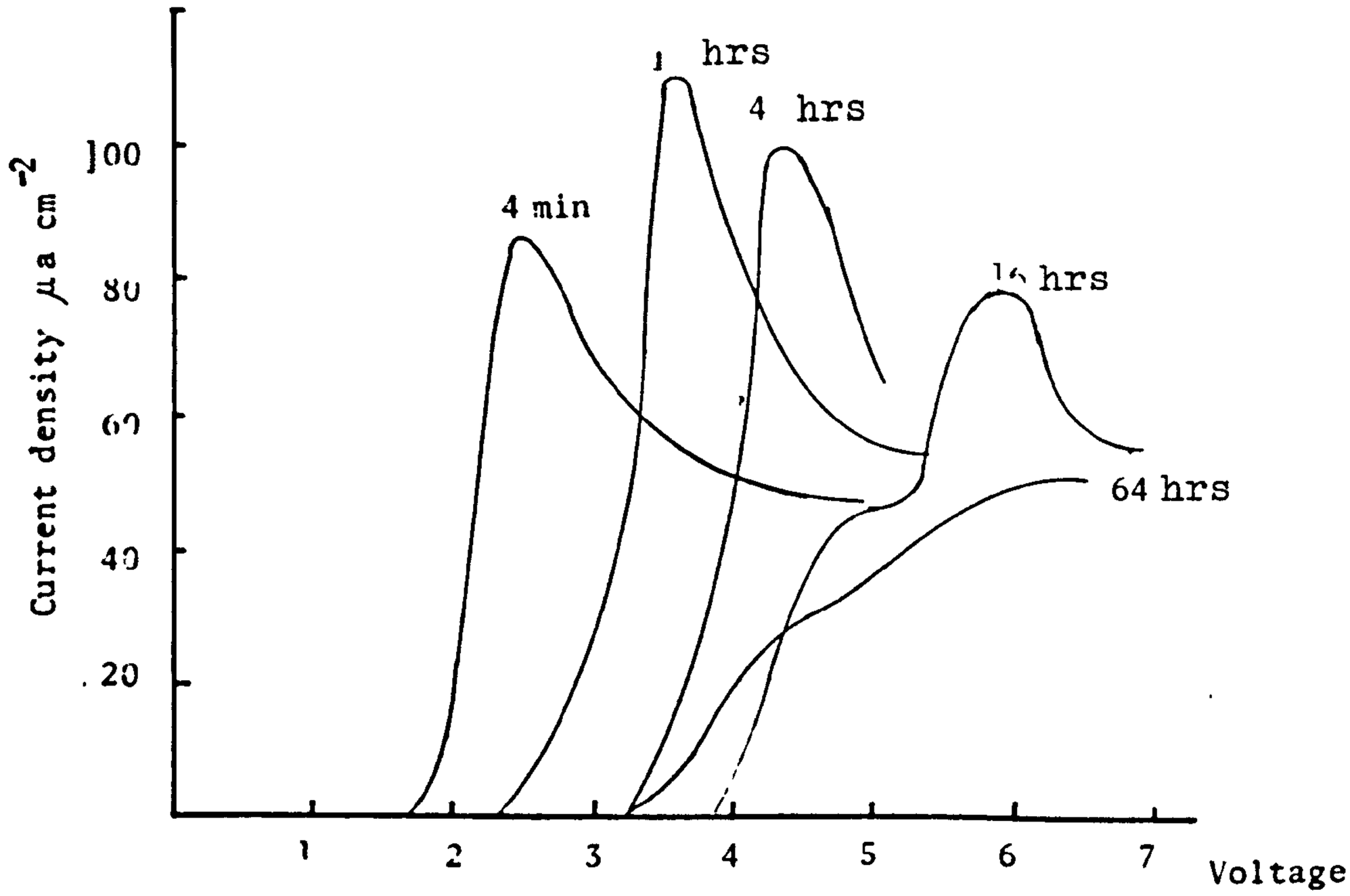

Fig.27 Influence of oxidation time at 250C on the polarisation curve for normal high purity aluminium.
(Dignam) 103

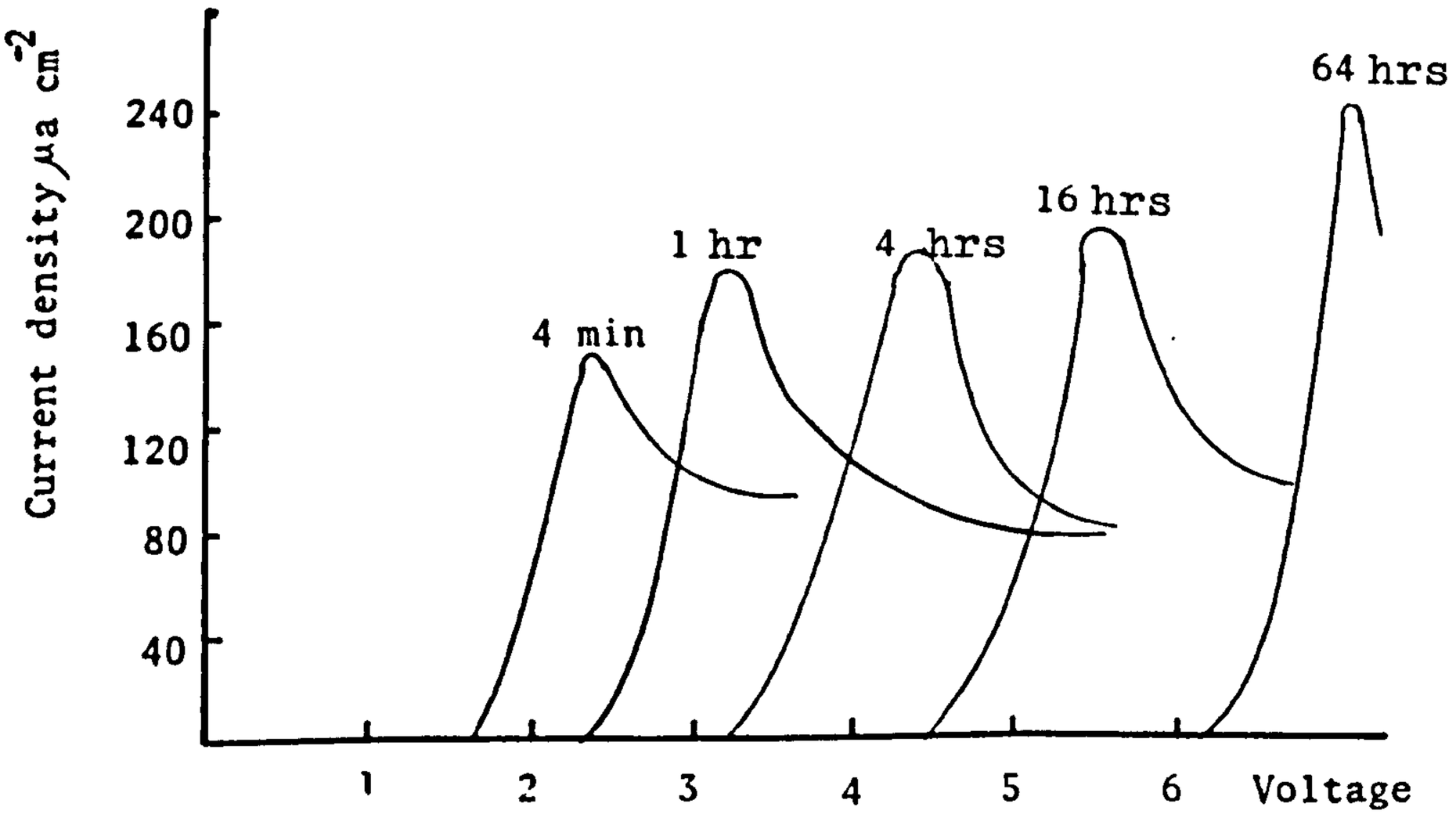

Fig.28 Influence of oxidation time at 450C on the polarisation curve for high purity aluminium containing 0.24% silicon.
(Dignam) 103

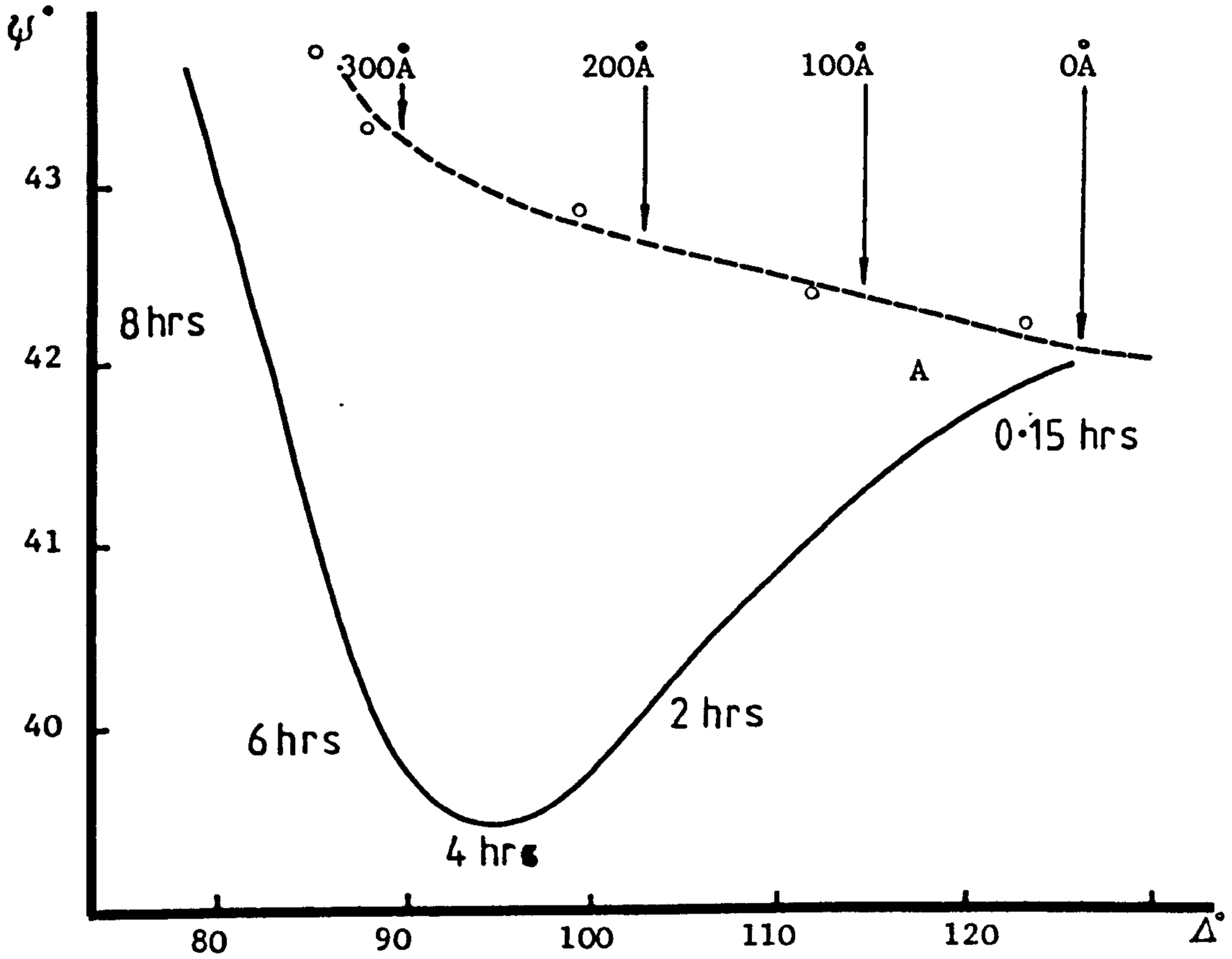

Fig. 29 Relationships between ψ and Δ .

° Experimental points obtained from evaporated alumina films on polished aluminium samples.

—— Obtained from air annealed samples (520 °C) Annealing times given in hours.

Badia[104]

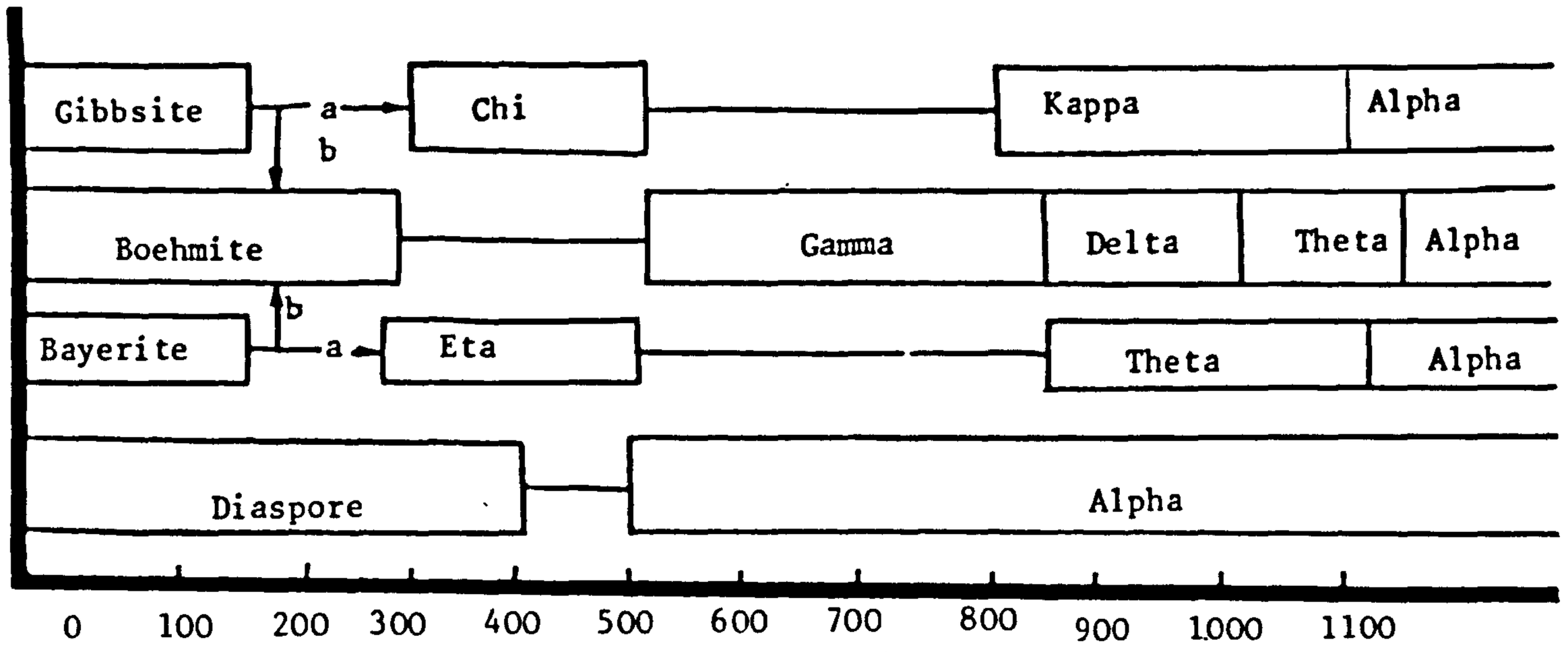

Figure 30 Dehydration sequences of alumina hydrates in air.

NOTE: Enclosed areas indicate range of stability. Open areas indicate range of transition.

Path b is favoured by moisture, alkalinity and coarse particle size(100 microns).

Path a by fine crystal size (below 10 microns)

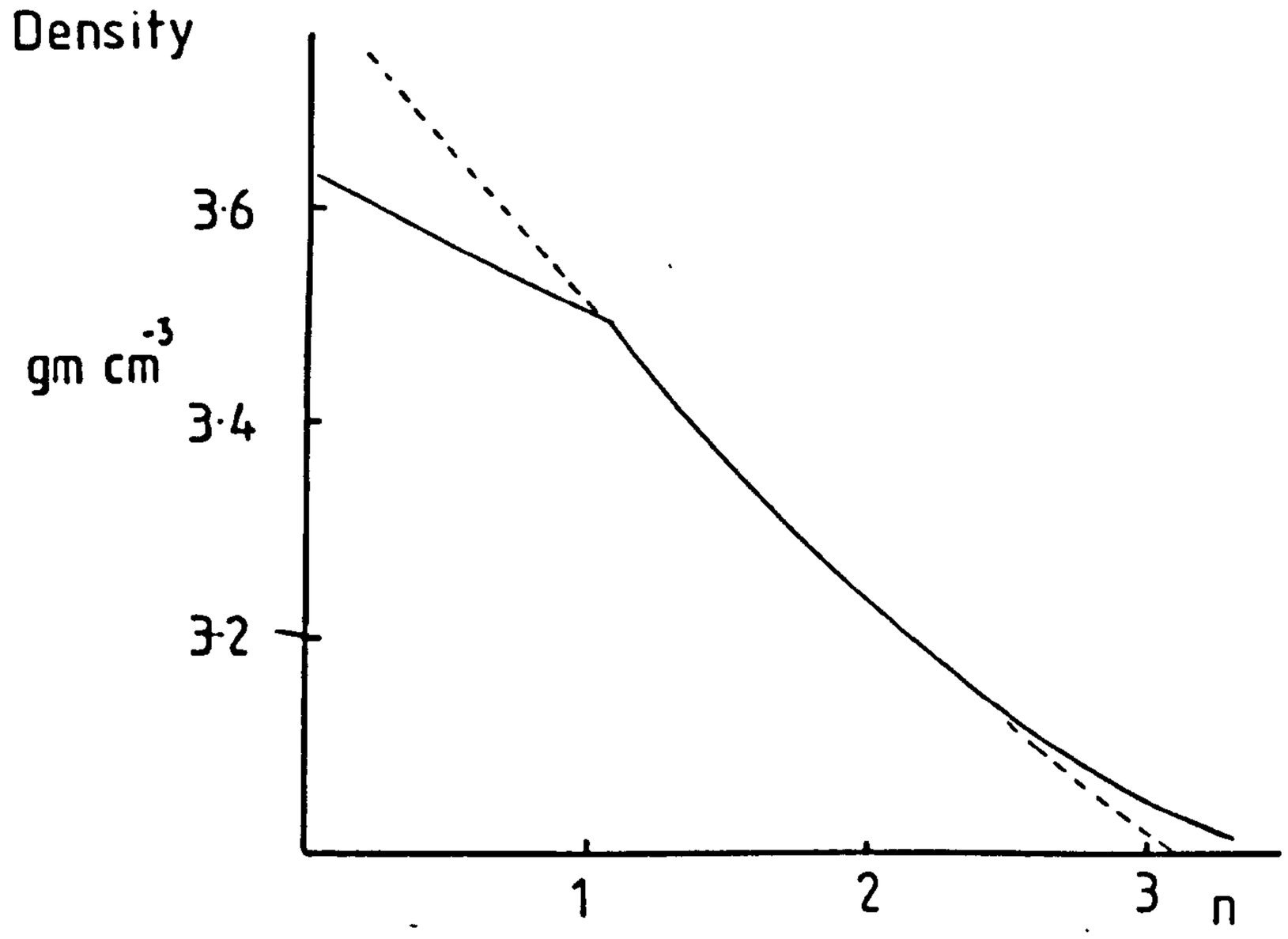

Fig.31 Density of various alumina samples as a function of water content.
(De Boer and Houben)[125]

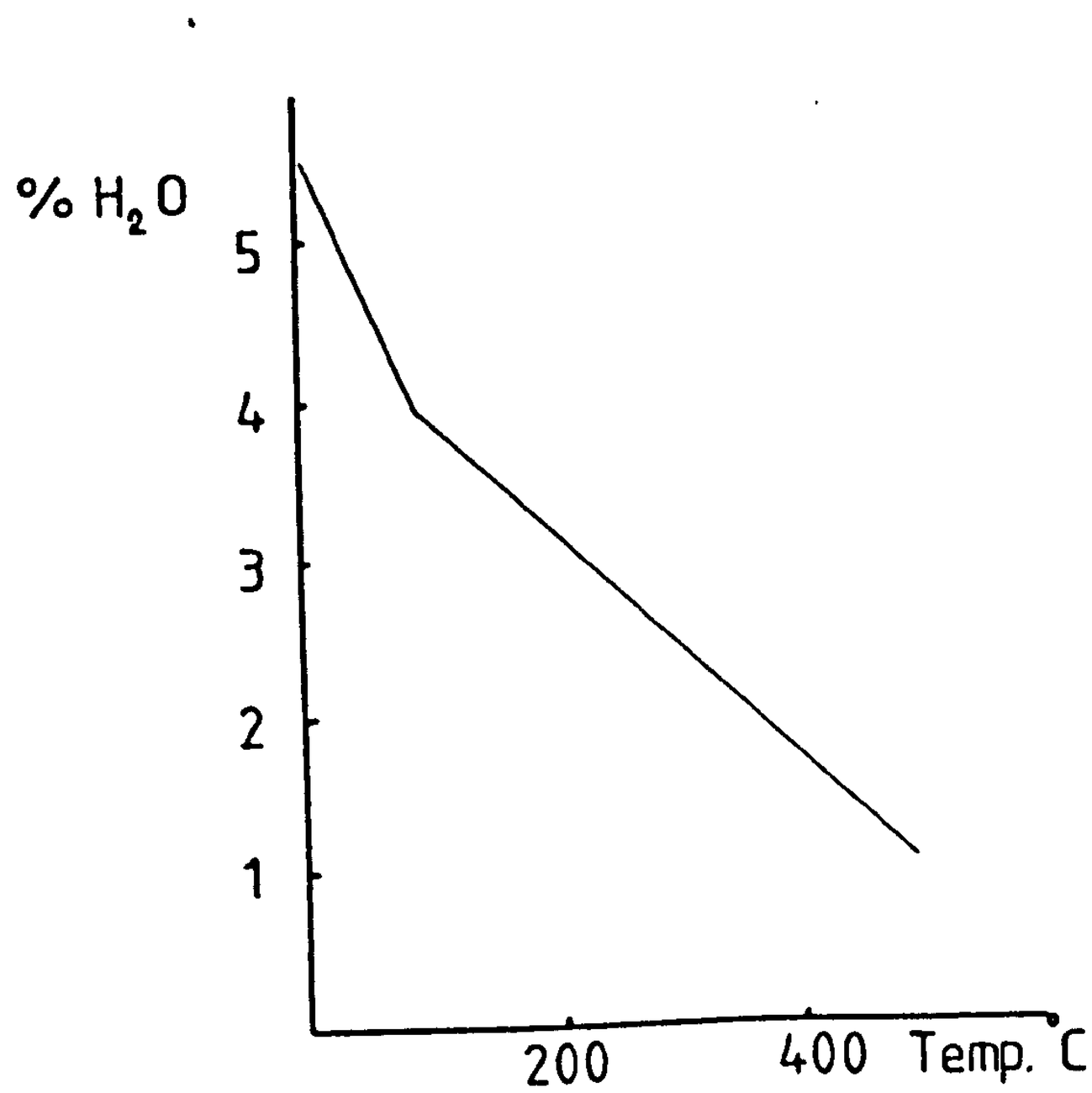

Fig.32 Percentage water in various alumina samples after heating for 8 hours at various temperatures.
(De Boer and Houben)[125]

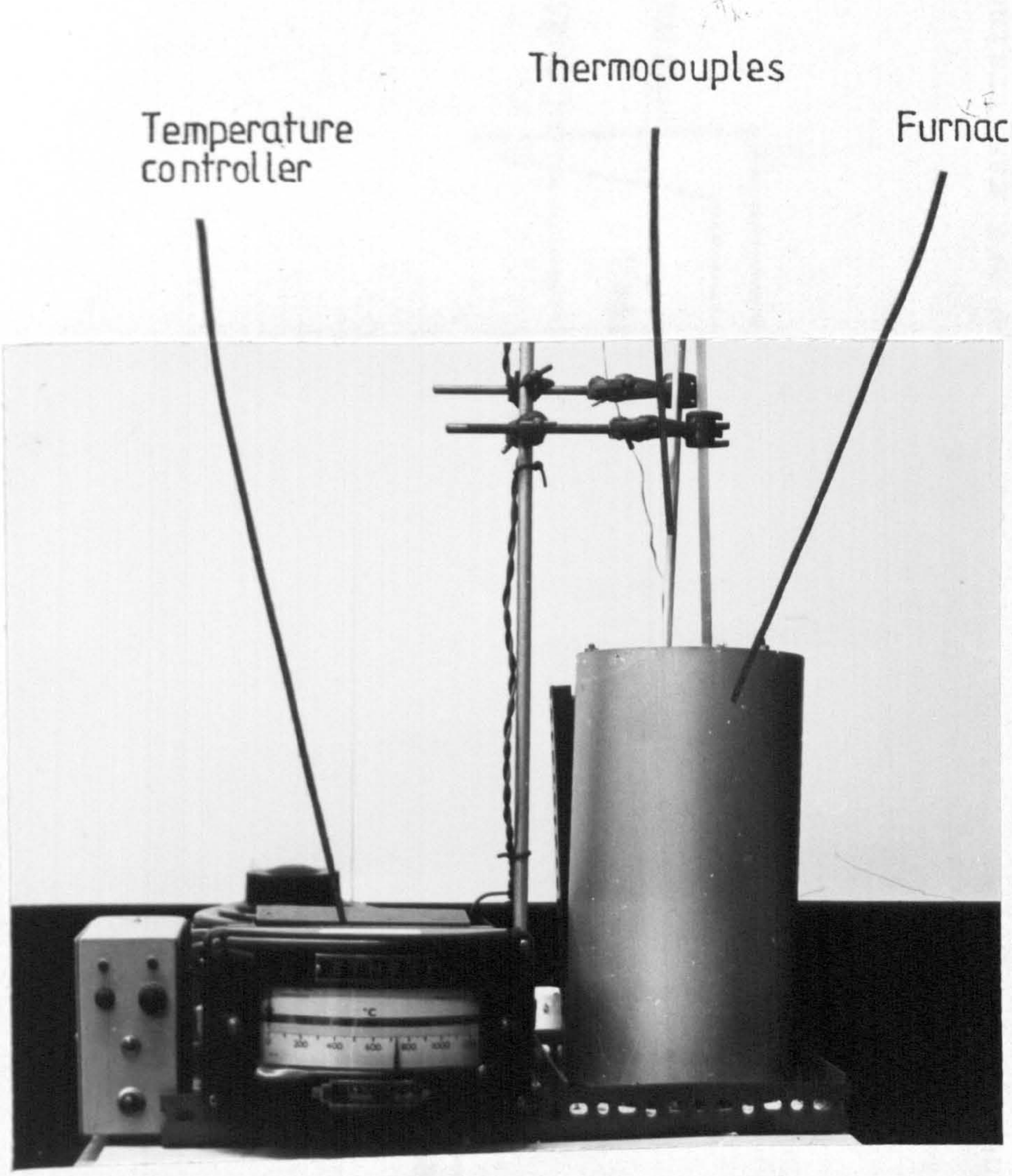

Fig.33 Melting and holding furnace.

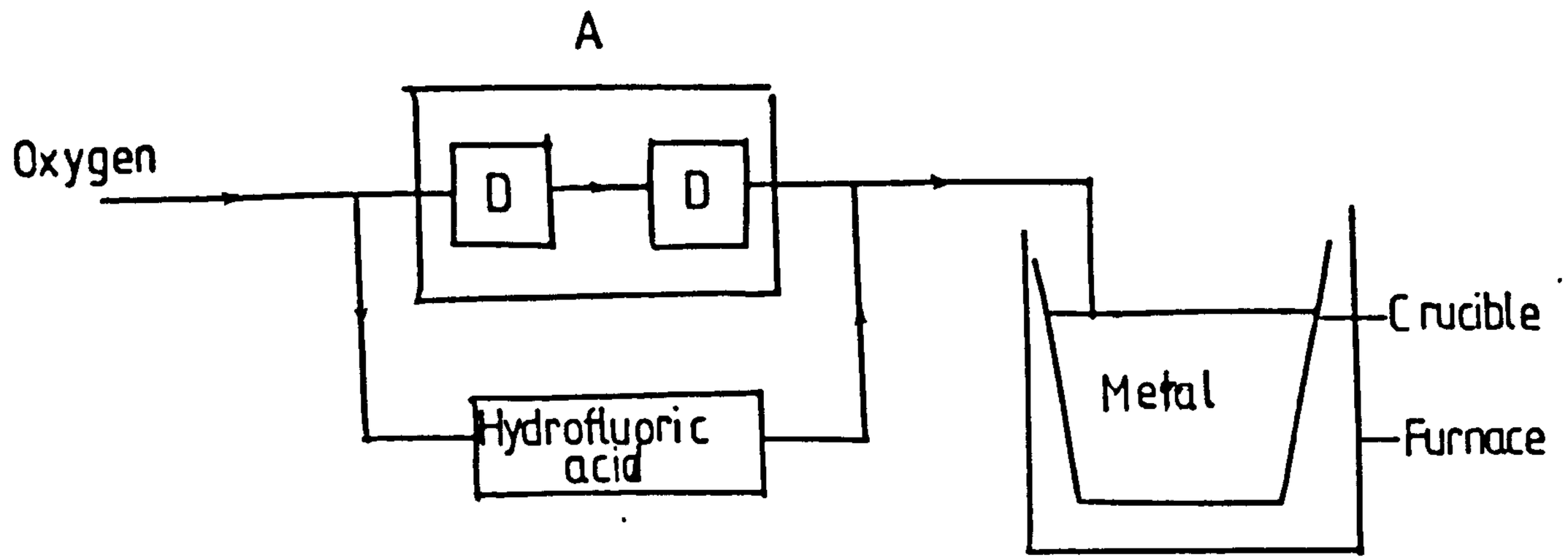

Fig.34 Schematic representation of melting furnace and gas trains

Water bath	A
Dreschal bottles	D

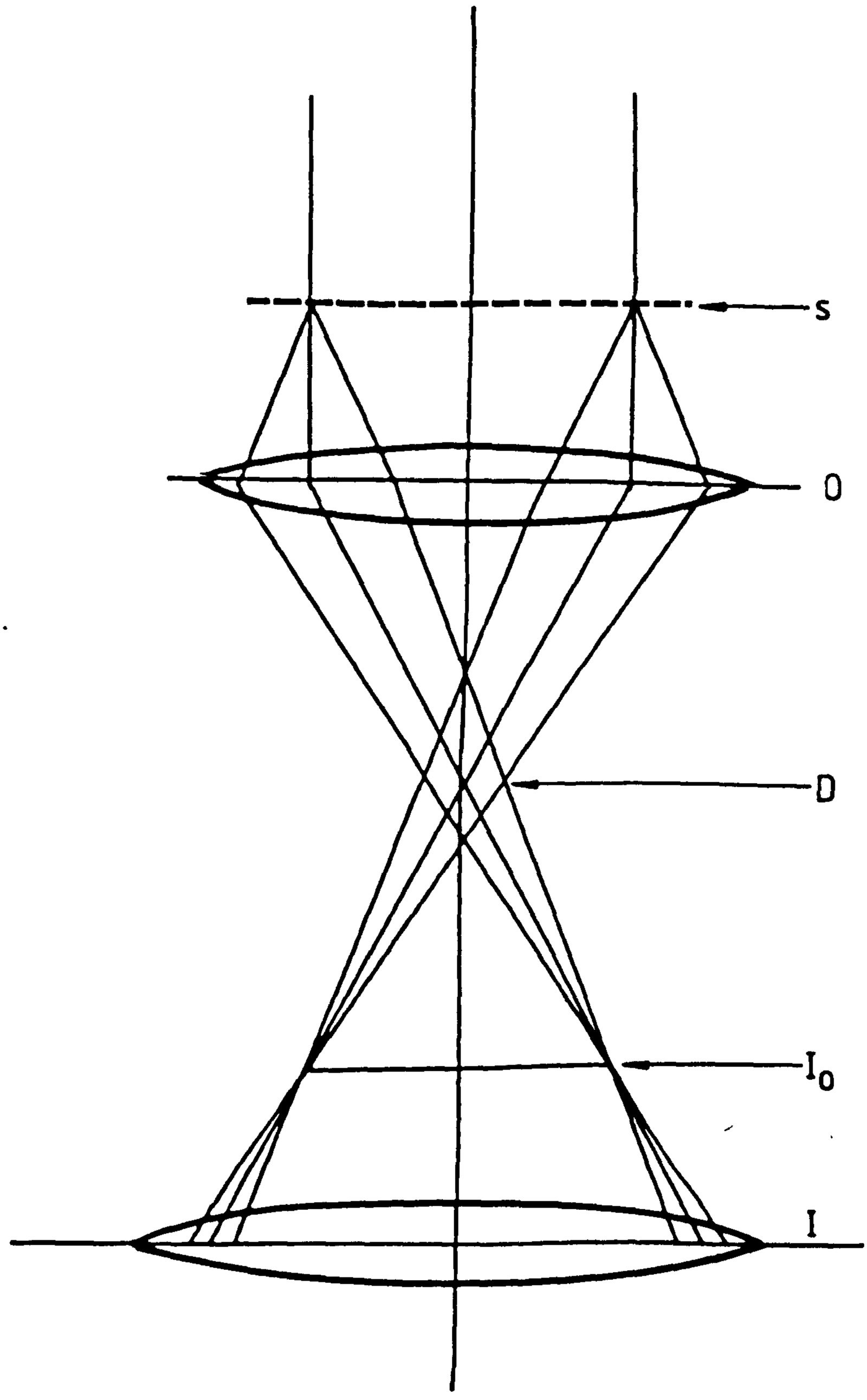

Fig.35. Formation of diffraction pattern(D) and intermediate image(I_0) of a crystalline specimen(s)by the objective lens(O). The intermediate lens(I)can be used to image either the intermediate image or diffraction pattern.

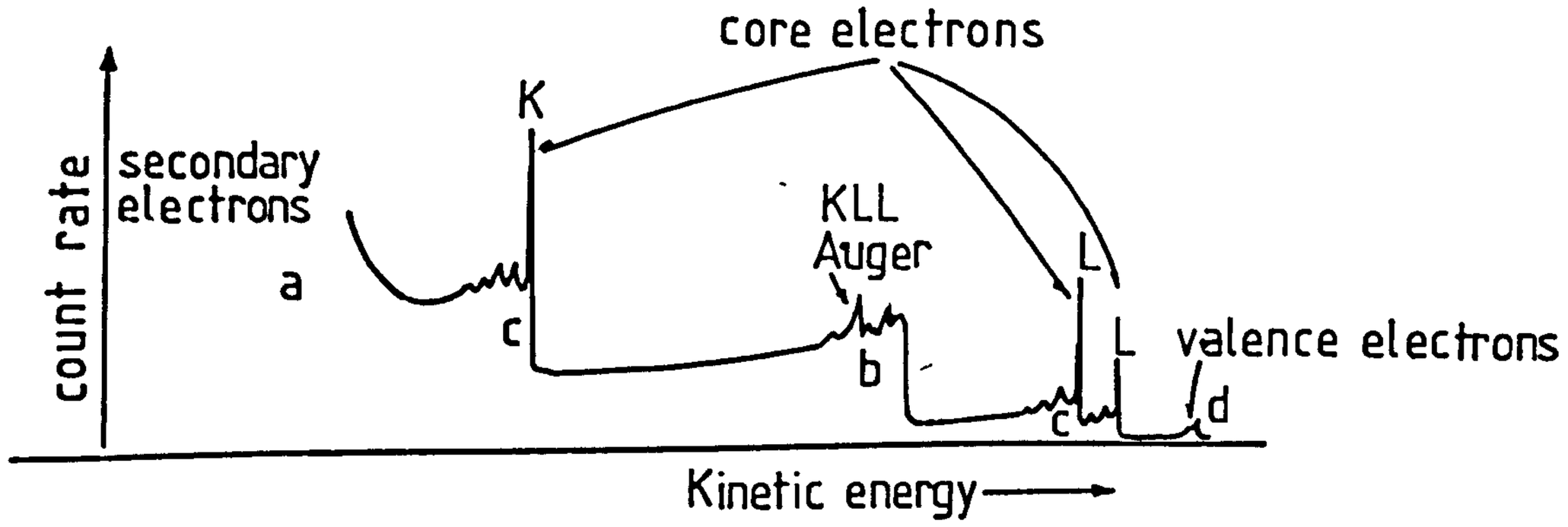

Fig. 36 A schematic XPS spectrum showing regions corresponding to secondary electrons (a) deexcitation of a hole in core shell by Auger process (b), primary excitation of core electrons (c), and primary excitation of valence electrons (d).

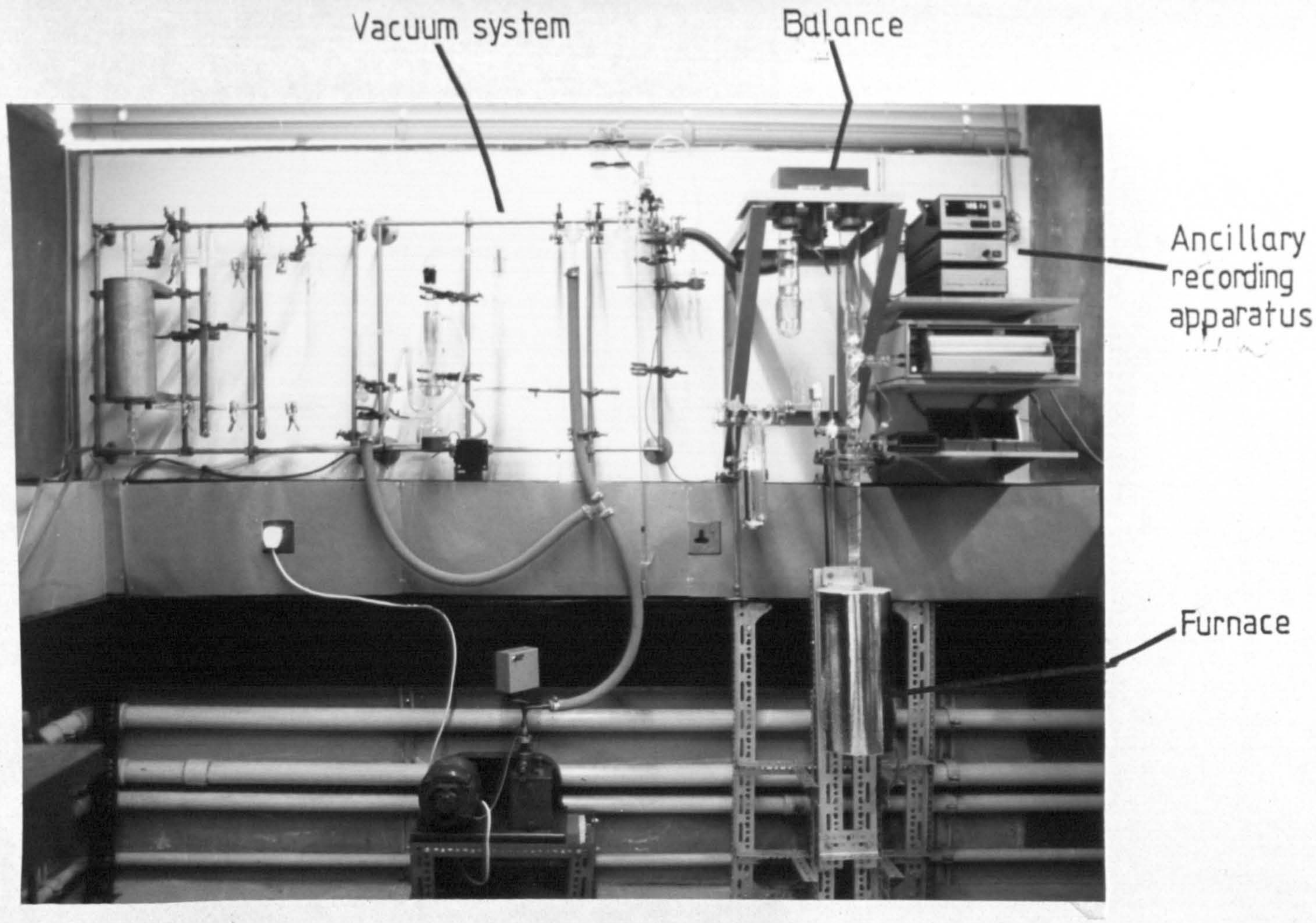

Fig.37 Microbalance apparatus

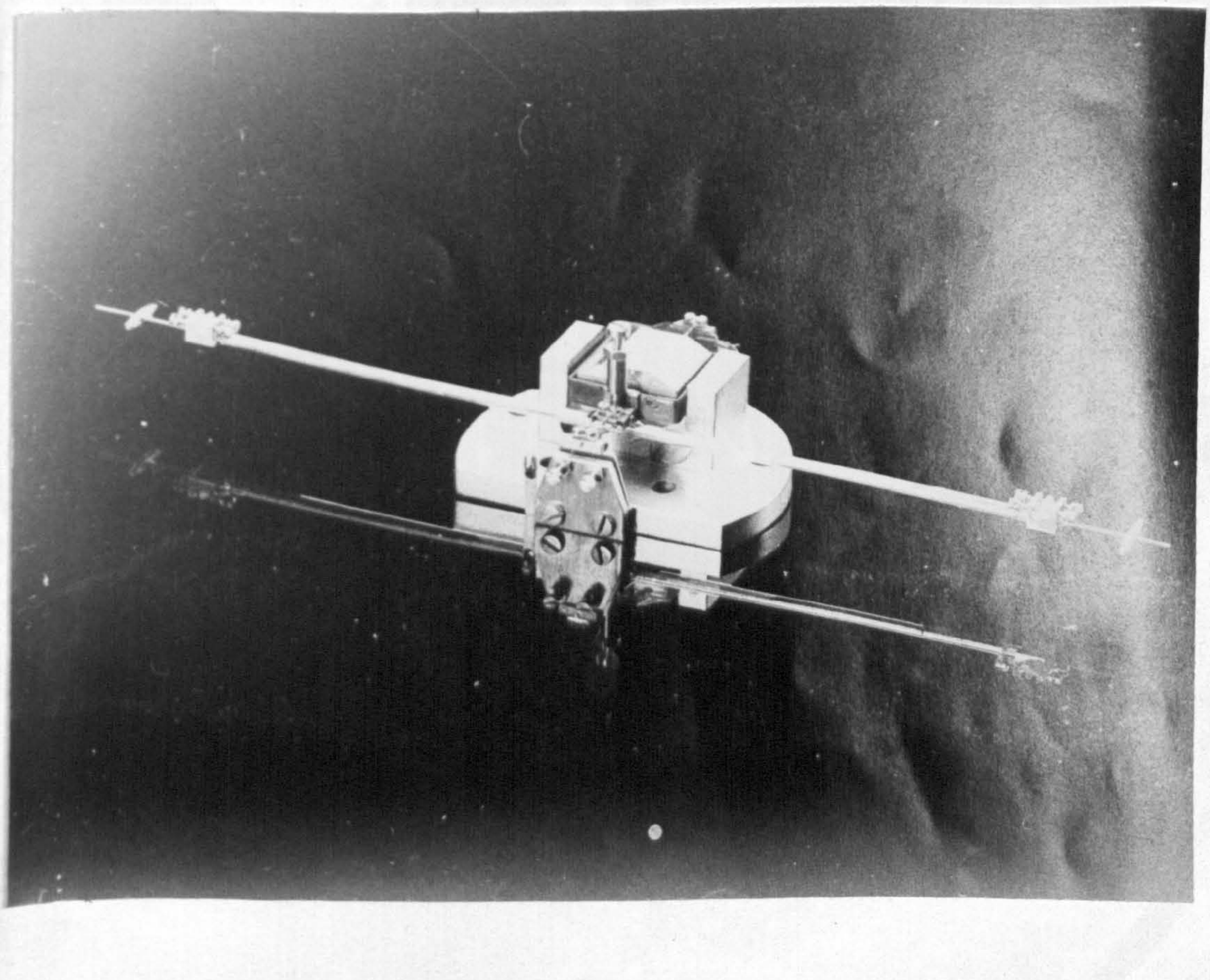

Fig.38 Balance beam.

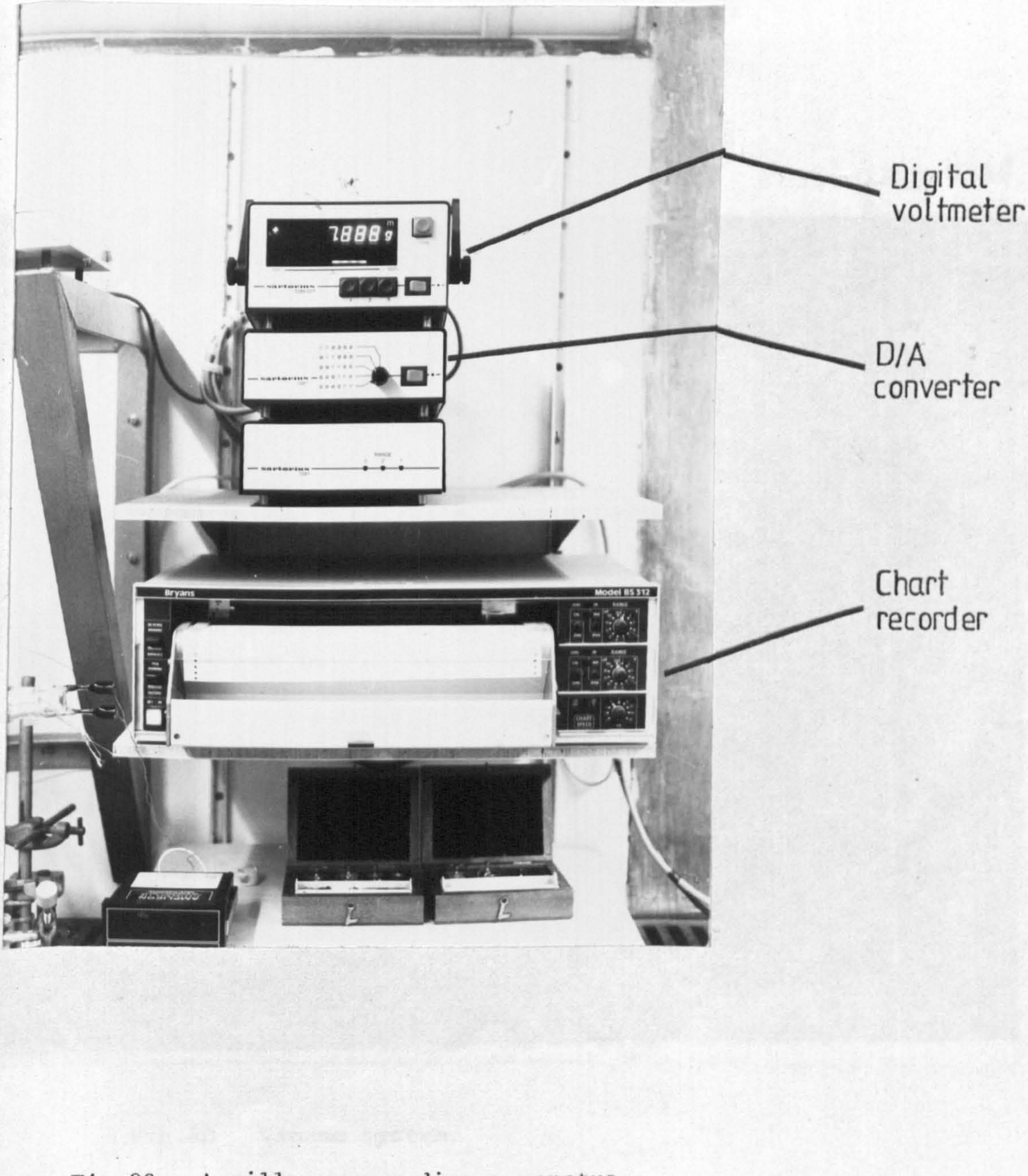

Fig.39 Ancillary recording apparatus.

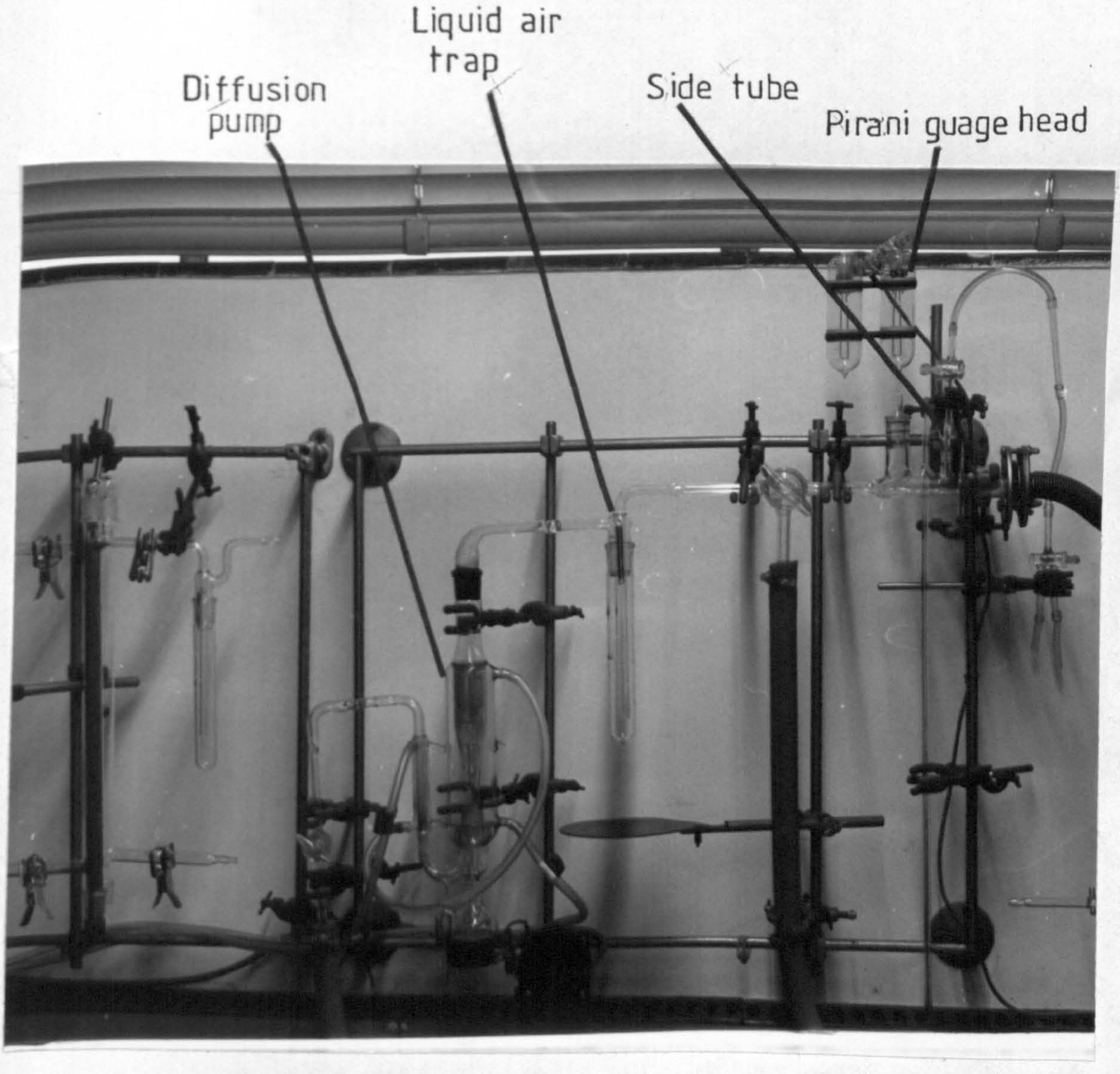

Fig.40 Vacuum system.

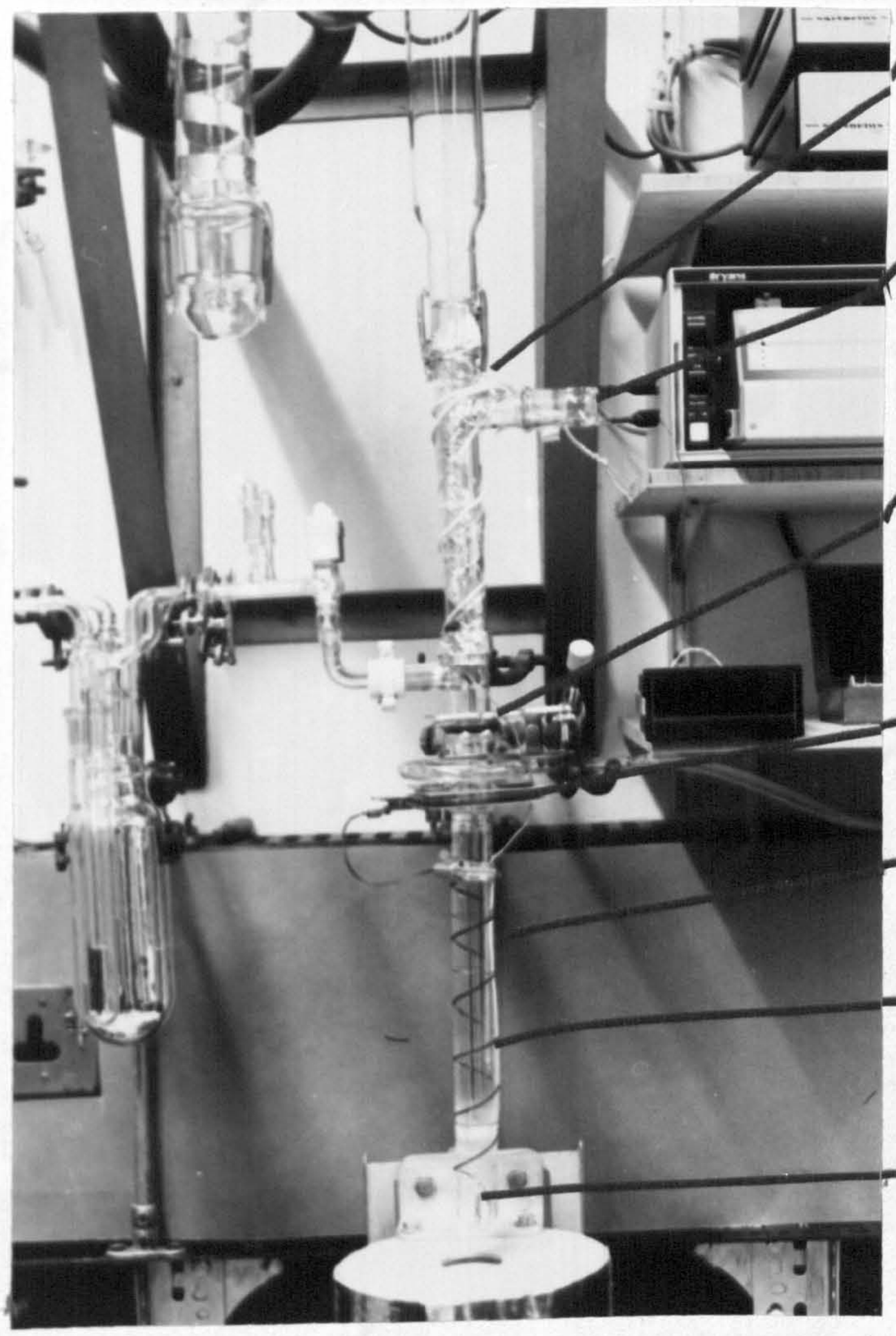

Fig. 41 Specimen chamber.

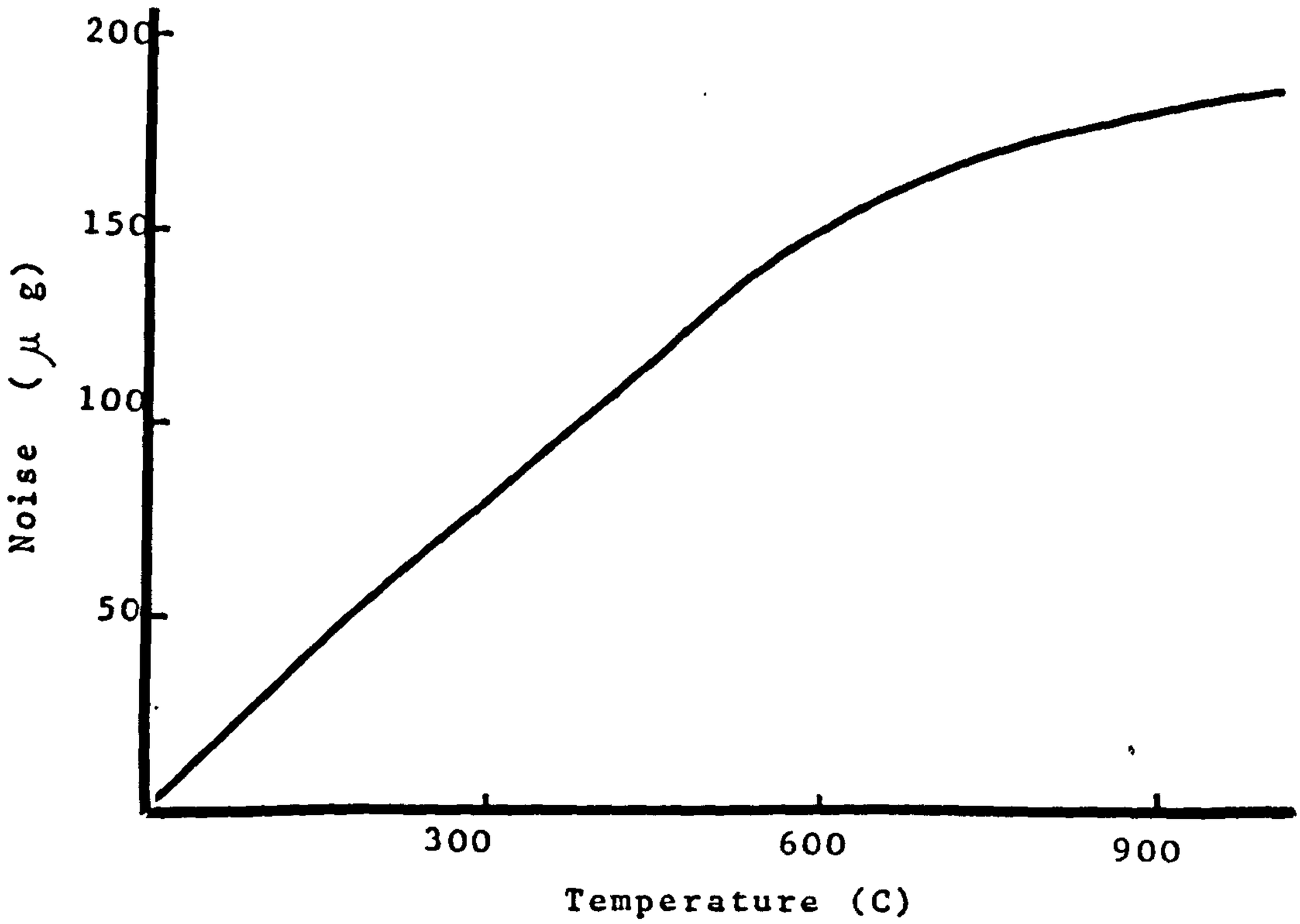

Fig.42a. Variation of 'noise' with temperature at constant pressure (1 atms)

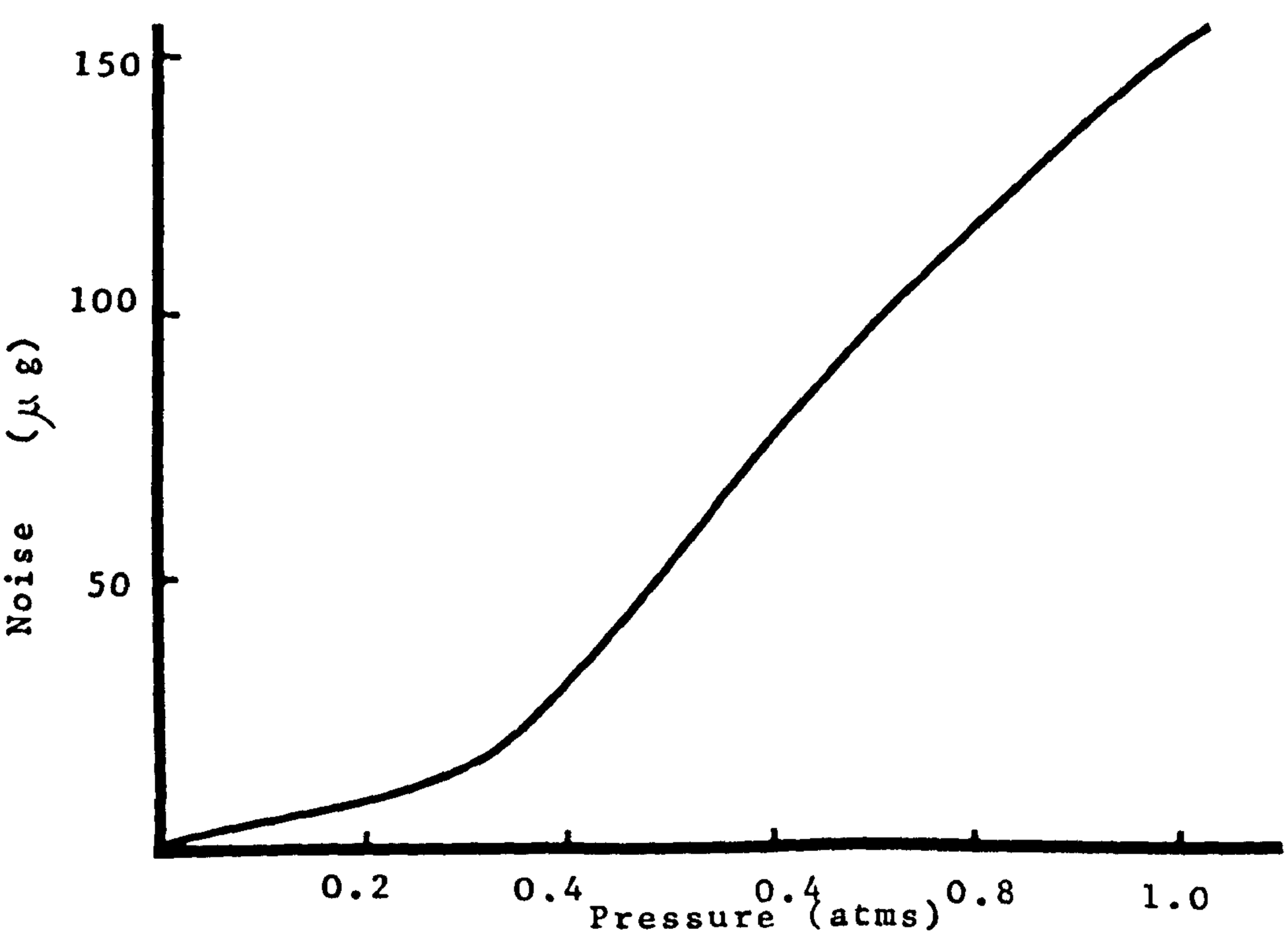

Fig.42b. Variation of 'noise' with pressure, at constant temperature (730°C)

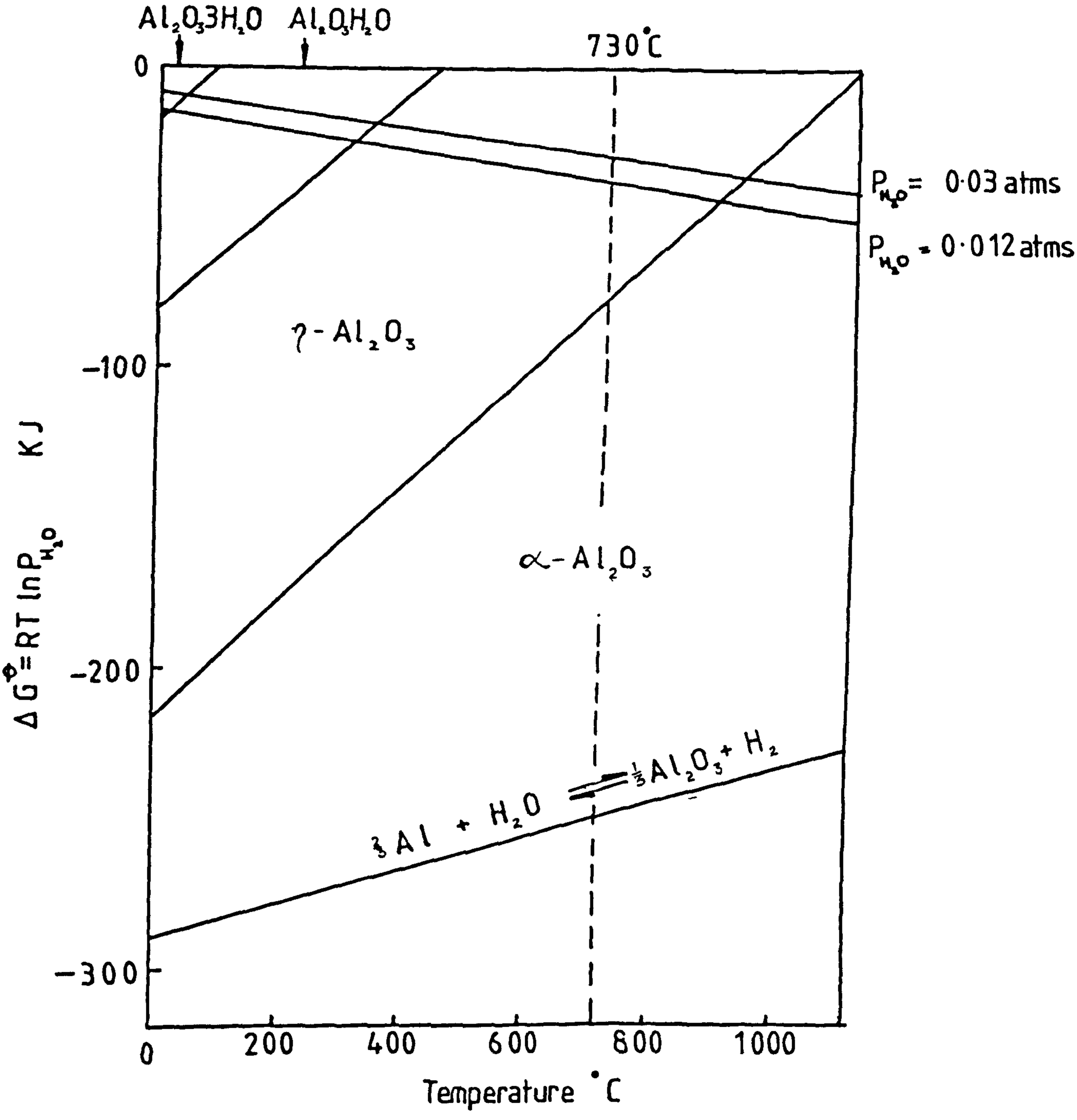

Fig 43 Water vapour potential diagram for alumina hydrates

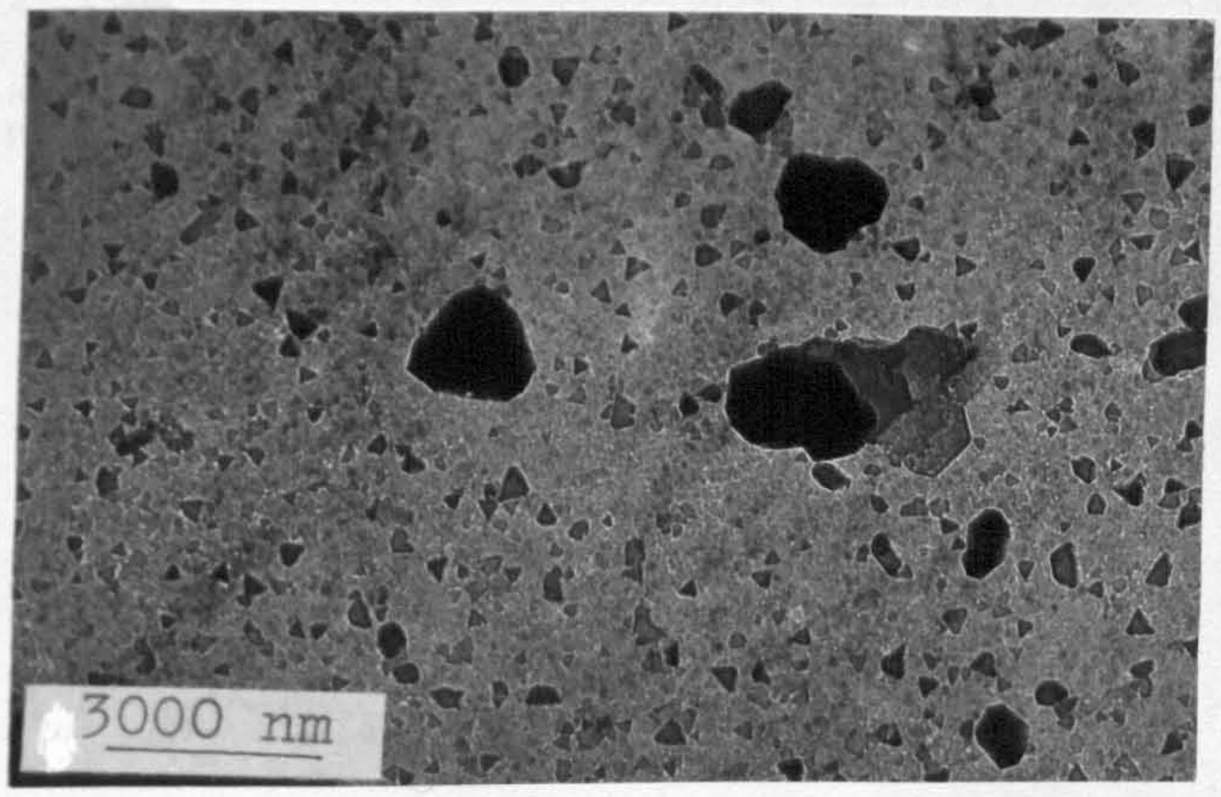

Fig.44a TEM of oxide film formed on pure aluminium at 730°C after 10 minutes exposure to moist oxygen, (P_{H_2O} · 0·03 atms.)

Fig 44b Selected area diffraction pattern of an oxide film formed on pure aluminium at 730 C after 10 mins exposure to moist oxygen (P_{H_2O} = 0.03 atms). The analysis (Table 9) shows that the film comprises $\alpha - Al_2O_3$ and $\eta - Al_2O_3$. Original negative magnified x2

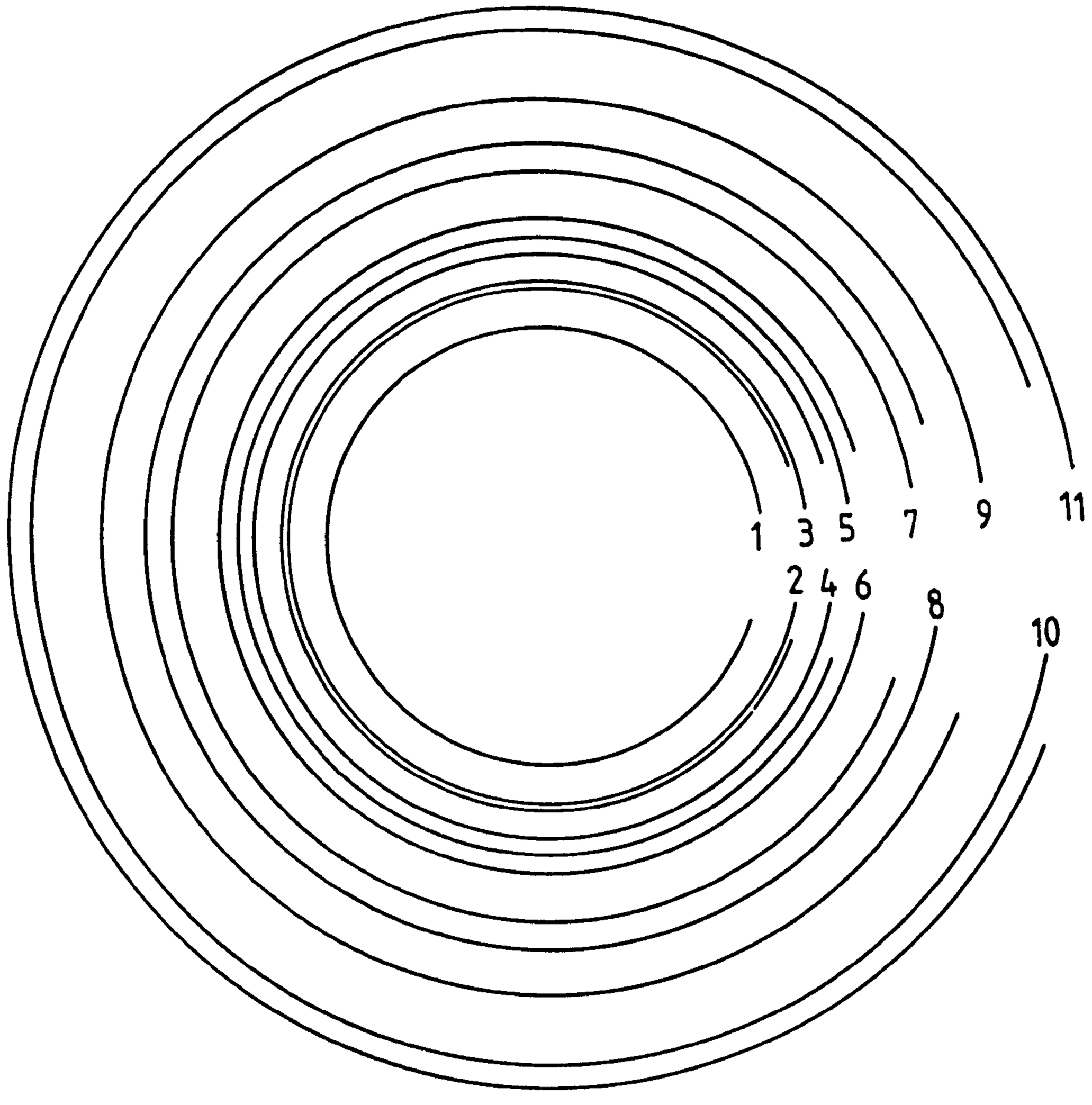
1
3
5
7
9
11
2
4
6
8
10

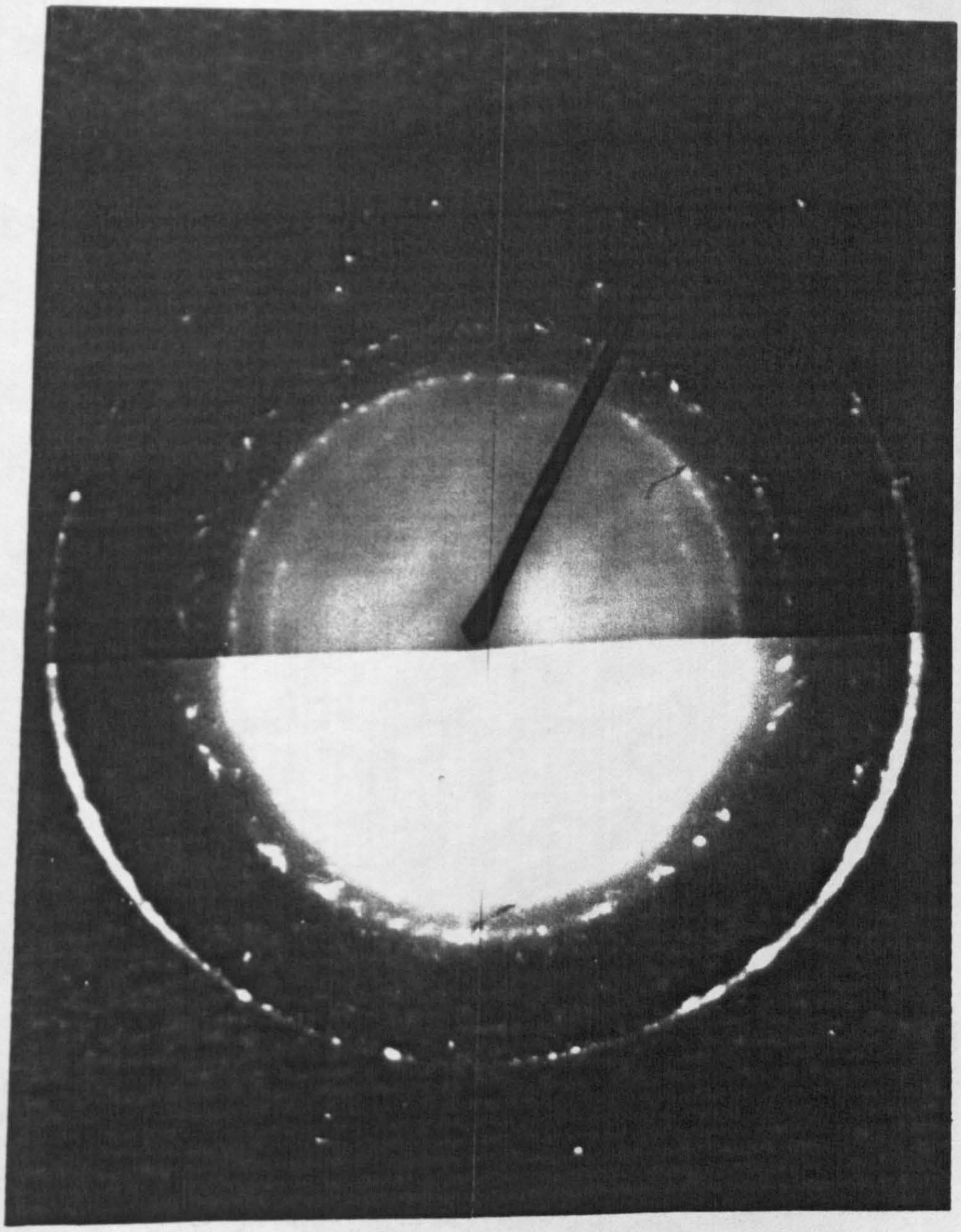

Fig. 44b. Selected area diffraction pattern of an oxide film formed on pure aluminium at 730^{o} C after 10 mins exposure to moist oxygen (P_{H_2O} = 0.03 atm)

The analysis (Table 9) shows that the film

comprises - Al_2O_3 and - Al_2O_3.

Original negative magnified x2.

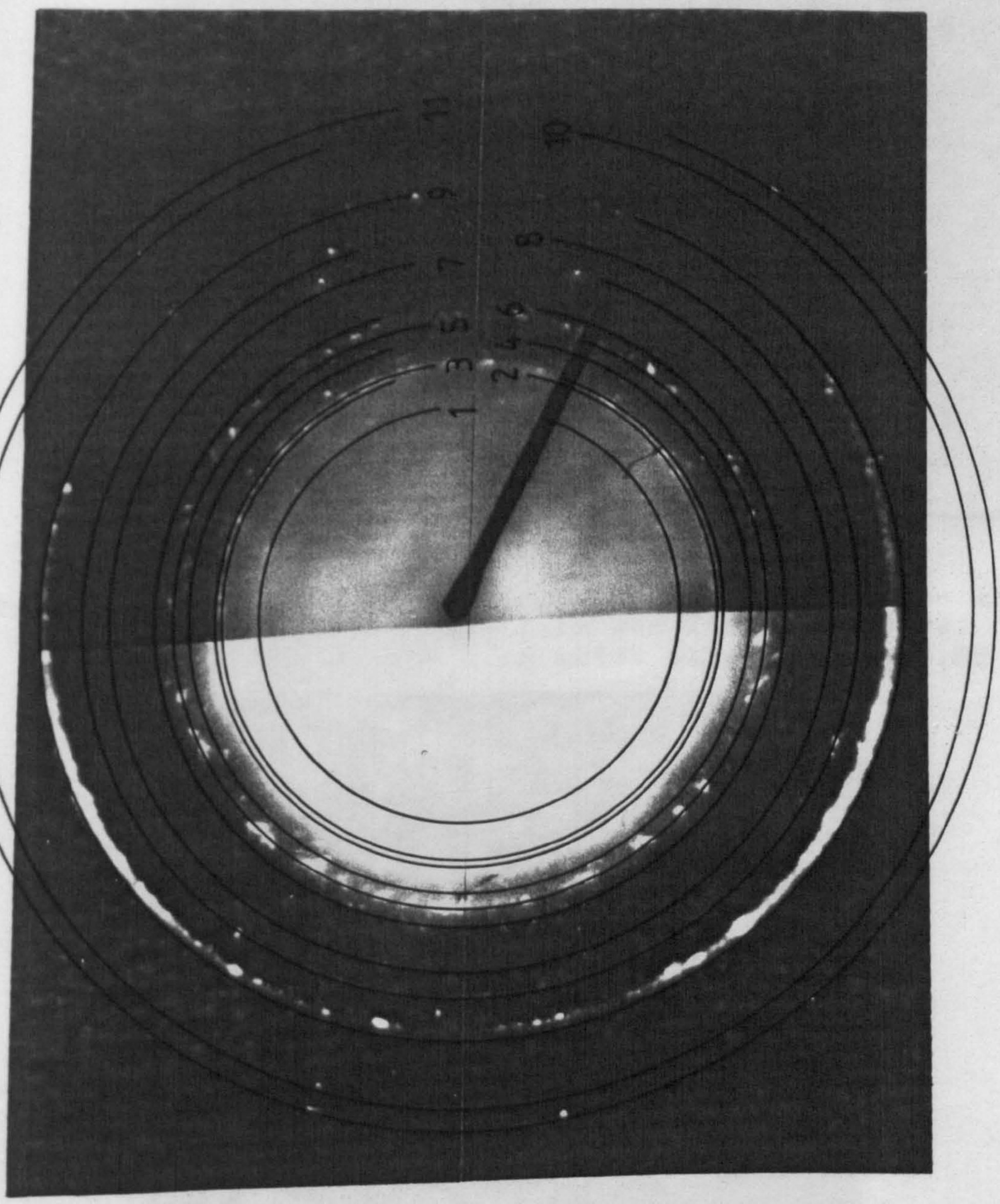

Fig. 44b. Selected area diffraction pattern of an oxide film formed on pure aluminium at 730^{o} C after 10 mins exposure to moist oxygen (P_{H_2O} = 0.03 atm)
The analysis (Table 9) shows that the film comprises - Al_2O_3 and - Al_2O_3.
Original negative magnified x2.

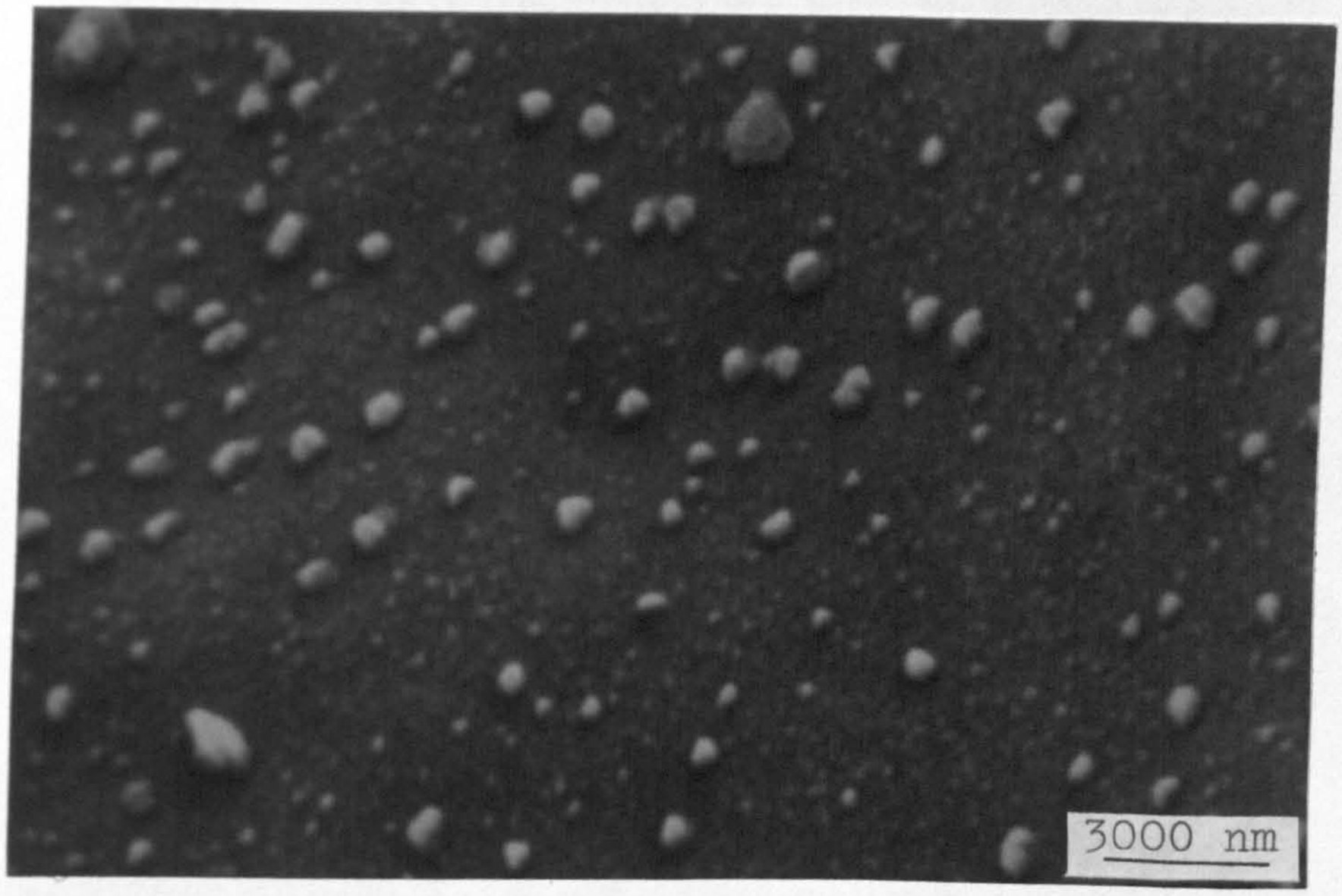

Fig.45 SEM of oxide/metal interface showing the α- Al_2O_3 crystals. The oxide film was formed on pure aluminium at 730 °C in moist oxygen (P_{H_2O} = 0.03 atms)

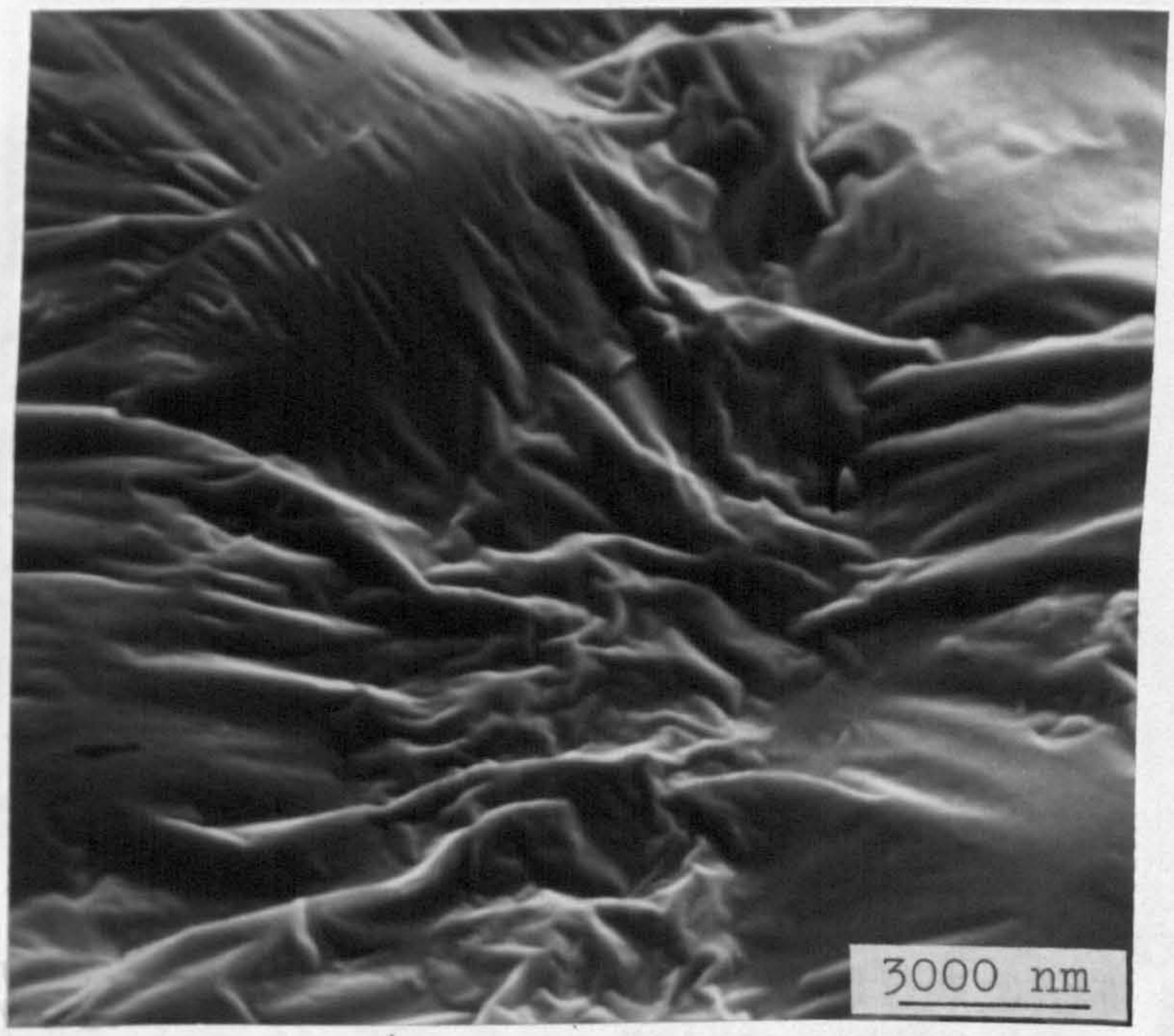

Fig.46 SEM of oxide/atms. interface showing the featureless γ-Al_2O_3 The film was formed on pure aluminium at 730 °C in moist oxygen (P_{H_2O} = 0.03 atms)

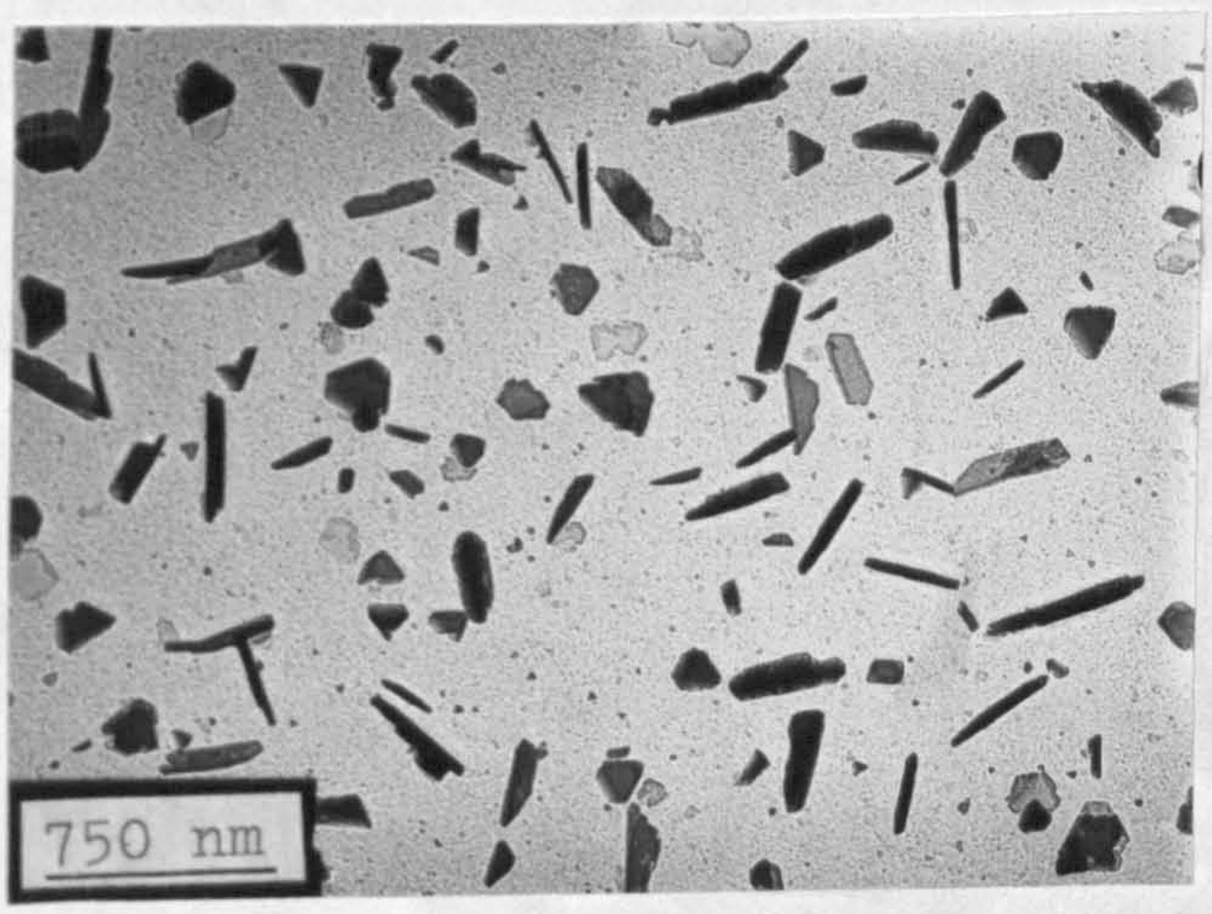

Fig. 47 TEM of oxide film formed on pure aluminium at 730 °C in moist oxygen (P_{H_2O} = 0.03 atms) showing coarse primary α- Al_2O_3.

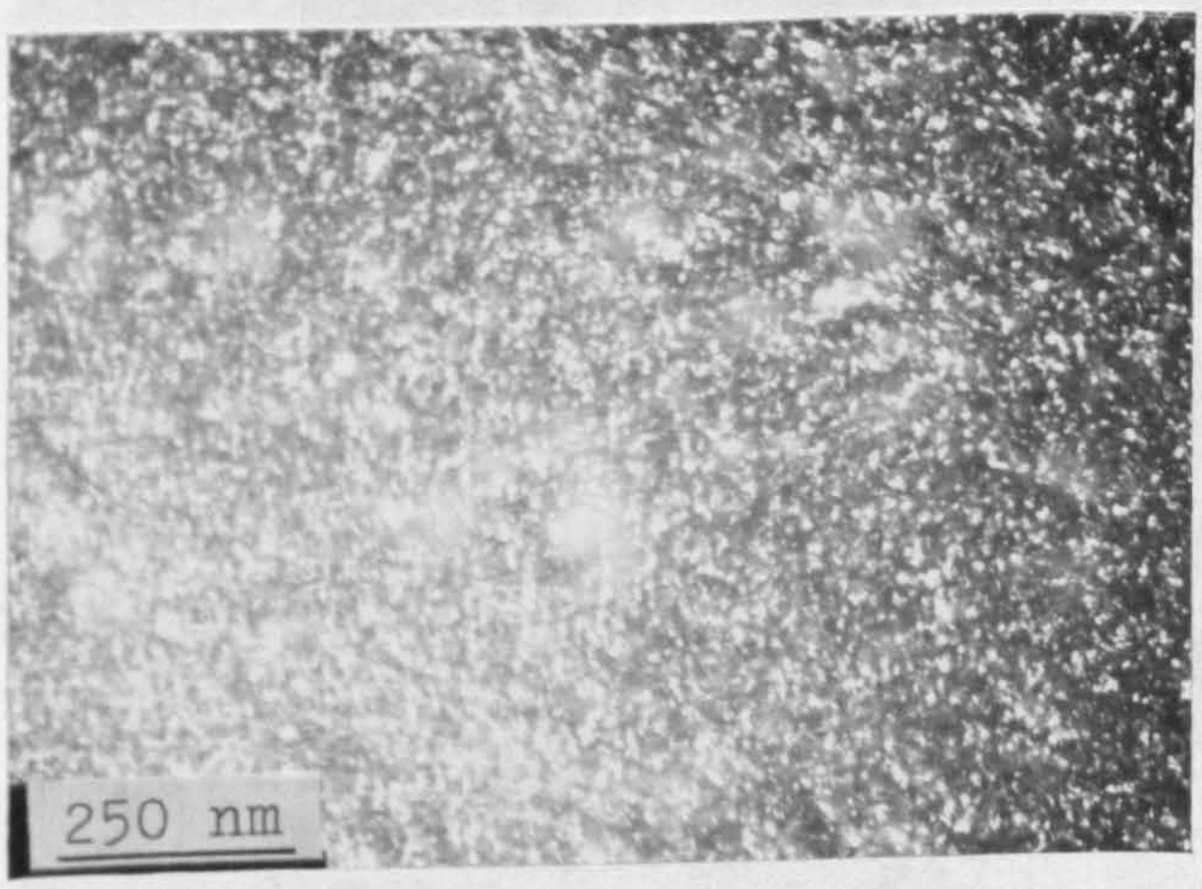

Fig.48 Dark field TEM showing the secondary α-Al_2O_3 crystallites. The oxide film was formed on pure aluminium at 730 °C in moist oxygen (P_{H_2O} = 0.03 atms.)

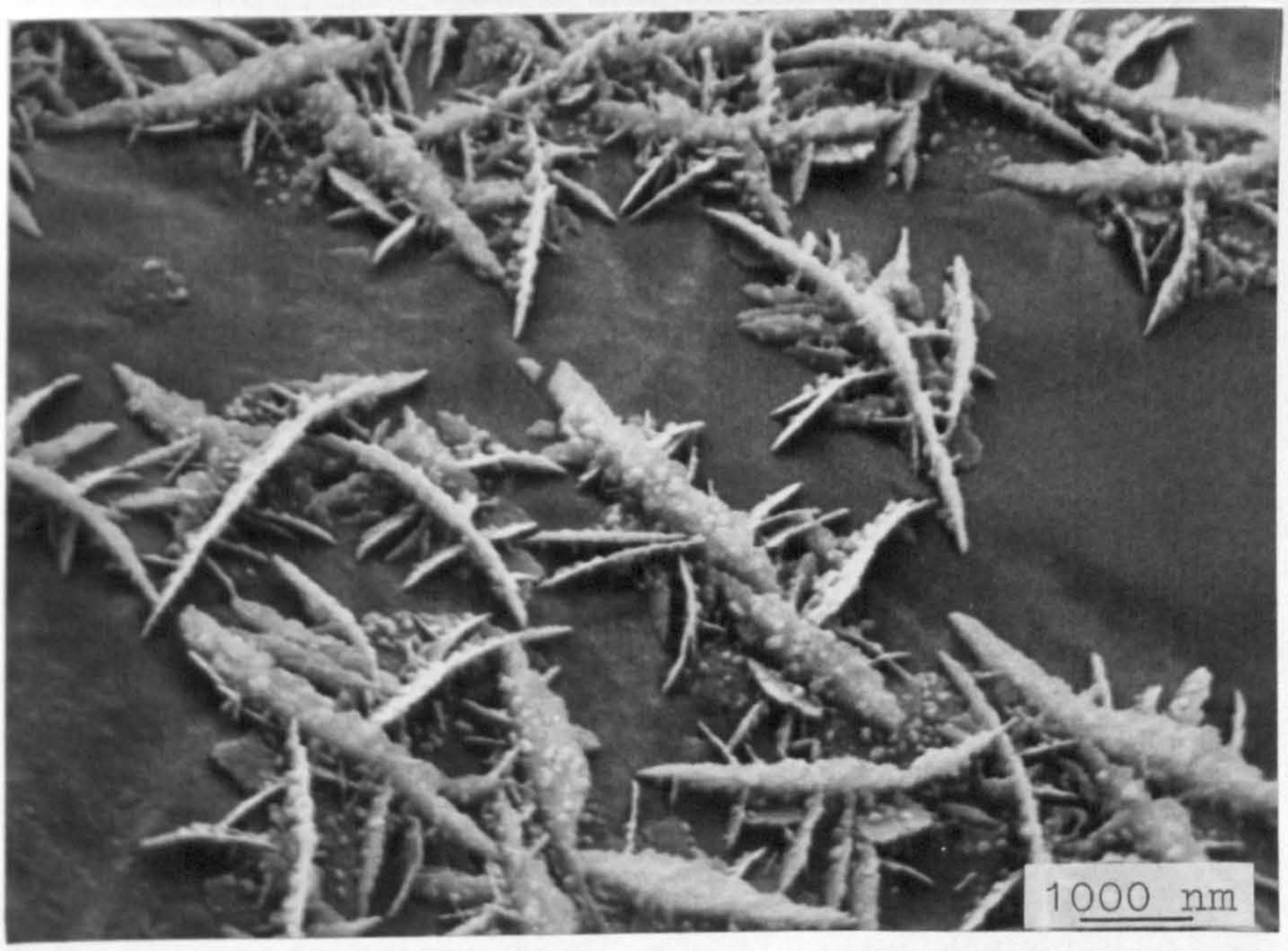

Fig.49a SEM of oxide film formed on pure aluminium at 730 °C in moist oxygen (P_{H_2O} = 0.03 atms.) showing acicular dendrites (Type a) at the oxide/metal interface.

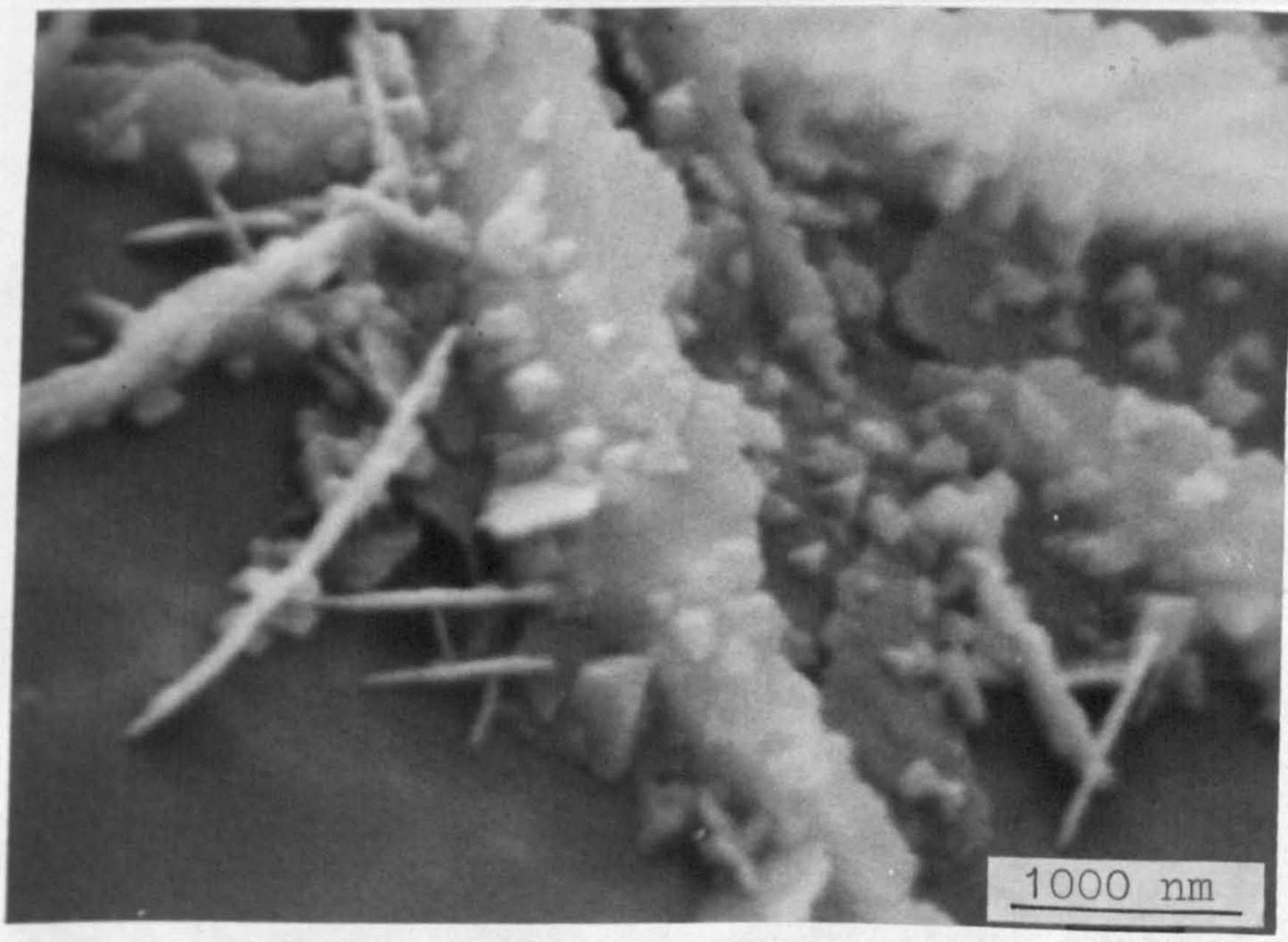

Fig.49b Type(a) morphology at higher magnification.

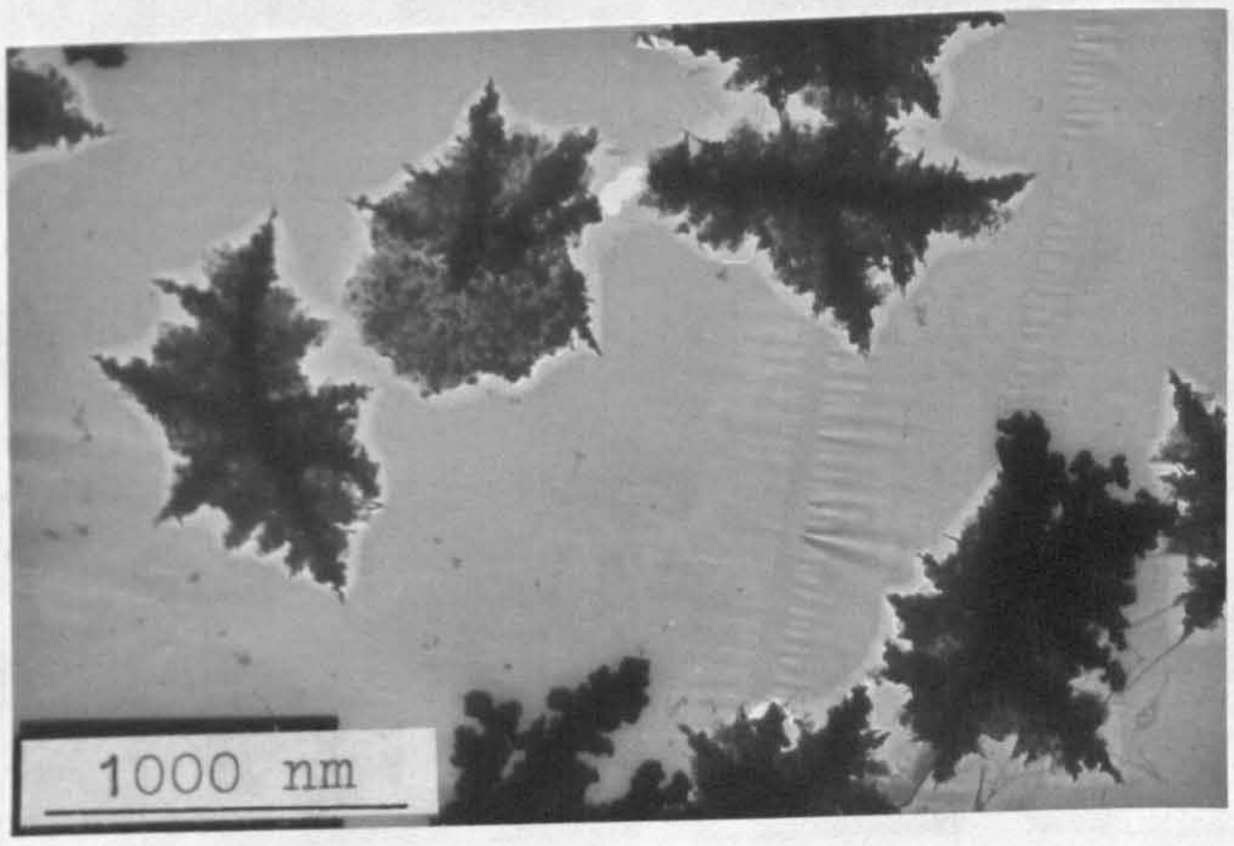

Fig.49c TEM of oxide film formed on pure aluminium at 730 °C in moist oxygen (P_{H_2O} = 0.03 atms.) showing acicular dendrites (Type a).

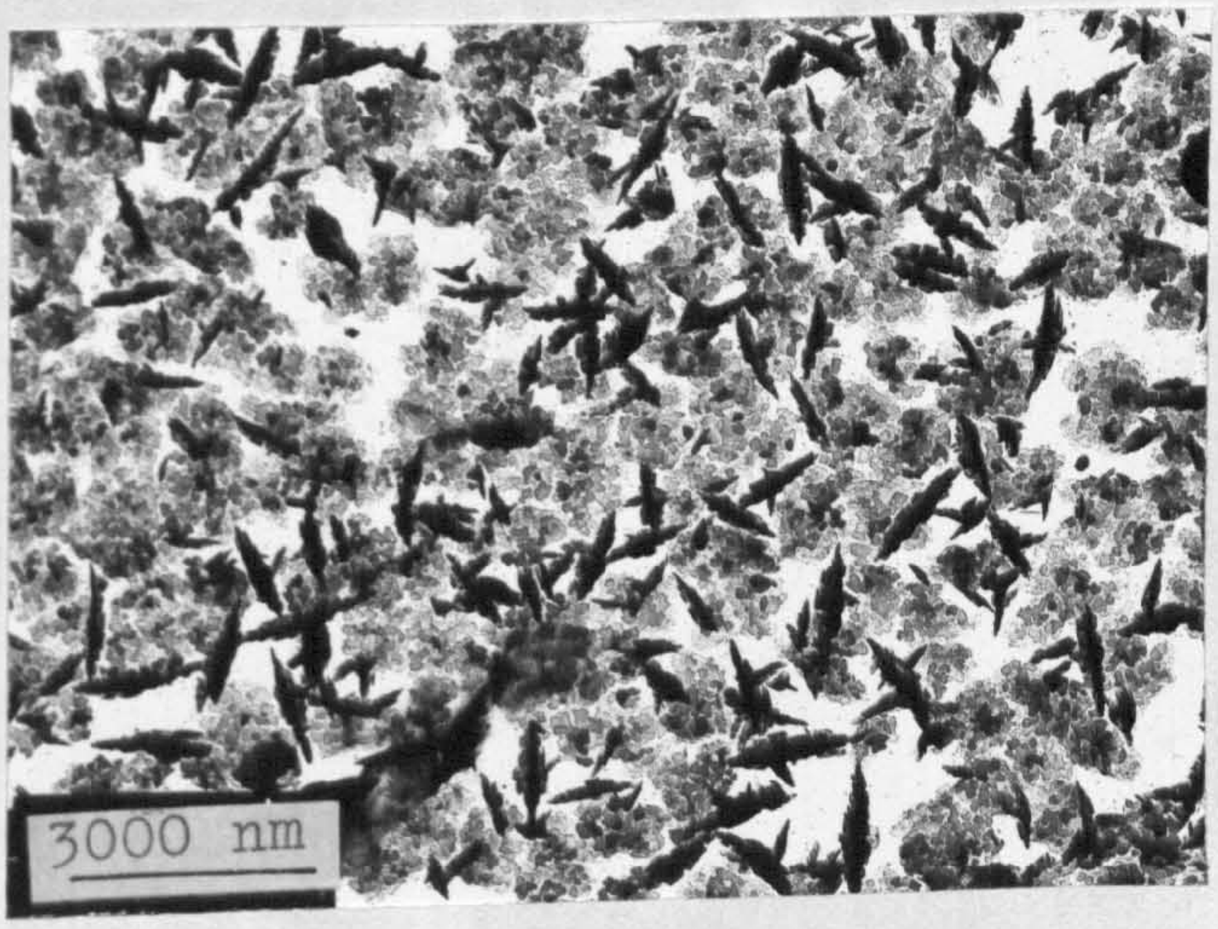

Fig.49d TEM of oxide film formedon pure aluminium at 730 °C in moist oxygen (P_{H_2O} =0.03 atms) showing acicular dendrites

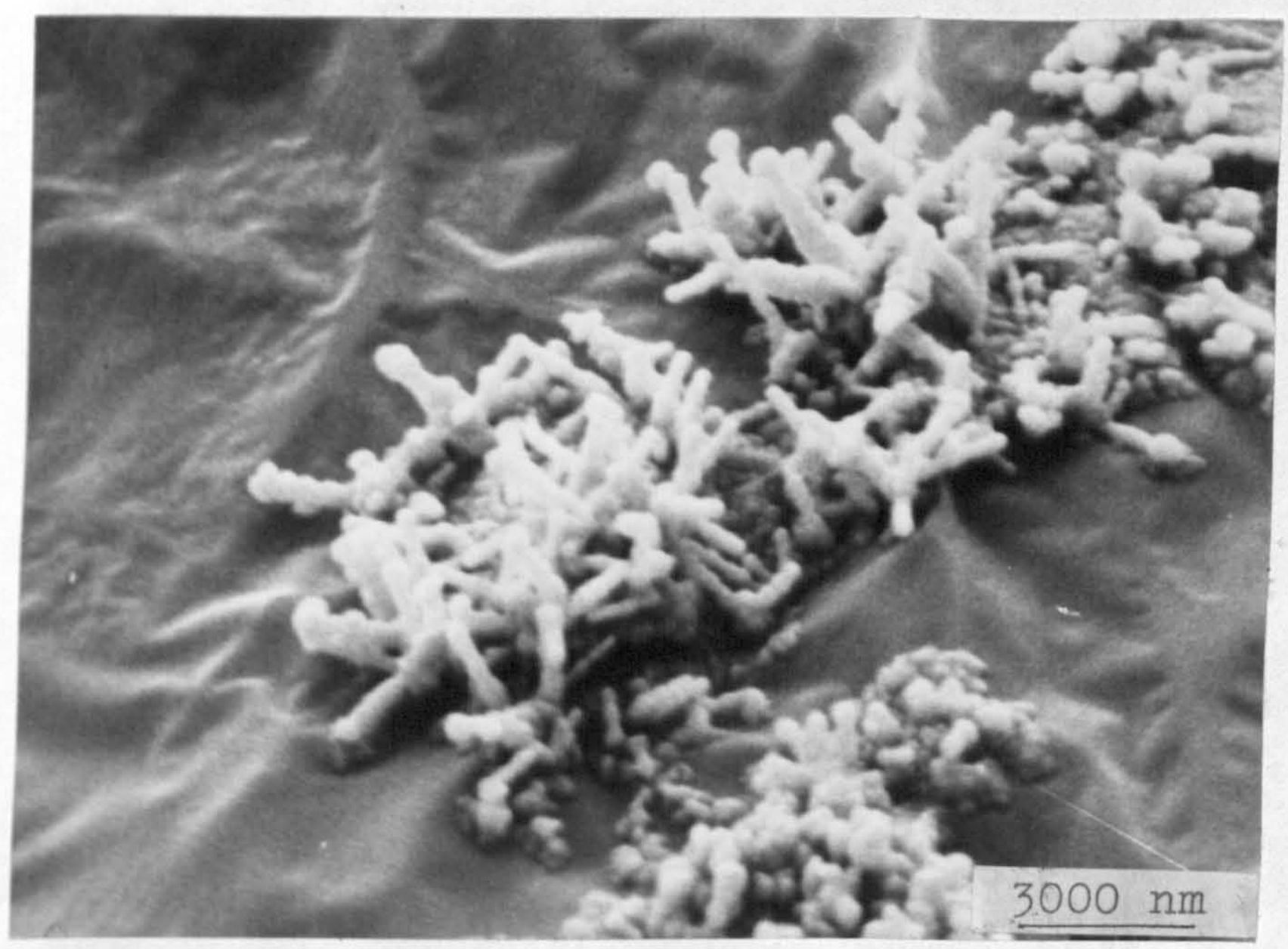

Fig.49e SEM of oxide film formed on pure aluminium at 730 °C in moist oxygen (P_{H_2O} =0.03 atms) showing globular dendrites (Type b) at the oxide/metal interface.

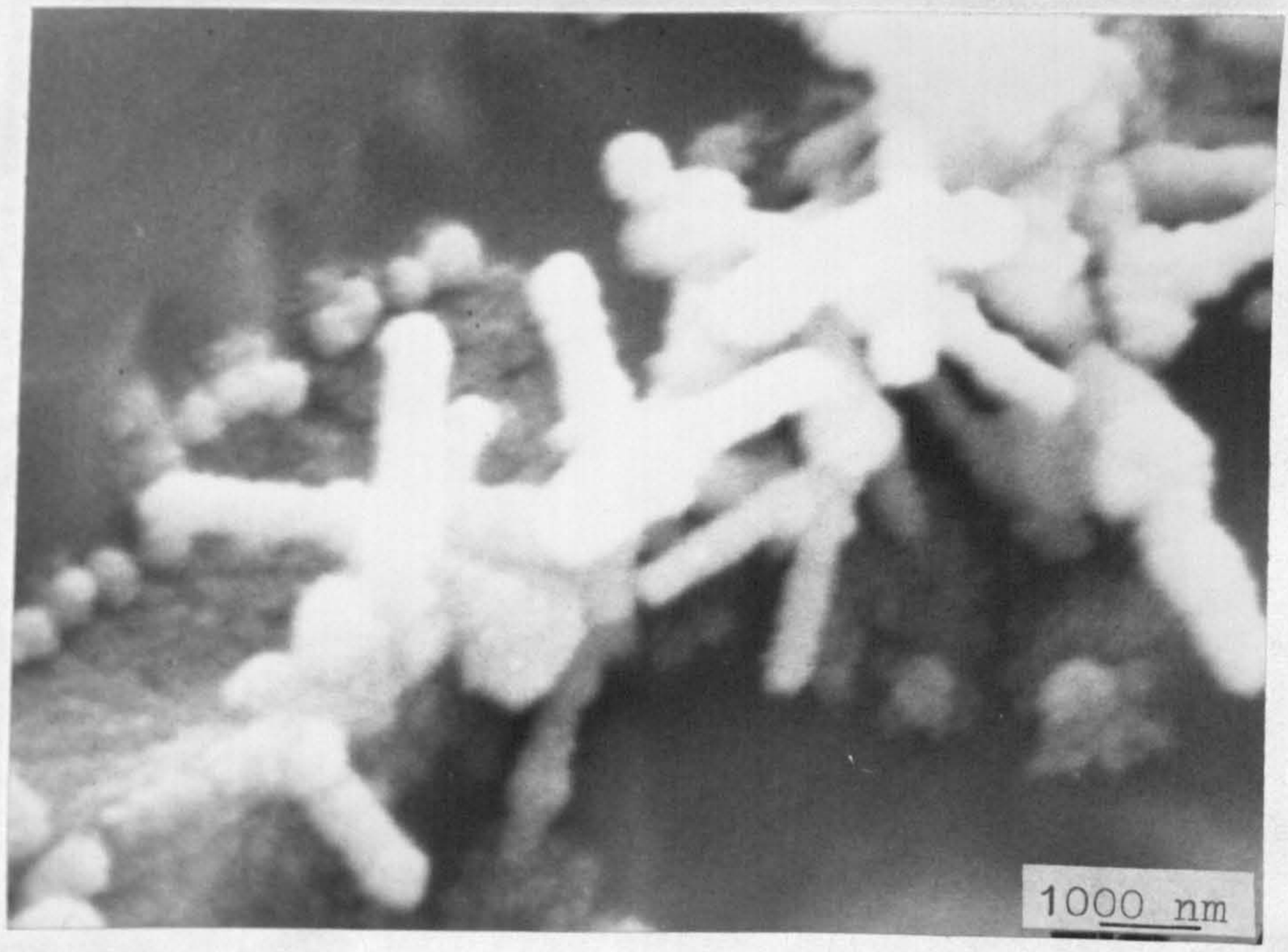

Fig.49f Type (b) morphology at higher magnification.

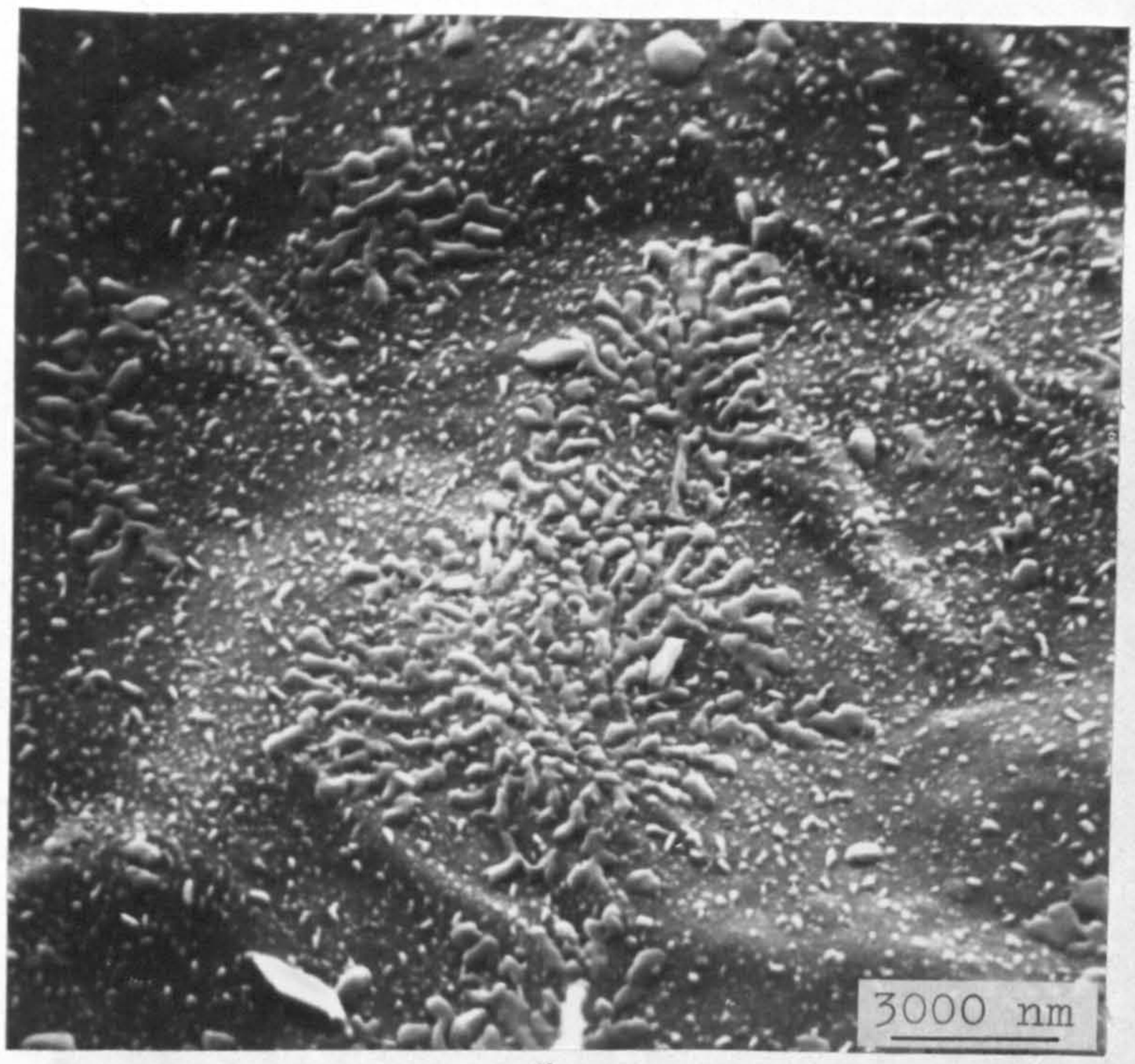

g

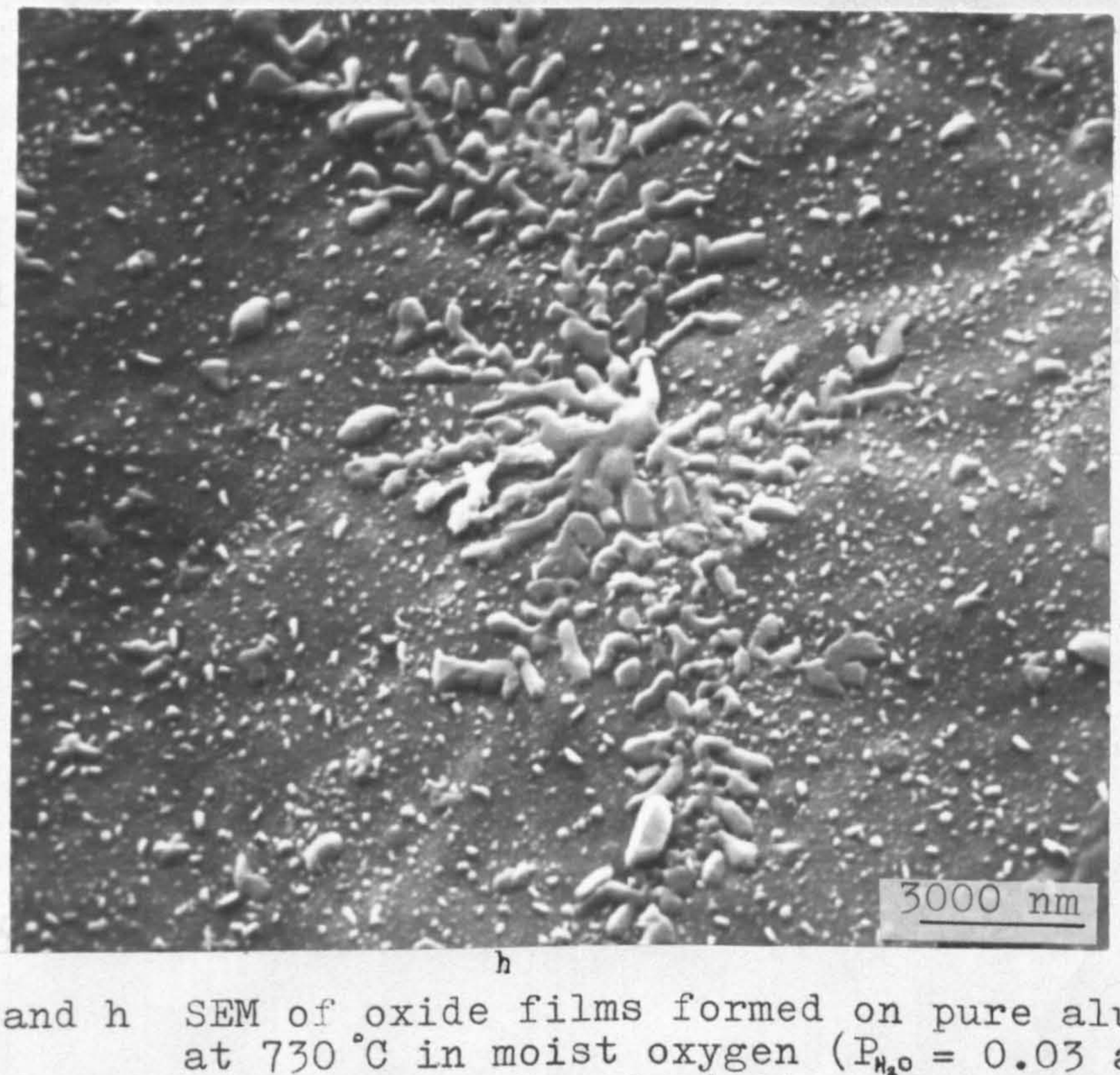

h

Fig.49g and h SEM of oxide films formed on pure aluminium at 730 °C in moist oxygen (P_{H_2O} = 0.03 atms) showing globular dendrites (Type b) at the oxide/metal interface.

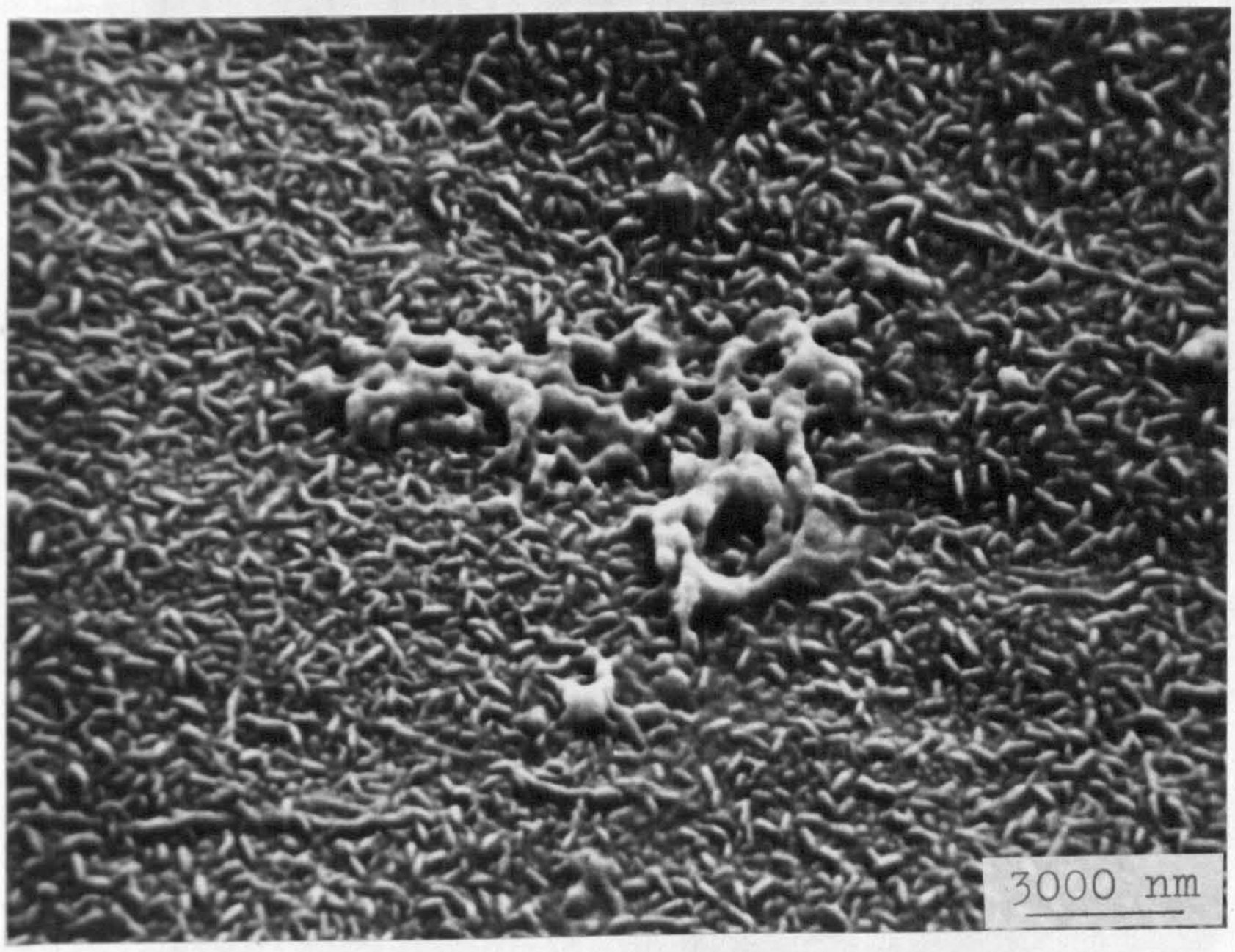

Fig.49i SEM of oxide film formed on pure aluminium at 730 °C in moist oxygen (P_{H_2O} = 0.03 atms) showing degenerate globular dendrites at the oxide/metal interface.

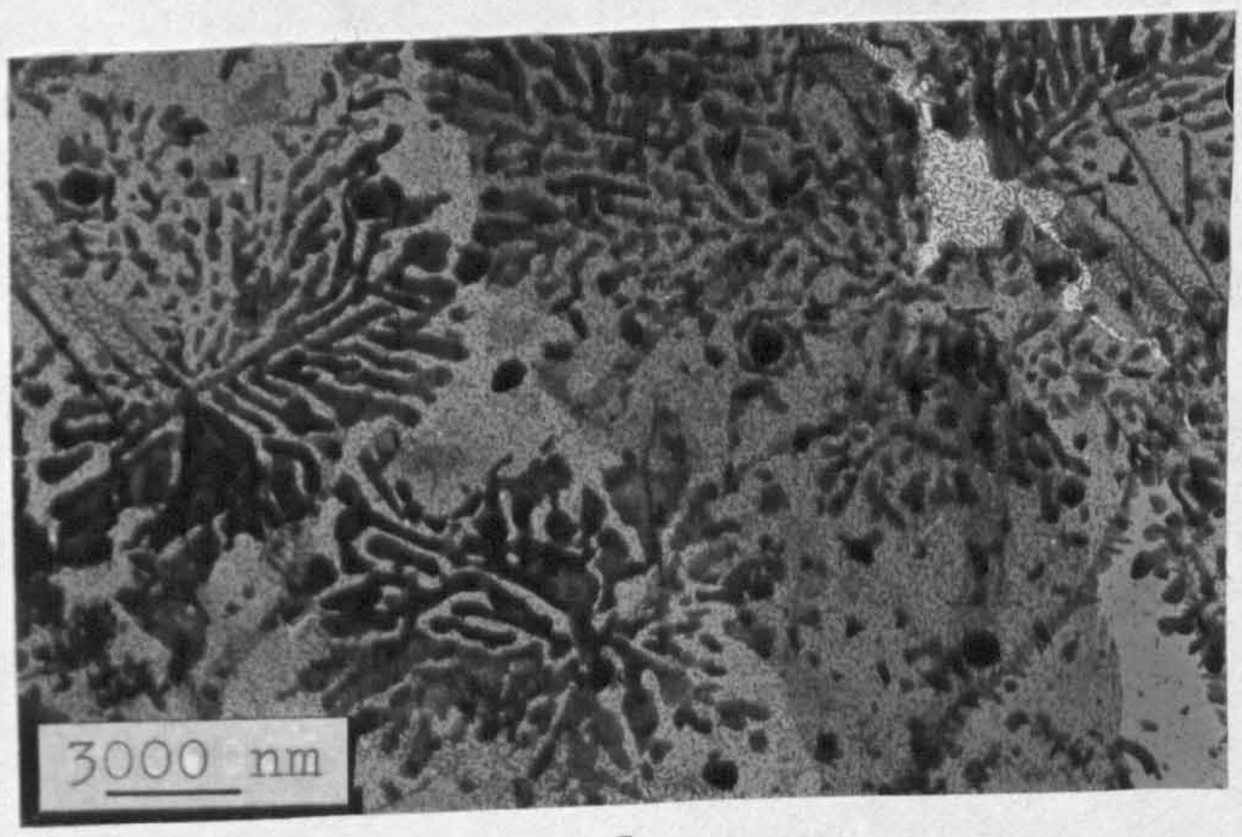

J

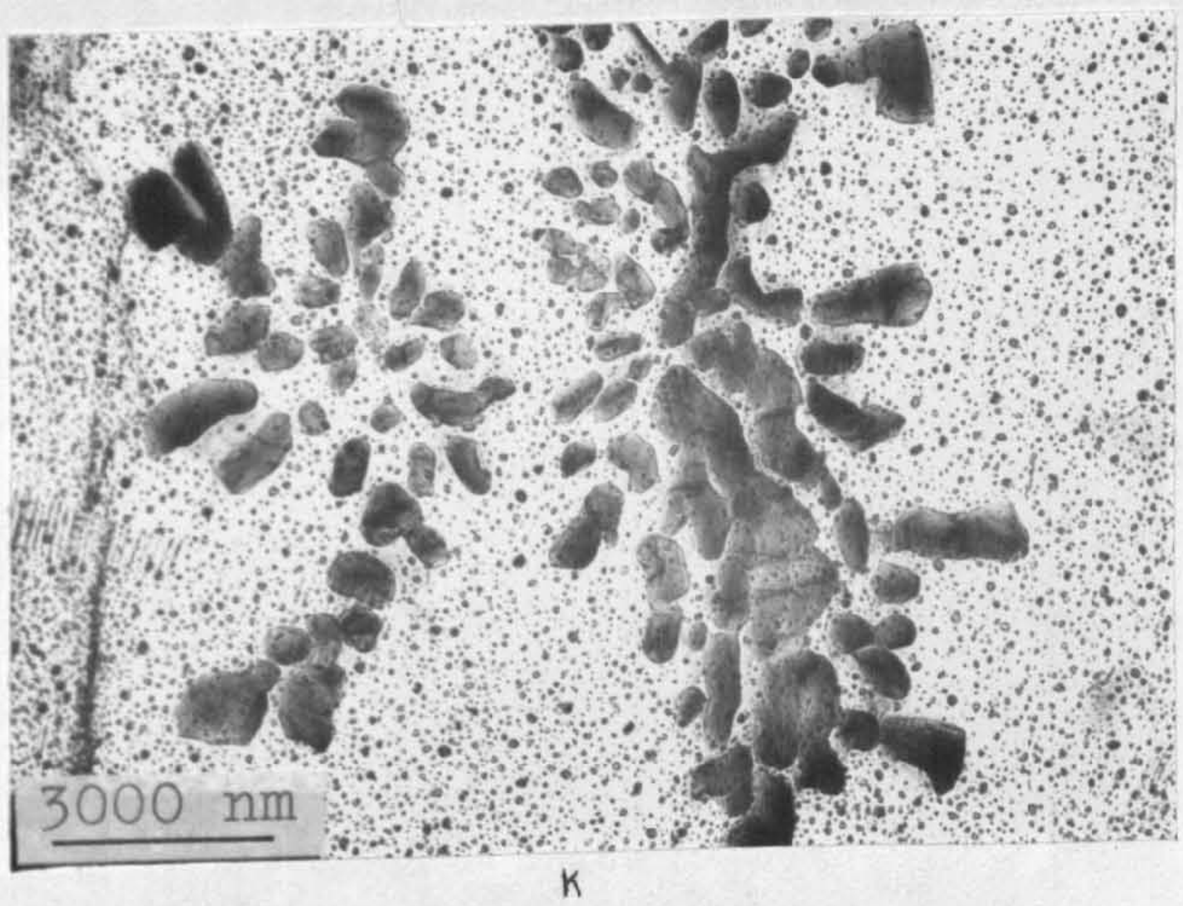

K

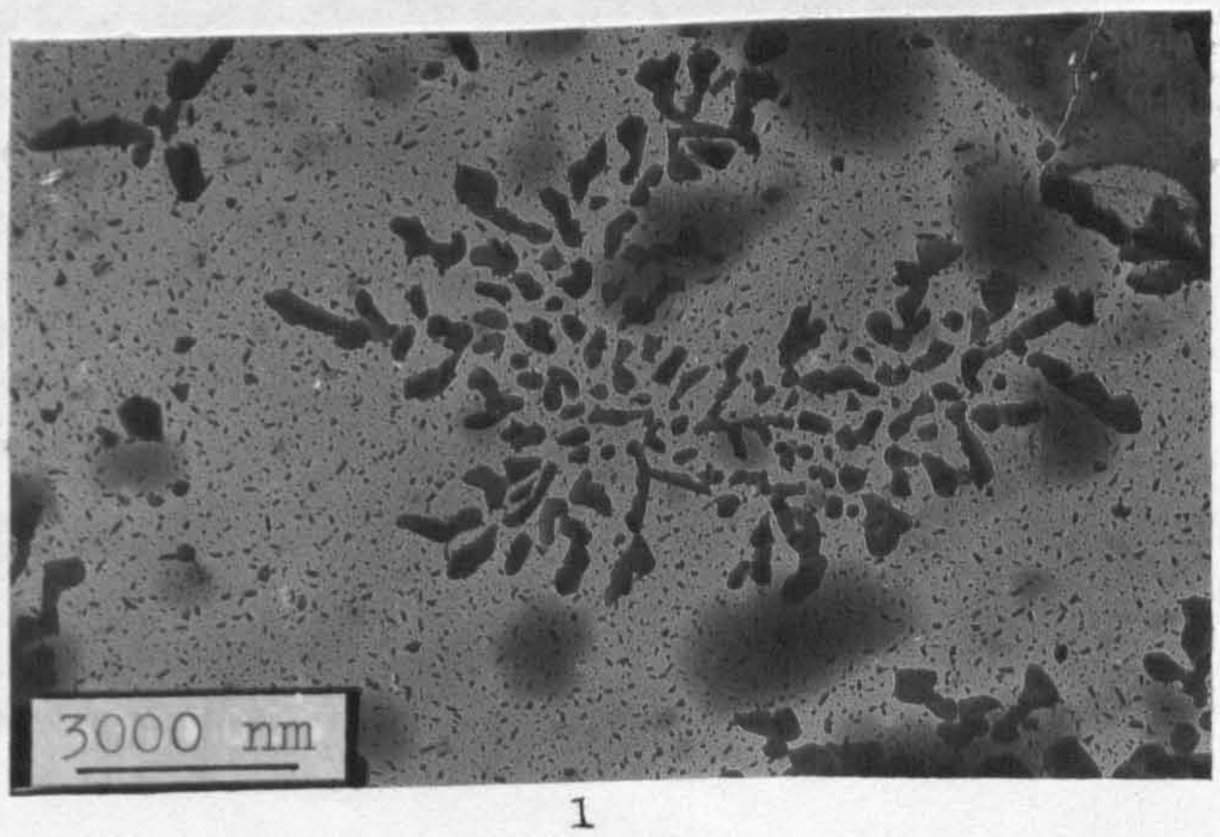

1

Figs.49 j,k,l TEM of oxide films formed on pure aluminium at 730 °C in moist oxygen (P_{H_2O} = 0.03 atms) showing degenerate dendrites (Type c)

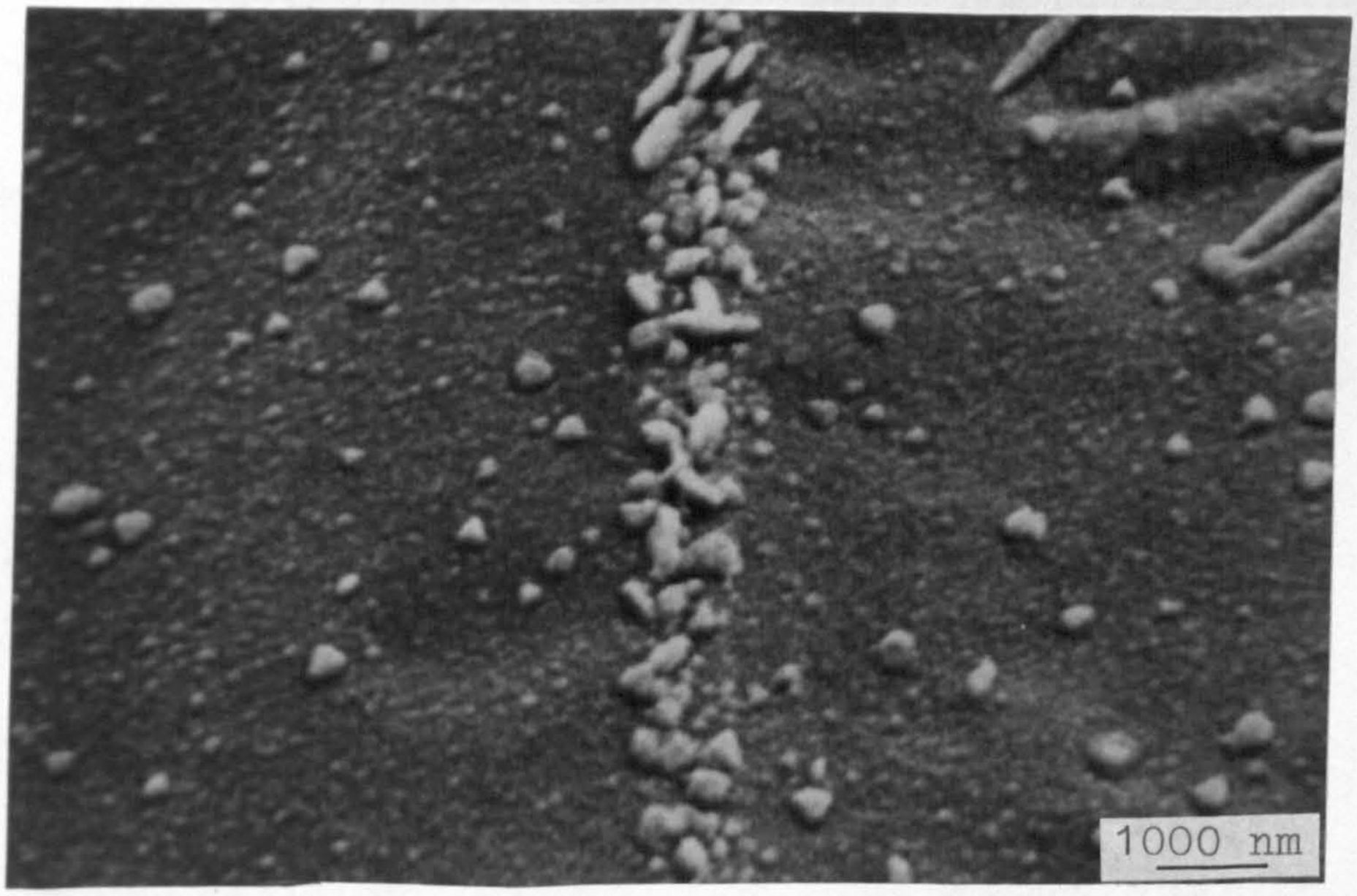

Fig. 49m SEM of oxide film formed on pure aluminium at 730 C in moist oxygen (P_{H_2O} = 0.03 atms) showing unassociated α-Al_2O_3 crystals (Type d) at the oxide/metal interface.

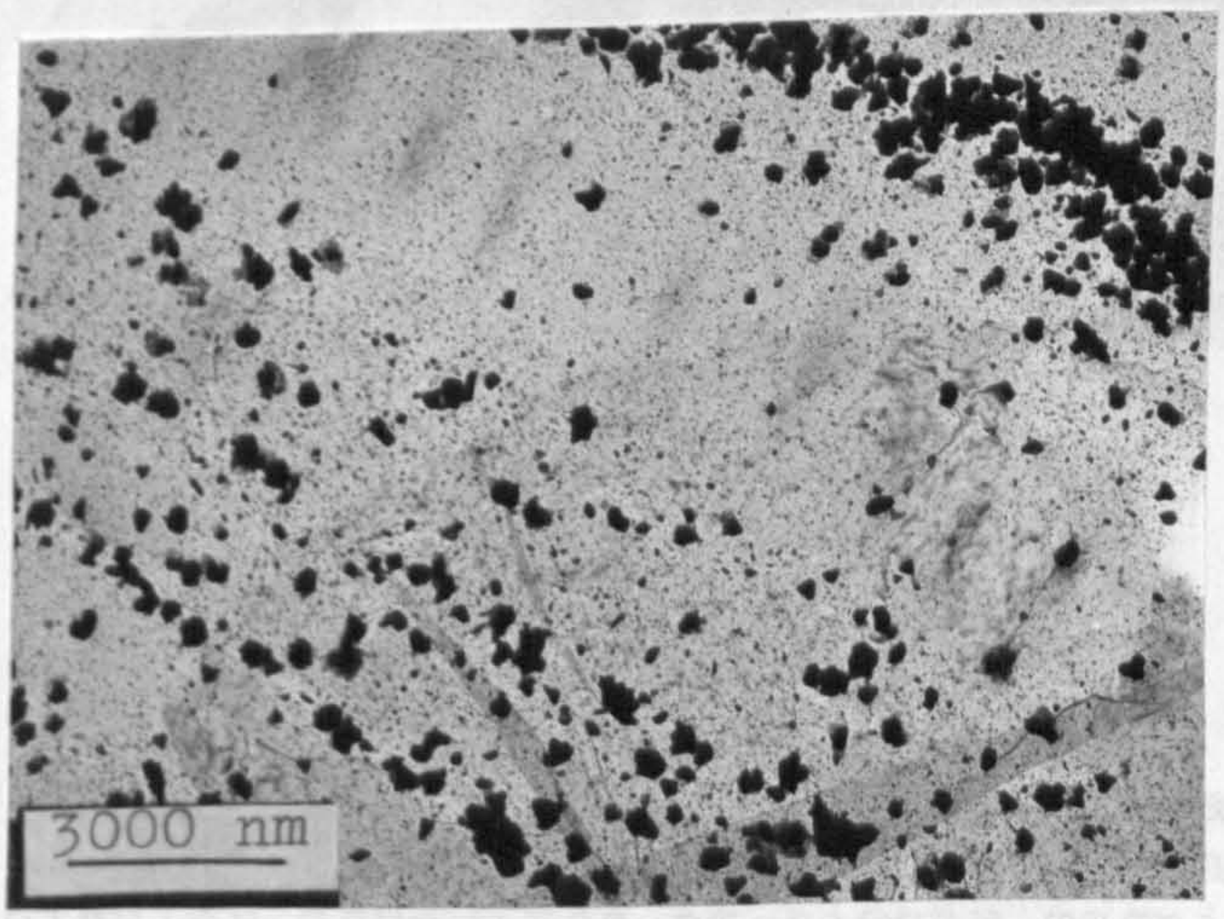

Fig. 49n TEM of oxide film formed on pure aluminium at 730 C in moist (P_{H_2O} = 0.03 atms) showing unassociated α-Al_2O_3 crystals (Type d)

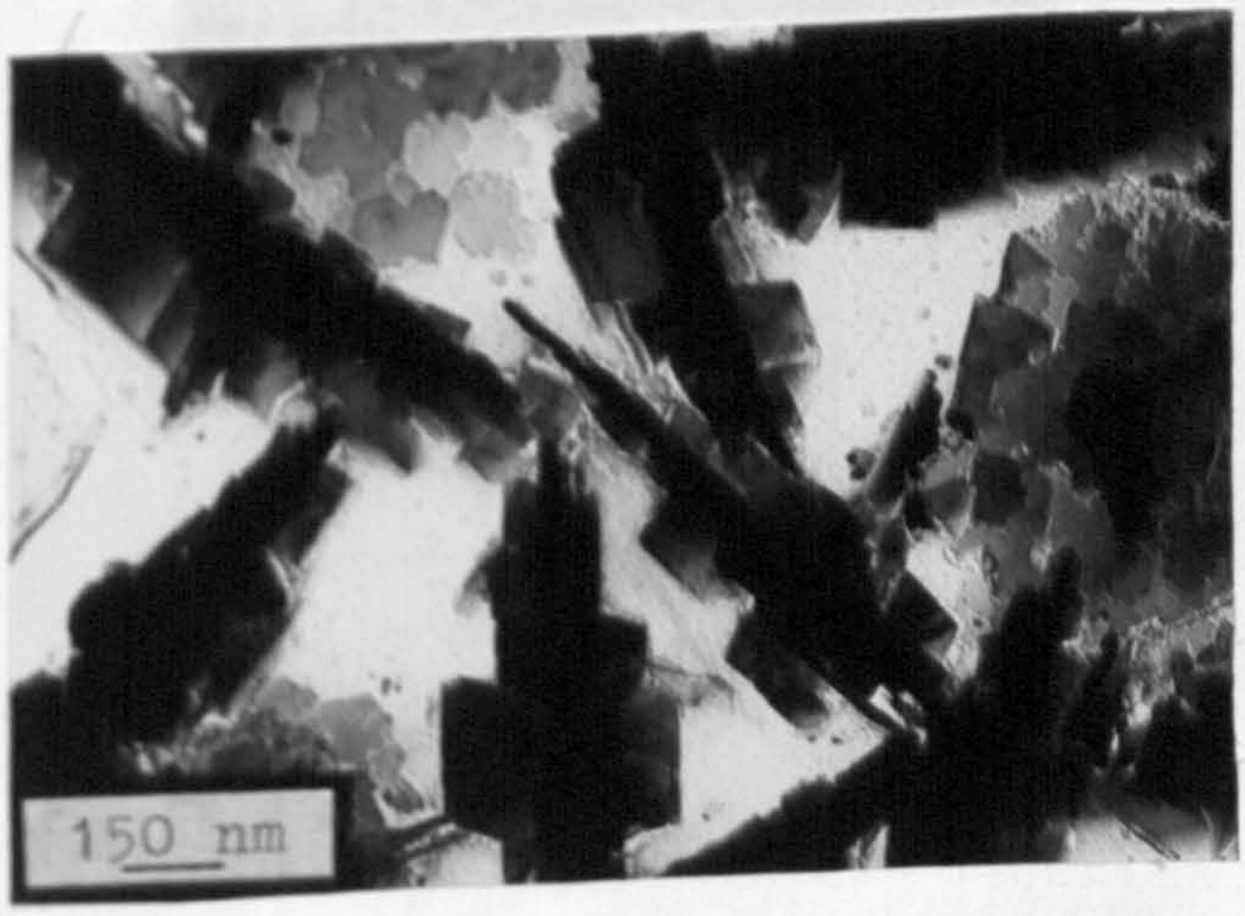

Fig. 50 TEM of oxide film formed on pure aluminium at 730 °C in moist oxygen (P_{H_2O} = 0.03 atms) showing acicular dendrites at higher magnification.

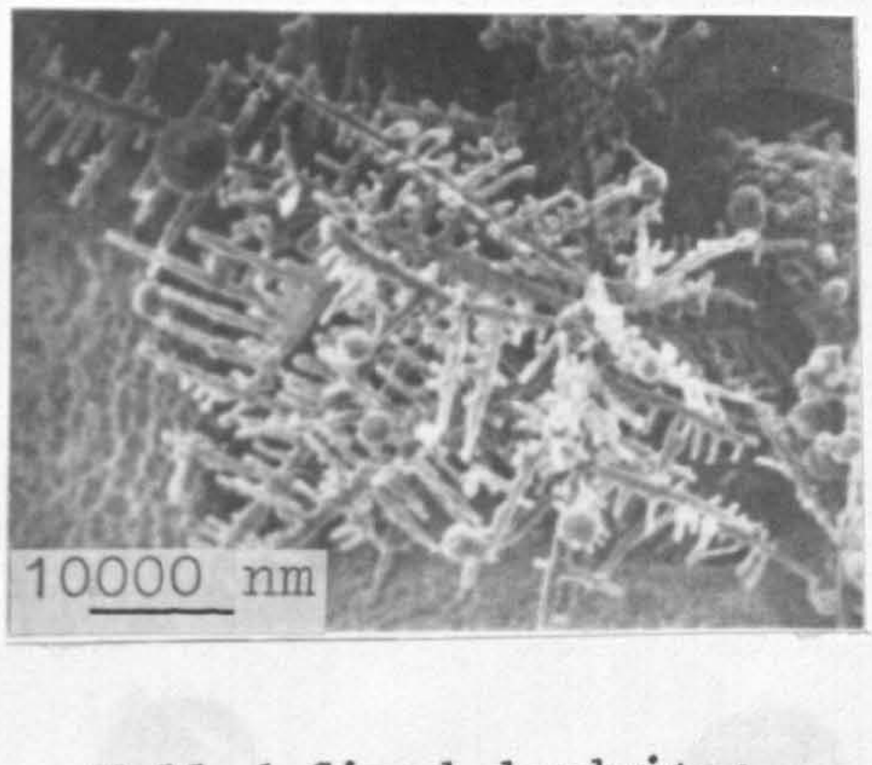

a) Well defined dendrites

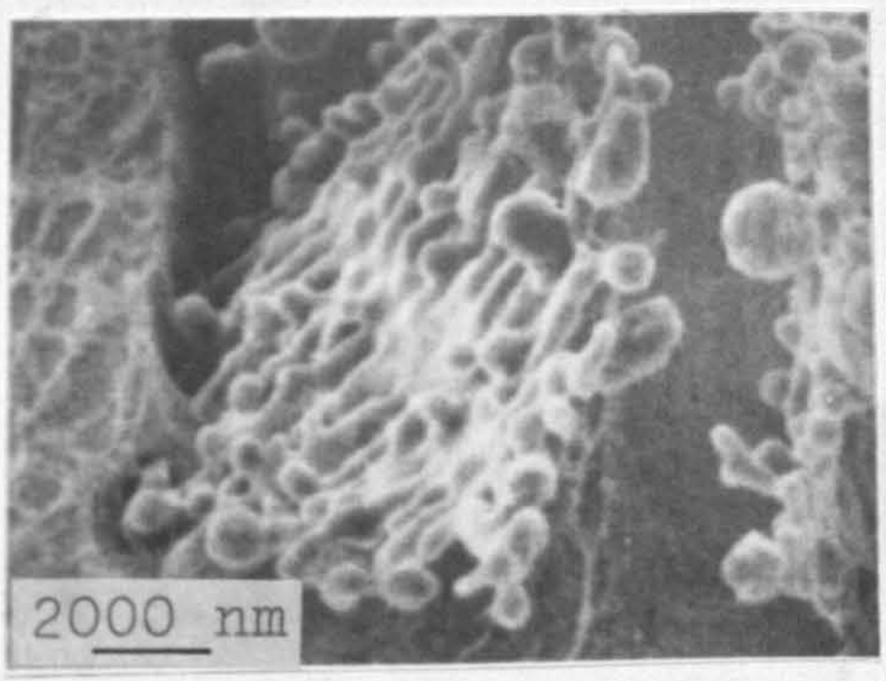

b) Degenerate dendrites

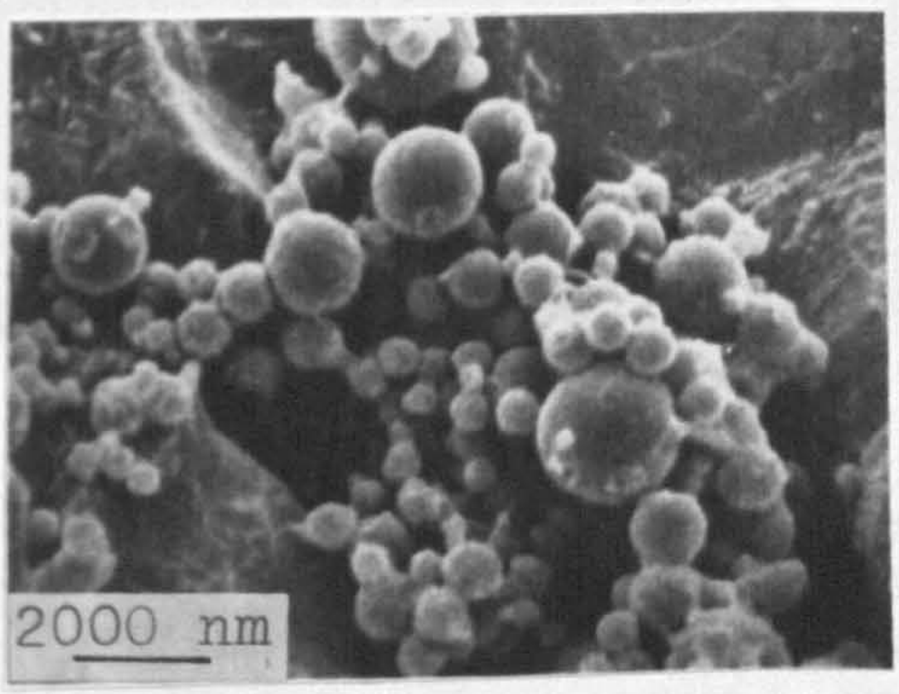

c) Globular morphology

Fig.51 Morphological variations of αAl_2O_3 inclusions formed in steel after deoxidation.

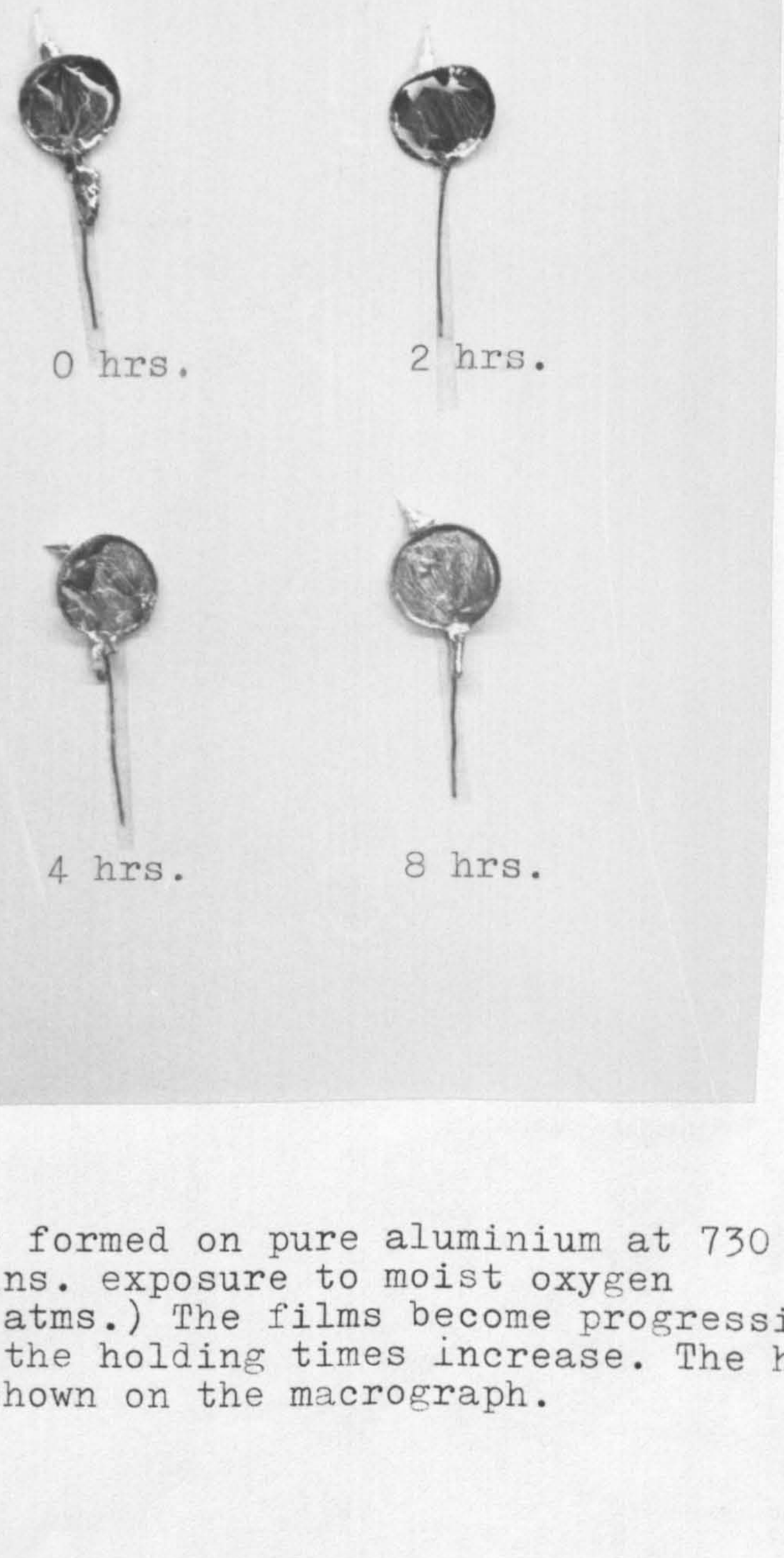

Fig 52 Oxide films formed on pure aluminium at 730 °C after 10 mins. exposure to moist oxygen (P_{H_2O} = 0.03 atms.) The films become progressively lighter as the holding times increase. The holding times are shown on the macrograph.

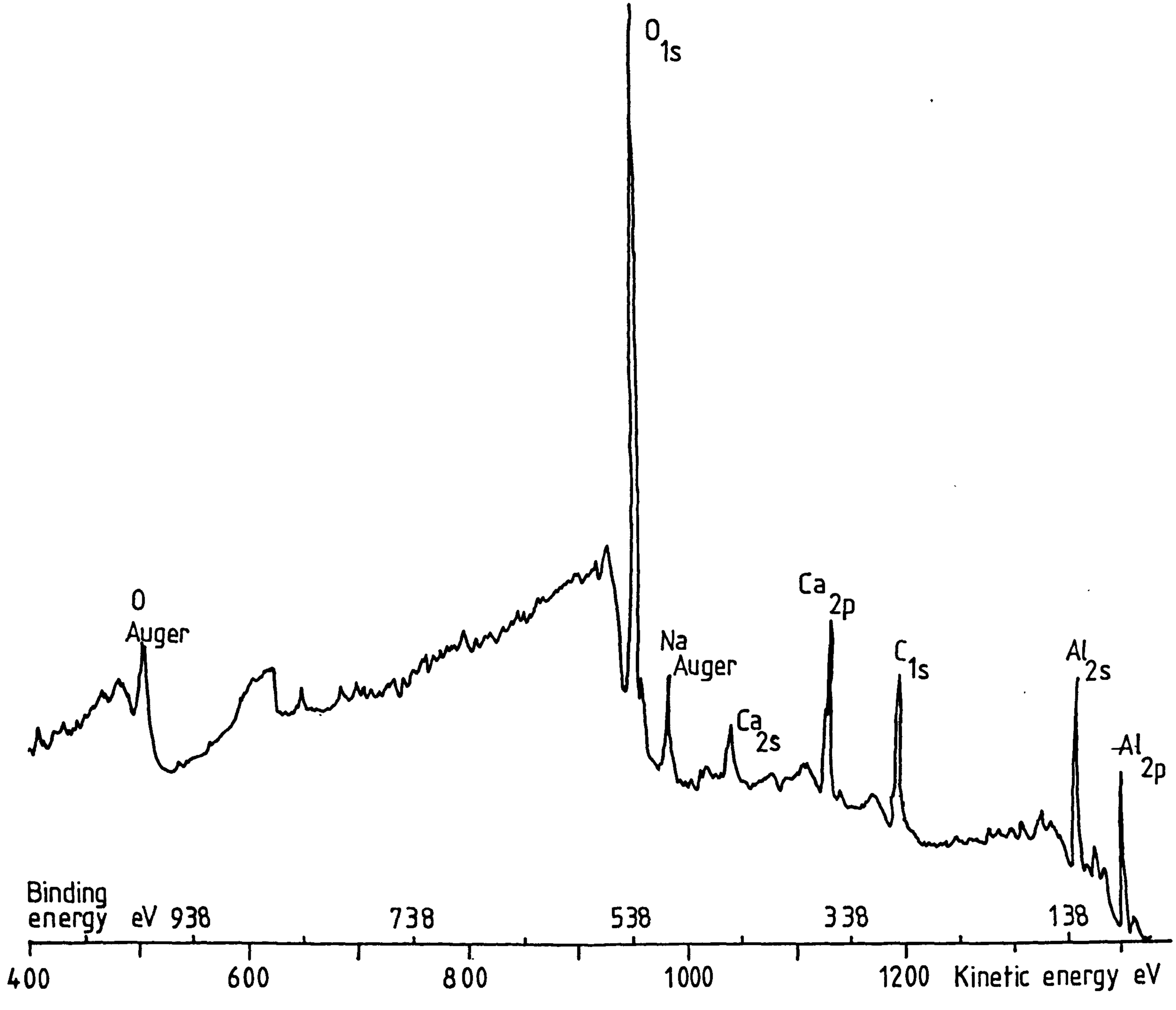
O 1s
O Auger
Na Auger
Ca 2s
Ca 2p
C 1s
Al 2s
Al 2p
Binding energy eV 938
738
538
338
138
400
600
800
1000
1200
Kinetic energy eV

Fig 53a XPS spectrum of oxide film formed on normal high purity aluminium (Billet A) at 730 °C in moist oxygen (P_{H_2O} =0.03 atms). The sample was sputtered with argon ions for 10 mins before obtaining the spectrum.

Excitation source	Al Kα (1486.6 eV)
	14 kV 13 mA
Source slit	2 mm
Collector slit	2 mm
Range	10^4 cps

Argon ion etching parameters

	2 mA
	5 kV

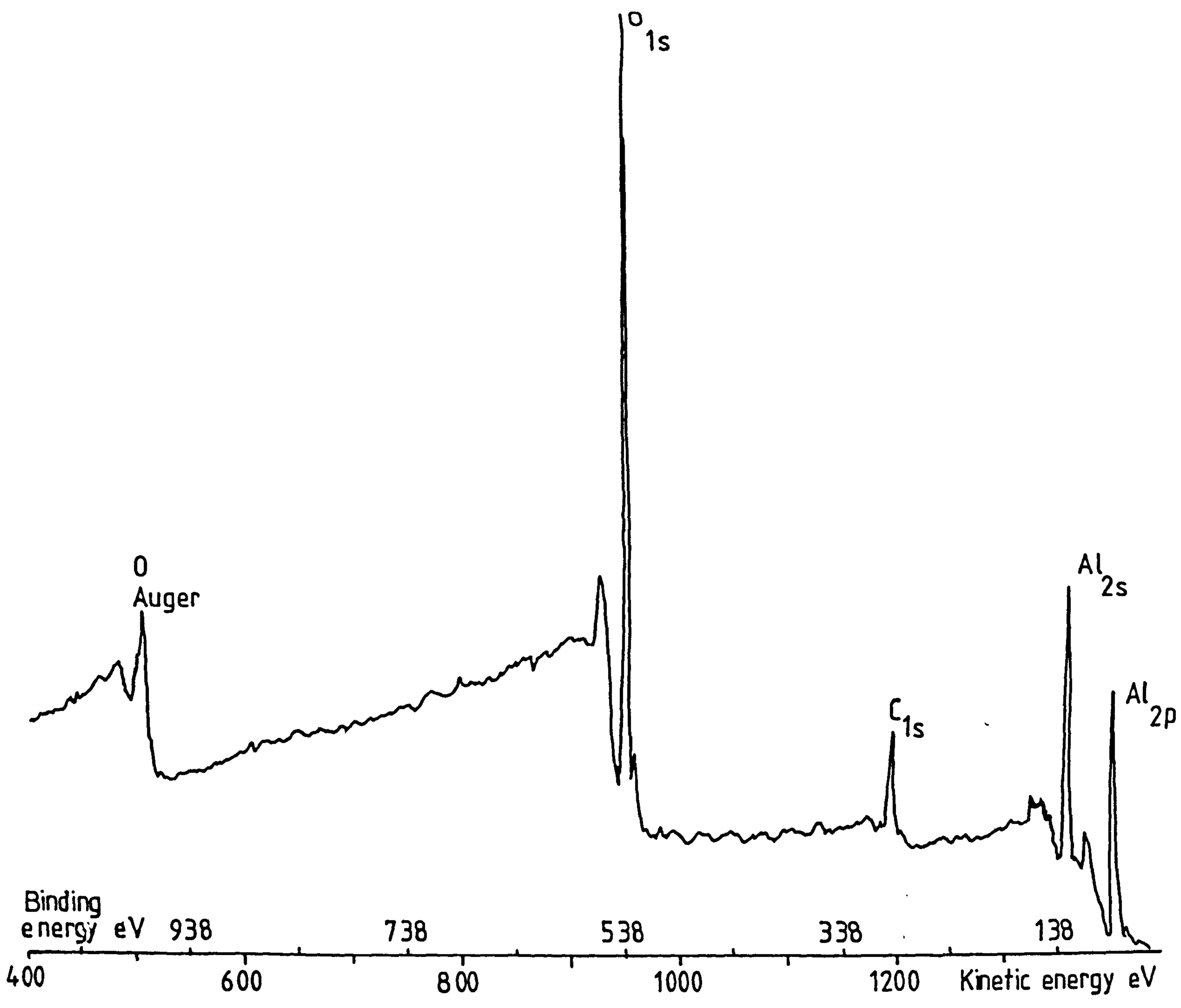
O
1s
O
Auger
Al
2s
Al
2p
C
1s
Binding
energy eV
938
738
538
338
138
400
600
800
1000
1200
Kinetic energy eV

Fig 53b XPS spectrum of oxide film formed on further purified high purity aluminium (Billet D) at 730 °C in moist oxygen (P_{H_2O} = 0.03 atms). The sample was sputtered with argon ions for 10 mins before obtaining the spectrum. A comparison of Fig 53a with Fig 53b shows that the levels of Ca and Na are greater in oxide film formed on high purity aluminium than in oxide film formed on further purified aluminium.

Excitation source	Al Kα (1486.6 eV)
	14 kV 13 mA
Source slit	2 mm
Collector slit	2 mm
Range	10^4 cps

Argon ion etching parameters

	2 mA
	5 kV

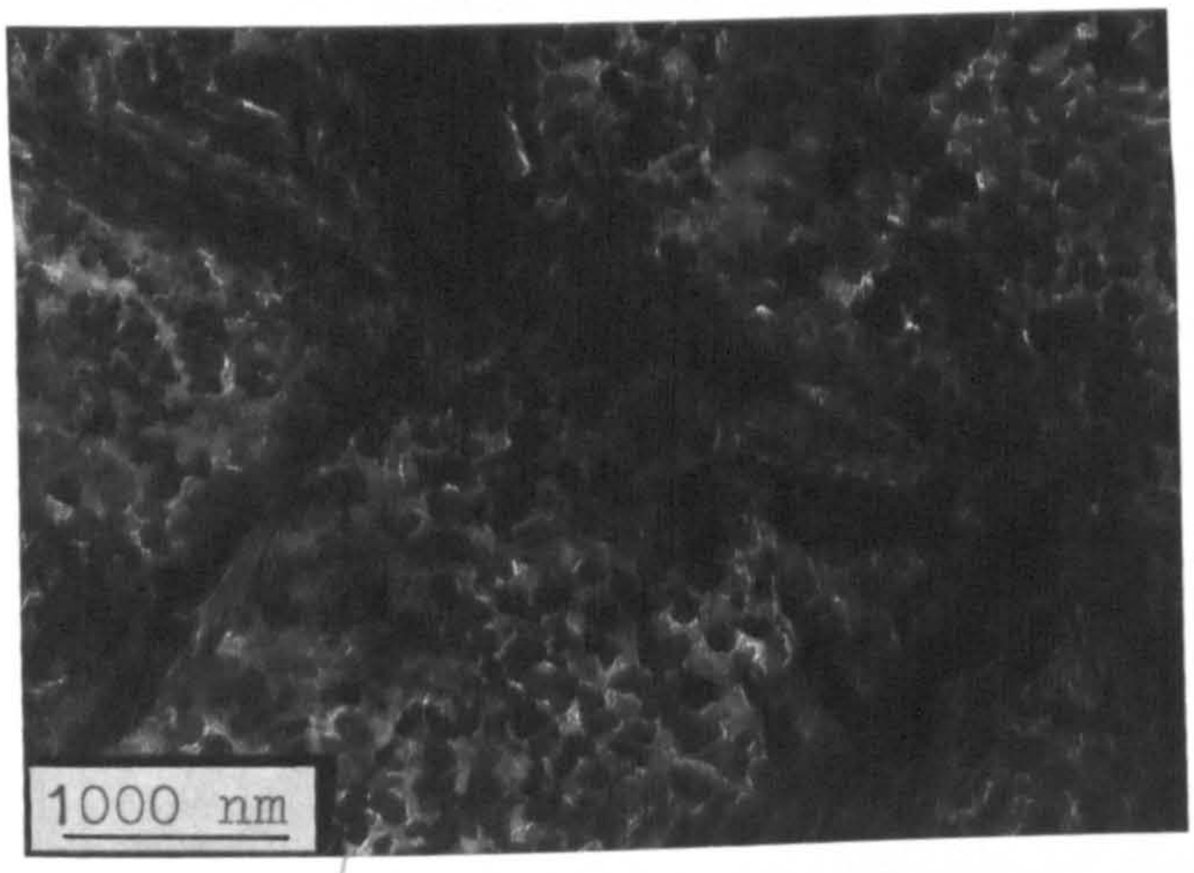

0 hrs.

Fig 54 a

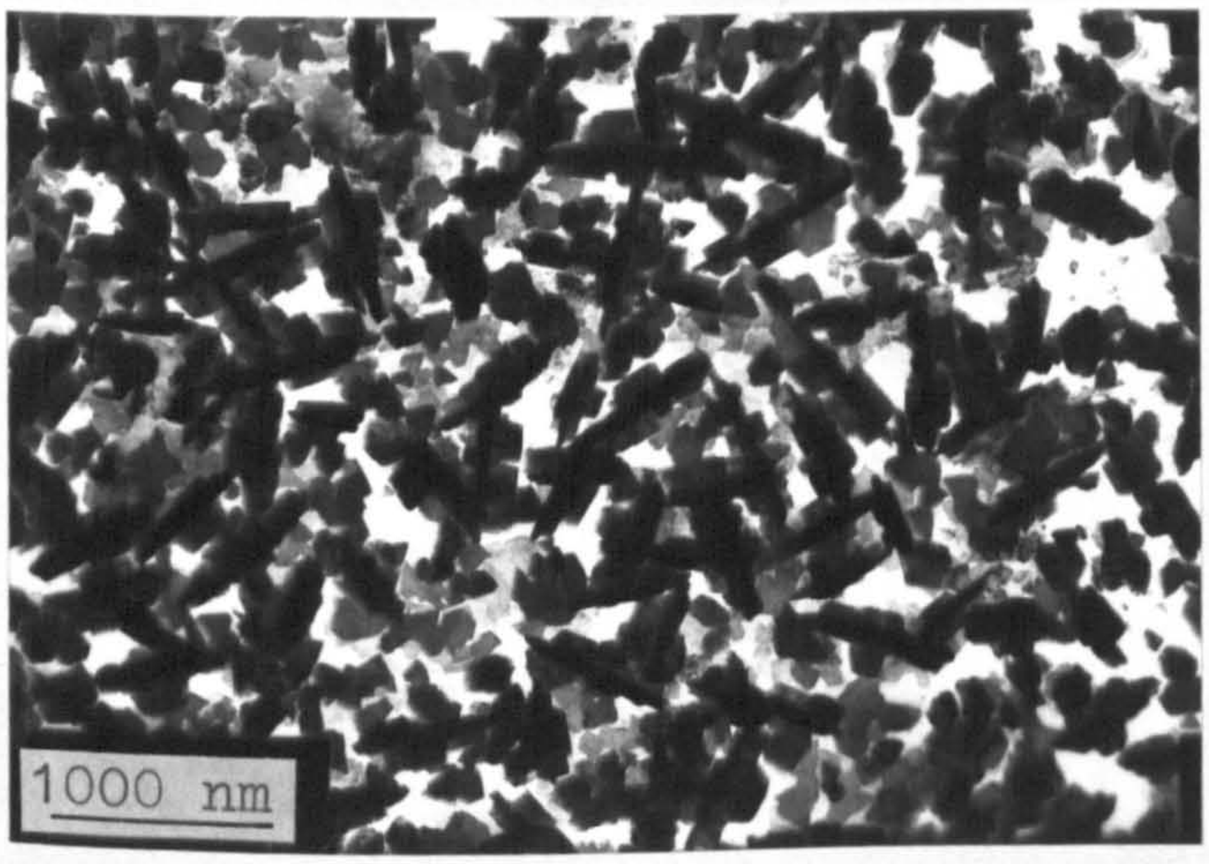

1 hrs.

Fig 54 b

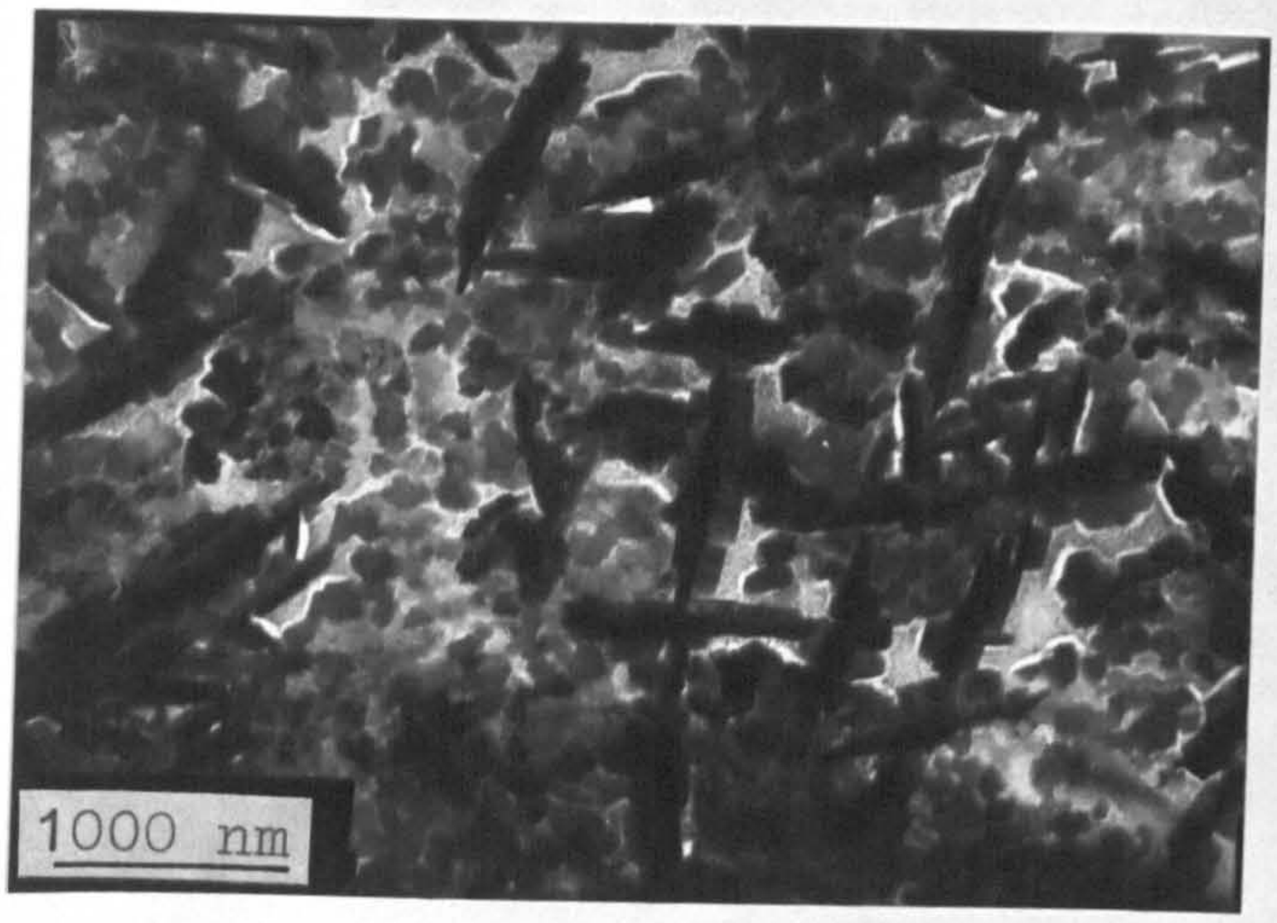

2 hrs.

Fig 54c

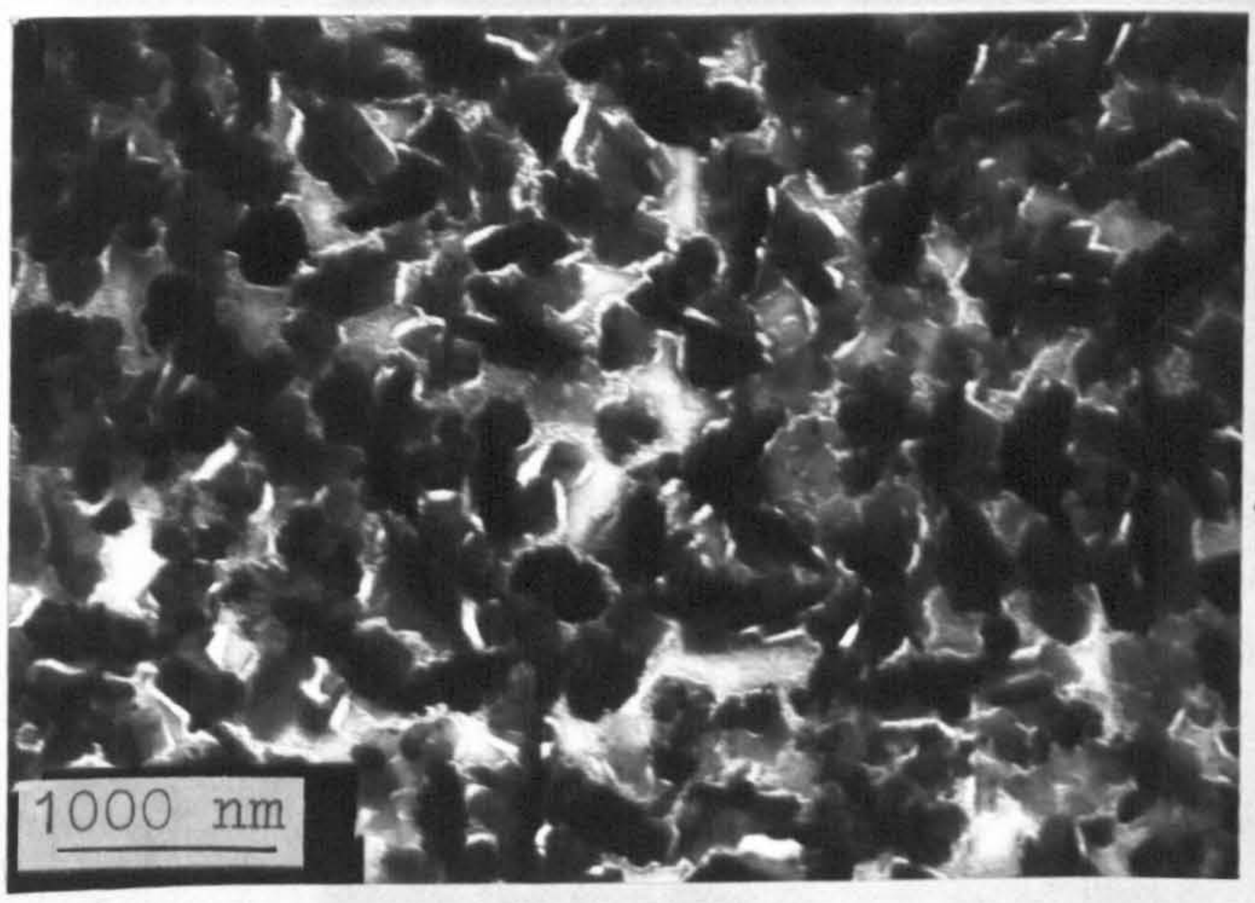

3 hrs

Fig 54 d

Fig 54 (a,b,c,d) TEM of oxide films formed on aluminium at 730 C in moist atmosphere (P_{H_2O} = 0.03 atms) illustrating the degeneration of acicular dendrites as holding times increace. (Holding times are shown on the micrographs.

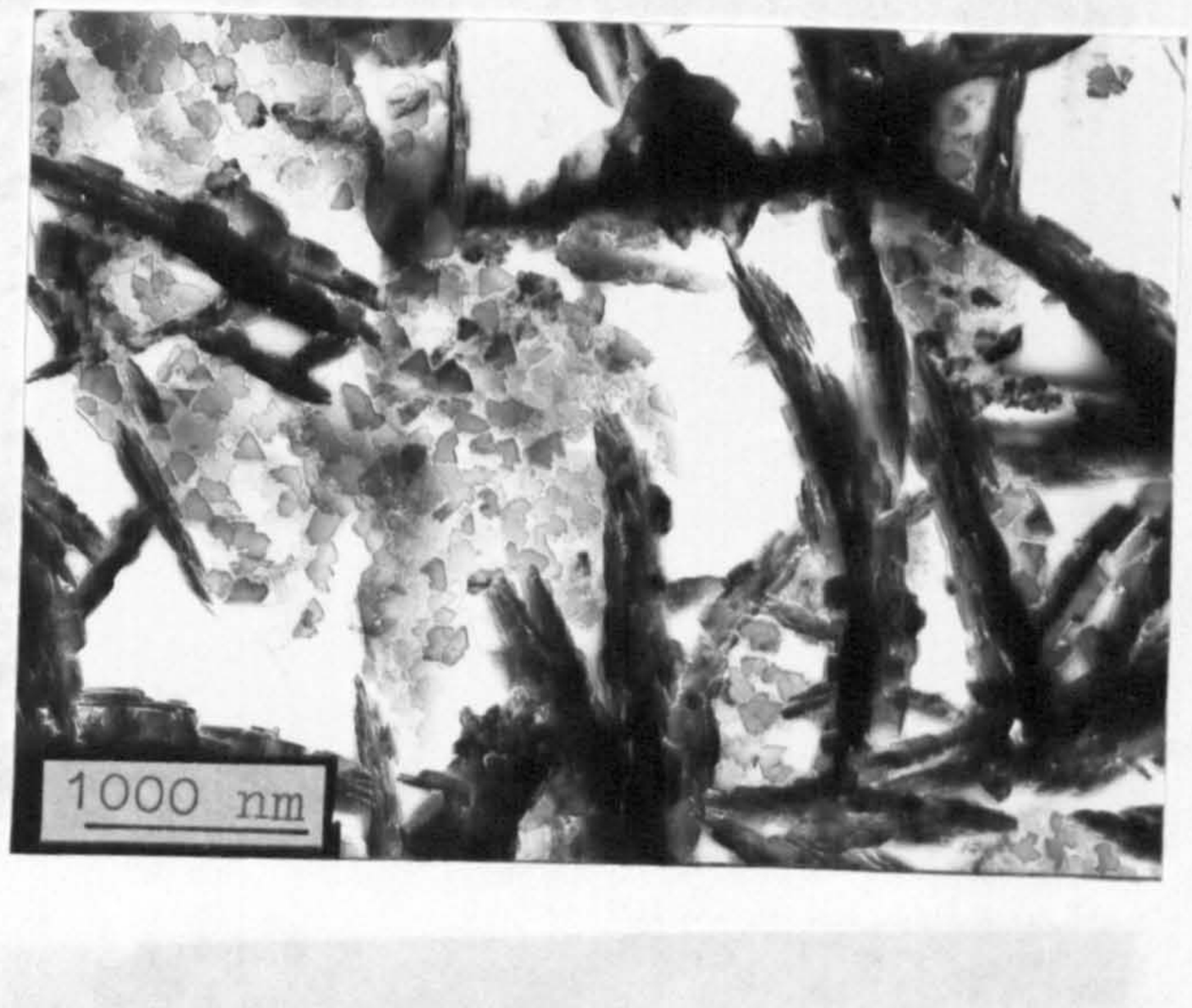

(a)

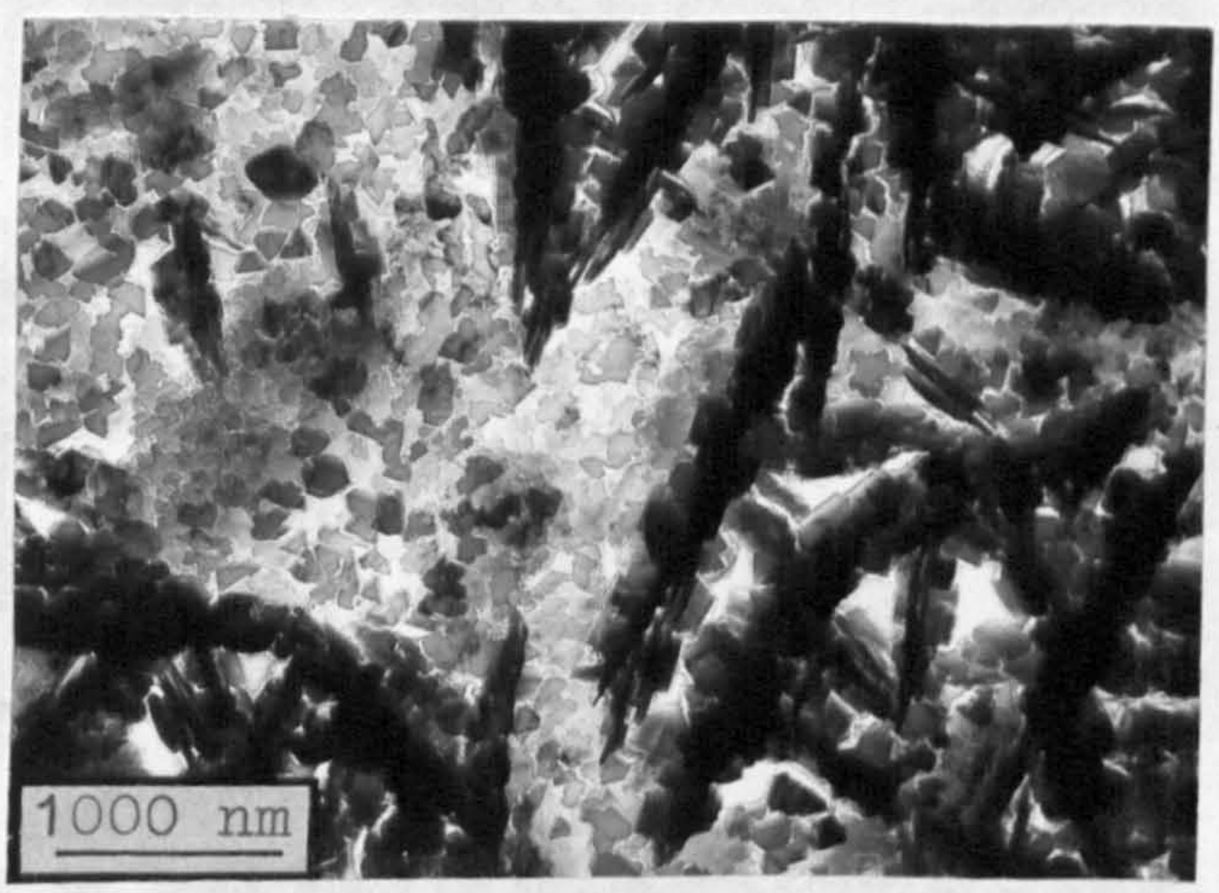

(b)

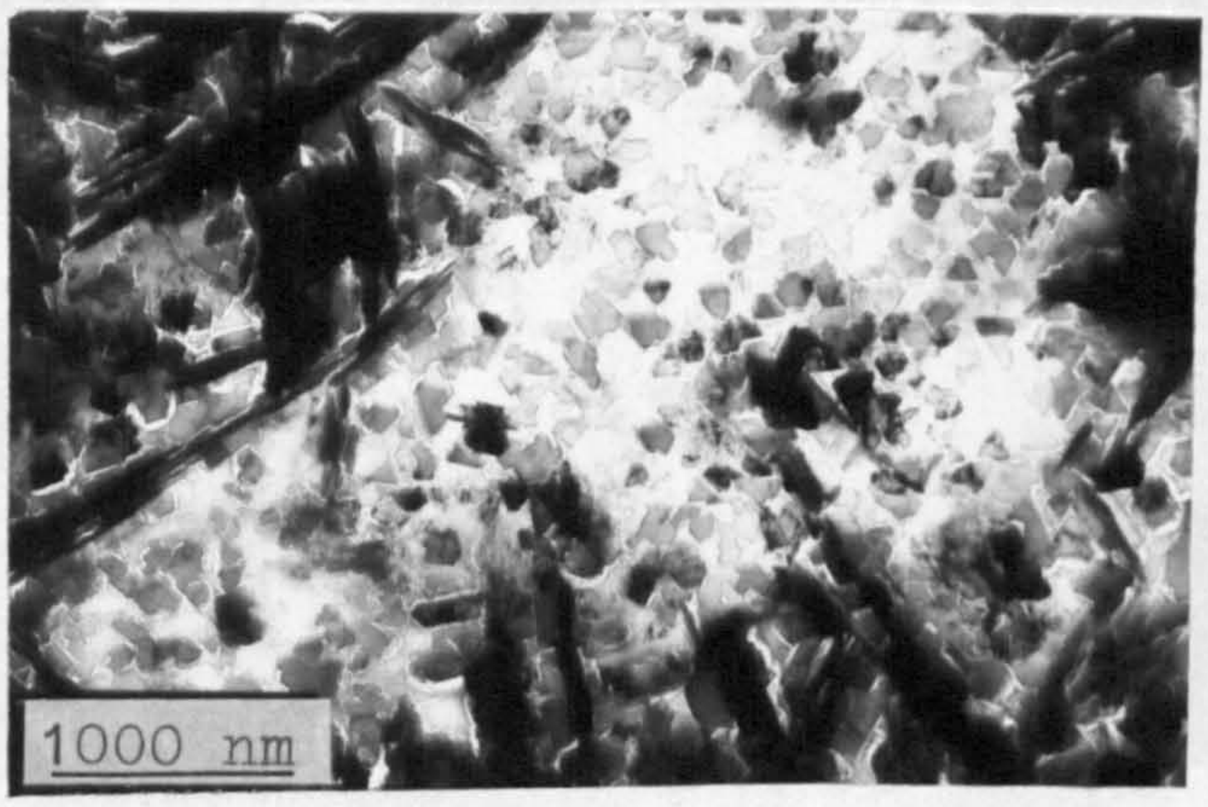

(c)

Fig.55 TEM of oxide films formed on normal high purity aluminium (Billet A) at 730 °C exposed to moist oxygen (P_{H_2O} = 0.03 atms) for (a) 5 mins,(b) 10 mins and (c) 40 mins.

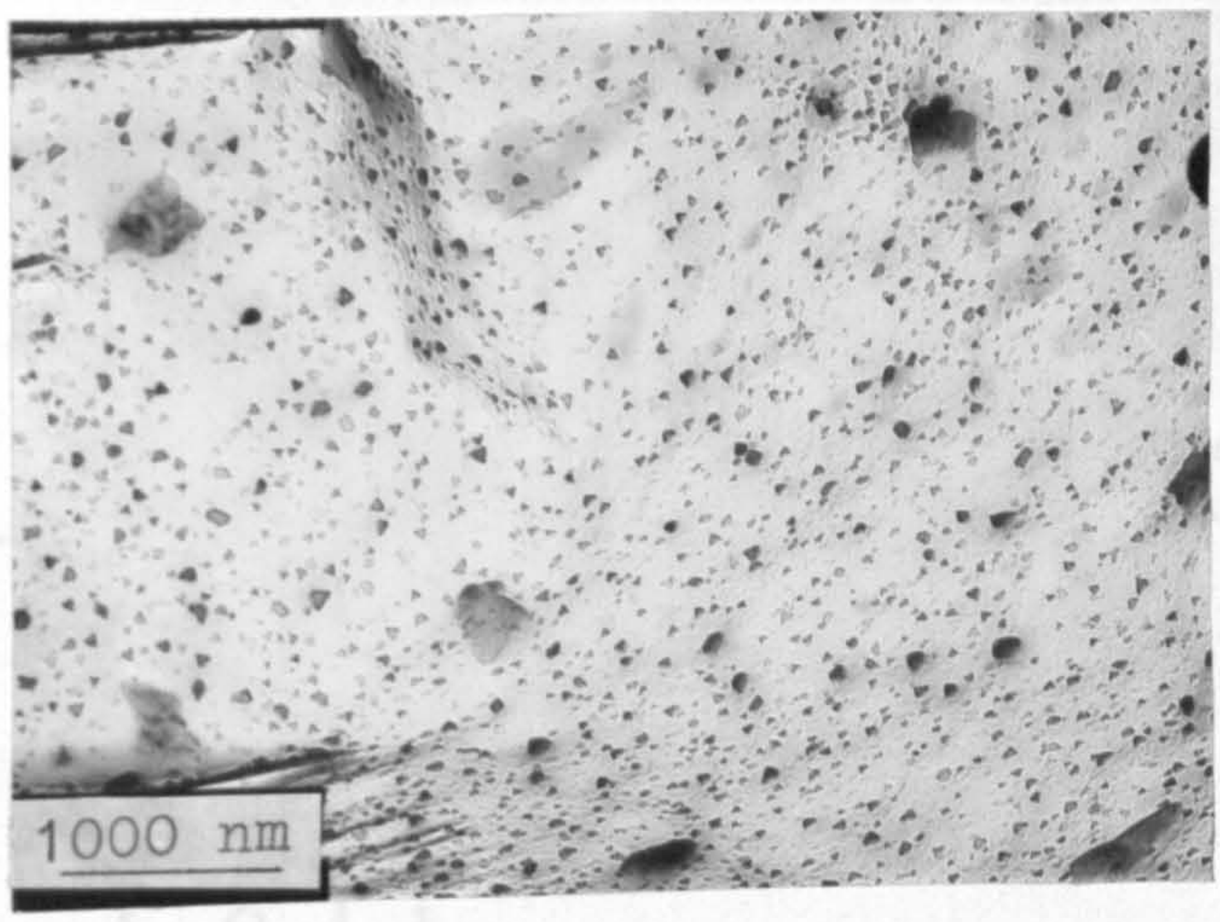

(a)

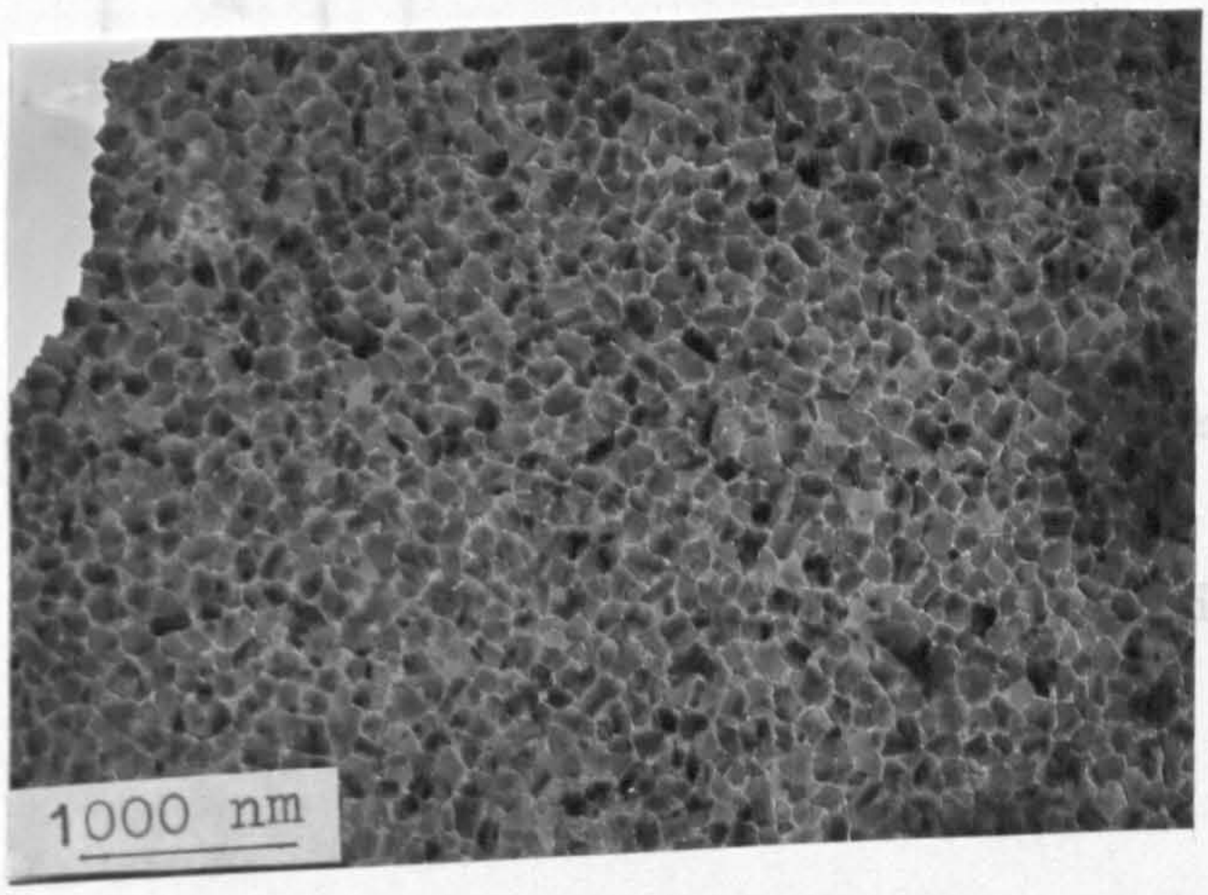

(b)

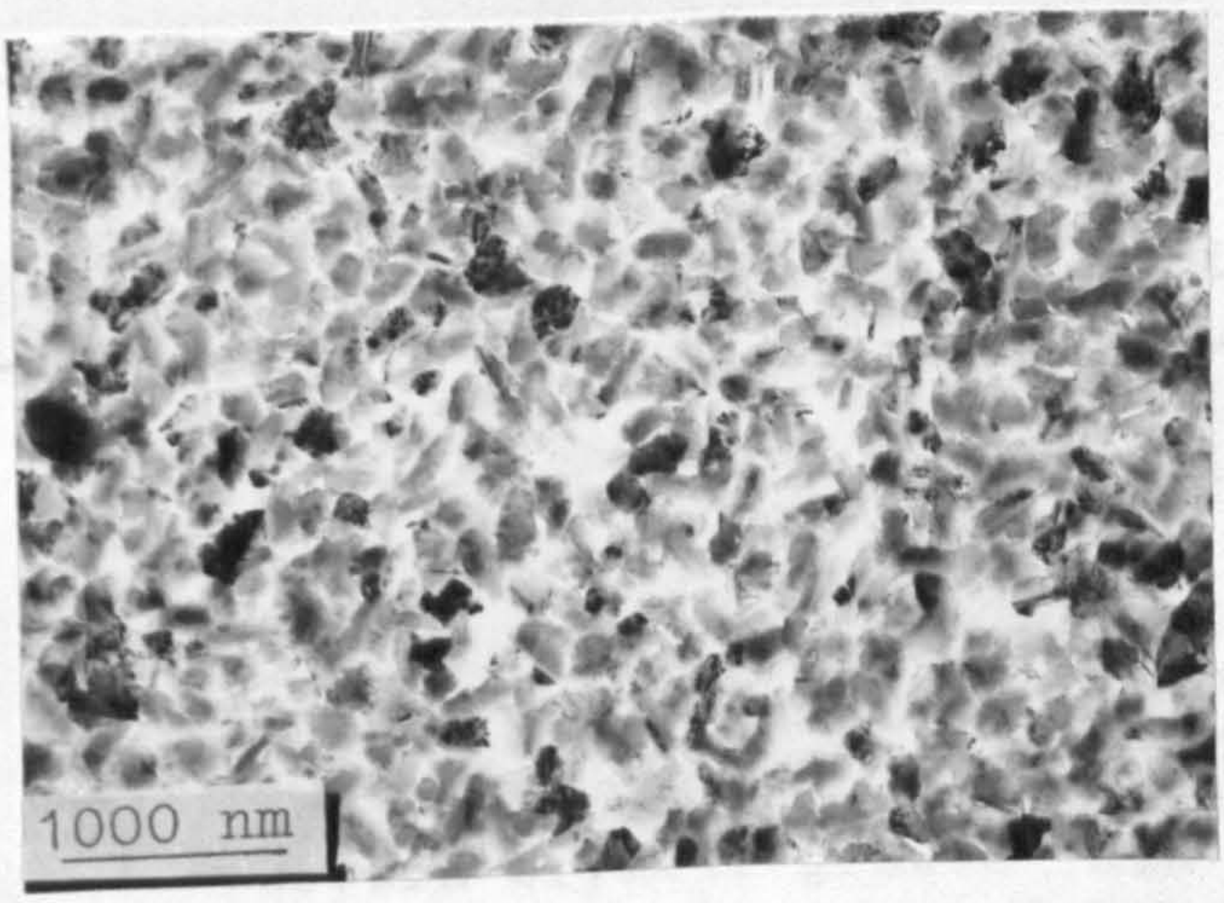

(c)

Fig.56 TEM of oxide films formed on further purified high purity aluminium (Billet D) at 730 °C exposed to moist oxygen (P_{H_2O} =0.03 atms) for (a) 1 min,(b)30 mins and (c)40 mins

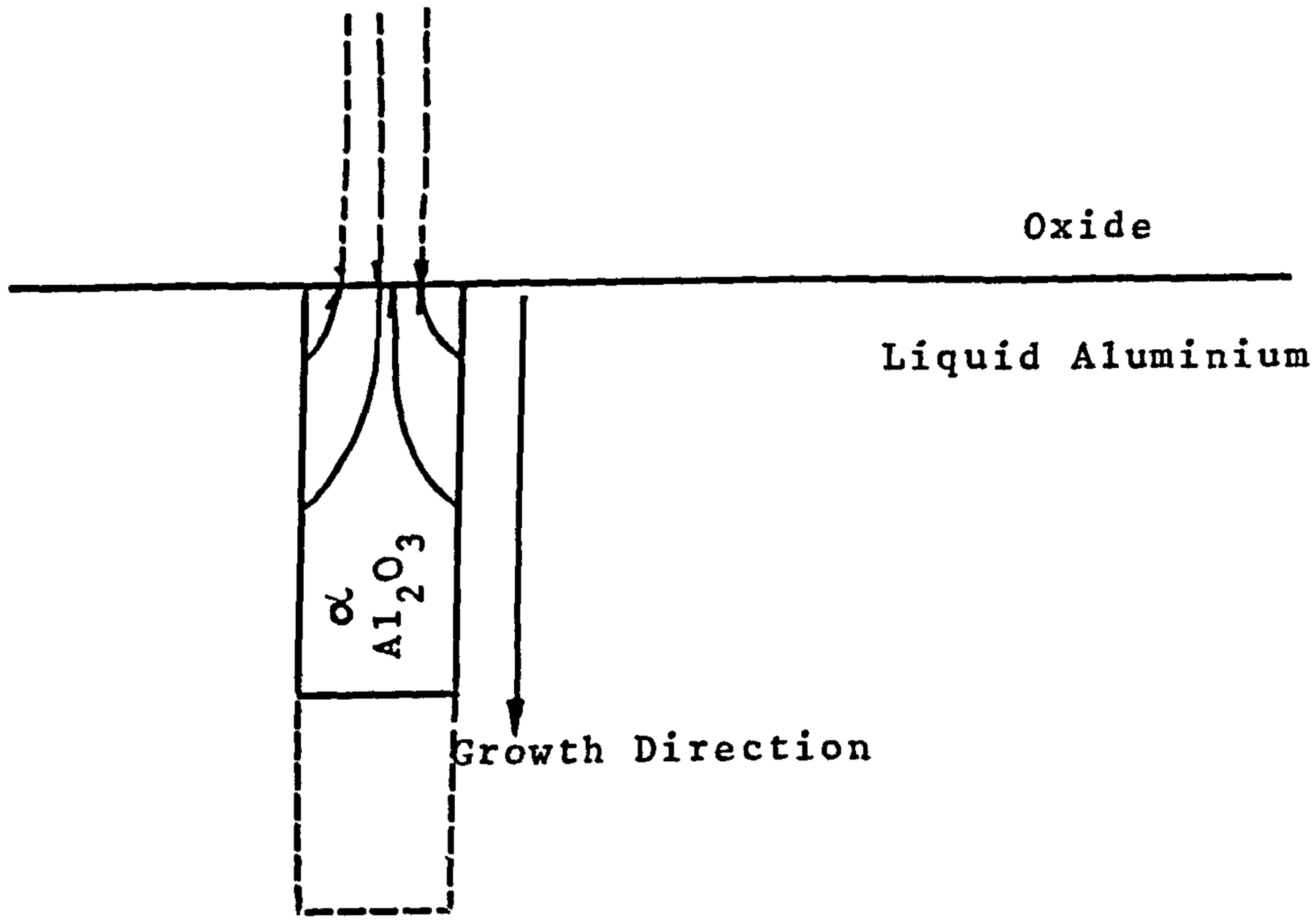

Figure 57 Schematic model for the formation of acicular α-Al_2O_3 dendrites. High oxygen activity at the metal/oxide interface facilitates crystal growth into the liquid metal.

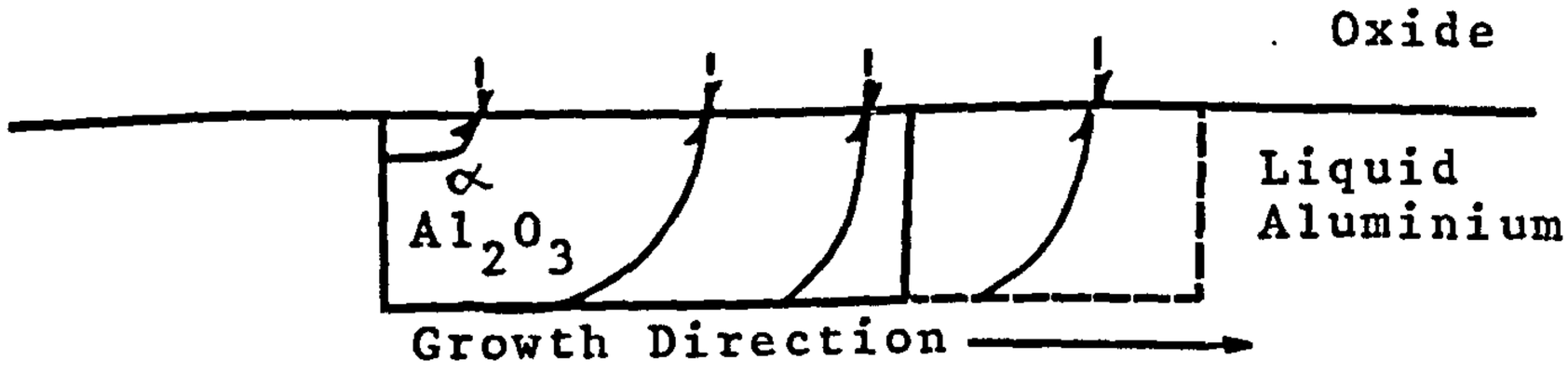

Figure 58 Schematic model for formation of globular α-Al_2O_3. Low oxygen activity at the metal/oxide interface cannot sustain crystal growth into the liquid metal, hence it grows laterally.

O^{2-}

Al^{3+}

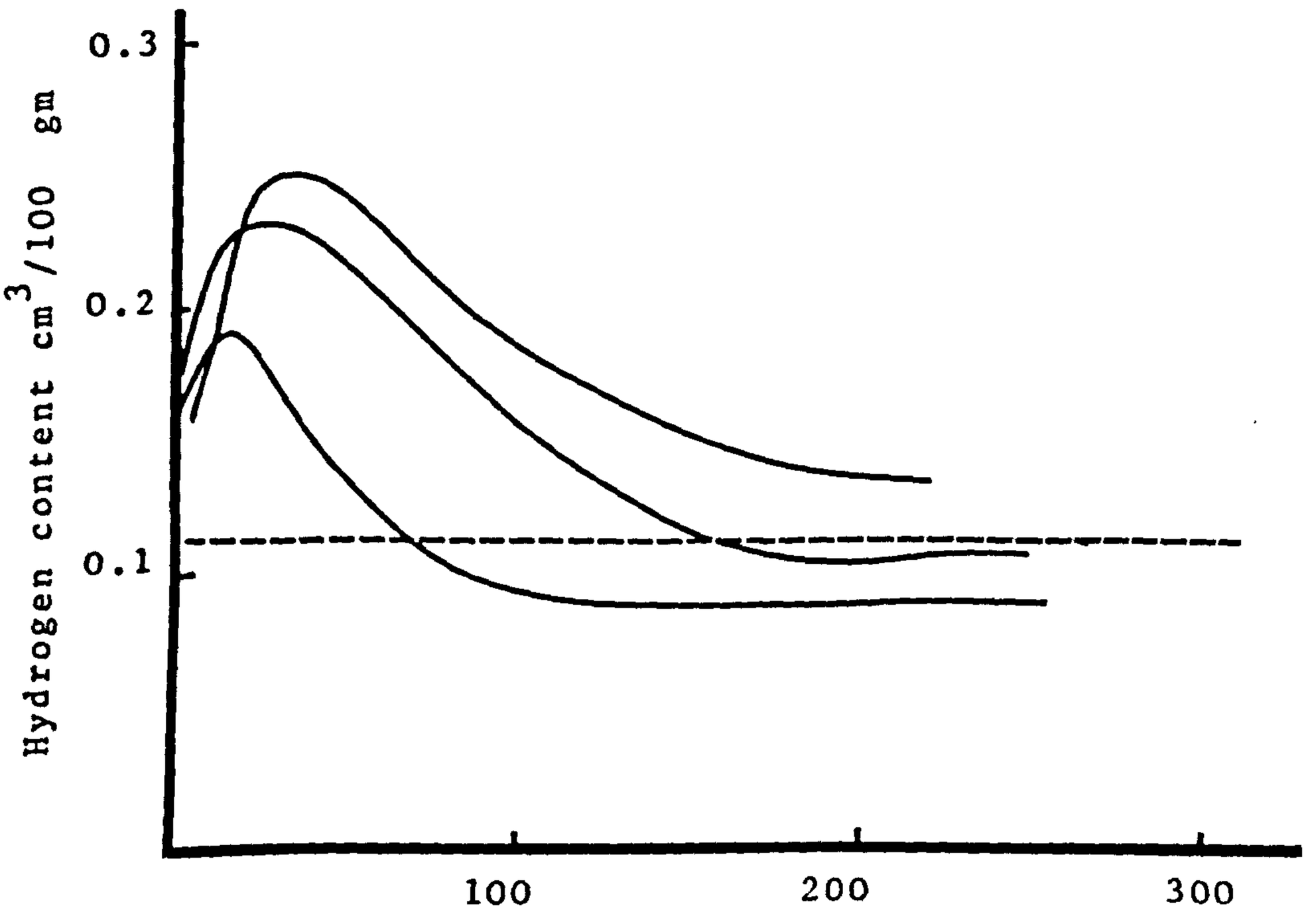

Fig.59. Hydrogen absorption by pure liquid aluminium exposed to humid environments (Stevenson)[159]

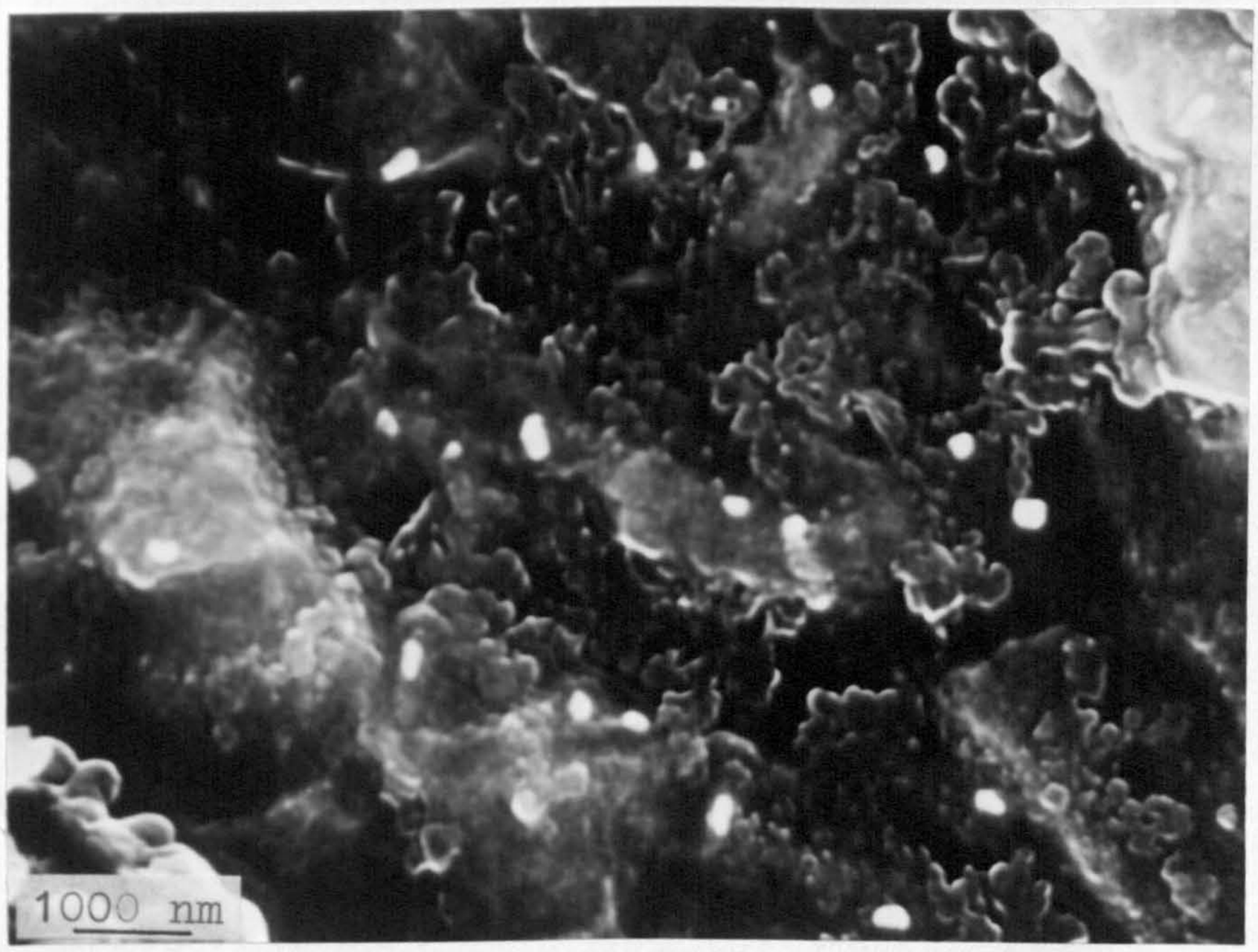

Fig 60 SEM of oxide/atms interface of an oxide film formed on pure aluminium at 730 °C exposed to dry oxygen. The degenerate dendrites resemble the $\alpha-Al_2O_3$ growths at the metal/oxide interface (Fig 49g and Fig 49h)

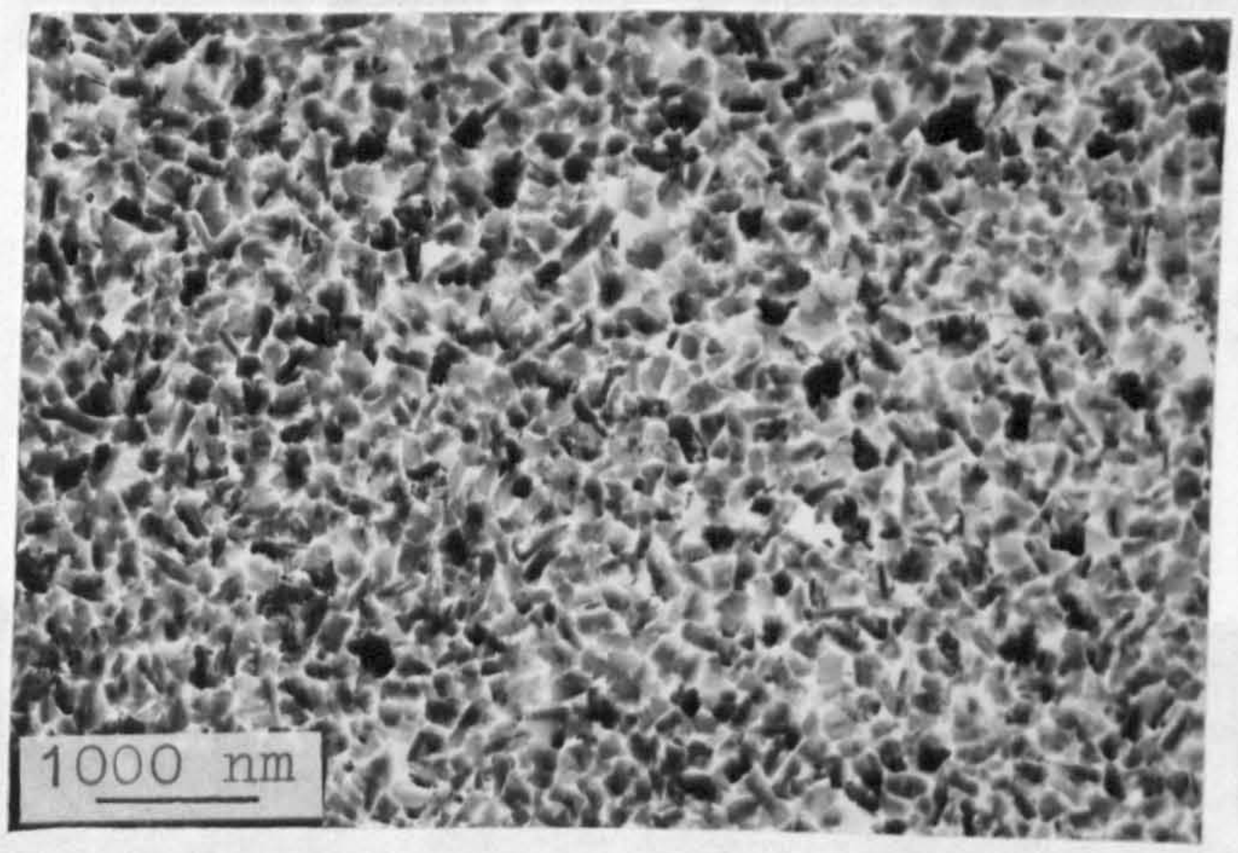

Fig.61(a) TEM of oxide formed after 1 min. on normal high purity aluminium at 730°C exposed to moist oxygen containing traces of volatile fluoride.

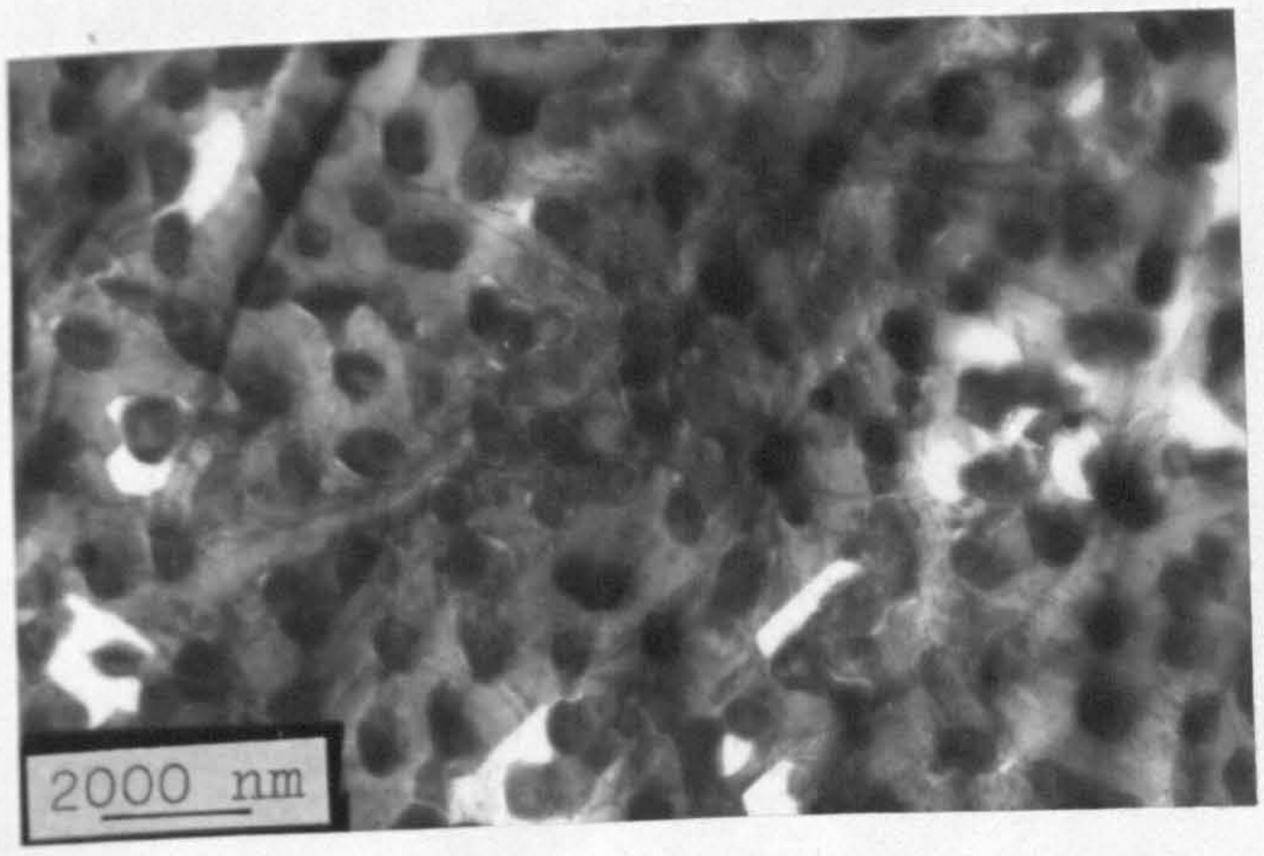

Fig.61(b) TEM of oxide formed on normal high purity aluminium(Billet A) at 730°C after 40 mins. exposure to moist atmosphere containing traces of volatile fluoride.

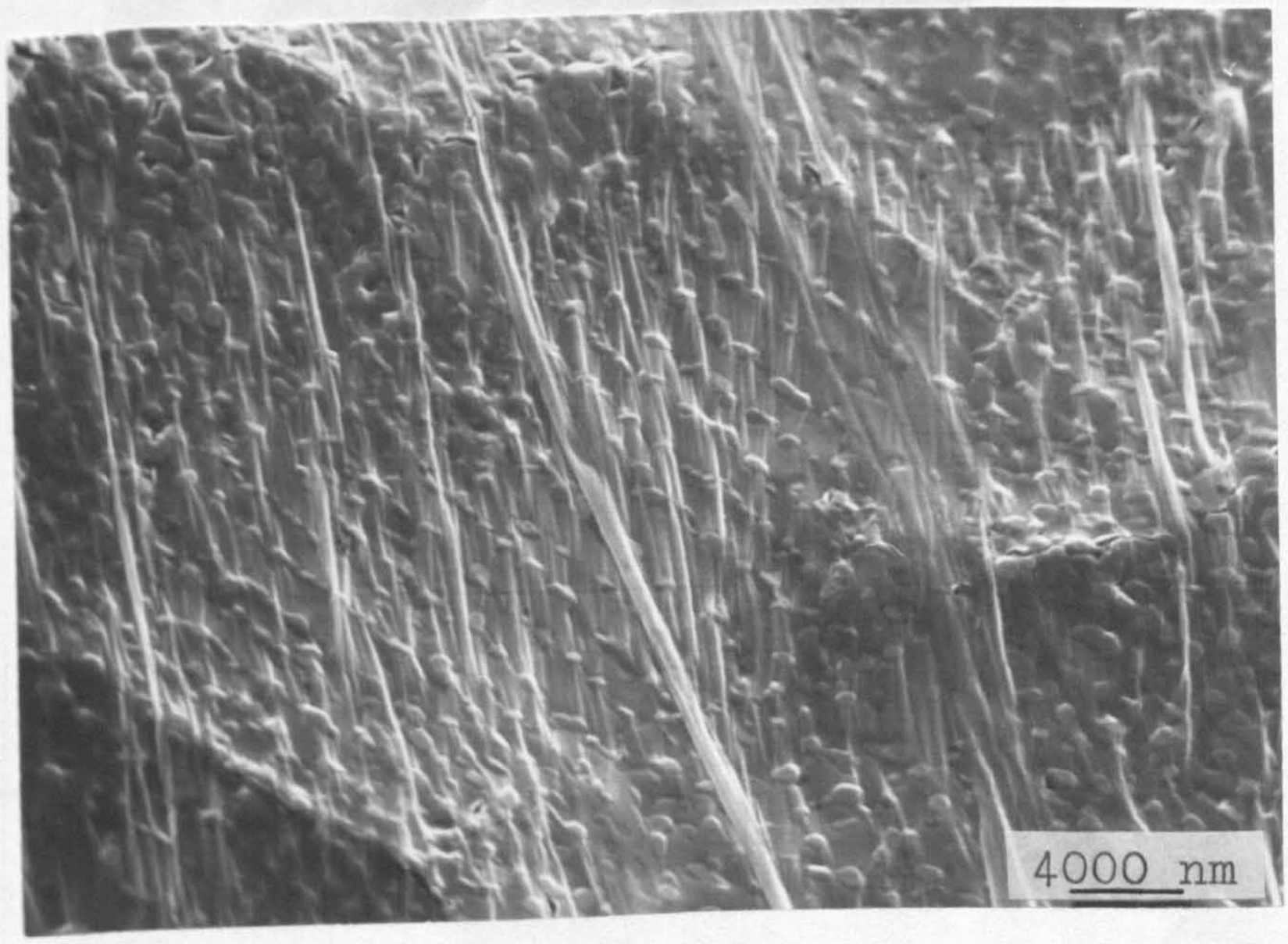

Fig.61(c) SEM of oxide/atmosphere interface of film shown in Fig.61(b)

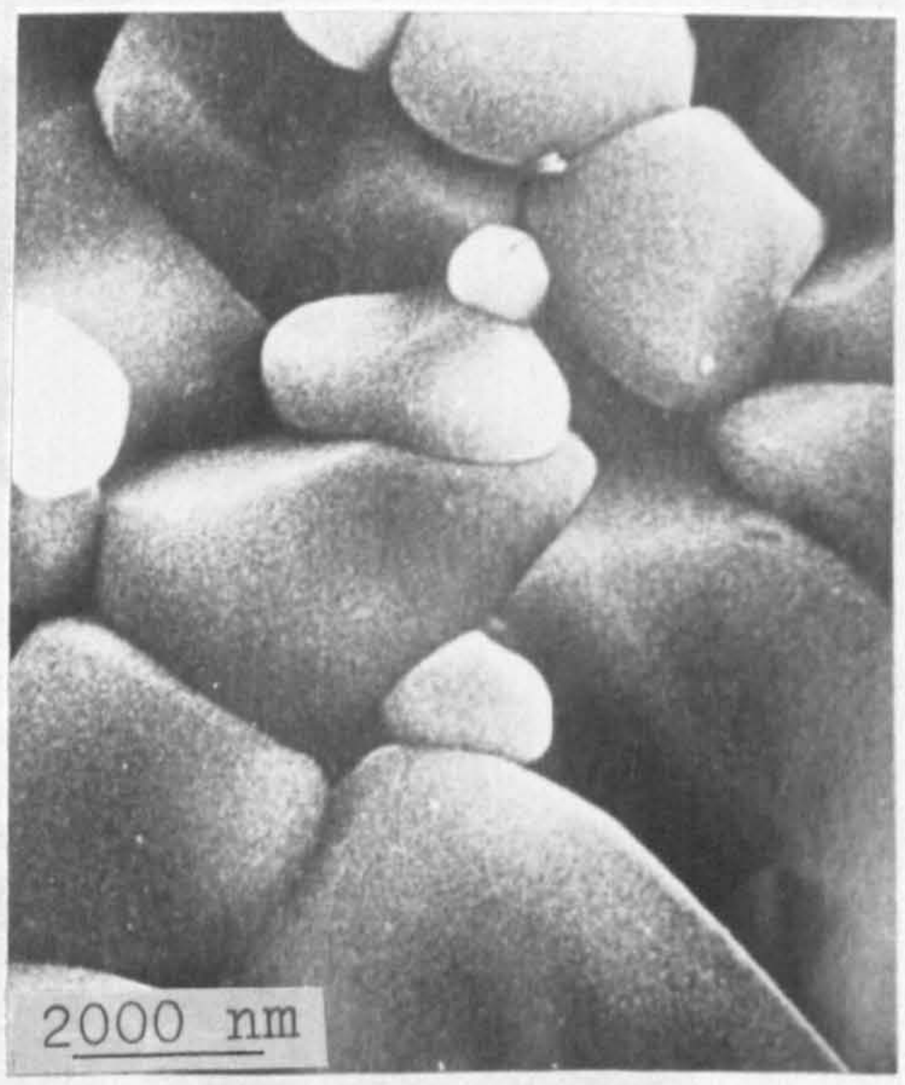

Fig.62(a) The structure of bulk α-Al_2O_3 after calcination at 1600°C.
(B.A. "An Atlas of Alumina")

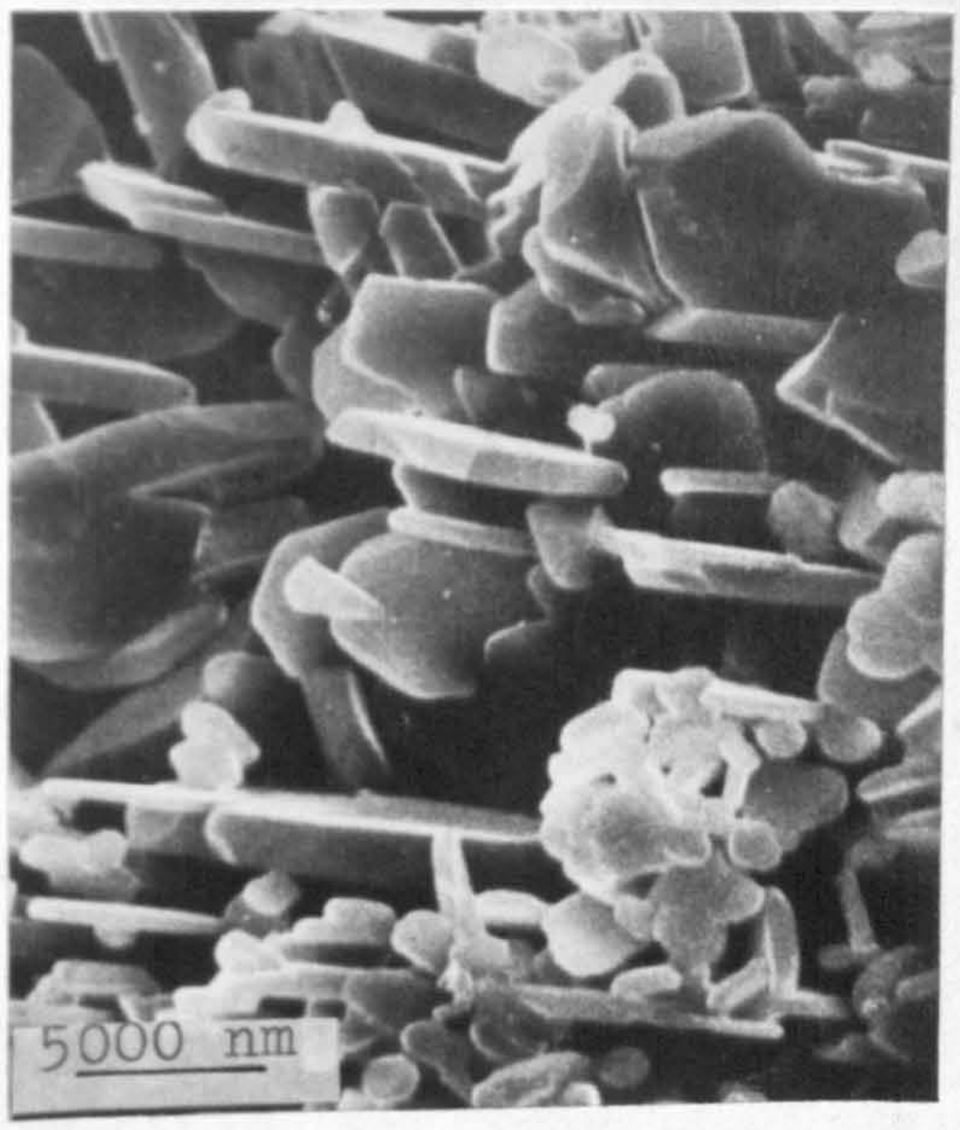

Fig.62(b)

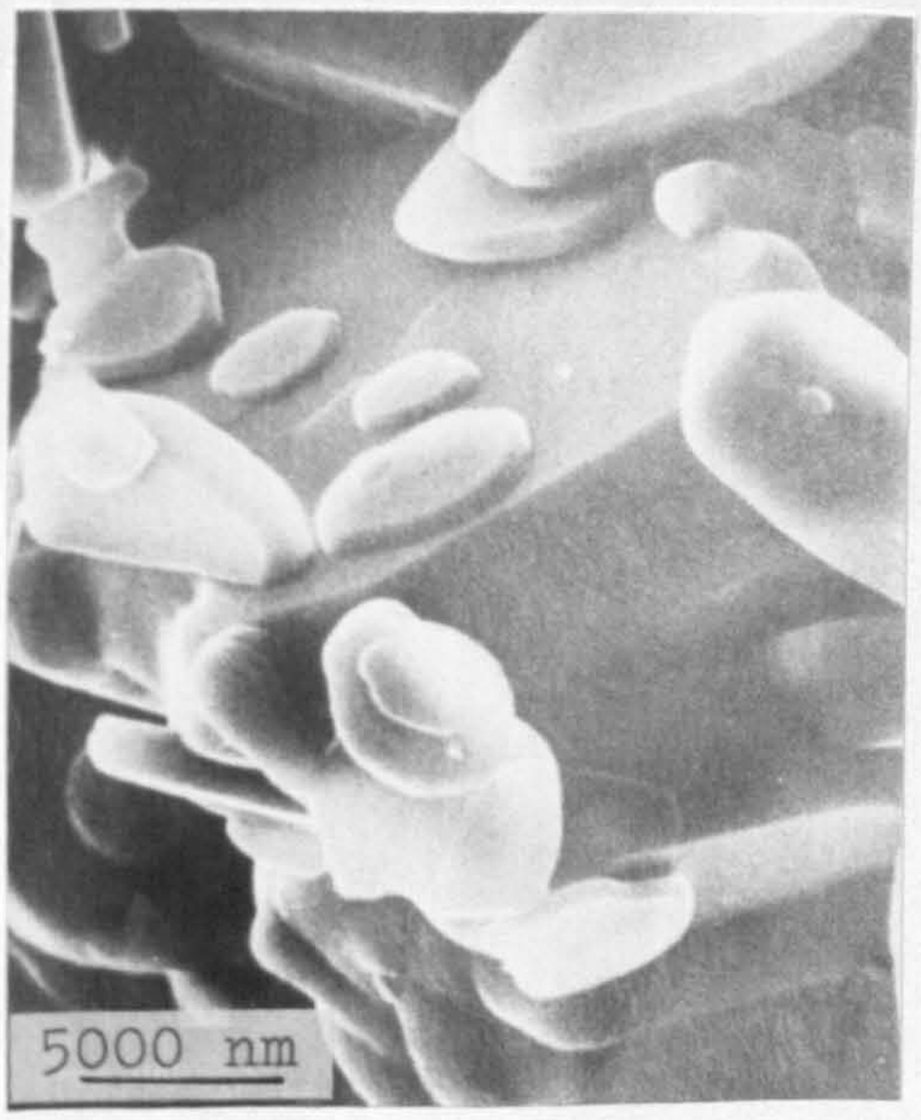

Fig.62(c)

Fig.62(b) and (c) Modifications of bulk α-Al_2O_3 shown in Fig.62(a) when calcined in an atmosphere containing fluorine.

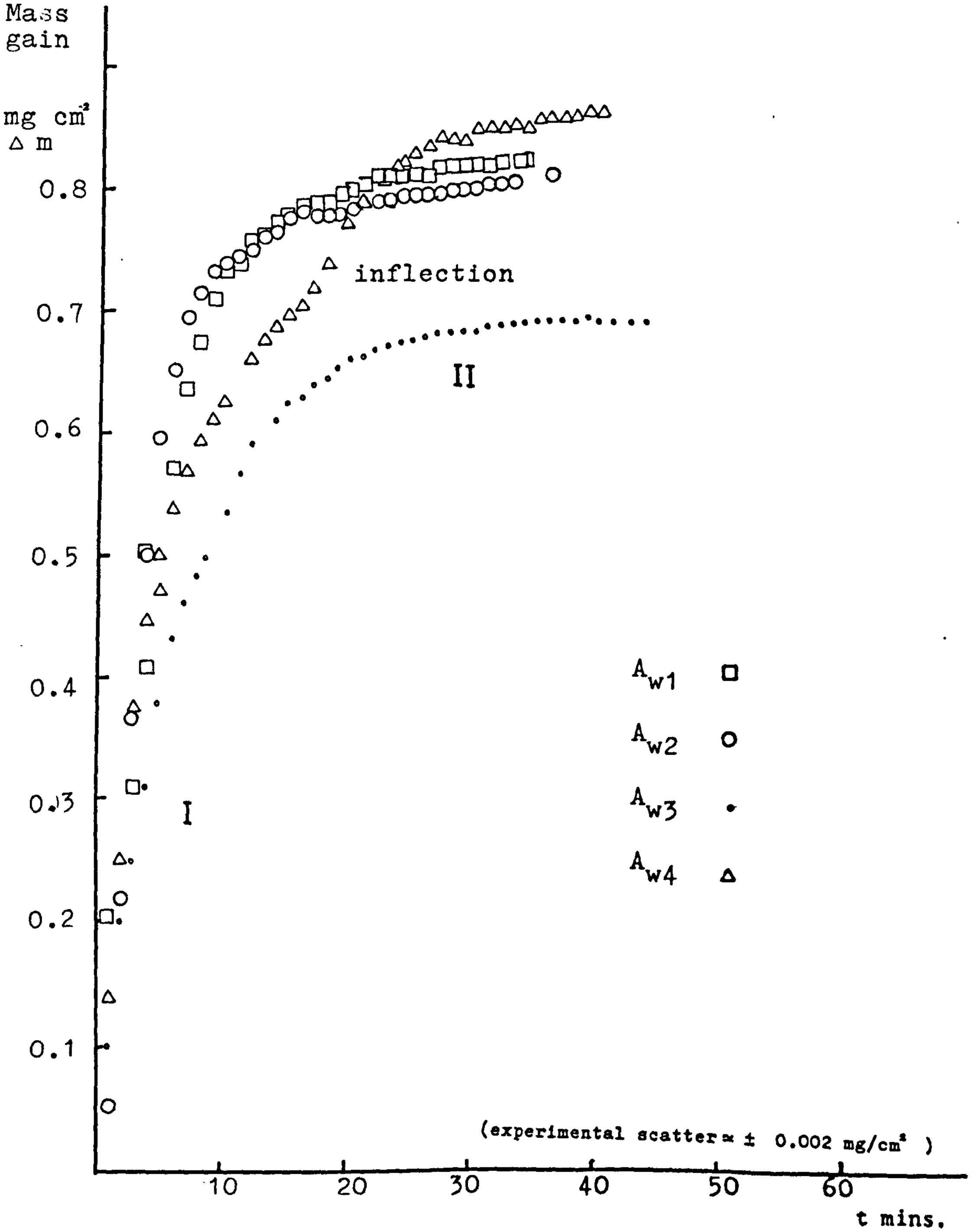

Fig 63a Oxidation of normal high purity aluminium (Billet A) at 1003 K (730 °C) in moist oxygen (P_{H_2O} 0.03 atms.)

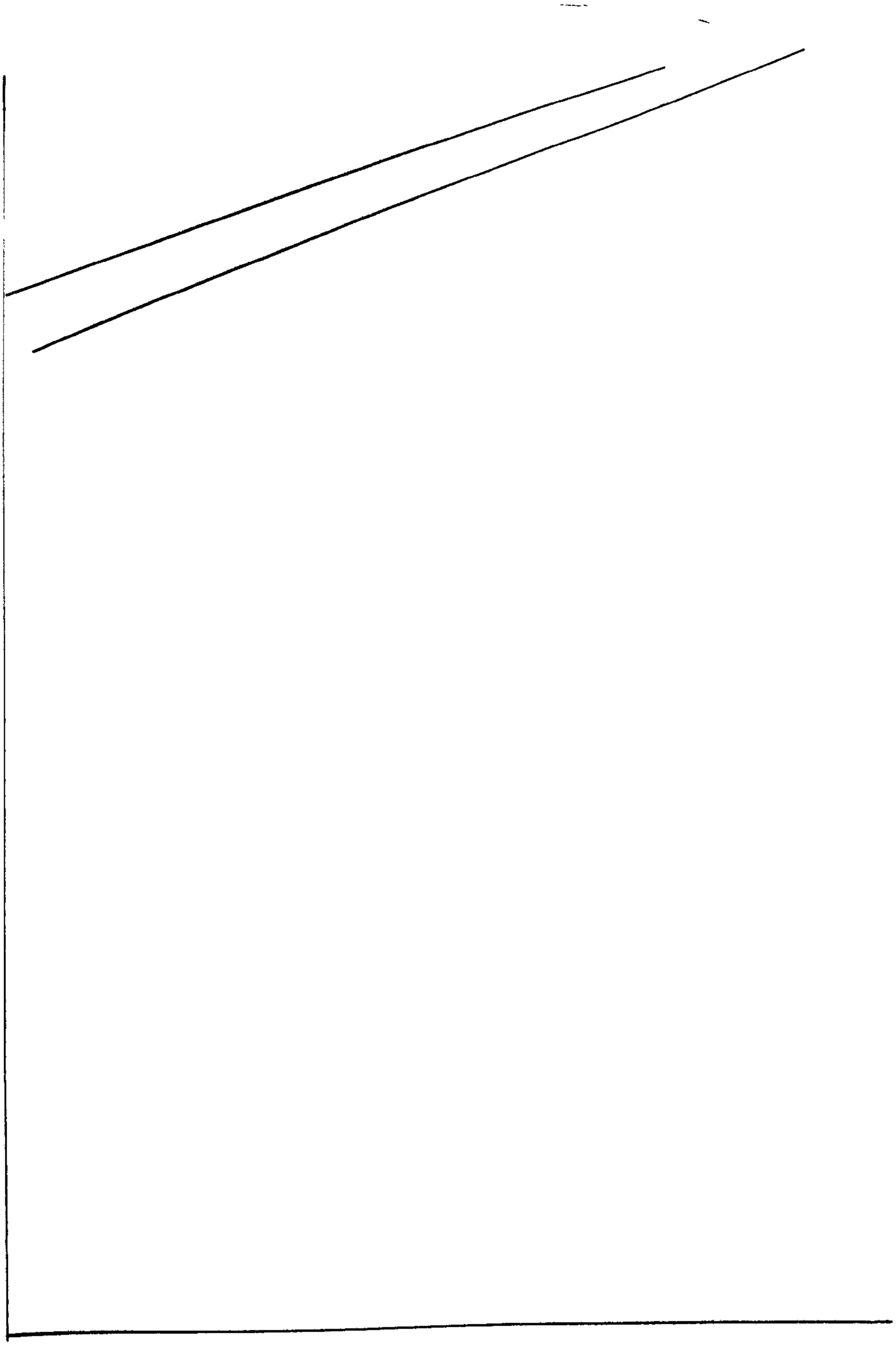

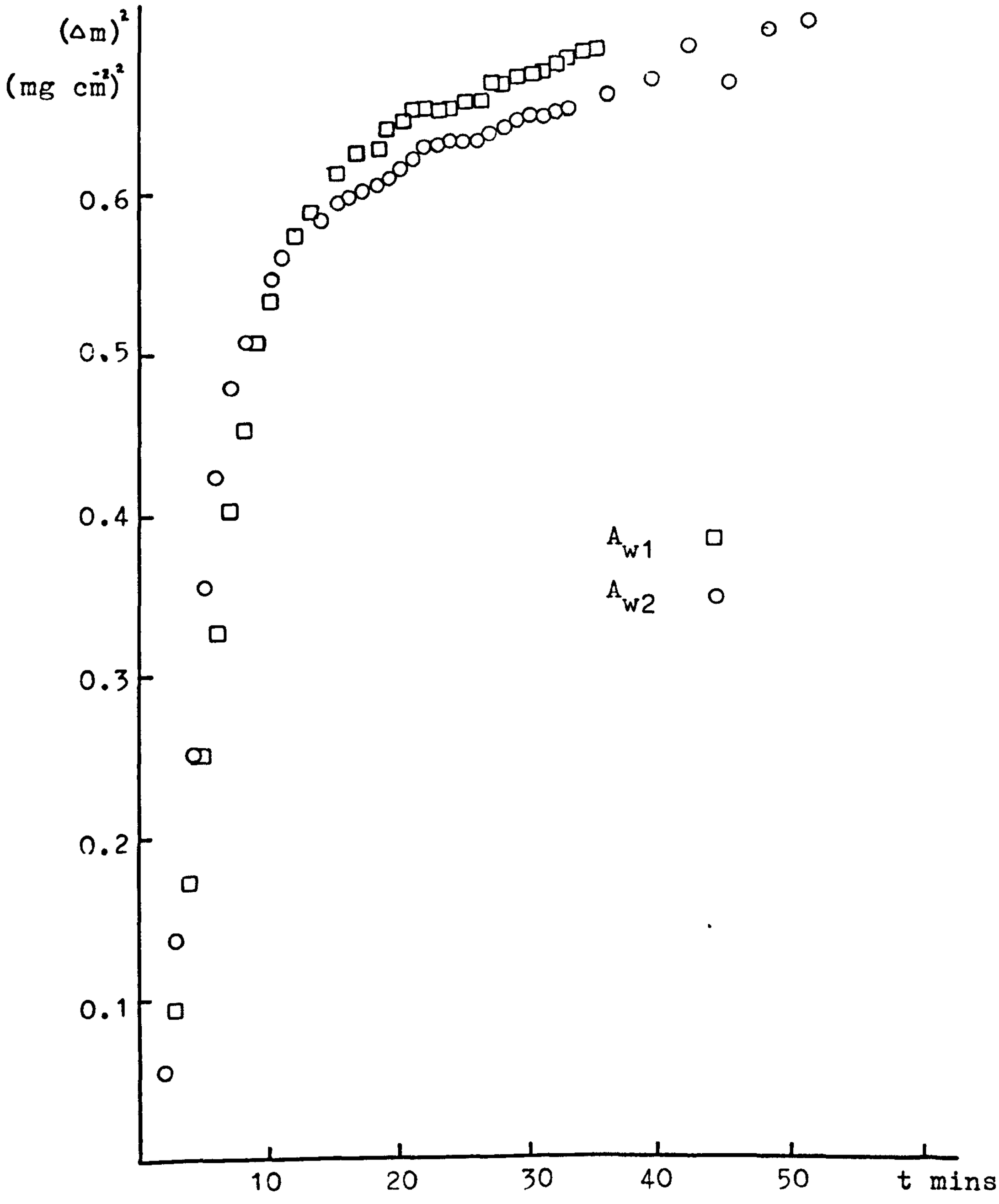

Fig.63b A_{w1} and A_{w2} from Fig.63a replotted on parabolic scale. $(\Delta m)^2$ plotted as a function of time showing parabolic kinetics in Stage II

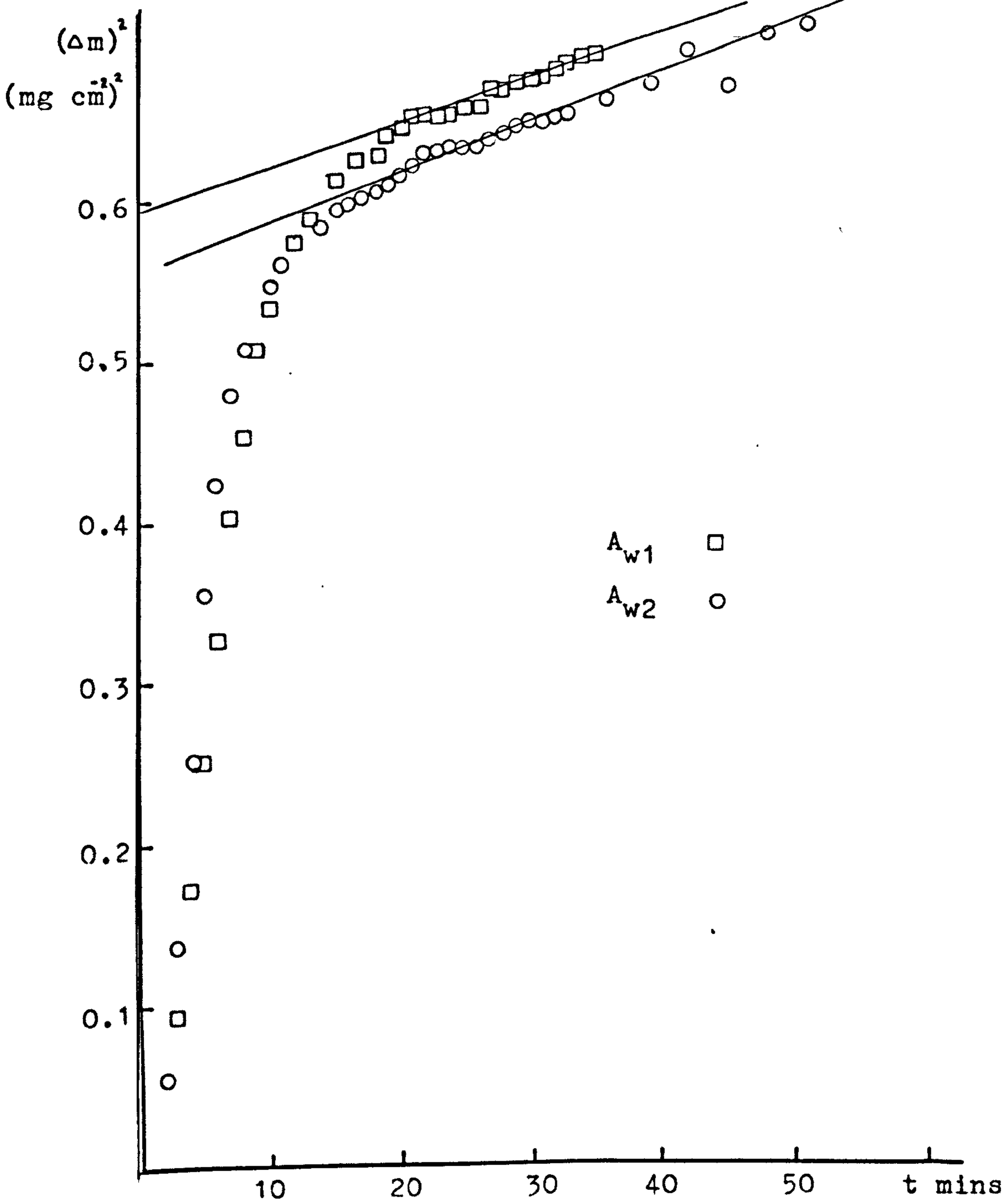

Fig.63b A_{w1} and A_{w2} from Fig.63a replotted on parabolic scale. $(\Delta m)^2$ plotted as a function of time showing parabolic kinetics in Stage II

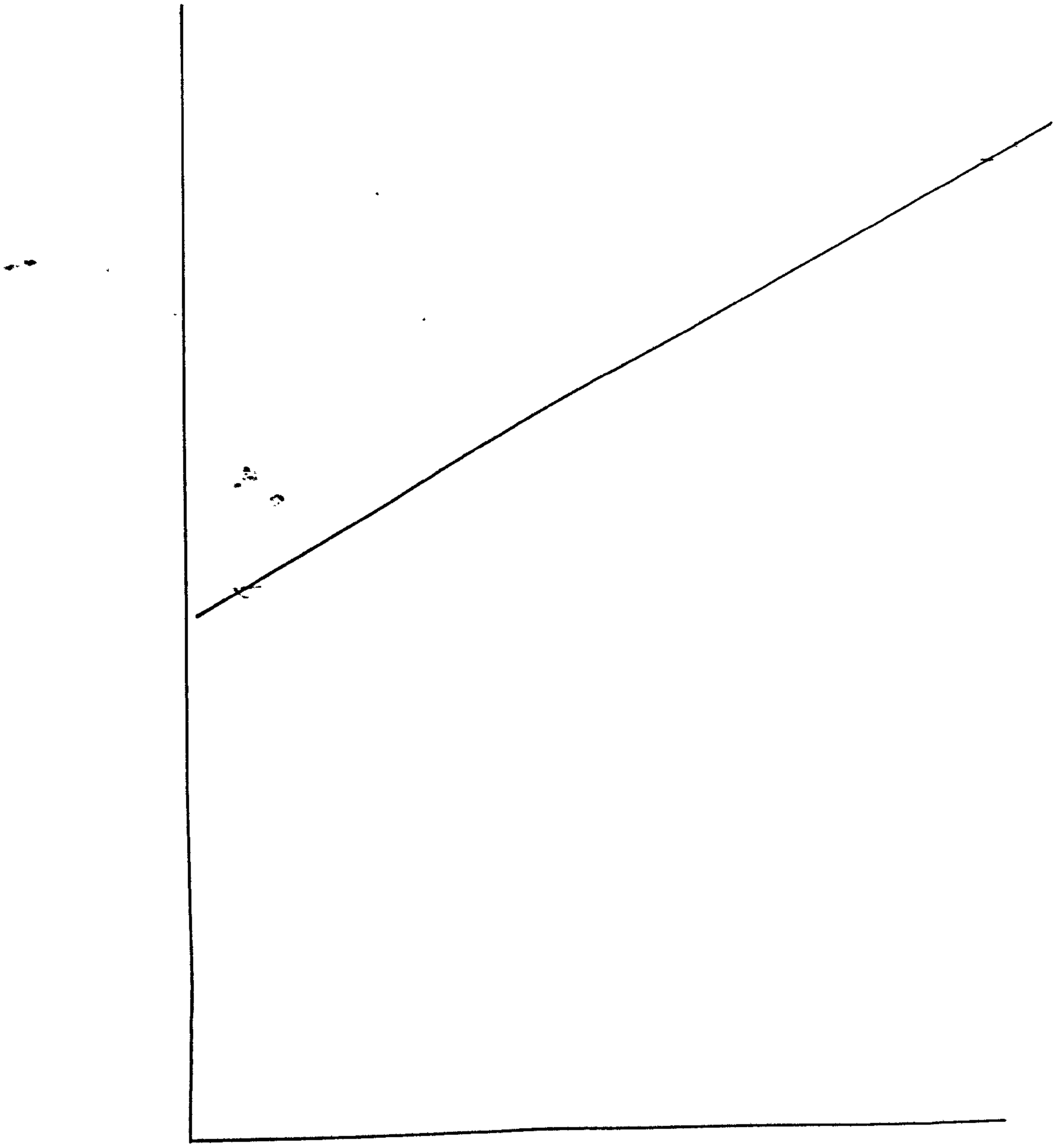

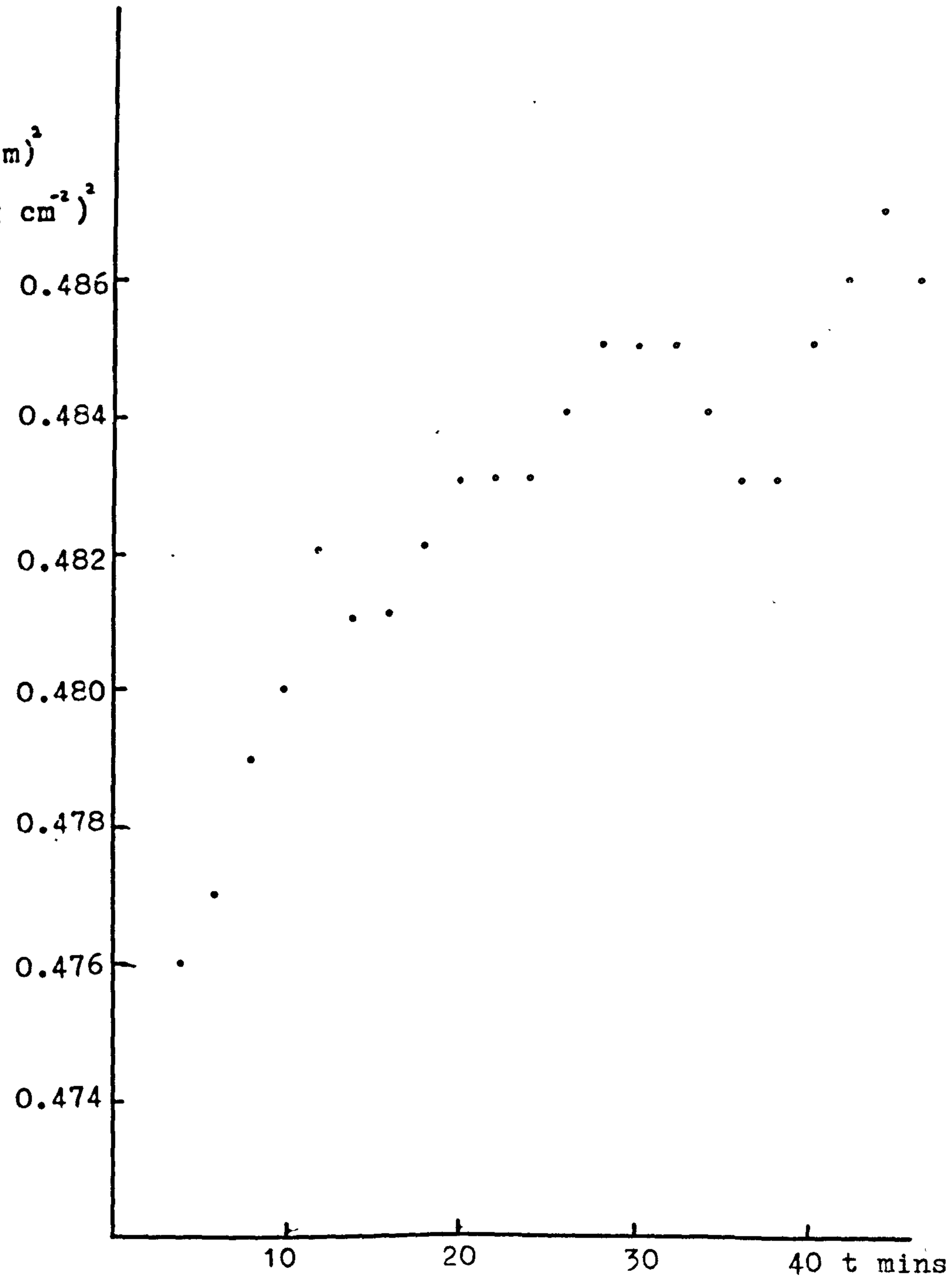

Fig 63c A_{W3} from Fig 63a replotted on parabolic scale. $(\Delta m)^2$ plotted as a function of time(t) showing parabolic kinetics in Stage II

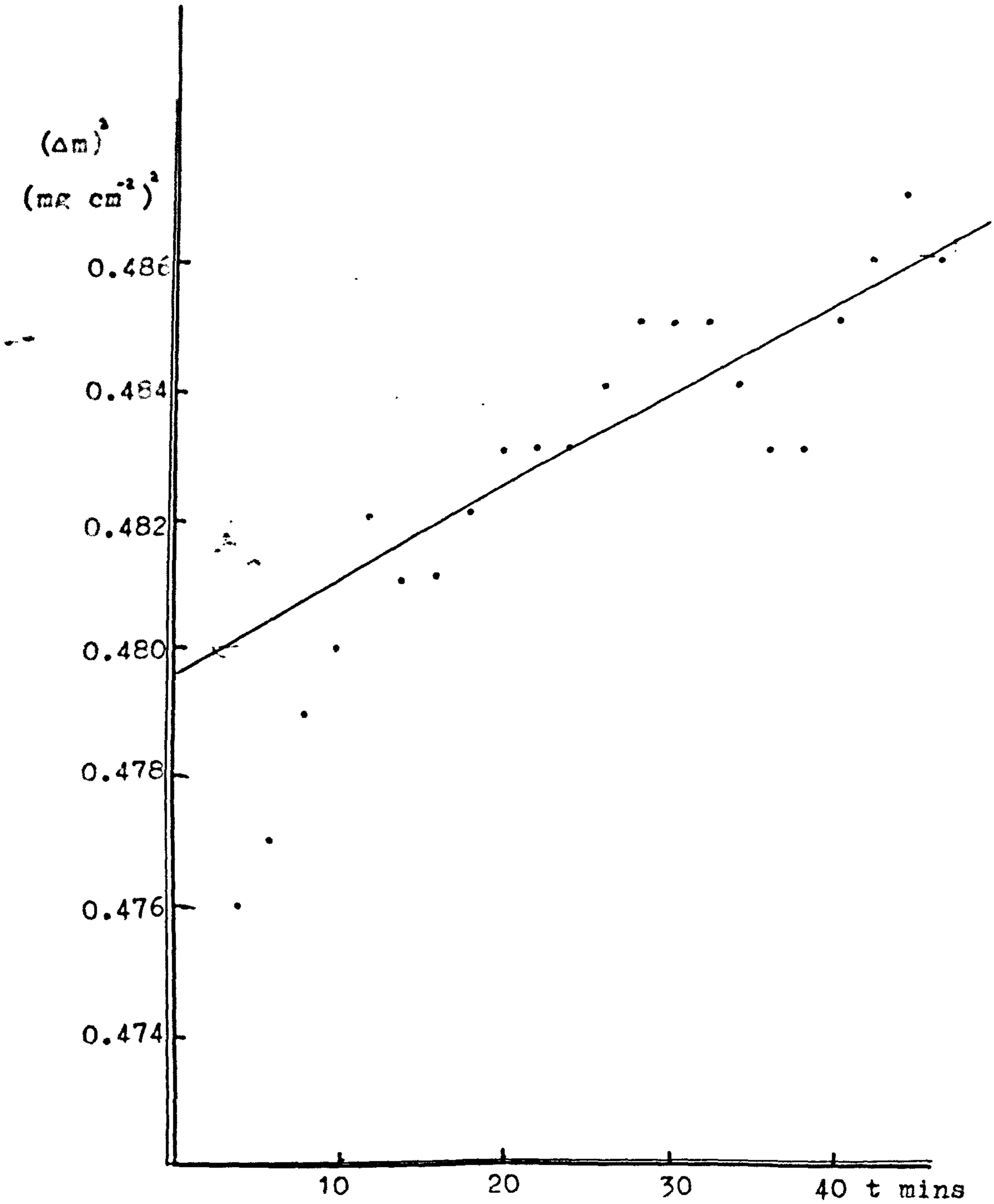

Fig 63c A_{W3} from Fig 63a replotted on parabolic scale. $(\Delta m)^2$ plotted as a function of time(t) showing parabolic kinetics in Stage II

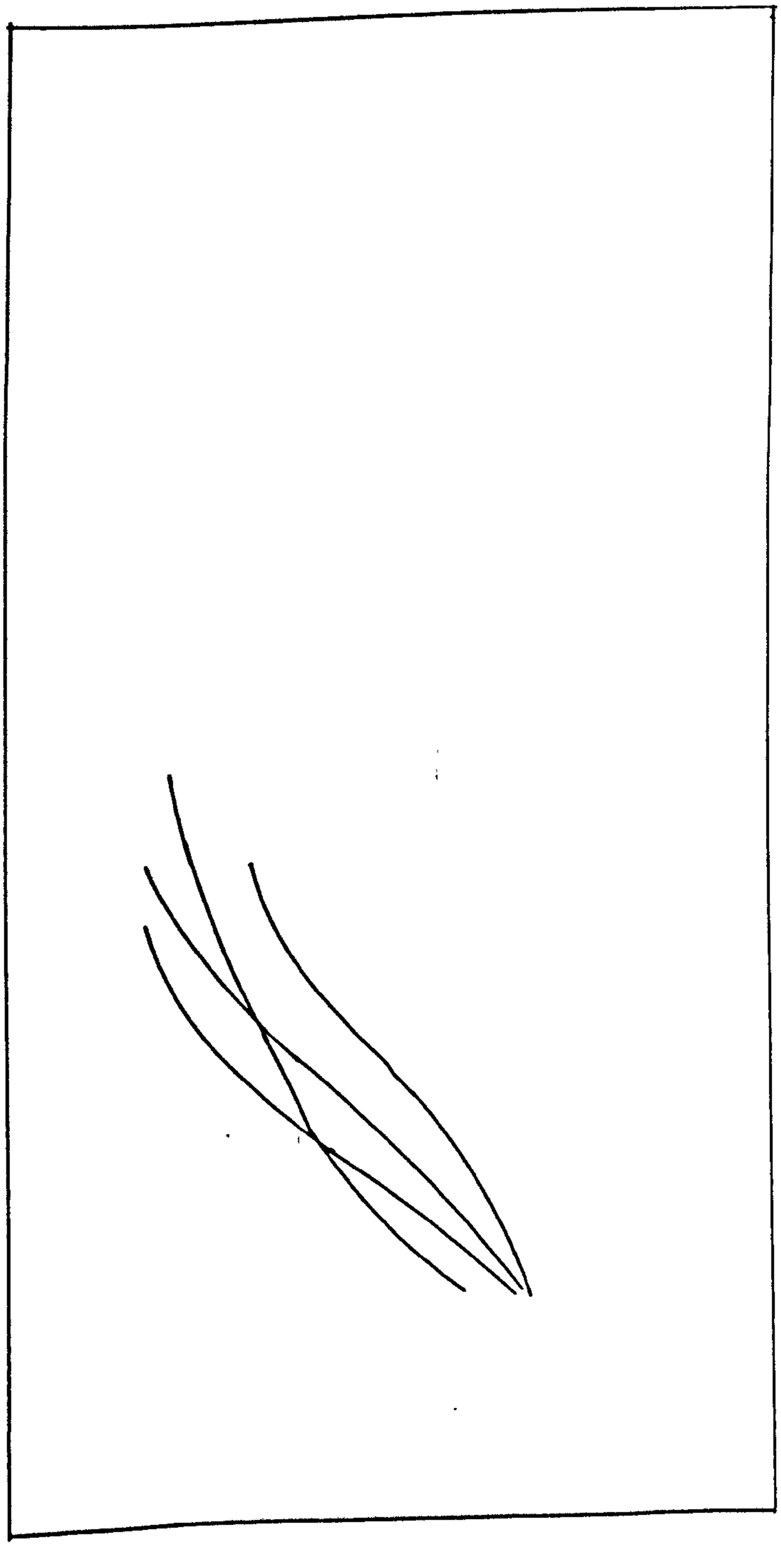

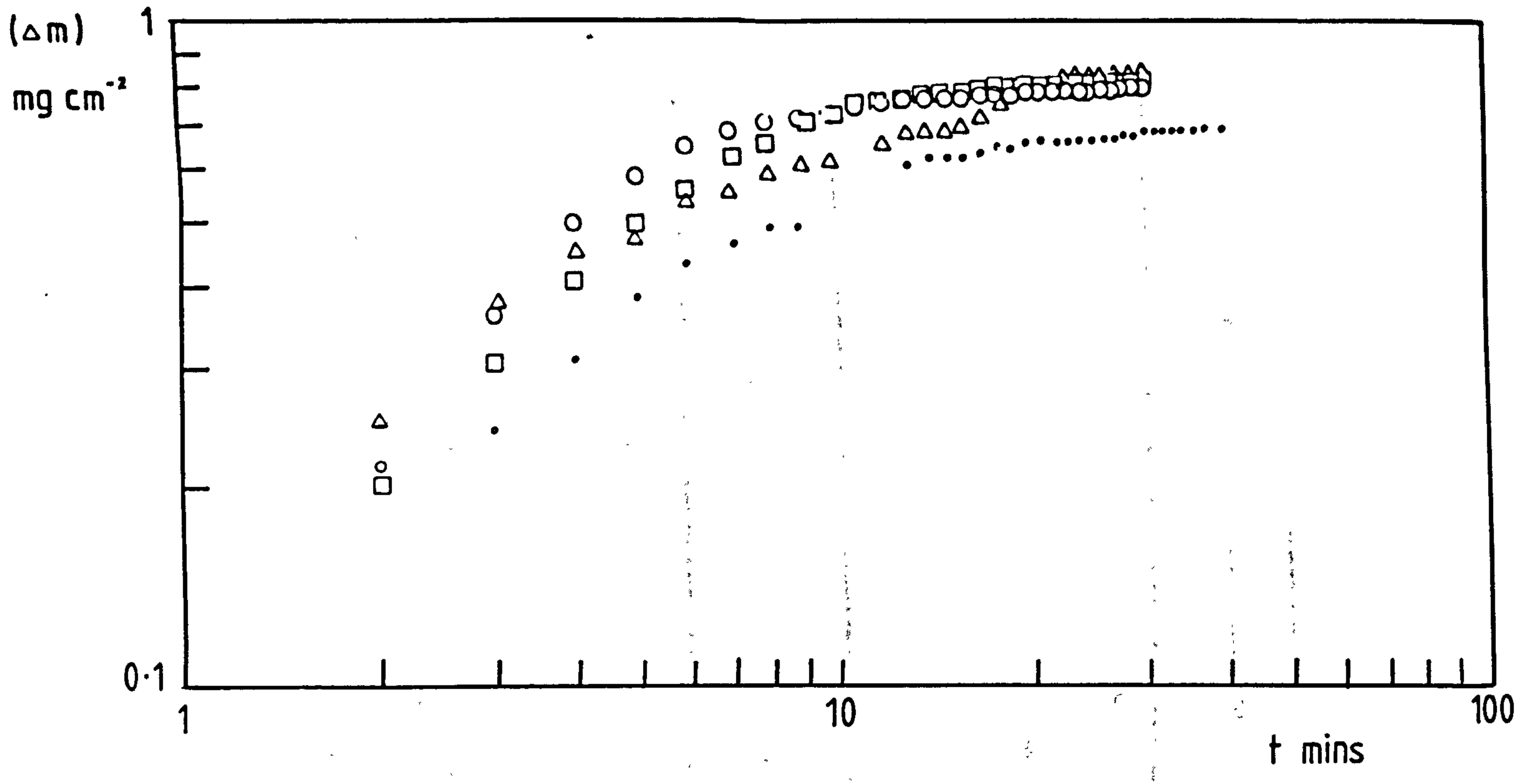

Fig 63d Fig 63a replotted on log/log scale, showing the kinetics in Stage I do not conform to a simple power law

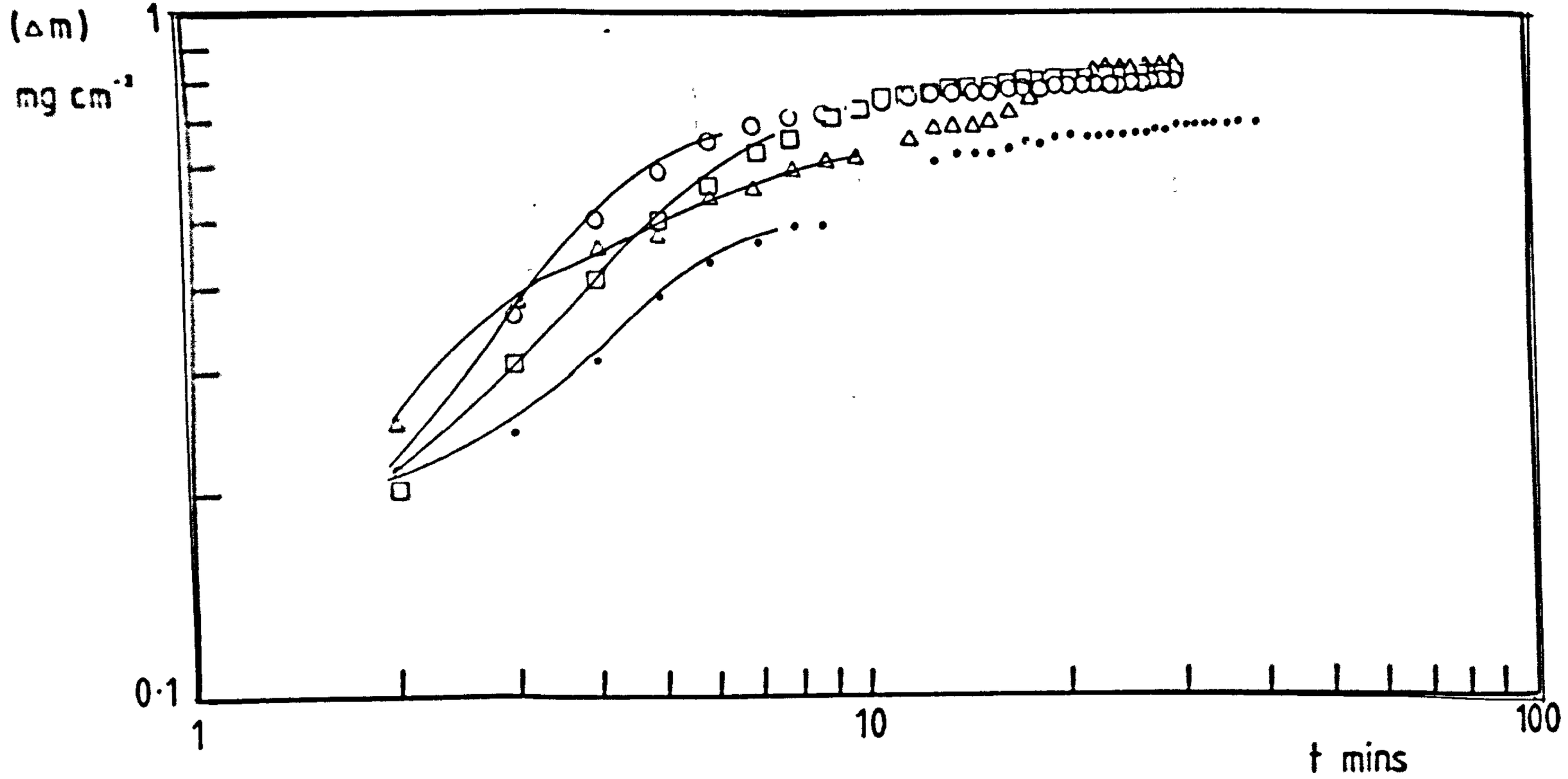

Fig 63d Fig 63a replotted on log/log scale, showing the kinetics in Stage I do not conform to a simple power law

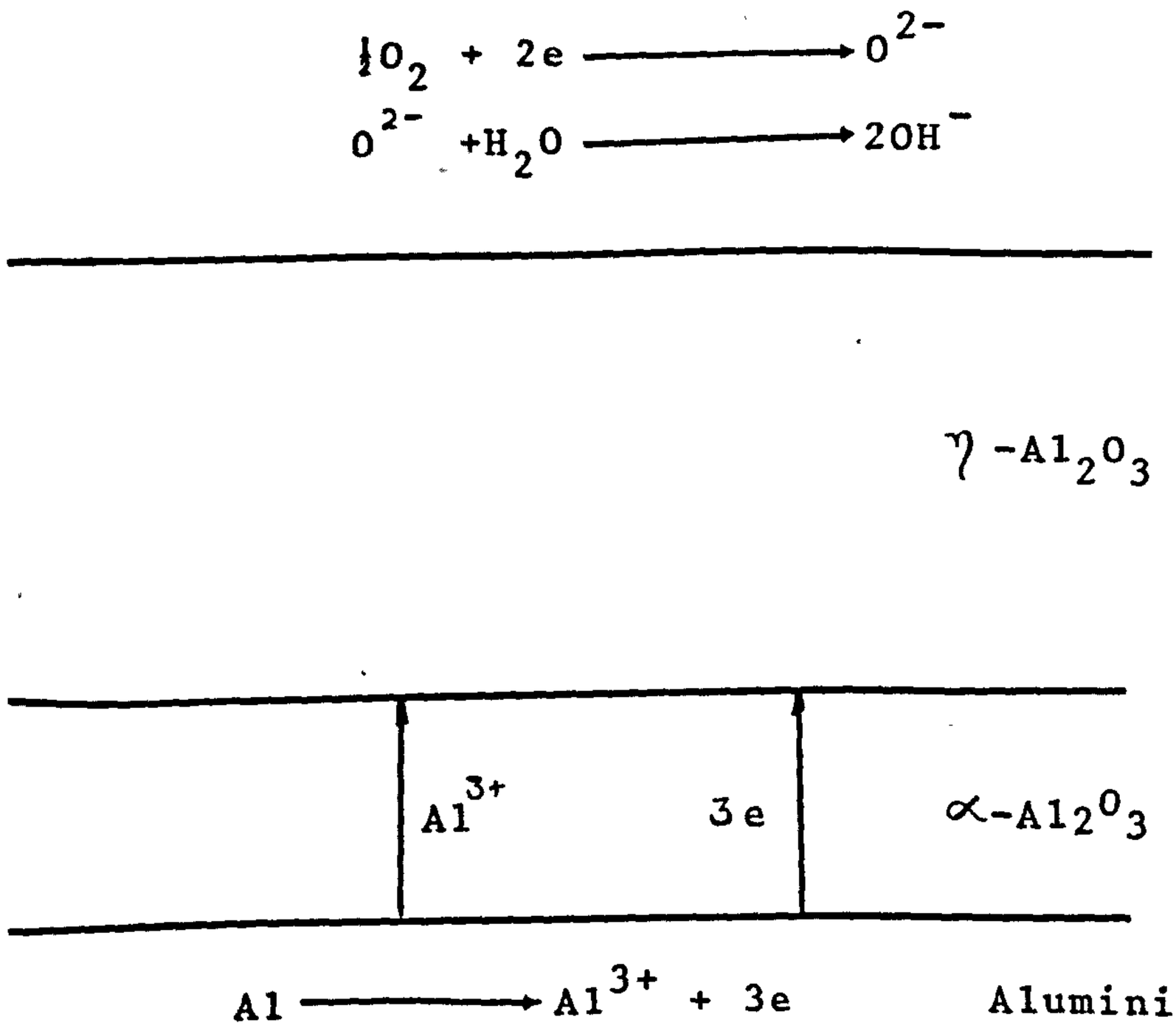

Fig 64 Schematic representation of transport within oxide films formed on pure aluminium at 730 °C in moist oxygen. When $\alpha\text{-}Al_2O_3$ subfilm is fully established the overall rate is controlled by transport of Al^{3+} through $\alpha\text{-}Al_2O_3$.

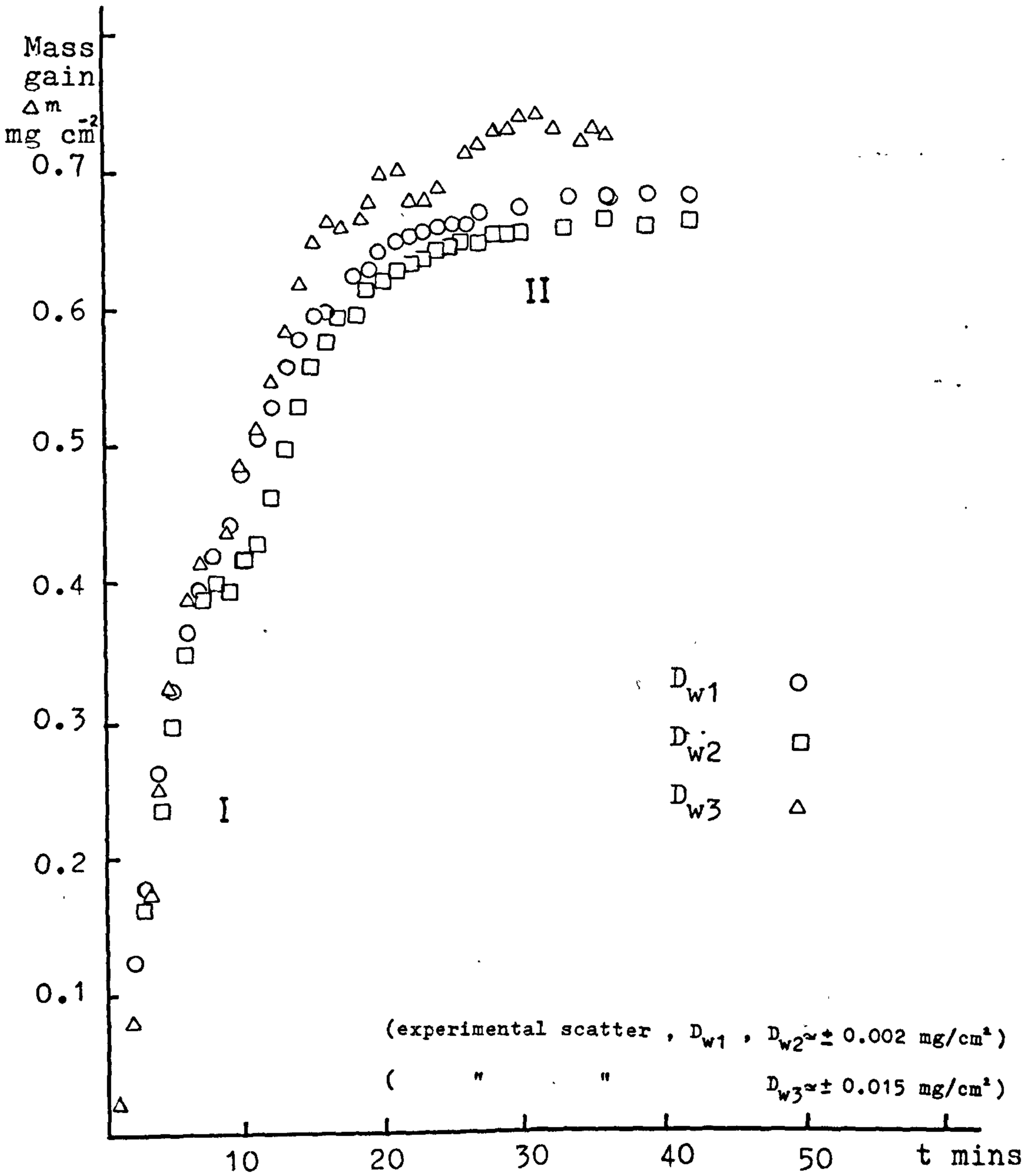

Fig 65a Oxidation of further purified normal high purity aluminium (Billet D) in moist oxygen (P_{H_2O}=0.03 atms.)

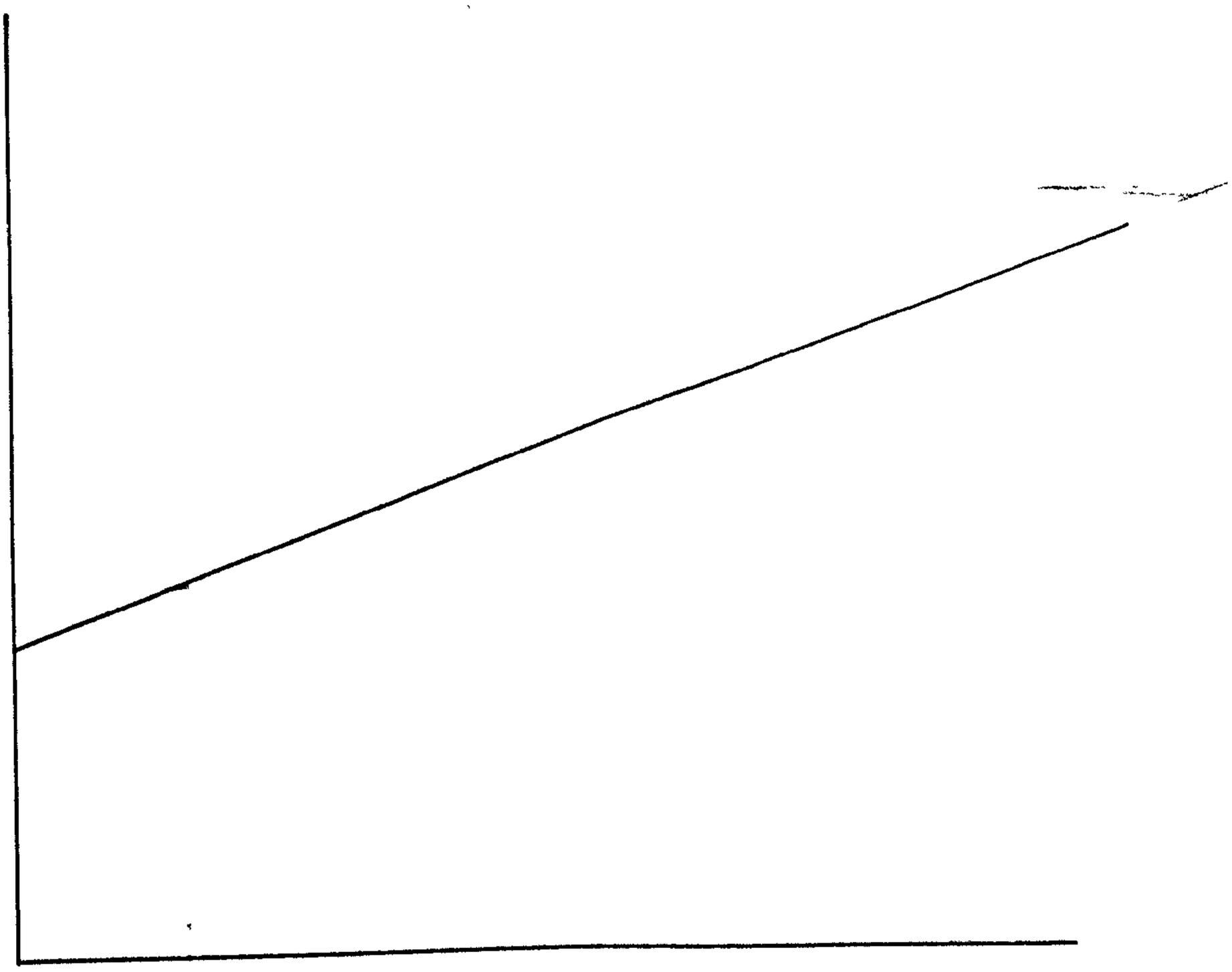

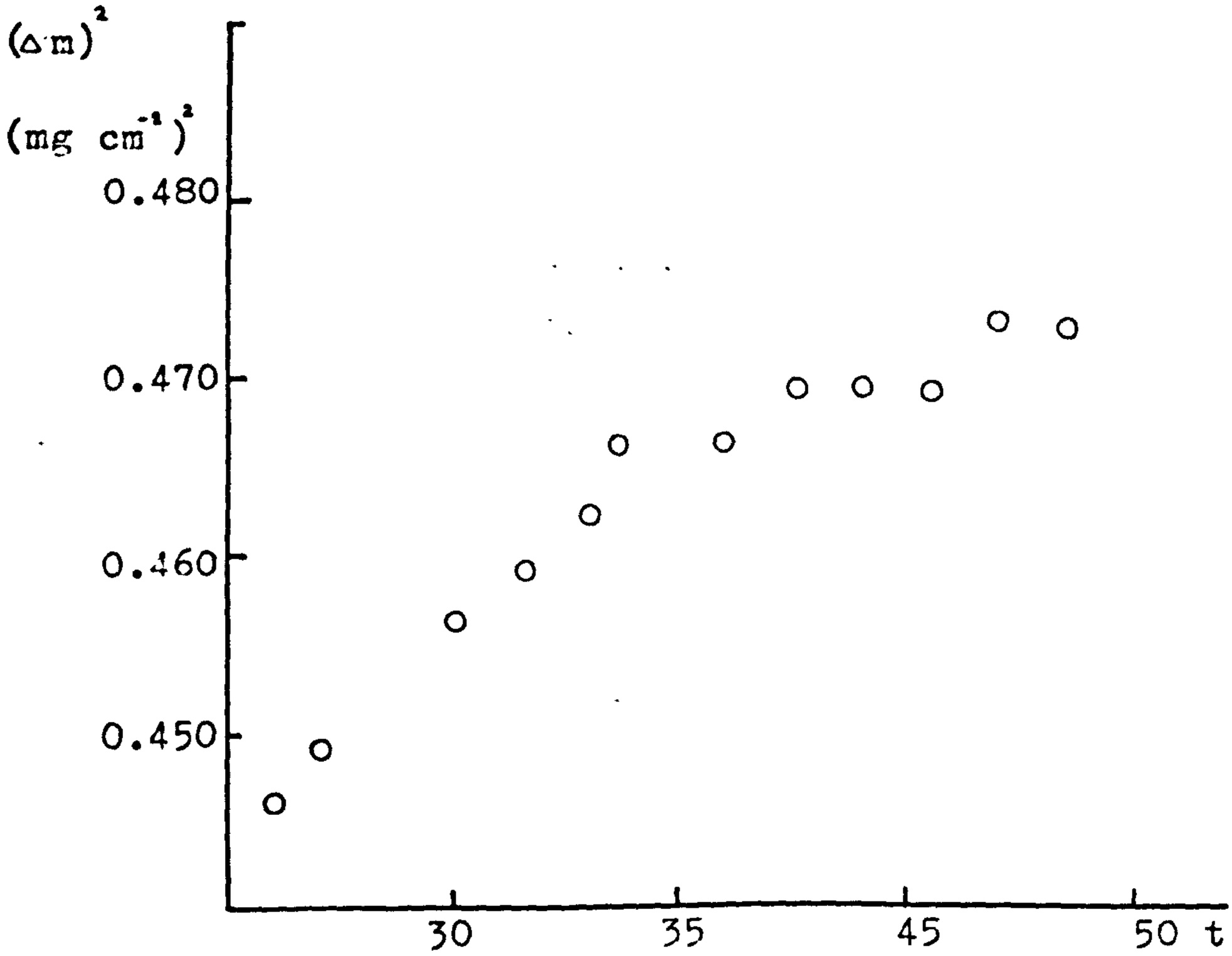

Fig 65b D_{w1} from Fig 65a replotted on parabolic scale. $(\Delta m)^2$ plotted as a function of time (t) , showing that the kinetics during Stage II conform to the parabolic law.

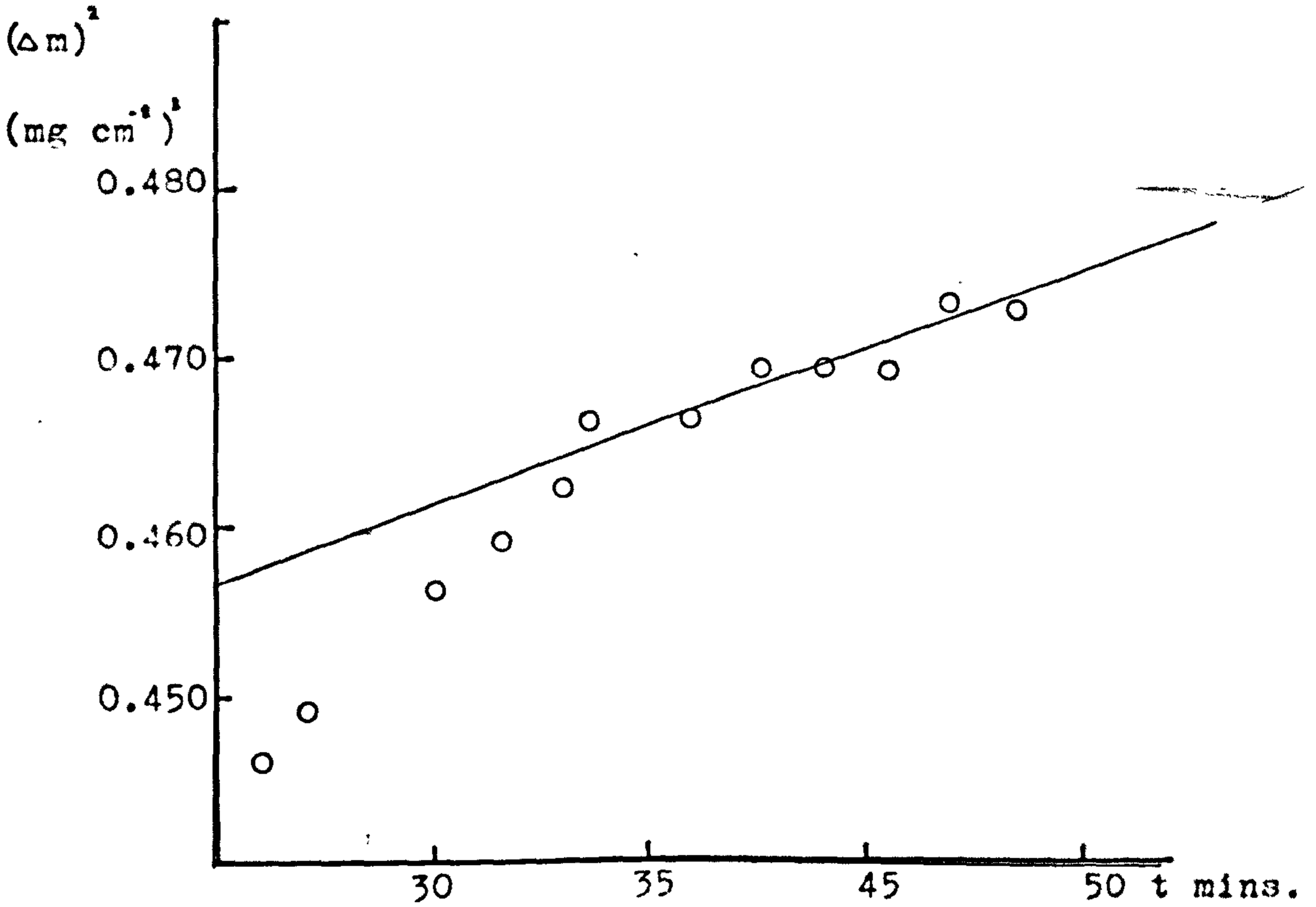

Fig 65b D_{w1} from Fig 65a replotted on parabolic scale. $(\Delta m)^2$ plotted as a function of time (t) , showing that the kinetics during Stage II conform to the parabolic law.

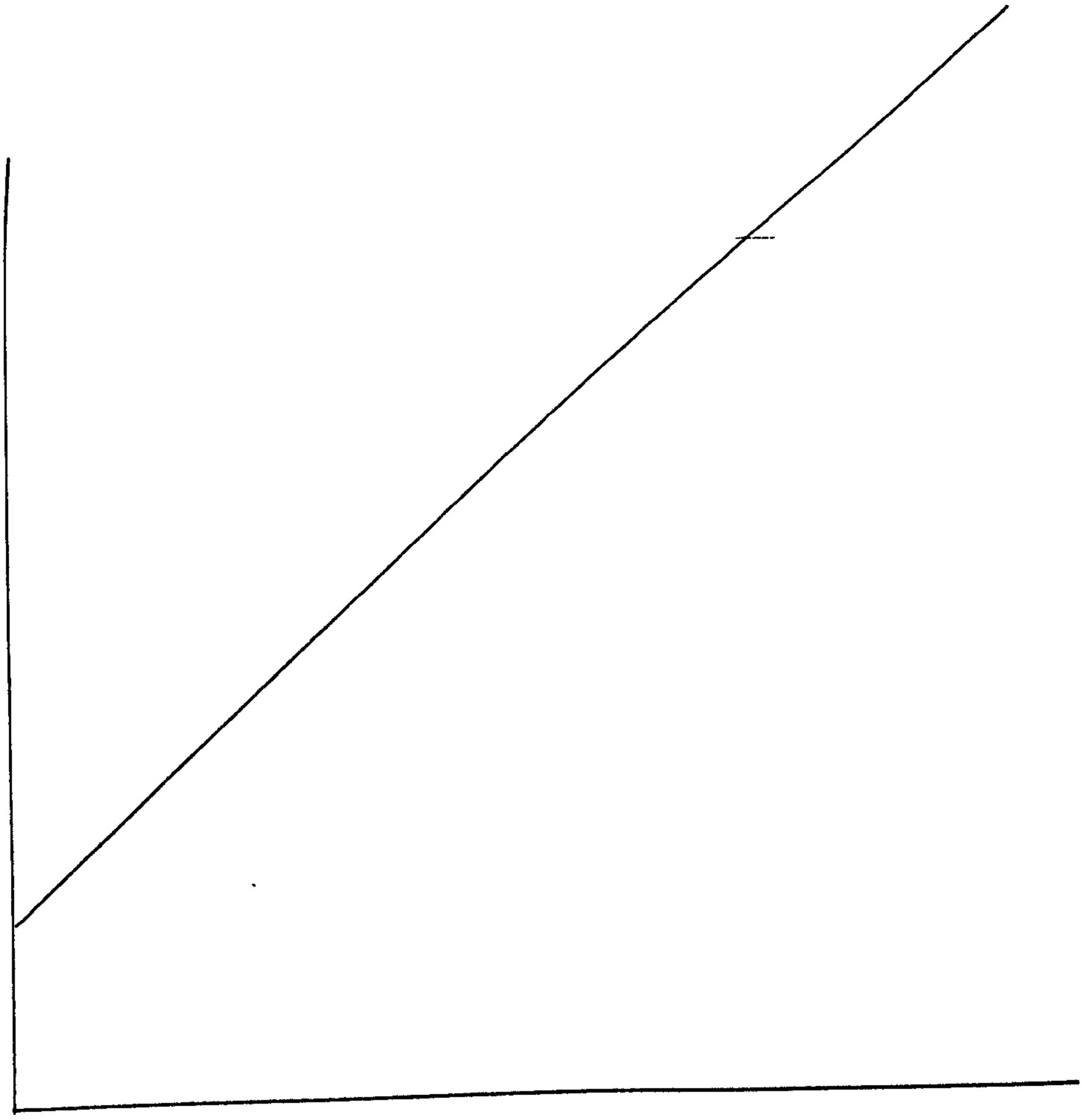

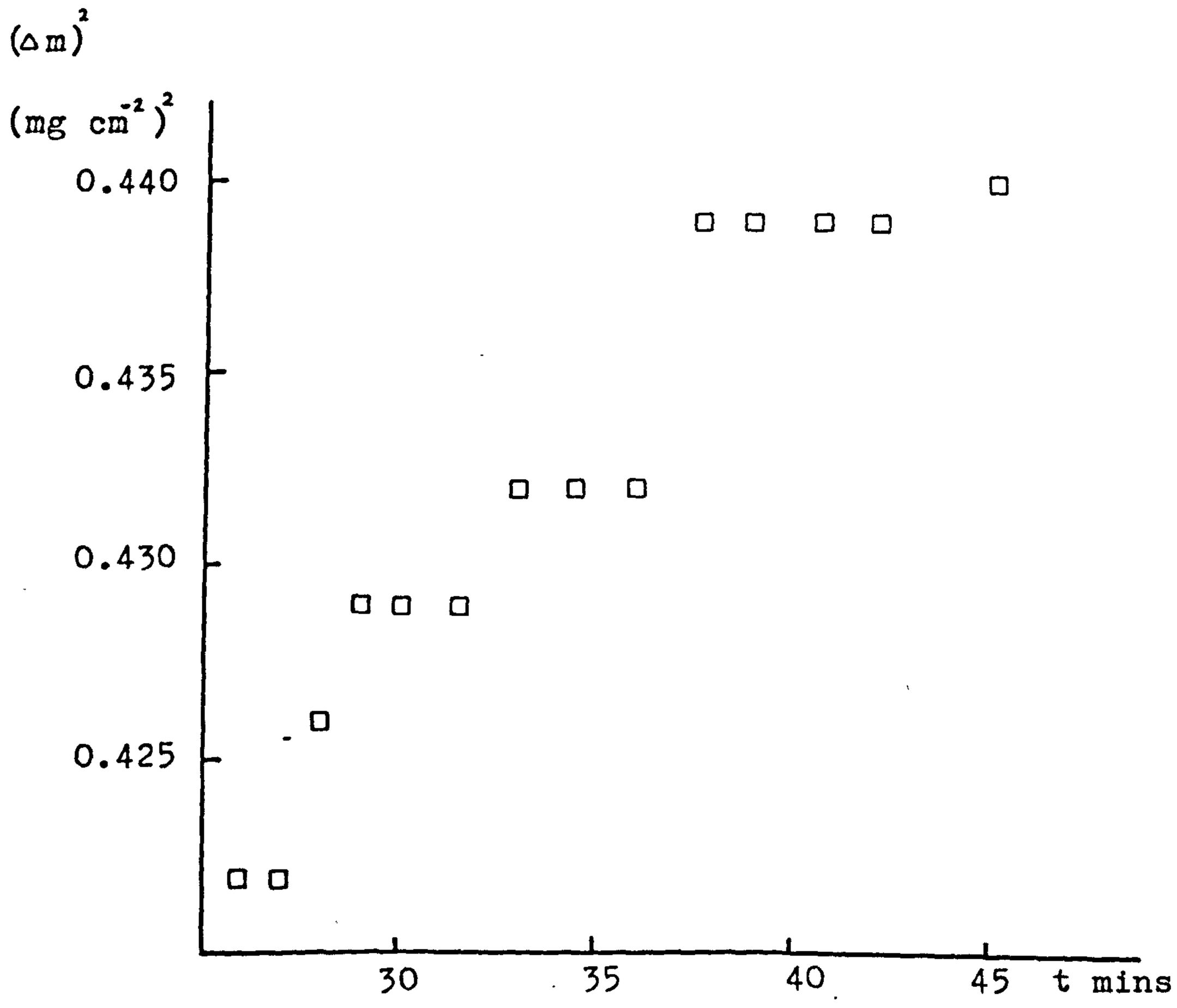

Fig 65c D_{w2} from Fig 65a replotted on a parabolic scale $.(\Delta m)^2$ plotted as a function of time (t) showing that the kinetics during Stage II conform to the parabolic law.

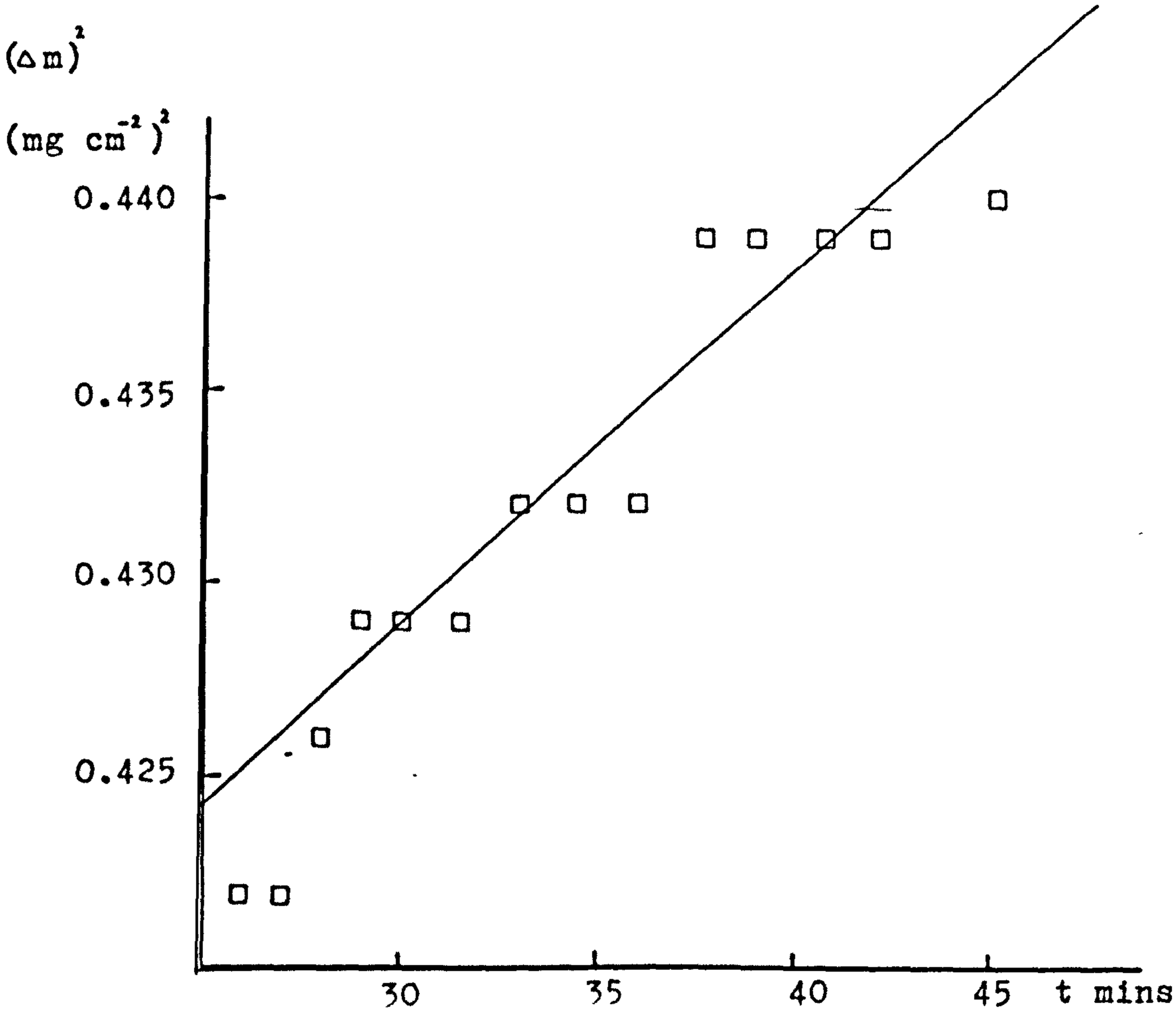

Fig 65c D_{w2} from Fig 65a replotted on a parabolic scale .$(\Delta m)^2$ plotted as a function of time (t) showing that the kinetics during Stage II conform to the parabolic law.

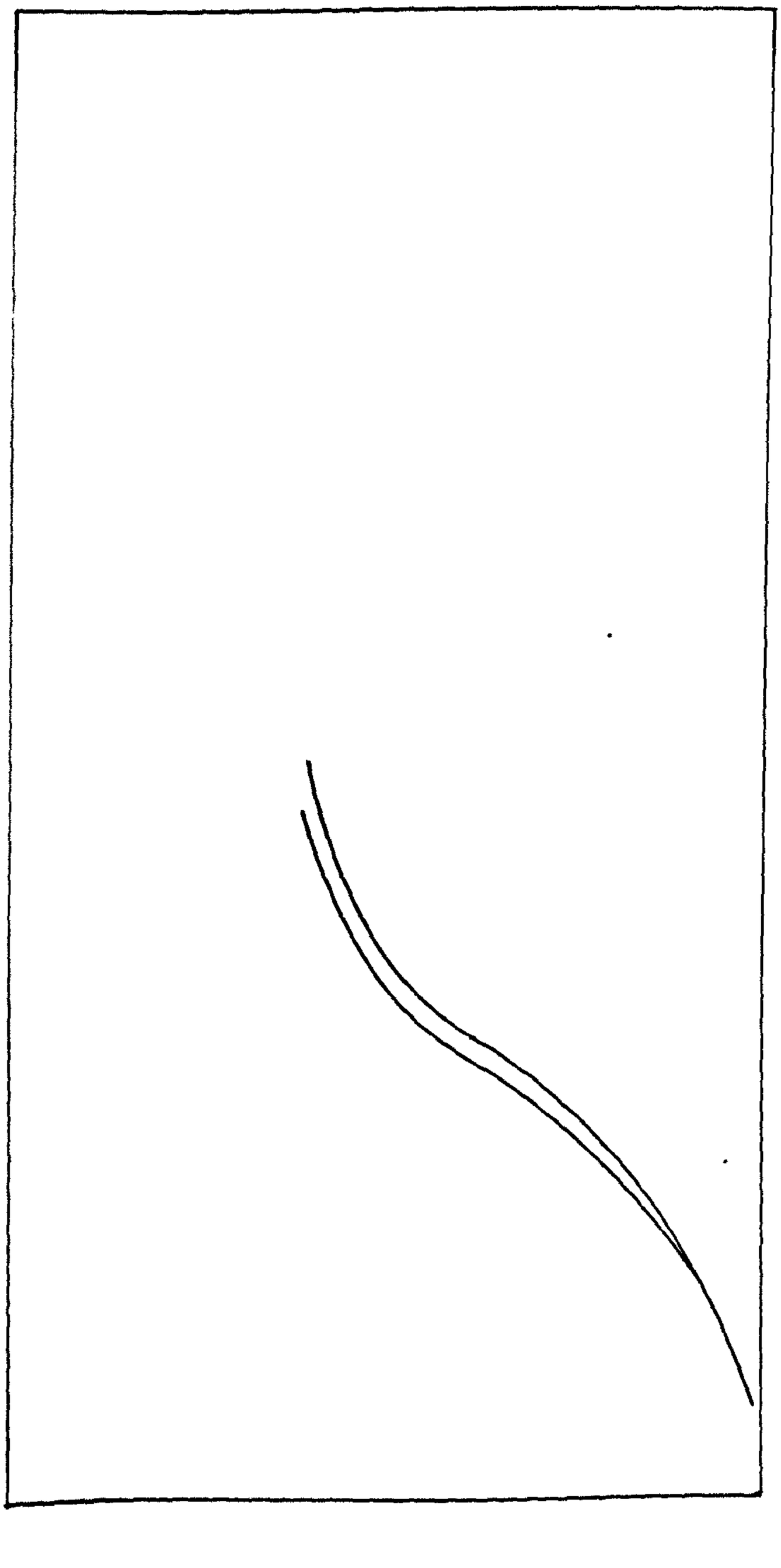

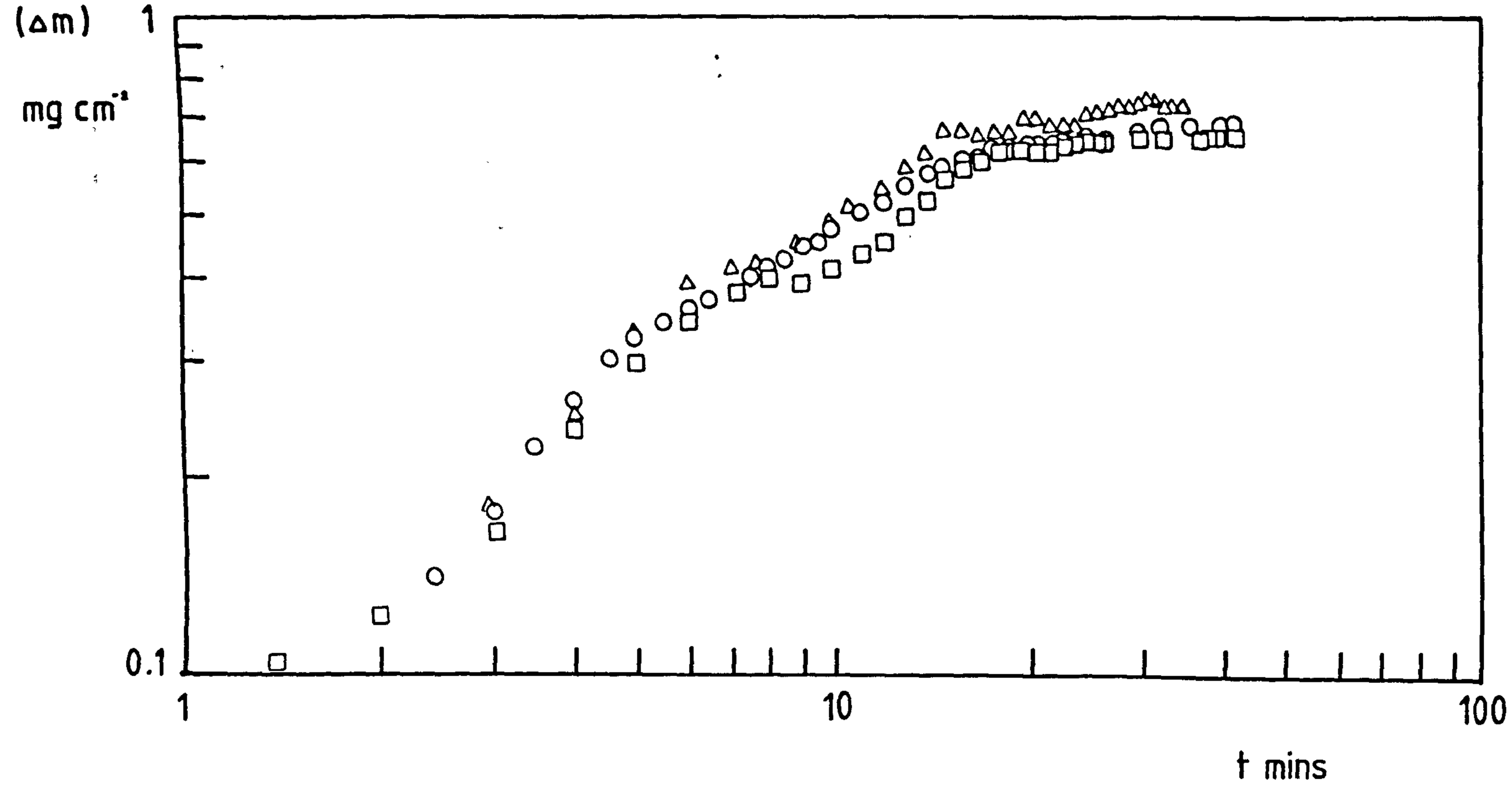

Fig 65d Fig 65a replotted on log/log scale showing that kinetics in Stage I do not conform to a simple power law.

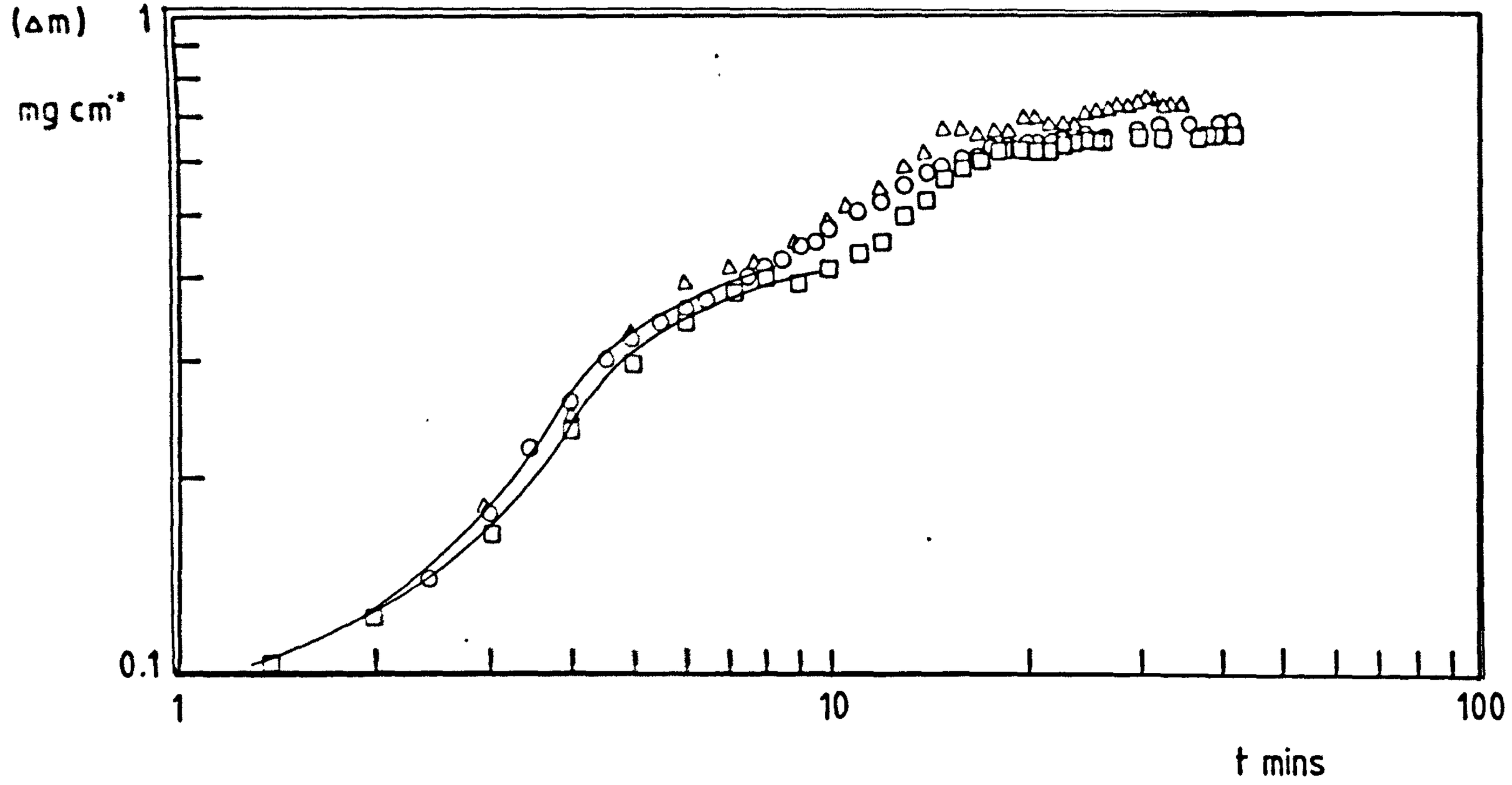

Fig 65d Fig 65a replotted on log/log scale showing that kinetics in Stage I do not conform to a simple power law.

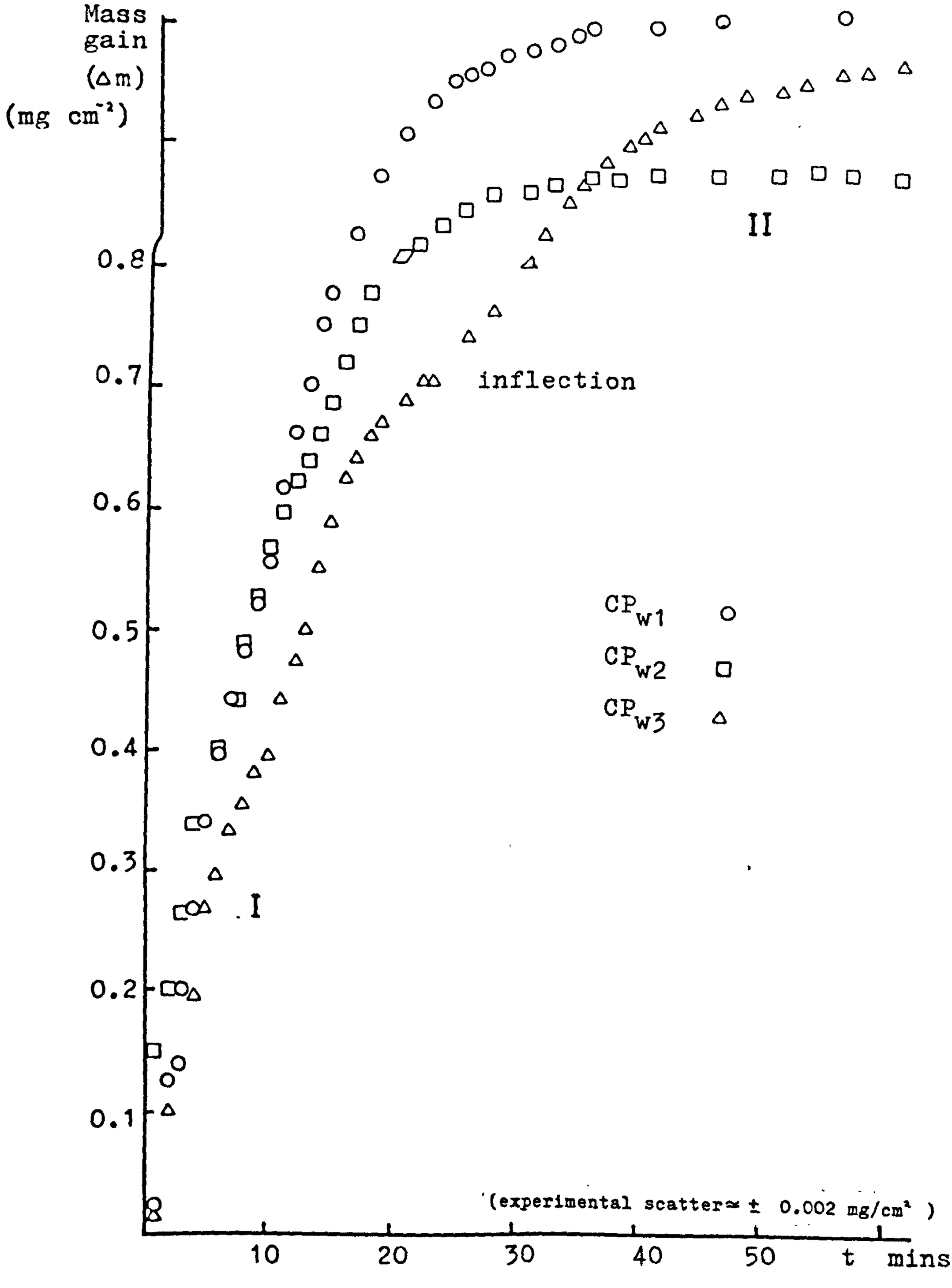

Fig 66a Oxidation of commercial purity aluminium at 1003 K (730 °C) in moist oxygen (P_{H_2O}=0.03 atms)

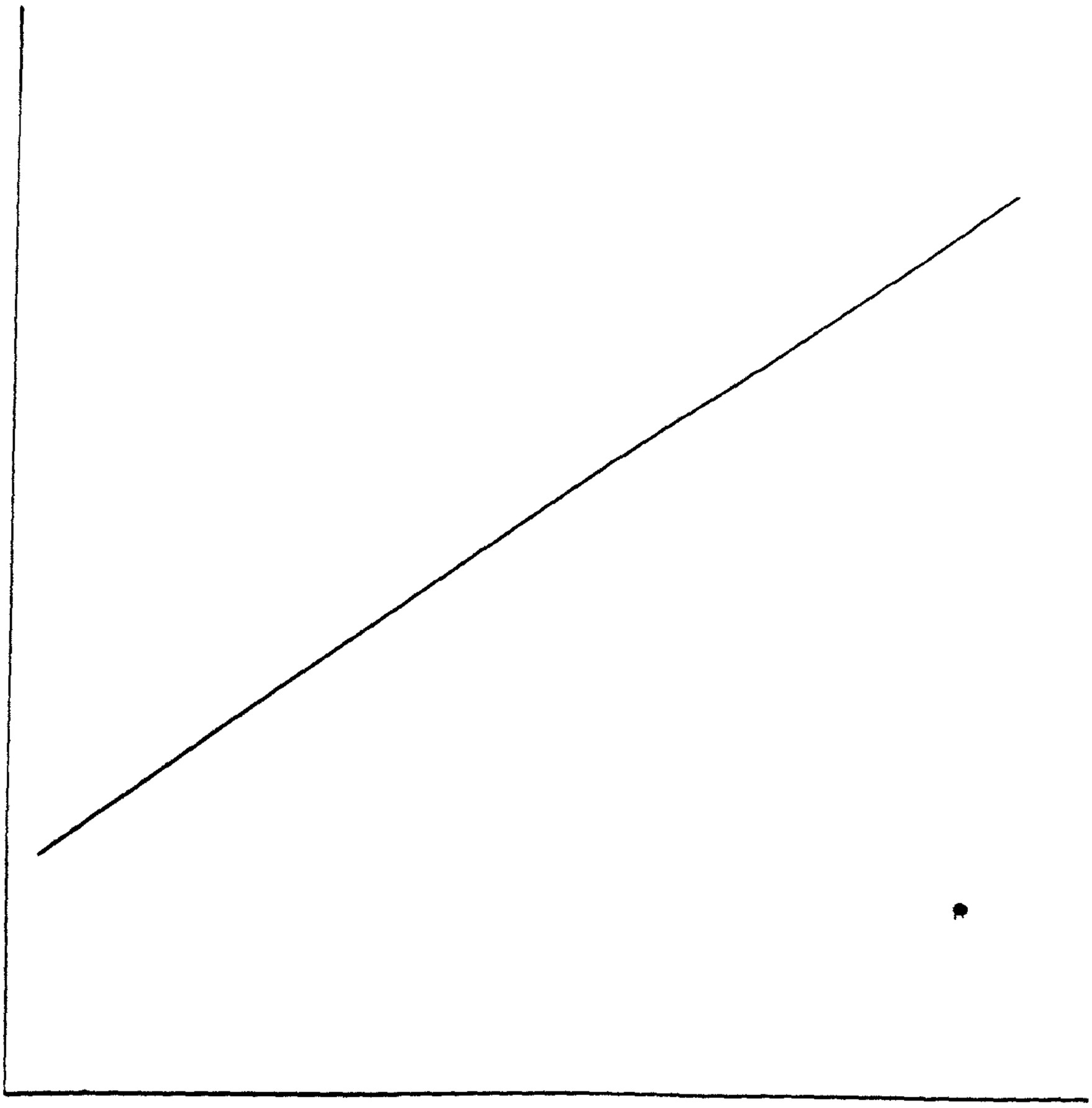

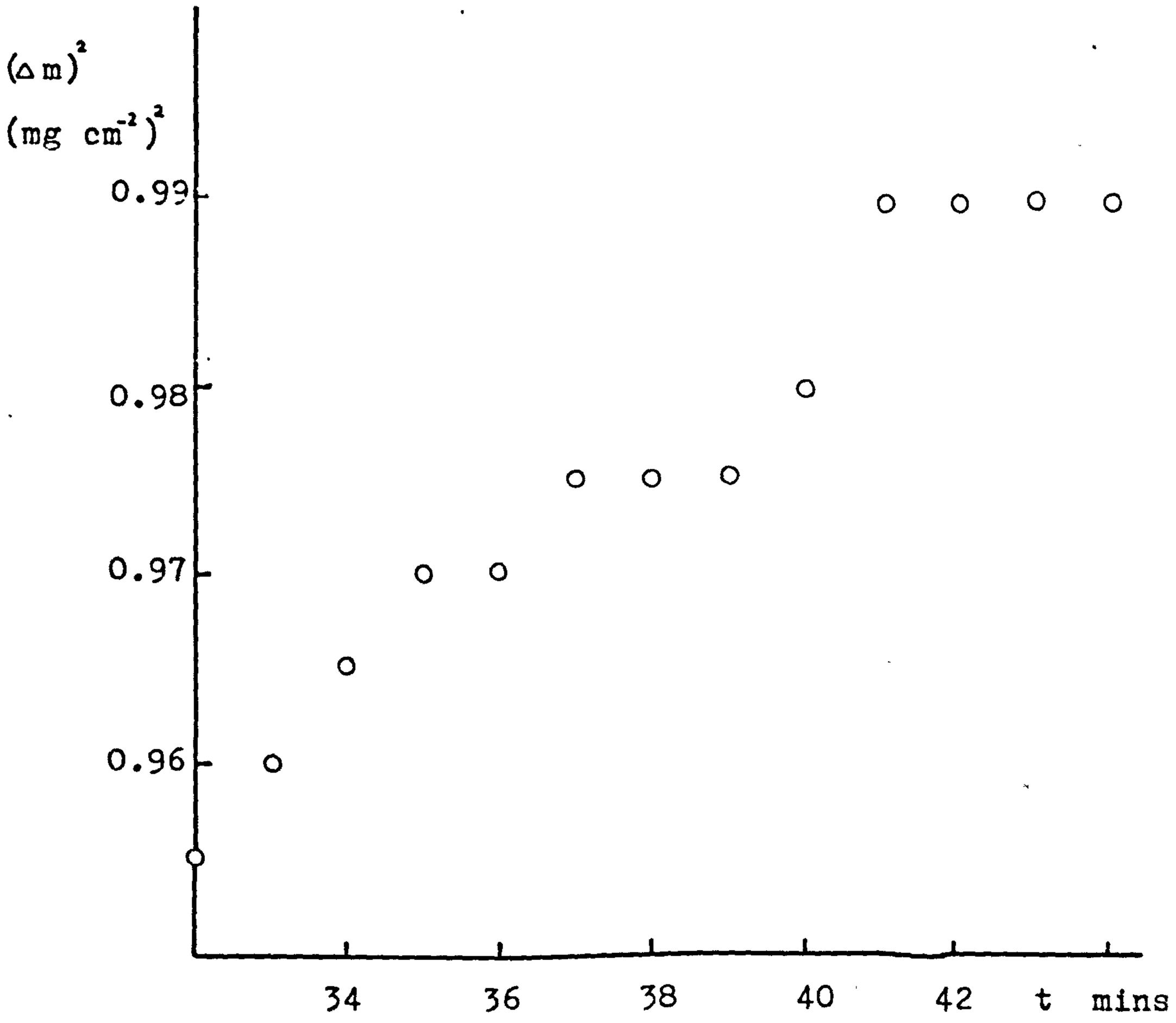

Fig 66b CP_{w1} from Fig 66a replotted on parabolic scale . $(\Delta m)^2$ plotted as a function of time (t) showing that the kinetics in during Stage II conform to the parabolic law.

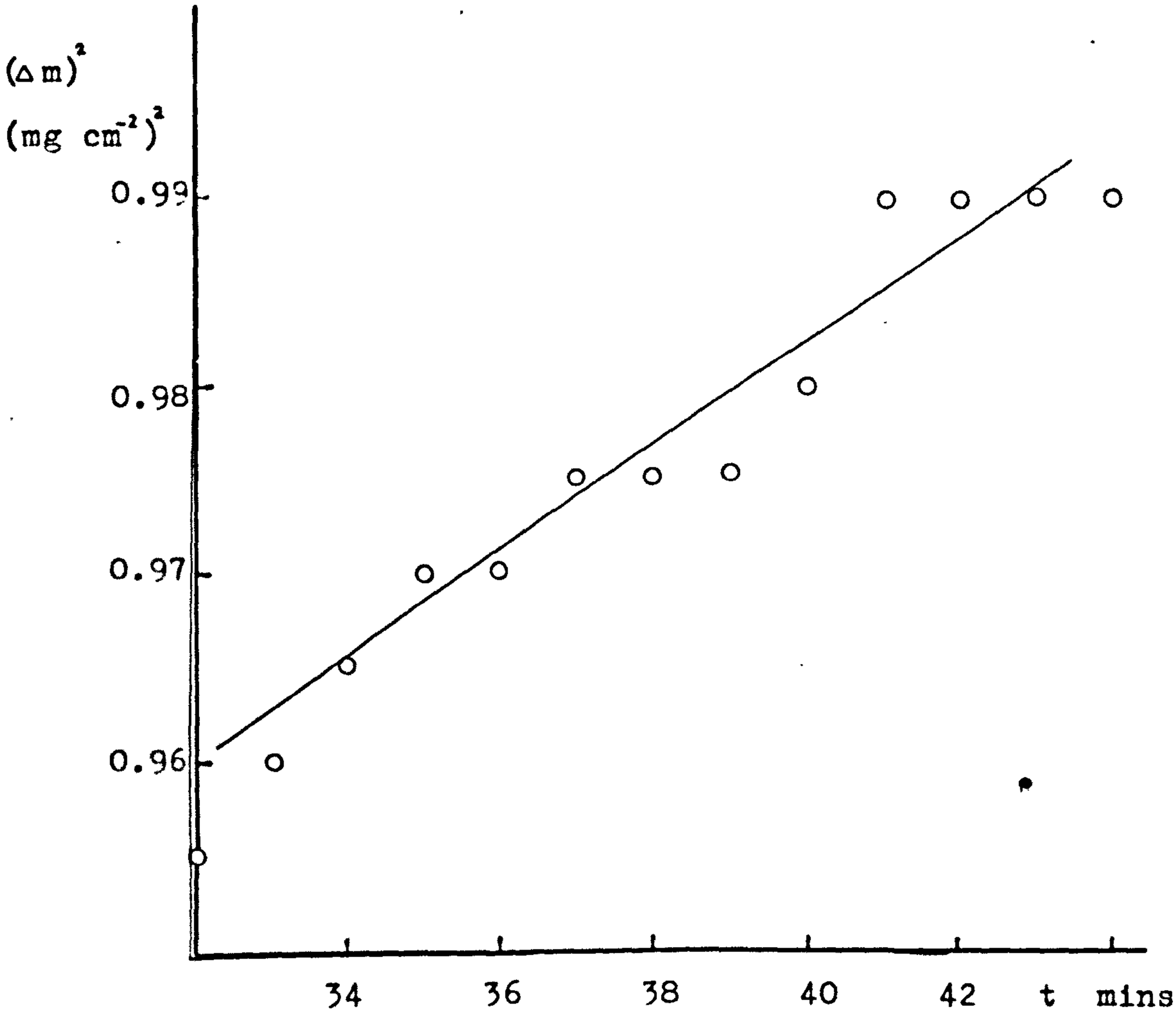

Fig 66b CP_{w1} from Fig 66a replotted on parabolic scale . $(\Delta m)^2$ plotted as a function of time (t) showing that the kinetics in during Stage II conform to the parabolic law.

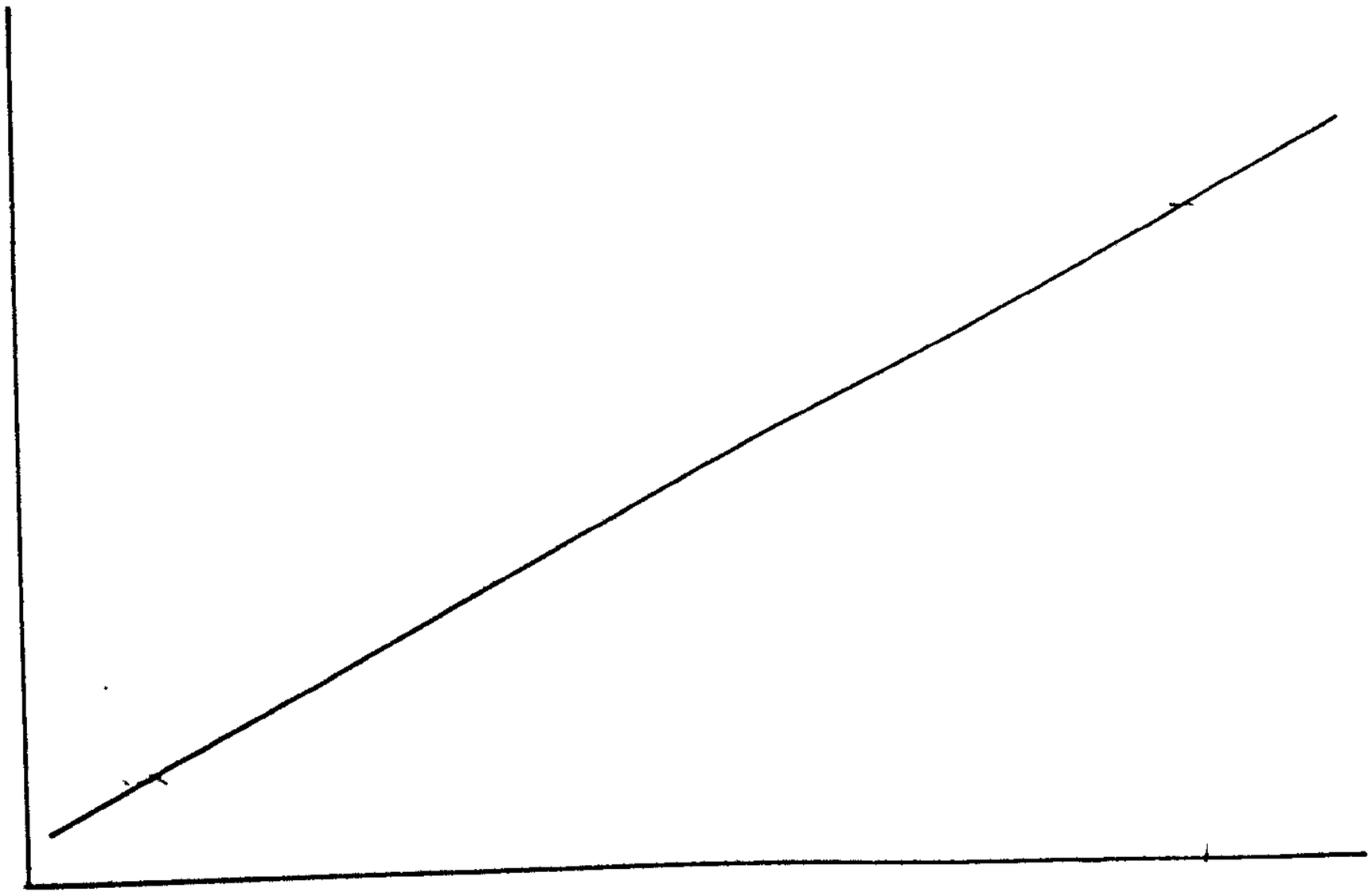

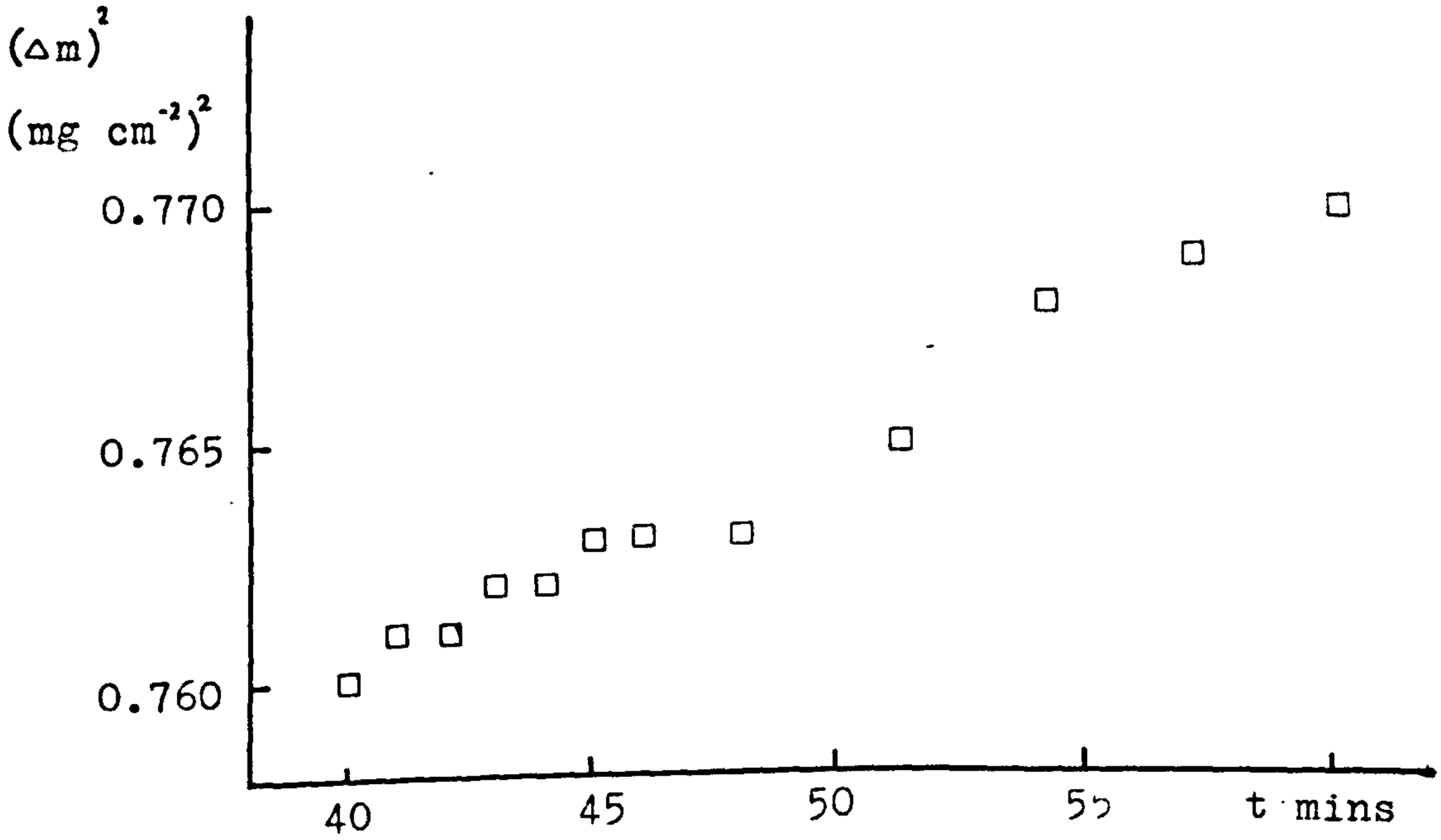

Fig 66c CP_{w2} from Fig 66a replotted on parabolic scale. $(\Delta\ m)^2$ plotted as a function time (t) showing that the kinetics in Stage II conform to the parabolic law.

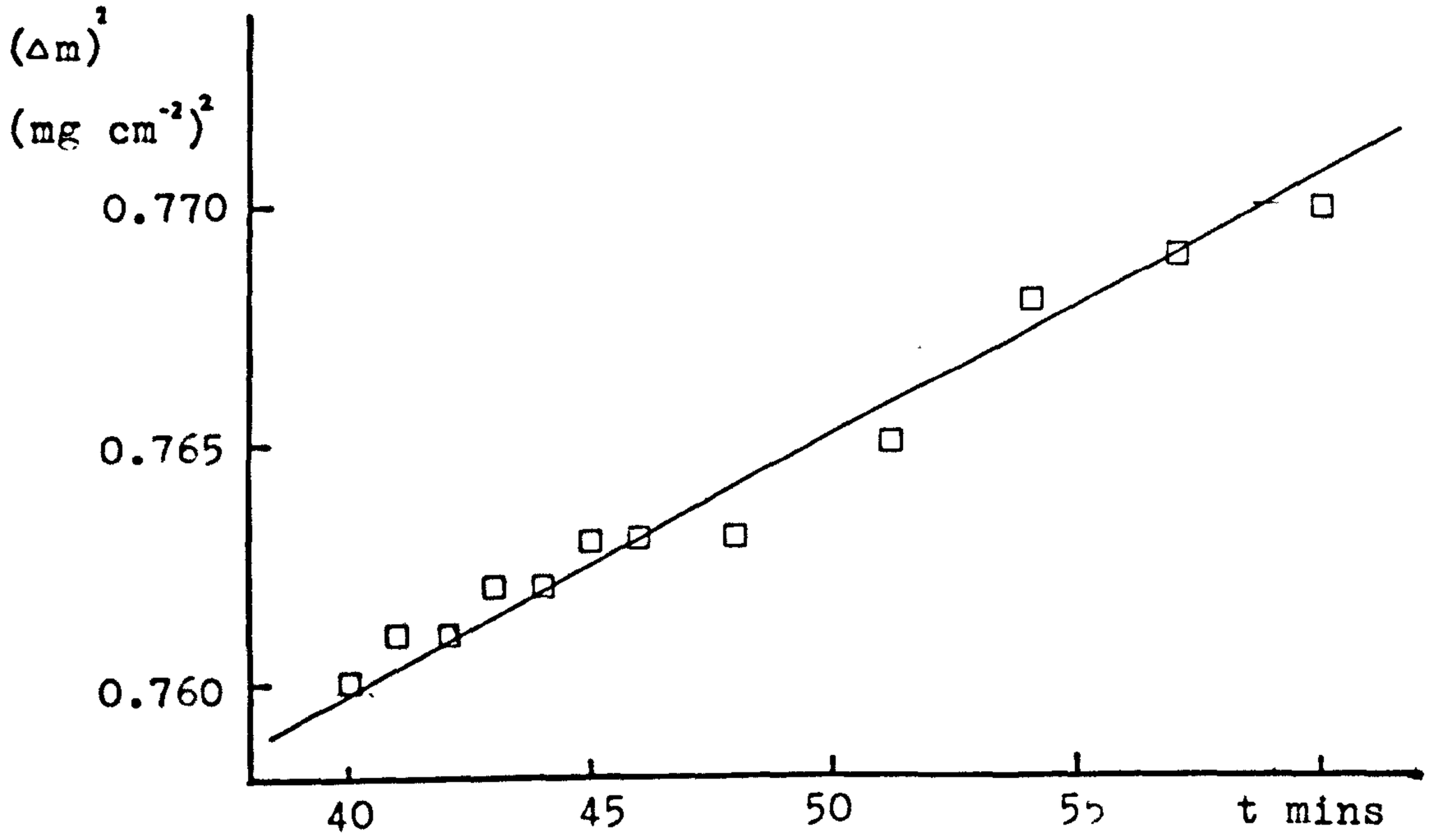

Fig 66c CP_{w2} from Fig 66a replotted on parabolic scale. $(\Delta m)^2$ plotted as a function time (t) showing that the kinetics in Stage II conform to the parabolic law.

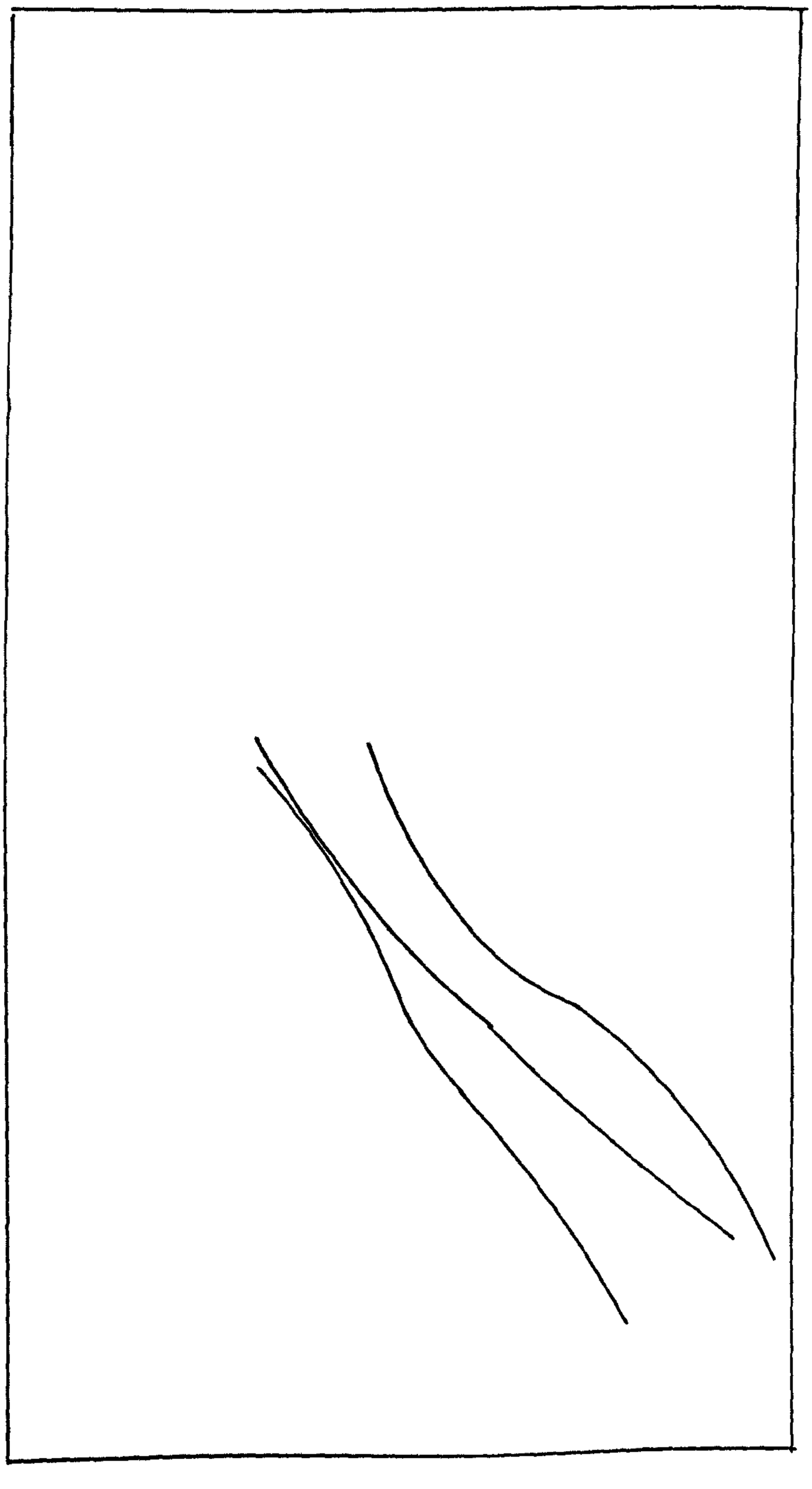

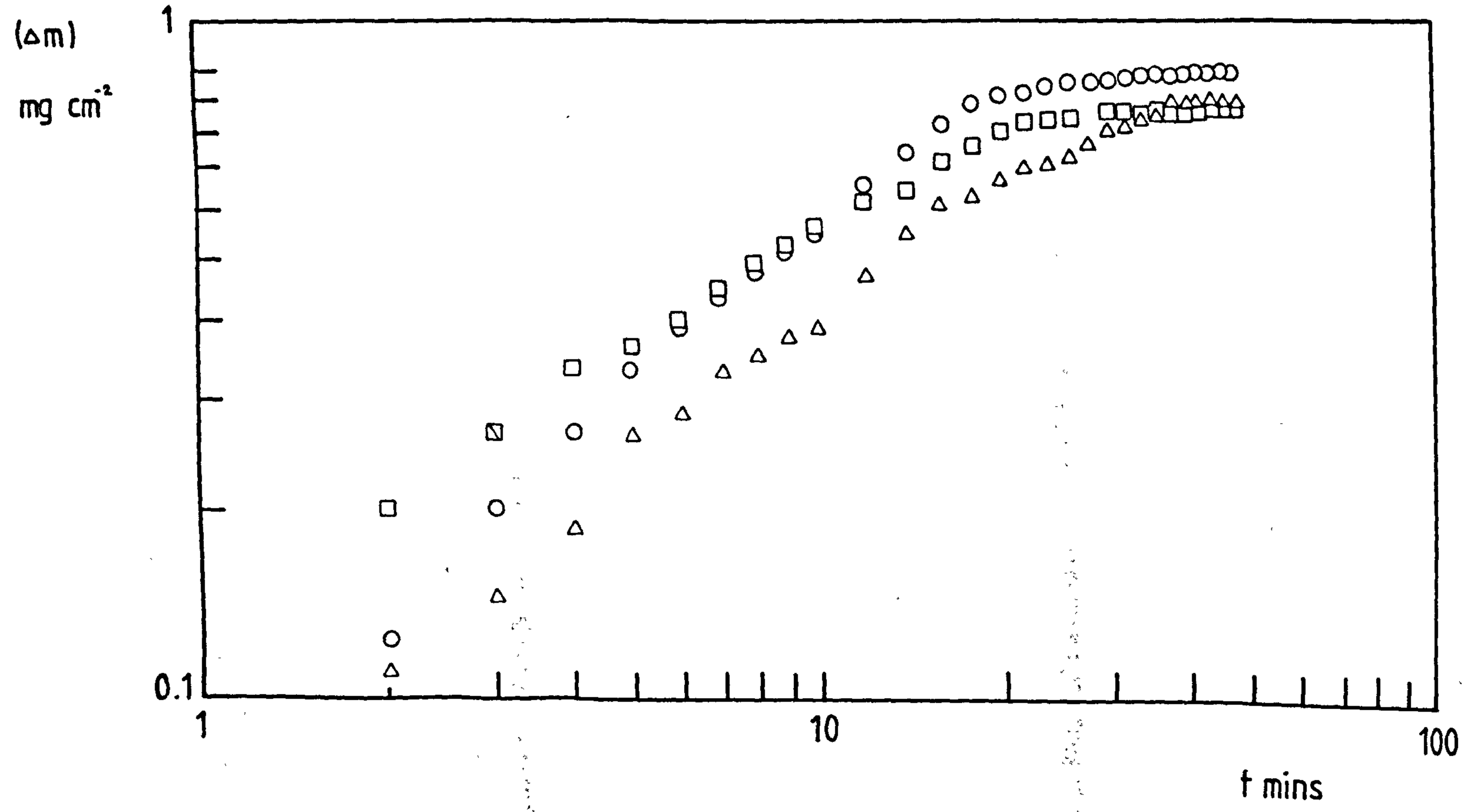

Fig 66d Fig 66a replotted on log/log scale showing that the kinetics in Stage I do not conform to a simple power law.

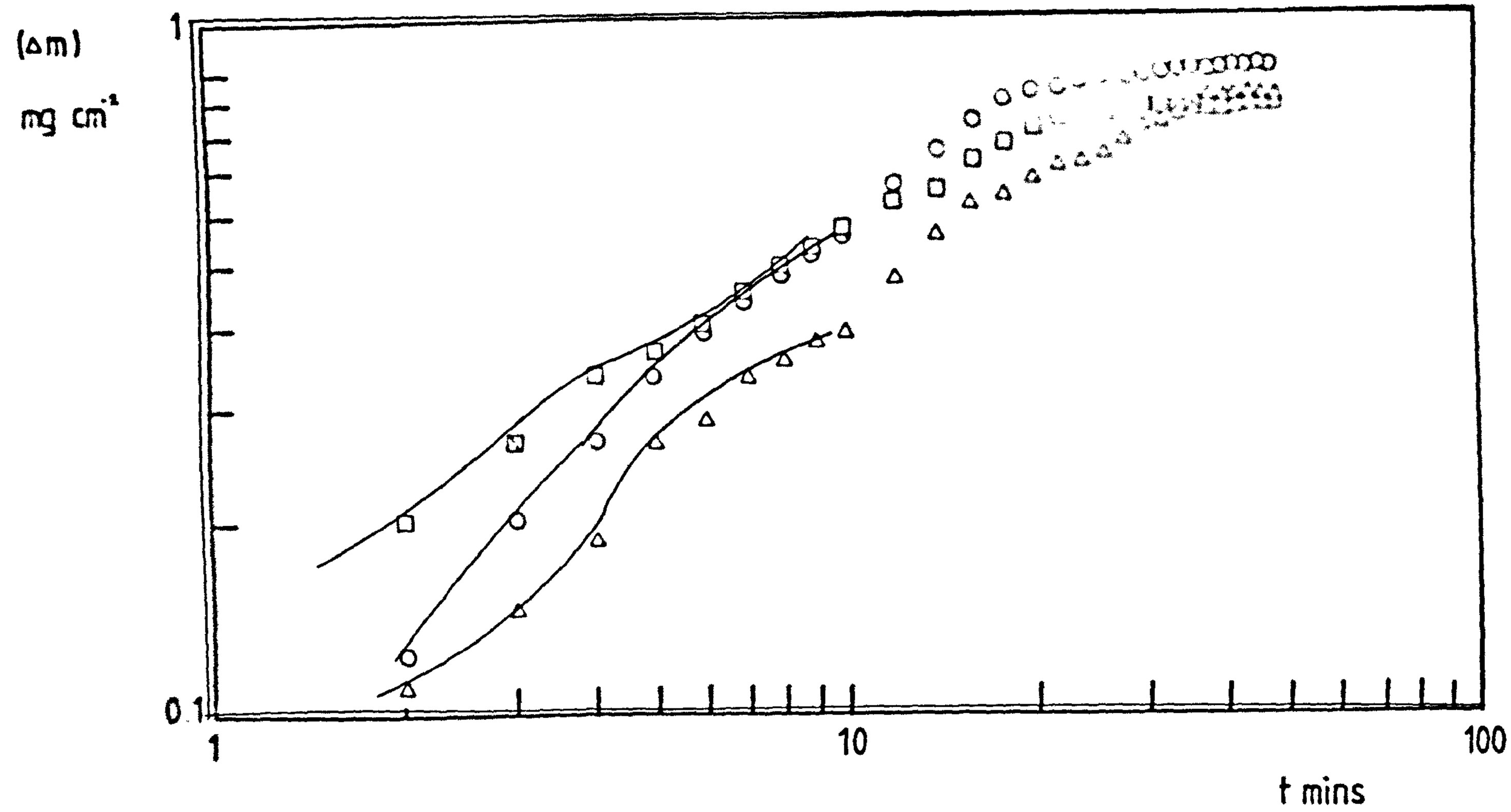

Fig 66d Fig 66a replotted on log/log scale showing that the kinetics in Stage I do not conform to a simple power law.

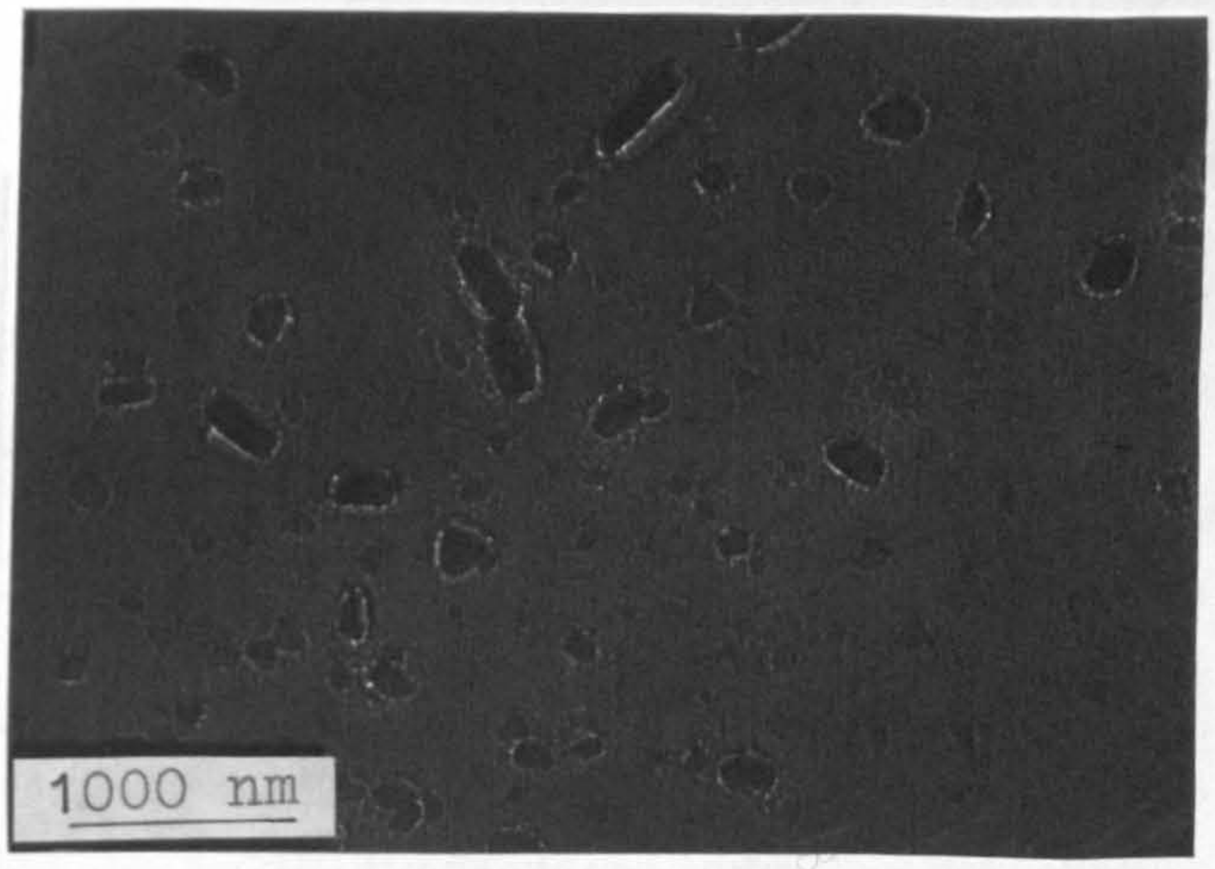

10 mins

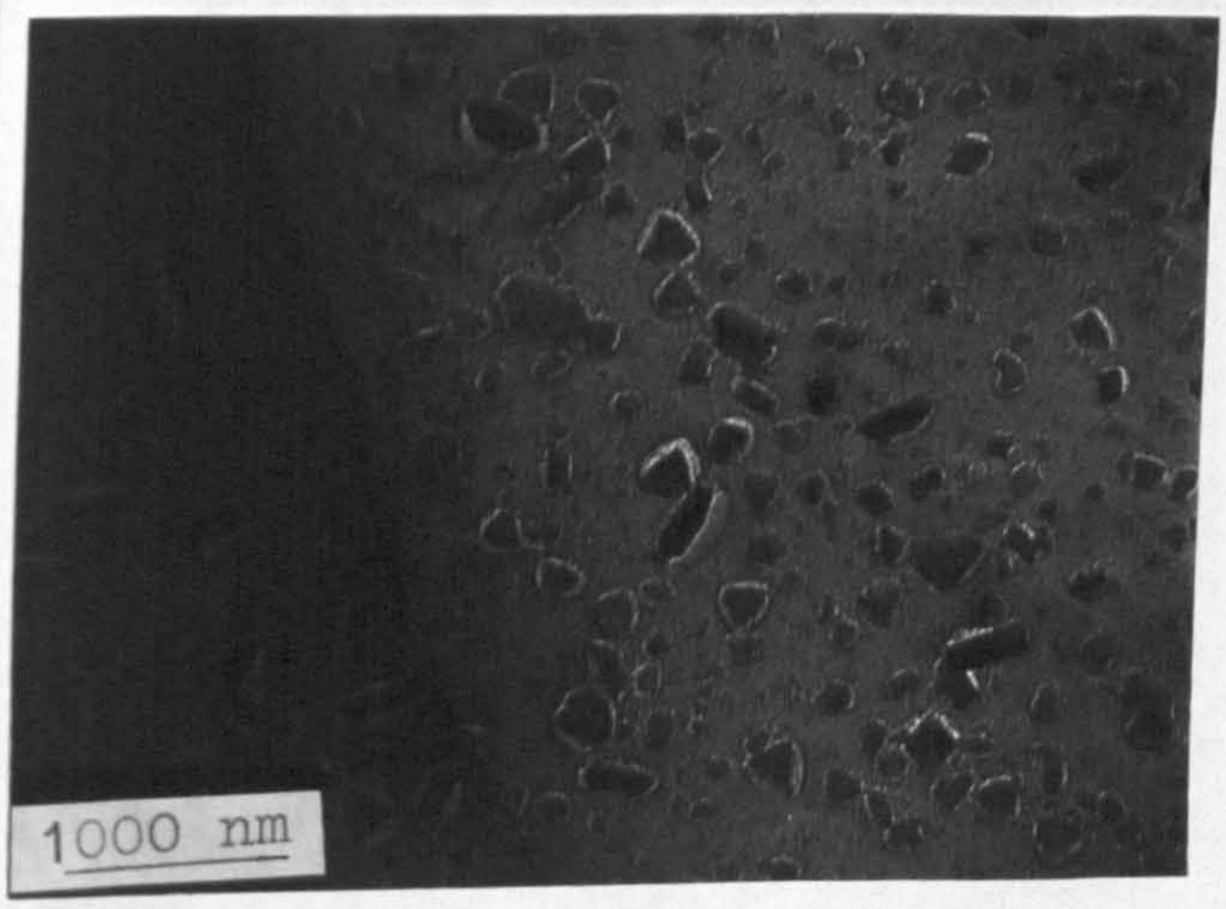

20 mins.

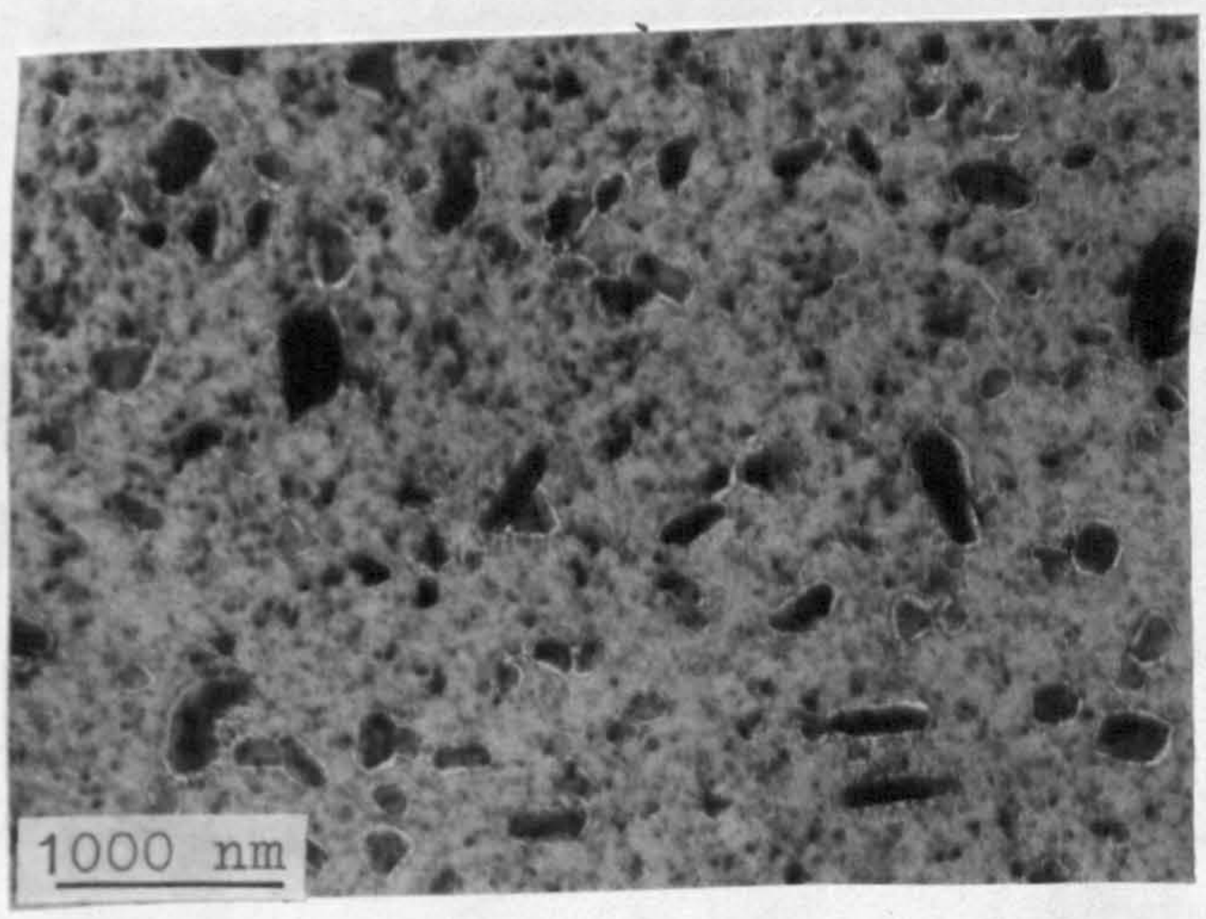

40 mins.

Fig 67 TEM of oxide films formed on CPAL at 730 °C in moist oxygen (P_{H_2O} = 0.03 atms.) A comparison with the micrographs shown in Fig 55 and Fig 56 shows a much slower establishment of α-Al_2O_3 subfilm.

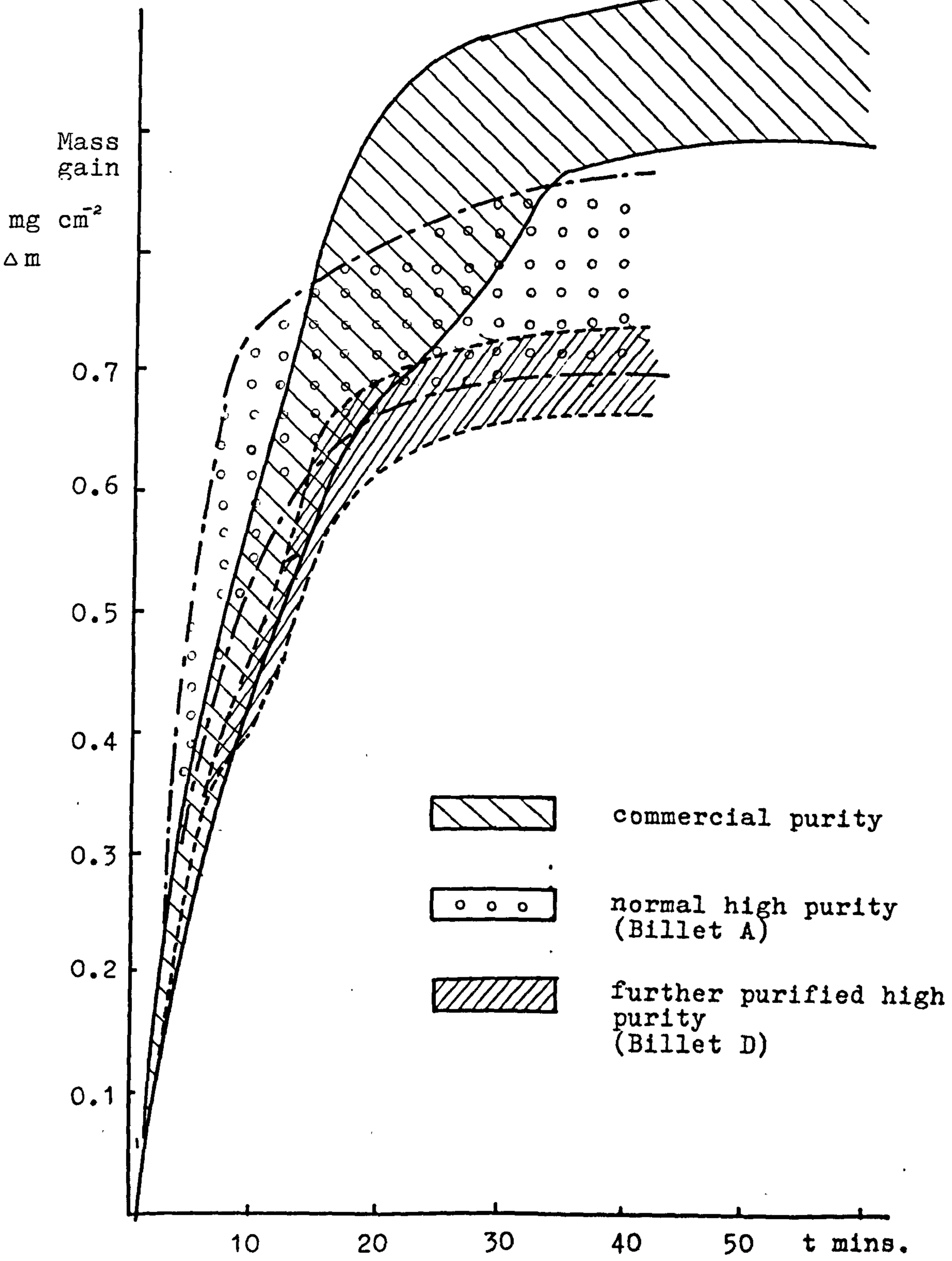

Fig 68 Comparison of oxidation kinetics in moist oxygen (P_{H_2O} = 0.03 atms) between samples obtained from

a) commercial purity aluminium
b) normal high purity aluminium (Billet A)
c) further purified aluminium (Billet D

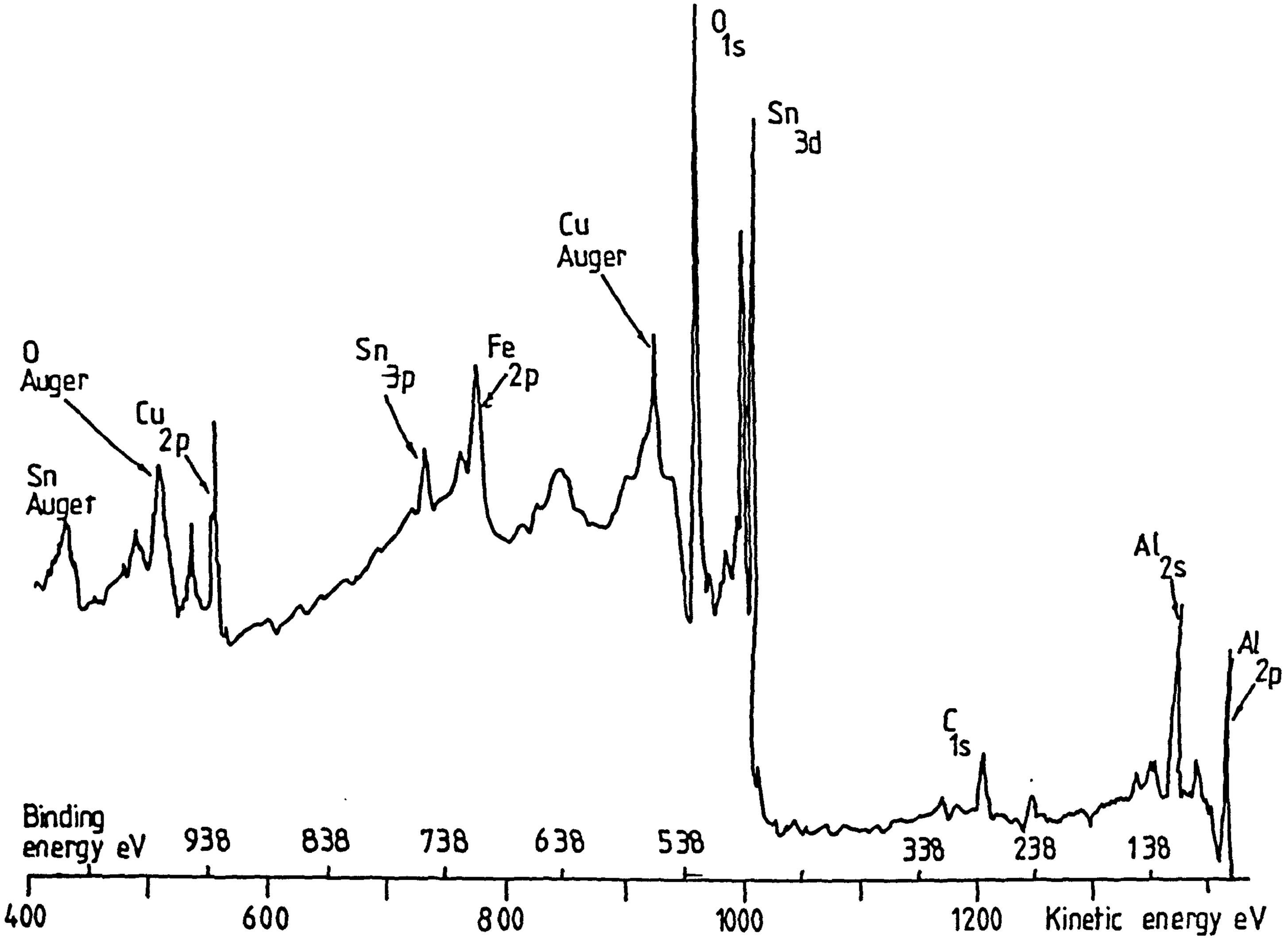
O
1s
Sn
3d
Cu
Auger
O
Auger
Cu
2p
Sn
3p
Fe
2p
Sn
Auger
Al
2s
Al
2p
C
1s
Binding
energy eV
938
838
738
638
538
338
238
138
400
600
800
1000
1200
Kinetic energy eV

Fig 69 XPS spectrum of an oxide film on CP AL at 730 C in moist oxygen (P_{H_2O} = 0.03 atms). The sample was sputtered with argon ions for 30 mins before the spectrum was obtained.

Excitation source	Al Kα (1486.6 eV)
	14 kV 13mA
Source slit	2mm
Collector slit	2mm
Range	10^4 cps

Argon ion etching parameters

2 mA

5 kV

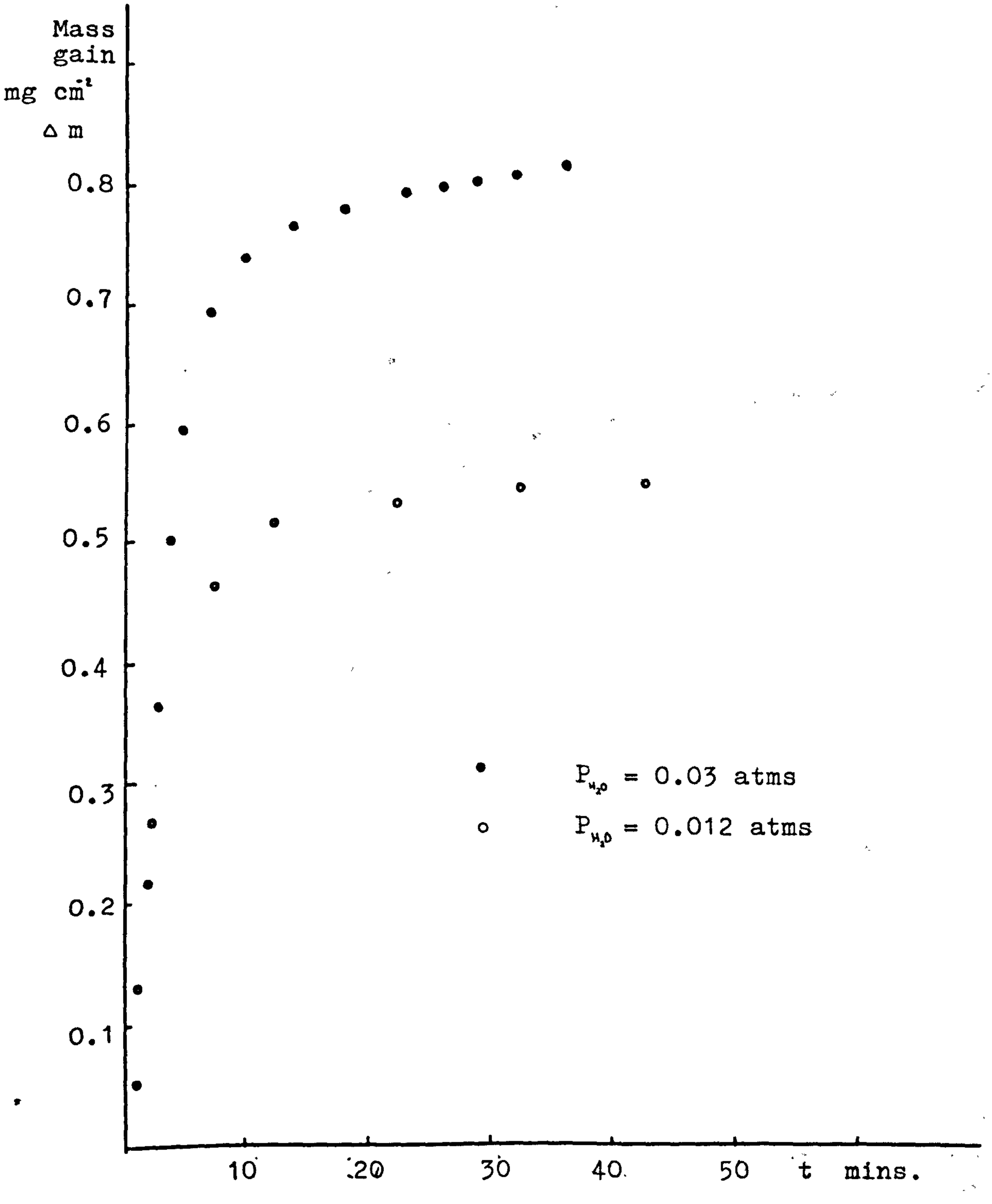

Fig 70 Oxidation kinetics of normal high purity aluminium at 730 °C in moist oxygen showing the influence of water vapour pressure .

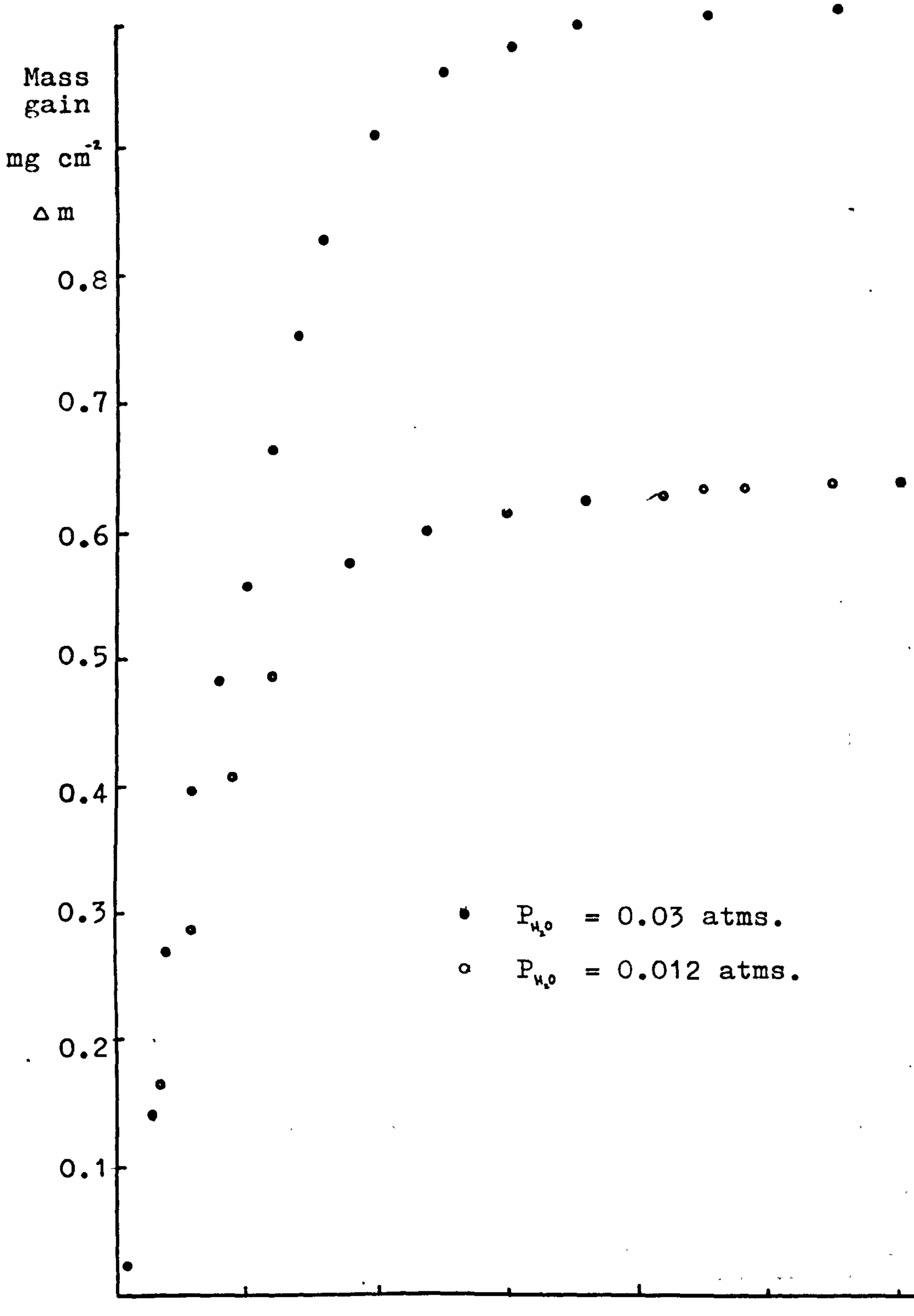

Fig 71 Oxidation kinetics of CPA1 at 730 °C in moist oxygen showing the influence of water vapour pressure

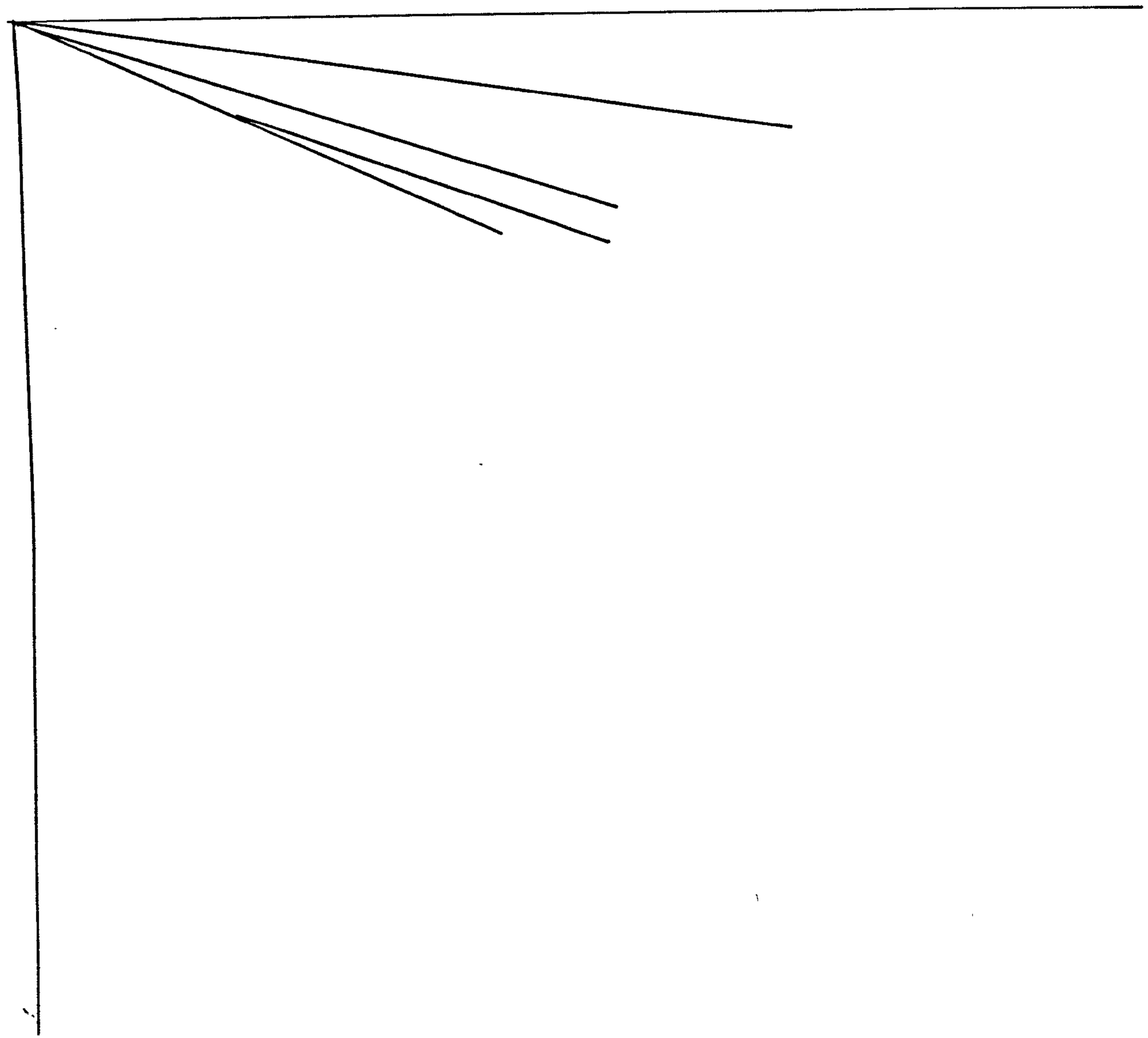

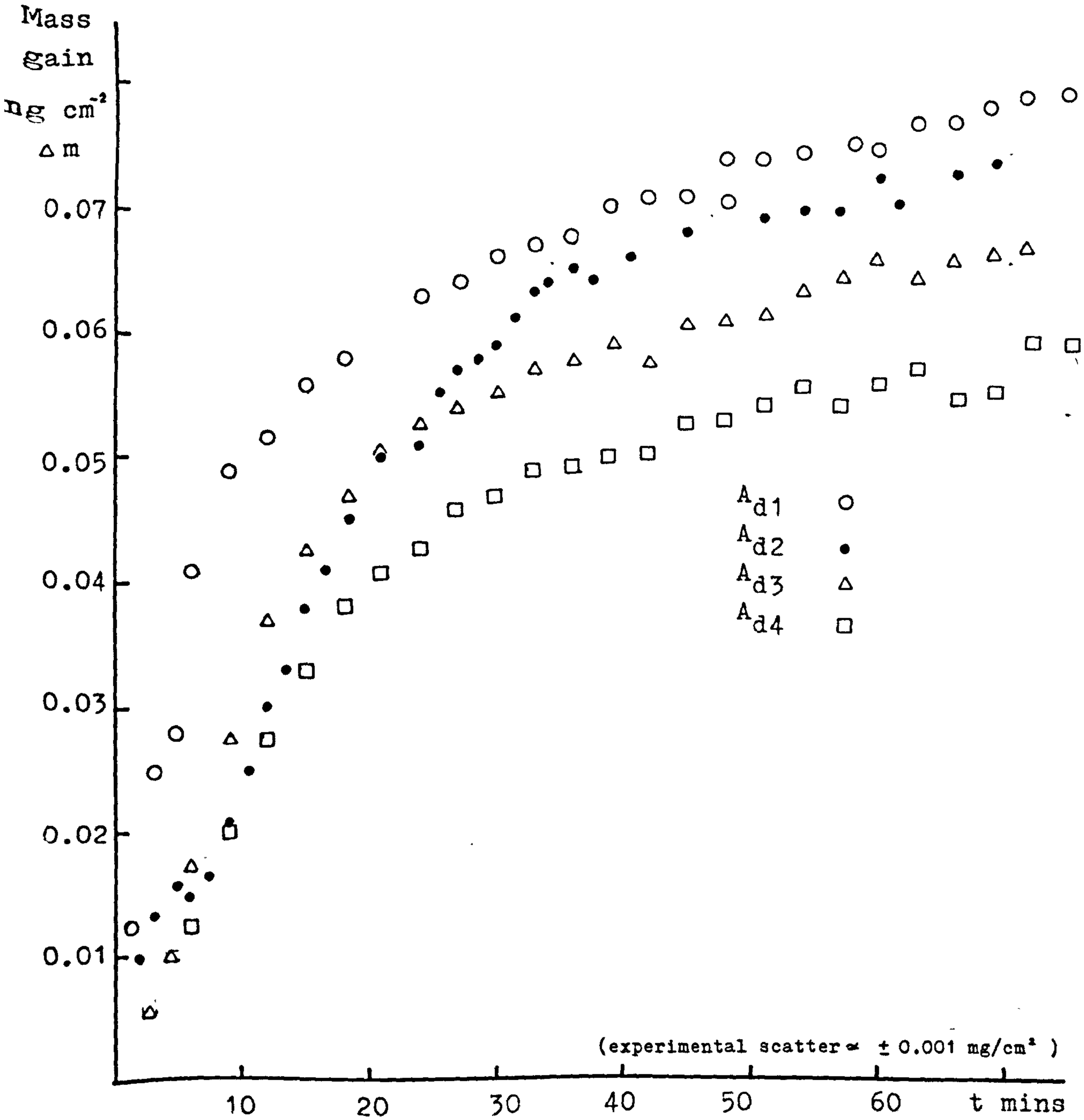

Fig 72a Oxidation of normal high purity aluminium (Billet A) at 1003 K (730 °C) in dry oxygen

Mass gain/unit area (Δm) plotted as a function time (t).

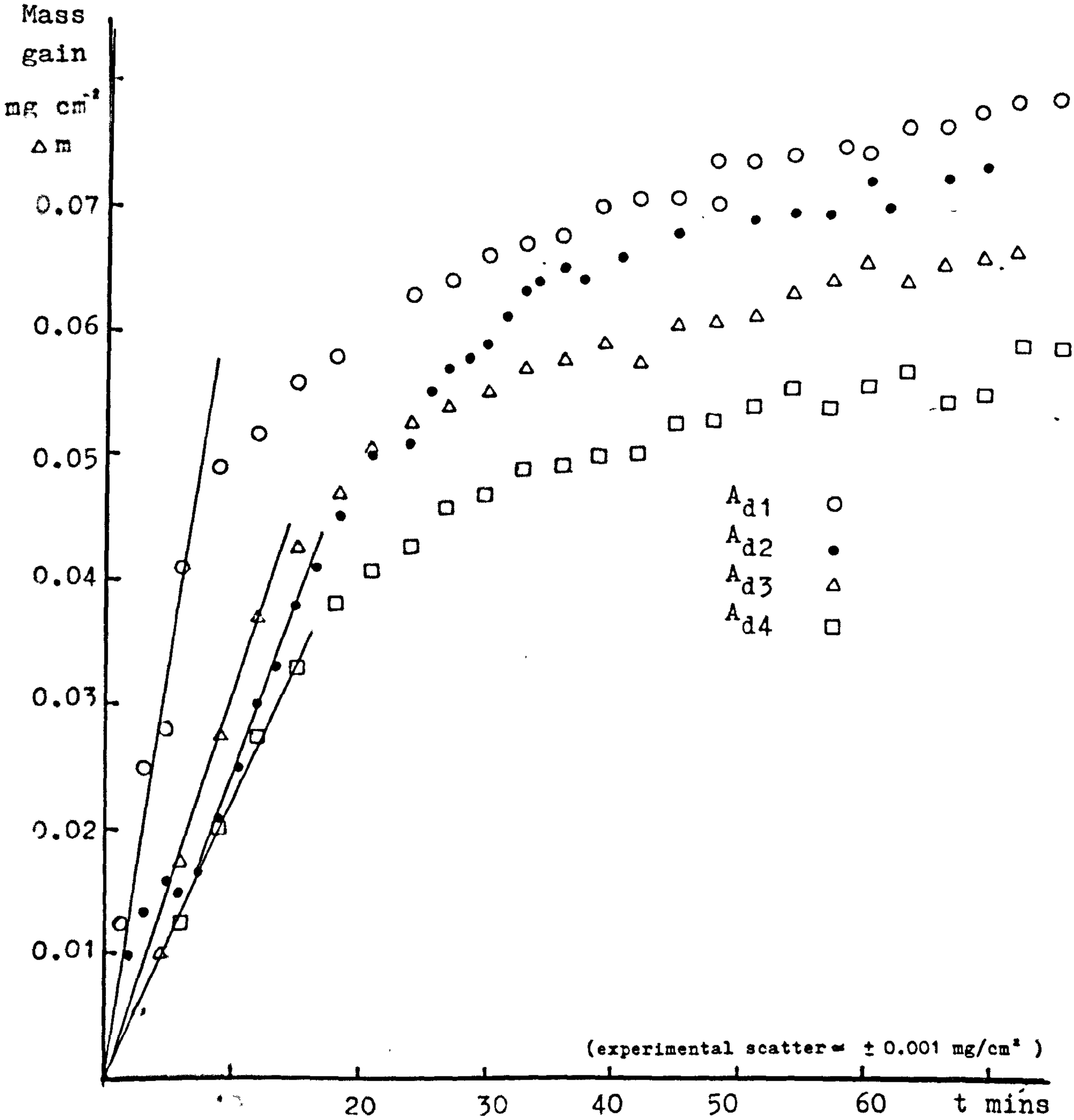

Fig 72a Oxidation of normal high purity aluminium (Billet A) at 1003 K (730 °C) in dry oxygen
Mass gain/unit area (Δm) plotted as a function time (t).

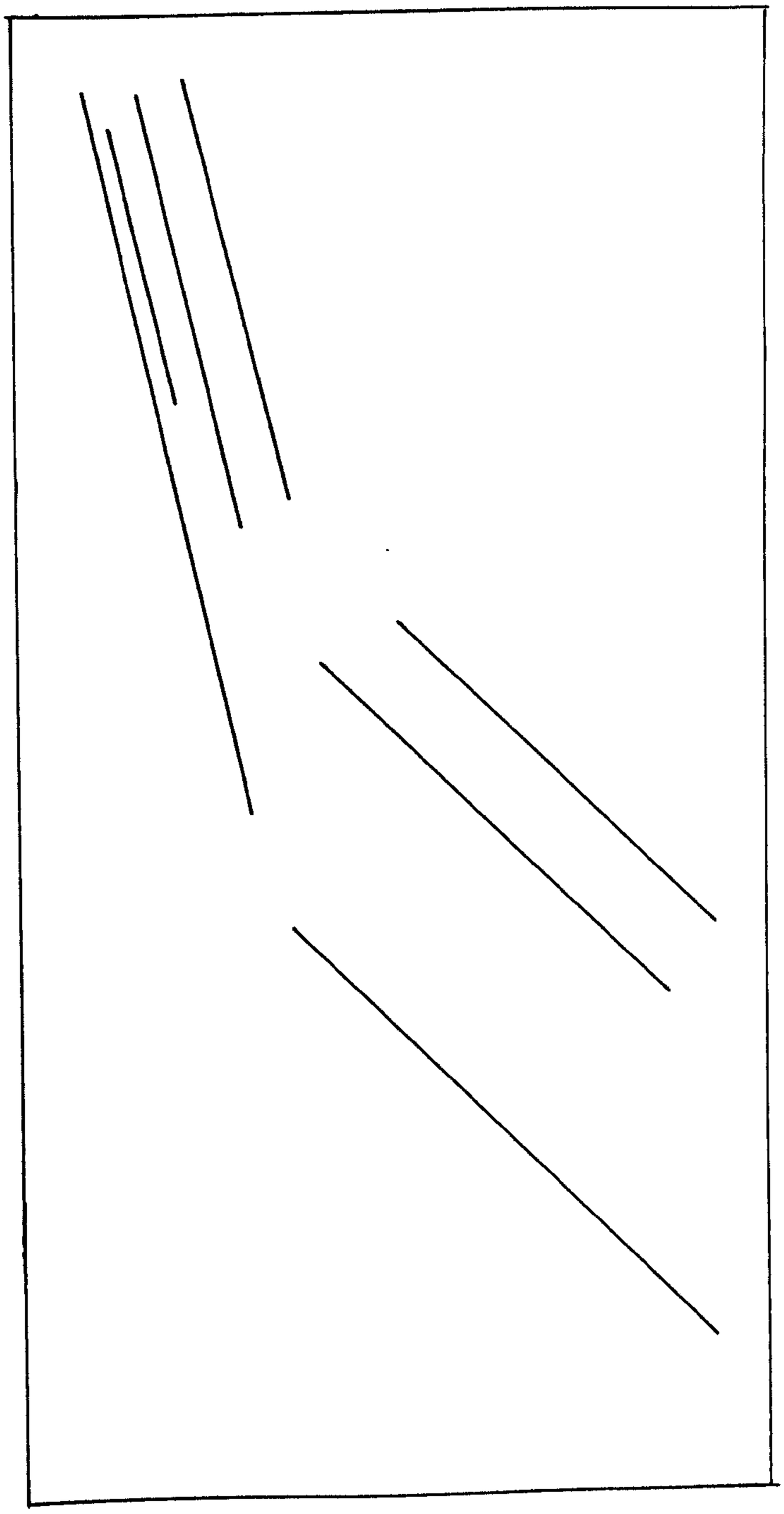

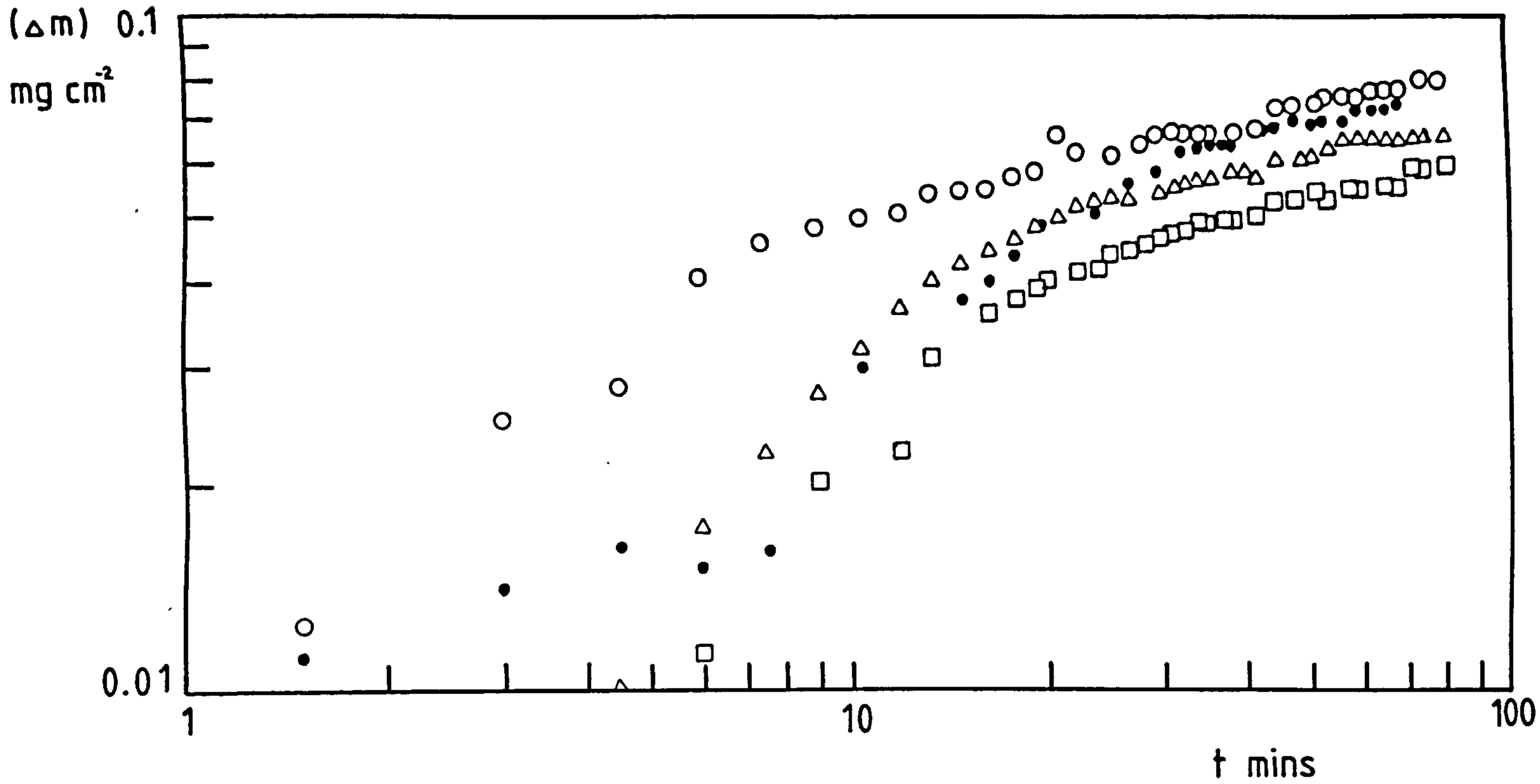

Fig 72b Oxidation of normal high purity aluminium (Billet A) at 730 °C in dry oxygen. Mass gain/unit area (△ m) replotted as a function of time on a log/log scale

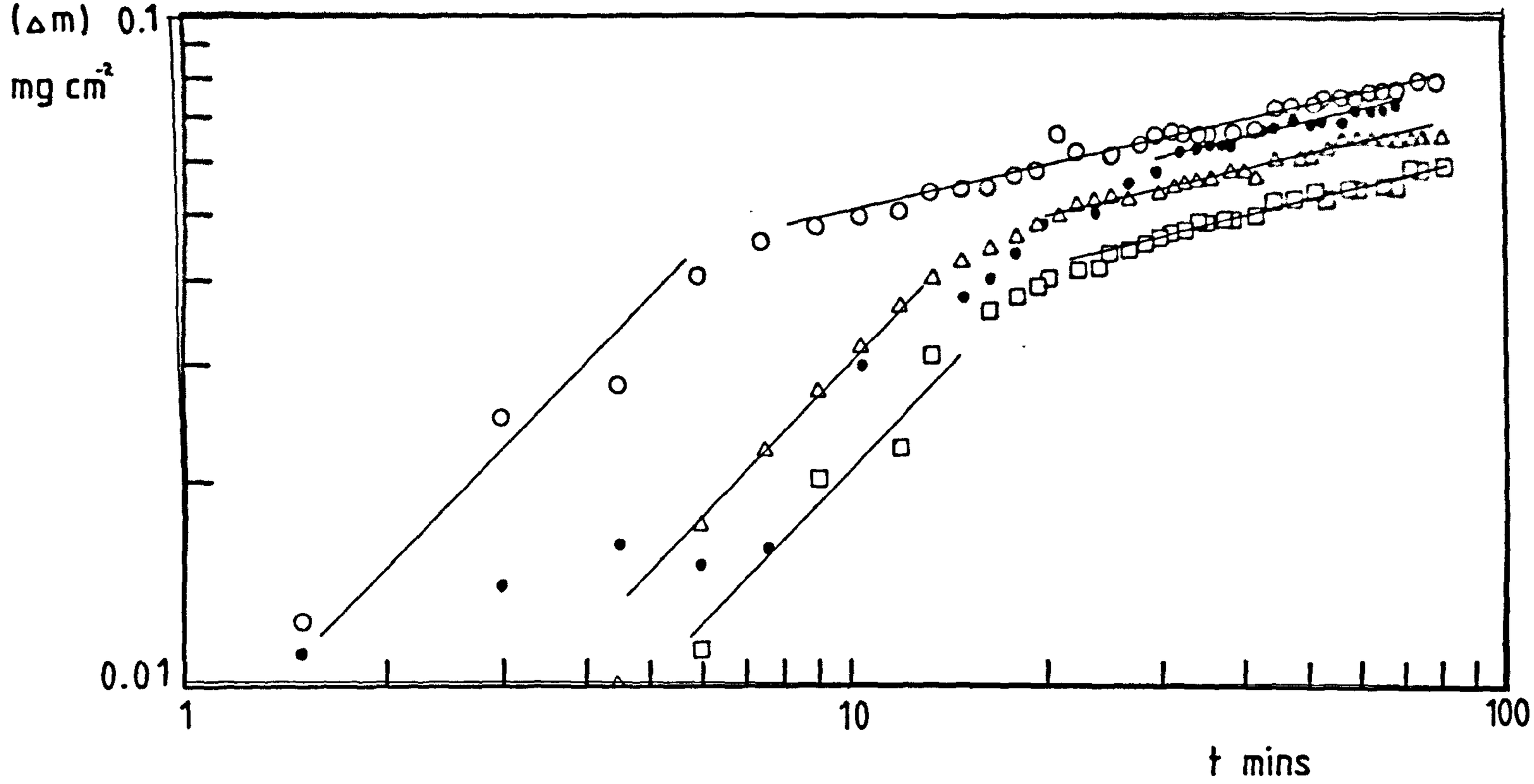

Fig 72b Oxidation of normal high purity aluminium (Billet A) at 730 °C in dry oxygen. Mass gain/unit area (Δ m) replotted as a function of time on a log/log scale

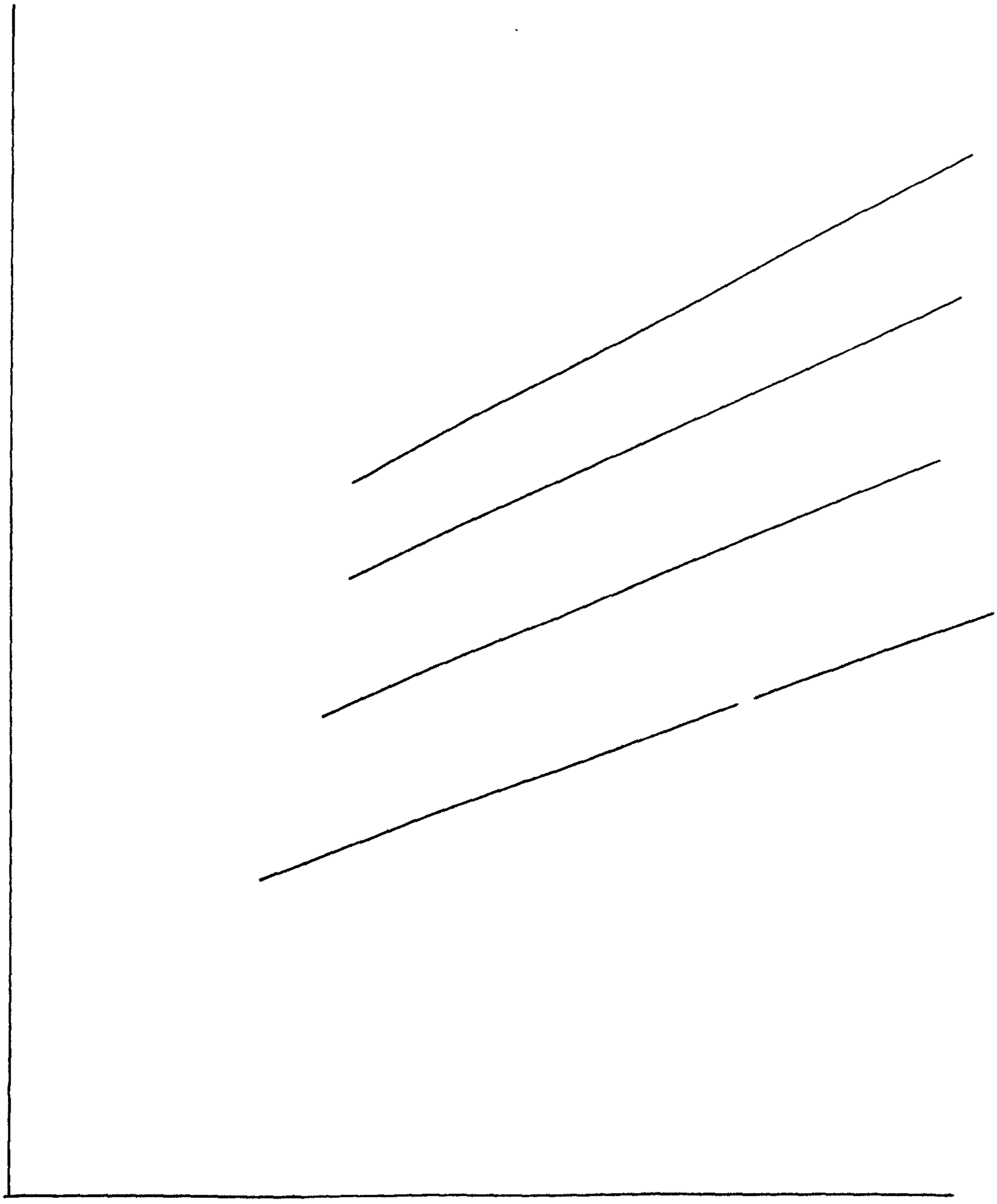

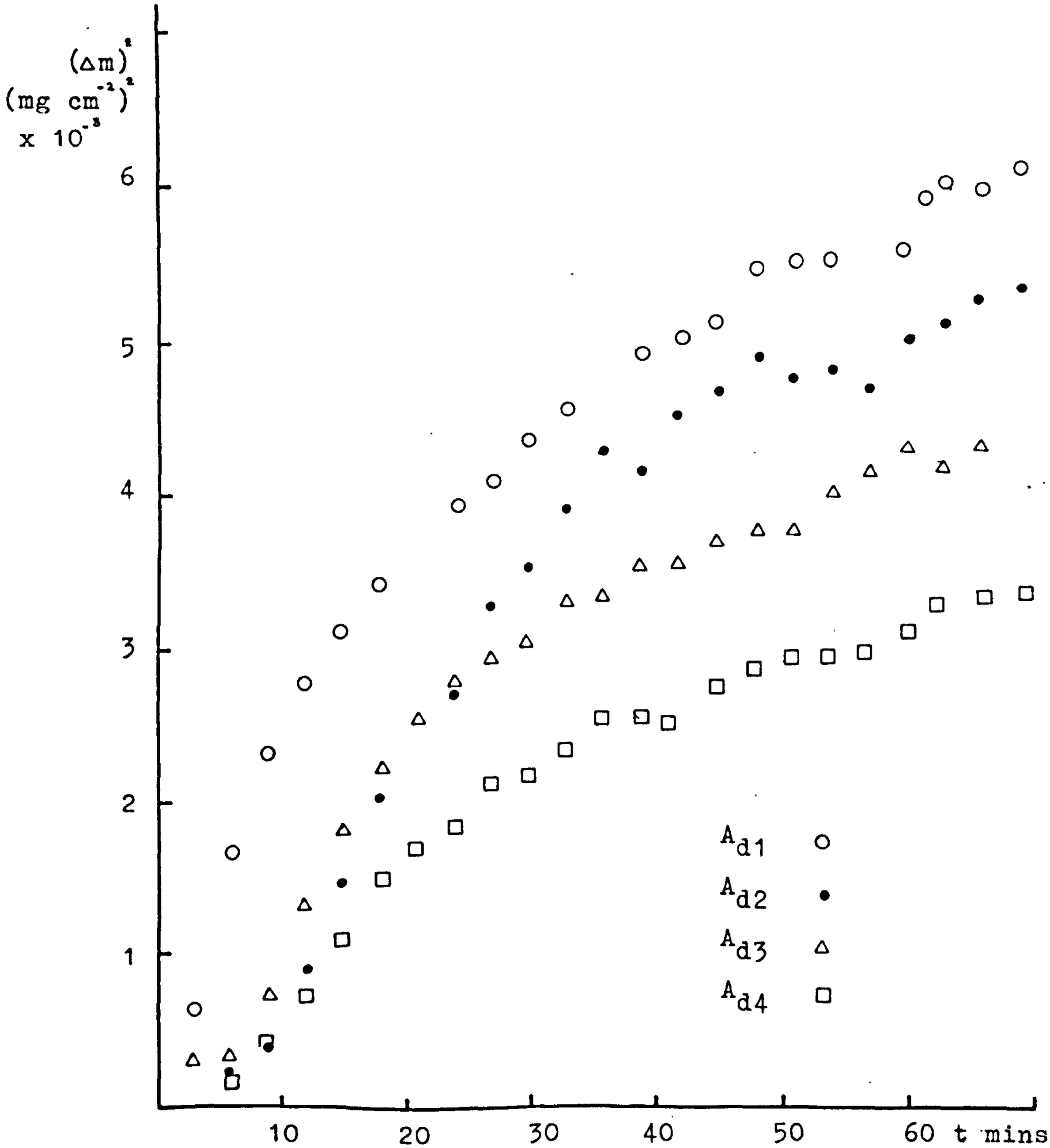

Fig 7 2c Fig 72a replotted on a parabolic scale. $(\Delta\ m)^2$ plotted as a function of time (t) showing the parabolic portions.

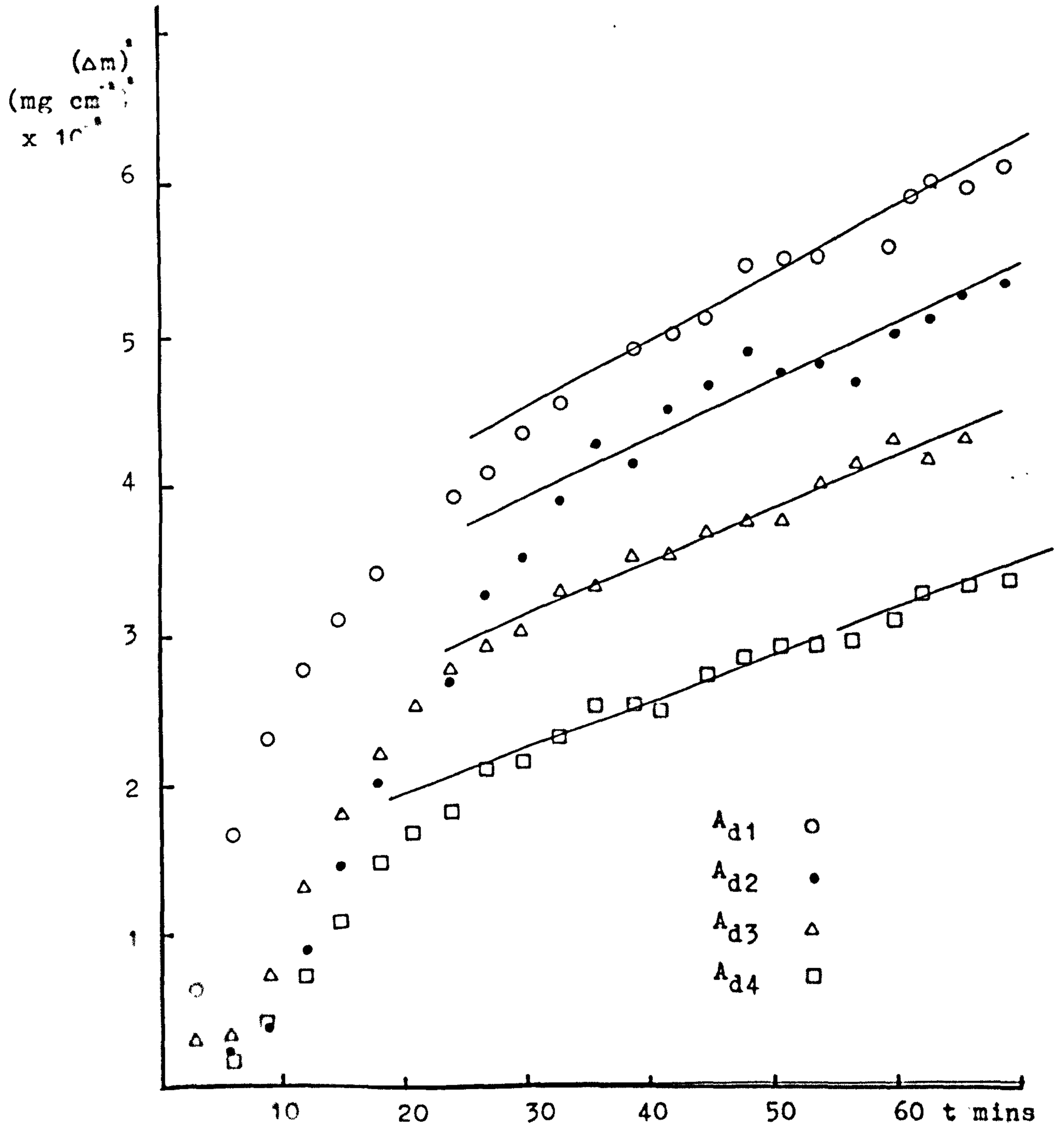

Fig 7 2c Fig 72a replotted on a parabolic scale. $(\Delta m)^2$ plotted as a function of time (t) showing the parabolic portions.

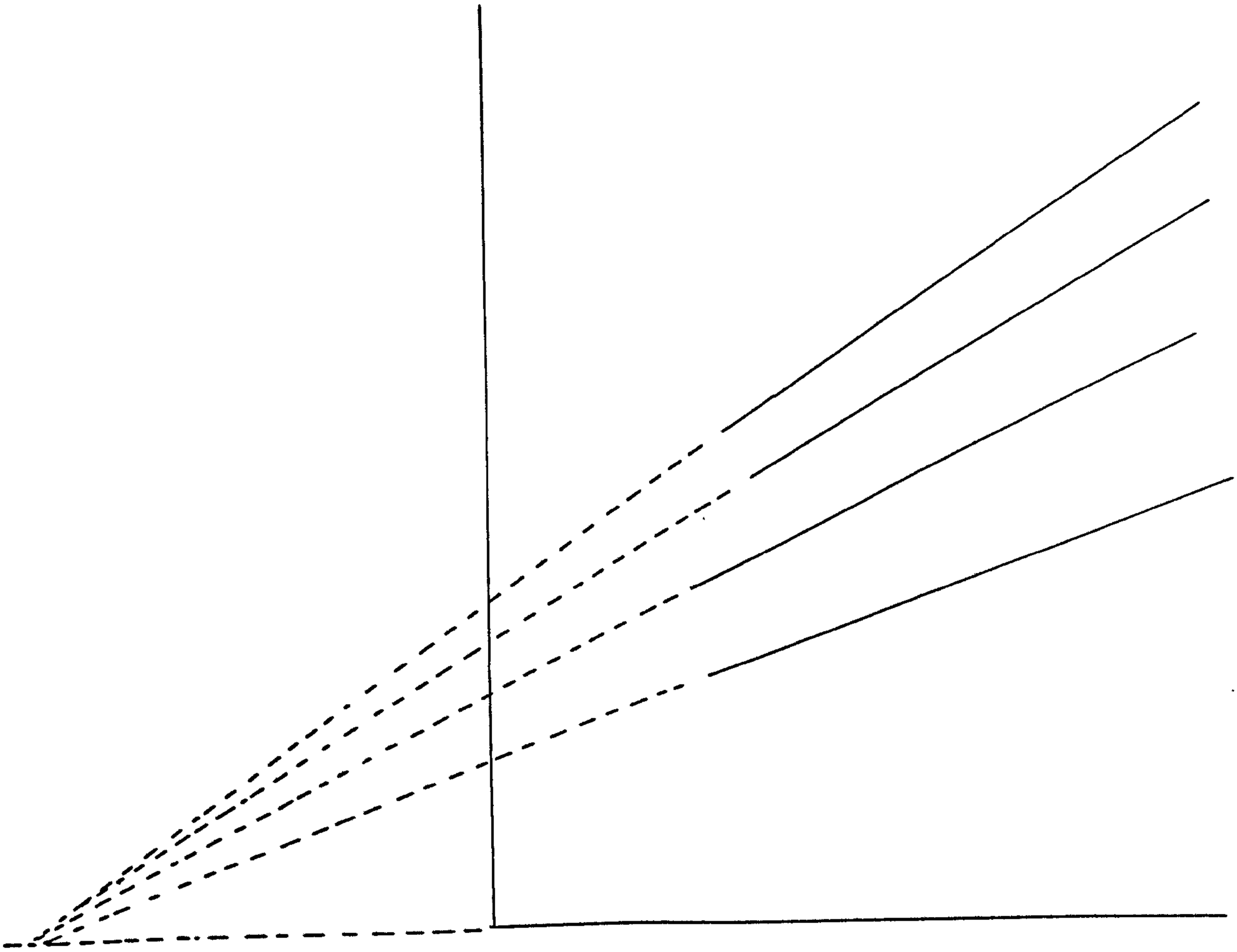

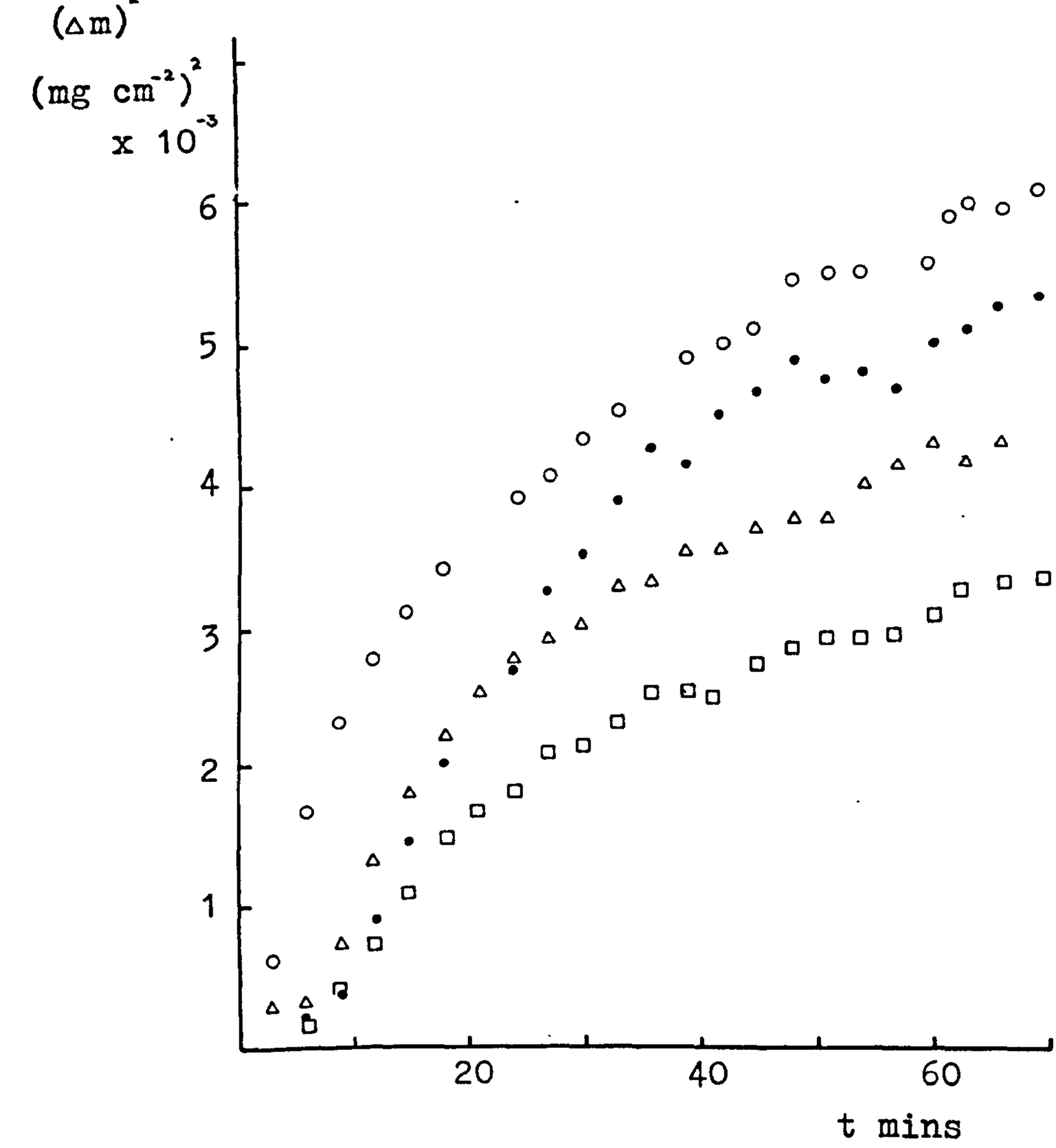

Fig 72d Fig 72c replotted to show common origin of parabolic regions.

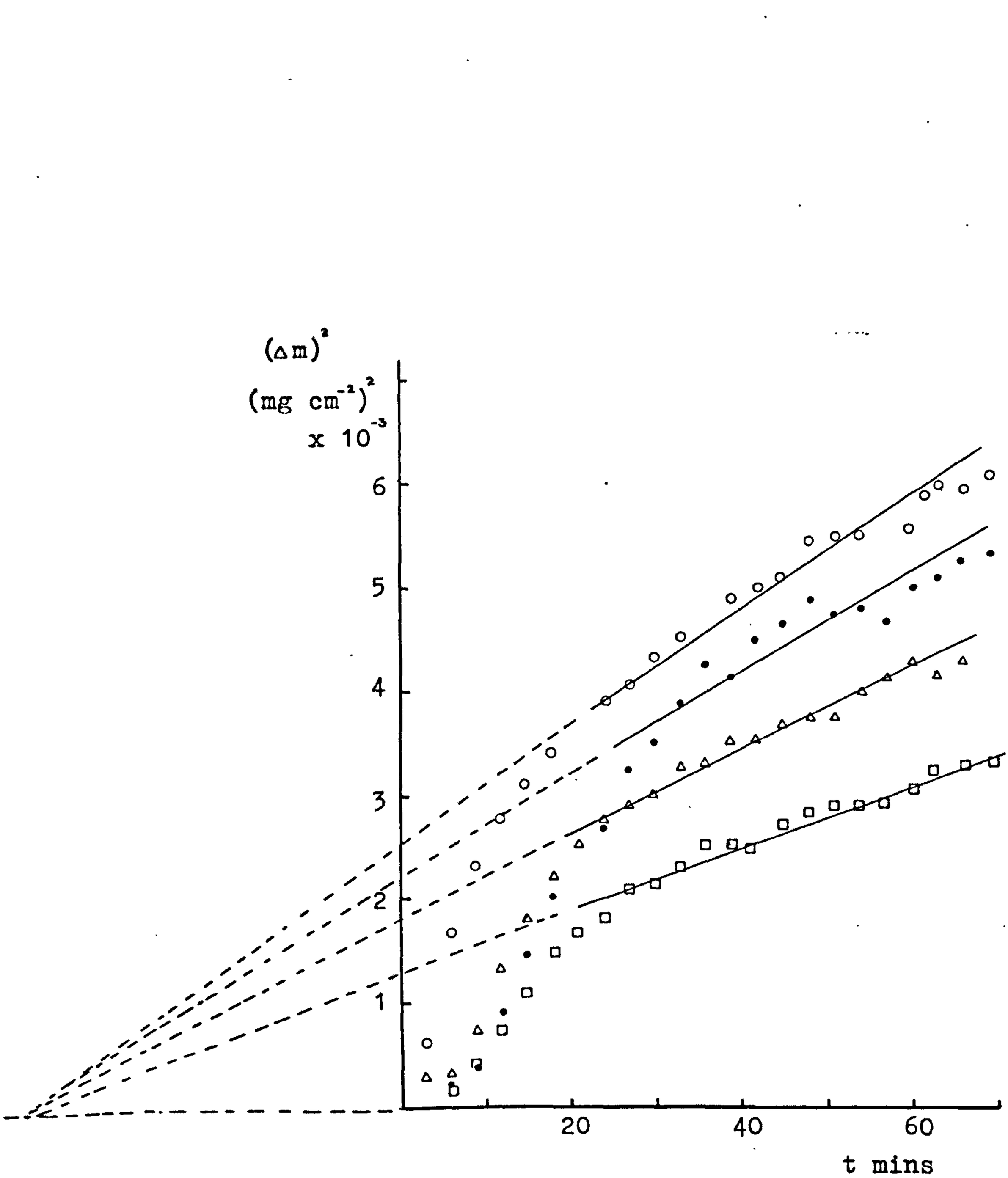

Fig 72d Fig 72c replotted to show common origin of parabolic regions.

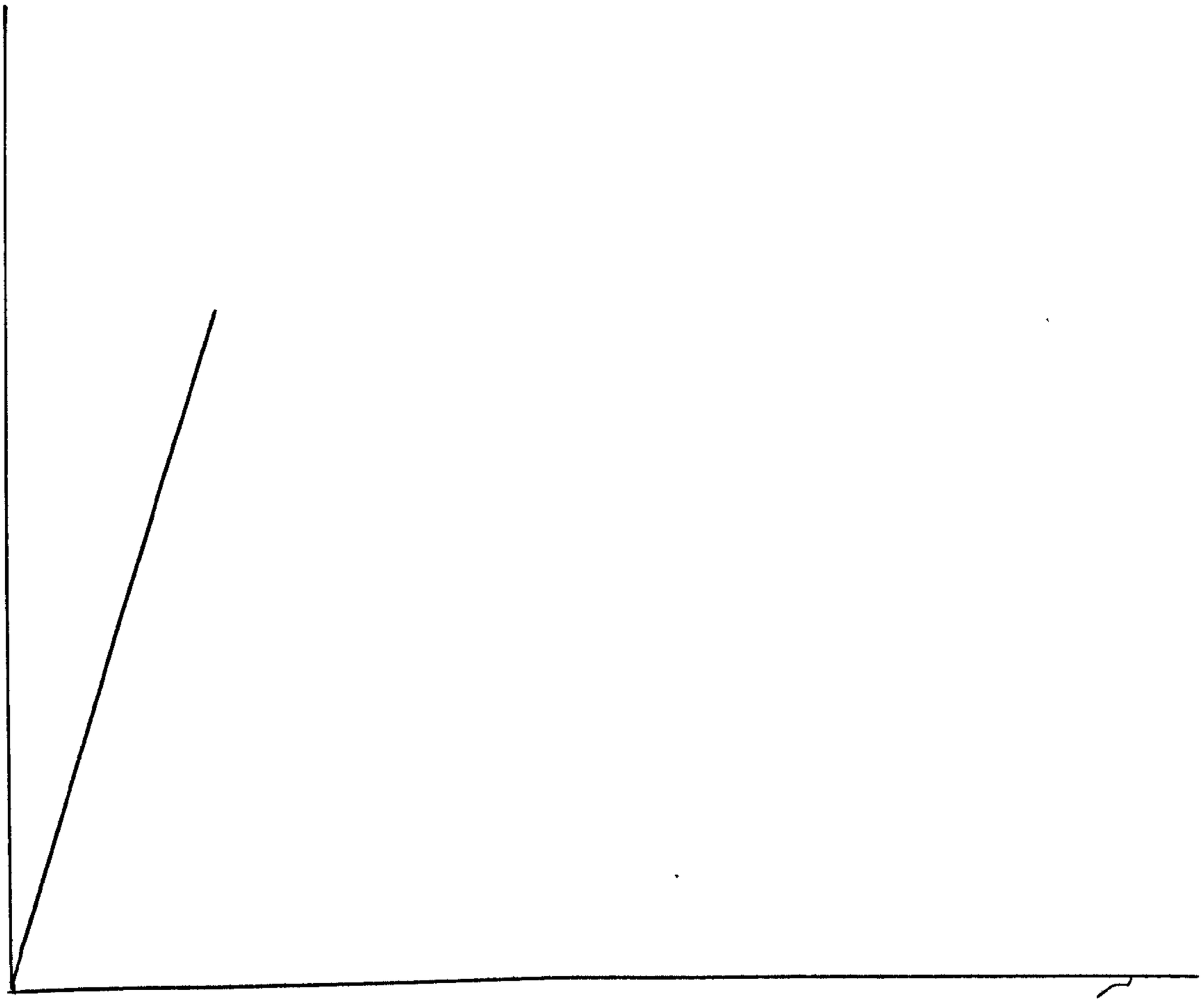

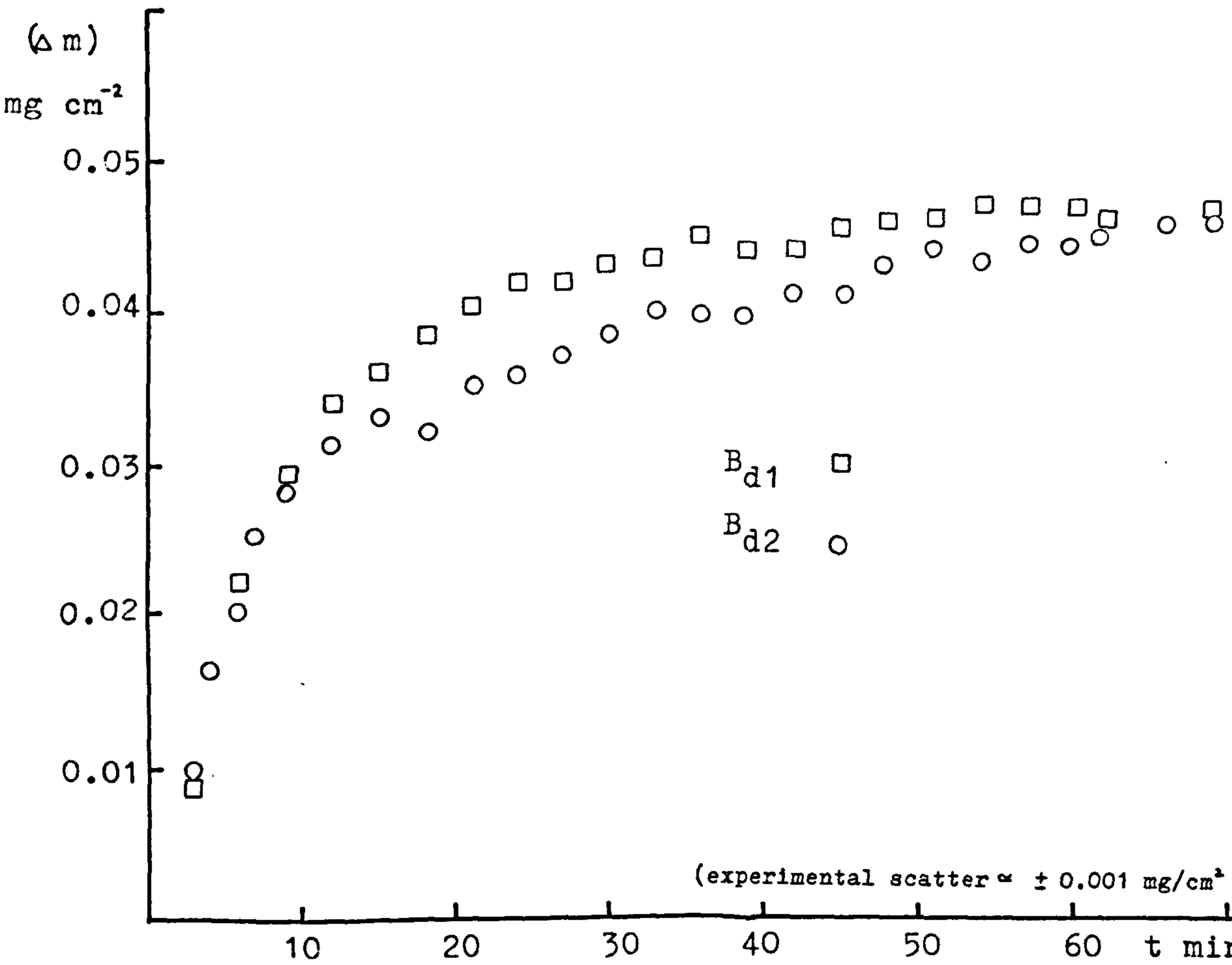

Fig 73a Oxidation of further purified high purity aluminium (Billet B) at 1003 K (730 °C) in dry oxygen
Mass gain / unit area (Δ m) plotted as a function of time (t).

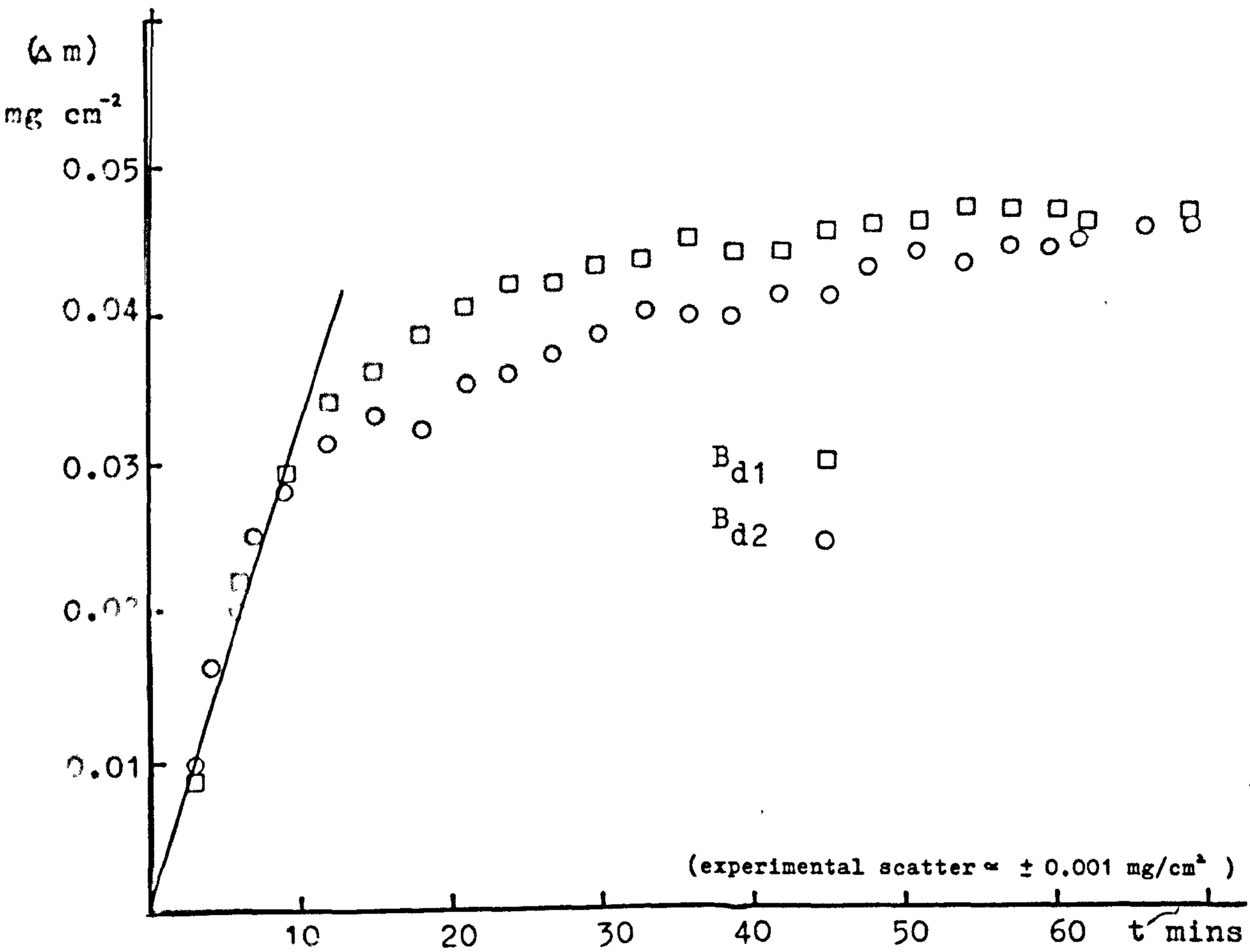

Fig 73a Oxidation of further purified high purity aluminium (Billet B) at 1003 K (730 °C) in dry oxygen
Mass gain / unit area (Δ m) plotted as a function of time (t).

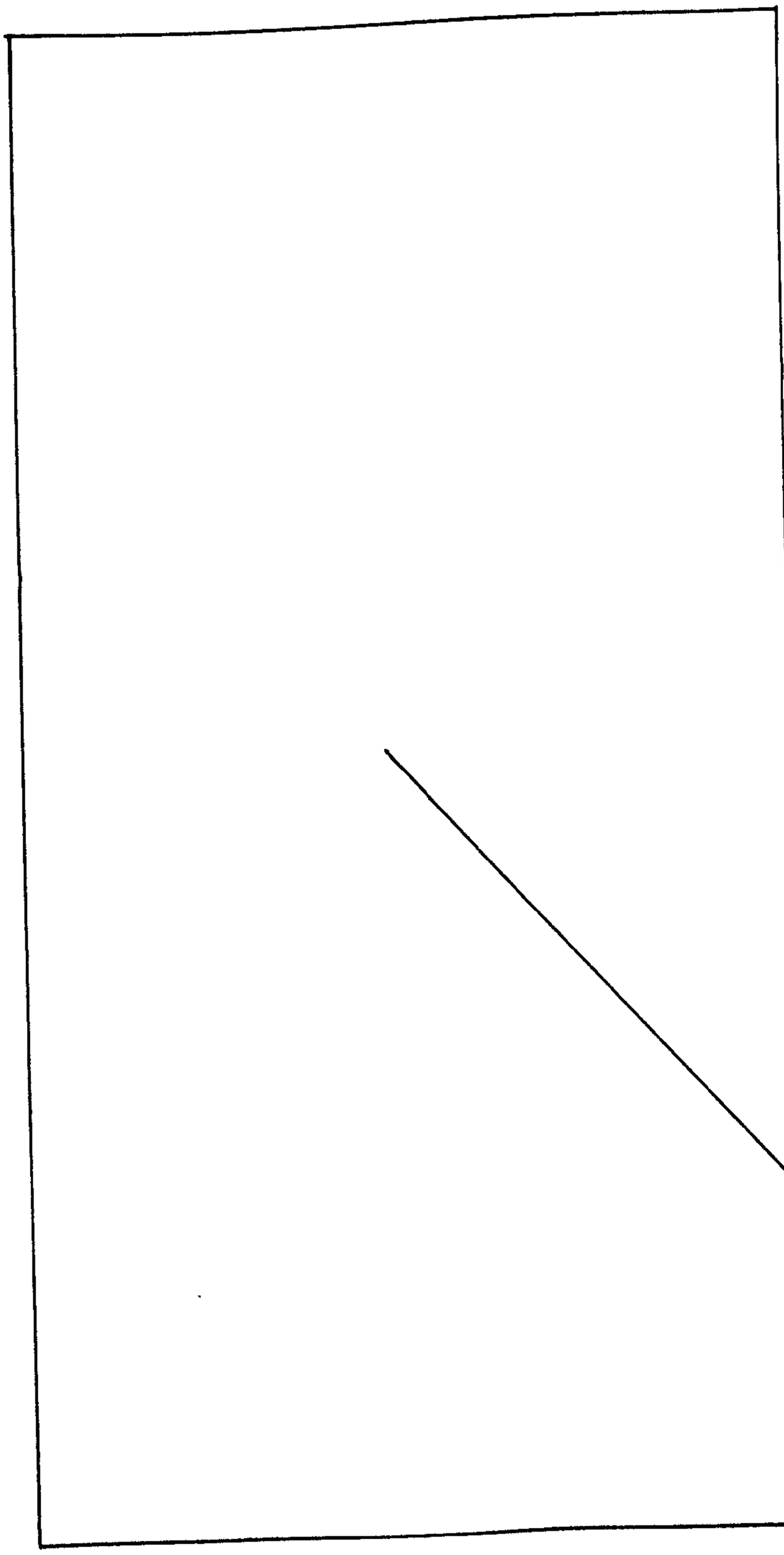

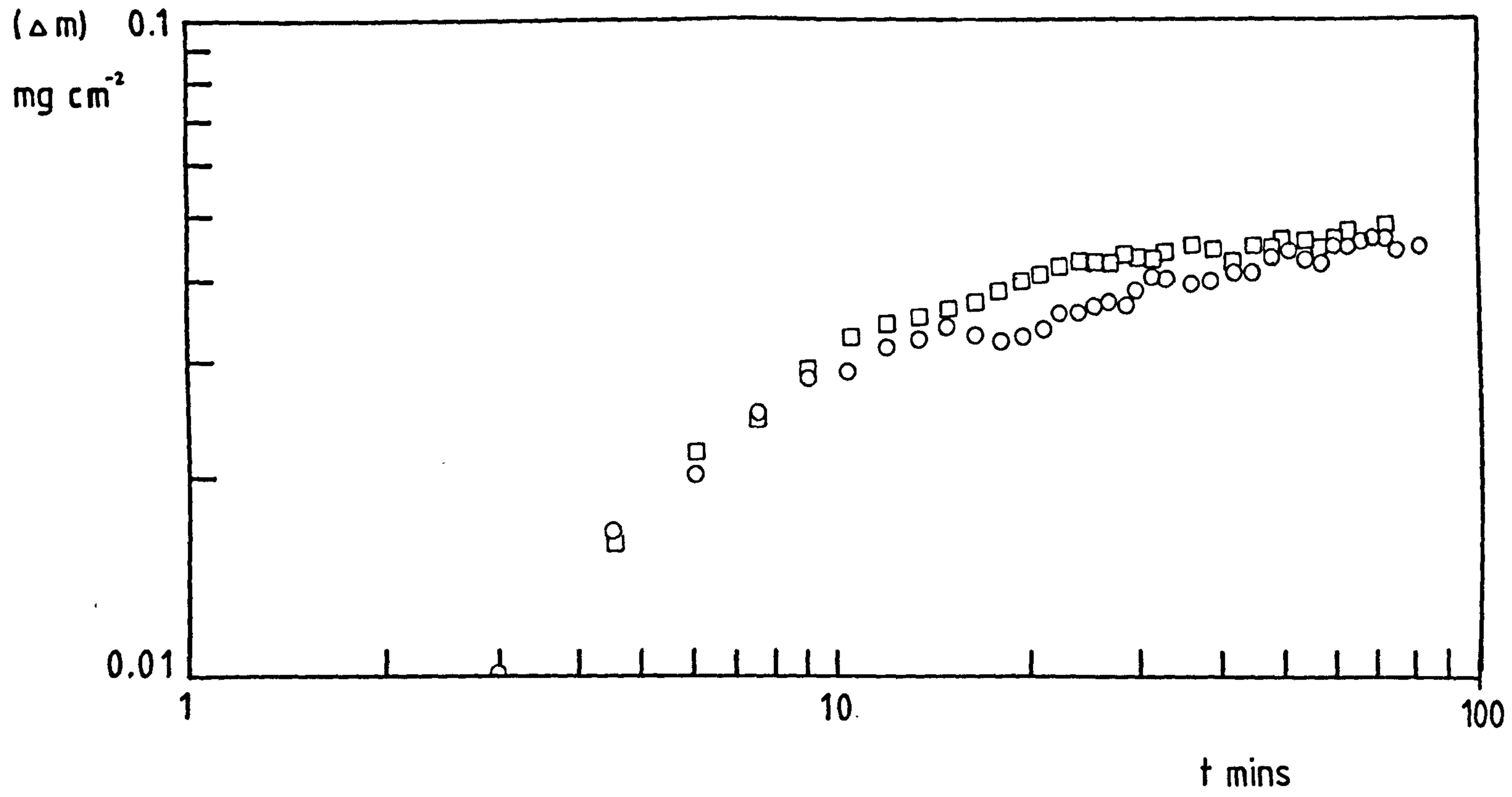

Fig 73b Oxidation of further purified high purity aluminium (Billet B) at 730 C in dry oxygen. Mass gain/unit area (Δm) replotted as a function of time on a log/log scale.

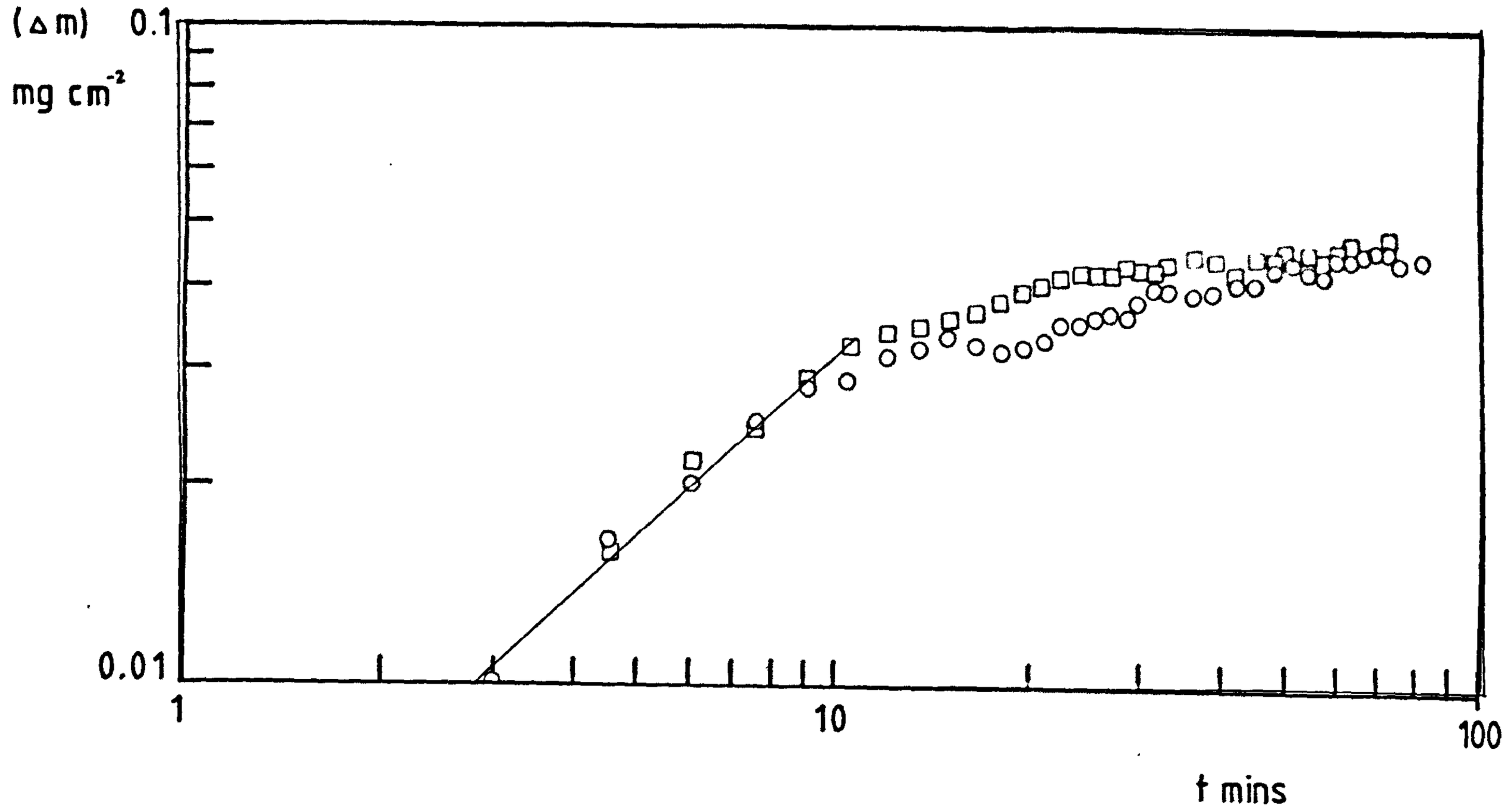

Fig 73b Oxidation of further purified high purity aluminium (Billet B) at 730 C in dry oxygen. Mass gain/unit area (Δm) replotted as a function of time on a log/log scale.

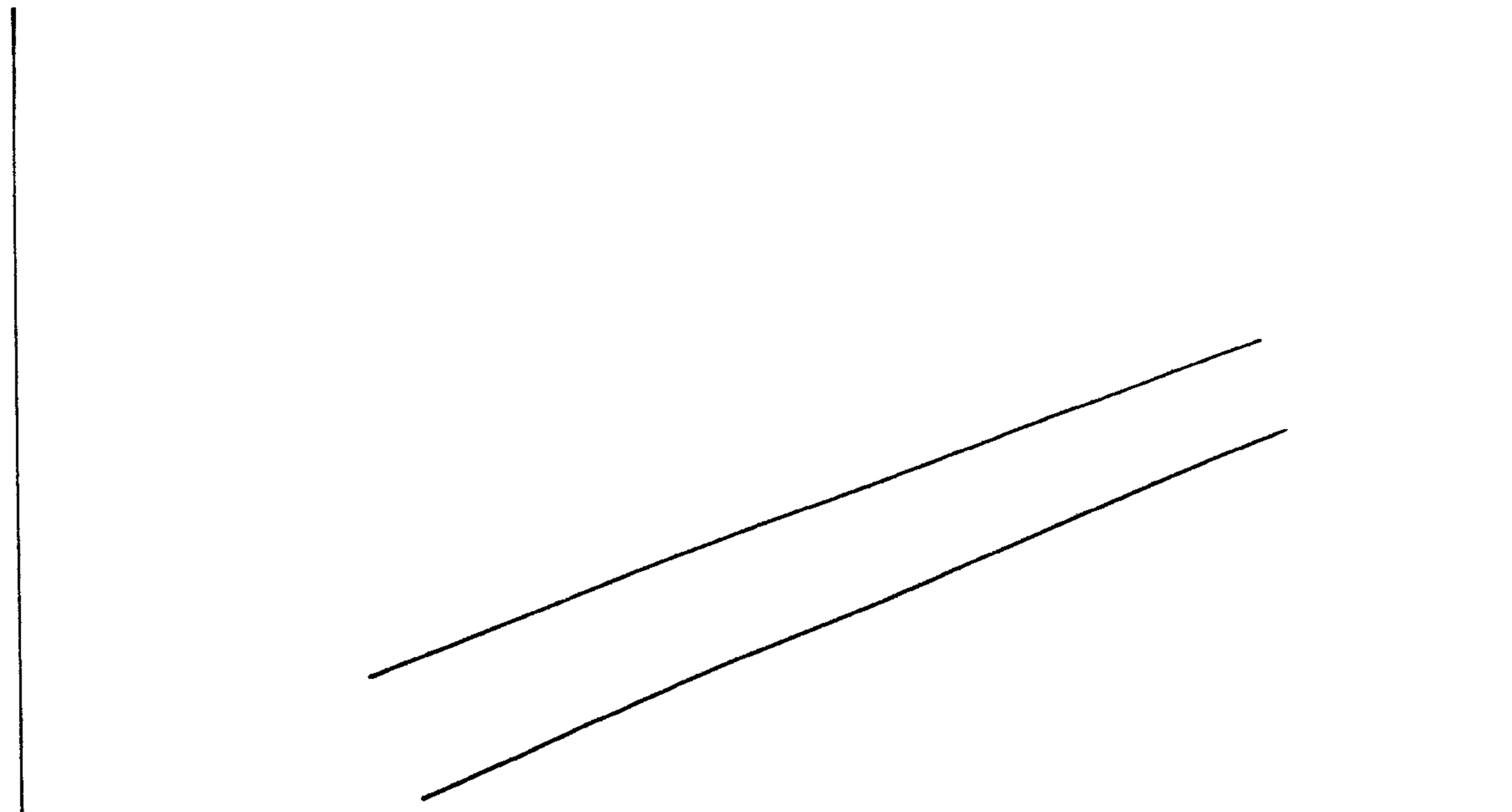

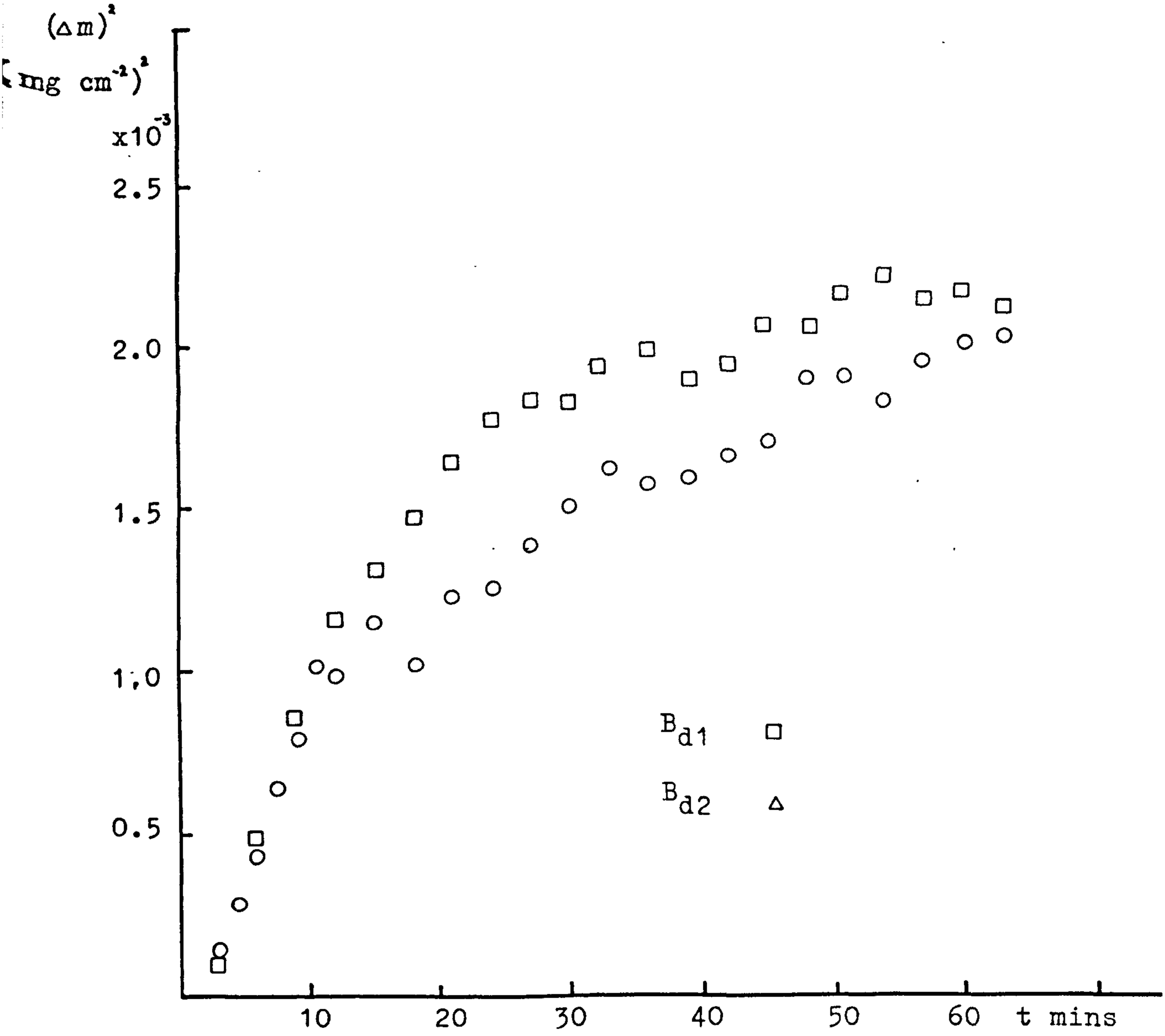

Fig 73c Fig 73a replotted on a parabolic scale . $(\Delta m)^2$ plotted as a function of time (t) showing the parabolic portions.

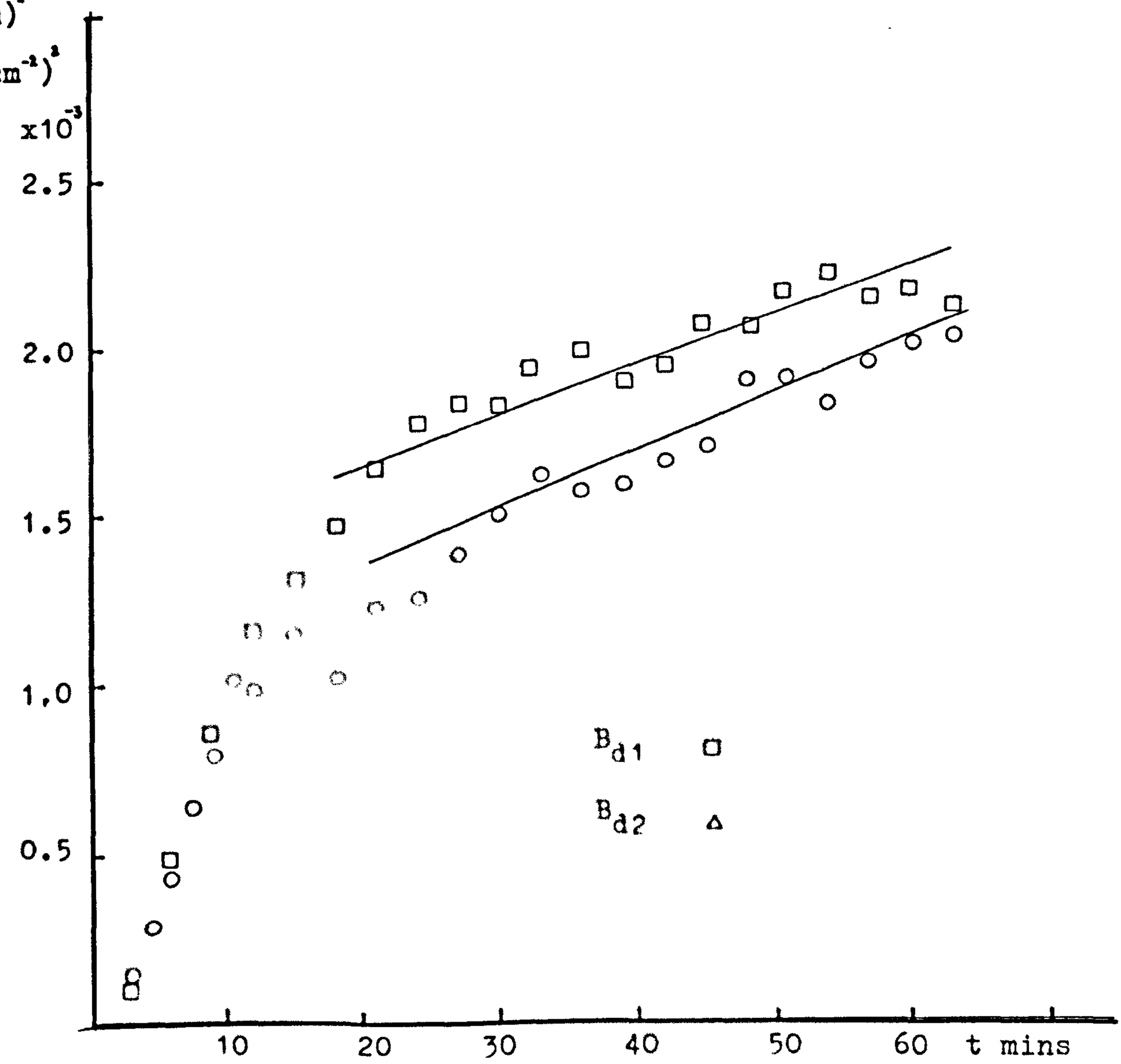

Fig 7_3c Fig 73a replotted on a parabolic scale . $(\Delta m)^2$ plotted as a function of time (t) showing the parabolic portions.

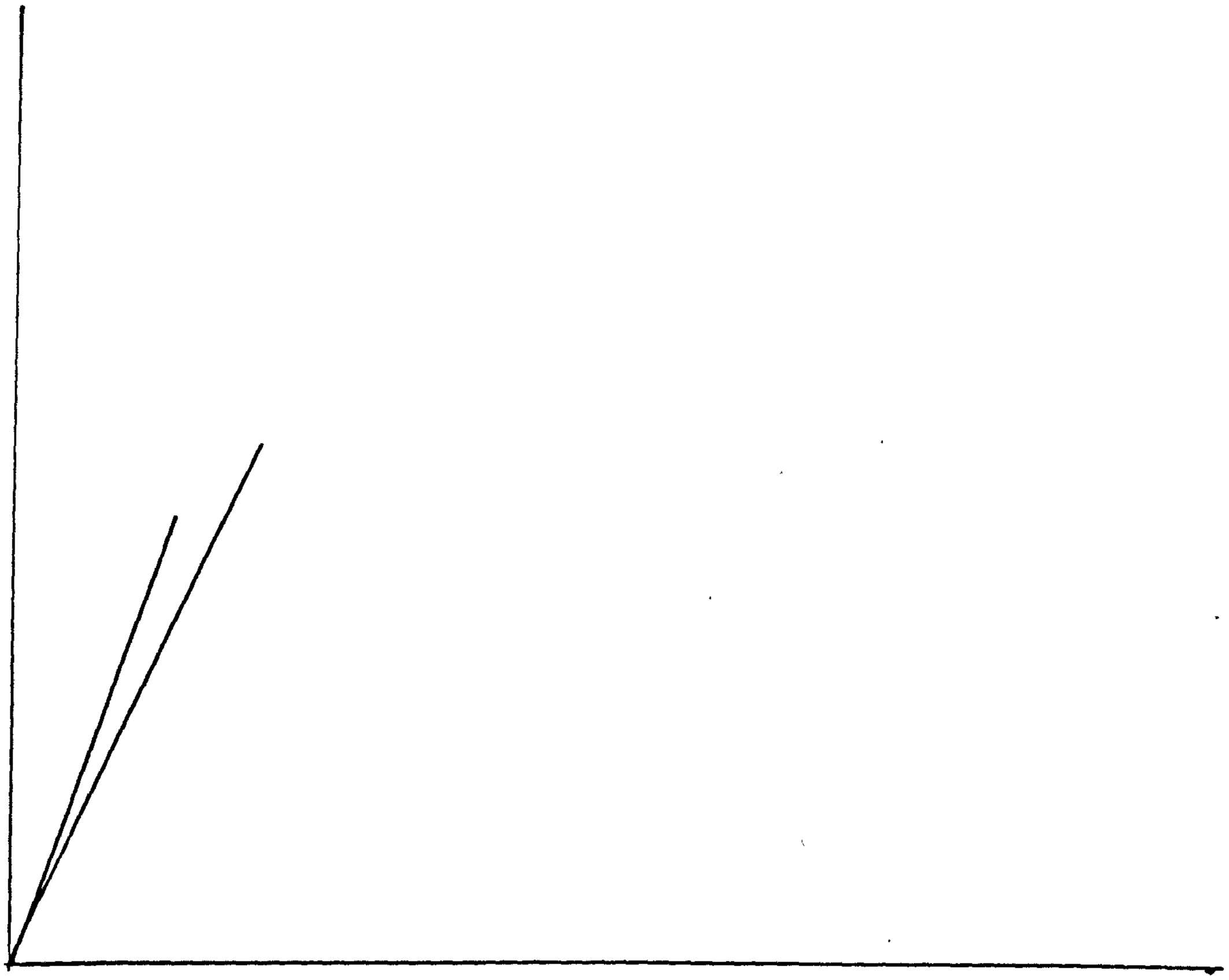

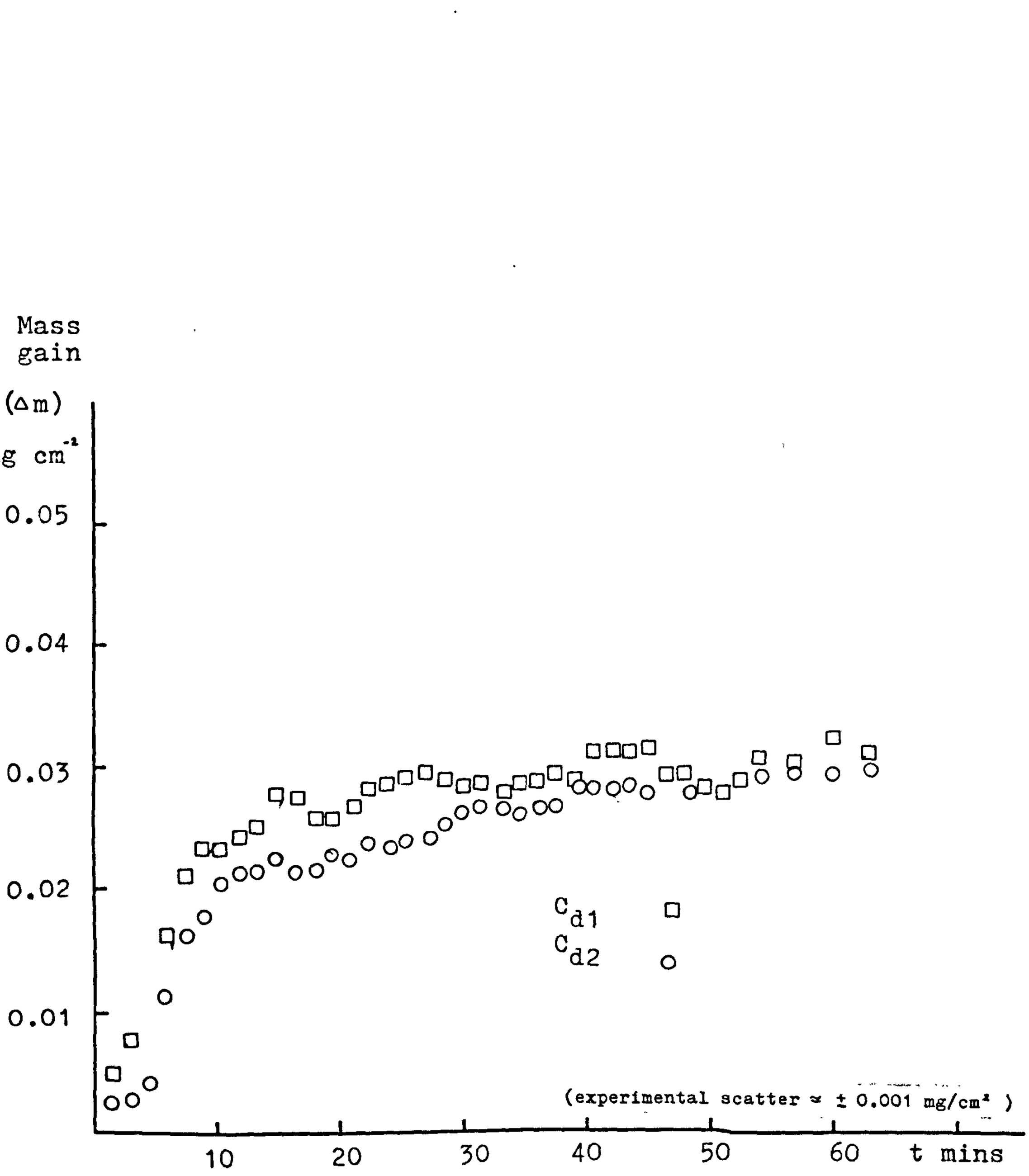

Fig 74a Oxidation of further purified high purity aluminium (Billet C) at 1003 K (730 °C) in dry oxygen . Mass gain /unit area (Δm) plotted as a function of time (t).

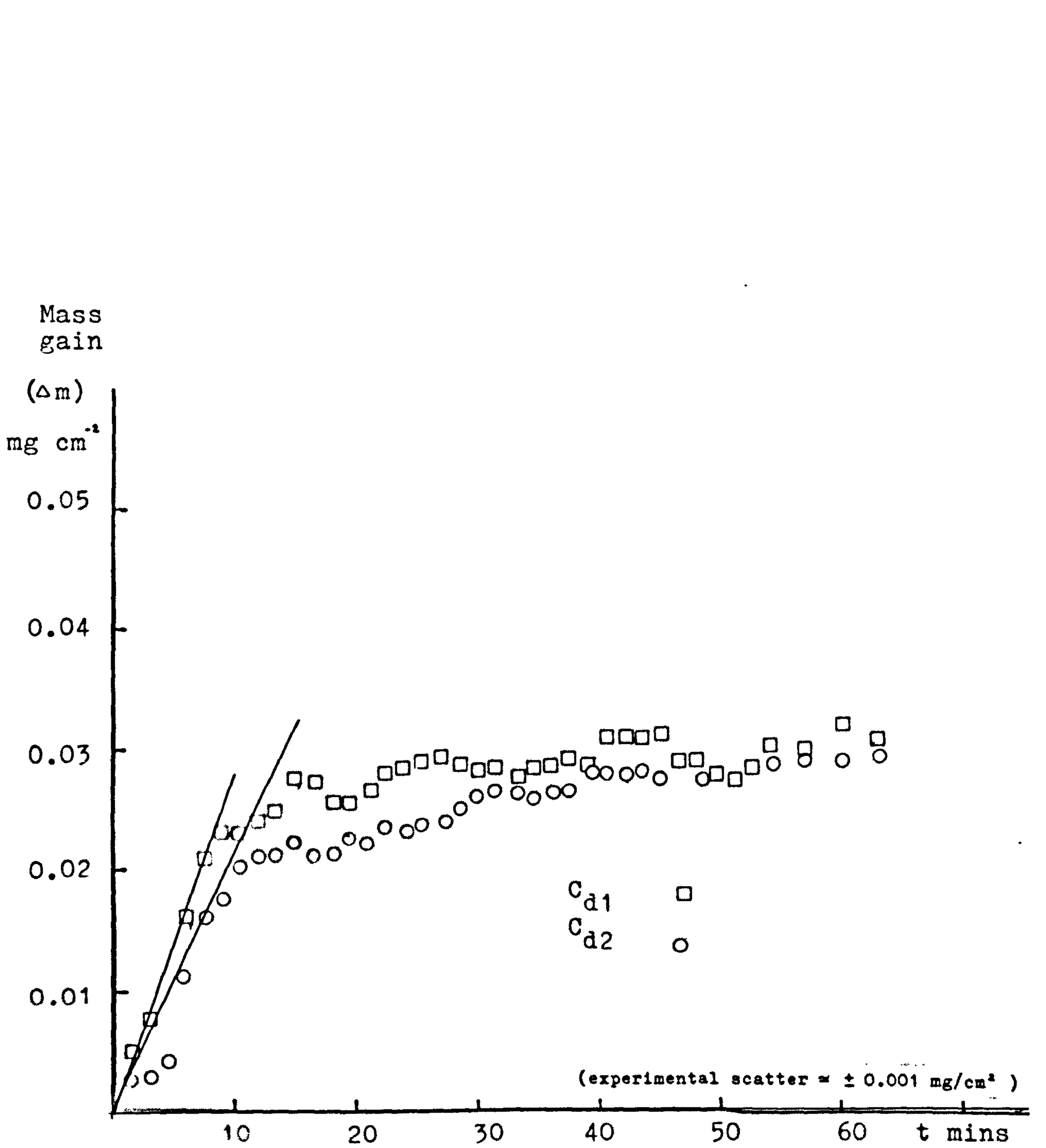

Fig 74a Oxidation of further purified high purity aluminium (Billet C) at 1003 K (730 °C) in dry oxygen . Mass gain /unit area (Δm) plotted as a function of time (t).

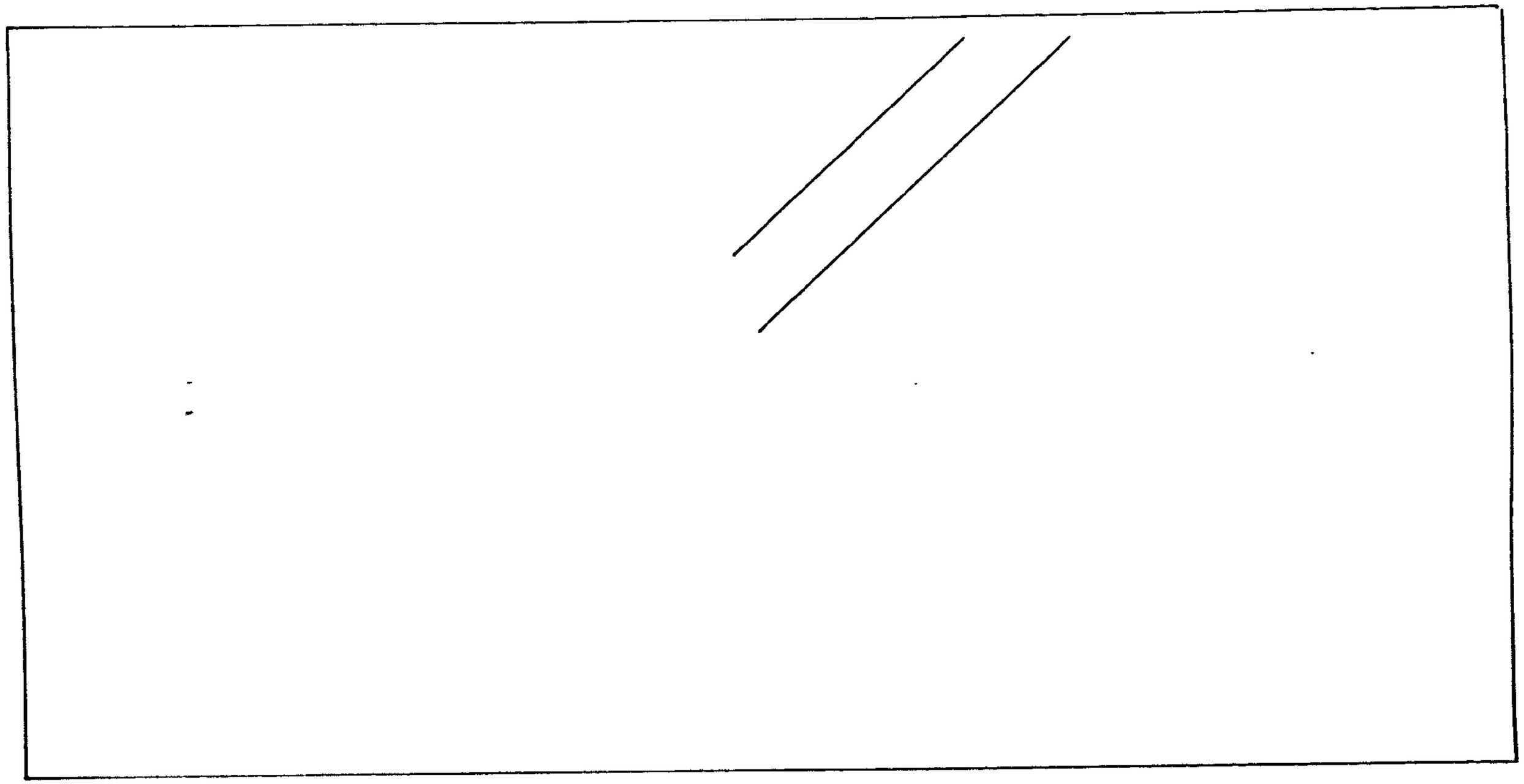

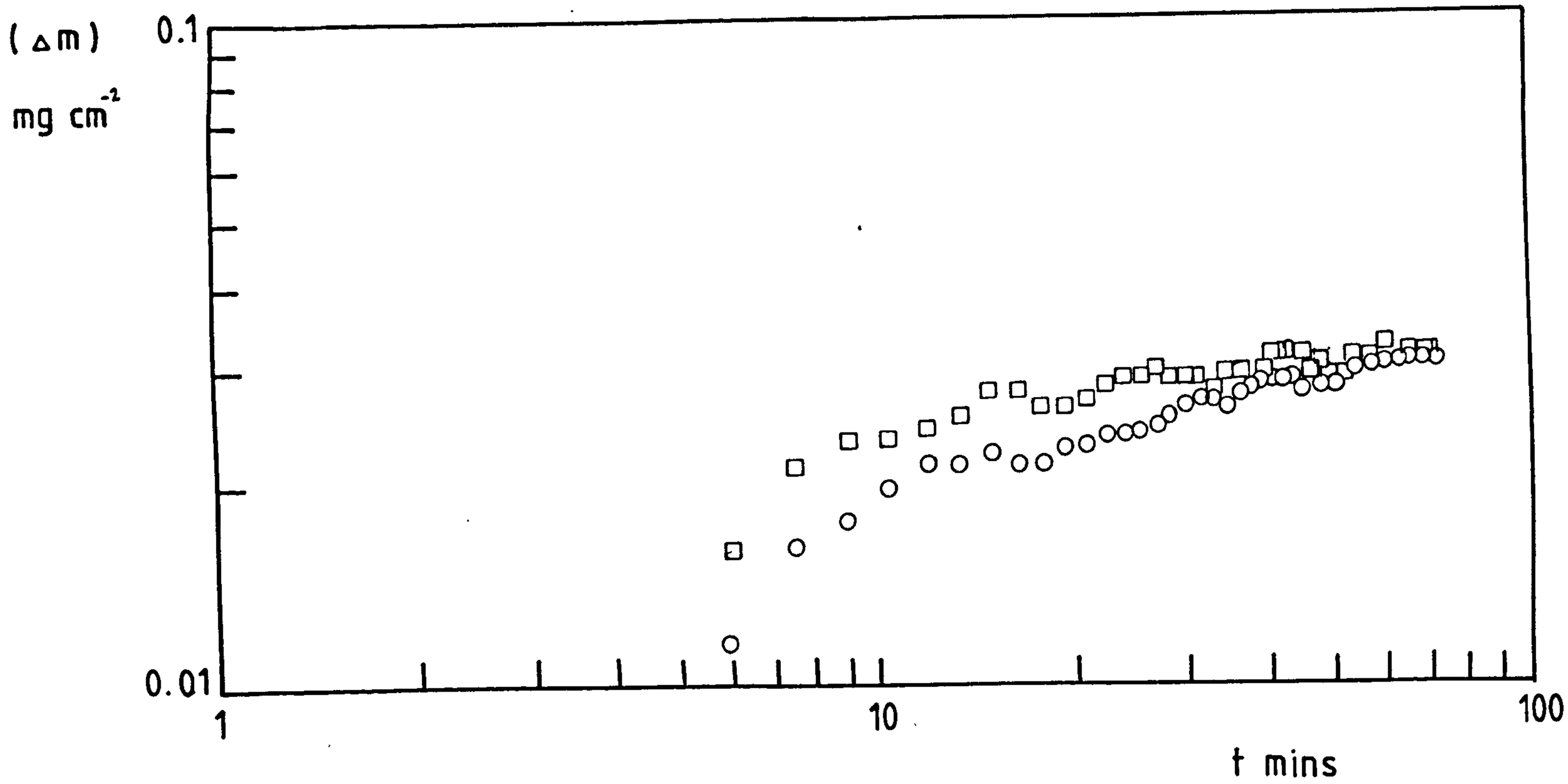

Fig 74b Fig 74a replotted on log/log scale

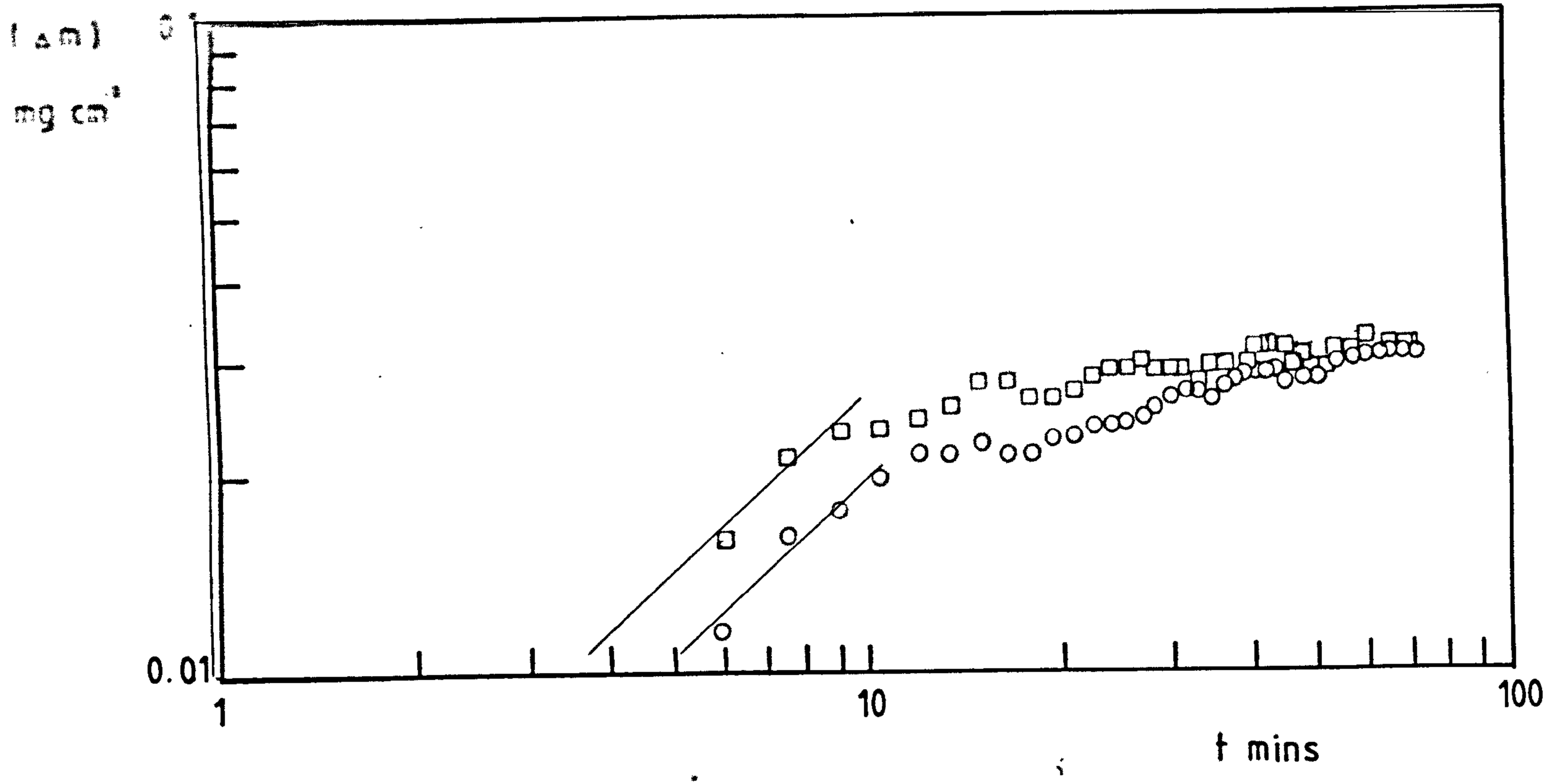

Fig 74b Fig 74a replotted on log/log scale

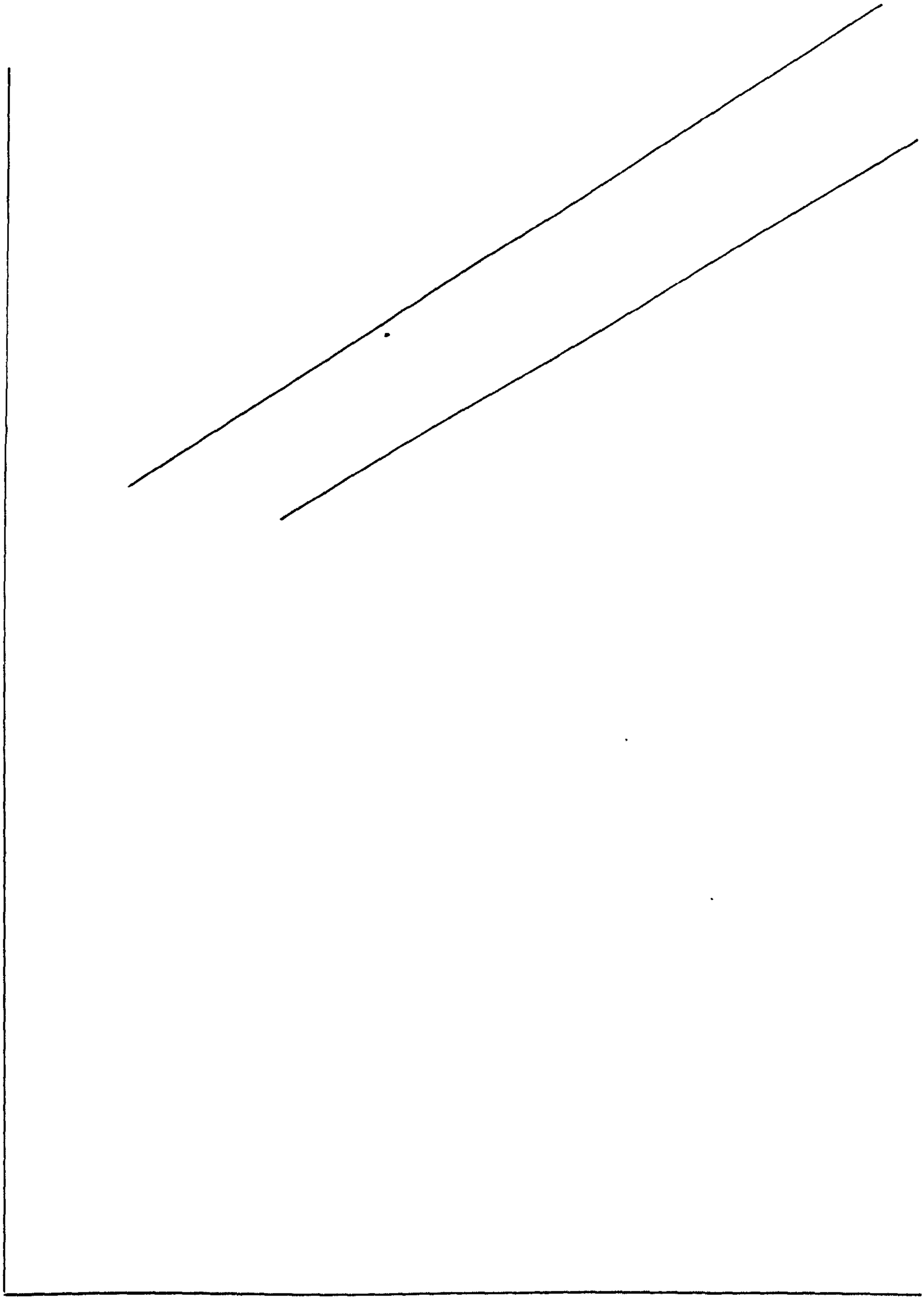

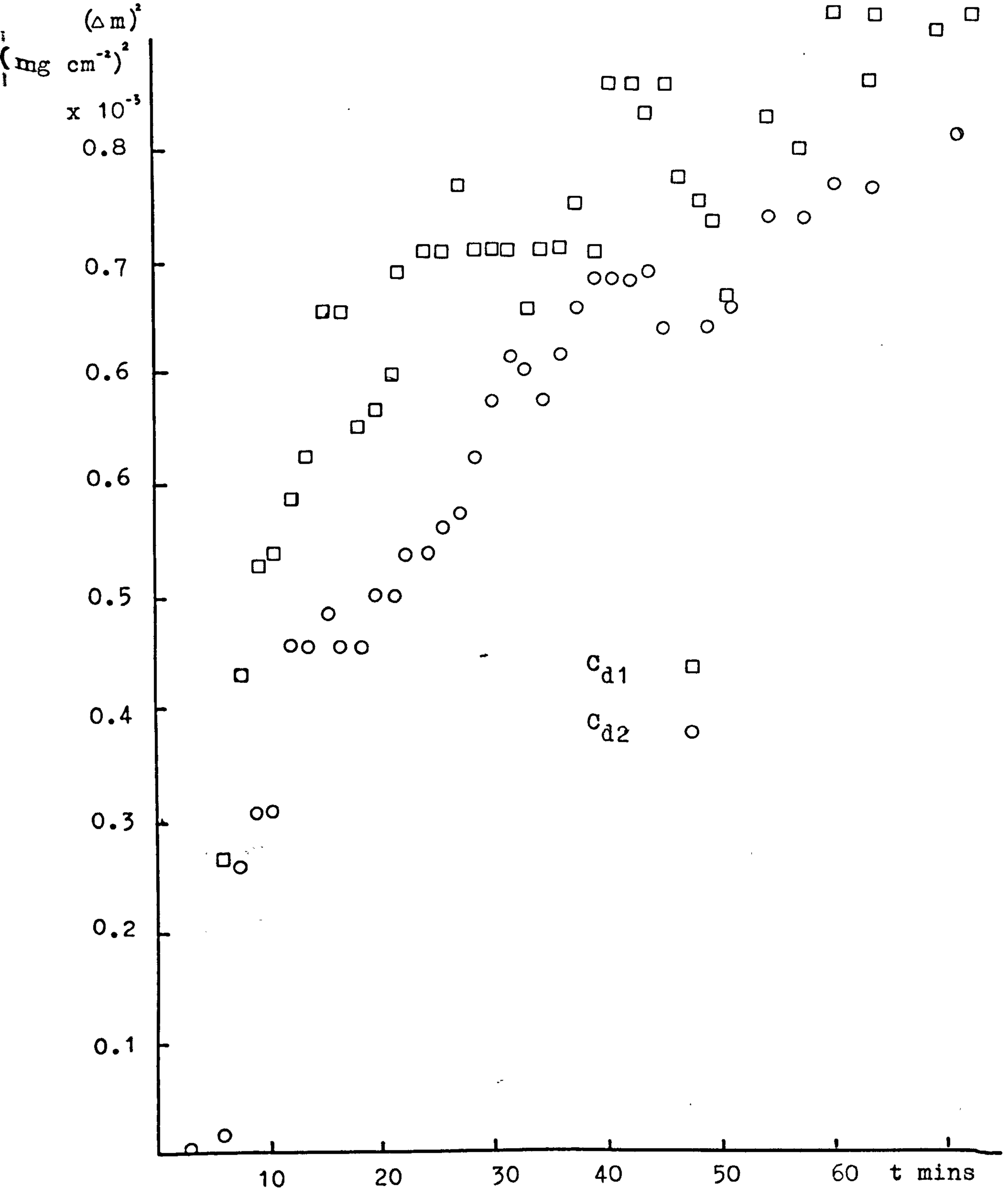

Fig 74c Fig 74a replotted on a parabolic scale. $(\Delta m)^2$ plotted as a function of time (t) showing parabolic portions.

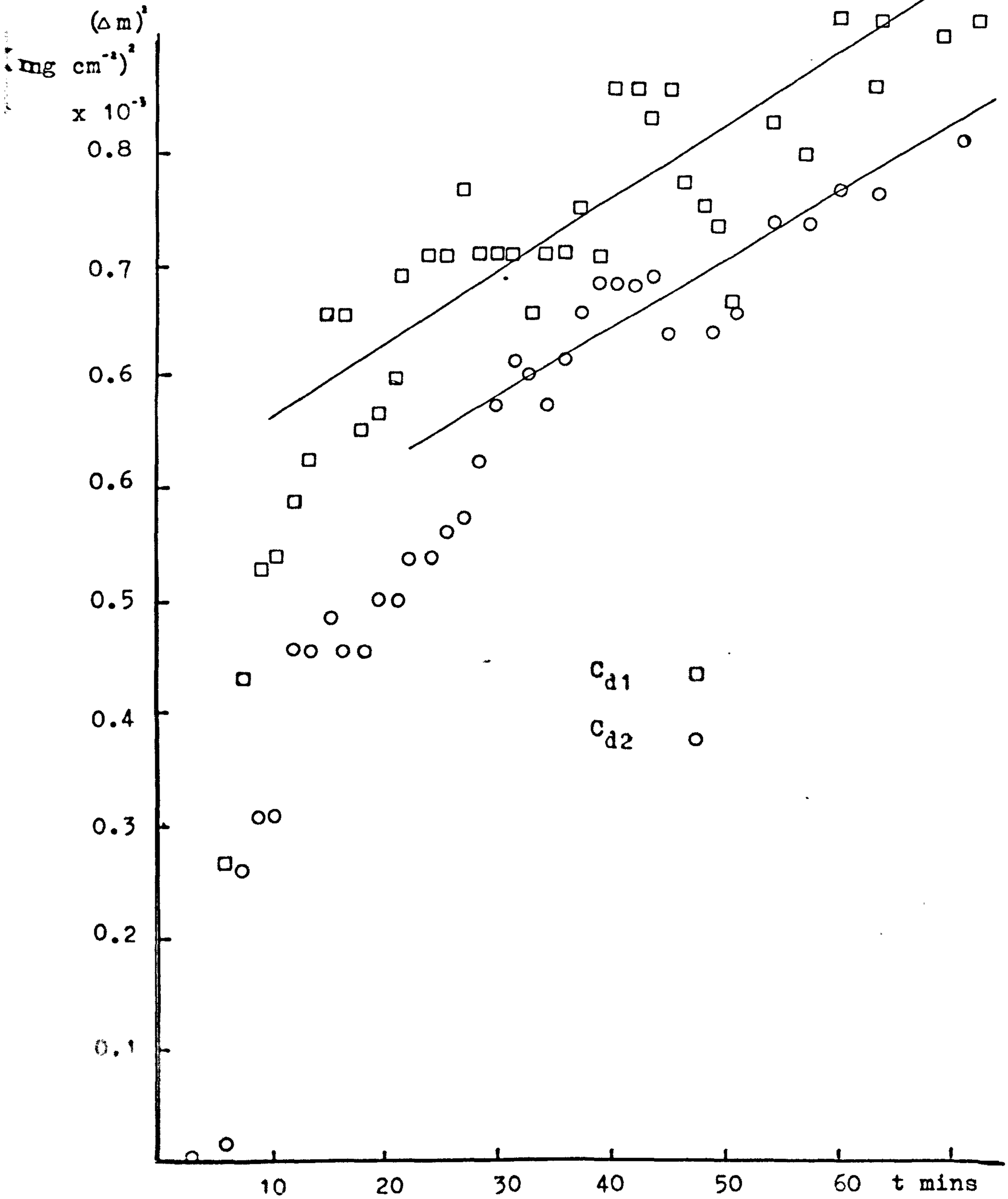

Fig 74c Fig 74a replotted on a parabolic scale. $(\Delta m)^2$ plotted as a function of time (t) showing parabolic portions.

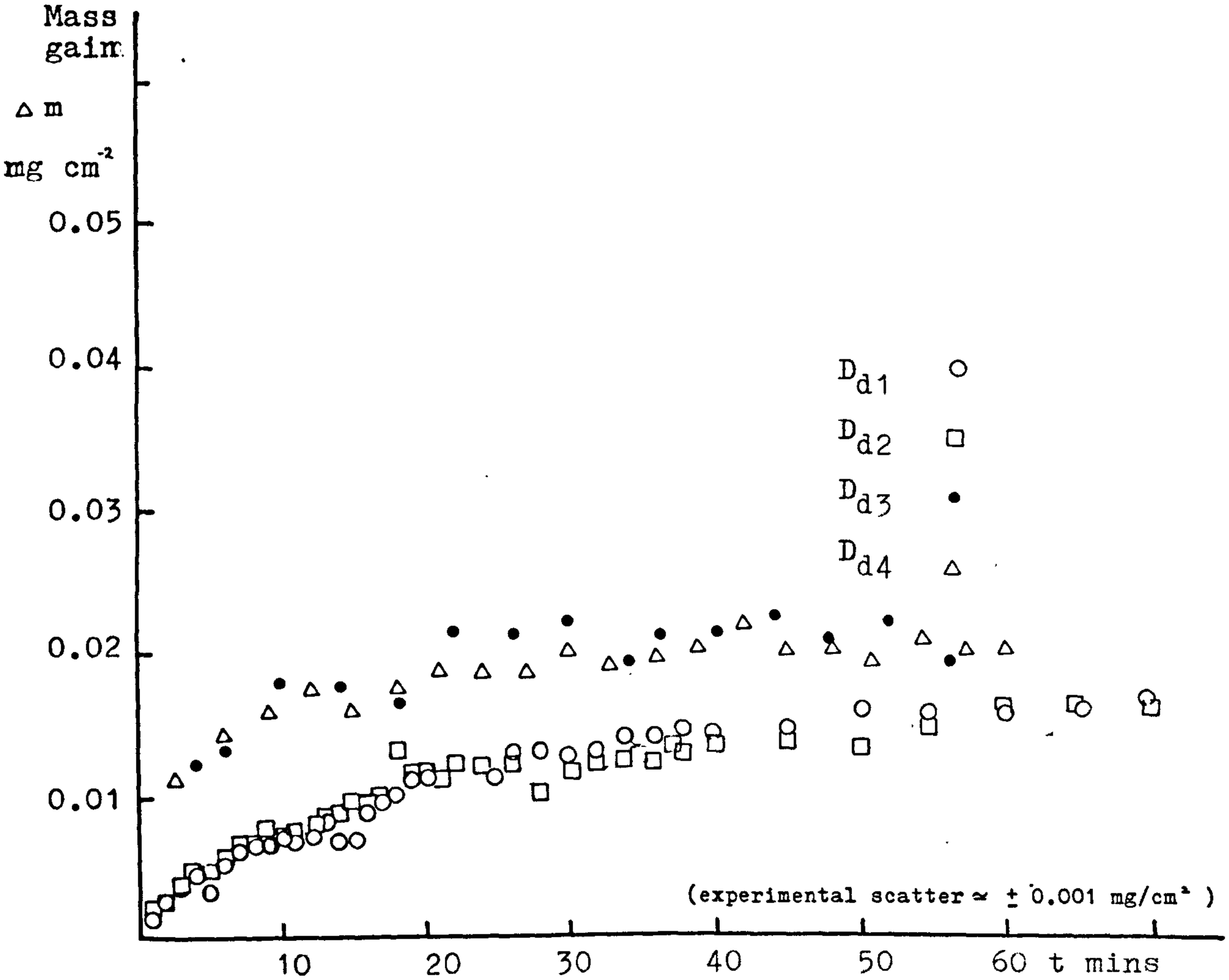

Fig 75a Oxidation of further purified high purity aluminium (Billet D) at 1003 K (730 C) in dry oxygen

Mass gain/unit area (Δ m) plotted as a function function of time (t).

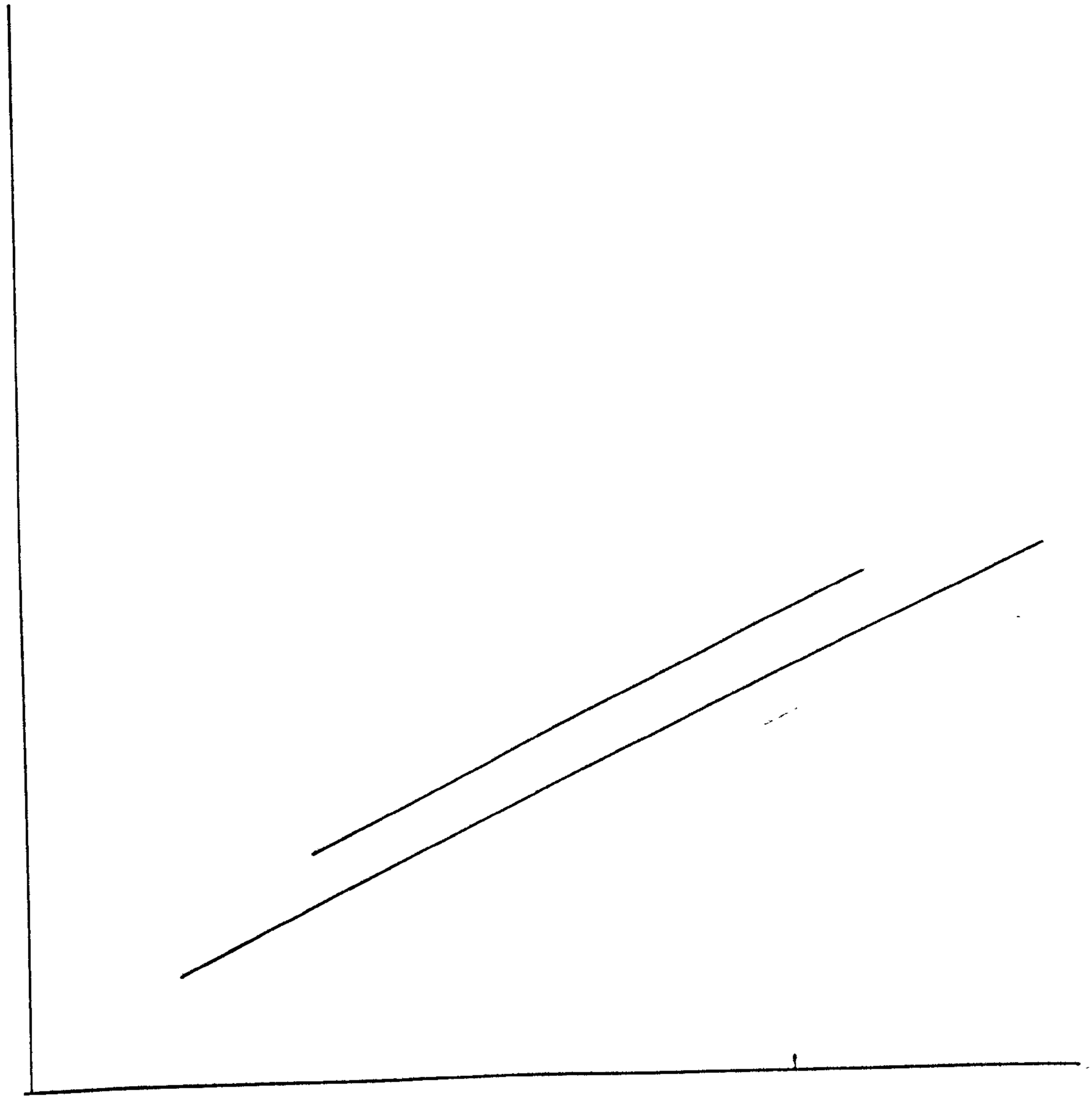

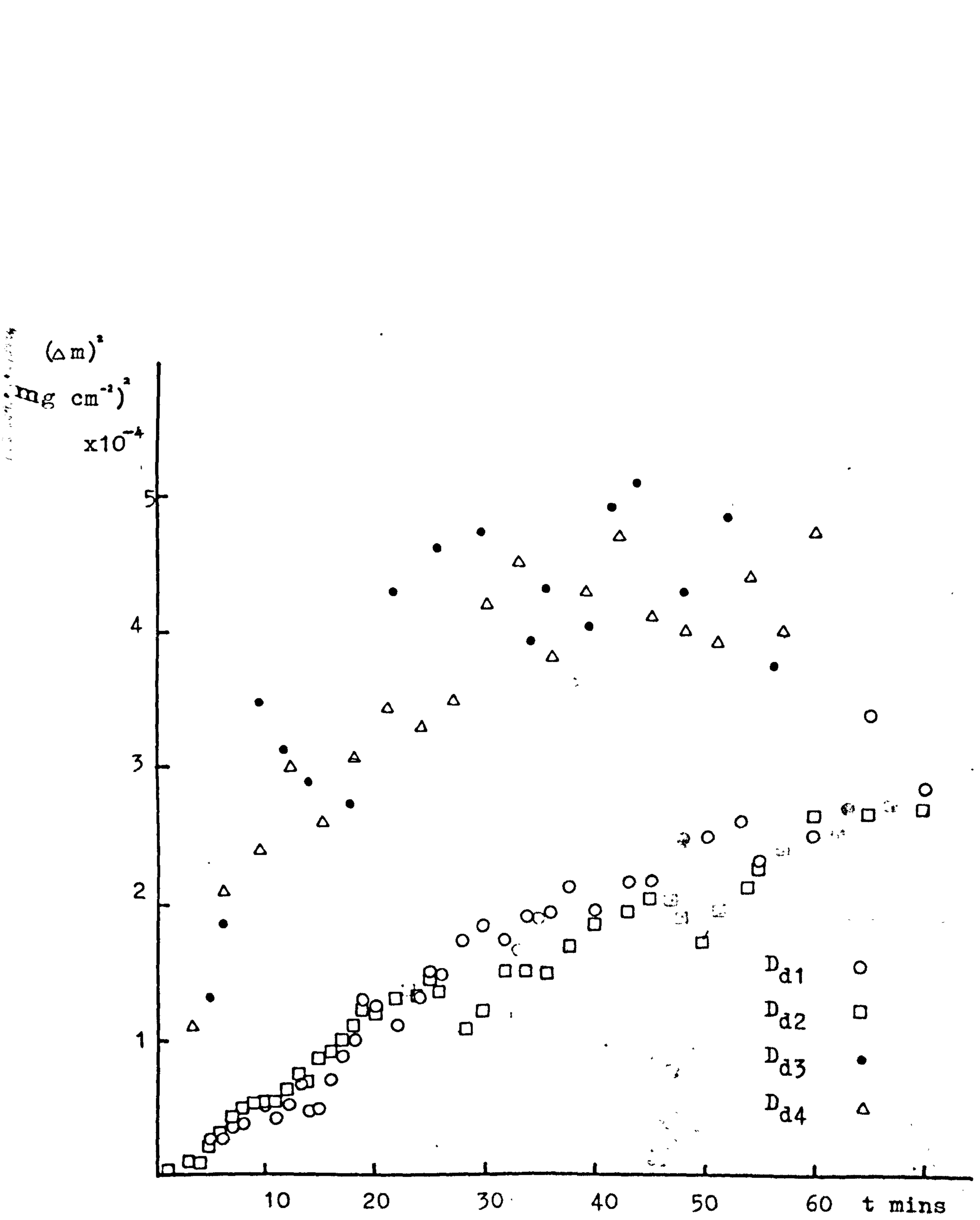

Fig 75b Fig 75a replotted on parabolic scale, showing parabolic portions in D_{d1} and D_{d2}. The experimental scatter in D_{d3} and D_{d4} does not allow the parabolic portions to be identified accurately.

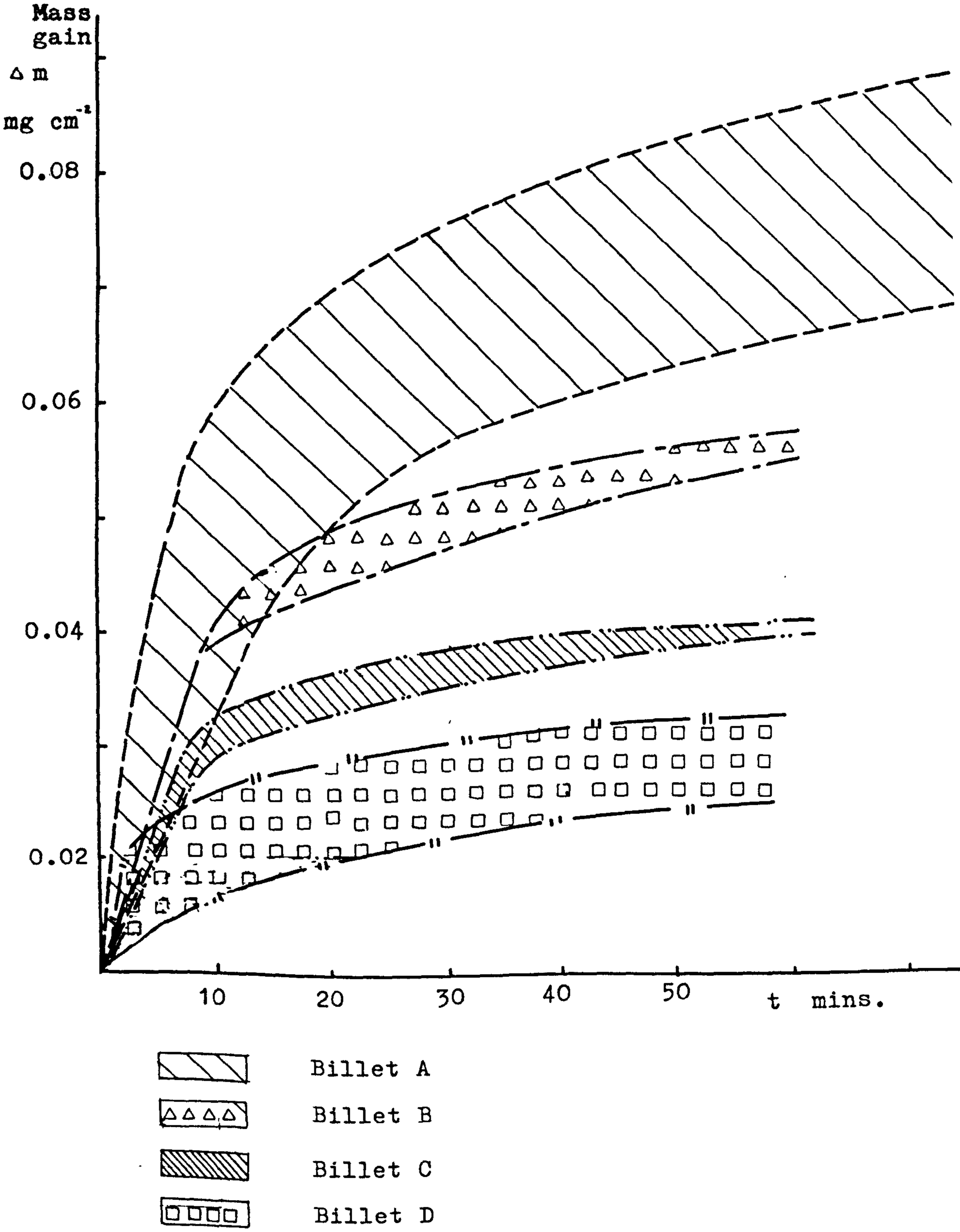
Mass gain
Δ m
mg cm⁻²
0.08
0.06
0.04
0.02
10
20
30
40
50
t mins.
Billet A
Billet B
Billet C
Billet D

Fig 76 Comparison of oxidation kinetics in dry oxygen at 730 °C between samples obtained from

a) normal high purity aluminium (Billet A)

b) further purified high purity aluminium

i	Billet B
ii	Billet C
iii	Billet D

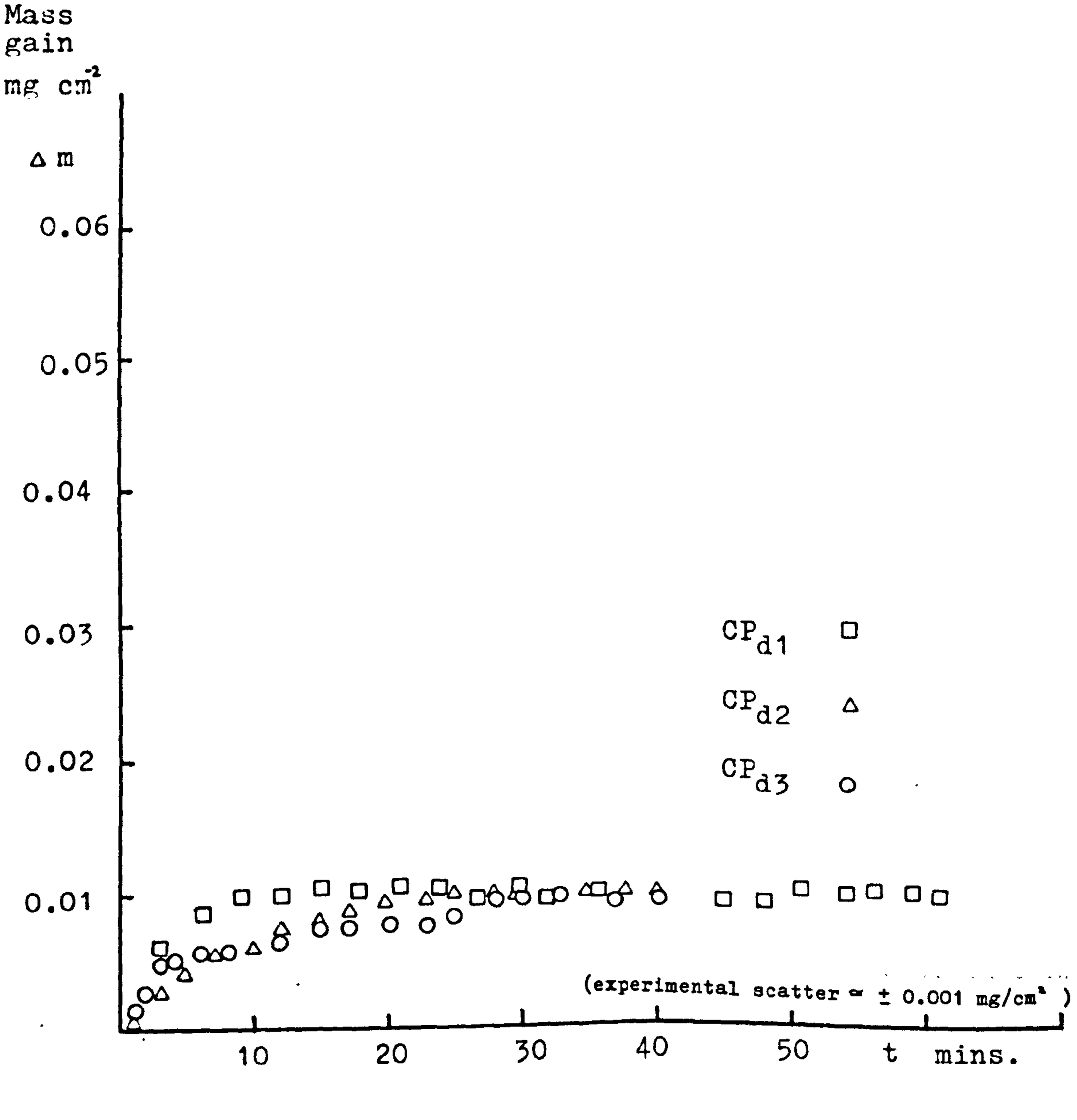

Fig 77a Oxidation kinetics in dry oxygen at 730 °C of samples obtained from commercial purity aluminium.

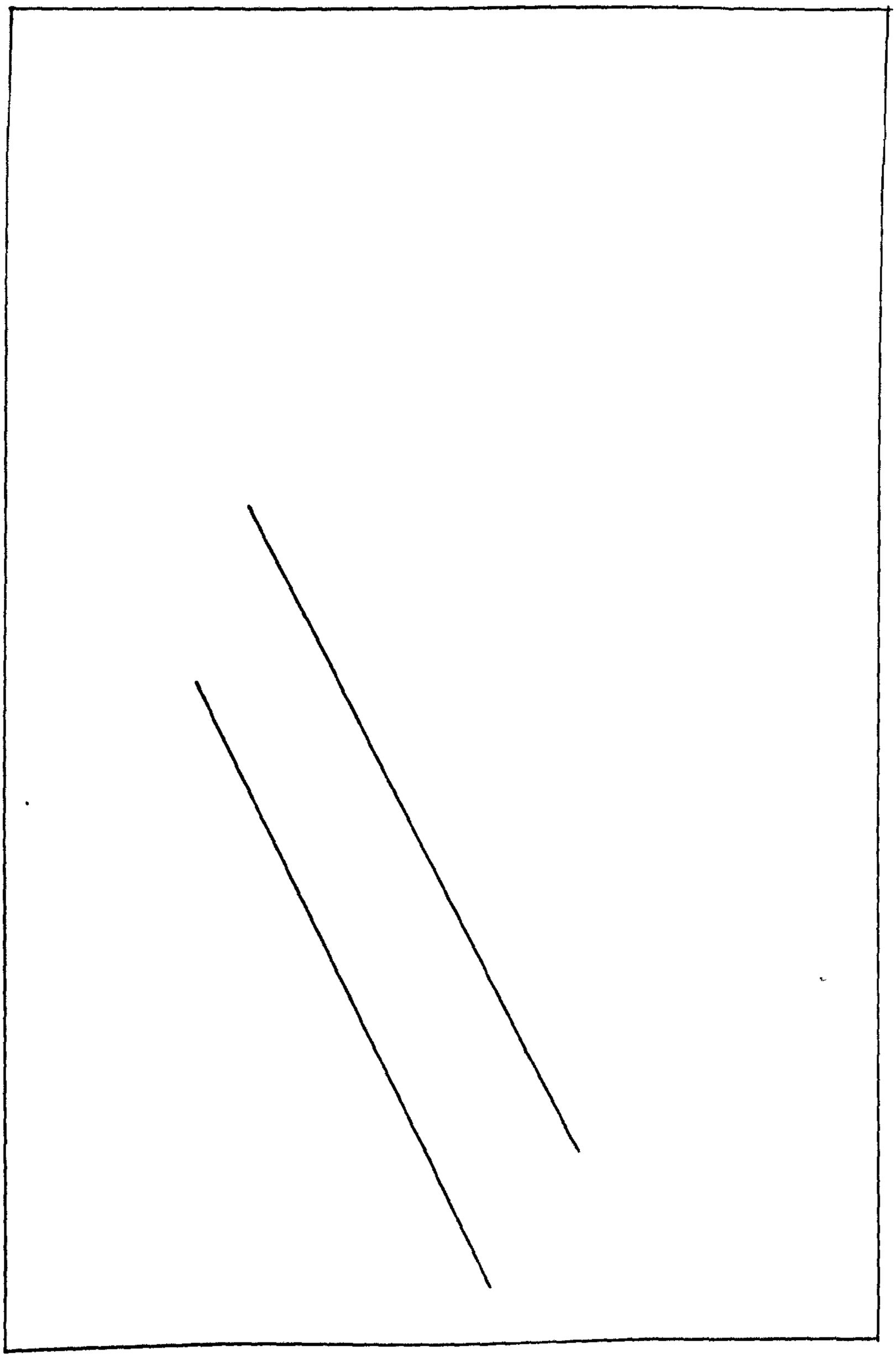

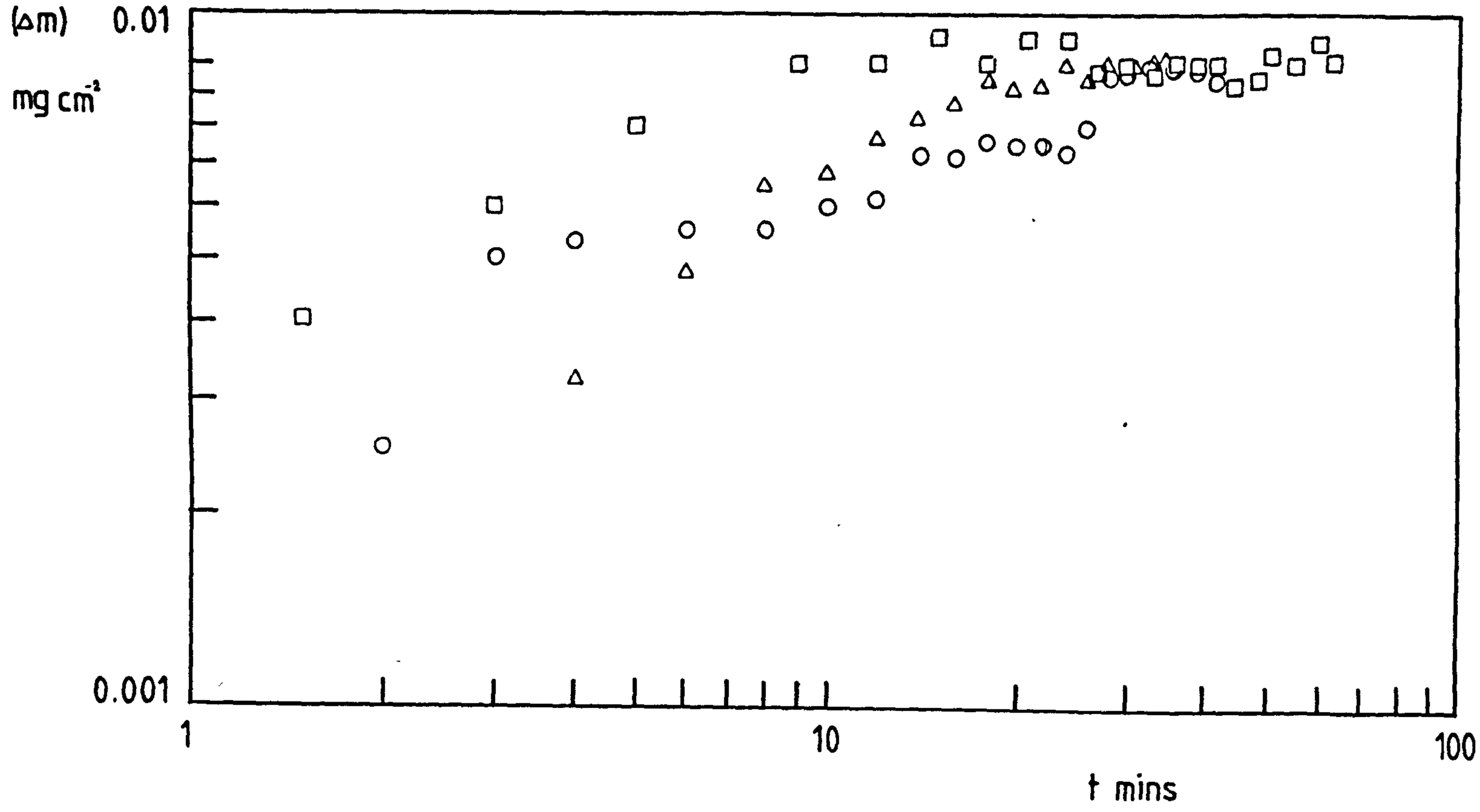

Fig 77b Fig 77a replotted on log/log scale

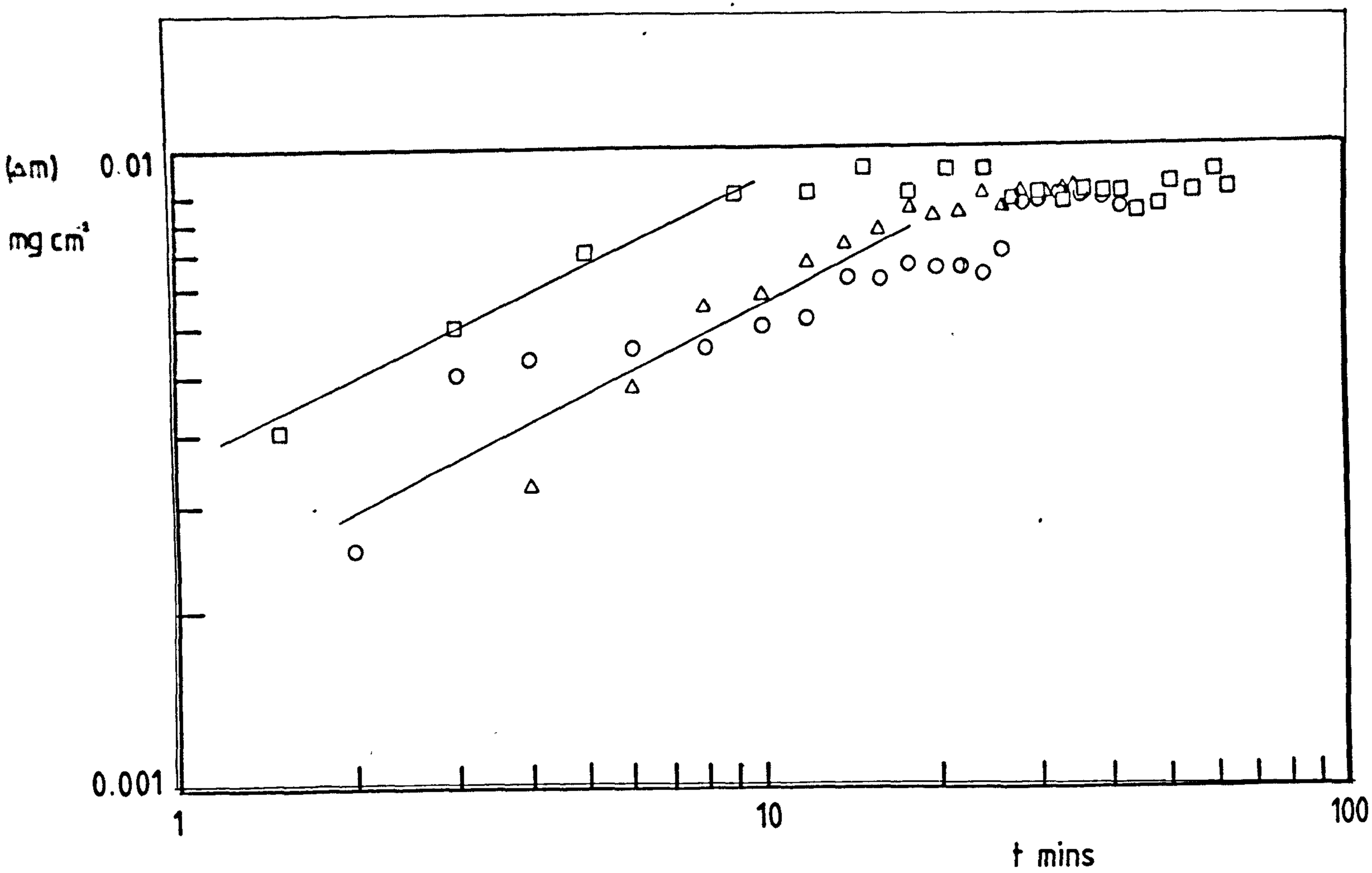

Fig 77b Fig 77a replotted on log/log scale

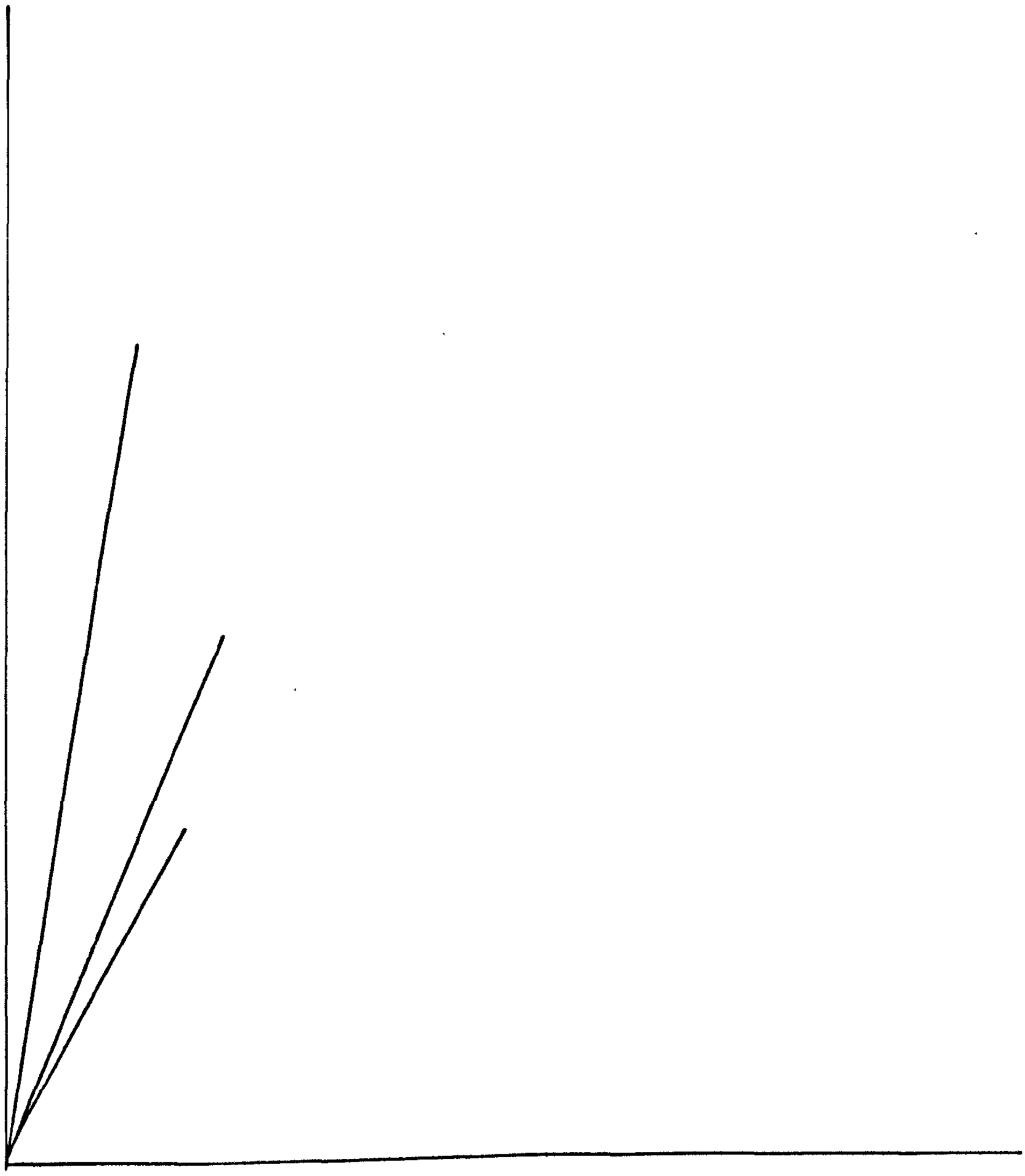

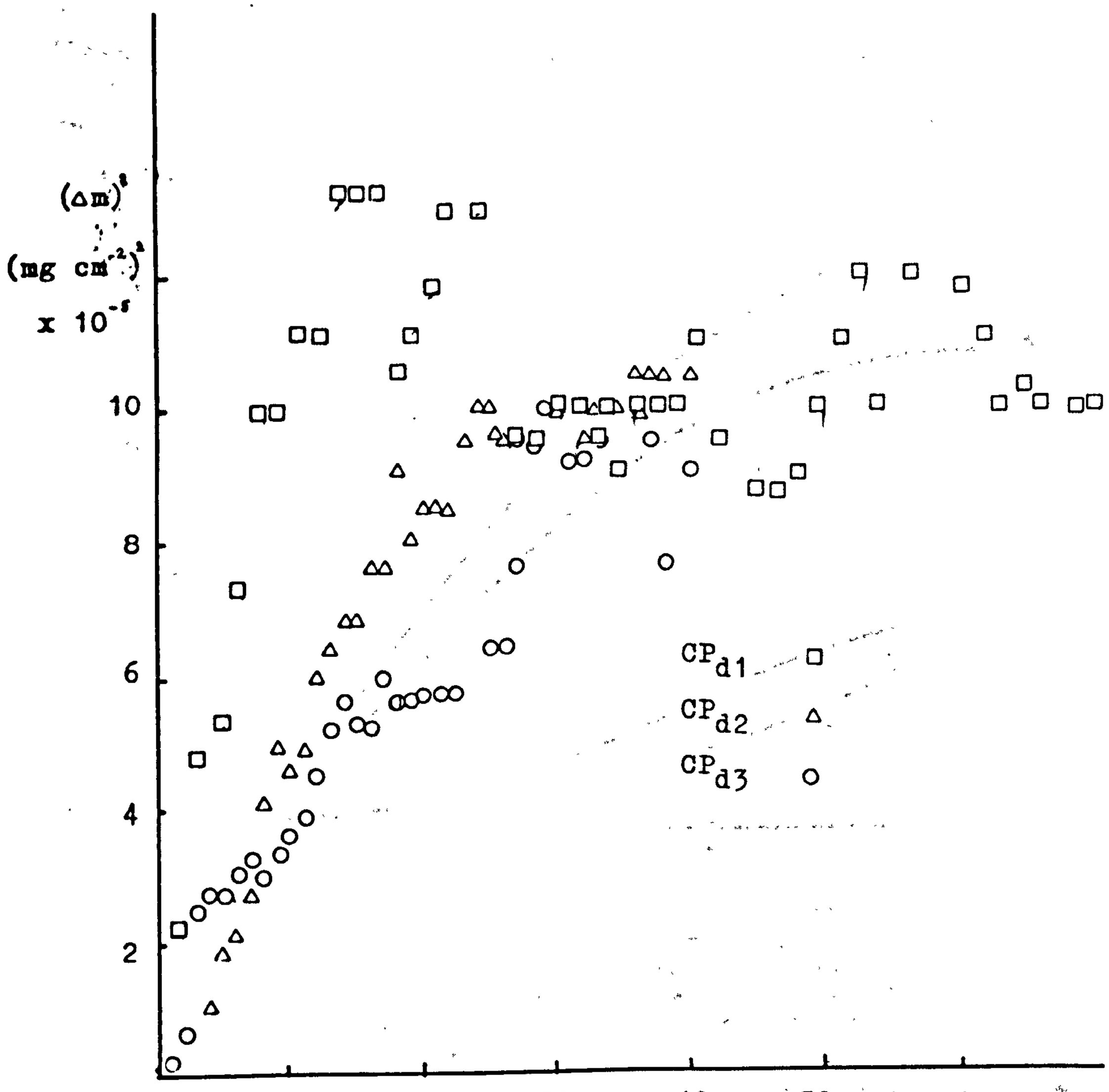

Fig 77c Fig 77a replotted on a parabolic scale . The kinetics conform to the parabolic law during t < 15 mins

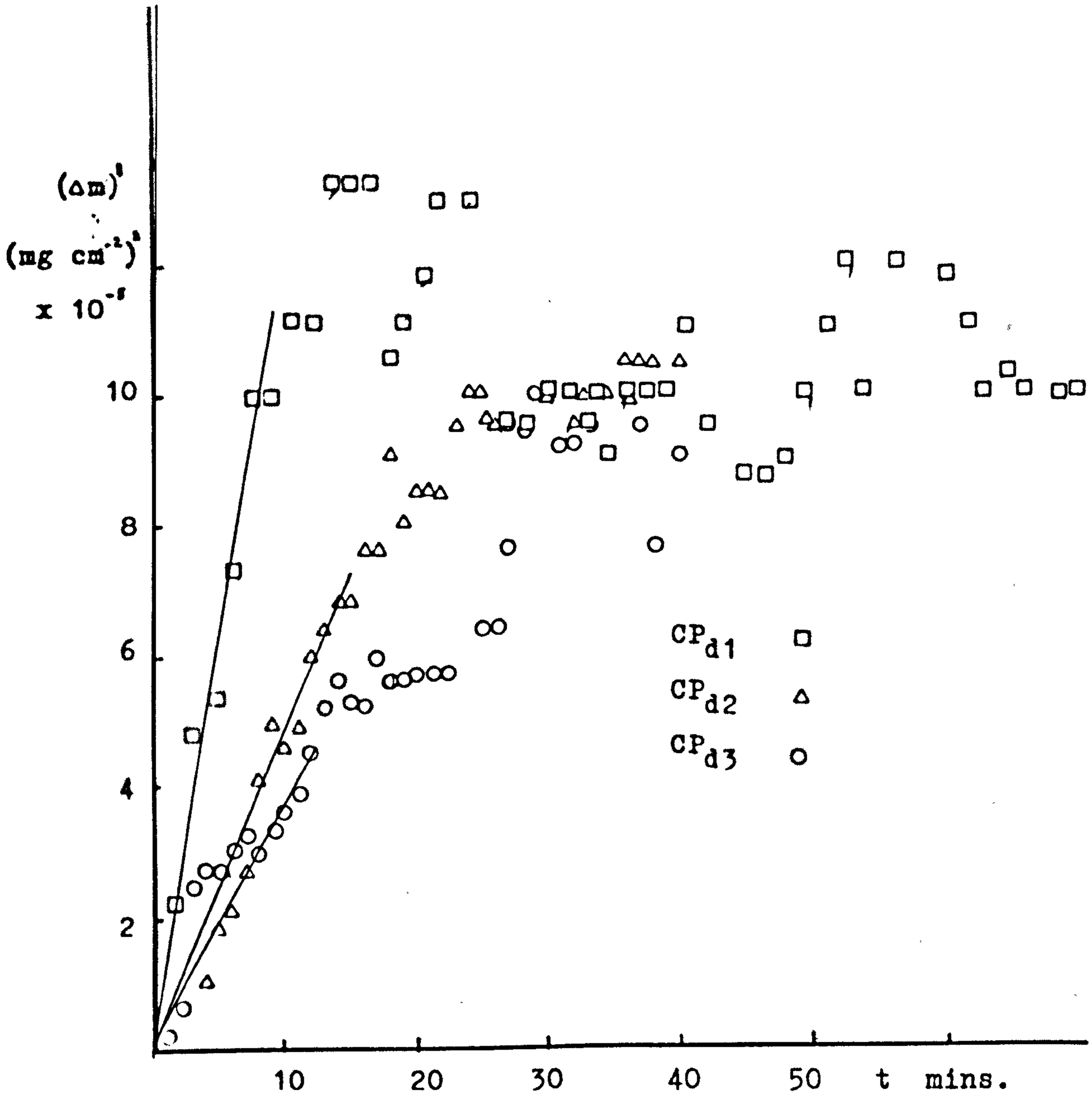

Fig 77c Fig 77a replotted on a parabolic scale . The kinetics conform to the parabolic law during t < 15 mins

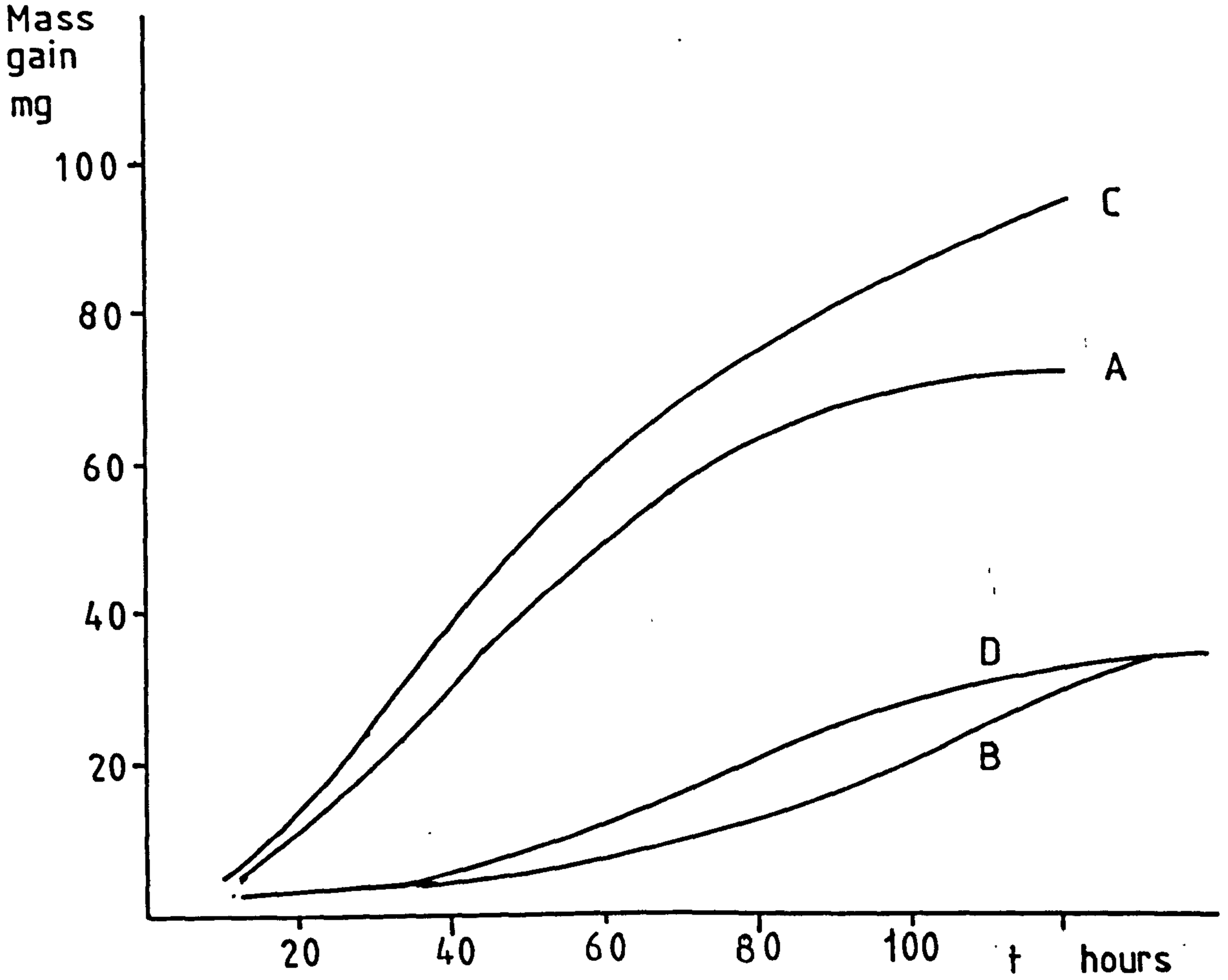

Fig 78 Oxidation kinetics at 800 C of samples obtained from pure aluminium ingots.
The variations in the kinetics of samples obtained from different ingots of the same nominal composition demonstrates the influence of impurities.
(oxidising surface area = 8.5 cm^2) Thiele"

INGOT	COMPOSITION				
	Al%	Fe%	Si%	Cu%	Na%
A	99.99	0.002	0.003	0.001	0.0008
B	"	"	0.004	"	0.0005
C	99.9	0.025	0.054	"	0.0013
D	"	0.030	0.031	"	< 0.0005

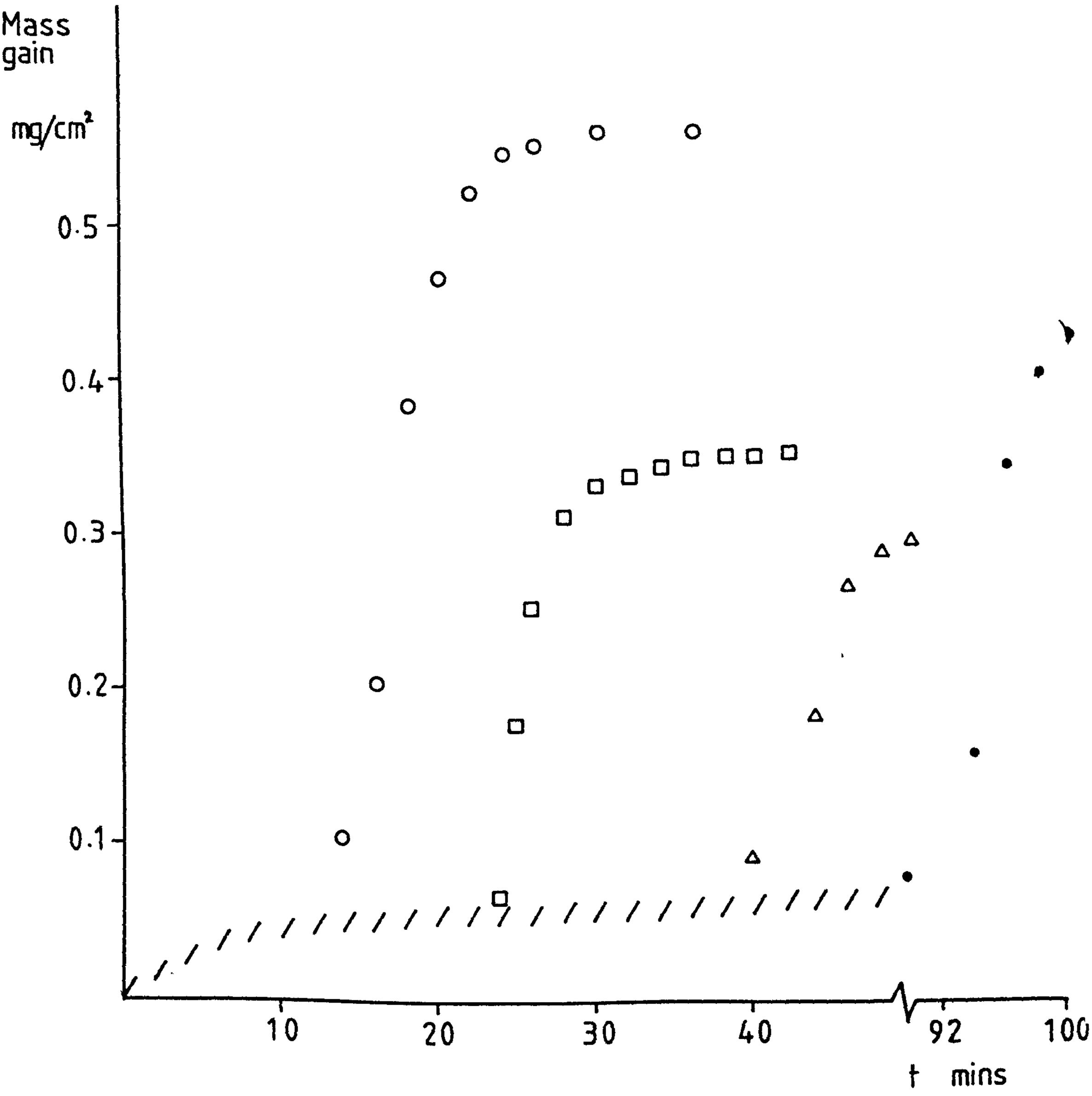
Mass gain
mg/cm²
0.5
0.4
0.3
0.2
0.1
10
20
30
40
92
100
t mins

Fig 79 Oxidation kinetics at 730 °C of samples obtained from normal high purity aluminium (Billet A) under two-stage test conditions.

///// Oxidation in dry atms

Moist oxygen (P_{H_2O} = 0.03 atms) introduced after

10 mins ○

20 mins □

40 mins △

90 mins ●

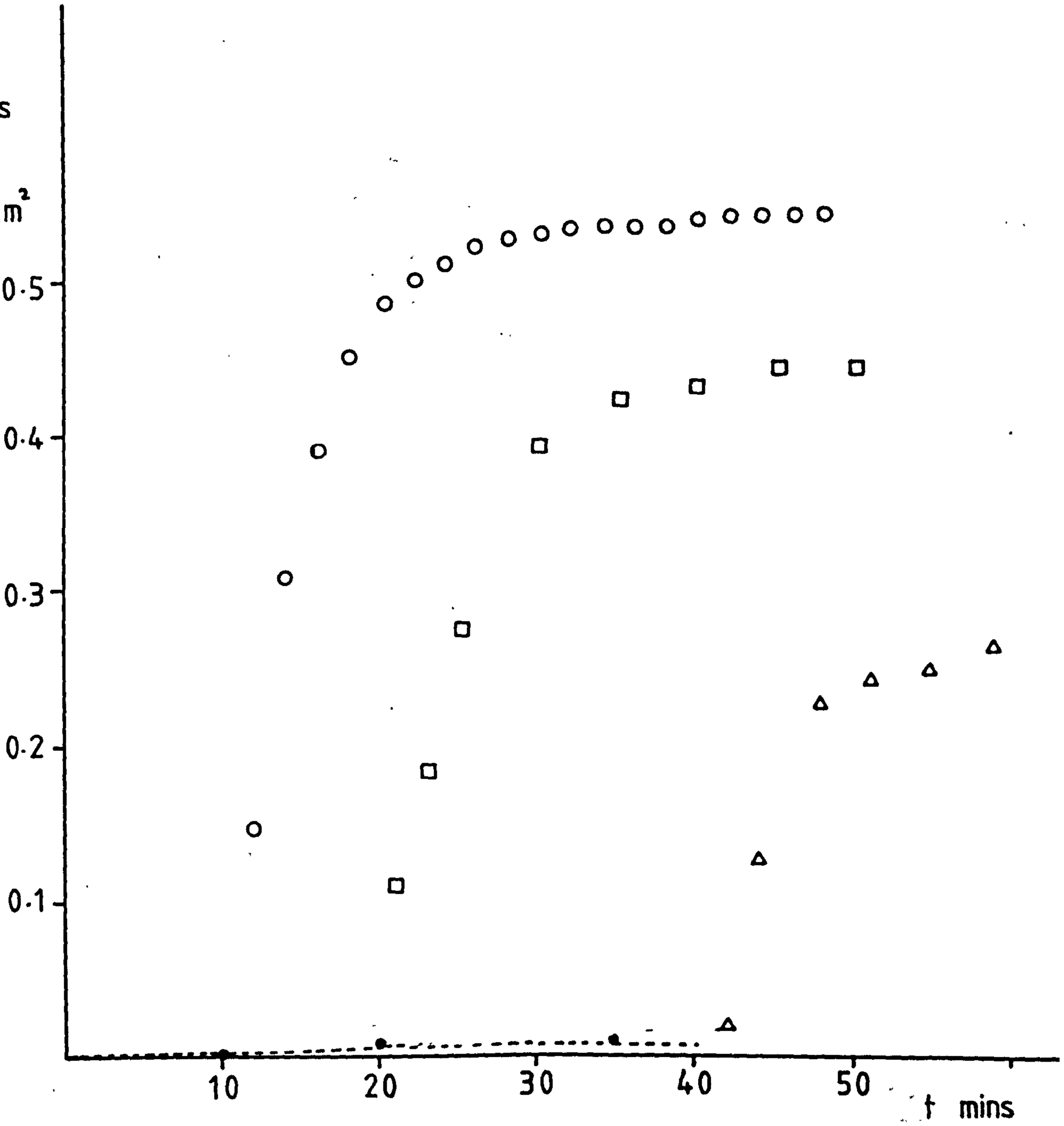

Fig 80. Oxidation kinetics at 730 °C of samples obtained from CP Al under two-stage test conditions

------- Oxidation in dry oxygen

Moist oxygen (P_{H_2O} = 0·03 atms) introduced after

10 mins ○

20 mins □

40 mins △

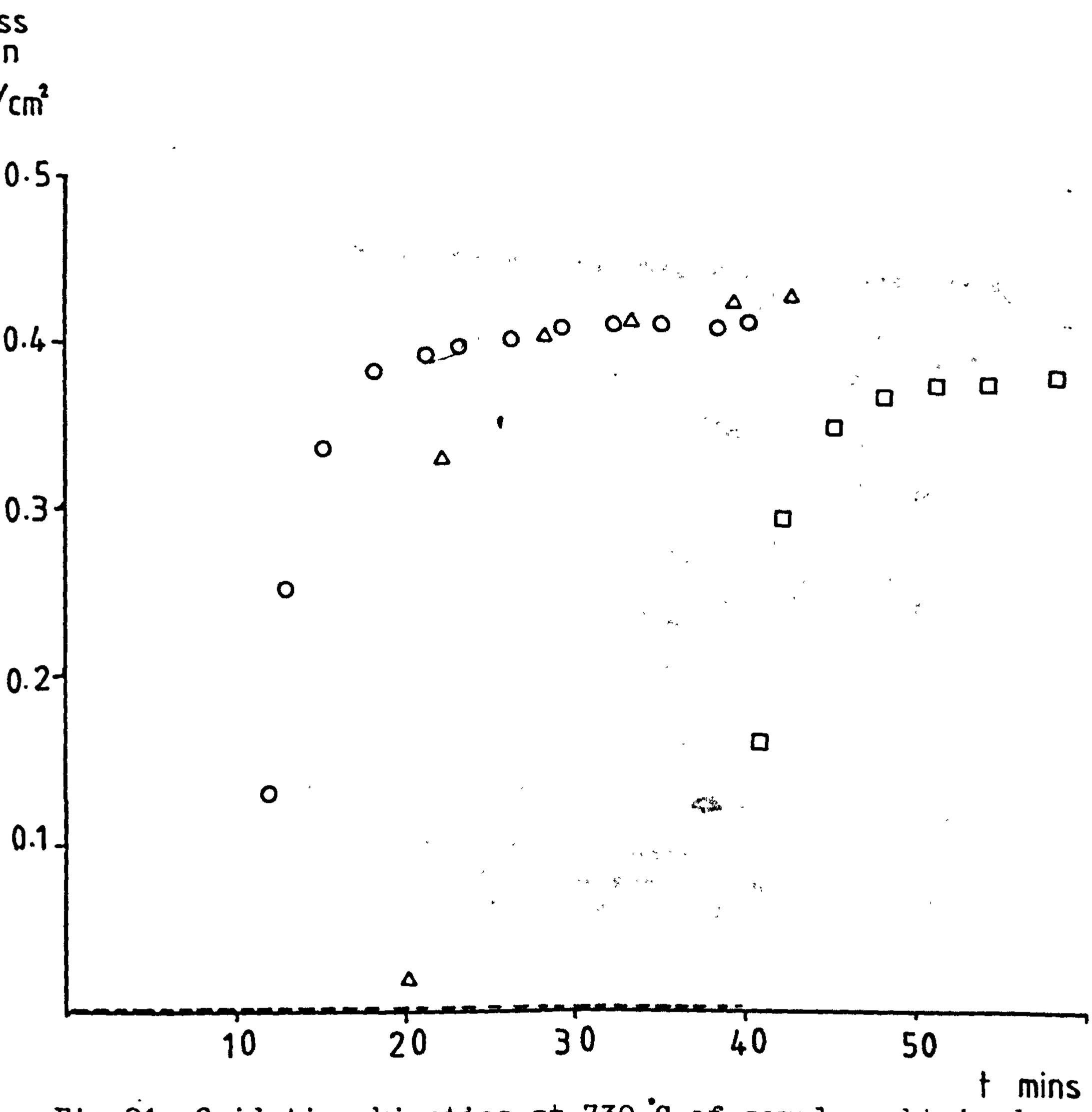

Fig 81 Oxidation kinetics at 730 °C of samples obtained from CP Al under two-stage test conditions

------ Oxidation in dry oxygen

Moist oxygen (P_{H_2O} = 0.012 atms) introduced after

10 mins ○

20 mins △

40 mins □

Fig.82. SEM showing the oxide/atmosphere interface of a sample which has been tested in a 'two-stage' experiment.

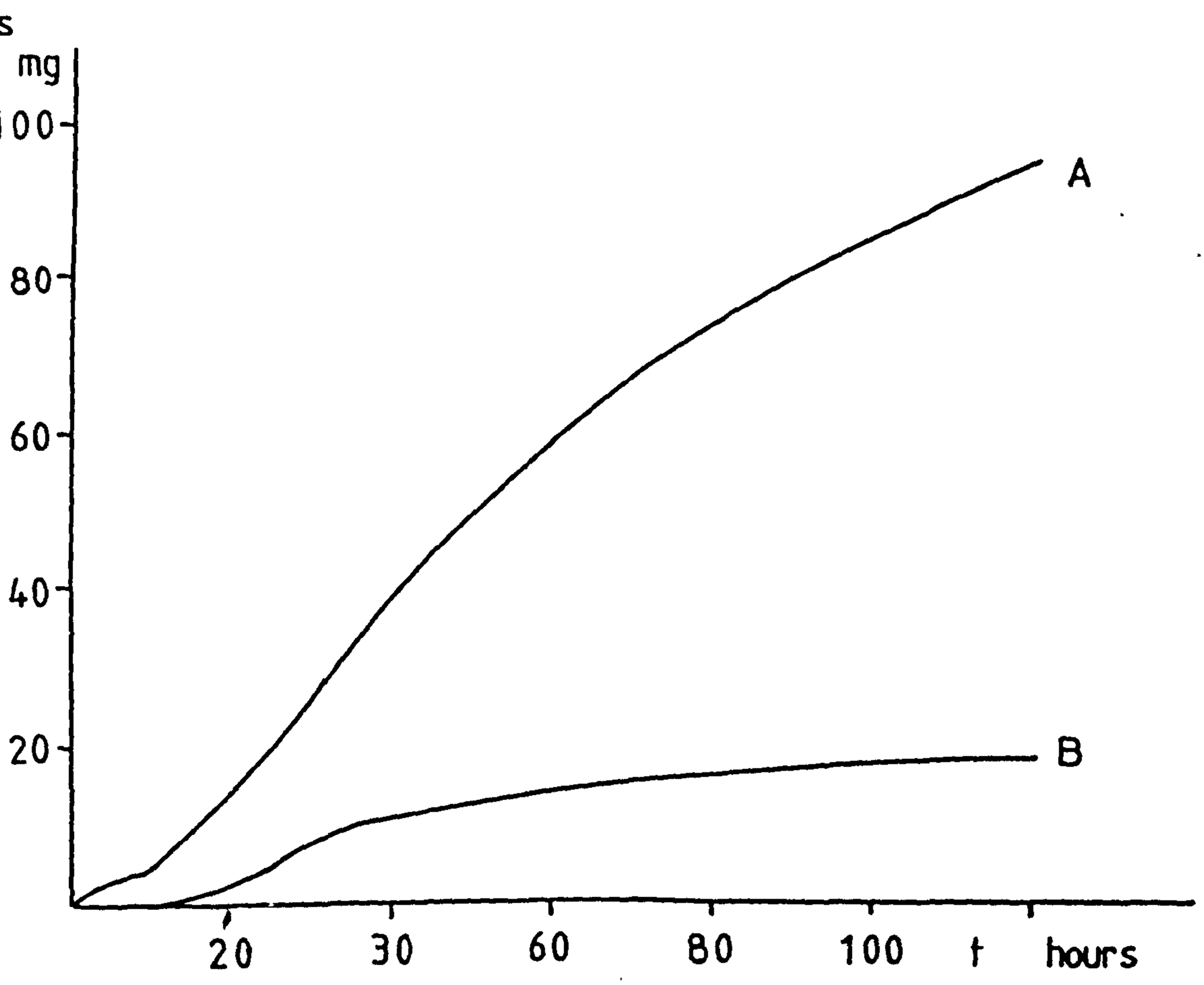

Fig 83 Oxidation kinetics at 800 C of samples obtained from pure aluminium (99.9% Al)
(oxidising surface area = 8.5 cm²)

A Dry atms

B Moist atms

Thiele"